Thèse n° 8777

Personalizable computational models of electrical spinal cord stimulation to restore function after neurological disorders

Présentée le 29 septembre 2021

Faculté des sciences de la vie
Unité du Prof. Courtine
Programme doctoral en génie électrique

pour l'obtention du grade de Docteur ès Sciences

par

Andreas ROWALD

Acceptée sur proposition du jury

Prof. D. Ghezzi, président du jury
Prof. G. Courtine, Dr M. Capogrosso, directeurs de thèse
Prof. S. Lempka, rapporteur
Prof. C. Moritz, rapporteur
Prof. S. Raspopovic, rapporteur

École
polytechnique
fédérale
de Lausanne

2021

Ἣ τὰν ἣ ἐπὶ τᾶς
— My mother

To my parents and sister…

Acknowledgements

I would like to express my gratitude to Prof. Grégoire Courtine for giving me the opportunity to conduct my PhD thesis in his lab. I have gained much from his supervision. Most importantly I have learnt about the value of beauty in envisioning the potential future an enlightened consciousness may inhabit.

I would like to thank Prof. Marco Capogrosso for his supervision during these years. He taught me much about research and leadership. Most importantly I learnt from him to stand up straight with my shoulders back.

I also want to show my appreciation to Dr. Fabien Wagner and Dr. Esra Neufeld, for being great teachers and whose kind nature and thoughtfulness pushed me through the most challenging times.

To my colleagues and friends that have shared my path these past few years: Thank you for all the wonderful moments we spent together; thank you for your support when times were tough and thank you for growing with me. Among many people I want to thank for many things I especially want to thank Salif Komi for always being by my side, Robin Demesmaeker for making the impossible possible, Edeny Baaklini for her openness, Andrea Galvez for sharing my sense of humor, Nathan Greiner for making me question everything, Beatrice Barra for letting me witness growth, Simon Borgognon for his kind nature, Marion Badi for struggling with me, Sara Conti for all the high jinks, Ismael Seáñez for his joyful nature, Kay Bartholdi for fighting together, Newton Cho for showing me what true strength is, Antonino Cassarà, Bryn lloyd, Hazael Montanaro, Fabio Becce and Stefano Mandija for their support in all technical questions I might have had, Edoardo Paoles for his professionalism, Sergio Hernandez, Gregory Dumont and Idriss Bachali for teaching me how to teach, Karen Minassian for sharing his encyclopedic knowledge and Emanuele Formento for being a great teacher.

Last but not least, I would like to thank my parents and my sister for their unconditional support and love.

Lausanne, 12 Mars 2021 A. R.

Abstract

Spinal Cord Injury (SCI) disrupts the communication between the brain and spinal circuits below the lesion, leading to a plethora of neurological impairments, including the loss of motor function. At present, the only medical practices to enhance recovery after paralysis are activity-based therapies. In severe cases, SCI-patients fail to produce active movements voluntarily and are therefore unable to fully benefit from these therapies. Epidural Electrical Stimulation (EES) applied over the lumbosacral spinal cord has demonstrated to enable locomotion in preclinical animal models and humans with SCI. EES may therefore play a pivotal role in the recovery of locomotion after SCI.

However, neither has EES reached the same level of efficacy in humans as in preclinical animal models, nor is there consensus on the definition of clinically meaningful stimulation protocols. In the absence of clear understanding on how EES promotes the formation of motor patterns, stimulation protocols have been largely based on empirical observations. Instead, hypothesis-driven definition of stimulation parameters has demonstrated superior efficacy in other neuromodulation therapies, such as deep brain stimulation.

In this thesis, I outline a computational approach to inform EES strategies for the recovery of neurological function after SCI. For this purpose, I leveraged a combination of finite element methods, neurophysical and neuromusculoskeletal models to refine our understanding on how EES promotes locomotion after SCI, inform the design of neuromodulation technologies and develop personalized EES treatments in humans with SCI.

In the first part of this thesis, I provide evidence that EES recruits proprioceptive and cutaneous afferents in the dorsal roots. I suggest that the recruitment of proprioceptive feedback circuits promotes the formation of motor patterns. In contrary, the continuous recruitment of cutaneous afferents may disrupt the production of locomotion. In the next chapter, I study interspecies difference of EES. I argue that these differences necessitate the adaption of stimulation protocols to enable translation of EES as a therapy from preclinical models to humans. I propose the application of spatiotemporal protocols with low-amplitude, high-frequency bursts to improve the efficacy of EES in humans. In the following chapter, I describe a technological framework that enables the implementation of such stimulation paradigms in people with SCI. I outline how personalized computational modeling can be used for treatment planning. I then summarize how I advanced this rudimentary computational tool into a computational framework for the rapid elaboration of highly realistic personalizable computational models. I explain how I leveraged this framework to inform the arrangements of electrodes on a paddle lead to enable locomotion in large and diversified patient-cohorts, perform preoperative treatment planning and validate the efficacy of both the lead and treatment planning protocol in individuals with severe, chronic SCI. Finally, I summarize how I translated my computational framework for other use-cases including the control of hemodynamics and the evaluation of an optoelectronic system to enable locomotion in preclinical models.

Key words: Spinal cord inury, epidural electrical stimulation, neuroprosthetics, locomotion, rehabilitation, computational neuroscience, finite element method, volume conductor models, neurophysical models, spinal sensorimotor circuits, spiking neural networks, neuromusculoskeletal modeling

Zusammenfassung

Rückenmarkverletzungen unterbrechen die Kommunikation zwischen dem Gehirn und den neuronalen Schaltkreisen unterhalb der Läsion, was zu einer Vielzahl von neurologischen Beeinträchtigungen, einschließlich des Verlusts motorischer Funktionen, führt. Derzeit sind die einzigen medizinischen Behandlungsmethoden, die die Genesung nach einer Lähmung fördern, aktivitätsbasierte Therapien. In schweren Fällen können querschnittsgelähmte Patienten keine aktiven Bewegungen ausführen und können daher nur bedingt von diesen Therapien profitieren. Epidurale Elektrische Stimulation (EES), die über das lumbosakrale Rückenmark angewendet wird, ermöglicht die Fortbewegung in präklinischen Tiermodellen und bei gelähmten Menschen. EES könnte daher eine zentrale Rolle bei der Wiederherstellung des Bewegungsapparats nach einer Querschnittslähmung spielen.

Die Anwendung von EES am Menschen ist, ungleich bei Tiermodellen, nur eingeschränkt effektiv. Darüberhinaus besteht kein Konsens über die Definition wirksamer Stimulationsprotokolle. In Ermangelung eines klaren Verständnisses darüber wie EES die Bildung motorischer Muster fördert, basierten Stimulationsprotokolle weitgehend auf empirischen Beobachtungen. Im Gegensatz dazu, haben hypothesengesteuerte Definitionen von Stimulationsparametern eine überlegene Wirksamkeit bei anderen Neuromodulationstherapien, wie der tiefen Hirnstimulation, gezeigt.

In dieser Dissertation skizziere ich einen computergestützten Ansatz, um EES-Strategien zur Wiederherstellung neurologischer Funktionen nach Verletzungen des Rückenmarks zu entwickeln. Zu diesem Zweck habe ich eine Kombination aus Finite-Elemente-Methoden, neurophysikalischen und neuromuskuloskelettalen Modellen genutzt, um mechanistische Erkentnisse über die Wiederherstellung des Bewegungsapparats mit EES zu gewinnen, Neuromodulationstechnologien zu entwickeln und personalisierte EES-Strategien für gelähmte Patienten zu entwerfen.

Im ersten Teil dieser These zeige ich, dass EES propriozeptive und kutane Afferenzen in den dorsalen Rückenwurzeln rekrutiert. Ich demonstriere, dass die Rekrutierung propriozeptiver Schaltkreise die Bildung motorischer Muster fördert. Ich suggeriere, dass die kontinuierliche Rekrutierung von kutanen Afferenzen die Fortbewegungsproduktion behindert. Im zweiten Teil, untersuche ich Differenzen in den Mechanismen von EES zwischen Spezien. Ich nutze dieses Verständnis um effiziente Stimulationsmuster, basierend auf der Anwendung von raumzeitlichen Protokollen mit hochfrequenten Bursts niedriger Amplitude, zu entwickeln. Im folgenden Kapitel beschreibe ich eine klinisch relevante Behandlungsweise von Bewegungseinschränkungen. Ich skizziere, wie personalisierte Computermodellierung für die Behandlungsplanung verwendet werden kann. Anschließend fasse ich zusammen, wie ich dieses rudimentäre Berechnungswerkzeug zu einer Technologie für die schnelle Ausarbeitung hochrealistischer, personalisierbarer Computermodelle weiterentwickelt habe. Ich erkläre, wie ich dieses Computermodelle für die Entwicklung von einem Rückenmarksimplantat, der präoperativen Behandlungsplanung und deren Validierung genutzt habe. Abschließend fasse ich zusammen, wie ich diese technologischen Entwicklungen auf andere Anwendungsfälle übertragen habe. Dies umschließt die Kontrolle von Blutdruck in querschnittsgelähmten Patienten und der Evaluierung eines optoelektronischen Systems.

Stichwörter: Rückenmarkverletzung, epidurale elektrische Stimulation, Neuroprothetik, Fortbewegung, Rehabilitation, theoretische Neurowissenschaft, Finite-Elemente-Methode, Volumenleitermodelle, neurophysikalische Modelle, spinale sensomotorische Schaltkreise, neuronale Netzwerke, neuromuskuloskeletale Modellierung

Contents

Acknowledgements **i**

Abstract **iii**

Zusammenfassung **v**

List of figures **xiii**

List of tables **lv**

1 Introduction **1**
1.1 Anatomy of the spine 4
1.1.1 The nervous system in a nutshell 4
1.1.2 Anatomical planes 6
1.1.3 The vertebral column 7
1.1.4 Organization of the vertebral canal 9
1.1.5 Variability of anatomical dimensions in the human spinal cord 10
1.2 Neural control of locomotion 11
1.2.1 Somatosensory system 12
1.2.2 Spinal locomotor network 17
1.2.3 Supraspinal control 19
1.3 Restoring locomotion after spinal cord injury 21
1.3.1 Activity-based therapies 22
1.3.2 Technological advancements to support activity-based therapies 23
1.3.3 Epidural electrical stimulation of the lumbosacral spinal cord 25
1.4 Computational modeling of epidural electrical stimulation in the spinal cord . 26
1.4.1 Finite element method for epidural electrical stimulation 27
1.4.2 Biophysical models of nervous structures 30
1.4.3 Neuromusculoskeletal modeling 33
1.5 Thesis outline 34

2 EES recruits proprioceptive and cutaneous afferents with vastly different consequences on the formation of motor patterns **39**
2.1 Abstract 41
2.2 Introduction 42

2.3 Results 43
2.3.1 EES recruits large-diameter afferent fibers in the entry zone 43
2.3.2 EES activates proprioceptive neurons 45
2.3.3 EES recruits proprioceptive feedback circuits to form motor patterns . . 47
2.3.4 Detrimental activation of Aβ-LTMR feedback circuits 49
2.3.5 Noradrenergic innervation of proprioceptive and Aβ-LTMR feedback circuits 52
2.3.6 Targeted pharmacotherapies potentiating the therapeutic efficacy of EES 58
2.3.7 Circuit-level mechanisms underlying the potentiation of EES 60
2.3.8 Voluntary control of walking in a preclinical model of severe SCI 65
2.4 Discussion 68
2.4.1 Proprioceptive gateways to spinal motor systems 68
2.4.2 Role of Aβ-LTMR feedback circuits 70
2.4.3 Implications for clinical applications 71
2.5 Materials and methods 72
2.5.1 Experimental model and subject details 72
2.5.2 Surgical procedures and post-surgical care 72
2.5.3 Ex-vivo calcium imaging in mouse DRGs 73
2.5.4 Behavioral testing and neurorehabilitation procedures 73
2.5.5 Electrophysiological experiments 75
2.5.6 Chemogenetics 76
2.5.7 Genetic labelling of low-threshold mechanoreceptor neurons 76
2.5.8 Virus production 76
2.5.9 Virus and tracer delivery procedures 77
2.5.10 Perfusion protocol 77
2.5.11 Immunohistochemistry 78
2.5.12 Fluorescent in-situ hybridization 78
2.5.13 Neuromorphological evaluations 79
2.5.14 Single-cell sequencing data processing 79
2.5.15 Dissection of mouse spinal cord with attached DRGs 80
2.5.16 Tissue clearing and 3D image acquisition 80
2.5.17 Hybrid computational model 81
2.5.18 Statistical procedures 84

3 Inter-species differences necessitate the adaption of EES-protocols to improve activity-based therapies in a clinical setting 85
3.1 Abstract 87
3.2 Introduction 87
3.3 Results 89
3.3.1 The probability of antidromic collisions during EES is higher in humans compared to rats 89

3.3.2 Computational models of proprioceptive feedback circuits during locomotion . . . 96
3.3.3 The range of EES parameters facilitating locomotion is limited in humans compared to rats . . . 101
3.3.4 Spatiotemporal EES protocols may remedy the limitations of continuous EES . . . 105
3.3.5 High frequency, low amplitude EES alleviates the disruptive effects of continuous EES . . . 106
3.4 Discussion . . . 110
3.4.1 EES erases proprioceptive information in humans, but not in rats . . . 110
3.4.2 Proprioceptive information must be preserved to enable locomotion with EES . . . 111
3.4.3 EES strategies that replace or preserve proprioceptive information . . . 112
3.5 Materials and Methods . . . 114
3.5.1 Computer simulations . . . 114
3.5.2 Experimental procedures in humans . . . 119
3.5.3 Experimental procedures in rats . . . 123
3.5.4 Statistics . . . 124

4 A technological framework to restore walking in paralyzed individuals with epidural electrical stimulation 125

4.1 Abstract . . . 127
4.2 Introduction . . . 127
4.3 Results . . . 128
4.3.1 Targeted neurotechnologies to deliver spatiotemporal stimulation during walking . . . 128
4.3.2 Targeted surgical implantation of individuals with a chronic cervical SCI 129
4.3.3 Targeting spatially selective regions of the spinal cord . . . 129
4.3.4 Targeted electrical stimulation enables control over the movement of single joints . . . 137
4.3.5 EES modulates cortical processes involved in producing movement . . . 137
4.3.6 Spatiotemporal stimulation restores the sequence of motoneuron activation for walking . . . 139
4.3.7 Voluntary control of adaptive and sustained locomotor movements overground . . . 147
4.3.8 Continuous stimulation failed to facilitate locomotor movements . . . 148
4.3.9 Rehabilitation improves walking capabilities with stimulation . . . 148
4.3.10 Rehabilitation promotes neurological recovery and restores walking without stimulation . . . 150
4.3.11 Targeted neurotechnologies supporting motor activities at home and in the community . . . 154
4.4 Discussion . . . 156

4.5 Materials and methods . . . 158
4.5.1 Clinical study and participants . . . 158
4.5.2 Surgical implantation . . . 159
4.5.3 Personalized computational model . . . 160
4.5.4 Evaluation of single-joint torque production . . . 163
4.5.5 Technological framework . . . 164
4.5.6 Configuration of targeted EES . . . 165
4.5.7 Clinical evaluations . . . 166
4.5.8 Study extension and technologies for use in the community . . . 167
4.5.9 Data processing . . . 168

5 Enabling immediate recovery of trunk and leg motor functions after complete paralysis with dedicated epidural electrical stimulation paradigms 173
5.1 Abstract . . . 175
5.2 Introduction . . . 175
5.3 Results . . . 176
5.3.1 Variability of spinal cord topological organisation . . . 176
5.3.2 Atlas of computational spinal cord models . . . 178
5.3.3 Optimized electrode arrangement . . . 180
5.3.4 Precise preoperative planning . . . 182
5.3.5 Intraoperative validation of model predictions . . . 190
5.3.6 Superior selectivity of the new electrode arrangement . . . 192
5.3.7 Configuration and real-time control of stimulation . . . 192
5.3.8 Immediate recovery of walking after complete paralysis . . . 194
5.3.9 Extension to other motor activities . . . 197
5.3.10 Recovery of independence in ecological settings . . . 198
5.4 Discussion . . . 200
5.5 Materials and Methods . . . 213
5.5.1 Study design and objectives . . . 213
5.5.2 Study participants . . . 214
5.5.3 Cadaver analysis . . . 214
5.5.4 Healthy volunteer MRI Data . . . 215
5.5.5 Structural MRI of the Thoracolumbar Spine . . . 216
5.5.6 Spinal cord fMRI . . . 217
5.5.7 Personalized hybrid computational models . . . 219
5.5.8 Atlas of computational spinal cord models . . . 227
5.5.9 Neurosurgical intervention . . . 227
5.5.10 Configuration of activity-specific stimulation programs . . . 228
5.5.11 Clinical evaluations . . . 229
5.5.12 Technological framework . . . 229
5.5.13 Data processing . . . 231
5.5.14 Statistics . . . 233

6 Application of personalizable computational models for the restoration of other neurological functions and development of novel neuromodulation paradigms 235
6.1 Hemodynamics can be controlled with EES in preclinical animal models and humans after SCI . . . 238
6.1.1 EES engages sympathetic circuitry in low thoracic segments to control hemodynamics . . . 238
6.1.2 Enabling clinical implementation with personalized computational models of the low thoracic spinal cord . . . 240
6.1.3 Outlook on personalized computational modeling for hemodynamic control with EES . . . 240
6.1.4 Computational modeling methods for hemodynamic control . . . 243
6.2 Evaluation of safety and efficacy of a novel optoelectronic system to manipulate neural substrates in the spinal cord of mice . . . 244
6.2.1 A computational model of the mouse lumbar spine to provide estimates of suitable dimensions for spinal implants . . . 244
6.2.2 A computational model of light penetration in the spinal cord of mice . 245
6.2.3 A computational model of heat diffusion with photostimulation protocols in mice . . . 247
6.2.4 Limitations and outlook of light propagation and heat diffusion simulations in the mouse spinal cord . . . 247
6.2.5 Computational modeling methods for safety and efficacy evaluations of optoelectronic devices in the spinal cord . . . 248
6.3 Guiding implant design for translational research . . . 249

7 Conclusions and perspectives 251
7.1 Summary of the main findings . . . 253
7.2 Perspectives . . . 254
7.2.1 Towards personalized treatment planning of neuromodulation therapies 255
7.2.2 Leveraging in-silico assessments for the design of neuromodulation technologies . . . 256
7.2.3 Optimizing EES-based rehabilitation strategies with in-silico investigations of neural adaptation mechanisms . . . 257
7.3 General conclusion . . . 258

Bibliography 293

Curriculum Vitae 295

List of Figures

1.1 Rostrocaudal organization of the spinal cord with a brief overview of functionalities associated with spinal nerves. Adapted with permission of World Health Organization, from World Health Organization and International Spinal Cord Society, 2013. 2

1.2 Various types of neurons. Republished with permission of McGraw-Hill, from Kandel, 2013; permission conveyed through Copyright Clearance Center, Inc.. . 5

1.3 Sketch of the rostrocaudal and dorsoventral axis (a), dorsoventral and mediolateral axis (b) and the antomical planes (c). Republished with permission of McGraw-Hill, from Kandel, 2013; permission conveyed through Copyright Clearance Center, Inc.. 6

1.4 Sketch of the vertebral column (left) and the anatomical organization of vertebrae in the cervical, thoracic and lumbar spine of humans (right). License-free picture from Ellen Bronstayn; Taken from: shutterstock.com. 8

1.5 A. 3D sketch of soft spinal tissues and anatomy of rootlets. B. Superior view of a sketch of a transverse cut of the spinal cord. C. Superior view of a sketch of a transverse cut of the white and gray matter. 9

1.6 The organization of cutaneous mechanoreceptors in the skin. Republished with permission of Elsevier, from Abraira and Ginty, 2013; permission conveyed through Copyright Clearance Center, Inc.. 15

1.7 Sketch of intrafusal muscle fibers (left), type Ia and II afferents (middle) and Ib afferents (right). Adapted with permission of McGraw-Hill, from Kandel, 2013; permission conveyed through Copyright Clearance Center, Inc.. 16

1.8 Sketch of the fundamental framework underlying locomotor control. CPGs generate the rhythm underlying locomotion. Spinal sensorimotor circuits process signals from proprioceptive and cutaneous sensory organs to adapt motor patterns to the environment. Supraspinal centers regulate the speed, onset and balance. Republished with permission of Annual Reviews, Inc., from Rossignol and Frigon, 2011; permission conveyed through Copyright Clearance Center, Inc.. 18

1.9 General overview of the supraspinal control of locomotion. 1.) Selection and initiation of locomotion involves multiple regions in the brain and brainstem. Firstly, the Basal Ganglia (BG) projects to the Motor Cortex (MCtx) via the Thalamus (Tha). The BG also projects to the Mesencephalic Locomotor Region (MLR), which includes the CuNeiform nucleus (CNf) and the PedunculoPontine Nucleus (PPN). The MLR projects through the Reticular Formation (RF) in the hindbrain to locomotor networks in the spinal cord to execute locomotion. 2.) Regulation of ongoing locomotion and posture maintenance is mediated by the vestibular and rubrospinal spinal pathways from the BrainStem Nuclei (BSN). The BSN receives input from the cerebellum which coordinates locomotion. For this purpose the cerebellum receives sensory feedback information from the spinal cord. 3.) Correction of locomotion due to visual stimulation originates in the Visuomotor Cortex (VCtx) and is mediated by the posterior Parietal Cortex (pPCtx) to the MCtx. Republished with permission of Springer Nature, from Kiehn, 2016; permission conveyed through Copyright Clearance Center, Inc.. . 20

1.10 Neuromodulation approaches for restoring function after spinal cord injury. Republished with permission of Elsevier, from James et al., 2018; permission conveyed through Copyright Clearance Center, Inc.. 25

1.11 An example of a highly refined patient-specific FEM. a. Preoperative Magnetic Resonance Imaging (MRI) scans were used to define the anatomy of an individual. Postoperative CT scans enabled the localisation of electrodes within this volume. b. This anatomy was translated into FEM objects and a bipolar simulus was approximated within this volume. Republished with permission of John Wiley and Sons, from Lempka et al., 2020; permission conveyed through Copyright Clearance Center, Inc.. 29

1.12 Multi-compartment double cable model of a mammalian, myelinated MA. Republished with permission of The American Physiological Society, from McIntyre et al., 2002; permission conveyed through Copyright Clearance Center, Inc.. . . 31

1.13 Overall structure of the motor and sensory axon model. Republished with permission of Springer Nature, from Gaines et al., 2018; permission conveyed through Copyright Clearance Center, Inc.. 32

2.1 Summary of the main findings in graphical form. EES promotes the formation of motor patterns by recruiting proprioceptive (Aα/Aβ) afferents. Inversly, the continuous recruitment of cutaneous low-threshold mechanoreceptor (Aβ-LTMR) afferents disrupts locomotion. 41

2.2 EES recruits proprioceptive neurons in the DRG. (A) High-resolution MRI-based reconstruction of the different tissues surrounding the spinal cord. Color-coded isopotentials showing the spread of the electric field following a single pulse of EES applied over the dorsal aspect of the spinal cord. (B) Electrical potential and generated currents following a single pulse of EES. (C) EES elicits action potentials along the activated fibers that propagate orthodromically towards the spinal cord and antidromically towards the periphery. The curves show the predicted propagation of excitation along a large-diameter, myelinated afferent fiber. (D) Recruitment thresholds for the activation of each class of sensory afferent fibers , Dorsal Column (DC) and Motor Axon (MA) when delivering EES at increasing stimulation intensity. (E) Cleared lumbosacral spinal cord with attached DRGs of a PVCre:R26LSL-tdTomato mouse. Insets highlight the curvilinear trajectory of proprioceptive afferent fibers and proprioceptive neurons in DRGs. Scale bars, 2mm (overview), 500µm (a), 200µm (b), 50µm for the inset and 200µm (c), respectively. (F) Timeline of calcium imaging experiments, conducted in PVCre:R26LSL-tdTomato mice (n = 5 per condition) under three experimental conditions: no stimulation, EES at 1.2x motor threshold and EES at 3x motor threshold. (G) Representative images of intracellular calcium release in L2 DRG for each condition. Asterisks highlight released intracellular calcium in PVON and/or PVOFF neurons. Scale bar, 50µm. (H) Bar plots reporting calcium release in L2 DRGs for each condition. EES at 1.2x motor threshold led to an increase in calcium release confined to PVON neurons. In contrast, PVOFF neurons did not release significantly more intracellular calcium at this stimulation intensity. **P = 0.003. ns, not significant. Two-way ANOVA followed by Tukey's post-hoc test. 44

2.3 Computational models and calcium imaging of proprioceptive neurons (A) MRI image of a rat vertebral column. Scale bars 1mm for the overview and 2mm for the insets, respectively. (B) MRI-based reconstruction of the L2 vertebra and spinal cord. (C) Reconstruction of the vertebral canal including the spinal cord and dorsal roots based on a sequence of consecutive MRI images. (D) Computer model of a myelinated fiber including a node of Ranvier (a) and the single components of the afferent fiber (MYSA, FLUT, STIN). (E) Calcium imaging experiments conducted in PVCre:R26LSL-tdTomato mice to visualize the activation of proprioceptive neurons in the dorsal roots in response to EES. (F) Timeline of the calcium imaging experiments. (G) Representative images of intracellular calcium release in L2 DRGs for each experimental condition and at each time point during the experiment. Asterisks indicate the released intracellular calcium in PVON and/or PVOFF neurons. Scale bar 50µm 46

2.4 EES engages proprioceptive feedback circuits to facilitate walking after SCI. (A) Scheme summarizing chemogenetic inactivation or activation of PVON neurons in DRGs. (B) Photograph showing mCherry-infected PVON neurons in the L4 DRG after AAV2/5-flex-hm4Di injection into the sciatic nerve. Scale bar 10 µm. DRG reconstruction displaying the ratio of PVON/mCherryON double-labelled neurons. (C) Photograph showing mCherry-infected PVON neurons in the DRG after AAV2/5-flex-hm3Dq injection into the sciatic nerve, as in (B). (D) Scheme illustrating reflex recordings in ankle flexor muscles in response to EES at L4 spinal level. Muscle responses are shown before and after 55 minutes post-CNO. (E) Bar plot reporting the relative change in the amplitude of muscle responses following CNO injection for each condition. ***P < 0.001, Two-way ANOVA followed by Bonferroni's post-hoc test. **P < 0.01, Two-way ANOVA followed by Bonferroni's post-hoc test. (F) Rats with contusion SCI stepping bipedally on a treadmill while supported by a robotic body weight support system. Joint kinematics were projected onto a 3D model of the hindlimbs to generate representative sequences of hindlimb movements in conjunction with EMG activity of extensor and flexor muscles of the ankle. EMG insets show muscle responses to each pulse of EES, indicated by arrows. (G) Bar plot reporting average scores on PC1, which quantifies the relative locomotor performance of PVCre-hm4Di rats with complete SCI under each experimental condition (n = 4 per condition) compared to rats with no injury. ***P < 0.0001. Two-way ANOVA followed by Bonferroni's post-hoc test. (H) Same functional experiments as in (G) in PVCre-hm3Dq rats. *P < 0.05. Two-way ANOVA followed by Bonferroni's post-hoc test. 48

2.5 Quantification of lesion size and functional outcomes. (A) Representative coronal section through a contusion epicenter at T8 (GFAP, Glial Fibrillary Acidic Protein). Scale bar 200µm. The contours of the lesion cavity at the epicenter are shown for all the main experimental rats. Scale bar 500 µm. (B) Bar graph reporting the area of spared tissue at the lesion epicenter for wild-type (n=4), PVCre-hm4Di (n=4) and PVCre-hm3Dq (n=4) rats. ns, not significant; $^*P < 0.05$; Non-paired Student's t-test. (C) PC analysis applied on 129 gait parameters averaged for each rat and condition (small circle). Large circles show the average per group. Bar plot showing average scores on PC1, which quantifies locomotor performance of PVCre-hm4Di and wild-type rats compared to non-injured rats (n=10). (D) Bar plots reporting average values of classic gait parameters with high factor loading on PC1. $^{***}P < 0.001$. Two-way ANOVA followed by Bonferroni's post-hoc test. (E) PC analysis to quantify locomotor performance in PVCre-hm3Dq rats (n=4). Bar plots report average scores on PC1 and average values of single gait parameters in PVCre rats (n=4) and non-injured wild-type rats (n=4). The activation of proprioceptive feedback circuits following CNO improved locomotor outcomes. PC1 score: $^*P < 0.05$. One-way ANOVA followed by Bonferroni's post-hoc test. Gait parameters: $^{**}P < 0.01$, $^*P < 0.05$. Two-way ANOVA followed by Bonferroni's post-hoc test. 51

2.6 EES recruits LTMR neurons in the DRG (A) Cleared lumbosacral spinal cord with attached DRGs of a RetCreER : R26LSL-tdTomato mouse. Insets highlight the curvilinear trajectory of LTMR afferent fibers and neurons in the spinal cord and DRGs. Scale bars, 500µm (overview), 200µm, 200µm (coronal view) and 50µm for the insets, respectively. (B) Representative images of intracellular calcium release in L2 DRGs. Calcium imaging was conducted on RetCreER : R26LSL-tdTomato mice for two experimental conditions: no stimulation (n=5) and EES at 1.2x motor threshold (n=5). Asterisks highlight the released intracellular calcium in RetON neurons. Scale bar, 50µm. (C) Bar plot reporting calcium release in L2 DRGs for each experimental condition. EES at 1.2x motor threshold led to an increase in calcium release in RetON neurons. $^{***}P < 0.001$ (D) Bar plot reporting the relative percentage of PVON and RetON DRG neurons activated by EES. $^{**}P < 0.01$. Non-paired Student's t-test. (E) Neurobiomechanical model of the hindlimbs in rats, including group-Ia afferents innervating the gastrocnemius muscle, and Aβ-LTMR innervating the foot sole. (F) Plots showing the firing rates of group-Ia and Aβ-LTMR afferents over the course of an entire gait cycle without and with EES. Arrows highlight the increased firing rates elicited by EES. 53

2.7 Noradrenergic α2a and α2c receptors are located on circuits activated by EES. (A) Noradrenergic receptor families. (B) Images showing α2aON and α2cON neurons in the DRGs of transgenic mice counterstained with an α2a and α2c in-situ hybridization probe (n=3 mice per line). Asterisks indicate double-labelled cells. Scale bars 20μm. Bar plots report that GFP reporter for both receptors are largely co-expressed with the α2a and α2c mRNA signal for all the studied regions of the spinal cord and DRGs. (C) Overview showing the location of cells expressing α2a (magenta) or α2c (cyan) receptor subtypes in the spinal cord and DRGs. (D) Representative images of GFP, PKC-γ, CGRP and Ib4 labelled dorsal horns displaying the distinct laminar location of α2aON and α2cON neurons. Scale bar 50μm for the overview, 25μm for the insets. (E) Images showing the expression of α2a and α2c receptor subtypes in DRGs. Scale bar 100μm for the overview, 20μm for the insets. (F) Polar plots displaying the phenotype of neurons expressing α2a or α2c in the DRGs. The picture shows α2aGFP and PV co-localization in the DRG, as highlighted with asterisks. Scale bar 10μm. (G) Polar plots displaying the phenotype of neurons expressing α2a or α2c in the various lamina of the spinal cord. The picture shows α2c-GFP and PV co-localization in neurons of laminae III/IV, as highlighted with asterisks. Scale bar 10μm. (H) Images showing vGlut1ON synapses from LTMR afferents that establish close appositions with an alpha2cON interneuron located laminae III/IV. (I) Images showing alpha2c and cfos co-localization in neurons located in laminae III/IV after 30 min of EES, as highlighted. (H) Images showing vGlut1ON synapses from LTMR afferents that establish close appositions with an α2cON interneuron located laminae III/IV. (I) Images showing α2c and cfos co-localization in neurons located in laminae III/IV after 30 min of EES, as highlighted with asterisks. Scale bars 5μm. Bar plot reporting the percentage of α2cON neurons co-localizing with cfos after EES versus no EES. ***P < 0.0001. Non-paired Student's t-test. (J) Images showing co-localization of α2c and RORα in interneurons located in laminae III/IV. Scale bars 10μm. Bar plot reporting the percentage of RORαON interneurons expressing α2a or α2c. ***P < 0.001. Non-paired Student's t-test. (K) Single-cell RNA sequencing experiment confirming the co-expression of α2c and RORα in a specific population of excitatory neurons (Glut_Elavl4_Meis2) located in the dorsal horn of the spinal cord. (L) Key molecular markers defining neurons (Glut_Elavl4_Meis2) expressing α2c and RORα. 54

2.8 Verification of the α2a and α2c GFP signals. (A) α2aON neurons counterstained with an α2a in-situ hybridization probe in laminae I/II and DRGs. Asterisks indicate double-labelling. Scale bars 10µm. (B) α2aON neurons in the brain and brainstem. Neurons expressing α2a receptors reproduced the previously documented topologies observed in the olfactory bulbs (Ob), cortex, hippocampus (HPC), thalamus and cerebellum (Cb). Scale bars, 1mm (overview), 100µm and 20µm (inset) (a), 100µm (b) and 100µm. (c) for the insets, respectively. (C) α2cON neurons counterstained with an α2c in-situ hybridization probe in laminae III/IV and DRGs. Asterisks indicate double-labelling. Scale bars 10µm. (D) α2cON neurons in the brain and brainstem. Neurons expressing α2c receptors reproduced the previously documented topologies observed in striatum (Str), islands of Calleja (ICj), cerebellum (Cb) and brainstem (Bst). Scale bars, 1mm (overview), 100µm and 20µm (inset) (a), 100µm (b) and 20µm (c) for the insets, respectively. 56

2.9 Phenotype of α2aON and α2cON neurons in the spinal cord and DRGs. (A) Overview showing the location of cells expressing α2a (magenta) or α2c (cyan) receptor subtypes in spinal cord and DRGs. (B) Images showing labelling of α2cON neurons in laminae III/IV and various neurotransmitters, scale bars 10µm. Pie charts indicate the percentage of α2aON neurons for each neurotransmitter in the respective area. (C) Labelling of α2cON neurons and various markers for sensory afferents in DRGs. Scale bars 10µm (D) Images showing labelling of α2aON neurons in laminae I/II and various neurotransmitters. Pie charts indicate the percentage of α2aON neurons for each neurotransmitter in the respective area. Scale bars 10µm (E) Images showing labelling of α2aON neurons in lamina X and various neurotransmitters. Scale bars 10µm (F) Labelling of α2aON neurons and various markers for sensory afferents in DRGs. Scale bars 10µm. 57

2.10 Targeted modulation of α2aON and α2cON circuits augments EES efficacy. (A) Effects of Clonidine and EES on stepping in α2a-/- and α2c-/- knockout mice with complete SCI. (B) Snapshots showing plantar stepping in α2a KO mice while α2c KO mice display complete paralysis. (C) Bar plot reporting average scores on PC1 for α2a (n=5) and α2c KO mice (n=5) compared to uninjured mice (n=6). ***P < 0.0001. Two-way ANOVA followed by Tukey's post-hoc test. (D) Effects of dual α2a antagonist/ α2c agonist and EES on stepping in rats with complete SCI. Conventions as in Fig. 2.4F. (E) Plots reporting the mean values of peak-to-peak amplitudes of muscle responses to EES (n = 5 rats). (F) Snapshots showing complete paralysis after administration of the dual α2a antagonist/ α2c agonist. Powerful stepping started as soon as EES was switched on. (G) PC analysis applied on 129 gait parameters. Small circles report mean values for each rat and condition, while the large circles correspond to the average for all rats. Bar plot reporting average scores on PC1 (n=6 injured rats and 10 non-injured rats). ***P < 0.0001. One-way ANOVA followed by Tukey's post-hoc test. (H) Bar plots showing average values of dragging duration and step height. ***P < 0.0001. One-way ANOVA followed by Tukey's post-hoc test. (I) Sequence showing hindlimb movements when turning EES on/off after the administration of the dual α2a antagonist/ α2c agonist. 59

2.11 Effect of Clonidine or 5HT agonists and EES on locomotor performance of mice with a complete SCI and lacking α2a or α2c receptors (A) Functional experiments were performed in α2a-/- and α2c-/- knockout mice with complete SCI. Stick diagram decompositions of right leg movements are shown for all the experimental conditions, indicated above each sequence. 5HT refers to a combination of an agonist to 5HT2A receptors (Quipazine) and antagonist to 5HT1A/7 receptors (8-OHDPAT). (B) PC analysis applied on 104 gait parameters averaged for each mouse and condition (small circle). Large circles represent the average per group. Bar plot showing the average scores on PC1 (locomotor performance) of α2a (n=5) and α2c (n=5) knockout mice compared to non-injured mice (n=6). ***P < 0.0001. Two-way ANOVA followed by Tukey's post-hoc test. (C) Bar plots showing average values of classic gait parameters with high factor loadings on PC1. ***P < 0.001. Two-way ANOVA followed by Bonferroni's post-hoc test. 61

2.12 Circuits potentiating EES with the dual α2a antagonist/α2c agonist. (A) Effects of the dual α2a antagonist/α2c agonist and EES on stepping in wild-type and Egr3-/- knockout mice with complete SCI. (B) EES fails to produce movements in mice lacking functional muscle spindles, in contrast to wild-type mice. (C) Bar plot reporting the average scores on PC1 (n=5 wild-type and n=4 Egr3KO (n=4) injured mice and n=5 non-injured mice. ***P < 0.0001. One-way ANOVA followed by Tukey's post-hoc test. (D) Effect of the dual α2a antagonist/α2c agonist on the muscle responses evoked by one pulse of EES. (E) Bar plots reporting the relative increase in the amplitude of muscle responses after the administration of the dual α2a antagonist/α2c agonist for each of the 5 tested rats. *P < 0.05, bootstrapping, two-sided. (F) Neuronal network used for simulations. Muscle responses to EES are shown without and with the activation of group-Ia/II afferents and inactivation of RoRα interneurons. (G) Adapted neuronal network wherein an inhibitory premotor interneuron has been interposed between RORα interneurons and motoneurons. Muscle responses shown in (F) are displayed for this adapted network. (H) Bar plots reporting the relative change in motoneuron firing during walking when RoRα interneurons are downregulated in the presence of EES. See neurobiomechanical simulations in Fig. S7. (I) Scheme summarizing monosynaptically-restricted tracing experiments to visualize inhibitory premotor interneurons receiving synaptic contacts from RORα interneurons. (J) Reconstruction showing the location of inhibitory PVON premotor interneurons in the spinal cord. (K) Image showing a rabiesON premotor interneuron co-localizing with PV in intermediate spinal cord lamina and receiving synaptic vGlut2ON synapses from RORαON interneurons. Scale bar 4μm. (L) 3D reconstruction of the interneuron shown in (J), including vGlut2ON synaptic contacts from RORαON interneurons. RabiesON/PVON neuron receives 6±2 synaptic contacts from RORαON interneurons. Scale bar 4μm. 62

2.13 Effects of RORα inactivation on in-silico electrophysiological recordings during locomotion with EES. (A) Schematic overview depicting the neural network connectivity of the modeled proprioceptive feedback circuits related to extensor (medial gastrocnemius) and flexor (tibialis anterior) muscles, and Aβ-LTMR feedback circuits related to the foot sole. (B) Realistic neurobiomechanical model of the rat hindlimb. Afferent firing profiles of group Ia and group-II afferents are calculated using muscle spindle models combined with recordings of leg kinematics and muscle activity (EMG) in rats. The firing profile of rapidly-adapting and slowly-adapting Aβ-LTMR afferent fibers innervating the foot sole are calculated based on in vivo recordings of Aβ-LTMR afferent during walking. (C) Relative difference of the neuronal firing rates for all the modelled cells and afferent populations under the conditions EES and EES + RORα inactivation over the course of the gait cycle. Results are expressed as a relative increase or decrease with respect to the natural firing rates during locomotion of healthy rats. The value 1 indicates a change of 100%. The color coding is adjusted for each neural element in order to facilitate the understanding of the amplitude of the changes. In particular the red and blue boxes highlight the more relevant changes following inactivation of RORα interneuron inactivation. 64

2.14 Potentiation of EES with the dual α2a antagonist/ α2c agonist requires functional proprioceptive feedback circuits (A) Functional experiments conducted in wild-type mice and in Egr3-/- knockout mice, which lacks functional muscle feedback circuits. Mice received a complete mid-thoracic SCI spindles and as under the dual α2a antagonist/ α2c agonist and EES. Stick diagram decompositions of right leg movements showing the functional outcomes for wild-type and Egr3 knockout mice under different experimental conditions. (B) PC analysis applied on 104 gait parameters averaged for each mouse and condition (small circle). Large circles represent the average per group. Bar plot showing the average scores on PC1 (locomotor performance) of injured wild-type (n=5) and Egr3KO (n=4) mice under the different experimental conditions compared to uninjured mice (n=5). ***P < 0.0001. One-way ANOVA followed by Tukey's post-hoc test. (C) Bar plots reporting average values of classical gait parameters with high factor loading on PC1. ***P < 0.0001 for dragging duration, ***P = 0.0001 for step height. Two-way ANOVA followed by Bonferroni's post-hoc test. 65

2.15 Voluntary control of locomotion in rats with a severe contusion SCI (A) Scheme illustrating tracing strategy to label descending noradrenergic axons and synapses in THCre rats. (B) 3D image showing the injection site in the r Rostral Ventro-Lateral Medulla (RVLM). Scale bar 300µm. (C) Images showing virus-infected neurons co-localizing with TH in the RVLM. Scale bar 10µm. (D) 3D rendering showing the interruption of noradrenergic descending fibers by the contusion. Scale bar 1.5mm, and 3D insets taken from above the contusion. Scale bars 500µm and 300µm, respectively. (E) Reconstructions of noradrenergic fibers above (T3) and below (L3) the contusion. Bar plot reports the count of noradrenergic fibers (n= 4 rats). Scale bar 500µm. ***P < 0.0001, paired Student's t-test. (F) Reconstruction of α2cON cells in the brainstem. Scale bar 500µm. Images showing α2cON neurons co-localizing with glutamate in the ventral gigantocellular nucleus (vGi). Scale bars 20µm. (G) Effects of EES and intrathecal versus systemic administration of the dual α2a antagonist/α2c agonist on voluntary control of overground locomotion in rats with contusion SCI. Convention as in Fig. 2.4F. (H) PC analysis of gait kinematics. Conventions as in Fig. 2.10G (n=6 injured and n=7 non-injured rats). ***P < 0.0001. One-way ANOVA followed by Tukey's post-hoc test. (I) Bar plots showing average values of step height and dragging duration. ***P < 0.0001. One-way ANOVA followed by Tukey's post-hoc test. (J) Chronophotography showing a rat unable to initiate locomotion after systemic (i.p.) injection of the dual α2a antagonist/α2c agonist and EES. Intrathecal (i.t.) injection of the same pharmacological agent resulted in powerful locomotion and the ability to cross the entire extent of the runway. 67

3.1 Probability of antidromic collisions during EES in rats and humans. A, Schematic illustration of antidromic collisions between EES-induced antidromic action potentials and natural action potentials traveling along the recruited proprioceptive afferent fibers. B,C, Probability for a natural action potential to collide with EES-induced antidromic action potential in the proprioceptive afferent fibers of rats (B; action potential propagation time along the entire length of the fiber: 2 ms) and in the proximal and distal proprioceptive afferent fibers of humans (C; action potential propagation time along the entire length of the fiber: 10 and 20 ms, respectively). The probability is calculated as a function of EES frequency and natural firing rate along afferent fibers. EES frequencies that are commonly used to facilitate locomotion in rats (Courtine et al., 2009; Moraud et al., 2016; van den Brand et al., 2012; Wenger et al., 2014) and humans (Angeli et al., 2014; S. Harkema et al., 2011; Huang et al., 2006; Minassian et al., 2004) are highlighted in blue. Physiological proprioceptive firing rates reported in rats (Hnk & lessler, 1973; Prochazka, 1999) and humans (Albert et al., 2006; Prochazka, 1996) are highlighted in red. Imp, impulse. 90

3.2 EES induces antidromic activity along proprioceptive afferents and disrupts proprioception. A, Recordings of antidromic activity from sensory nerves during EES. Needle and surface electrodes were inserted in peripheral nerves and over muscles, respectively, as depicted in the scheme. Continuous EES (20 Hz, monopolar pulses, black cathode and red anode) was delivered for approximatively one minute. Averaged evoked potentials (±SEM, n 1200) are shown for subject 1 and subject 3. Evoked potentials highlighted in blue, red and grey were respectively classified as antidromic afferent volleys, efferent orthodromic activity, and far-field potentials (e.g. electromyographic activity of nearby muscles). B, Sensory AIS scores relative to the L1-S2 dermatomes for the two subjects that performed the Threshold To Detection of Passive Movement (TTDPM) test. C, Setup of the TTDPM test. Randomly selected flexion or extension movements were imposed to the knee joint of subject 1 (top). A movement speed of 0.5 degree per second and a maximum allowed range of motion of 15 degrees was used. Subject 3 (bottom) was not able to perceive movement direction. Hence, only the ability to detect extension movements was assessed. A movement speed of 1 degree per second and a maximum allowed range of motion of 30 degrees was used. EES configurations used to target knee flexor and extensor muscles are reported. D, Bar plots reporting the detection angle (median ± 95% CI) and error rate (percentage correct trials ± 95% CI) on the TTDPM test performance without EES and when delivering continuous EES (50 Hz) at 0.8 and 1.5 times motor response threshold amplitudes. Black dots report the detection angle for successful trials, while red dots and red crosses indicate false positive and failure to detect movement within the allowed range of motion, respectively. The detection angle statistic (median ± 95% CI) was only computed when the subjects successfully completed 10 trials. *, $P < 0.05$, Clopper-Pearson interval. 91

3.3 Impact of continuous EES on the threshold to detection of passive movement test performance. Bar plots reporting the detection angle (median ± 95% CI) and error rate (percentage correct trials ± 95% CI) on the TTDPM test performance without EES and when delivering continuous EES at 0.8 and 1.5 times motor response threshold amplitudes and a range of EES frequencies. Different EES frequencies were tested on subject 1 (10 Hz, 50 Hz, 100 Hz) and subject 3 (30 Hz, 50 Hz). At 1.5 motor response threshold amplitude, EES frequencies below 50 Hz induced spasms in the muscles and were thus not tested. Black dots report the detection angle for successful trials, while red dots and red crosses indicate false positive and failure to detect movement within the allowed range of motion, respectively. The detection angle statistic (median ± 95% CI) was only computed when the subjects successfully completed 10 trials. *, $P < 0.05$, Clopper-Pearson interval. 94

3.4 Effect of EES on the natural modulation of proprioceptive circuits during passive movements. A, Configuration of the experimental setup for humans. The subjects were secured in a robotic system that moved the ankle or knee joint passively within the reported range of motion. EES electrodes were configured to target a muscle mobilized during the selected joint movement, as highlighted in red for each subject. B, Plots showing EES pulses, EMG activity of the tibialis anterior, and changes in knee joint angle during passive oscillations of the knee for three different EES frequencies (20, 40 and 60 Hz) in subject 2. The rectangular windows highlight muscle responses induced by a single pulse of EES. Red and grey arrows depict the onset of the stimulation pulse and of the muscle response, respectively. C, The cycle of joint oscillation was divided into 10 bins of equal durations during which muscle responses were extracted and regrouped. Superimposed muscle responses are displayed for each bin for two EES frequencies (subject 2). Muscle responses used to compute the normalized modulation depth are depicted in light blue. D, Bar plots reporting the median and 95% CI of the normalized modulation depth, for every EES condition tested and for the different subjects. Low frequencies of stimulation often induced spasms in the muscles. Consequently, subjects 2 and 3 could not be tested with EES frequencies below 20 and 10 Hz, respectively. *, $P < 0.05$, bootstrap. E-G, Configuration of the experimental setup for rats with severe contusion SCI (250 kdyn).) and results following the same conventions as in (B-D) for humans. . . 97

3.5 Impact of continuous EES on proprioceptive afferent firings during locomotion in rats and humans. A, Layout of the computational models built for rats and humans. The components highlighted in brown are tuned to match the anatomical and physiological features of rats versus humans. B, Spiking neural network model of muscle spindle feedback circuits for a pair of antagonist muscles. Mn, motoneuron. Ex, excitatory interneurons. Iai, Ia-inhibitory interneurons. The synapses highlighted with an asterisk (*) are tuned to match the known properties of humans and rats. C, Estimated stretch profiles and afferent firing rates of ankle flexor and extensor muscles over an entire gait cycle in rats (top) and humans (bottom). D, Impact of EES on the natural firing rate profiles of group-Ia afferents innervating a flexor muscle of the ankle during locomotion in rats (left) and humans (right). From left to right: averaged firing rate profiles of the simulated population of afferent fibers over one gait cycle, mean afferent firing rate (± SEM, n = 10 gait cycles), modulation depth of afferents firing rate profiles (mean ± SEM, n=10 gait cycles), and total amount of sensory information erased by EES. Results are reported over a range of EES frequencies. Top and bottom panels reports the results for EES amplitudes recruiting 40% (top) or 80% (bottom) of the entire population of modelled group-Ia afferents. 99

3.6 Interactions between EES and muscle spindle feedback circuits during locomotion in rats and humans. A,B, Impact of EES on the natural activity of Ia-inhibitory interneurons and on the activation of motoneurons during locomotion in rats and humans. Left, average firing rate profiles and modulation depth of the Ia-inhibitory interneuron populations embedded in the flexor or the extensor neural network (mean ± SEM., n = 10 gait cycles). Right, average firing rate profiles and mean firing rate during the active phase for motoneurons embedded in the flexor or the extensor neural network (mean ± SEM., n = 10 gait cycles. The impact of EES frequencies and amplitudes are reported in the top and bottom panels, respectively. EES amplitude was set to a value recruiting 60% of the modelled Ia afferents when EES frequency was modulated, while EES frequency was set to 60 Hz when the amplitude was modulated. 100

3.7 Impact of EES amplitude on muscle activity and leg kinematics during locomotion on a treadmill — Subject 1. A, AIS leg motor score. B, Configuration of electrodes targeting the left and right posterior roots projecting to the L1 and L4 segments. Continuous EES was delivered through these electrodes to facilitate locomotion. C, EMG activity of flexor (semitendinosus/tibialis anterior) and extensor (rectus femoris/soleus) muscles spanning the right knee and ankle joints, together with the changes in the knee ankle and foot height trajectories over four gait cycles without EES and with EES delivered at 0.9, 1.2 and 1.5 motor response threshold amplitude. EES frequency was set to 40Hz. D, Bar plots reporting the averaged root mean square activity of the recorded muscles, the averaged range of motion of the knee and ankle angles, and the average step height (mean ± SEM). *, P < 0.05, ***, P < 0.001, Wilcoxon rank-sum test. 101

3.8 Impact of EES frequencies on muscle activity and leg kinematics during locomotion in rats and humans. A, Experimental setup in rats. Rats with a severe contusion SCI were positioned a robotic body weight support system located above a treadmill. Continuous EES was applied over L4 and L2 segments through chronically implanted electrodes secured over the midline of the dorsal spinal cord. B, EMG activity of the tibialis anterior muscle and foot height trajectory over two gait cycles without EES and with EES delivered at 40 Hz, 60 Hz and 80 Hz. C, Bar plots reporting the mean step height (± SEM) for the different tested EES frequencies. Dashed lines report the linear regression between the EES frequency and the step height. Slope (m) and R2 are reported. ***, $P < 0.001$ t-test slope > 0. D, Experimental setup in humans. Subjects were positioned in a robotic support system that provided personalized forward and upward forces to the trunk. Subjects were asked to step on the treadmill while holding the handlebars, since they were not able to step independently with the hands free. E, EMG activity of flexor (semitendinosus/tibialis anterior) and extensor (rectus femoris/soleus) muscles spanning the right knee and ankle joints, together with the changes in the knee ankle and foot height trajectories over four gait cycles without EES and with EES delivered at 20 Hz, 40 Hz and 80 Hz in subject 1. EES amplitude was set to 1.2 times the motor response threshold. Notice the opposite modulation of EMG activity in extensor and flexor muscles with increase in frequencies together with the co-activation of flexor muscles with extensor muscles. F, Bar plots reporting the averaged root mean square activity of the recorded muscles, the averaged range of motion of the knee and ankle angles, and the average step height (mean ± SEM) for subject 1. *, $P < 0.05$, ***, $P < 0.001$, Wilcoxon rank-sum test. The same results are reported for subjects 2 and 3 in Fig. 3.9 and 3.10. 103

3.9 Impact of EES frequency and amplitude on muscle activity and leg kinematics during locomotion on a treadmill — Subject 2. The results displayed in Fig. 3.8 and Fig. 3.10 for subject 1 are reported for subject 2 using the same conventions. 104

3.10 Impact of EES frequency and amplitude on muscle activity and leg kinematics during locomotion on a treadmill — Subject 3. The results displayed in Fig. 3.8 and Fig. 3.9 for subject 1 are reported for subject 3 using the same conventions. 105

3.11 Spatiotemporal EES protocols encoding proprioceptive sensory information. A, Estimation of spatiotemporal stimulation profiles that match the natural flow of proprioceptive information generated from flexor and extensor muscles of the ankle during gait. From left to right: estimated averaged firing rate profiles of group-Ia, group-II and group-Ib (equivalent to the muscle activity) afferents over a gait cycle, and the sum of these profiles that yielded the estimated stimulation profiles. B, Percentage of primary afferents that are recruited when applying the estimated spatiotemporal stimulation profile and during continuous stimulation. C, Impact of the estimated spatiotemporal stimulation profile on the modulation of muscle spindle feedback circuits from flexor and extensor muscles, including from left to right: group-Ia afferents firings, bar plots reporting the averaged mean firing rate and modulation depth of primary afferents (mean ± SEM., n = 10 gait cycles), overall percentage of sensory information erased by EES, modulation of Ia-inhibitory interneurons, and motoneuron activity. For comparison, the impact of continuous EES on the group-Ia afferent firings is also reported. Results of simulations are shown for a range of EES amplitudes. Conventions are the same as in Fig. 3.6. 107

3.12 High-frequency low-amplitude EES protocols preserve proprioceptive information. A, Realistic models of alpha motoneurons and of the strength and distribution of group-Ia synaptic contacts. B, Simulations showing the response of motoneurons to a singe pulse of EES at an amplitude recruiting 45% of the afferent population, and to a high-frequency bursts (5 pulses, 600 Hz) at an amplitude recruiting 15% of the afferent population. Windows show a zoomed view of the motoneuron membrane potential depolarizations in response to the pulses of EES (arrows). Right: plots showing the percentage of recruited motoneurons and the average (mean ± SEM) latency before the onset of an action potential. C, Responses recorded from the tibialis anterior muscle following a single pulse of EES (left) and high-frequency bursts of EES (right) applied to the lumbar (L2) spinal cord of rats with severe contusion SCI over a range of amplitudes and burst frequencies. The grey arrow indicates the responses induced by a single pulse of EES at the motor response threshold amplitude, emphasizing the need to deliver high amplitudes to elicit responses with single pulses compared to high-frequency bursts. D, Heatmaps representing the power of the motor response to single pulses (column on the left) and high-frequency bursts (matrix on the right) of EES over a range of EES amplitudes and bursts frequencies, for 5 rats. EES amplitude is reported as a multiple of motor response threshold, amplitude corresponding to the response highlighted by the black box. The highlighted column corresponds to the bursts with a frequency inducing the largest motor responses. Right, latencies of motor responses elicited by EES bursts with the frequency highlighted in the black boxes, at increasing amplitudes. E, Impact of continuous high-frequency low-amplitude EES protocols (600 Hz, 20% recruited afferents) on the modulation of the muscle spindle feedback circuits, following the same conventions as in Fig. 3.6. For comparison, the impact of continuous EES on the group-Ia afferent firings is also reported. . 108

3.13 Integrate and fire motoneuron model. A, Schematic of the integrate and fire model and of the different synapses contacting this cell. B, Simulated Inhibitory and Excitatory Post-Synaptic Potentials (IPSPs/EPSPs) induced by the activation of a single Ia-inhibitory interneuron or a single group-Ia afferent fiber, respectively. C, Excitation threshold of our realistic alpha motoneuron model (Moraud et al., 2016). D, Number and amplitude of experimental (Harrison & Taylor, 1981; McIntyre & Grill, 2002; Munson et al., 1980) and modelled EPSP/IPSPs induced from the synaptic contacts originating from group-Ia afferents (s1), group-II excitatory interneurons (s2), and Ia-inhibitory interneurons (s3). 116

3.14 Adaptation of the rat neural network to humans. A, Model layout of the hybrid rat-human computational model used to tune the human neural network weights. W1, w2, w3 and w4 represent the weights of the neural network connections that have been modified to adapt the rat neural network to the human one. B, Systematic search results. W1 and w3 were ranged together between 1 and 2 times the weight used in the rat network, while w2 and w4 were ranged between 1 and 4 times. Bar plots report the percentage of simulations that fulfilled the defined fitness criteria. Selected weights that have been used for further simulations are highlighted with an arrow. C, Effect of EES on the natural activity of Ia-inhibitory interneurons and on the production of motor patterns during locomotion, in the hybrid rat-human model for the selected set of synaptic weights. Panels on the left report the average firing rate profiles of the Ia-inhibitory interneuron populations associated to either the flexor or the extensor network, as well as their modulation depth (mean ± SEM, n = 10 gait cycles). Similarly, right-most panels represent the average firing rate profiles of motoneurons and their mean firing rate activity during the phase in which they are active (mean ± SEM, n = 10 gait cycles). Effects of different EES frequencies and amplitudes are reported on the top and bottom panels, respectively. 118

4.1 Technology and study design. a, Targeted neurotechnologies enable walking after SCI. Multidirectional assistance of trunk movements during overground locomotion while 3D kinematics, ground reaction forces and EMG activity are recorded wirelessly. An implantable pulse generator connected to a 16-electrode paddle array was used to target the posterior roots projecting to specific motor neuron pools, illustrated for hip flexors and ankle extensors. Real-time processing of residual kinematics ensures that targeted EES coincides with movement intent. b, Study timeline 129

4.2 Surgical procedure and technological framework. a, Surgery. Step 1: high-resolution MRI for pre-surgical planning. The entry point into the epidural space is based on the position of the conus. Step 2: placement of subdermal and intramuscular needle EMG electrodes for key leg muscles and paraspinal (PS) muscles. A subdermal needle is inserted over the sacrum and used as a return electrode for stimulation. Bottom, schematic of the 16-electrode paddle array. Step 3: surgical openings based on pre-surgical planning, typically between the L1 and L2 vertebrae, which are identified through intraoperative X-ray. The mediolateral positions of the paddle array are evaluated with X-ray and recordings of EMG responses following single pulses of EES delivered to the most rostral or most caudal midline electrodes. Step 4: the rostrocaudal position of the paddle array is optimized using EMG responses to single-pulse EES delivered to the electrodes located at each corner of the paddle array. The aim is to obtain strong ipsilateral responses in hip flexors with the most rostral electrodes and strong ipsilateral responses in ankle extensors with the most caudal electrodes. Step 5: implantable pulse generator (IPG) placed within the abdomen. Once connected to the paddle array, the impedance of the electrodes is evaluated to verify that all the components are properly connected. Step 6: post-surgical CT scan showing the location of the paddle array with respect to the vertebrae in each participant. b, Technological framework and surgical procedure. Step 1: participants wear reflective markers that are monitored using infrared cameras. An algorithm assigns the markers to the joints in real-time. Step 2: the spatiotemporal trajectory of the foot around a calculated centre of rotation (centroid, updated every 3 s) is converted into angular coordinates that trigger and terminate EES protocols when a user-defined threshold is crossed. Step 3: EES commands are transmitted to the IPG via Bluetooth (1) to a module that converts them into infrared signals (2), which are then transferred to the stimulation programmer device (2). Step 4: the stimulation programmer transmits EES commands into the IPG (4) via induction telemetry, using an antenna (3) taped to the skin and aligned to the IPG. EES is delivered through the paddle array (5). 130

4.3 Configuration of targeted EES. a, Distribution of motor neuron pools within the spinal cord (Sharrard, 1964). b, Map of motor neuron activation underlying isometric torque production in a healthy subject (consistent across three repetitions and subjects). c, Personalized computational model of EES. Simulated map of motor neuron activation following EES targeting the L1 and S2 posterior roots. d, Electrophysiological experiments were used to determine optimal electrodes and amplitudes for targeting specific spinal cord regions. EMG responses when delivering single-pulse EES at increasing amplitudes are shown (grey traces). Motor neuron activation maps correspond to optimal amplitudes (black traces). Circular plots report EMG amplitude (in grey scale) at increasing amplitudes (radial axis). White circles show optimal amplitudes; polygons quantify selectivity at this amplitude. e, Instrumented chair used to measure single-joint torques. f, Targeted EES enables voluntary force production by paralysed muscles. Isometric torque and EMG activity while delivering targeted EES, including quantification (n = 3 repetitions, P1). Gmax, gluteus maximus; Il, iliopsoas; MG, medial gastrocnemius; RF, rectus femoris; Sol, soleus; ST, semitendinosus; TA, tibialis anterior; VLat, vastus lateralis. 133

4.4 Identification of electrode configurations to target selected posterior roots. Step 1: single-pulse EES and EMG recording setup. Step 2: Motoneuron pools are located in specific segments, which informs on the relative recruitment of each posterior root with EES. For example, electrodes targeting the L3/L4 posterior roots will elicit the strongest EMG responses in the knee extensors. A personalized computational model of EES allows the performance of simulations that evaluate the relative activation of a given posterior root with a given electrode over the entire range of amplitude. Each curve corresponds to an electrode. The highlighted curve corresponds to selected electrode after Step 3-5. Step 3: Single pulses of EES are delivered through the subset of electrodes identified with simulations. The EMG responses are recorded over a broad range of EES amplitude. Step 4: The EMG responses are concatenated, averaged for each EMG amplitude, and the peak-to-peak amplitude of the average responses calculated to elaborate a recruitment curve for each recorded leg muscles (black traces: targeted muscles). Step 5: The polar plots display the normalized EMG responses (greyscale) when delivering single–pulse EES at increasing amplitudes (radial axis), where the white circle highlights the optimal EES amplitude and the polygon quantifies the relative muscular selectivity at this amplitude. The motoneuron activation maps are shown for the optimal amplitudes. Step 6: Decision tree to validate or optimize electrode configurations. The selected electrode is tested during standing since the position of the paddle array with respect to the spinal cord can change between supine and standing. In this example, the selectivity improves during standing. When the selectivity is not deemed sufficient, the current is steered toward the targeted posterior roots using multipolar configurations. The example shows the increased selectivity of a multipolar configuration with 2 cathodes surrounded by 3 anodes, compared to the 2 corresponding monopolar configurations. These results are verified experimentally and with computer simulations. 134

4.5 Spatial selectivity of targeted electrode configurations. Monopolar configurations (shown on paddle array schematics) experimentally selected to target the left and right posterior roots associated with hip flexion (L1), knee extension (L3), ankle flexion (L4) and ankle extension (S1) for the three participants. The circular plots and motor neuron activation maps use the same conventions as in Fig. 4.3 and Fig. 4.4 (median of n = 4 pulses). The normalized selectivity index is reported above each motor neuron activation map. This index represents the percentage of posterior root selectivity for the electrode configuration selected experimentally, with respect to the maximum posterior root selectivity that can be achieved among all monopolar configurations (all selectivity indices obtained from computational simulations). Note that in P2, the electrode selected experimentally to target the right S1 root was located on the midline and resulted in bilateral activation within computational. 136

4.6 Single-joint movements enabled by targeted EES. Step 1: participants are placed in standardized positions to allow assessment of voluntary torque production at a single joint (isometric contractions) without and with targeted EES. Step 2: EES protocols elaborated from single-pulse experiments (Figs. 4.3, 4.7) are optimized for each task using multipolar configurations and adjustments of EES amplitude and frequency. Step 3: sequence of each trial. Participants were asked to produce a maximal voluntary contribution, but failed in most cases, as evidenced by the absence of EMG activity during this period. While they continued trying to activate the targeted muscle, EES was switched on. After a few seconds, participants were instructed to stop their voluntary contribution. After a short delay, EES was switched off. For each sequence, the produced torque and EMG activity of the key agonist and antagonist muscles acting at the targeted joint were calculated over the four indicated phases of the trial. Plots report the measured torques and EMG activity during the various phase of the trial for the left legs of all participants for the four tested joints (cyan, flexor; magenta, extensor), together with EES parameters and electrode configurations. All measurements were performed before rehabilitation, except for hip extension in P1 and P2 (not tested before), and ankle extension in P3 (no capacity before rehabilitation), which were carried out after rehabilitation. Targeted EES enabled or augmented the specific recruitment of the targeted muscle, which resulted in the production of the desired torque at the targeted joint, except for ankle extension of P2. Plots show quantification of the EMG activity and torque for n = 3 trials per condition. Note that hip flexion can be enabled or augmented with EES targeting L1 and/or L4 posterior. 138

4.7 Configuration of spatiotemporal EES for walking. a, EMG activity during walking in healthy individuals. Spatiotemporal map of motor neuron activation highlights hotspots (mean, n = 12 gait cycles, representative subject). Equipotential lines represent 45–75% activation. b, Functional target of each hotspot. c, Map of motor neuron activation following 500-ms bursts of targeted EES during standing. Bar plots show Pearson's correlations for each hotspot (mean ± s.e.m., n = 12 bursts, ***P < 0.001; one-way ANOVA, post hoc Tukey's Honest Significant Difference (HSD) test). d, EMG activity and map of motor neuron activation during EES or without EES after a motor complete SCI while stepping on a treadmill with support and assistance (P3). EES timing is indicated along foot trajectories (bottom right; n = 73 steps) and below motor neuron activation maps. e, Spatiotemporal EES sequence for data shown in d. f, Mean (± s.e.m.) modulation of EMG amplitude in flexor and extensor muscles during walking with increasing EES frequencies (n = 20, 15, 16, 17, 15, 16, 15 gait cycles for 20, 25, 30, 40, 60, 80, 100 Hz, respectively; P3). 140

4.8 Voluntary control of adaptive and sustained locomotion. a, Spatiotemporal EES enables voluntary control of overground walking. Chronophotography, tibialis anterior (TA) EMG activity and foot vertical position during overground walking with gravity-assist and sticks while EES is switched on, then off, then on. Leg motor scores shown on muscles in diagrams: 0, total paralysis; 1, palpable or visible contraction; 2, active movement, gravity eliminated; 3, active movement against gravity; 4, active movement against some resistance; 5, active movement against full resistance. b, Spatiotemporal EES enables voluntary control of leg kinematics. Overground walking when participants were requested to perform steps with normal heights and then exaggerated step elevations. c, Spatiotemporal EES enables sustained walking. Consecutive values of step height and EMG activity over 60 min of walking with EES (P1: 1.2 km; P2, P3: 1 km). Experiments in a, b were repeated at least five times; the experiment in c was performed once, but participants routinely walked for 60 min during training. BWS, bodyweight support. 141

4.9 Modulation of EEG activity during volitional contraction of leg muscles without and with EES. a, Recordings of EEG activity while participants were asked to produce an isometric torque at the knee joint without and with continuous EES targeting motor neuron pools innervating knee extensors, as shown in b. b, Superimposed EEG responses (n = 40 repetitions) and temporal changes in the topography of average activity over the cortical surface after the onset of EES, as indicated above each map. The onset was calculated from the onset of EMG responses in the targeted vastus lateralis muscle (insets). The stimulation elicited a robust event-related response over the left sensorimotor cortex with a latency of 90 ± 40 ms for P1 and P3, and of 170 ± 40 ms for P2 (full range of the peaks and middle of this range indicated). c, Average normalized time–frequency plots (n = 40 trials) showing ERD and ERS over the Cz electrode (central top electrode) for each individual during the voluntary activation of knee extensor muscles without and with EES. Schematic drawings (left) indicate the motor scores of the tested legs, including the targeted muscles (*), at the time of enrolment in the study. Both legs were tested in P1 owing to his asymmetric deficits. d, Normalized average power (mean ± s.e.m.) of the β-band over the Cz electrode during ERS from 0 to 500 ms after termination of contraction without and with continuous EES (n = 40 repetitions for each condition, individual data points shown except for outliers more than 3 median absolute deviations away from the median). ***P < 0.001 (permutation tests, see Methods). 142

4.10 Configuration of spatiotemporal EES to enable walking. a, Spatial configuration. Step 1: select electrode configurations from single-pulse experiments to target the three hotspots underlying the production of walking in healthy individuals (weight acceptance: L3; propulsion: S1; swing: L1/L4). Step 2: optimize EES amplitude and frequency while delivering EES during standing. Multipolar configurations can be used to refine selectivity of EES protocols. Example shows continuous EES targeting the right L3 posterior root to facilitate right knee extension during standing, and trains (500 ms) of EES targeting the right L1 posterior root stimulation to facilitate hip flexion. Two EES frequencies are shown (P3). b, Temporal configuration. Step 3: decision tree to select the best strategy to configure the temporal structure of EES protocols. If the participant is able to initiate leg movements consistently, use closedloop EES based on real-time processing of foot trajectory. If the participant is not able to initiate consistent leg movements but can feel when EES is applied, use open-loop EES. If the participant is not able to generate movement and cannot feel EES, use closed-loop EES combined with physiotherapist assistance to move the legs. Step 4: real-time monitoring of the spatiotemporal trajectory of the feet. The trajectory is modelled as a foot rotating in space around the centroid of the movement (updated every 3 s). Angular thresholds determine the onset and end of EES protocols. Step 5: example showing the effect of three different angular thresholds on the onset of EES and resulting kinematics and EMG activity, including the quantification of kinematics for each step and condition that enables selecting the optimal onset of EES trains (P1). The same approach is used to optimize the duration of each train. c, Comparisons between closed-loop and open-loop EES. Plots show the vertical displacements of the left and right feet and successive step heights during walking with spatiotemporal EES delivered in closed loop versus open loop, showing the reduced variability of step height during pre-programmed EES sequences (P1). d, Resulting EMG patterns. Step 6: example of the progressive addition of EES protocols targeting specific hotspots. Plots show the quantification of EMG activity for the displayed muscles (n = 7 gait cycles for no EES and n = 9 gait cycles for each stimulation condition, P2). Step 7: EES amplitudes and frequencies are adjusted to avoid detrimental interactions between the different EES protocols and thus obtain the desired kinematic and EMG activity. Plots report the modulation of EMG activity and kinematics with increases in EES amplitude and frequency (mean ± s.e.m.; amplitude data: n = 10, 12, 12, 30, 19, 12, 11, 10 gait cycles for amplitudes in increasing order, P2; frequency data: n = 20, 15, 16, 17, 15, 16, 15 gait cycles for frequencies in increasing order, P3). . . . 144

4.11 Targeted modulation of muscle activity during walking. Each panel reports the same representative data and quantification for one participant. Left, EMG activity of leg muscles during walking on a treadmill without EES (EES OFF) and with spatiotemporal EES (EES ON) while applying 50%, 45% and 70% body weight support for participants P1, P2 and P3, respectively. Stance and swing phases are indicated by grey and white backgrounds, respectively. The personalized spatiotemporal EES sequence (open loop) is schematized at the top right. The colours of each EES protocol refer to the targeted hotspots: weight acceptance (salmon), propulsion (magenta) and swing (cyan). These colours are used in the EMG traces to indicate the temporal window over which each targeted EES protocol is active. The bar plots report the amplitude of muscle activity without EES and with spatiotemporal EES, for which the quantification was performed over the entire burst of EMG activity and during each temporal window with targeted EES. The temporal windows are labelled with a number that refers to the spatiotemporal EES sequence. These results show the pronounced increase in the EMG activity of the targeted muscles (P1, no EES: n = 7 gait cycles, EES: n = 11 gait cycles; P2, no EES: n = 9 gait cycles, EES: n = 9 gait cycles; P3, no EES: n = 10 gait cycles, EES: n = 57 gait cycles). The average spatiotemporal trajectories of both feet with respect to the hip in the sagittal plane are shown for walking without EES and with spatiotemporal EES. The presence of targeted EES is indicated with the same colour code. Plots at bottom right show the relationships between EES frequency and the modulation of the EMG activity of flexor (blue) and extensor (magenta or salmon) muscles and maximum amplitude of hip movements during walking (mean ± s.e.m.; P1: n = 14, 17, 15, 19 gait cycles for increasing frequencies; P2: n = 13, 16, 10, 17, 12 gait cycles for increasing frequencies; P3: n = 20, 15, 16, 17, 15, 16, 15 gait cycles for increasing frequencies). ***P < 0.001. Student's t-test. 146

4.12 Volitional adaptations of walking during otherwise unchanged spatiotemporal EES. a–c, Quantifications of experiments shown in Fig. 4.8a–c for each participant. a, Step height and TA EMG activity with and without EES during overground walking (P1, EES ON: n = 7 gait cycles; P2, EES ON: n = 16 gait cycles; P3, EES ON, n = 7 gait cycles). b, Step height and TA EMG activity during normal steps and when participants were requested to perform exaggerated step elevations during overground walking (P1, n = 15 normal gait cycles, n = 11 exaggerated gait cycles; P2, n = 31 normal gait cycles, n = 23 exaggerated gait cycles; P3, n = 14 normal gait cycles, n = 10 exaggerated gait cycles). c, Step height and TA EMG activity during the first and last 30 steps extracted from a sequence of 1 h of locomotion on a treadmill (n = 30 gait cycles for all conditions). ***P < 0.001; n.s., non-significant; Student's t-test. d, EMG activity of representative leg muscles, vertical displacements of the foot and anteroposterior oscillations of the leg (virtual limb joining the hip to the foot) while P2 was walking continuously on the treadmill with spatiotemporal EES (open loop). The participant was asked to suppress the effects of EES and stand during one cycle of open-loop spatiotemporal EES sequence, highlighted in brown (SKIP), whereas he actively contributed to the production of movement the rest of the time. Plots report the quantification of step height and TA EMG activity during walking and when skipping steps for each participant (P1, n = 13 normal gait cycles, n = 1 skipped cycles; P2, n = 36 normal gait cycles, n = 3 skipped gait cycles; P3, n = 11 normal gait cycles, n = 2 skipped cycles). e, EMG activity of two representative muscles, vertical displacements of the foot and anteroposterior oscillations of the leg while P1 was walking on the treadmill and the speed of the belt increased progressively from 0.8 to 2 km h–1. Plots show relationships between treadmill speed and mean stride length and TA EMG activity in all participants (P1: n = 9, 9, 9, 9, 10, 18, 15, 9, 9 gait cycles for increasing speeds; P2: n = 13, 10, 7, 8, 10, 9 gait cycles for increasing speeds; P3: n = 8, 8, 10, 9, 9, 8 gait cycles for increasing speeds; s.e.m. shown). The range of tested speeds was adapted to the walking ability of each participant. 149

4.13 Rehabilitation mediates neurological recovery. a, Improved mobility after rehabilitation. Chronophotography shows P1 and P2 transiting from sitting to walking with crutches without EES; P3 progresses overground with a walker and EES; repeated at least three times on different days. b, Plots reporting changes in 6-min and 10-m walk tests for P1 and P2. Tests were performed without gravity-assist, following clinical guidance. For P3 plots report changes in walking distance during rehabilitation and walking speed with EES (with transparent body weight support). c, Evaluations of isometric torque production for each joint, quantified before surgery and after rehabilitation without EES for P1 and P2, and with EES for P3. d, Changes in lower limb motor and sensory scores after rehabilitation. Changes in motor and sensory scores on Abbreviated Injury Scale (AIS) 151

4.14 Comparison between continuous and spatiotemporal EES during overground walking. Each panel represents one participant who is attempting to walk overground with gravity-assist without EES (left), with continuous EES (middle) and with spatiotemporal EES (right). EMG activity of representative leg muscles, vertical position of the foot and distance covered by the foot in the forward direction are displayed for each experimental condition. Continuous EES is applied throughout the trial (red). For P2 and P3, we optimized EES protocols that targeted the posterior roots on both sides, whereas EES was applied over the most rostral and most caudal midline electrodes for P1, as shown next to each plot. Spatiotemporal EES is represented using the same colour scheme as in Fig. 4.7 and Fig. 4.11. The plots report quantification of EMG activity, step height and mean speed (based on distance covered) for the three experimental conditions (P1, n = 6, 7, 8 gait cycles for no EES, continuous EES and spatiotemporal EES; P2, n = 17, 7, 9 gait cycles for no EES, continuous EES and spatiotemporal EES; P3, n = 6, 10, 9 gait cycles for no EES, continuous EES and spatiotemporal EES). ***P < 0.001; **P < 0.01; n.s., non-significant. One-way ANOVA, post hoc Tukey's HSD. These recordings were repeated on at least three different days for each participant. 152

4.15 Rehabilitation program and evolution of walking capacity. a, Rehabilitation programs were continuously personalized on the basis of the current motor performance of participants. Walking capacities evolved in phases (b). For this reason, the relative percentage of training in the various tasks has been divided into clusters, which correspond to the evolution of walking capacities. To facilitate the sustained production of reproducible locomotor movements (Fig. 4.10c), EES was delivered in open-loop mode during gait rehabilitation. b, Walking capacities evolved through stereotypical phases that are illustrated in the snapshots. c, Plots showing the progression of the three participants along the phases of recovery during the rehabilitation program, and during the subsequent 6 months for P1 and P2. P3 had just completed the rehabilitation program at the time of submission of this study. 153

4.16 Spatiotemporal EES in ecological settings. a, System to support activities of daily living. Tablet featuring a mobile App allows participants to select EES sequences, delivered in open loop or closed loop based on Inertial Measurement Units (IMUs) located on both feet or attached onto the cranks and frame of a trike. 1. A personalized voice-controlled watch allows the user to switch EES on or off. 2. IMUs detect foot or crank motion during walking or cycling. 3. Controller sends commands to the patient programmer. 4. Spatiotemporal EES is adjusted in a closed loop. b, Walking and cycling activities in ecological settings are enabled by spatiotemporal EES. 154

4.17 Changes in muscle mass and quality and recovery of voluntary movements with and without EES in participant P3. a, Skeletal muscle mass and quality were assessed at the pre- and post-rehabilitation time points using X-ray attenuation from CT images obtained at the abdomen (L3 vertebra) and mid-thigh (25 cm above femorotibial joint space). Muscle mass was determined by measuring the Cross-Sectional Areas (CSAs) of muscle tissues, while muscle quality was reflected by CT attenuation numbers (in Hounsfield Units, HU) within the CSAs. Muscle segmentations were performed semi-automatically using ImageJ and muscle-specific HU thresholds (–29 to 150 HU). Plots report the substantial changes in muscle mass at mid-thigh, for both flexor and extensor muscles, and of trunk muscles. Muscle quality was also improved at both levels: total mid-thigh, left: 52.9 to 56.1 HU, right: 51.9 to 56.7 HU; total L3, 45.9 to 48.3 HU. This increase in CT attenuation numbers between the baseline CT scan and the follow-up imaging reflected the decrease in muscle fibre lipid content at the mid-thigh and abdomen. These evaluations were part of a protocol amendment obtained when enrolling P3. b, Assessment of voluntary torque production at the ankle (extension) with targeted EES before and after rehabilitation. Conventions are as in Fig. 4.6. c, Snapshots showing voluntary extension of the left leg against the direction of gravity together with the concomitant sequence of EMG activity in the extensor and flexor muscles of this leg. The zoomed window shows the relationship between the movement and the EMG activity, indicated with the numbers. This participant presented flaccid paralysis, and had thus no control over leg muscles before the surgery. This movement was observed repeatedly at the end of the rehabilitation period. 155

4.18 Performance of closed-loop spatiotemporal EES to enable walking and cycling outside the laboratory. a, P1 and P2 were asked to walk freely overground with a walker (no body weight support) for 6 min. The concomitant vertical displacements of the foot show the consistency of EES triggering events despite variable foot kinematics and voluntary breaks. The trajectory of the centre of mass is shown from a top view to illustrate the ability to steer locomotion along any desired path. EES protocols took into account the deficits of each participant (cyan, EES targeting hip flexion; magenta, EES targeting knee and ankle extension). Histograms indicate the number of detected foot-off events for the represented leg as a function of the latency with respect to real foot-off events. The confusion matrix associated with these detections is represented below, as a percentage of the real events that were correctly or incorrectly classified. Detections were considered valid if they occurred between 400 ms before and 100 ms after real foot-off events, as highlighted in green on histograms (P1, n = 49 gait cycles; P2, n = 79 gait cycles). b, Closed-loop spatiotemporal EES was delivered in P3 using an electric trike powered by hand and foot pedals. Traces show EMG activities of the targeted hip flexor and knee extensor muscles on one leg together with the tangential acceleration of the pedal and power generated at the foot pedal. Plots report the quantification of flexor and extensor EMG activities, peak tangential accelerations and generated power without and with EES. Successive ankle trajectories during cycling are shown together with the timing of EES protocols targeting the hip flexor and knee extensor muscles. The histograms and confusion matrices report the performance of the controller following the same conventions as in a, except that the correct detection window was restricted to 50 ms before and 100 ms after the desired crank position (P3: n = 73 pedalling cycles). ***P < 0.001. Student's t-test. 157

5.1 Anatomical quantification and personalizable computational models. a, Human spinal cord, including a visualization of the targeted thoracic, lumbar and sacral dorsal roots. b, Spinal cord topology from 27 adult individuals were quantified from MRI/CT scans of 15 healthy volunteers and anatomical measurements of 12 cadavers. Each bar or dot reports measurements from one individual. Three complete anatomical models are shown from individuals with widely different topologies. c, Automated framework to elaborate anatomical models of spinal cord tissues from high-resolution MRI and CT images. d, Discretization of anatomical models as voxels using rectilinear (structured) gridding. e, Distribution of electric potential when delivering one pulse of EES. f, Compartmental cable models incorporating the entire range of afferents and efferents are initialized in the rootlets. g, Relative recruitment of afferents and efferents when delivering a single pulse of EES with increasing amplitude. 177

5.2 Personalizable computational models of the interactions between EES and the spinal cord. Step 1, High-resolution MRI images enable clear-cut visualization of spinal tissues, including individual dorsal roots. Step 2, CT images enable reconstructing the tridimensional geometry of vertebral bodies. Step 3, Elaboration of highly realistic anatomical models from MRI and CT scans. Step 4, Automatic generation of rootlets based on the identification of the uppermost rootlet (shown in red) in high-resolution MRI acquisitions. Rootlet trajectories are interpolated from this rootlet, using the measured segment length as a reference. Step 5, Splines representing the nerve fibers are automatically generated inside the rootlets. For this purpose, points are initialized in each cross-section based on a weighted superposition of the points constituting the cross-section itself. These points are connected to generate splines. Step 6, Conductivity maps are imposed on each voxel of the discretized finite element models. The white matter and rootlets require an anisotropic conductivity map. Functionality has been implemented in Sim4Life for that purpose that generates anisotropic conductivity maps by solving a diffusion problem with suitable boundary conditions in the tissues of interest and locally aligning conductivity tensors with the gradient of the obtained solution. Step 7, Compartmental cable models are initialized along each spline to integrate the nerve fibers. 179

5.3 Optimal arrangement of electrodes. a, Highlight of the four features that guided the positioning of the electrodes on the new paddle lead. These features were studied using computational experiments detailed in panels b, c, d, and e. b, Generalized model reconstructed from averaging all the spinal cords of the atlas. The length of the new paddle lead was calculated from this model. c, A grid of 7 x 5 electrodes was positioned over each targeted rootlet bundle, here shown for the L1 dorsal root. Simulations computed a selectivity index for each electrode of the grid to determine the distributions of the lateral electrodes (red rectangle). d, Due to the inherent variability of dorsal root distributions and putative deviations during surgical placement, the selectivity of the cathodes may require adjustments (e.g. simulated offset as blue rectangle). Simulations determined that lateral shifts of the cathodes compensate for deviations in the medial direction, while anodes located over the midline steer current with bipolar stimulation. e, Distribution of electrical potentials when delivering unipolar versus multipolar stimulation over the dorsal roots agglutinated within the thecal sac. The transverse arrangement of electrodes enables steering the current toward the targeted sacral dorsal roots. f, Arrangement of electrodes on the new paddle lead. 182

5.4 Importance of modeling rootlet bundles. Step 1, Models of the same spinal cord wherein the dorsal roots are modelled as single tubular structures (left) versus multiple tubular structures mimicking the topology of rootlet bundles observed in humans (right), as shown in Step 2, side by side comparison of the rootlet bundles in the model and in a real spinal cord. To create the model of the rootlets, we determined the entry point of the uppermost rootlet for each spinal segment, and then populated the space from the uppermost rootlet of a given dorsal root to the uppermost rootlet of the next dorsal root by distributing rootlets homogeneously across this space. Step 3, A pulse of EES was delivered with increasing intensities through the electrode depicted in step 1, over the L3 dorsal root. The plots show the resulting recruitment curve of each dorsal root. The explicit models of rootlets led to pronounced differences in the recruitment curves of each dorsal root. Step 4, Performance of the new paddle lead evaluated in 15 computational models of the atlas. The top left electrode of the paddle lead was positioned over the dorsal root innervating the L1 spinal segment, as depicted in the model on the left. The plot on the left reports the selectivity of this electrode for each model, organized laterally based on the length of the spinal cord (as reported in Fig. 5.1). The plot on the right reports the selectivity of the bottom left electrode to recruit the dorsal root projecting to the S1 spinal segment. Lower Panel, Horizontal bar plots on the left report the variability of the width of the dorsal root entry zone (n = 15 healthy volunteers). Horizontal bar plots on the right report the variability of length of each spinal segment (n = 27 spinal cords). The bar plot between these two plots reports the variability of the width of the dorsal root entry zones and of the length of spinal segments. ***, $P < 0.0001$, t-test. 183

5.5 Preoperative planning and intraoperative validation. a, CT scan combined with structural and functional MRI acquisitions enabled the personalization of computational models predicting the interactions between the location of EES and the recruitment of afferents in the dorsal roots. b, For each participant, simulations (left) calculated the relative selectivity of the paddle lead for 6 positions separated by 2 mm, as shown in the vertical bars positioned over the computational model, and their enlarged version next to each bar. The selectivity of electrodes located at each corner of the paddle lead is aggregated in a combined (color coded) selectivity index. The same procedure was conducted intraoperatively (right) for three positions of the paddle lead, including the optimal position predicted by the model. Representations are the same as in the computational simulations. The final surgical positioning of the paddle lead is displayed in the reconstructed CT images. c, Bar plots reporting the selectivity of electrodes from the new paddle lead (in red) and Specify 5-6-5 (in grey) to recruit muscles eliciting hip flexion and ankle extension. d, Bar plots reporting the amplitude of muscle responses when stimulating with monopolar versus multipolar electrode configurations, showing the ability of the transverse electrode arrangement to selectively recruit sacral roots despite the agglutination of all lumbar dorsal roots within the stimulated region. 185

5.6 Identification of the projectome from propriospinal neurons. Step 1, Acquisition of functional MRI from the spinal cord in response to the recruitment of proprioceptive afferents from specific leg muscles. The muscle spindles are recruited either by stretching the muscles in which they are embedded (the limb is mobilized by a physiotherapist, aided with audio cues), or by applying muscle tendon vibration using MR-compatible pneumatic vibrators (synchronized with MRI triggers). Two runs are acquired for each muscle. Only the right leg muscles are tested. In addition to the functional volume series, T2 anatomical images and physiological (heart rate, respiratory) signals are acquired. Step 2, Raw fMRI volume series are repeatedly acquired every 2.5 s (TR) in functional runs lasting about 7 minutes. Step 3, A two staged motion correction (3D and then 2D slice-by-slice) is applied for each run. First, the volumes are registered to their respective averaged-in-time image using 3D rigid body realignment. Secondly, taking as reference the averaged-in-time corrected volume, a slice-by-slice 2D realignment is applied thus accounting for the non rigid property of the spinal cord. Step 4, The motion corrected series are spatially smoothed, volume by volume with 3D gaussian kernel with Full Width at Half Maximum (FWHM) of $2x2x6mm^3$. Step 5, The motion-corrected series are again averaged through time. The cerebrospinal fluid and white matter are segmented from this mean functional image. Step 6, Physiological signals (heart rate and respiratory) acquired concomitantly to the fMRI volumes are used to model physiological noise (RETROICOR based procedure). If no signals are available, noise regressors are built with component based noise extraction (aCompCor). Step 7, Acquisition timings corresponding to the task-design, pre-processed (motion corrected, smoothed) fMRI volume series and physiological noise regressors are submitted to a specific first level generalized linear model. A second level fixed effects analysis (subject level, task specific) is performed by combining the two runs. Whenever possible, multiple comparison corrections are performed ($Z > 2$, $pcorr < 0.05$). Step 8, Spinal segments are identified from high-definition T2-ZOOMit structural images that allow visualization of the dorsal roots. Spinal segments are then reported in the T2 anatomical image acquired in each run. Step 9, Using non-rigid transformations, the mean functional images are co-registered to the T2 anatomical image. Step 10, Thresholded activity patterns resulting from the generalized linear model are coregistered to the anatomical image. The projectome of proprioceptive neurons innervating the mobilized muscles are extracted and mapped to the anatomical model. Step 11, Projectomes from the three participants, and for comparison, averaged myotome distribution measured electrophysiologically in a large population of patients undergoing surgery. The color dots represent reconstructed projectome from key leg muscles. Vertical color bars represent mean population distribution of muscular motor hotpots. The projectomes differed across the participants. In particular, the projectome identified in P3 revealed an unexpected inversion of the projectome from ankle antagonists. This rostrocaudal inversion was confirmed electrophysiologically. 186

5.7 Preoperative planning for optimal placement of the new paddle lead. Step 1, CT, MRI and fMRI acquisitions allow to personalize a computational model of the interactions between EES and the spinal cord for each participant. Step 2, The insertion of the new paddle lead within the spinal canal is visualized in the model to anticipate bony structures or ligaments that could deviate the trajectory. Step 3, The new paddle lead is positioned at 6 locations separated by 2 mm, thus covering the entire region of the spinal cord targeted by the therapy. The same procedure was applied to the Specify 5-6- 5 lead, except that 2 additional locations were necessary to cover the entire region since this lead is shorter than the new paddle lead. Step 4, The plot shows the recruitment of each dorsal root when simulating the delivery of EES at increasing intensities through the electrodes located at the corners of the paddle lead. Step 5, The recruitment of dorsal roots is translated into the recruitment of motor pools based on a transformation matrix that maps the recruitment of afferents to the recruitment of motor pools. The transformation matrix was either based on the averaged location of motor pools across the human population (Schirmer et al., 2011), or the projectome of proprioceptive neurons from key leg muscles identified from fMRI. Step 6, Applying the transformation matrix depicted in Step 5 allows to convert the predicted recruitment of dorsal roots shown in Step 4 into a prediction of motor pool recruitment. Step 7, For each position of the lead, the recruitment of the targeted motor pools compared to the non-targeted motor pools is measured to obtain a selectivity index. For each position of the paddle lead, the selectivity index for the tested electrode is color coded, and the selectivity between the tested locations interpolated to obtain a continuum. Step 8, The selectivity indices obtained for the electrodes located at each corner of the paddle lead (from left to right, targeting motoneurons eliciting hip flexion or ankle extension) are aggregated into a combined selectivity index that defines the performance of the paddle lead at the tested position. The optimal position for the paddle lead was defined as the position for which the highest combined selectivity index was obtained (most yellow rectangle). Step 9, Optimal position of the new paddle lead predicted based on a personalized computational model but a generic distribution of motoneuron locations. Step 10, Intraoperative quantification of the combined selectivity index, and thus identification of the optimal position of the new paddle lead. The predicted optimal position of the paddle lead based on a personalized model with the identified projectomes of proprioceptive neurons matched the optimal position validated intraoperatively, whereas simulations based on the averaged location of motor pools across the human population failed to predict the optimal position. Step 11-13, The procedures described in Steps 8-10 were repeated for the Specify 5-6-5 paddle lead. Note that the intraoperative validation of the optimal position of the Specify 5-6-5 was restricted to one position to minimize the duration of the surgical intervention. 188

5.8 Impact of model abstractions to determine the optimal position of the paddle lead. Step 1, Generalized computational model of the interaction between EES and the spinal cord, including the location of motoneurons from key leg muscles. Step 2, Personalized computational model of the interaction between EES and the spinal cord for the three participants. The models are aligned with the generalized model depicted in Step 1. Step 3, Simulations predict the optimal position of the new paddle lead for each participant, following the procedures explained in Extended Data Figure 4, but based on various model abstractions, as explained in the boxes above each prediction. Step 4, The optimal position of the new paddle lead was validated intraoperatively, as explained in Fig. 5.7, and is shown on a CT scan reconstruction. The horizontal yellow line passing through the top electrodes of the paddle lead highlights the optimal position, thus allowing a direct comparison between the various predictions and the optimal position. The fully personalized models achieved the best performance. 191

5.9 Configuration of activity-dependent stimulation programs. a, Library of optimized anode and cathode configurations and stimulation frequencies to modulate motor pools associated with the key phases of gait, as highlighted with the color code. b, Sequence of muscle activity underlying walking in healthy people, converted into a spatiotemporal map of motoneuron activity that highlights the timing and location of motor hotspot activation; translated into a preprogrammed sequence of stimulation bursts (template) that aims to reproduce this activation pattern. Color code as in (a). The configurations of electrodes targeting each hotspot are derived from the library, and injected into this template. c, Software enabling live adjustments of stimulation patterns and parameters based on real-time feedback from muscle activity and kinematic sensors that are synchronized with stimulation sequences. d, Walking on a treadmill with stimulation after less than one hour of configuration, including sequence of stimulation and underlying muscle activity. e, Independent walking between parallel bars less than one week after the onset of the therapy. f, Chronophotography of sit-to-stand, swimming, leg-press and motomed exercises enabled by activity-specific stimulation programs, displayed at the bottom of each chronophotography. 193

5.10 Purpose software for configuration, optimisation, evaluation and implementation of activity. Step 1, A custom-built software named GDrive+ integrates signals from video cameras, sensors of muscle activity, and inertial measurement units (accelerometers and gyroscopes) in real-time and wirelessly. Each configuration of electrodes targeting a given hotspot/muscle group is color-coded in the interface, and is visualized onto the kinematic and physiological signals when EES is turned on. This synchronized visualization provides direct feedback to configure and optimize activity-specific stimulation programs. This configuration is performed via dedicated graphical interfaces that allow to change the timing and parameters of stimulation directly onto a stimulation scheduler and ergonomic windows, including touch screens. This software allows the configuration and personalization of activity-dependent stimulation programs in less than one hour. Step 2, EES commands are transmitted to the Implantable Pulse Generator (IPG) via Bluetooth (1) to a module that converts them into infrared signals (2), which are then transferred to the stimulation programmer device (2). The stimulation programmer transmits EES commands into the IPG via induction telemetry (4), using an antenna (3) taped to the skin and aligned to the IPG. EES is delivered through the paddle array (5). This communication chain allows the control of up to 4 concomitant stimulation waveforms in real-time, with a response latency of approximately 120 ms. Step 3, A handheld tablet and connected smartwatch (1) running our custom-made software App provide user-friendly interfaces for therapists and participants to select activity-specific stimulation programs (2) and to adapt relevant stimulation parameters of these programs (3) to perform rehabilitation exercises or support activities of daily living. Custom-built ergonomic clickers (4) or inertial measurement units (5) are placed on the body or assistive devices to ensure that the stimulation is delivered with a timing corresponding to the intended movement. 195

5.11 Configuration of trunk-specific stimulation programs. a, Stimulation of the dorsal root projections to the T12 spinal segment modulates trunk and abdominal muscles, b, as shown in muscle responses. c, Temporal course (color-coded) of coronal plane trunk trajectory elicited by side-specific stimulation. d, Chronophotography of a sequence of trunk flexion and extension. The onsets highlight trunk posture at rest without and with a stimulation program optimized for modulation of motor pools innervating trunk muscles. e, Bar plots reporting the time necessary to complete the return phase (extension) of the flexion / extension sequence of trunk movements for the 3 participants, compared to 5 healthy individuals (Mann- Whitney test, *, p<0.05; **, p<0.01). 197

5.12 Recovery of independence in the community. a, Chronophotography of independent walking outdoors after 6 months of practice with activity-specific programs. b, Progressive recovery of weight bearing capacity during walking over the course of the 6 months of practice. c, Bar plots reporting performance in the six-minute walk test and ten-meter walk test before and after neurorehabilitation with activity-specific stimulation programs. No assistance was provided during these tests. d, Standing for extensive periods of time for boxing or enjoying a drink at a high table of a bar. e, Stimulation programs for trunk stability while paddling were developed in the lab, and then used to support paddling activity on a lake. Bar plots report the number of paddle strokes per minute with and without EES. f, Bar plots reporting changes in thigh and trunk muscle mass, quantified as total/specific cross-sectional area. g, Amplitude of muscle activity for each of 1240 strokes performed over one hour. Bar plots report the mean amplitude of muscle activity without EES (gray), and calculated during the 100 first and 100 last cycles (red). Photographs illustrate the setting for the development of cycling stimulation, and its use community settings. 199

5.13 Configuration of activity-specific stimulation protocols. Step 1, The participant is lying supine in a relaxed posture. Wireless sensors are positioned over selected leg muscles to monitor electromyographic signals in conjunction with leg kinematics using an optical 3D motion capture system. Step 2, Intraoperative imaging of the final paddle lead position guides the realignment of the paddle lead with respect to the personalized model of the interactions between EES and the spinal cord. The optimal cathode to target specific motoneurons are inferred based on the location of the electrodes with respect to the dorsal roots and location of motoneurons identified from fMRI measurements. Step 3, The performance of the preselected optimal cathode is assessed using trains of pulses delivered with predefined frequency ranges that are optimal for the targeted motoneurons. Step 4, The muscle responses are quantified from 40 to 500 ms after stimulation onset, and then normalized with respect to a baseline window selected 500ms before stimulation onset. The relative amplitudes of muscle responses are represented in a polar plot that allows to appreciate the relative recruitment of each muscle. Step 5, A physiotherapist grades the precision of the elicited movements and muscle activity based on a simple clinical scale that enables the quick adjustment of anode and cathode configurations to achieve the most optimal selectivity. Step 6, This procedure enables the rapid elaboration of a library of anode and cathodes targeting specific muscles and motor hotspots, which are then implemented in preprogrammed stimulation templates that aim to reproduce the natural activation of muscles during the desired activity. 203

5.14 Configuration of frequency-specific EES trains to elicit functional muscular and kinematic activity. Step 1, Configuration of electrodes to target the hotspots associated with weight acceptance (top) and whole-leg flexion (bottom). Example from participant P3. EES bursts are delivered at 20 Hz. (weight acceptance, optimal frequency for motoneurons innervating extensor muscles) and 100 Hz (whole-leg flexion, optimal frequency for motoneurons innervating flexor muscles) to elicit muscle responses, recorded from the Iliopsoas (Il), Rectus Femoris (RF), Vastus Lateralis (VLat), Semitendinosus (ST), Tibialis Anterior (TA), Gastrocnemius Medialis (MG), and Soleus (Sol) muscles (mean response, n=5 repetitions). The muscles associated with the targeted hotspot are color-coded. Polar plots report the normalized muscle responses, using the same convention as in Fig. 5.13. Polar plot units are normalized with respect to the baseline (n-fold). Bar plots report the amplitude of associated kinematic responses from each joint, and the selectivity indexes for targeted and non-targeted muscles. Step 2, Similar representations are shown for participant P1. 205

5.15 Immediate recovery of independent stepping with EES. Step 1, Kinematic and muscle activity underlying stepping on a treadmill without and with EES on the very first day of stimulation for the 3 participants. Bar plots report quantification of the muscle activity, and the range of motion for the hip, knee and ankle in both conditions. Muscular activities are quantified as Mean Absolute Value over their expected phase of activity. Step 2, Number of independent steps performed during the very first day of stimulation. Step 3, Chronophotographies showing normal and voluntarily exaggerated steps while stimulation parameters remain otherwise unchanged. Bar plots report the mean step length quantified during normal and exaggerated steps (Mann-Whitney test, *, $p<0.05$; **, $p<0.01$; ***, $p<0.001$,****, $p<0.0001$). 207

5.16 Selective recruitment of trunk muscles. Step 1, Trunk and abdominal muscles are primarily innervated by motoneurons located in the thoracic region of the spinal cord. The new paddle array enables targeting the dorsal roots projecting to the T12 spinal segment, allowing the recruitment of trunk and abdominal muscles. Step 2, Single pulses of EES at increasing amplitude are delivered over electrodes to evaluate their ability to recruit trunk and abdominal muscles. Muscle responses are calculated, normalized, and then represented in a polar plot. The selectivity of trunk/abdominal versus leg muscle activation is calculated with a selectivity index formula. Side-specific recruitment of trunk and abdominal muscles is obtained with the upper electrodes of the new paddle lead. Step 3, Polar plots reporting the activation of trunk/abdominal muscles versus leg muscles when delivering EES through various electrodes of the new paddle lead, as indicated by the number referring to the electrodes depicted in step 2. Step 4, Trains of EES are delivered through the same electrodes as in Step 2 to elicit kinematic responses. For each tested electrode, the panels depict the mean time-dependent trajectory of trunk and knee movements in the plane perpendicular to the direction of gravity, and bar plots reporting the mean amplitude of trunk and knee movement in abduction or adduction. Electrodes 1 and 4, which are located over the top row of the new paddle lead, elicited side-specific trunk movement without disturbing knee movements. 208

5.17 Immediate recovery of trunk control. Step 1, Participant P2 performing repeated front pull movement on a medicine ball without stimulation (black/EES OFF) and with EES targeting the T12 dorsal root (red/EES ON). Radius of curvature of the lumbar region is measured at position 3, which is the most difficult position for the participants to stabilize. Exercises were repeated 4-5 times in each condition (EES OFF/ON). Step 2, Representation of the trunk muscles engaged in the execution of the task (grey) and EES targeted muscles (red), together with the electrode configuration to target the subset of these muscles affected by the SCI. Step 3, Bar plots reporting the radius of curvature of the lumbar region at position 3 and the execution time of the whole exercise for each participant (Mann-Whitney test, *, $p<0.05$; **, $p<0.01$). Step 4, Participant P2 performing repeated lumbar lordosis correction in four-point kneeling position in the absence of stimulation (black/EES OFF) and with a stimulation program that targeted trunk, abdominal and gluteus muscles to stabilize the four-point kneeling position (red/EES ON). Radius of curvature of the lumbar region is measured at the time of maximal contraction and maximal relaxation of the lower back. Exercises were repeated 4-5 times in each condition (EES OFF/ON). Step 5, Same as Step 2. Step 6, Bar plots reporting the lumbar curvature without and with stimulation. Step 7, Participant P2 performing repeated front shoulder raise in the absence of stimulation (black/EES OFF) and with EES (red/EES ON). Exercises were repeated 4-5 times in each condition (EES OFF/ON). Step 8, Same as Step 2. Step 9, Changes in position of the wrist in the vertical plane during the front shoulder raise movement, showing improved symmetry and range of motion with EES turned on. The bar plot reports the execution time of this task with and without EES, and in healthy individuals for comparison. Step 10, Dips lifting hip. In the absence of stimulation, the participant (P1) is able to lift his own body-weight but is not able to lift his pelvis (black). With EES, he is able to activate his lower abdominal and oblique muscles to lift his pelvis on both sides. Step 11, The participant (P1) is using a torso rotation machine at the gym. In the absence of stimulation, he is able to rotate to both sides lifting 10kg. EES enables him to perform this exercise with twice this weight as represented on the bar plot. . . . 210

5.18 Volitional activation of muscles. a, While lying in a supine position, participants were requested to attempt to perform three successive flexions of the right hip without EES and in the absence of any facilitation manoeuvres. Data is shown before the neurosurgical implantation and after 6 months of neurorehabilitation supported by EES. b, EMG activity was recorded from the right Iliopsoas. Two out of 3 participants with complete sensorimotor paralysis recovered volitional activation of the Iliopsoas muscle with EES turned off. 212

6.1 Overview of computational models developed for hemodynamic control with EES. a. Hybrid computational model of low thoracic and lumbar rat spinal cord. b. Recruitment profiles from cathodic stimuli applied over electrodes mapped out in a. c. Sketch of the electric field as a result of a FEM approach in model a. c. Hypothesized circuitries underlying hemodynamic control with the recruitment of large-diameter, myelinated afferent fibers. e. Results of circuit-level modeling of proposed circuitries in d. f. Recruitment profile of simulation and experimental validation of mediolateral shifts in cathodic origin of stimulation applied at L2 segment. g. Personalized hybrid compuational model of an individual with SCI to confirm stimulation strategy in-silico. h. Blood pressure change in-vivo in response to stimulation outlined in g. 241
6.2 3D volume of mouse spinal cord. a. CT-reconstruction of skeletal system. b. Transverse crosssection of MRI images. c. Reconstruction of lumbar spinal cord outlines suitable dimensions of implant. 245
6.3 Simulations showing the penetration of light through spinal tissues with various power densities. a. Transverse crosssection of blue-light (wavelength 600 nm) penetration. b. Transverse crosssection of blue and red-light (wavelength 470 nm) penetration. c. Sagital view of blue-light penetration. 246
6.4 Transverse crosssection of heat diffusion in the spinal cord with 6mA (50 $\frac{mW}{mm^2}$), 12mA (100 $\frac{mW}{mm^2}$), 18mA (150 $\frac{mW}{mm^2}$) 247
6.5 Segmentation of high-resolution MRI and CT images enables a 3D reconstruction of the spinal cord in Non-Human Primates (NHPs) and rats. 250

List of Tables

1.1 Sensory fibers listed by diameter and myelination. 12
1.2 Sensory modalities and respective sensory organs. Information was obtained from Abraira and Ginty, 2013. 13

2.1 Kinematic, Kinetic and EMG parameters. 50

3.1 Subjects' data and neurological status according to the International Standards for Neurological Classification of Spinal Cord Injury. 93

4.1 Subjects' neurological status according to the International Standards for Neurological Classification of Spinal Cord Injury at study entry and after completion of the five-month training program. *Reason for AIS C classification in spite of motor scores of 0 throughout all lower extremity key muscles is the presence of voluntary anal contraction. 132
4.2 Weights of agonist and antagonist muscle groups for the calculation of selectivity indices from EMG data. 170
4.3 Myotome of average population. 171

5.1 Demographic and neurological status of participants 213
5.2 Acquisition parameters for MR pulse sequences to image thoracolumbar spine. 216
5.3 Normalized patient-specific projectome as obtained from fMRI. 225
5.4 Myotome of average population. Taken from (Wagner et al., 2018). 226
5.5 Weights of agonist and antagonist muscle groups in the legs for the calculation of selectivity indices for preoperative treatment planning. 226
5.6 Weights of agonist and antagonist muscle groups in the legs for the calculation of selectivity indices from EMG data. 232
5.7 Weights of agonist and antagonist muscle groups of the trunk muscles for the calculation of selectivity indices from EMG data. 233

1 Introduction

The term Spinal Cord Injury (SCI) refers to damage to the spinal cord. This damage can be the result of diseases such as cancer. However, in up to 90 % of cases SCI is due to trauma (Alizadeh et al., 2019). This physical damage to the nervous tissue of the spinal cord occurred with an estimated global incidence rate between 133 and 226 thousand cases in 2007 (B. B. Lee et al., 2014). The affected individuals suffer from a variety of symptoms that differ substantially on an inter-subject level. As the damage occurs at the spinal cord, which itself is composed of nervous tissue, any neurological function that is mediated by the spinal cord can be altered. The severity and range of affected functionalities depend on two factors: 1.) The place of the injury along the spinal cord and 2.) the severity of the injury. This simple rule originates from the segmentalized nature of the spinal cord, which organizes itself along the rostrocaudal axis to control neurological functionalities closest to itself (Fig. 1.1). This topological arrangement is particularly prevalent in the control of motor function, which is the focus of this thesis. The most rostral part of the spinal cord, which is located in the neck and referred to as the cervical spinal cord is assigned to the control of upper limb motor function. The division just below the cervical spine, the thoracic spine, affects muscles found in the chest, back and abdomen. The lower two partitions of the spinal cord, which emerge below the thoracic spine as the lumbar and sacral spine in that order, act on the muscles of the hip and lower limbs. As both hip and leg muscles play an important role in the upright locomotion of humans, the last two spinal divisions are often denominated together as the lumbosacral segments. The underlying neural circuits may act partially independent from the brain but must eventually communicate with it. In a spinal cord injured subject this communication is interrupted at the location of the injury and impaired to the degree of the injury. Any functionality caudal to the lesion may therefore be affected. It is therefore not surprising that some form of loss of lower limb control is reported in most spinal cord injured patients. Roughly 65 % of SCIs result in either partial or complete paraplegia and the remaining 35 % in either partial or complete tetraplegia (Wyndaele & Wyndaele, 2006). The resulting impairment of locomotion, leaves affected individuals dependent on other means of transport such as the use of wheelchairs. During my PhD I set my goal to enable SCI patients to reclaim some form of independence. This ultimately entailed the recovery of lost functionality after SCI.

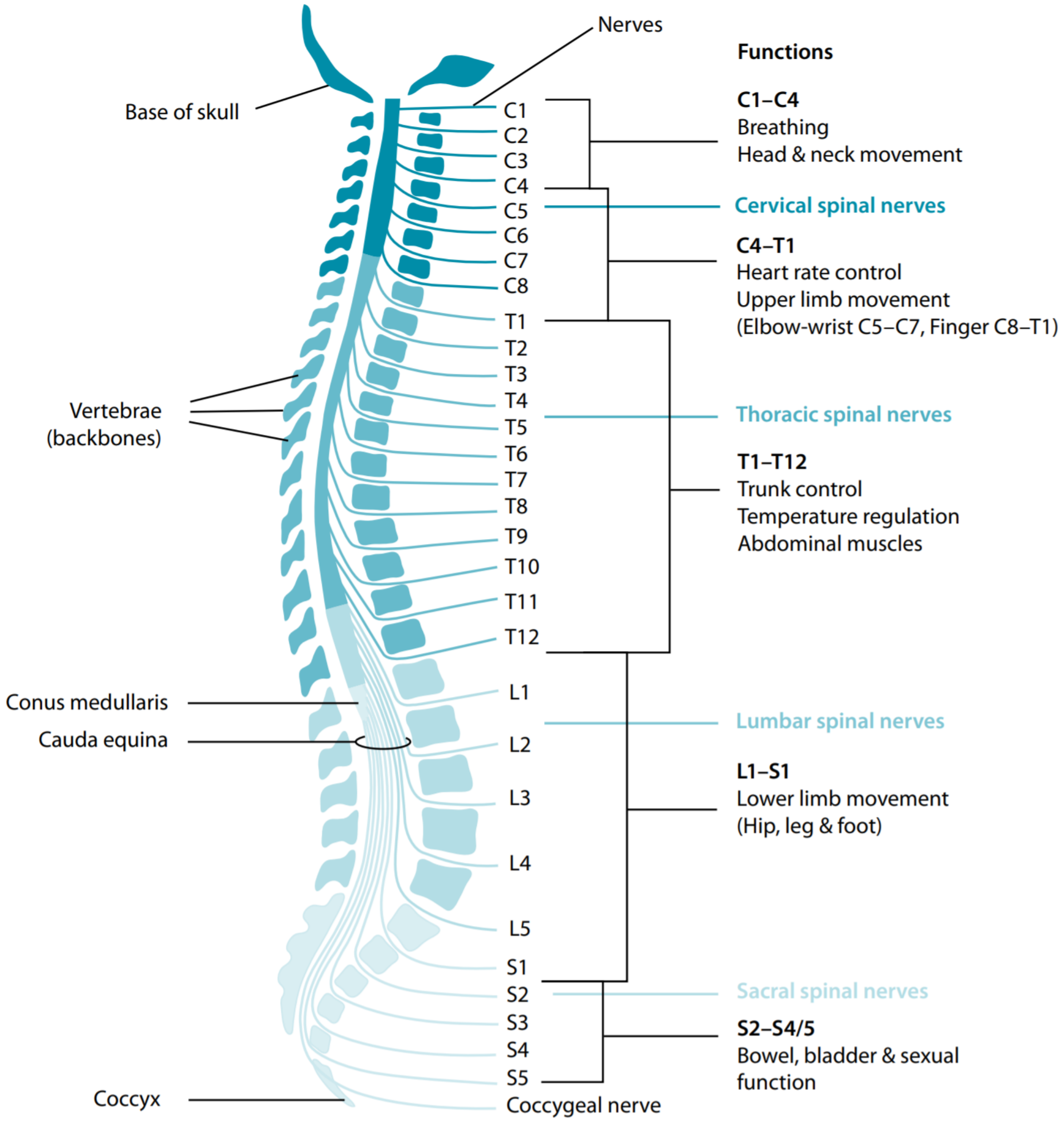
Nerves
Base of skull
Functions
C1
C2
C3
C4
C5
C6
C7
C8
C1–C4
Breathing
Head & neck movement
Cervical spinal nerves
C4–T1
Heart rate control
Upper limb movement
(Elbow-wrist C5–C7, Finger C8–T1)
T1
T2
T3
T4
T5
T6
T7
T8
T9
T10
T11
T12
Vertebrae
(backbones)
Thoracic spinal nerves
T1–T12
Trunk control
Temperature regulation
Abdominal muscles
Conus medullaris
Cauda equina
L1
L2
L3
L4
L5
Lumbar spinal nerves
L1–S1
Lower limb movement
(Hip, leg & foot)
S1
S2
S3
S4
S5
Coccygeal nerve
Sacral spinal nerves
S2–S4/5
Bowel, bladder & sexual
function
Coccyx

Figure 1.1: Rostrocaudal organization of the spinal cord with a brief overview of functionalities associated with spinal nerves. Adapted with permission of World Health Organization, from World Health Organization and International Spinal Cord Society, 2013.

In order to reclaim the lost functionality after SCI this impaired communication between the brain and spinal cord must be in some way recovered. This might either be done through an artificial bridge that circumvents the injury and reintroduces the neural signal through technological means or by leveraging neuroplasticity to re-wire the connection through spared or re-grown tissues. Although a plethora of potential medical interventions can and have been imagined, to this date, the only common medical practices for enhancing neurological recovery are activity-based therapies (Behrman et al., 2017; Field-Fote et al., 2005; Jones et al., 2014).

The underlying hypothesis is simple, volitional engagement of compromised neurological pathways may result in beneficial reorganization of neuronal pathways. However, in contrary, these therapeutic avenues are hindered by the inability of the affected individual to control those functions they wish to improve upon. This conundrum can be simply formulated in the case of locomotion: The affected invididual lost the ability to walk, to recover walking, the individual needs to walk, which the individual cannot. This vicious cycle prompted the development of multifaceted neurotechnologies (Borton et al., 2013) such as lower limb exoskeletons, bodyweight support systems, functional electrical stimulation of muscles, brain stimulation and spinal cord neuromodulation therapies that all share the same goal: enable patients to sustain active movements during task–specific training to enhance the spontaneous reorganization of neuronal pathways.

Among these therapeutic avenues Epidural Electrical Stimulation (EES) applied over the dorsal aspect of the lumbosacral spinal cord has demonstrated impressive restorative effects on the capacity to produce weight-baring standing and walking in animal models of SCI (Asboth et al., 2018; Capogrosso et al., 2016; van den Brand et al., 2012). Originally, EES established itself as a technology for the management of neurological pain (Shealy et al., 1967). Less than 10 years after that, EES was introduced to alleviate spasticity due to Multiple Sclerosis, and it was anecdotally noticed that patients improved in motor function (Cook, 1976). EES was also identified to reduce spasticity (Barolat, 1988) and allow for voluntary mobility across the knee or ankle in several SCI patients, further indicating its utility in supplementing motor activation (M. Dimitrijevic et al., 1986). In conjunction with activity-based training, Courtine et al., 2009 noticed use-dependent plastic changes in sensorimotor circuits caudal to the injury site in animal-models. Transition to human application demonstrated that EES facilitated weight-baring standing, stepping and volitional movement of leg muscles (S. Harkema et al., 2011). Mounting evidence suggests that intentional control of movement of the lower limbs (Angeli et al., 2014; Grahn et al., 2017) as well as independent stepping (M. L. Gill et al., 2018) can be achieved with EES even after motor complete paralysis.

Despite its therapeutic potential, EES has yet to prove itself as a rehabilitative and/or assistive device for SCI patients. Although it is generally accepted that recovery of locomotion is possible when stimulation is applied over the dorsal aspect of the lumbosacral spinal cord, the exact stimulation paradigms that should be used remains a topic of heated debate. The technology and its use-case in SCI patients is too young to draw conclusive evidence about the robustness of various approaches in large and diversified patient-cohorts. This was the question I aimed to tackle in this work. The aim of this work is to aid in the translation of EES as a medical technology for the recovery of neurological deficits after SCI in large and diversified patient-cohorts. My particular focus was the recovery of locomotion after SCI.

In the past, computational modelling has been one of the primary driving factors in understanding the mechanisms underlying the neuromodulation with epidural electrical stimulation (Capogrosso et al., 2013; Moraud et al., 2016; Rattay et al., 2000). In recent years computational modeling has been considered as a key component to accelerate clinical developments (Capogrosso & Lempka, 2020). Particularly, patient-specific computer models have the capacity to aid in clinical translation of neuromodulation technologies (Lempka et al., 2020). For this reason, in my work I aimed at leveraging subject-specific computational modeling to:

1. Contribute to the mechanistic understanding of the interactions between neuromodulation technologies and the neural sensorimotor circuitry underlying locomotion,
2. design personalizable stimulation paradigms targeted at improving locomotion after paralysis,
3. aid in the design of spinal cord stimulation devices tailored to recover locomotion in large and diversified patient cohorts,
4. and translate my work for use in the treatment of other neurological disorders and the development of novel neuromodulation paradigms.

In order to accomplish these goals, I must first clarify specific theoretical understandings underlying the nervous system and its interactions with neuromodulation technologies. In this chapter, I will start by first providing a basic overview of the spinal cord anatomy. I will then give special attention to the neural control of locomotion and its underlying circuitry. Thereafter, I will discuss the possible therapeutic avenues for restoring locomotion after spinal cord injury. I will focus this discussion on the recovery of locomotion with spinal cord stimulation. Then, I will provide a brief overview of the state-of-the-art technologies available for leveraging computational modeling to study neuromodulation technologies. Finally, I provide an outline of how I contributed to advancements in the field of personalizable computational modeling for the restoration of neurological functions.

1.1 Anatomy of the spine

1.1.1 The nervous system in a nutshell

The cornerstone of the nervous system is formed by electrically excitable cells called neurons (Fig. 1.2), forming neural networks transmitting signals electrochemically through connections called synapses. Across the nervous system there are various highly specialized neurons specifically evolved to accomplish their respective tasks. These neurons are structurally similar in that they are comprised of a cellular body or soma, the axon - a thin tubular structure that carries the output signal to the synapse - and the dendrites, which receive the signals from other neurons. The axon of some neurons is wrapped by a thin sheath - the myelin sheath, increasing the speed of electical information conduction. The myelinated axon is subdivided into myelinated portions called internodes and unmyelinated sections referred to as nodes of Ravier.

Electrical information is mediated by neurons through various ions. The ion exchange between the neuron and its surrounding is imperative to the transmission of electrical information through the neuron. To accomplish this task ion channels and ion pumps are distributed throughout the neurons membrane. These pumps regulate the potential difference between the intracellular and extracellular space of the membrane. This membrane potential has an approximate value of -65 mV at resting state.

In the presence of an external stimuli the membrane potential can be altered. In the case of membrane potential increase the membrane is said to be depolarized. The opposite case is referred to as hyperpolarization. Due to particularly dramatic changes in ion potentials the membrane potential can exhibit a very rapid and huge depolarization followed by hyperpolarization lasting approximately 1ms. This event is called Action Potential (AP).

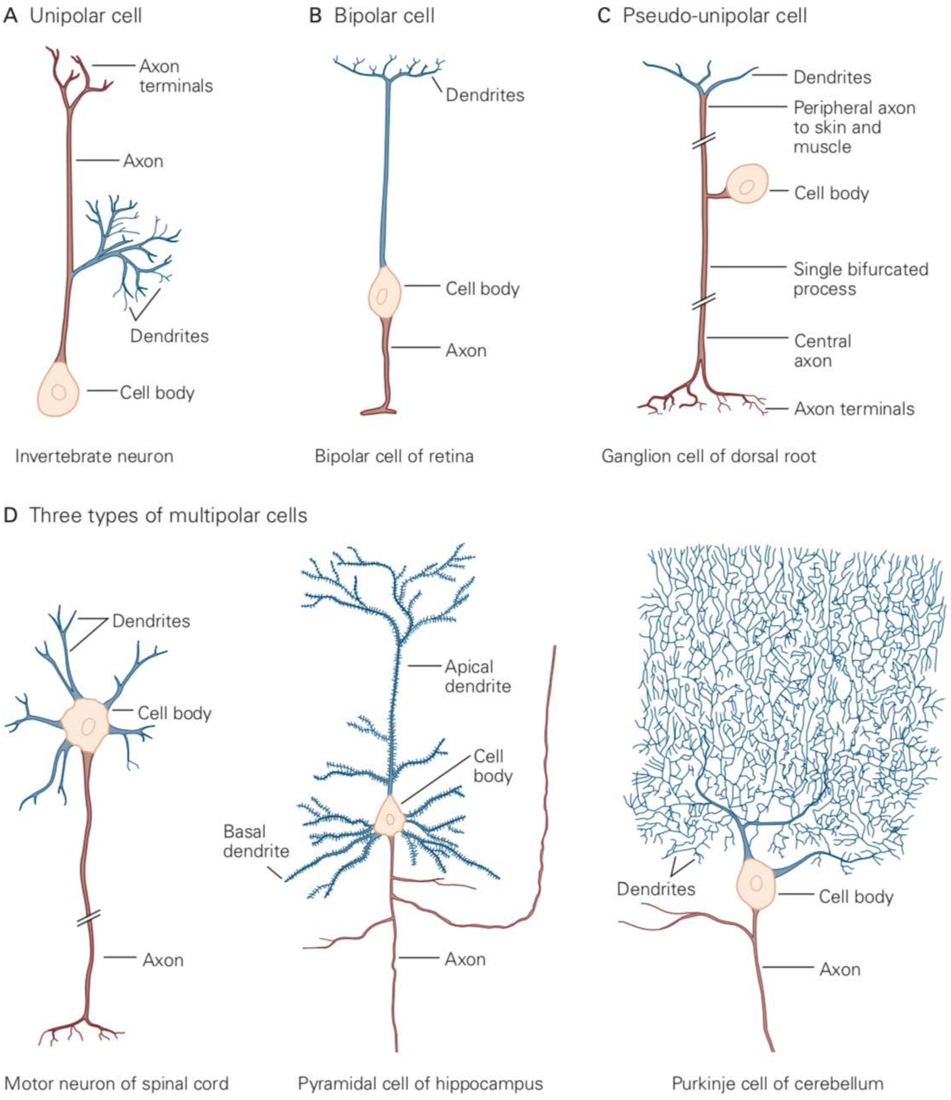
A Unipolar cell
Axon terminals
Axon
Dendrites
Cell body
Invertebrate neuron
B Bipolar cell
Dendrites
Cell body
Axon
Bipolar cell of retina
C Pseudo-unipolar cell
Dendrites
Peripheral axon to skin and muscle
Cell body
Single bifurcated process
Central axon
Axon terminals
Ganglion cell of dorsal root
D Three types of multipolar cells
Dendrites
Cell body
Axon
Motor neuron of spinal cord
Apical dendrite
Cell body
Basal dendrite
Axon
Pyramidal cell of hippocampus
Dendrites
Cell body
Axon
Purkinje cell of cerebellum

Figure 1.2: Various types of neurons. Republished with permission of McGraw-Hill, from Kandel, 2013; permission conveyed through Copyright Clearance Center, Inc..

The AP is the primary communicating signal of the neuron. The AP travels along the axon until it reaches the synaptic terminals at the distal end of the axon. Here specific molecules named neurotransmitters are released in consequence. The neurotransmitters may bind to receptor channels on the post-synaptic membrane of the next neuron, causing depolarization or hyperpolarization of the following neuron in the process. In this manner of synaptic transmission, signals are relayed from one neuron to another.

The complex architecture of neurons in the mammalian nervous system can be roughly divided into two substructures: The Central Nervous System (CNS) and the Peripheral Nervous System (PNS). The latter is defined by the nervous tissue outside the CNS, while the CNS is comprised of two substructures: The brain and the spinal cord. In this thesis I aim to discuss neuromodulation of the spinal cord. Hence, in this chapter I will focus solely on the spine.

1.1.2 Anatomical planes

In order to visually assess the tridimensional structure of the spine on a two-dimensional medium such as this thesis, I must first clarify the terminology below by which I will consistently refer to various cross-sectional views throughout this document. The terminology is summarized and depicted in Fig. 1.3.

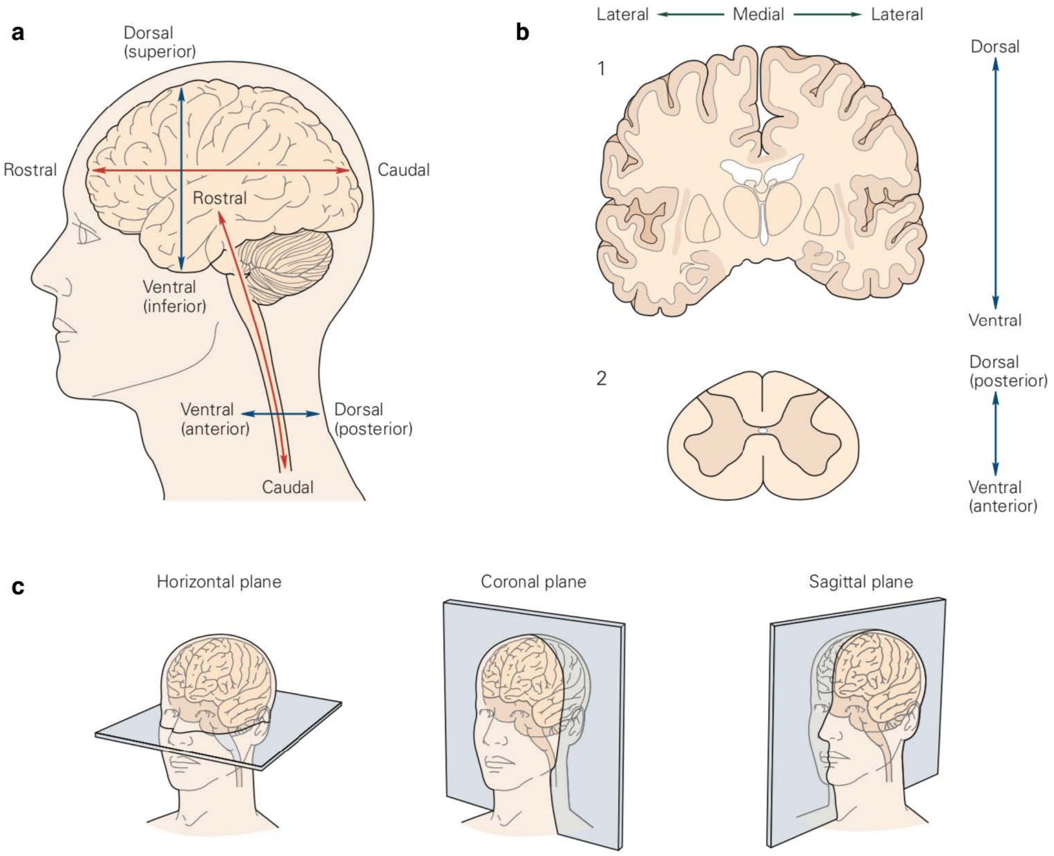
a
Dorsal
(superior)
Rostral
Caudal
Rostral
Ventral
(inferior)
Ventral
(anterior)
Dorsal
(posterior)
Caudal
b
Lateral
Medial
Lateral
1
Dorsal
Ventral
2
Dorsal
(posterior)
Ventral
(anterior)
c
Horizontal plane
Coronal plane
Sagittal plane

Figure 1.3: Sketch of the rostrocaudal and dorsoventral axis (a), dorsoventral and mediolateral axis (b) and the antomical planes (c). Republished with permission of McGraw-Hill, from Kandel, 2013; permission conveyed through Copyright Clearance Center, Inc..

The coordinate system, I will be using, spans three axis defined as:

- Rostrocaudal axis: Direction from head to feet. The rostral vector points towards the head, the caudal vector points towards the feet.
- Mediolateral axis: Direction from inside the spine to the hands. The medial vector points from the hands to the spin. The lateral vector points from the spine to the hands.
- Dorsoventral axis: Direction from the back to the chest. The dorsal vector (also sometimes referred to as posterior) points from the spine to the back. The ventral vector (also sometimes reffered to as anterior) points from the spine to the chest.

It is worth mentioning that this coordinate system is rotated by 90° when assessing the brain (Fig. 1.3). However, the above mentioned definitions will hold true when assessing the spine. The two-dimensional planes of view are defined by the axis missing:

- Horizontal/Transversal/Transverse: Along the rostrocaudal direction.
- Coronal: Along the dorsoventral direction.
- Sagital: Along the mediolateral direction.

1.1.3 The vertebral column

The spinal cord is embedded within the vertebral column, that runs along the rostrocaudal axis of the body. The vertebral column is a series of approximately 33 bones called vertebrae, separated by layers of cartilage named intervertebral discs. It forms the fundamental axis of the upper body. The column supports the weight of the body above the pelvis and aids in movement and posture of the upper body. It critically protects the soft tissues inside the vertebral canal, also named vertebral foramen. The structure of the segments of the spine is visualized in Fig. 1.4.
Each vertebrae is remarkably similar to each other. Although there are some clear anatomical differences, all vertebrae are divisible into two parts: The vertebral body on the ventral side and vertebral arch on the dorsal aspect of the body. The vertebral body is composed of one single semi-cylindrical geometry that bares the predominant load placed on the vertebrae. The vertebral arch on the other hand is further subdivisible into:

- Spinous processes: A central elongation at the dorsal aspect of the arch.
- Transverse processes: A transverse elongation that extends both left and right laterally to the arch. In the thoracic vertebrae, the transverse processes articulate with the ribs.
- Pedicles: The connection points at the lateral sides merging the vertebral body with the arch.

- Laminae: The connections points between transverse and spinous processes.
- Articular processes: Joints between one vertebra and its superior and inferior counterparts. The articular processes are located at the intersection of the laminae and pedicles.

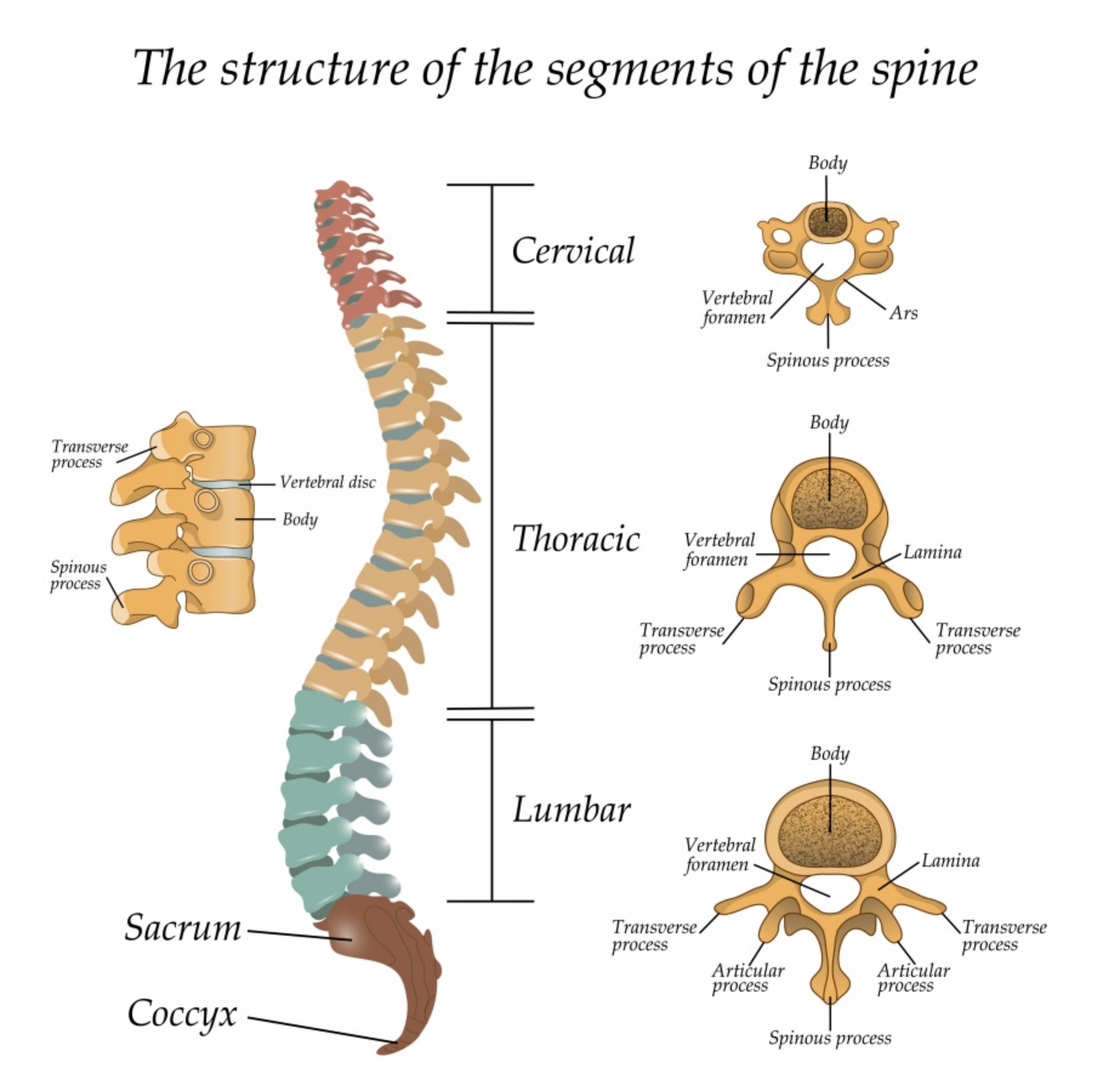
The structure of the segments of the spine
Cervical
Thoracic
Lumbar
Sacrum
Coccyx
Transverse process
Vertebral disc
Body
Spinous process
Body
Vertebral foramen
Ars
Spinous process
Body
Vertebral foramen
Lamina
Transverse process
Transverse process
Spinous process
Body
Vertebral foramen
Lamina
Transverse process
Transverse process
Articular process
Articular process
Spinous process

Figure 1.4: Sketch of the vertebral column (left) and the anatomical organization of vertebrae in the cervical, thoracic and lumbar spine of humans (right). License-free picture from Ellen Bronstayn; Taken from: shutterstock.com.

The vertebral column can be subdivided into five different regions. From rostral to caudal the vertebral column can be classified into a cervical, thoracic, lumbar, sacral and coccygeal area. The usual number of vertebrae in humans per region is 7 for cervical, 12 for thoracic, 5 for lumbar, 5 for sacral and 4 for coccygeal.

The total number of vertebrae and the grouping formula into its subdivisions exhibit a large degree of inter-subject variability. There is little consensus on the exact applicability of the aforementioned guidelines. Frey, 1930 suggests that these rules apply to $\frac{3}{4}$th of the population, while studies from Rosenberg, 1920 and Simons, 1951 suggest an applicability of $\frac{2}{3}$rd on the population.

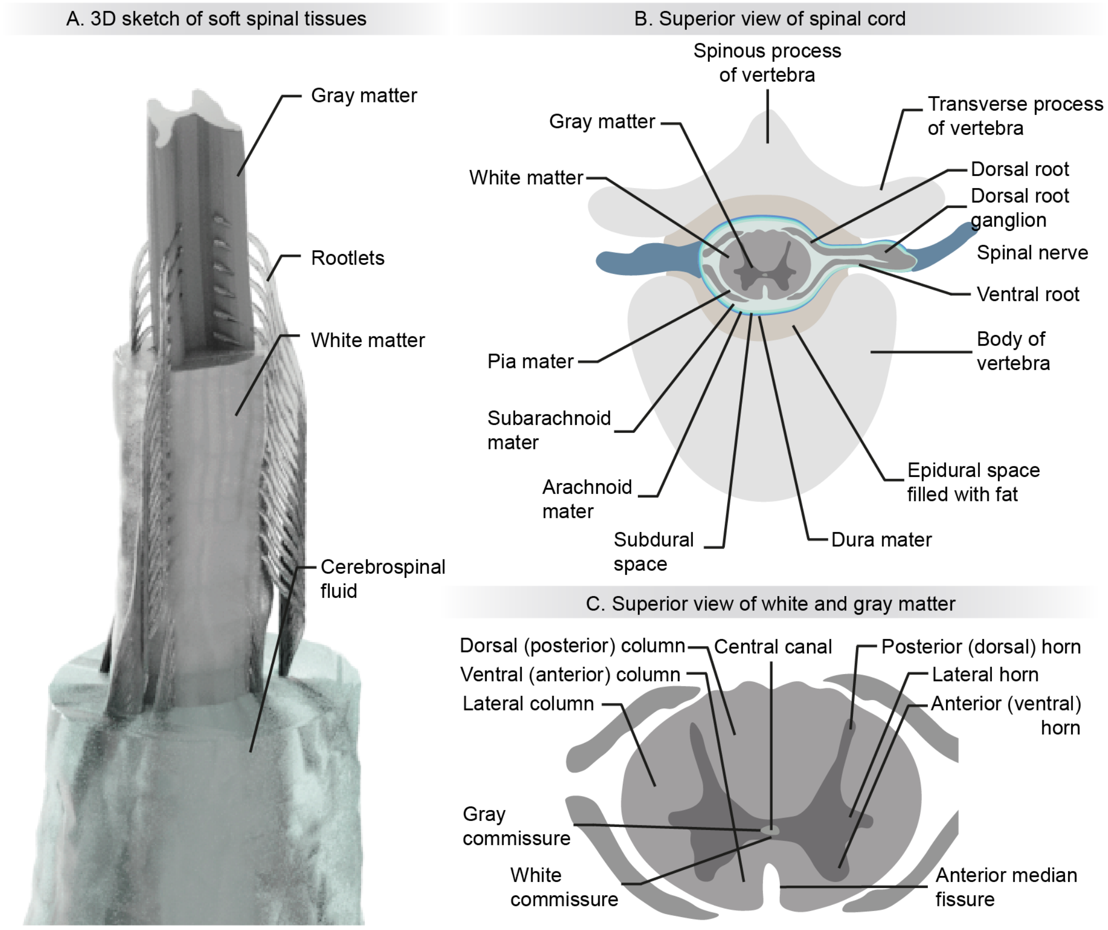

A. 3D sketch of soft spinal tissues

B. Superior view of spinal cord

C. Superior view of white and gray matter

Gray matter
Rootlets
White matter
Cerebrospinal fluid
Spinous process of vertebra
Gray matter
Transverse process of vertebra
White matter
Dorsal root
Dorsal root ganglion
Spinal nerve
Ventral root
Pia mater
Body of vertebra
Subarachnoid mater
Epidural space filled with fat
Arachnoid mater
Subdural space
Dura mater
Dorsal (posterior) column
Central canal
Posterior (dorsal) horn
Ventral (anterior) column
Lateral horn
Lateral column
Anterior (ventral) horn
Gray commissure
White commissure
Anterior median fissure

Figure 1.5: A. 3D sketch of soft spinal tissues and anatomy of rootlets. B. Superior view of a sketch of a transverse cut of the spinal cord. C. Superior view of a sketch of a transverse cut of the white and gray matter.

1.1.4 Organization of the vertebral canal

The vertebral canal is filled with various soft tissues, that are visualized in Fig. 1.5. The nervous tissues inside the vertebral canal are protected by three membranous coverings referred to as meninges. These are from outermost to innermost dura, arachnoid and pia. The space between the dura mater and vertebral structures contains blood vessels and fat. The dura mater is in close contact with the arachnoid mater. The space behind the arachnoid mater is filled with a liquid called CerebroSpinal Fluid (CSF). The dura and its constituents are named dural sac.

The spinal cord is the elongated structure protruding caudally from the brain in the dural sac. It is composed of two tissues. At the center of it there is the Gray Matter (GM). Along the transversal plane, the GM resembles the shape of a butterfly. The protruding wings of this butterfly shape are named by the aspect towards which they extend, namely the dorsal and ventral horn. The GM is encapsulated by the White Matter (WM). Along the transversal plane the WM is elliptical in nature, with a thin fissure at its ventral aspect, named the anterior median fissure. The GM is made up of neural bodies, their dendritic trees and axons that form a complex architecture of synaptic connections. The WM on the other hand is constituted of longitudinal nerve fibers running along the rostrocaudal axis. The WM terminates on average somewhere around the L1 and L2 vertebrae. Along its ventral and dorsal side, it is innervated by spinal nerve roots. The spinal nerve roots connect the PNS to the CNS. They enter into the spinal canal below the pedicles of a vertebrae. The spinal nerve roots connect to the spinal cord splitting into multiple smaller structures along their trajectory, the spinal rootlets, before entering into the WM. The spinal roots on the dorsal aspect of the spinal cord, transport sensory information from the PNS to the CNS. The ventral roots inhabit Motor Axons (MAs) connecting the CNS to muscle fibers. It is important to note that the spinal roots are named by their associated vertebrae. They refer to the vertebrae below which they enter into the spinal canal. The notable exceptions are the cervical roots, which are all but the last associated in their enumeration by the cervical vertebrae above which they enter into the spinal cord. Importantly, I must note that while the rootlets in the cervical spinal cord run almost horizontally along the transverse plane in the spinal canal, this trajectory gets progressively more bent along the rostrocaudal axis when looking at rootlets further caudally in the spinal cord (see Fig. 1.5).

1.1.5 Variability of anatomical dimensions in the human spinal cord

For the purpose of this thesis, it is of utmost importance to discuss the anatomical dimensions in the lumbar and sacral spinal cord in humans. First, I must define the key anatomical parameters that will play an important role in the coming chapters. These are:

- Segmental length: The rostrocaudal dimension from the most rostral rootlet of a single nerve root to the most rostral rootlets of the succeeding spinal nerve root.
- Dorsal Root Entry Zone (DREZ): The mediolateral merging point on the WM at the dorsal rootlets.
- Ventral Root Entry Zone (VREZ): The mediolateral merging point on the WM at the ventral rootlets.
- Rootlet diameter: The diameter of a single rootlet of a spinal nerve root.

- Rootlet number: The number of rootlets emerging from a single spinal nerve root innervating a specific spinal segment.

Many studies have successfully quantified key anatomical parameters in the human spinal cord (Frostell et al., 2016; Ko et al., 2004; Liu et al., 2015; Mendez et al., 2020; Toossi et al., 2020). Unfortunately, the anatomical assessment of the segmental length in the lumbar and sacral spinal cord not only exhibits a significant deviation between subjects in a single study, but the various studies disagree on the exact anatomical dimensions on the segmental length (Frostell et al., 2016; Ko et al., 2004; Mendez et al., 2020; Toossi et al., 2020). In turn, vertebral bone length seems to exhibit a significantly lower variability (Mendez et al., 2020). This discrepancy in anatomical variability between segmental length and vertebrae bone length contributes to the substantial variation in the rostrocaudal position of spinal cord segments relative to the vertebral column (Cadotte et al., 2014). This makes locating the spinal segments with anatomical landmarks a challenging feat.

Similar observations hold true for the other anatomical parameters. However, rootlet diameters seem to be less variable between subjects (Liu et al., 2015), although ventral rootlet diameter may exhibit more inter-subject variability than dorsal rootlet diameter (Mendez et al., 2020). In turn, rootlet numbers seem to be highly variable (Liu et al., 2015). This may be due to the fact that lumbar and sacral segments are innervated by a continuum of rootlets, that at least for the dorsal aspect can be described as well-organized and linear (Mendez et al., 2020). With relatively consistent spinal rootlet diameters, the number of rootlets necessary to innervate a spinal segment depends on the segmental length. As this value is highly variable between subjects, the number of rootlets may be highly variable as a consequence.

The entry zone of the dorsal roots (DREZ) and ventral roots (VREZ) are hugely important for spinal cord stimulation. It is important to note that there is little variation in the anatomical parameters surrounding the DREZ such as its width (Mendez et al., 2020). However, these parameters are difficult to evaluate for the VREZ (Mendez et al., 2020). This may be due to the fact that the dorsal rootlets enter the DREZ in something approximating a single line along the rostrocaudal axis (Mendez et al., 2020). The VREZ on the other hand is less organized (Mendez et al., 2020).

1.2 Neural control of locomotion

Locomotion is one of the most basic functions of humans and animals. It is defined as the capacity to move from one place to another. This entails a whole range of transportation modes such as walking, stepping or swimming. These movements seem effortless and can happen in the absence of conscious decision making. This automaticity comes at the price of a highly complex architecture of neural connections in vertebrates, that can be roughly organized into three levels of control: The brain, the spinal cord and the PNS.

Firstly, planning and initiation of locomotion originates in supraspinal areas such as the cortex, midbrain, hindbrain, cerebellum and basal ganglia (Drew & Marigold, 2015; Dubuc et al., 2008; Grillner & Robertson, 2015; Jordan et al., 2008). This information is down-propagated through descending pathways to spinal circuits. These spinal circuits are composed of multiple layers of interneurons that can produce the rhythm and pattern of locomotion (Grillner, 2003; Kiehn, 2006). These well-coordinated bursts of activities ultimately reach ensambles of MotoNeurons (MNs) in the ventral horn of the GM. MN pools are connected to distinct muscles via their axons, which are located in the ventral roots (Sharrard, 1964). In this way, harmonic activity patterns reach the muscular system, culminating in well-coordinate and rhythmic movements (Kiehn, 2006, 2016; Sherrington, 1910). In turn, the muscular system together with the rest of the body is permeated with sensory organs, that provide a dynamic representation of the body and its environment. The resulting sensory activity is transmitted back to the spinal cord through the dorsal roots. It enables the spinal circuits to rapidly adjust the movement to functional motor behaviors that are environmentally appropriate by calibrating nervous activity to adjust for different stepping speeds, levels of load imposed during stepping and unpredictable perturbations (Kiehn, 2006, 2016; Rossignol et al., 2006).

Unfortunately, the precise organization of the neural mechanisms underlying locomotion is still a matter of debate. Particularly in humans, where only indirect evidence is collectable, the neural control of locomotion remains enigmatic (Dietz, 2003). Several observations, however, suggest that the neural circuits controlling locomotion are broadly conserved across mammals (Danner et al., 2015; Dominici et al., 2011; Grillner, 2011; Nadeau et al., 2010). Therefore, it is reasonable to assume that neural control of locomotion is similarly organized across species. In the following chapters, I will give a broad overview of the various levels of organization underlying the neural control of locomotion. Unless stated otherwise, I will assume that the discussed mechanisms apply to all mammalian species.

1.2.1 Somatosensory system

The sensory system is often colloquially classified into five sensory modules. These are gustation, vision, olfaction, balance and hearing. In reality, a sixth sense is present in humans and animals: Somatosensation. Its sensory information originates from various sensory organs distributed across the body and process information in respect to several modalities that enable humans and animals alike to guide their movements, while minimizing the risk of injury. From the sensory organ, the nervous activity travels across the axons of afferent neurons from the PNS to the CNS through the spinal roots. Distinct groups of afferent fibers can be attributed to specific sensory organs. A broad overview is given in Table 1.2.

Fiber	Diameter	Myelination
Aα	10-20 μm	Yes
Aβ	7-15 μm	Yes
Aδ	2-5 μm	Thin
C	0.1-0.5 μm	No

Table 1.1: Sensory fibers listed by diameter and myelination.

Afferents can be roughly classified by their respective diameter and myelin content. The respective values are species-dependent. Table 1.1 depicts this categorization for humans.

Modality	Response to	Sensory organ	Afferent
Nociception	mechanical stimulation	high threshold mechanonociceptors	Aβ,Aδ, C
	mechanical and thermal stimulation	thermal nociceptors	Aδ, C
	chemical substances	chemical nociceptors	Aδ, C
	all of the above	polymodal nociceptors	Aδ, C
	inflammation or injury	silent nociceptors	Aδ, C
Thermoception	warm/hot	bulboid corpuscle	C
	cool/cold	bulboid corpuscle	Aδ
Mechanoreception	rapid vibration	Pacinian corpuscles	Aβ
	light touch	Meissner's corpuscles	Aβ
	sustained pressure	Merkel's discs	Aβ
	deep tension	bulboid corpuscle	Aβ
	touch, pressure, stretch, tickle and itch	Free nerve endings	Aβ, Aδ, C
	hair follicle deflection	longitudinal lanceolate ending	Aβ, Aδ, C
	stretch of blood vessel	Baroreceptor	Aβ, Aδ, C
Proprioception	intramuscular stretch	Muscle spindles	Aα,Aβ
	tendon stretch and passive muscle stretch	Golgi tendon organs	Aα

Table 1.2: Sensory modalities and respective sensory organs. Information was obtained from Abraira and Ginty, 2013.

Multiple afferents are bundled together into single roots. Which dorsal root contains which afferent is dependent on the location of the sensory organ in the body. In turn, which ventral root contains which efferent is dependent on the location of the innervated muscle in the body. These two informations are key in the pursuit of restoration of motor function after paralysis. I will explain why this is the case in section 1.3. For now, I need to make two definitions that will be invaluable in the coming chapters. Firstly, I will refer to the innervation pattern of proprioceptive sensory afferents in the segments of the spinal cord as the projectome. Secondly, I will utilize the commonly used terminology of myotome to refer to the innervation pattern of MAs in the segments of the spinal cord.

Although the projectome is not well established in humans, a lot of studies have tried to decipher the myotome in humans (Schirmer et al., 2011; Sharrard, 1964). These studies demonstrate a rostrocaudal distribution with upper limb muscles innervated in the cervical spinal cord, trunk muscles innervated in the thoracic spinal cord and lower limb muscles innervated in the lumbar and sacral spinal cord. In particular the myotome of lower limb muscles is interesting to me as it will help me to recover locomotion with spinal cord stimulation. It is important to note that these studies also demonstrate a large degree of inter-subject variability in the innervation pattern. Sharrard, 1964 suggests that on average one or two spinal nerve roots innervate a particular muscle in a given individual. However on a group level the distribution of the innervation pattern widens significantly. As an example, the iliopsoas muscle is primarily innervated by the L1 spinal nerve root (Schirmer et al., 2011; Sharrard, 1964). However, Schirmer et al., 2011 was able to demonstrate that among all the subjects he studied there are subpopulations of individuals with innervation patterns in spinal roots between L2-S1 of the iliopsoas muscle.

Of all sensory modalities, cutaneous and proprioceptive sensory organs play a particularly important role in walking. In the next section, I give a broad overview over their spinal sensorimotor interactions.

Cutaneous sensory feedback

Cutaneous sensory organs in the skin encode information in regard to the perception of touch (Abraira & Ginty, 2013). Many cutaneous sensory organs, often referred to as mechanoreceptors, can be differentiated depending on their respective sub-modality. A rough classification can be made into two families of mechanoreceptors: Light-Threshold MechanoReceptors (LTMRs) and High-Threshold MechanoReceptors (HTMRs). A summary of all LTMR and HTMR sensory end organs is visualized in Fig. 1.6.

The former include Merkel's discs, Meissner's corpuscles, Pacinian corpuscles and free nerve endings that sense innocuous mechanical stimulation. With the exception of longitudinal lanceolate ending, which are also innervated by Aδ and C afferents, all other LTMRs are mediated by Aβ afferents (Abraira & Ginty, 2013).

In turn, HTMRs respond to harmful mechanical stimuli. HTMRs are composed of free nerve endings and are innervated by Aβ, Aδ and C afferents (Abraira & Ginty, 2013).

Lastly, mechanoreception can also take place in the autonomic nervous system. These baroreceptors encode information regarding the stretch of blood vessels to maintain systemic blood pressure at a relatively constant level, especially during a change in body position. They can be divided into high and low pressure baroreceptors and are innervated by Aβ, Aδ and C afferents (Chapleau et al., 2006).

Cutaneous sensory input may have numerous effects on locomotion. Firstly, cutaneous sensory signals may be involved in the fine control of the feet during locomotion (Bouyer & Rossignol, 2003a). Secondly, cutaneous stimulation applied at the feet modulates motor output dramatically (Rossignol et al., 2006). Lastly, cutaneous sensory signals can both initiate and stop the spinal network activity underlying locomotion (Fleshman et al., 1984; Rossignol et al., 2000; Viala & Buser, 1974).

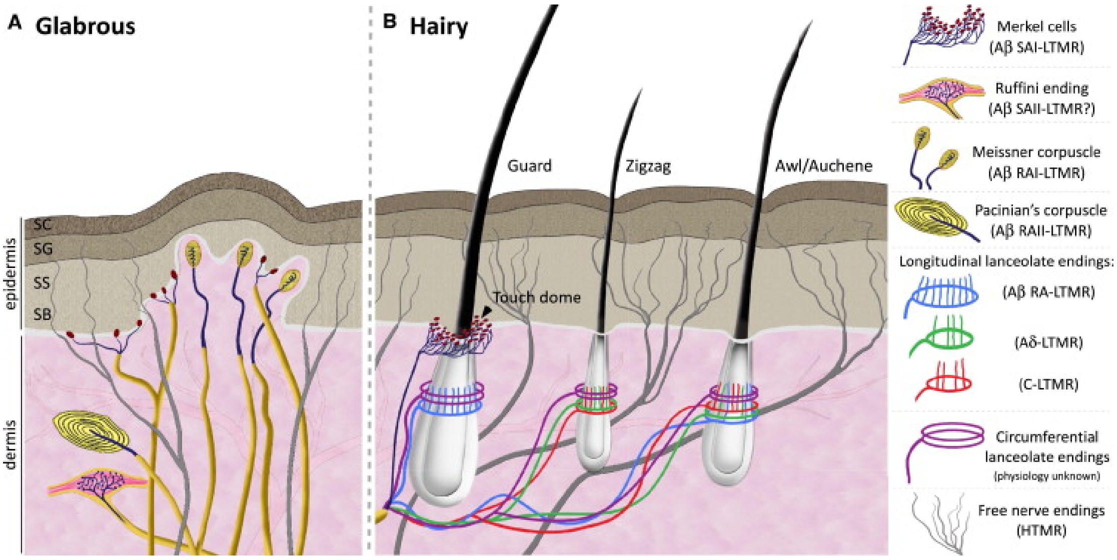
A Glabrous
B Hairy
SC
SG
SS
SB
epidermis
dermis
Guard
Zigzag
Awl/Auchene
Touch dome
Merkel cells
(Aβ SAI-LTMR)
Ruffini ending
(Aβ SAII-LTMR?)
Meissner corpuscle
(Aβ RAI-LTMR)
Pacinian's corpuscle
(Aβ RAII-LTMR)
Longitudinal lanceolate endings:
(Aβ RA-LTMR)
(Aδ-LTMR)
(C-LTMR)
Circumferential
lanceolate endings
(physiology unknown)
Free nerve endings
(HTMR)

Figure 1.6: The organization of cutaneous mechanoreceptors in the skin. Republished with permission of Elsevier, from Abraira and Ginty, 2013; permission conveyed through Copyright Clearance Center, Inc..

Proprioceptive sensory feedback

Proprioceptive sensory organs can be divided into muscles spindles and Golgi Tendon Organs (GTOs). These sensory organs are located throughout the musculoskeletal system and are innervated by afferents as depicted in Fig. 1.7.

Muscle spindles are located in the muscle belly and are composed of intrafusal muscle fiber which themselves are attached to neighboring extrafusal fibers. Each intrafusal fiber is constructed of a central non-contractile element and two contractile compartments, one at each extremity. The central element is innervated by two types of afferents: Type Ia and type II afferents. These afferents transduce muscle length information encoded in the muscle stretch. Both types of afferents respond slightly different to muscle stretch information and their firing rates can be expressed as summarized in Eqn. 1.1 and 1.2 (Prochazka & Gorassini, 1998a, 1998b). Ia-afferents are part of the Aα fiber family, while type II afferents are categorized as Aβ fibers.

$$f_{Ia}(t) = f_{Ia} + 2 \cdot d(t) + 4.3 \cdot sign(v(t)) \cdot |v(t)|^{0.6} + 50 \cdot EMG_{env}(t) \tag{1.1}$$

$$f_{II}(t) = f_{II} + 13.5 \cdot d(t) + 20 \cdot EMG_{env}(t) \tag{1.2}$$

Here, the firing rates of type Ia $f_{Ia}(t)$ and type II $f_{II}(t)$ afferent fibers is determined by the stretch of their muscle fibers $d(t)$, the rate of change of this muscle stretch $v(t)$, their respective mean firing rates f_{Ia}, f_{II} and the envelope of the ElectroMyoGraphy (EMG) activity EMG_{env}. The other important sensory information encoded in proprioceptive signals is the force generated by a muscle. This information is extracted by GTOs located in the musculotendinous junction. GTOs are innervated by type Ib afferents. Their firing rate can be calculated by means of the normalized EMG activity and its second-order differential ΔEMG as described in Eqn. 1.3 (Prochazka & Gorassini, 1998a, 1998b). Ib afferents are categorized as Aα fibers.

$$f_{Ib}(t) = \frac{4500 \cdot EMG \cdot (\Delta EMG + 0.15) \cdot (\Delta EMG + 1.5) \cdot (\Delta EMG + 16)}{(\Delta EMG + 0.2) \cdot (\Delta EMG + 2) \cdot (\Delta EMG + 37) \cdot (\Delta EMG + 12)} \tag{1.3}$$

Proprioceptive signals are major driving factors in the production of motor output during locomotion. They reinforce and adapt MN activity, regulate the timing of locomotion and similarly to cutaneous signals can initate and block locomotion (Courtine et al., 2009; Dietz & Duysens, 2000; K. Pearson, 2008; Rossignol et al., 2006; Takeoka et al., 2014). To accomplish this wide range of complex tasks, the proprioceptive circuitry in the spinal cord has a sophisticated architecture. A few key features can be extracted that are of huge importance for the coming chapters.

Firstly, Ia afferents, located in a muscle, form excitatory monosynaptic connections with the homonymous MN pool. Albeit to a lower extent, they also form connections to other synergistic muscles. They are also involved in more complex di- and oligosynaptic circuits as described in chapter 1.2.2. Secondly, while group II afferents form disynaptic excitatory pathways with the homonymous muscle, they may also be able to evoke a flexion reflex (Rossignol et al., 2006). Finally, although the exact circuitry of the Ib afferents remains enigmatic, they may play an important role in weight-bearing during locomotion through oligosynaptic connections (Dietz & Duysens, 2000).

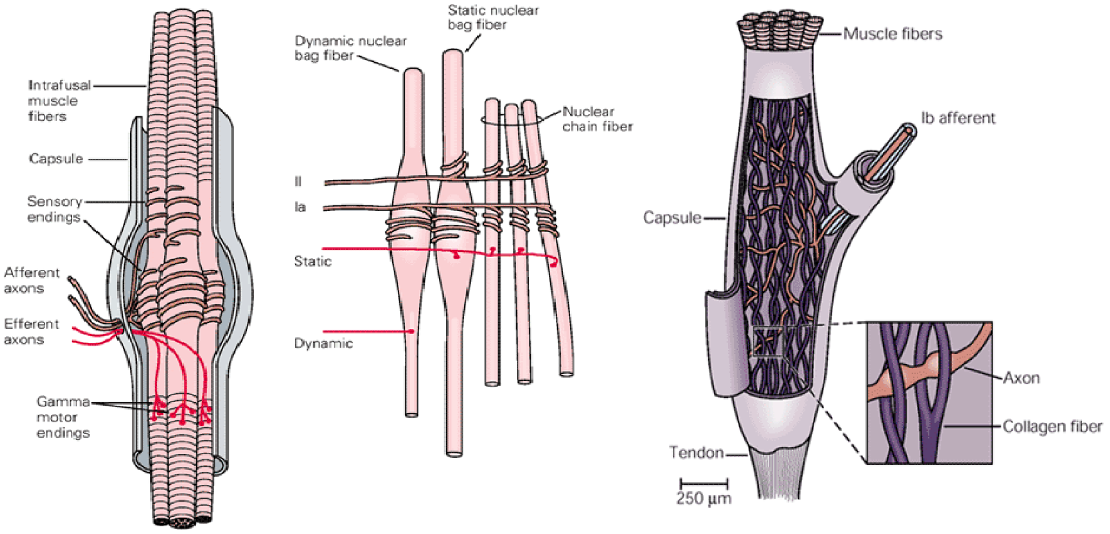
Intrafusal muscle fibers
Capsule
Sensory endings
Afferent axons
Efferent axons
Gamma motor endings
Dynamic nuclear bag fiber
Static nuclear bag fiber
Nuclear chain fiber
II
Ia
Static
Dynamic
Muscle fibers
Ib afferent
Capsule
Axon
Collagen fiber
Tendon
250 µm

Figure 1.7: Sketch of intrafusal muscle fibers (left), type Ia and II afferents (middle) and Ib afferents (right). Adapted with permission of McGraw-Hill, from Kandel, 2013; permission conveyed through Copyright Clearance Center, Inc..

1.2.2 Spinal locomotor network

Experiments with deafferented cats with a complete transection of the spinal cord revealed that the spinal cord can produce rhythmic alternating activity of the flexor and extensor muscles of the ankle in the absence of this sensory information (Brown & Sherrington, 1911, 1912). It is for this reason that Brown hypothesized that neural networks within the spinal cord, successively termed Central Pattern Generators (CPGs), have the intrinsic ability to generate the pattern of muscle activations underlying locomotion (Brown, 1914) (see Fig. 1.8). These muscle activations can be broadly classified into three tasks. Firstly, neurons in the locomotor CPG generate the rhythm and pattern of muscle contraction (Kiehn, 2006, 2016). Secondly, muscle activities need to be coordinate within a limb to ensure alternation of flexor-extensor pairs (Kiehn, 2006, 2016). Lastly, activity between pairs of limbs need to be regulated (Kiehn, 2006, 2016). These movement patterns are produced in the spinal cord by circuits that may:

- Produce the rhythm underlying locomotion and set the speed of locomotion,
- ensure bilateral coordination
- and control intra-limb coordination.

In the following segments I will quickly review the intrinsic organization of these three locomotor networks.

Rhythm generating circuits
While the source of rhythm generation in the spinal cord remains unknown in humans, studies in lamprey, rodents and cats suggest the source of rhythm generation to be excitatory, glutamatergic neurons with ipsilateral projections to MNs (Goulding, 2009; Kiehn, 2016). Direct evidence for this hypothesis stems from studies in mice, which demonstrate that optogenetic activation of spinal glutamatergic neurons elicit locomotor activity (Hägglund et al., 2010; Hägglund et al., 2013). In turn, blocking crossed inhibitory acitivity and ipsilateral inhibitory interneurons do not shut down rhythm generation in the lamprey (Cangiano & Grillner, 2003, 2005), in rodents (Bonnot et al., 2002; Bracci et al., 1996; Kjaerulff & Kiehn, 1997; Kremer & Lev-Tov, 1997) and in cats (Kato, 1987; Noga et al., 1987).

Bilateral coordinating circuits
Locomotion requires the coordination of muscles on the left and right side of the body. This function is primarily encoded in Commissural Neurons (CNs) localized in the ventral spinal cord (Matsuyama et al., 2006; Nissen et al., 2005; Stokke et al., 2002). CNs provide this crucial bilateral communication by projecting to the contralateral side of the spinal cord. Despite securing the alternation of muscle activity on both sides of the body, CNs regulate left-right coordination at different speeds of locomotion. This multifaceted task-regulation is enabled by modular organization of CNs, that include both excitatory and inhibitory pathways (Butt & Kiehn, 2003; Jankowska et al., 2005; Jankowska, 2008; Quinlan & Kiehn, 2007).

On the one hand cross inhibition may be achieved by two different populations of CNs: 1.) Inhibitory CNs ($V0_D$) that act directly on contralateral MNs or interneurons and 2.) excitatory CNs ($V0_V$) activating inhibitory neurons premotor interneurons (Butt & Kiehn, 2003; Quinlan & Kiehn, 2007). On the other hand cross excitation may be accomplished by excitatory CNs ($V0_3$) synapsing on contralateral MNs or interneurons (Y. Zhang et al., 2008). The former dual inhibition supports alternating muscle activity across the cord. Indeed, both pathways seem to be necessary as suppression or ablation of either circuitry leads to unwanted synchronicity in contralateral activity (Talpalar et al., 2013; Talpalar et al., 2011). The latter excitatory pathway is tuned to support left-right synchronization such as hopping or galloping.

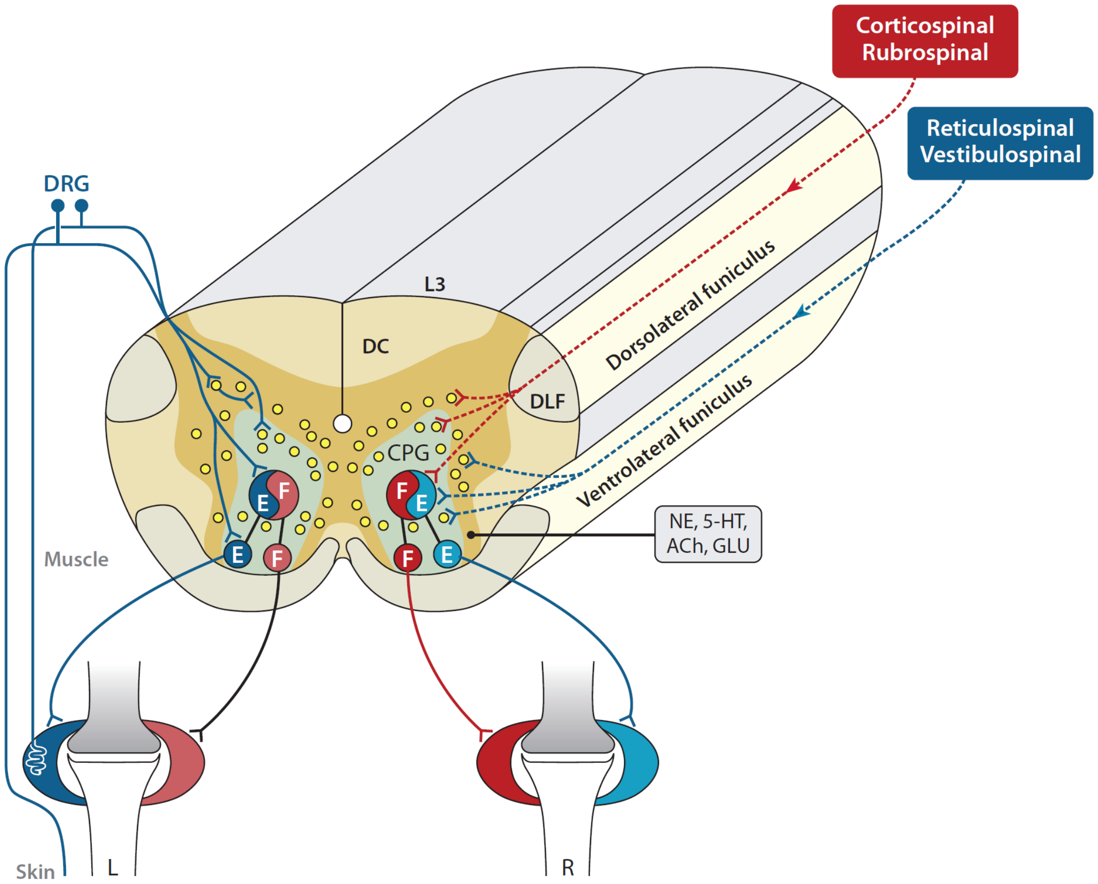
Corticospinal
Rubrospinal
Reticulospinal
Vestibulospinal
DRG
L3
DC
DLF
Dorsolateral funiculus
Ventrolateral funiculus
CPG
E
F
F
E
E
F
F
E
NE, 5-HT,
ACh, GLU
Muscle
Skin
L
R

Figure 1.8: Sketch of the fundamental framework underlying locomotor control. CPGs generate the rhythm underlying locomotion. Spinal sensorimotor circuits process signals from proprioceptive and cutaneous sensory organs to adapt motor patterns to the environment. Supraspinal centers regulate the speed, onset and balance. Republished with permission of Annual Reviews, Inc., from Rossignol and Frigon, 2011; permission conveyed through Copyright Clearance Center, Inc..

Coordination of flexors and extensors

Alternation of flexor and extensor MNs on the same side necessitate inhibitory networks.

While CNs play a role in this ipsilateral coordination, they cannot be the major contributing factors, as this alternating pattern persists in hemisected cords, where crossing connections have been removed (Bonnot et al., 2002; Kato, 1987; Kjaerulff & Kiehn, 1997). Instead, ipsilateral inhibitory networks must be strongly involved in flexor-extensor coordination. Many populations of interneurons have been identified to potentially play a crucial role in the generation of the alternating activity. In particular, Ia-InterNeurons (Ia-INs) and Renshaw Cells (RCs) have been suspected to play a major part in this coordination, as both cell populations are rhythmically active during locomotion (McCrea et al., 1980; Noga et al., 1987; Pratt & Jordan, 1987).

RCs are inhibitory neurons that are excited via recurrent collaterals from MNs. RCs project back to these MNs, effectively inhibiting these MNs in phase with the MN activity. Ia-INs are last-order interneurons that are innervated by group Ia afferents of one muscle while inhibiting MNs of anatgonistic muscles out of phase. Simultaneously, pools of antagonistic Ia-INs mutually inhibit each other and are inhibited by RCs (Hultborn, 1976; Hultborn et al., 1971; Kiehn, 2016). Studies in mice demonstrated that the reciprocal Ia inhibitory pathway is sufficient to create alternation of flexor and extensor MNs (Talpalar et al., 2013; Talpalar et al., 2011). Astonishingly, even in the absence of excitatory pathways this circuitry is sufficient for the generation of rhythmic activity in flexor-extensor pairs (Talpalar et al., 2013; Talpalar et al., 2011). In turn blocking the synaptic output of Ia-INs disrupts the flexor-extensor alternation (J. Zhang et al., 2014).

1.2.3 Supraspinal control

Supraspinal centers play a crucial role in the planning and initiation of locomotion. A rough division can be made between cortical structures and the brainstem, although numerous subcortical structures such as the cerebellum and the basal ganglia are also involved in locomotor control (Jordan et al., 2008; Ray et al., 2011; Takakusaki, 2013; Takakusaki et al., 2015). From a control theory point of view, initiation of locomotion can be roughly subdivided into voluntary or automatic processes. The former involve cortical areas while the latter arises in the limbic system. Secondly, the control of locomotion including onset, speed, termination and other high-level features is largely reliant on the brainstem. A notable exception are fine voluntary adjustments which are directly controlled by the cerebral cortex through the corticospinal tract.

In this section I will briefly review the role of the brainstem as well as cortical and subcortical areas in locomotion.

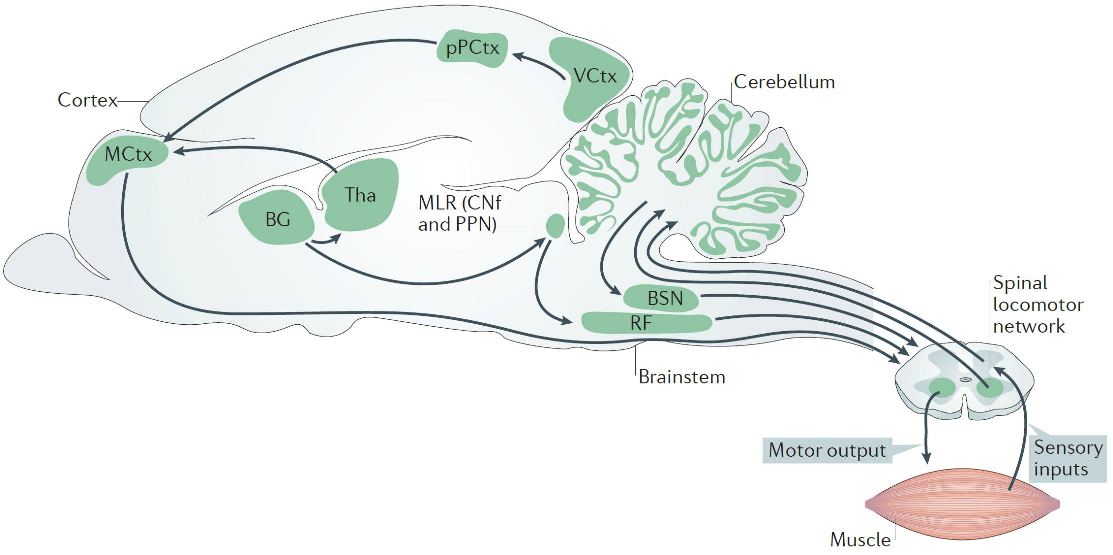

Figure 1.9: General overview of the supraspinal control of locomotion. 1.) Selection and initiation of locomotion involves multiple regions in the brain and brainstem. Firstly, the Basal Ganglia (BG) projects to the Motor Cortex (MCtx) via the Thalamus (Tha). The BG also projects to the Mesencephalic Locomotor Region (MLR), which includes the CuNeiform nucleus (CNf) and the PedunculoPontine Nucleus (PPN). The MLR projects through the Reticular Formation (RF) in the hindbrain to locomotor networks in the spinal cord to execute locomotion. 2.) Regulation of ongoing locomotion and posture maintenance is mediated by the vestibular and rubrospinal spinal pathways from the BrainStem Nuclei (BSN). The BSN receives input from the cerebellum which coordinates locomotion. For this purpose the cerebellum receives sensory feedback information from the spinal cord. 3.) Correction of locomotion due to visual stimulation originates in the Visuomotor Cortex (VCtx) and is mediated by the posterior Parietal Cortex (pPCtx) to the MCtx. Republished with permission of Springer Nature, from Kiehn, 2016; permission conveyed through Copyright Clearance Center, Inc..

The brainstem

Many structures of the brainstem may be involved in locomotion. In animals three major regions were able to be identified. These are namely: The Mesencephalic Locomotor Region (MLR), the Subthalamic Locomotor Region (SLR) and the Cerebellar Locomotor Region (CLR) (Grillner, 1981; Mori, 1987; Mori et al., 1999; P. Stein, 1997). Here, I restrict my assessment of the brainstem to these three regions.

The MLR in particular may play an important role in locomotion as electrical stimulation of the MLR can trigger full weight-bearing treadmill locomotion (Shik et al., 1969). It receives inputs from the premotor cortices (Matsuyama & Drew, 1997) and the limbic and hypothalamic areas (Grillner, 1981; Sinnamon, 1993). The MLR excites the rhythm generating system through the reticulospinal tract and activates monoaminergic descending pathways (Takakusaki et al., 2004; Takakusaki, 2008; Takakusaki et al., 2006). The reticulospinal tract is hypothesized to both activate rhythm generating networks in the spinal cord to initiate locomotion and controls postural muscles (Rossignol et al., 2006; Takakusaki et al., 2004). The monoaminergic descending pathways may have various functions including the regulation of spinal cord sensitivities to descending and sensory signals (Takakusaki, 2013).

The SLR also activates the rhythm-generating system. It is able to do this either directly or through indirect connections via the MLR (Grillner, 1981; Rossignol et al., 2006; Sinnamon, 1993). As it is part of the hypothalamus its role in motor behaviors is speculated to be linked to emotional decision-making.

The CLR in the mid-part of the celebellum is associated with the hook bundle of Russel and projects to the vestibular nuclei in the brainstem. It possibly also activates the rhythm-generating system through these projections. (Mori et al., 1999).

Cortical and subcortical areas

Cortical and subcortical structures play an important role in the survival of animals. Planning environmentally appropriate locomotion to circumvent obstacles or organizing complex muscle activation patterns in convoluted situations such as hunting undoubtedly involves cortical and subcortial areas (Kalaska, 2009; Rizzolatti et al., 2014). Here, I focus primarily on elucidating the function of the Posterior Parietal Cortex (PPC) and the MCtx.

The PPC is essential for planning gait modification in response to visual stimulation (Andujar et al., 2010; Beloozerova & Sirota, 2003; Marigold et al., 2011). Certain population of cells in the PPC alter their discharge activity already 2-3 steps prior to reaching an obstacle suggesting the PPC to contribute to estimation of spatial and temporal information concerning the obstacle (Andujar et al., 2010).

Contrary to the PPC that demonstrates neural activity prior to the step over an obstacle, the MCtx becomes primarily active during the step. This may hint at a pronounced role of the MCtx in execution of modified movements. To this end, the MCtx projects towards the spinal cord through Pyramidal Tract Neurons (PTNs) both directly through the corticospinal tract and indirectly through the brainstem (Amos et al., 1990; Beloozerova & Sirota, 1993; Drew, 1993; Drew et al., 1996; Drew et al., 2008). Whether the MCtx controls high-level features of locomotion or modifies muscle activities remains unclear (Drew & Marigold, 2015).

1.3 Restoring locomotion after spinal cord injury

In the last chapter, I explained that supraspinal centers play an essential role in planning and initiation of locomotion. After SCI the communication between the supraspinal centers and the spinal cord is interrupted. However, generally the spinal circuits in the lumbosacral spinal cord and the PNS remains intact. As these nervous tissues generate the rhythm underlying locomotion, coordinate muscle activity within one leg and between legs as well as alter motor activity to accomodate movement in the environment, humans and animals with SCI retain the capacity to elicit involuntary movements. However, due to the lack of supraspinal activity the locomotor circuits decline into an altered state (Rossignol & Frigon, 2011).

We can therefore divide the goal of a rehabilitation strategy into two sub-goals: 1.) The proper functioning of the locomotor circuitry must be recovered and 2.) the communication between supraspinal centers and the spinal cord must be re-established. Beyond this scientific description the end goal is to promote patient care and cure. This entails rehabilitation across all healthcare setting including acute care, inpatient rehabilitation, outpatient rehabilitation, community fitness, wellness and integration as well as clinical decision-making and practice (Behrman et al., 2017). At the core of this definition stand activity-based therapies in the medical reality (Behrman et al., 2017; Field-Fote et al., 2005; Jones et al., 2014). In this chapter, I introduce activity-based therapies and their scientific basis. I then move on to technological advancement in the management of spinal cord injury. Finally, I highlight the special role of EES in this endeavour.

1.3.1 Activity-based therapies

Classification of SCI
Firstly I must introduce a metric by which I can classify the severity of impairment in people affected with SCI. The International Standards for Neurological Classification of SCI (ISNCSCI) is currently the gold standard to describe the level of impairment. It relies on a series of functional tasks performed by the individual to differentiate neurological functioning between complete (AIS A), sensory-incomplete (AIS B), motor-incomplete (AIS C or D) or normal (AIS E) (Kirshblum & Waring, 2014).

Locomotor training
Intensive locomotor training can result in functional improvements in individuals with chronic incomplete SCI (AIS C or D) (S. J. Harkema et al., 2012). This finding has been the result of decades of pre-clinical research demonstrating that treadmill training is sufficient to restore locomotion in spinal cats (Barbeau et al., 1987; Belanger et al., 1996) as well as several other species (*Handbook of physiology : a critical, comprehensive presentation of physiological knowledge and concepts*, 1977). The rehabilitative nature of locomotor training may be mediated by sensory signals generated during stepping, that promote reorganization through activity-dependent plasticity mechanisms (Bouyer & Rossignol, 2003b; Edgerton et al., 2008; Rossignol & Frigon, 2011). In particular muscle spindles seem to be implicated in the recovery of locomotion through activity-based therapies (Goldberger, 1977; Takeoka et al., 2014). Unfortunately, the exact mechanisms of how sensory signals aid in the reorganization of supraspinal control and spinal locomotor networks remain unclear.
This lack of scientific understanding might explain the considerable variability that is observed in clinical improvement of individuals with chronic, motor-incomplete SCI (Jones et al., 2014). Furthermore, gait-rehabilitation strategies have yet to demonstrate significant improvements in people with clinically complete lesions (Dietz et al., 1995; Wirz, 2001). However, these results might also implicate that additional technological interventions are necessary to promote functional recovery of locomotion after SCI.

1.3.2 Technological advancements to support activity-based therapies

Pharmacological neuromodulation
After a traumatic SCI, the nervous tissue at the site of the injury is impaired. To add insult to injury, the initial mechanical damage is followed by a secondary injury cascade further deteriorating the state of the spinal cord. The spinal cord undergoes a dramatic alteration that includes many mechanisms (Ahuja & Fehlings, 2016). However, the spinal circuits below the lesion are still technically intact, although functionally dormant. This is due to the fact that descending excitatory inputs are lost, while inhibitory neurotransmitters aggregate in the spinal cord (Hultborn, 2003; Tillakaratne et al., 2000). This results in an overall decrease of excitability in the neural circuits (Rossignol & Frigon, 2011). To counteract this depression of excitability, various pharmacological interventions such as $\alpha 2$ agonists, glycinergic agonists, serotonergic agonists, and GABAergic antagonists have been proposed (Barbeau & Rossignol, 1990; Chau et al., 1998; de Leon et al., 1999; Edgerton et al., 2008; Forssberg & Grillner, 1973; Robinson & Goldberger, 1985; Rossignol & Frigon, 2011). These pharmacological agents have demonstrated strong modulatory effects in preclinical animal models that ultimately enable the generation of motor pattern formation. Unfortunately, the translation of the pharmacotherapies to human application has been largely unsuccessful thus far (Dietz et al., 1995; Rossignol & Frigon, 2011). Additionally, high costs and stringent clinical regulations in relation to these therapeutic avenues have spiked the interest in electrical stimulation as an alternative treatment (Hay et al., 2014; D. W. Howells et al., 2013; Travessa et al., 2017).

Electrical neuromodulation
Electrical neuromodulation technologies can be grouped by the type of nervous tissue that is stimulated (see Fig. 1.10). In this way, we can classify three types of neuromodulations techniques: 1.) Peripheral nervous system stimulation, 2.) brain stimulation and 3.) spinal cord stimulation.

The most established form of neuromodulation for SCI is direct electrical stimulation of the peripheral nervous system (James et al., 2018). There exist a plethora of commercially available functional electrical stimulation devices that can used in a clinical or ecological setting (James et al., 2018). These devices either directly activate efferent or afferent fibers or stimulate a muscle directly. The latter case is referred to as Functional Electrical Stimulation (FES). PNS stimulating technologies have the capacity to enable various movements in the upper and lower extremities as well as the trunk (Ho et al., 2014). In this way, stimulation of the PNS enables locomotion after SCI and can support activity-based therapies. However, this form of electrical neuromodulation has three major disadvantes: 1.) It causes rapid muscle fatigue, 2.) it obscures biofeedback and 3.) voluntarily-produced muscle activity is masked by the direct elicitation of muscle contractions (Duffell & de Neufvillle Donaldson, 2020). Hence, PNS stimulation alone may not be optimal for enabling recovery of locomotion after SCI (Duffell & de Neufvillle Donaldson, 2020).

In recent years, PNS stimulation has been increasingly combined with Brain-Machine Interfaces (BMI). The BMI enables the recording and decoding of brain activity, that can be reproduced as muscular activity through technologies such as FES (Bouton et al., 2016). BMIs demonstrate impressive results in either bypassing the injury or enhancing neuroplasticity (Jackson & Zimmermann, 2012; Krucoff et al., 2016). Despite encouraging outcomes BMIs are currently linked to an abundance of adoption hurdles, including high costs and specialised technologies and expertise (James et al., 2018).

While BMIs aim to record brain activity, brain stimulation aims to increase descending activity through residual pathways between spinal and supraspinal circuits (Kumru et al., 2017). As many regions in the brain are involved in the production of locomotion, there exists a wealth of experimental techniques that aim to target these regions. Two notable examples are Deep Brain Stimulation (DBS) and direct motor cortex stimulation. DBS has successfully been used in the treatment of Parkinson's disease, dystonia and essential termor in the past and has recently been proposed to aid in motor production after SCI through stimulation of subcortical locomotor regions (Bachmann et al., 2013; Hentall & Gonzalez, 2011; Mahlknecht et al., 2015). Direct motor cortex stimulation with epidurally implanted electrodes has also demonstrated recovery of skilled motor functions in preclinical animal models (Martin, 2016). DBS and direct motor cortex stimulation are both highly invasive and therefore carry a significant risk. Instead, non-invasive techniques such as transcranial Direct Current Stimulation (tDCS) and Transcranial Magnetic Stimulation (TMS) relies on non-invasive application of electrical and magnetic stimulation respectively. TMS has even been studied in individuals with SCI and demonstrated improvements in hand function and locomotion (Alexeeva & Calancie, 2014; Gomes-Osman & Field-Fote, 2015; Kumru et al., 2016). Unfortunately, TMS also carries with it significant technological limitations and usability requirements that need to be ameliorated for widespread use (James et al., 2018). In contrast to TMS, tDCS is easy to integrate into the clinical routine. Due to its cost-efficiency, absence of adverse events and clinical acessibility, tDCS is an attractive treatment option for SCI (James et al., 2018). Unfortunately, tDCS studies have mostly been carried out in healthy individuals thus far and clinically relevant data in individuals with SCI is sparse (Gomes-Osman & Field-Fote, 2013, 2015; Murray et al., 2015; E. Park et al., 2014). Further research is necessary to evaluate its efficacy on the recovery of locomotion after SCI.

Finally, electrical stimulation can be applied to the spinal cord directly. Although many experimental placements of electrodes exist that have their respective advantages and disadvantages, such as subdural or intradural stimulation (Sharpe & Jackson, 2014), the two most common stimulation strategies are transcutaneous and epidural spinal cord stimulation. In transcutaneous Spinal Cord Stimulation (tcSCS) the electrodes are placed on the skin over the vertebral column. Exciting evidence suggests that tcSCS can modulate the excitability of spinal and supraspinal circuits (Bocci et al., 2015; Bocci et al., 2014), improve upper limb strength, grasping (Inanici et al., 2018) and provide volitional stepping-like movements after SCI (Y. P. Gerasimenko et al., 2015). Due to its non-invasive and inexpensive nature and the fact that tcSCS can be done with conventional, commercially available stimulation devices, tcSCS is an attractive neuromodulation strategy (James et al., 2018). The drawback is that it most likely targets the neural structures necessary for the recovery of locomotion (with both tcSCS and EES) less specifically than EES. What those structures are and how EES works is discussed in the next section.

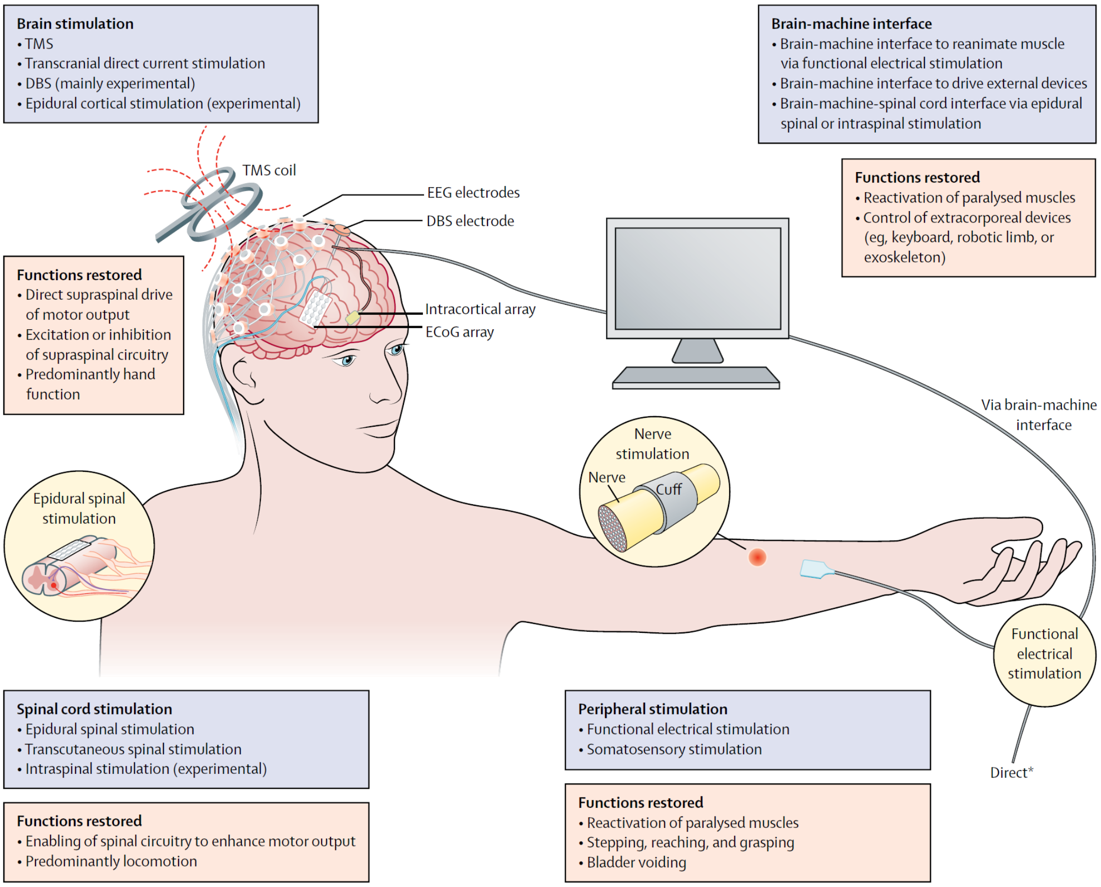
Brain stimulation
• TMS
• Transcranial direct current stimulation
• DBS (mainly experimental)
• Epidural cortical stimulation (experimental)
Brain-machine interface
• Brain-machine interface to reanimate muscle via functional electrical stimulation
• Brain-machine interface to drive external devices
• Brain-machine-spinal cord interface via epidural spinal or intraspinal stimulation
Functions restored
• Reactivation of paralysed muscles
• Control of extracorporeal devices (eg, keyboard, robotic limb, or exoskeleton)
TMS coil
EEG electrodes
DBS electrode
Functions restored
• Direct supraspinal drive of motor output
• Excitation or inhibition of supraspinal circuitry
• Predominantly hand function
Intracortical array
ECoG array
Via brain-machine interface
Nerve stimulation
Nerve
Cuff
Epidural spinal stimulation
Functional electrical stimulation
Direct*
Spinal cord stimulation
• Epidural spinal stimulation
• Transcutaneous spinal stimulation
• Intraspinal stimulation (experimental)
Functions restored
• Enabling of spinal circuitry to enhance motor output
• Predominantly locomotion
Peripheral stimulation
• Functional electrical stimulation
• Somatosensory stimulation
Functions restored
• Reactivation of paralysed muscles
• Stepping, reaching, and grasping
• Bladder voiding

Figure 1.10: Neuromodulation approaches for restoring function after spinal cord injury. Republished with permission of Elsevier, from James et al., 2018; permission conveyed through Copyright Clearance Center, Inc..

1.3.3 Epidural electrical stimulation of the lumbosacral spinal cord

Contrary to the non-invasive tcSCS, prior to EES an electrode lead is placed on the dorsal surface of the spinal cord. Although originally used as a treatment for chronic pain (Deer et al., 2014; Wall, 2003), clinical studies demonstrated that EES applied over the lumbosacral spinal cord can enable individuals with chronic motor or sensory complete (AIS A-B) (Angeli et al., 2014; S. Harkema et al., 2011) SCI to make small voluntary leg movements during stimulation. These initial results were followed up by studies combining EES with activity-based therapies that demonstrate that individuals with chronic motor complete SCI achieved treadmill and over-ground walking as well as independent standing and trunk stability (Angeli et al., 2018; M. L. Gill et al., 2018).

However, these clinical studies seem to indicate that only a limited range of EES parameters can provide a therapeutic effect in humans (Angeli et al., 2014; S. Harkema et al., 2011). Preclinical efforts demonstrated that modulation of certain stimulation parameters can improve precise control of motor output during gait (Capogrosso et al., 2016; Wenger et al., 2014). Given the vast parameter space, optimization of stimulation parameters with very limited empirical data is necessarily suboptimal. Instead, optimization with computational modeling could accelerate efforts to improve the therapeutic capacity of EES.

Having said that, to this date, the mechanisms underlying the interaction between EES and the lumbosacral spinal cord remain enigmatic. Computational and experimental efforts suggest that EES primarily recruits large-diameter, myelinated afferent fibers (Capogrosso et al., 2013; Y. P. Gerasimenko et al., 2006; Minassian et al., 2007; Rattay et al., 2000). These fibers are of type Aα and Aβ. As can be seen in Table 1.1, Aα and Aβ afferents predominantly innervate proprioceptive and cutaneous sensory organs. Additionally, experiments in rodents also indicate that muscle-spindle feedback circuits play a crucial role in the ability of EES to enable locomotion (Takeoka et al., 2014). Muscle-spindle circuits form mono- and disynaptic pathways with MNs (see chapter 1.2.2). In this way, the recruitment of large-diameter, myelinated afferents may activate MNs and increase excitability of the whole spinal locomotor network (Angeli et al., 2014; Danner et al., 2015). Particularly, the increased excitability of spinal circuits may augment their sensitivity to sensory feedback and residual descending inputs, enabling the emergence of locomotion (Edgerton et al., 2008).

Remarkably, EES has a certain specificity associated to itself that is primarily dependent on the shape of the electrodes, their position relative to the excitable structure, the duration, intensity and polarity of the stimulus signal as well as its repetition rate (Rattay et al., 2000). This indicates that EES can be tuned to elicit specific movement patterns at will. This discovery ultimately culminated in the development of spatiotemporal stimulation strategies that aim to reproduce the migration of motor pool activity in the spinal cord during locomotion (Capogrosso et al., 2016; Cappellini et al., 2010; Wenger et al., 2016; Wenger et al., 2014). However, this undertaking is hindered by the vast variability of anatomical dimensions and innervation patterns in large and diversified patient-cohorts (see chapter 1.1.5 and 1.2.1).

In this thesis I aimed at leveraging computational modeling to enable the efficacious and robust translation of spatiotemporal EES into a clinical setting. In the next chapter I provide the state-of-the-art technological capacity of computational modeling technologies that I leveraged and improved upon throughout my thesis.

1.4 Computational modeling of epidural electrical stimulation in the spinal cord

Computational models offer three major benefits to the scientific, industrial and clinical communities that strive to develop and apply neuromodulation technologies (Capogrosso & Lempka, 2020). Firstly, translating what we know about a specific subsystem of the nervous system into an in-silico representation immediately reveals what we do not yet know or understand about the underlying nervous structures and can therefore drive experimental research (Markram et al., 2015). Secondly, computational frameworks provide a virtual testing ground in which interactions between neuromodulation technologies and neural structures can be studied at a speed that is limited only by the available computational resources and in this manner can accelerate the development of new technologies, the optimization of existing technologies and aid in the deconstruction of underlying mechanisms (Mcintyre & Foutz, 2013). Lastly, computational models can be personalized and in this manner provide a useful tool for preoperative strategy planning, personalization of treatment and development of technologies that are robust in large and diversified patient-cohorts (Lempka et al., 2020).

In the case of EES, computational models were first developed to understand the distribution of electric fields in the spinal cord (Coburn & Sin, 1985) and how these stimuli interact with long myelinated fibers (Coburn, 1985). In this context, 3D volumes were generated that approximate the tissues of the thoracic spinal cord and a Finite Element Method (FEM) was applied to numerically approximate the electric field following a simulated stimulus (Coburn & Sin, 1985). These estimations of the electric field were coupled with a biophysical model of the myelinated nerve axon to interpret the neurophysiological effects (Coburn, 1985). This methodology has since been expanded significantly and translated to other parts of the spinal cord with different targeted neural structures, but at its core it continues to this day (Bossetti et al., 2007; Capogrosso et al., 2013; Holsheimer, 2002; Ladenbauer et al., 2010; Lempka & Patil, 2018; Lempka et al., 2020; McIntyre et al., 2002; Rattay et al., 2000; Rattay et al., 2003; Rattay, 1986).

For the remainder of this work, I will refer to computational models that combine FEMs with biophysical models of nervous tissues as hybrid computational models. These hybrid models suggested that EES engages the spinal circuits underlying locomotion trans-synaptically through the recruitment of large-diameter, myelinated afferent fibers (Capogrosso et al., 2013). However, as previously discussed in chapter 1.2.2, these sensory afferents also regulate the production of MN activity in the spinal cord (Edgerton et al., 2008). It is therefore imporant to include the circuit-level interactions between the EES-induced recruitment pattern of spinal circuits and their natural activity during locomotion. This study can be enabled by feeding recruitment patterns extracted from hybrid computational models into artificial representations of complex networks controlling locomotion and using biomechanical models to generate natural firing patterns of sensory afferents (Moraud et al., 2016). I will refer to this type of modeling as neuromusculoskeletal modeling.

In the following chapter, I describe the theoretical basis of FEMs, biophysical modeling of nervous structures and neuromusculoskeletal modeling, that form the basis of my own work. I aim to pay particular attention to outline the current state-of-the-art to enable the reader to understand the advances I made in my own work towards using personalizable computational modeling to restore neural function after neurological disorders.

1.4.1 Finite element method for epidural electrical stimulation

At their core FEMs for EES aim to provide numerical approximations of the electromagnetic field in the spinal cord. Electric and magnetic fields can be described by Maxwell's equations. This simply requires perfect knowledge of the electric charge density ρ and electric current density j in all mediums with their respective electric permittivities ϵ and magnetic permeabilities μ at all points x in space and all times t. Unfortunately, this prior comprehension is not always feasible given the average human lifespan and the vastness of the universe.

Luckily, a few approximations can tremendously reduce the complexity of this feat. Firstly, we can consider our problem to be quasi-static, which simply means that the electromagnetic field at a single time t is considered to be induced as if the sources at that instant were stationary (Plonsey & Heppner, 1967). This reduces the problem to a series of instants during and immediately after the application of an electrical stimulus. Secondly, we must assume that the displacement current (i.e. the current induced by free and bound charges within materials) is negligible in comparison to the ohmic current of the applied stimulus. These two assumptions enable us to reformulate Maxwell's equations into the Poisson equation described in Eqn. 1.4.

$$\nabla(\sigma\nabla V(x)) = \nabla j_i(x) \tag{1.4}$$

Here σ refers to the conductivity of the medium, V is the electric potential and j_i is the current density impressed by a source.

Third, if we assume $\nabla j_i(x)$ to be much larger in a certain region of space v_0 than anywhere else, then we can neglect the term $\nabla j_i(x)$ in Eqn. 1.4 for all x outside of v_0. In this case Eqn. 1.4 transforms into Eqn. 1.5.

$$\nabla(\sigma\nabla V(x)) = 0 \tag{1.5}$$

The remaining issue is space. In theory, Eqn. 1.5 must be solved at all points in space. This problem can be solved through the introduction of volume conductor models with boundary conditions. We simply restrict our region of interest to the immediate volume around the source of stimulation. In our case EES is applied to the lumbosacral spinal cord. Hence, we must recreate all the tissues described in chapter 1.1 artificially. There exists very little consensus on how the anatomy of the spine should be represented. In the past these anatomical tridimensional volumes have mostly been generated by roughly approximating the shape and anatomical dimensions of the biological tissues from anatomical measurements (Coburn & Sin, 1985; Holsheimer, 2002; Ladenbauer et al., 2010; Rattay et al., 2000). Although, in recent years these volume conductor models have vastly improved in anatomical realism even taking into account medical imaging datasets for reconstruction purposes (Greiner et al., 2021; Howell et al., 2014). Unfortunately, as described in chapter 1.1.5, there exists large variability of anatomical parameters between subjects. Hence, there is considerable drive to fully personalize the anatomical dimensions through segmentation of medical imaging datasets (Lempka et al., 2020). Despite, these advances many anatomical structures are often being omitted due to technical difficulties in acquiring and segmenting these tissues. The most crucial are the bundles of rootlets inside the dura, which inhabit the afferent fibers that EES supposedly recruits (Capogrosso et al., 2013; Rattay et al., 2000). It is also important to note that some tissues like the thin dura mater can be excluded from the model when their respective conductivities do not dramatically affect the resulting field (Ladenbauer et al., 2010; Rattay et al., 2000).

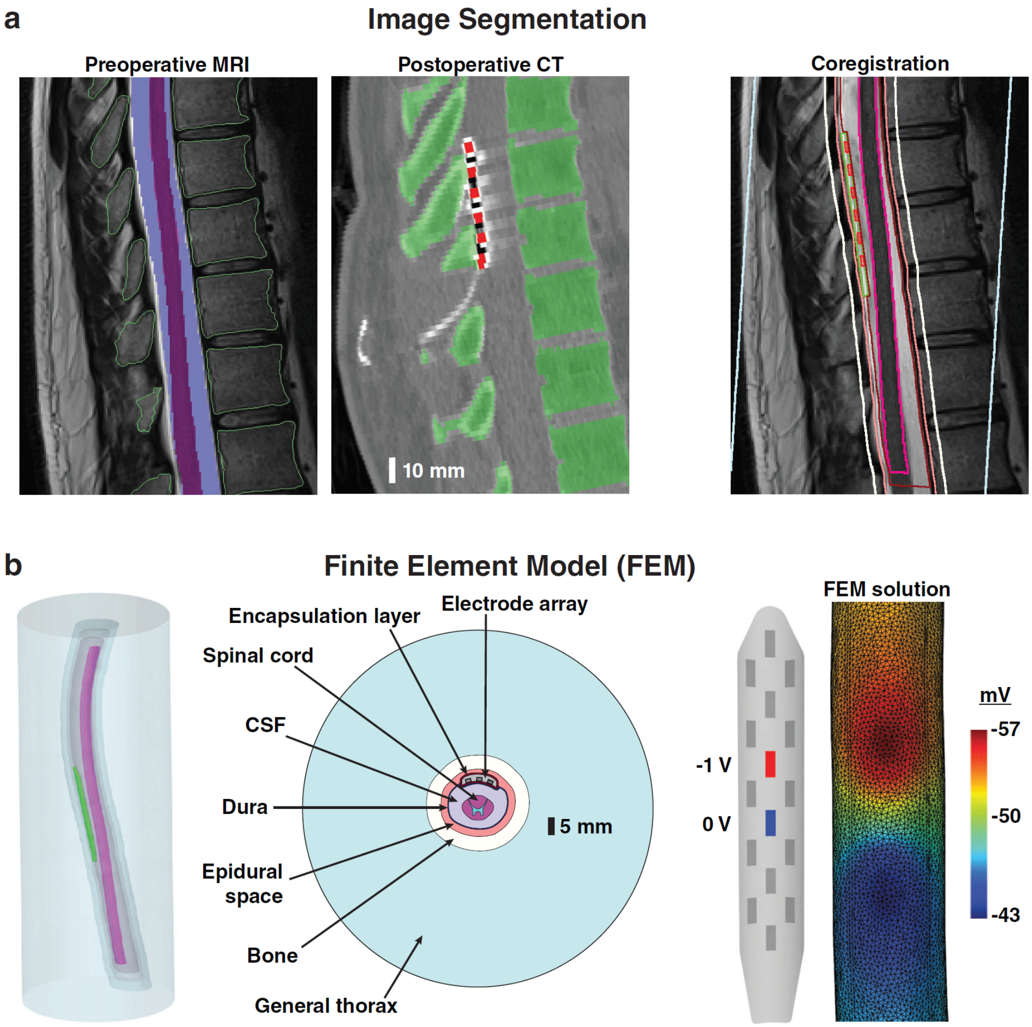
a
Image Segmentation
Preoperative MRI
Postoperative CT
10 mm
Coregistration
b
Finite Element Model (FEM)
Encapsulation layer
Electrode array
Spinal cord
CSF
Dura
Epidural space
Bone
General thorax
5 mm
FEM solution
-1 V
0 V
mV
-57
-50
-43

Figure 1.11: An example of a highly refined patient-specific FEM. a. Preoperative Magnetic Resonance Imaging (MRI) scans were used to define the anatomy of an individual. Postoperative CT scans enabled the localisation of electrodes within this volume. b. This anatomy was translated into FEM objects and a bipolar simulus was approximated within this volume. Republished with permission of John Wiley and Sons, from Lempka et al., 2020; permission conveyed through Copyright Clearance Center, Inc..

The next step in obtaining a numerical solution to Eqn. 1.5 inside the lumbosacral spinal cord is to discretize the space into a finite amount of homogeneous representations. For this purpose, mesh engines are being employed. For the most parts two types of mesh engines can be differentiated: Structured and unstructured. In a structured mesh, a finite amount of volumes such as voxels are placed inside the entirety of the volume conductor model and each volume is denoted to be part of a specific tissue. The conductivity of this element is assumed to be fully characterized by the conductivity of the medium at this point as if it was homogeneous in this space. If the conductivity is isotropic, it is fully characterized by a scalar value. In case the medium is anisotropic, a scalar value needs to be assigned to each orthonormal vector of a basis in a local coordinate system. The same procedure holds true in an unstructured mesh, with the notable exception that volumes such as tetrahedrals are fitted inside the volume denoted by its respective boundary. Both methods enable the calculation of Eqn. 1.5 only if the entire volume is finite, requiring the existence of boundary conditions, that specify 1.) what happens inside the volume in its entirety and the outside that is assumed to not exist and 2.) what happens at the interface of each volume.

In volume conductor models, two types of boundary conditions are commonly used: Dirichlet conditions and von Neumann conditions. Dirichlet boundary conditions assume that the potential at a point x is any fixed real scalar value. As such we can for example express the cathode that normally injects current into the lumbosacral spinal cord to have a fixed value of 1V. The anode that returns this current may be assumed to have a value of -1V. And the boundary between the spinal cord and its surrounding may be approximated to be 0V.

Alternatively, von Neumann conditions may be applied that specify what happens to the derivative of the Potential normal to the boundary rather than its absolute value. In this case $\vec{n}\nabla V = j_B$, where $\vec{n}$ is the projection vector normal to the boundary, and j_B can be any flux. It is often convenient to assume $j_B = 0$.

It is important to note, that all the steps described in this overview do not necessarily need to be applied in exactly this way. Other solutions can be imagined. However, the workflow as it is laid out here, enables the numerical approximation of the electric field inside the lumbosacral spinal cord. One of the most refined examples of the described workflow, that I am aware of, is described in Fig. 1.11

1.4.2 Biophysical models of nervous structures

In the last chapter, I gave a broad overview on how to estimate the electric field inside the spinal cord with FEMs. In order to predict the effect of this field on the nervous tissues, it needs to be coupled with an electrical represention of these tissues. At their core, biophysical models of nerve fibers aim to do this by accurately representing the ion channels and morphology of nerve fibers. Here, I present the primary biophysical models of nerve fibers that I used in the development of this thesis.

Modeling large-diameter, myelinated afferent and efferent axons as sensory and motor MRG models

One of the most widely used neurophysical model of a nerve fiber is the MRG model, which aims to represent a mammalian myelinated motor nerve fiber (McIntyre et al., 2002). This multi-compartmental model alternates electric representations of nodes of Ranvier with myelinated internodal compartments. Each internodal section is comprised of 2 paranodel myelin attachment segments (MYSA), 2 paranodal main segments (FLUT) and 6 internodal segments (STIN). The non-linear membrance ionic conductances of the nodes of Ranvier were modeled as fast (Naf) and persistent (Nap) sodium, slow potassium (Ks) and linear leakage conductances (Lk) in parallel with the nodal capacitance (Cn). The passive internodal compartments were represented by linear conductances (Gm in parallel with Cm) and the internodal axolemma (Gi in parallel with Ci) (see Fig. 1.12).

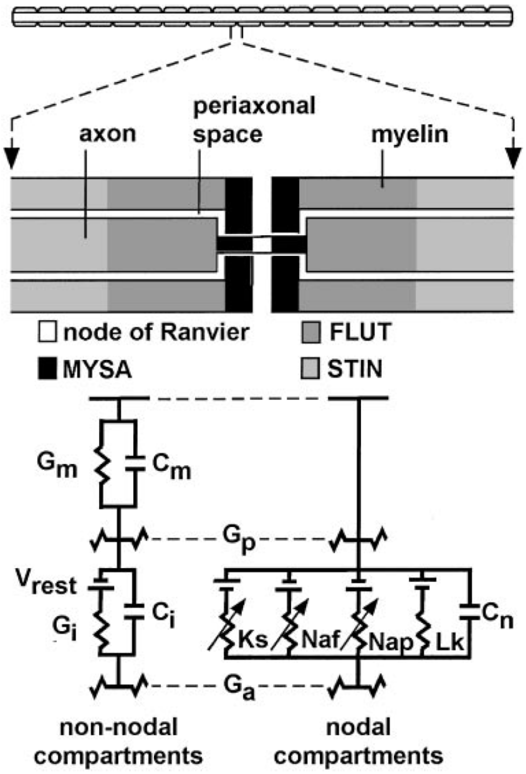

Figure 1.12: Multi-compartment double cable model of a mammalian, myelinated MA. Republished with permission of The American Physiological Society, from McIntyre et al., 2002; permission conveyed through Copyright Clearance Center, Inc..

For most of my work, I used a slight alteration to the MRG-model (Gaines et al., 2018). This model included fast Potassium channels (Kf) in the nodal compartment and split up the single conductance of the internodal channels into fast (Kf), slow (Ks) and hyperpolarization-activated cyclic-nucleotide-gated (H) channels while also including a linear leakage conductance (Lk) (see Fig. 1.13).

For the MA models, the parameters were largely retained, but parameters for the additional conductances were added from the literature (J. Howells et al., 2012; Röper & Schwarz, 1989). Similarly, for the sensory axons, these parameters were used to tune the fiber model to represent the sensory axon (J. Howells et al., 2012; Röper & Schwarz, 1989). The original MRG model and the presented alteration have been developed and validated for fixed diameters of the nerve axons.

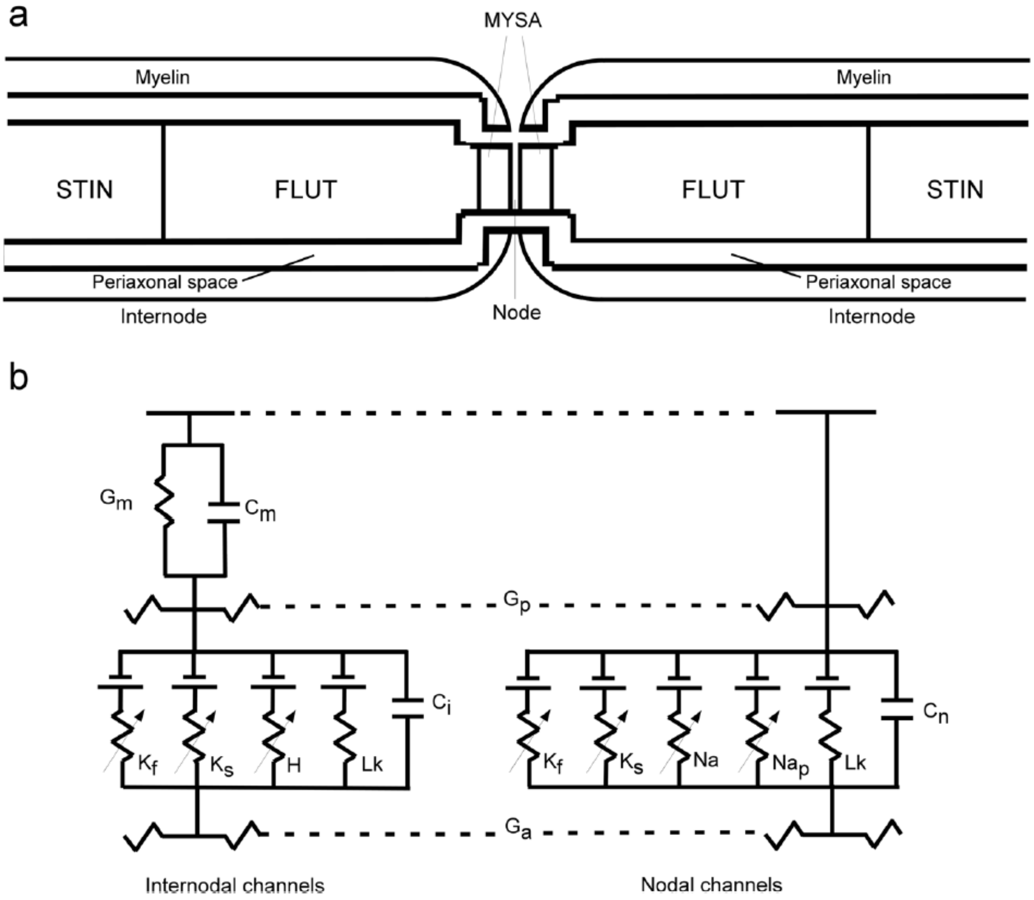
a
MYSA
Myelin
Myelin
STIN
FLUT
FLUT
STIN
Periaxonal space
Periaxonal space
Internode
Node
Internode
b
G_m
C_m
G_p
C_i
K_f
K_s
H
Lk
K_f
K_s
Na
Na_p
Lk
C_n
G_a
Internodal channels
Nodal channels

Figure 1.13: Overall structure of the motor and sensory axon model. Republished with permission of Springer Nature, from Gaines et al., 2018; permission conveyed through Copyright Clearance Center, Inc..

Simplifying biophysical models with Sweeney models

Although the MRG-model and its variations offer a great opportunity to study the interactions between neuromodulation technologies and the neural structures they aim to target, due to their complexity the necessary simulations are computationally expensive. When trying to quickly formulate hypothesis on neuromodulation technologies, a simpler variant of a nerve axon is desirable. In this case, I employed a model of a myelinated axon derived from rabbits (Sweeney et al., 1987). Here, the nodes of Ranvier are only represented by voltage-dependent sodium channels, voltage-dependent leakage channels and nodal capacitance. The internodal myelin is assumed to be a perfect insulator.

Modeling unmyelinated afferents with Sundt models

In order to represent the unmyelinated C-fibers I utilized a model derived by Sundt and colleagues (Sundt et al., 2015). Here, the axon is not divided into nodes of Raniver and internodes, but is simply constructed of voltage-gated sodium and delayed-rectifier potassium channels.

1.4.3 Neuromusculoskeletal modeling

In the last chapter, I discussed how to evaluate the effect of a neuromodulation technology on nervous tissues with a combination of FEMs and biophysical models of nerve axons. This methodology is immensely powerful to understand the manipulation of electric potential within these neural structures but lacks the capacity to decipher circuit-level interactions, that are a direct result of the artificial stimuli. For this purpose, neuromusculokeletal modeling can be employed. Fundamentally, neuromusculokeletal models can be divided into three components: A model of the neural circuits, a model of the musculoskeletal system, and their link.

Circuit-level models

The neural circuits underlying a subsystem of the nervous system can be modeled with different levels of abstractions depending on the phenomenon of interest. In the work of this thesis, I was primarily interested in analyzing dynamic behaviour of the spinal circuits linked to locomotion. In this case, spiking neural networks can be employed. I either modeled single neurons with biophysically realistic models (Wallen et al., 1992) or with integrate-and-fire neurons (Burkitt, 2006; Stienen et al., 2007). The former were particularly interesting when investigating the neuromodulatory effects of pharmacological agents. The latter are often sufficient and preferential due to their relatively cheap computational costs, to understand circuit-level responses to synaptic or artificial inputs. In the following chapters, I describe circuit-level models that receive input from proprioceptive and cutaneous sensory afferents. APs are artifically elicited in these afferents from recruitment patterns of hybrid computational models. Additionally, these afferents undergo natural firing patterns that can be calculated as described in chapter 1.2.1, if the appropriate parameters are known from the musculoskeletal system.

Model of the musculoskeletal system

The musculoskeletal system must be modeled in two parts: the skeletal system and the coupled muscles. The skeletal system can approximated as rigid body segments with defined inertal and mass properties. These segments are connected by constraints that approximate the joints.

Joint movements are then computed by equations of motions that leverage muscle contraction dynamics from joint moments (Buchanan et al., 2004). In this way a movement can be simulated.

Linking neural circuits models with musculoskeletal models

Circuit models and musculoskeletal models can be coupled in different ways. In the work described in this thesis, I exclusively used musculoskeletal models to calculate natural afferent firing patterns from kinematic recordings. This necessitates datasets of kinematic movement that are being imposed on the musculoskeletal model. This enables the collection of changes in muscle length that are necessary for the calculation of proprioceptive firing patterns (see Eqn. 1.1 and Eqn. 1.2). These firing profiles are being fed back into the spiking neural network model to supply natural activity to the spinal circuits while simultaneously coinciding with recruitment patterns of hybrid computational models. Ultimately, this culminates in an approximation of circuit-level behaviours during EES-enabled locomotion.

1.5 Thesis outline

In the most broad view possible, in my work, I aimed at restoring nervous function after neurological disorders. For this purpose, I decided to focus primarily on enabling locomotion in individuals in SCI. As I laid out in this introduction, the only common medical practices for enhancing neurological recovery are activity-based therapies (Behrman et al., 2017; Field-Fote et al., 2005; Jones et al., 2014). I also highlighted the tremendous potential of EES to support activity-based therapies in individuals with SCI (Angeli et al., 2018; M. L. Gill et al., 2018). However, I also explained that the efficacy and robustness of this approach is limited by the novelty of this approach and our limited understanding of the underlying mechanisms (Capogrosso & Lempka, 2020; Capogrosso et al., 2013; Edgerton et al., 2006). I hypothesized that hypothesis-driven strategies could ameliorate this situation (Capogrosso & Lempka, 2020). It is for this reason, that I decided to leverage computational modeling to investigate the mechanisms through which EES facilitates locomotion and to exploit this knowledge to develop hypothesis-driven strategies to improve EES therapies. I approached this goal by dividing it into three sub-goals:

- Refine our understanding of which nervous structures are recruited through EES and how they interact with natural afferent activity during locomotion.
- Design specific spinal cord stimulating electrode arrays tailored to patient anatomy.
- Develop personalizable EES strategies to target specific motor pools to enable locomotion.

In this section I will explain how I approached these goals and which advancements I have made towards them. Please note that in this overview, as well as in the initial introduction of all coming chapters, I will use the singular first person form (I) to highlight my own contributions and the plural first person form (we) to indicate the contribution of a team of people - including myself - to each presented result and innovation.

Computational studies suggested that EES predominantly recruits large-diameter, myelinated, proprioceptive and cutaneous afferent fibers in the dorsal roots (Capogrosso et al., 2013; Rattay et al., 2000). It is well established that proprioceptive muscle-spindle feedback circuits play an important role in enabling stepping with EES after SCI (Takeoka et al., 2014). Computational and experimental efforts suggested that EES works in synergy with the natural activity pattern of muscle-spindle feedback circuits to enable locomotion (Moraud et al., 2016). However, little is known about the role of cutaneous afferents in this interplay between EES and activity-based therapies. This was the predominant question I aimed to tackle in **chapter 2**. First, I built a computational framework that enabled me to build an anatomically highly-realistic volume conductor model of the rat spinal cord. I translated this model into a hybrid computational model combining a FEM including anistropic, inhomogeneous conductivity maps with accurate biophysical models of nervous structures to confirm the claim that EES recruits only large-diameter, myelinated, proprioceptive and cutaneous afferent fibers in amplitude ranges commonly used for locomotion therapy. In combination with my co-authors, we validated this hypothesis using neuron-specific calcium imaging of dorsal root ganglia. We leveraged chemogenetics, electrophysiological and behavioral experiments to establish that while the recruitment of proprioceptive afferents leads to the formation of motor patterns during EES, the recruitment of certain subtypes of cutaneous afferents disrupts this motor pattern. I then expanded an existing neuromusculoskeletal model (Moraud et al., 2016) to include a subsystem of cutaneous spinal circuits and was able to suggest that the recruitment of cutaneous afferents was detrimental to the production of locomotion. These results led to the development of pharmacological intervention therapies that in conjunction with EES seem to result in the production of robust locomotion in preclinical model of SCI.

Unfortunately, these pharmacotherapies are not yet available for use in humans. I therefore strived to investigate how the clinical translation of existing EES-enabled activity-based therapies may be improved upon. For this purpose, me and my co-authors investigated the mechanisms of EES in humans compared to animal models in **chapter 3**. Me and my co-authors translated an existing neuromusculoskeletal model (Moraud et al., 2016) for its applicability in humans. The resulting simulation results suggested that, unlike in rodents, in humans EES blocks the natural firing activity of proprioceptive sensory signals traveling along the recruited axon. We utilized a series of experiments in rats and individuals with SCI to verify this hypothesis. We leveraged computational simulations and behavioral experiments to define amplitudes and frequencies of EES that may not interfere with natural sensory activity during locomotion. As these parameter ranges were shockingly limited, we utilized our neuromusculoskeletal model to identify stimulation protocols that might improve the efficacy of EES. These stimulation protocols rely on the targeted recruitment of proprioceptive sensory afferents linked to specific muscles with appropriate timing to reproduce the migration map of MN pools during locomotion (Formento et al., 2018).

In **chapter 4**, I describe the work I carried out in a consortium assembled around the research groups of Grégoire Courtine and Jocelyne Bloch that worked on enabling activity-based therapies in individuals with incomplete SCI. Our objective was to leverage the results from **chapter 3** and implement and test these targeted stimulation strategies in a clinical setting. For this purpose, we utilized a commercially available neurostimulation device to target proprioceptive afferent fibers in the dorsal roots of the lumobsacral spinal cord. However, as I described in chapter 1.1.5, the human spinal cord exhibits a large degree of anatomical variability between humans. To my knowledge, there is no consensus to this date on where to implant an electrode array in the lumbosacral spinal cord to accurately target these dorsal roots. In order to guide the surgical implantation, I built a computational framework based on my work in chapter 2, that supports the development of personalized hybrid computational models of each study participant. I performed computer simulations to confirm the pre-operative implantation strategy and the multipolar stimulation paradigms to accurately reproduce the migration map of MN pools during locomotion. Ultimately, we were able to demonstrate that spatiotemporal spinal cord stimulation enables activity-based training of the study participants, while continuous stimulation fails to facilitate locomotor movements (Wagner et al., 2018).

Thereafter, I aimed at improving my approach from chapter 4. This endeavour is described in **chapter 5**. Firstly, the need to generate personalized computational models was not only computationally expensive but also necessitated a level of abstraction in anatomical parameters I was unsatisfied with. I wanted to test whether increasing the level of realism in anatomical parameters would make a difference in the optimization of electrode location. I adapted my computational framework to enable the rapid generation of highly personalized hybrid computational models including volume conductor models that accurately capture the participants anatomy and the biophysical properties of the proprioceptive afferents. I generated an atlas of personalized computational models from high-resolution medical imaging datasets of healthy volunteers. I noticed, not only that this improved anatomical accuracy yielded different results to lesser abstractions of the computational model, but also that the commercially available neurostimulation device was necessarily suboptimal for the purpose of EES-enabled locomotion. I leveraged anatomical analysis and computational modeling to inform the placement of electrodes on a new paddle lead that should improve the robustness of accurately targeting proprioceptive afferents in large and diversified patient-cohorts. I developed personalized computational models of individuals with complete SCI that were to be implanted with this new paddle lead, to guide the surgical implantation. Then, I worked with the previously described consortium to recover the participants ability to stand, walk, cycle, swim and control their trunk.

In **chapter 6**, I tested the viability of my computational framework to be translated for use in other neurological disorders and the development of novel neuromodulation paradigms. I started by verifying that my approach, which has previously been successful in humans, could also be used for the design of neuromodulation devices in preclinical animal models. I then explored whether I could leverage my computational framework for testing the viability of novel neuromodulation strategies in the use-case of optogenetic stimulation of the lumbosacral spinal cord in preclinical models. Finally, I directed my attention to targeting different neurological functions by focusing on the control of hemodynamics. I utilized a combination of hybrid computational models and circuit-level models to support the mechanistic understanding of hemodynamic control with EES and confirm stimulation paradigms for the control of hemodynamic stability following SCI.

In the last chapter (**chapter 7**), I discuss the potential of the proposed strategies to support the efficacious and robust implementation of neuromodulation strategies in a clinical setting. Special attention is given to the use-case of treatment planning for the restoration of locomotion in people with SCI and the design of neuromodulation technologies with hybrid computational models. I also speculate about future directions in improving EES-based rehabilitation strategies with in-silico investigations of neural adaptation mechanisms. Lastly, I highlight future research directions, that may enable the development of a robust and viable therapy for restoring locomotion in individuals with SCI.

2 EES recruits proprioceptive and cutaneous afferents with vastly different consequences on the formation of motor patterns

Activity-based therapies combined with EES of the spinal cord promotes locomotion in animal models and humans with paralysis (Angeli et al., 2018; Courtine et al., 2009; M. L. Gill et al., 2018; S. Harkema et al., 2011; Wagner et al., 2018). However, the development of EES strategies has thus far been mainly based on empirical observations. This strategy is intrisically suboptimal due to the vast space of variables that may have an effect of EES.

Instead, hypothesis-driven stimulation strategies may improve recovery of motor deficits in a more robust and efficacious manner. Unfortunately, the mechanisms underlying the neuromodulation of spinal circuits with EES remain largely enigmatic. Computational modelling and behavioural experiments revealed that EES may recruit large-diameter, myelinated afferent fibers in the dorsal roots (Capogrosso et al., 2013; Y. P. Gerasimenko et al., 2006; Rattay et al., 2000). These afferents fibers predominantly mediate information from proprioceptive and cutaneous sensory organs. Although, many studies suggest a beneficial interaction of EES and proprioceptive muscle-spindle feedback circuits that may facilitate motor control, to this date there is no direct evidence for the recruitment of proprioceptive afferent fibers with EES (Moraud et al., 2016; Takeoka et al., 2014). Furthermore, very little is known about the interaction between EES and cutaneous afferent fibers.

In this chapter, I present a work, that aimed to address the interaction of EES and proprioceptive and cutaneous LTMR afferents. For this purpose, I generated a highly-realistic volume conductor model of the lumbosacral spinal cord of a rat to suggest, that EES recruits Aα and Aβ afferents in the dorsal roots, at thresholds substantially lower than all other nerve fibers and neurons. This result is in line with previous works (Capogrosso et al., 2013; Y. P. Gerasimenko et al., 2006; Rattay et al., 2000). We provided experimental validation for these claims through neuron-specific calcium imaging of dorsal root ganglia in rodents. We leveraged chemogenetics, targeting proprioceptive neurons, to indicate that the recruitment of proprioceptive feedback circuits directly relates to the formation of motor patterns during EES. I extended a neuromusculoskeletal model, that we established previously, to include cutaneous

Low-Threshold MechanoReceptor (Aβ-LTMR) feedback circuits. I performed neurobiomechanical simulations that indicate, that the continuous recruitment of these afferents with EES, may be detrimental to the production of locomotion. Due to this result, we reasoned, that tuning the gain of proprioceptive and Aβ-LTMR feedback circuits in opposite directions would potentiate the therapeutic efficacy of EES. Investigating receptor subtypes in the spinal cord enabled us to support the design of a targeted pharmacotherapy, that aims to accomplish this in rodents. This pharmacotherapy potentiated muscle responses to EES, which resulted in robust locomotion in preclinical models of complete SCI and severe contusion SCI.

Related publication and personal contributions

The content of this chapter is adapted - with permission of the co-authors - from the following manuscript: Kay Bartholdi*, Quentin Barraud*, **Andreas Rowald***, Nicholas D James, Newton Cho, Thomas H. Hutson, Laetitia Baud, Emanuele Formento, Claudia Kathe, Jordan W. Squair, Jimmy Ravier, Nathalie Mestdagh, Eric Jnoff, Nofar Engelhard, Silvestro Micera, Victoria E. Abraira, Simone Di Giovanni, Pavel Musienko, Marco Capogrosso & Grégoire Courtine, "**Deconstruction of spinal circuits engaged by epidural electrical stimulation and restoring locomotion after paralysis**", in preparation.
* contributed equally to this work

Personal contributions: Conceived and developed a computational framework, adapted medical imaging protocols, collected and analyzed medical imaging datasets, developed the computational models, performed computer simulations, performed behavioural experiments in rodent models, collected and analyzed data from behavioural experiments, figures preparation, manuscript editing.

2.1 Abstract

Epidural Electrical Stimulation (EES) of the lumbosacral spinal cord enables walking in people with paralysis. However, the underlying mechanisms remain enigmatic. Here, we demonstrate that EES recruits both proprioceptive (Aα/Aβ) and cutaneous Low-Threshold MechanoReceptor (Aβ-LTMR) afferents. This preferential activation is due to the location, topology, myelin content and diameter of these afferents. Targeted modulation of proprioceptive neurons revealed that motor patterns emerge from the repeated recruitment of proprioceptive feedback circuits. Instead, the unanticipated recruitment of Aβ-LTMR feedback circuits with EES deteriorates locomotion. EES disrupts light touch information encoded in Aβ-LTMR afferents and transmitted downstream through glutamatergic interneurons expressing the RORα nuclear orphan receptor. This understanding guided the design of a noradrenergic pharmacotherapy that upregulates proprioceptive feedback circuits while downregulating Aβ-LTMR/RORα feedback circuits. This sensory gating potentiated the efficacy of EES, enabling robust locomotion in paralyzed rats. These findings will support the design of targeted and more effective neuromodulation therapies.

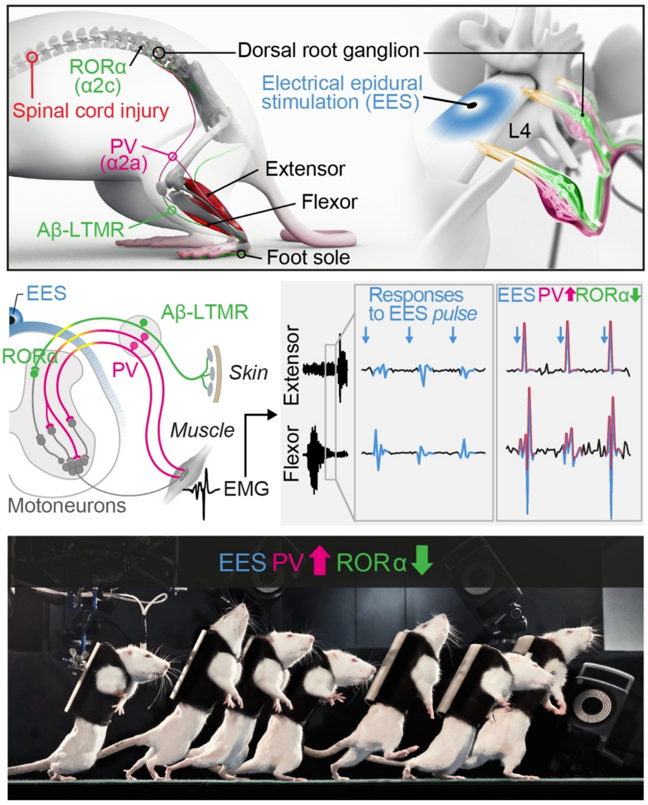
RORα
(α2c)
Spinal cord injury
Dorsal root ganglion
Electrical epidural
stimulation (EES)
L4
PV
(α2a)
Extensor
Flexor
Aβ-LTMR
Foot sole
EES
Aβ-LTMR
RORα
PV
Skin
Muscle
EMG
Motoneurons
Extensor
Flexor
Responses
to EES pulse
EES PV⬆ RORα⬇
EES PV⬆ RORα⬇

Figure 2.1: Summary of the main findings in graphical form. EES promotes the formation of motor patterns by recruiting proprioceptive (Aα/Aβ) afferents. Inversly, the continuous recruitment of cutaneous low-threshold mechanoreceptor (Aβ-LTMR) afferents disrupts locomotion.

2.2 Introduction

Electroceuticals – the regulation of targeted brain and spinal circuits with electrical stimulation – is broadening the spectrum of therapeutic options to treat or alleviate symptoms associated with various neurological disorders (Borton et al., 2013; Famm et al., 2013). The most common treatments involve deep brain stimulation of the basal ganglia in people with Parkinson's disease or tremor (Limousin et al., 1998), and epidural spinal cord stimulation to alleviate neuropathic pain (Shealy et al., 1967). However, the number of neurological conditions that may be addressed with electroceuticals is expanding quickly.

A recent achievement is the recovery of walking in people with paralysis when EES is applied to the lumbosacral spinal cord. Three independent studies documented this recovery in a few individuals with chronic Spinal Cord Injury (SCI), offering promise that electroceuticals could mediate functional gains for people with paralysis (Angeli et al., 2018; M. L. Gill et al., 2018; Wagner et al., 2018). However, our understanding of the circuit-level mechanisms through which EES modulates spinal circuits remain limited, despite the importance of this knowledge to design precise and effective strategies that can target the heterogenous population of patients with SCI.

While the mechanisms of EES remain debated, a long-assumed hypothesis is the activation of motoneurons trans-synaptically through the recruitment of afferent pathways (Capogrosso et al., 2013; Formento et al., 2018; Y. P. Gerasimenko et al., 2006; Rattay et al., 2000). Computational models suggested that when EES is applied over the dura mater of lumbosacral segments, the electrical current flows within the cerebrospinal fluid where it depolarizes large-diameter, myelinated afferent fibers (Capogrosso et al., 2013; Ladenbauer et al., 2010; Rattay et al., 2000). These afferent fibers primarily innervate muscle proprioceptors that transmit information about the length and change in length of a muscle, as well as the tension applied to its tendon. Albeit to a lesser extent, afferent fibers recruited by EES may also include the large-diameter, myelinated low-threshold mechanoreceptors (Aβ-LTMRs) afferents that convey information about innocuous light touch sensation (Capogrosso et al., 2013; Holsheimer, 2002). These afferent pathways form feedback circuits that regulate the activation of motoneurons during locomotion, both directly and indirectly through the modulation of spinal interneurons involved in motor control (Arber, 2012; Grossmann et al., 2010; Kiehn, 2016; Moraud et al., 2016). These sensory feedback circuits integrate afferent information and descending commands to coordinate the formation of motor patterns underlying a variety of locomotor behaviors (Bourane et al., 2015; Mayer et al., 2018; Takeoka et al., 2014; Windhorst, 2007).

Here, we sought to investigate these hypothetical mechanisms. Specifically, our aim was to deconstruct the spinal circuits through which EES enables walking after paralysis, and leverage this knowledge to develop a therapy that targets the circuit-level mechanisms of EES to potentiate this treatment.

For this purpose, we combined finite element modeling and neurobiomechanical simulations with a series of anatomical, electrophysiological and behavioral experiments in transgenic rats and mice. To ease their understanding, we summarize the logic and main results of these experiments. Modeling of electrical fields induced by EES indicated that the location, curvilinear trajectory, high myelin content, and large diameter of Aα and Aβ afferents favor their recruitment with EES, at thresholds substantially lower than all other nerve fibers and neurons. Neuron-specific calcium imaging of Dorsal Root Ganglia (DRG) confirmed that, within the range of relevant amplitudes to enable walking, EES near-exclusively recruits proprioceptive and Aβ-LTMR neurons in DRGs. We then demonstrated that the recruitment of proprioceptive afferents activates motoneurons via proprioceptive feedback circuits, eliciting a succession of reflex responses in leg muscles that are locked to each pulse of EES. Using chemogenetics targeted in proprioceptive neurons, we established a causal relationship between the recruitment of proprioceptive feedback circuits and the formation of motor patterns during EES. Contrary to proprioceptive afferents, Aβ-LTMR afferents are only transiently activated during locomotion. Consequently, neurobiomechanical simulations suggested that the continuous recruitment of these afferents with EES was detrimental to the production of locomotion. We then reasoned that tuning the gain of proprioceptive and Aβ-LTMR feedback circuits in opposite directions would potentiate the therapeutic efficacy of EES. Noradrenergic pharmacotherapies targeting α2 receptors are commonly used to modulate these feedback circuits in patients with chronic pain or spasticity (Maupas et al., 2004; Nance et al., 1985; Pertovaara, 2006). We thus asked whether α2 receptor subtypes exhibit a differential expression onto proprioceptive and Aβ-LTMR feedback circuits that could support the design of a targeted pharmacotherapy to test our hypothesis. We found a profuse expression of α2a receptors in proprioceptive neurons, whereas in the spinal cord, α2c receptors were only expressed in a specific population of interneurons receiving a dense innervation from Aβ-LTMR afferents. The activation of α2 receptors induces a G-protein mediated decrease of neuronal activity (Pertovaara, 2006; Shen et al., 1992; Surprenant & North, 1988). Consequently, we repurposed a dual α2a antagonist / α2c agonist that upregulated the gain in proprioceptive feedback circuits while downregulating the gain in Aβ-LTMR feedback circuits. As predicted, this targeted noradrenergic pharmacotherapy potentiated muscle responses to EES, which resulted in robust locomotion in preclinical models of complete SCI and severe contusion SCI.

2.3 Results

2.3.1 EES recruits large-diameter afferent fibers in the entry zone

To identify the neural structures directly recruited by EES, we developed an anatomically and neuro-functionally realistic model of the lumbosacral spinal cord in adult rats. First, we acquired high-resolution MRI datasets to reconstruct the spinal cord and vertebrae (Fig. 2.2A and Fig. 2.3A-C). We discretized this reconstruction into a finite element model that allowed us to characterize the distribution of electrical currents and potentials resulting from the application of EES over the spinal cord (Fig. 2.2A-C).

We incorporated the entire spectrum of afferent fiber populations (Aα, Aβ, Aδ and C) located in the posterior roots and dorsal columns. We also modelled α-MotoNeurons (MNs) and their Motor Axon (MA), and positioned interneurons in the dorsal horn. We ensured that the myelin compositions, electrical properties, anatomical dimensions and tridimensional topologies were functionally realistic and specific for each modelled neural element (Fig. 2.3D).

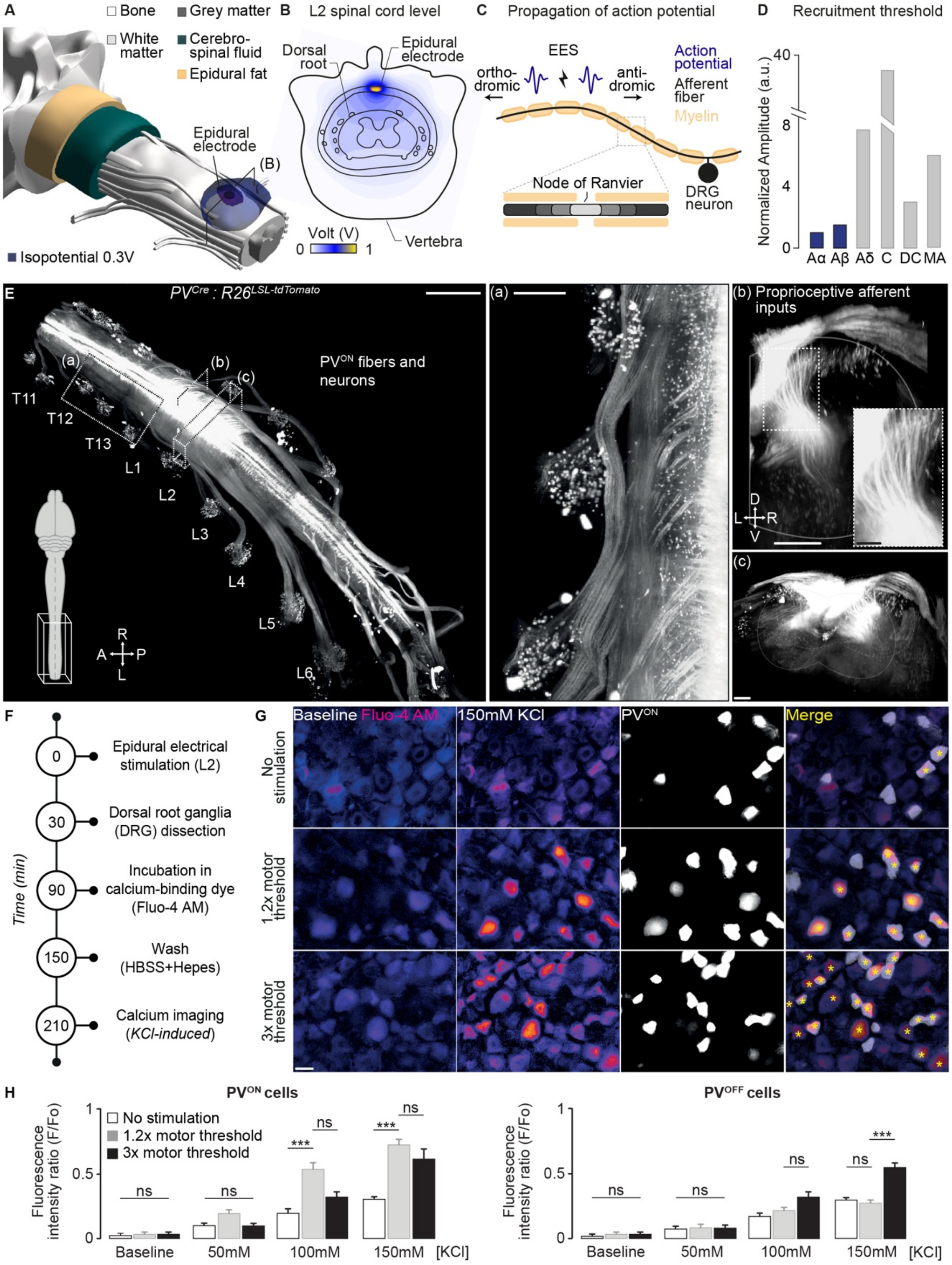
A
□ Bone
■ Grey matter
□ White matter
■ Cerebro-spinal fluid
■ Epidural fat
Epidural electrode
(B)
■ Isopotential 0.3V
B
L2 spinal cord level
Dorsal root
Epidural electrode
Volt (V)
0
1
Vertebra
C
Propagation of action potential
EES
ortho-dromic
anti-dromic
Action potential
Afferent fiber
Myelin
Node of Ranvier
DRG neuron
D
Recruitment threshold
Normalized Amplitude (a.u.)
40
8
4
0
Aα
Aβ
Aδ
C
DC
MA
E
PV^Cre : R26^LSL-tdTomato
(a)
(b)
(c)
T11
T12
T13
L1
L2
L3
L4
L5
L6
PV^ON fibers and neurons
R
A
P
L
(a)
(b) Proprioceptive afferent inputs
D
L
R
V
(c)
F
Time (min)
0
Epidural electrical stimulation (L2)
30
Dorsal root ganglia (DRG) dissection
90
Incubation in calcium-binding dye (Fluo-4 AM)
150
Wash (HBSS+Hepes)
210
Calcium imaging (KCl-induced)
G
Baseline Fluo-4 AM
150mM KCl
PV^ON
Merge
No stimulation
1.2x motor threshold
3x motor threshold
H
PV^ON cells
Fluorescence intensity ratio (F/Fo)
1
0.5
0
□ No stimulation
■ 1.2x motor threshold
■ 3x motor threshold
ns
ns
***
ns
***
ns
Baseline
50mM
100mM
150mM
[KCl]
PV^OFF cells
Fluorescence intensity ratio (F/Fo)
1
0.5
0
ns
ns
ns
ns
***
Baseline
50mM
100mM
150mM
[KCl]

Figure 2.2: EES recruits proprioceptive neurons in the DRG.

Figure 2.2: (Continued) (A) High-resolution MRI-based reconstruction of the different tissues surrounding the spinal cord. Color-coded isopotentials showing the spread of the electric field following a single pulse of EES applied over the dorsal aspect of the spinal cord. (B) Electrical potential and generated currents following a single pulse of EES. (C) EES elicits action potentials along the activated fibers that propagate orthodromically toward the spinal cord and antidromically towards the periphery. The curves show the predicted propagation of excitation along a large-diameter, myelinated afferent fiber. (D) Recruitment thresholds for the activation of each class of sensory afferent fibers , Dorsal Columns (DC) and Motor Axons (MA) when delivering EES at increasing stimulation intensity. (E) Cleared lumbosacral spinal cord with attached DRGs of a PVCre:R26LSL-tdTomato mouse. Insets highlight the curvilinear trajectory of proprioceptive afferent fibers and proprioceptive neurons in DRGs. Scale bars, 2mm (overview), 500µm (a), 200µm (b), 50µm for the inset and 200µm (c), respectively. (F) Timeline of calcium imaging experiments, conducted in PVCre:R26LSL-tdTomato mice (n = 5 per condition) under three experimental conditions: no stimulation, EES at 1.2x motor threshold and EES at 3x motor threshold. (G) Representative images of intracellular calcium release in L2 DRG for each condition. Asterisks highlight released intracellular calcium in PVON and/or PVOFF neurons. Scale bar, 50µm. (H) Bar plots reporting calcium release in L2 DRGs for each condition. EES at 1.2x motor threshold led to an increase in calcium release confined to PVON neurons. In contrast, PVOFF neurons did not release significantly more intracellular calcium at this stimulation intensity. **P = 0.003. ns, not significant. Two-way ANOVA followed by Tukey's post-hoc test.

Simulations predicted that the probability of recruiting Aα- and Aβ-afferent fibers with EES was very high, which contrasted with the low probability of depolarizing Aδ and C afferents (Fig. 2.2D). Simulations additionally predicted that EES applied over lumbar segments exerted no relevant influence on interneurons, motoneurons and motor axons (Fig. 2.2D). In the model, the depolarization of Aα- and Aβ-afferent fibers predominantly occurred where they exhibit a high degree of curvature that favors their recruitment with electrical fields. This depolarization triggers action potentials that propagate along the axon in both directions, thus activating spinal circuits orthodromically and sensory neurons in the DRGs antidromically (Fig. 2.2C). Electrodes (cathode) positioned over the midline additionally recruited some branches of Aα- and Aβ-afferent fibers within the dorsal columns (DC) (Fig. 2.2D).
Together, these simulations predicted that EES primarily recruits Aα- and Aβ-afferent fibers, in particular where they exhibit a high degree of curvature that promotes their activation.

2.3.2 EES activates proprioceptive neurons

We next thought to verify these predictions with experimental quantifications using transgenic mice and rats that allowed us to target specific neuronal populations.

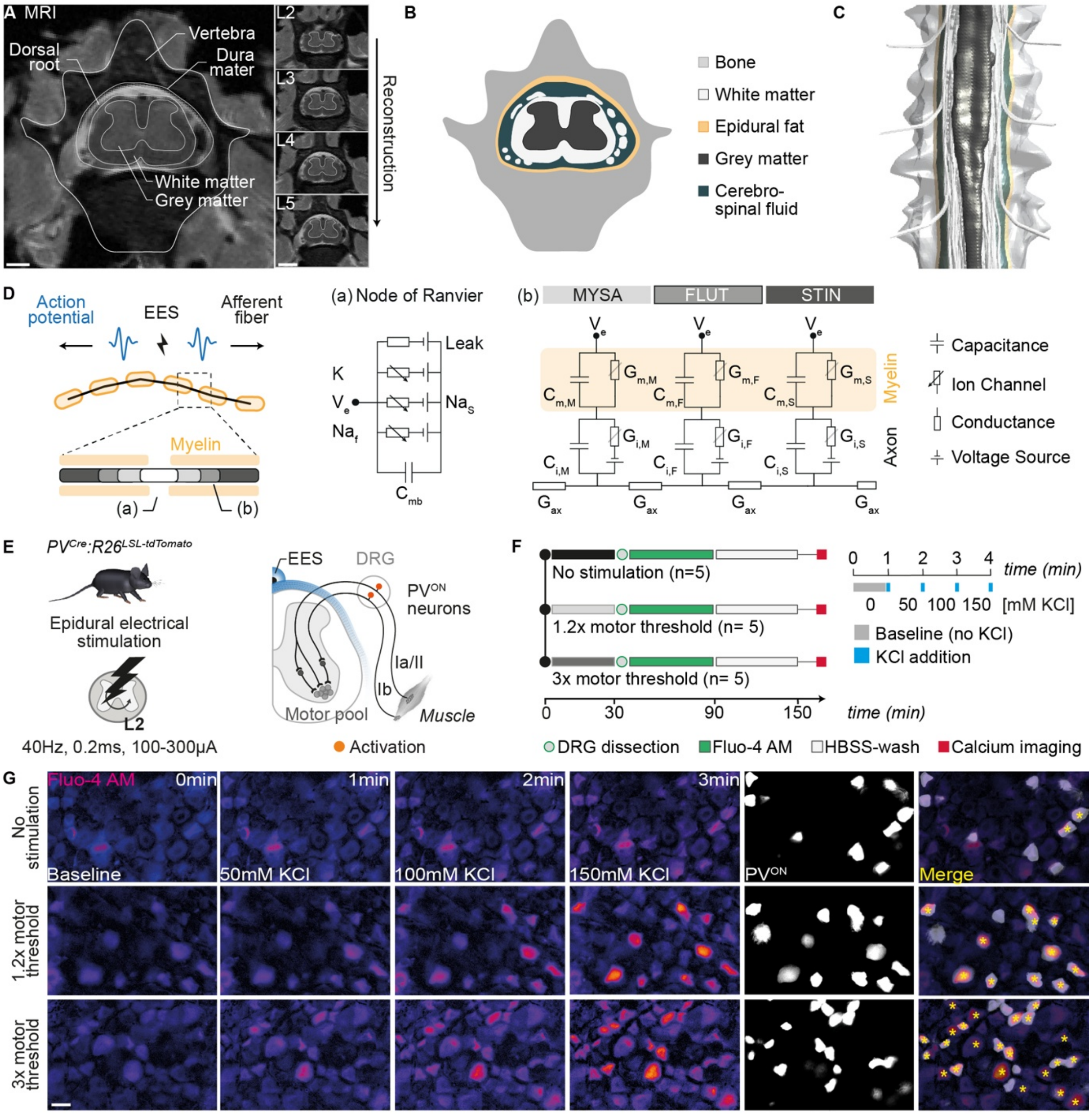
A MRI
Dorsal root
Vertebra
Dura mater
White matter
Grey matter
L2
L3
L4
L5
Reconstruction
B
Bone
White matter
Epidural fat
Grey matter
Cerebro-spinal fluid
C
D
Action potential
EES
Afferent fiber
Myelin
(a)
(b)
(a) Node of Ranvier
Leak
K
V_e
Na_s
Na_f
C_mb
(b) MYSA
FLUT
STIN
V_e
G_m,M
G_m,F
G_m,S
C_m,M
C_m,F
C_m,S
Myelin
G_i,M
G_i,F
G_i,S
C_i,M
C_i,F
C_i,S
Axon
G_ax
Capacitance
Ion Channel
Conductance
Voltage Source
E
PV^Cre:R26^LSL-tdTomato
Epidural electrical stimulation
L2
40Hz, 0.2ms, 100-300µA
EES
DRG
PV^ON neurons
Ia/II
Ib
Motor pool
Muscle
Activation
F
No stimulation (n=5)
1.2x motor threshold (n= 5)
3x motor threshold (n= 5)
0
30
90
150
time (min)
0 1 2 3 4
time (min)
0 50 100 150 [mM KCl]
Baseline (no KCl)
KCl addition
DRG dissection
Fluo-4 AM
HBSS-wash
Calcium imaging
G
Fluo-4 AM
0min
1min
2min
3min
No stimulation
1.2x motor threshold
3x motor threshold
Baseline
50mM KCl
100mM KCl
150mM KCl
PV^ON
Merge

Figure 2.3: Computational models and calcium imaging of proprioceptive neurons (A) MRI image of a rat vertebral column. Scale bars 1mm for the overview and 2mm for the insets, respectively. (B) MRI-based reconstruction of the L2 vertebra and spinal cord. (C) Reconstruction of the vertebral canal including the spinal cord and dorsal roots based on a sequence of consecutive MRI images. (D) Computer model of a myelinated fiber including a node of Ranvier (a) and the single components of the afferent fiber (MYSA, FLUT, STIN). (E) Calcium imaging experiments conducted in PVCre:R26LSL-tdTomato mice to visualize the activation of proprioceptive neurons in the dorsal roots in response to EES. (F) Timeline of the calcium imaging experiments. (G) Representative images of intracellular calcium release in L2 DRGs for each experimental condition and at each time point during the experiment. Asterisks indicate the released intracellular calcium in PVON and/or PVOFF neurons. Scale bar 50µm

We first verified that proprioceptive afferent fibers exhibit a topological configuration that promotes their activation with EES. Proprioceptive neurons express the protein ParValbumin (PV) (Arber et al., 2000).To visualize proprioceptive afferent fibers, we cleared the posterior roots, DRGs and lumbosacral spinal cord of PV^{Cre}:$R26^{LSL-tdTomato}$ mice. CLARITY-optimized light-sheet microscopy confirmed that proprioceptive afferent fibers enter the spinal cord through a continuum of rootlets with highly curved trajectories prone to depolarization with electrical currents (Fig. 2.2E).

We then asked whether EES leads to the preferential activation of proprioceptive neurons located in the DRGs. We imaged intracellular calcium levels in the DRGs of PV^{Cre}:$R26^{LSL-tdTomato}$ mice in response to EES applied during 30 min over the L2 spinal cord segment (n = 5 mice per group, Fig. 2.2F and Fig. 2.3E-G). We parametrized EES at the intensity (1.2 X muscle response threshold) and frequency (40 Hz) commonly used to enable walking after SCI. This stimulation led to a significant increase in the levels of calcium released from intracellular stores of PV^{ON} neurons (Fig. 2.2G-H). In contrast, PV^{OFF} neurons required stimulation intensities as large as three times the muscle response threshold to exhibit a similar increase in calcium levels. At this intensity, EES did not recruit additional PV^{ON} neurons, indicating that PV^{ON} cells activated by EES were nearly all recruited at the intensities commonly delivered to enable walking with EES (Fig. 2.2G-H and Fig. 2.3G).

2.3.3 EES recruits proprioceptive feedback circuits to form motor patterns

We next sought to understand how the recruitment of proprioceptive feedback circuits leads to motor pattern formation, and ascertain their pivotal role in enabling locomotion with EES after SCI. To expose this causality, we expressed inhibitory (h4mDi) or excitatory (h3mDq) designer receptor exclusively activated by designer drug (DREADD) in proprioceptive neurons located in the DRGs. To target proprioceptive neurons, we injected AAV2/5-hSyn-flex-h4mDi-mCherry or AAV2/5-hSyn-flex-h3mDq-mCherry into both sciatic nerves of PV^{Cre} rats (Fig. 2.4A). Post-mortem quantification of L4 DRGs revealed that 46 ± 2.1% (h4mDi, Fig. 2.4B) and 54 ± 1.2% (h3mD,Fig. 2.4C) of PV^{ON} neurons expressed the DREADD-tag mCherry.

A single pulse of EES applied over the L4 spinal segment elicited muscle responses that we recorded from the ElectroMyoGraphic (EMG) activity of tibialis anterior muscles (Fig. 2.4D). These responses have previously been suggested to be associated with the recruitment of proprioceptive feedback circuits (Y. P. Gerasimenko et al., 2006). Silencing PV^{ON} DRG neurons with the DREADD agonist Clozapine N-Oxide (CNO) near-completely abolished these responses, whereas CNO had no influence on these responses in wild-type rats (Fig. 2.4D-E). Instead, the potentiation of PV^{ON} DRG neurons with excitatory DREADDs significantly increased the amplitude of muscle responses ($p < 0.01$, Fig. 2.4D-E).

The rats received a severe mid-thoracic (T8) contusion SCI (250 kdyn) that led to complete paralysis associated with quiescent EMG activity in leg muscles (Fig. 2.4F and Fig. 2.5A-B). Continuous EES immediately enabled bipedal stepping on a treadmill while the rats were supported against gravity in a robotic system (Fig. 2.4F). Analysis of EMG activity in leg muscles revealed that each burst was elaborated from a succession of muscle responses linked to each pulse of EES (Fig. 2.4F).

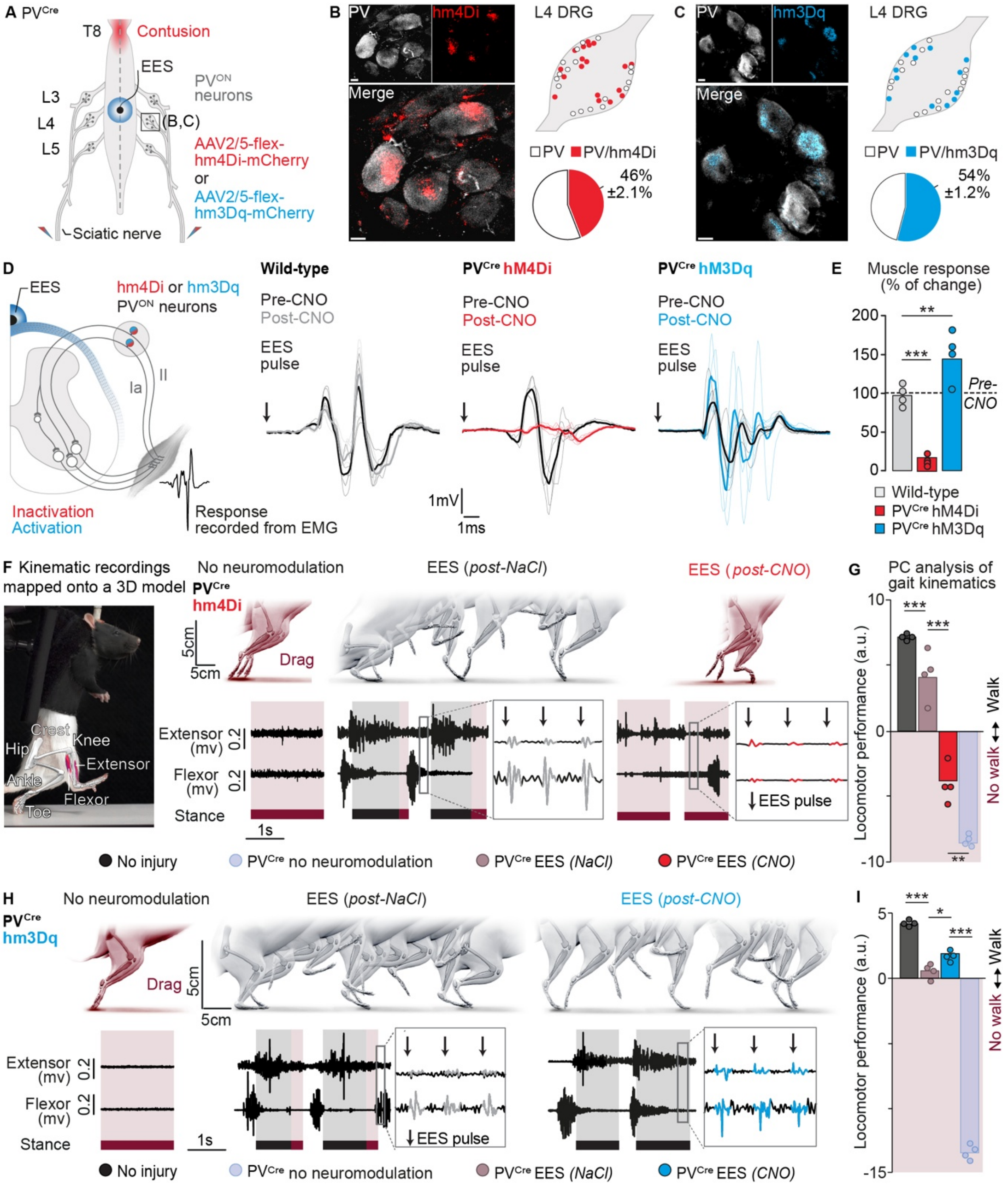

Figure 2.4: EES engages proprioceptive feedback circuits to facilitate walking after SCI. (A) Scheme summarizing chemogenetic inactivation or activation of PVON neurons in DRGs. (B) Photograph showing mCherry-infected PVON neurons in the L4 DRG after AAV2/5-flex-hm4Di injection into the sciatic nerve. Scale bar 10 µm. DRG reconstruction displaying the ratio of PVON/mCherryON double-labelled neurons. (C) Photograph showing mCherry-infected PVON neurons in the DRG after AAV2/5-flex-hm3Dq injection into the sciatic nerve, as in (B). (D) Scheme illustrating reflex recordings in ankle flexor muscles in response to EES at L4 spinal level. Muscle responses are shown before and after 55 minutes post-CNO.

Figure 2.4: (Continued) (E) Bar plot reporting the relative change in the amplitude of muscle responses following CNO injection for each condition. ***P < 0.001, Two-way ANOVA followed by Bonferroni's post-hoc test. **P < 0.01, Two-way ANOVA followed by Bonferroni's post-hoc test. (F) Rats with contusion SCI stepping bipedally on a treadmill while supported by a robotic body weight support system. Joint kinematics were projected onto a 3D model of the hindlimbs to generate representative sequences of hindlimb movements in conjunction with EMG activity of extensor and flexor muscles of the ankle. EMG insets show muscle responses to each pulse of EES, indicated by arrows. (G) Bar plot reporting average scores on PC1, which quantifies the relative locomotor performance of PVCre-hm4Di rats with complete SCI under each experimental condition (n = 4 per condition) compared to rats with no injury. ***P < 0.0001. Two-way ANOVA followed by Bonferroni's post-hoc test. (H) Same functional experiments as in (G) in PVCre-hm3Dq rats. *P < 0.05. Two-way ANOVA followed by Bonferroni's post-hoc test.

Silencing PV^{ON} DRG neurons blocked these muscle responses, which led to the near complete suppression of locomotion ($p < 0.001$, Fig. 2.4F). On the contrary, the activation of excitatory DREADDs increased the amplitude of muscle responses to EES during walking, which translated into improved locomotor performance ($p < 0.05$; Fig. 2.4H-I and Fig. 2.5E).

We quantified locomotor performance by applying a Principal Component (PC) analysis onto a comprehensive set of 129 kinematic, kinetic and EMG parameters (Table 2.1) calculated from high-resolution recordings (Fig. 2.4G and Fig. 2.5C-D). PC1 captured 40% of the total variance in gait patterns, and segregated the experimental groups and conditions. Consequently, locomotor performance was quantified based on the scores of each rat along PC1 (Fig. 2.4G). Silencing proprioceptive feedback circuits deteriorated locomotor performance, leading to gait patterns equivalent to those measured without EES (Fig. 2.4D-E). Instead, increasing the gain of these circuits promoted gait patterns that shared many features with those of non-injured rats (Fig. 2.4F-G and Fig. 2.5).

These results not only demonstrate that EES activates leg muscles through the recruitment of proprioceptive feedback circuits, but also show that augmenting the gain in these circuits improves the ability of EES to enable locomotion.

2.3.4 Detrimental activation of Aβ-LTMR feedback circuits

We next asked whether EES also recruits Aβ-LTMR afferent fibers, as predicted in simulations. LTMR neurons are molecularly defined by the unique expression of the Ret receptor at embryonic days E10-E11 (Abraira et al., 2017; Bourane et al., 2015; Zimmerman et al., 2019), which we targeted using $Ret^{CreER} : R26^{LSL-tdTomato}$ mice (Luo et al., 2009).

Computed gait parameters for PC analysis		
Gait timing		Velocity
Cycle duration		Whole limb angle velocity (minimal)
Movement velocity		Hip joint angle velocity (minimal)
Stance duration		Knee joint angle velocity (minimal)
Swing duration		Ankle joint angle velocity (minimal)
Stance duration in percentage of whole cycle		MTP joint angle velocity (minimal)
Interlimb coordination		Whole limb angle velocity (maximal)
Double stance (in % of gait cycle duration)		Hip joint angle velocity (maximal)
Stride length		Knee joint angle velocity (maximal)
Step length		Ankle joint angle velocity (maximal)
Step height		MTP joint angle velocity (maximal)
Step height normalized to stance height		Whole limb angle velocity
Path length		Hip joint angle velocity
Features of limb endpoint trajectory		Knee joint angle velocity
Stance width		Ankle joint angle velocity
Body weight support by the postural prosthesis		MTP joint angle velocity
Maximal backward position of the foot		(Intra-limb) coordination
Maximal forward position of the foot		Temporal coupling between crest and thigh oscillation
Maximal endpoint velocity		Temporal coupling between thigh and shank oscillation
Timing of the maximal endpoint velocity		Temporal coupling between shank and foot oscillation
Endpoint acceleration		Temporal coupling between foot and toe oscillation
Endpoint velocity		Correlation of crest and thigh oscillation
Orientation of the velocity vector at swing onset		Correlation of thigh and leg oscillation
Drag duration		Correlation of leg and foot oscillation
Relative drag duration (% of swing duration)		Correlation of foot and toe oscillation
Stability		Correlation of hip and knee oscillation
Amplitude of lateral trunk position		Correlation of knee and ankle oscillation
Sagittal trunk movement		Correlation of ankle and MTP oscillation
Sagittal trunk velocity		Timing of crest-thigh (minimal)
Variability of vertical hip-midpoint oscillation		Timing of crest-thigh (maximal)
Variability of medio-lateral hip rotation		Timing of thigh-shank (minimal)
Forward movement of the center of mass		Timing of thigh-shank (maximal)
Lateral oscillation of the center of mass		Timing of shank-foot (minimal)
Joint angles and limb segment oscillations		Timing of shank-foot (maximal)
Crest oscillation (minimal elevation)		Degree of linear coupling between joint oscillations (PC1)
Thigh oscillation (minimal elevation)		Degree of linear coupling between joint oscillations (PC2)
Shank oscillation (minimal elevation)		Degree of linear coupling between joint oscillations (PC3)
Foot oscillation (minimal elevation)		Similarity to healthy gait
Toe oscillation (minimal elevation)		Correlation between limb oscillation of healthy and injured leg
Whole limb oscillation (minimal elevation)		Correlation between hip oscillation of healthy and injured leg
Crest oscillation (maximal elevation)		Correlation between knee oscillation (healthy and injured leg)
Thigh oscillation (maximal elevation)		Correlation between ankle oscillation (healthy and injured leg)
Shank oscillation (maximal elevation)		Correlation between MTP oscillation of healthy and injured leg
Foot oscillation (maximal elevation)		Variability of gait
Toe oscillation (maximal elevation)		Variability of foot trajectory in the forward direction
Whole limb oscillation (maximal elevation)		Variability of foot trajectory in the sagittal plane
Hip joint angle (maximal)		Variability of foot trajectory in the 3-dimensioal room
Knee joint angle (maximal)		Variability of gait cycle duration
Ankle joint angle (maximal)		Variability of stride length
MTP joint angle (maximal)		Variability of double stance duration
Whole limb adduction		Variability of step height
Foot adduction		Variability of path length
Hip joint angle (minimal)		Variability of max endpoint velocity
Knee joint angle (minimal)		Kinetics
Ankle joint angle (minimal)		Vertical ground reaction force
MTP joint angle (minimal)		Parameters measured from EMG activity
Whole limb abduction		Burst onset of extensor
Foot abduction		Burst end of extension
Crest oscillation		Burst duration of extensor
Thigh oscillation		Mean amplitude of extensor
Shank oscillation		Integral of extensor activity
Foot oscillation		Root mean square of extensor activity
Toe oscillation		Burst onset flexor
Whole limb oscillation		Burst end of flexor
Hip joint angle		Burst duration of flexor
Knee joint angle		Mean amplitude of flexor
Ankle joint angle		Integral of flexor activity
MTP joint angle		Root mean square of flexor activity
Whole limb medio-lateral oscillation		Co-contraction of the flexor and extensor muscle

Table 2.1: Kinematic, Kinetic and EMG parameters.

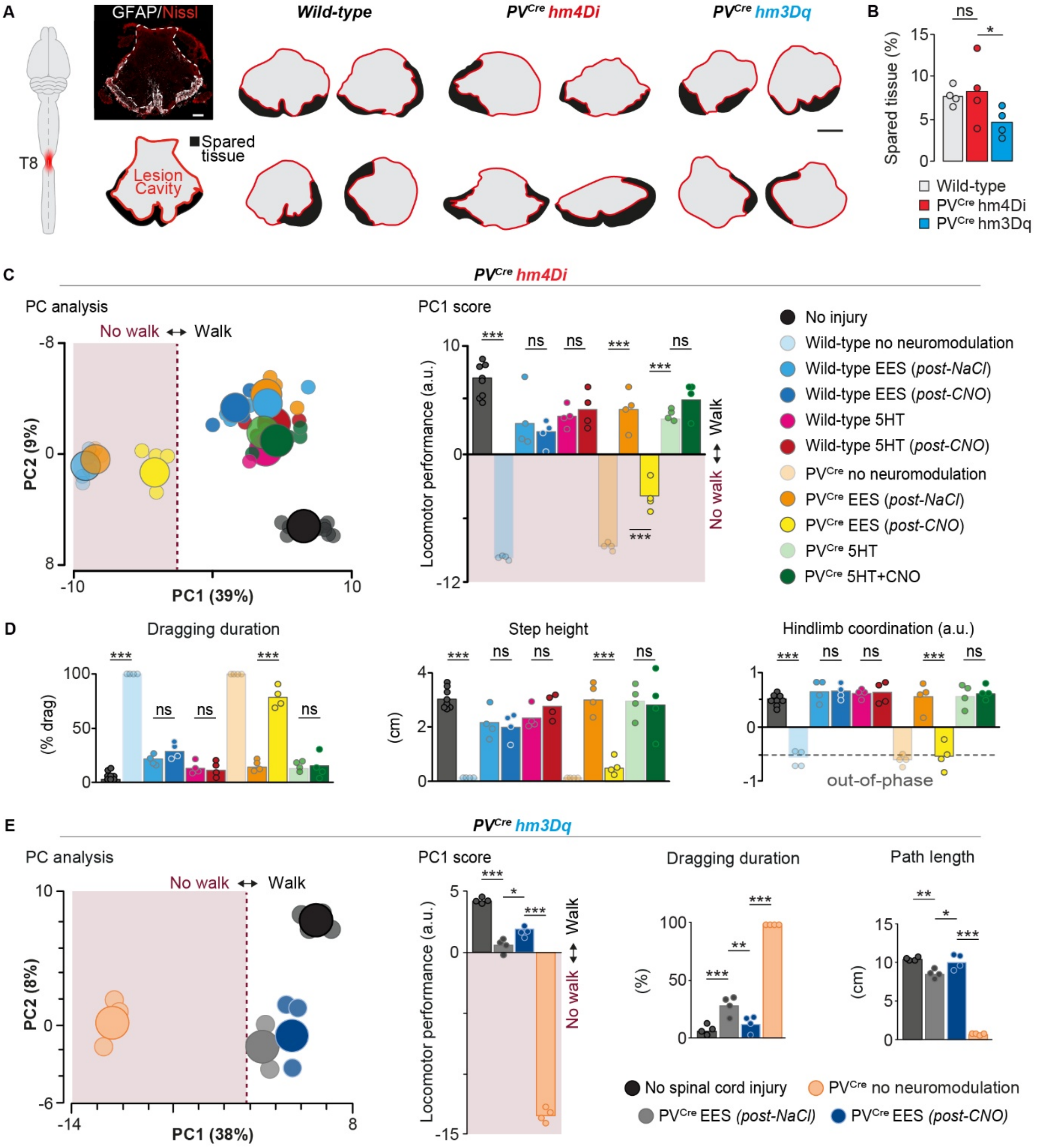

Figure 2.5: Quantification of lesion size and functional outcomes. (A) Representative coronal section through a contusion epicenter at T8 (GFAP, Glial Fibrillary Acidic Protein). Scale bar 200µm. The contours of the lesion cavity at the epicenter are shown for all the main experimental rats. Scale bar 500 µm. (B) Bar graph reporting the area of spared tissue at the lesion epicenter for wild-type (n=4), PVCre-hm4Di (n=4) and PVCre-hm3Dq (n=4) rats. ns, not significant; *P < 0.05; Non-paired Student's t-test. (C) PC analysis applied on 129 gait parameters averaged for each rat and condition (small circle). Large circles show the average per group. Bar plot showing average scores on PC1, which quantifies locomotor performance of PVCre-hm4Di and wild-type rats compared to non-injured rats (n=10). (D) Bar plots reporting average values of classic gait parameters with high factor loading on PC1. ***P < 0.001. Two-way ANOVA followed by Bonferroni's post-hoc test.

Figure 2.5: (Continued) (E) PC analysis to quantify locomotor performance in PVCre-hm3Dq rats (n=4). Bar plots report average scores on PC1 and average values of single gait parameters in PVCre rats (n=4) and non-injured wild-type rats (n=4). The activation of proprioceptive feedback circuits following CNO improved locomotor outcomes. PC1 score: $^{*}P < 0.05$. One-way ANOVA followed by Bonferroni's post-hoc test. Gait parameters: $^{**}P < 0.01$, $^{*}P < 0.05$. Two-way ANOVA followed by Bonferroni's post-hoc test.

As observed with proprioceptive afferent fibers, CLARITY-optimized light-sheet microscopy of Ret^{CreER} : $R26^{LSL-tdTomato}$ confirmed that Aβ-LTMR afferent fibers enter the spinal cord through a continuum of rootlets with highly curved trajectories prone to depolarization with electrical currents (Fig. 2.6A).

We then imaged intracellular calcium levels in the DRGs of Ret^{CreER} : $R26^{LSL-tdTomato}$ mice in response to 30 min of EES applied over the L2 spinal cord (n = 5, Fig. 2.6B). This stimulation led to an increased release of calcium from intracellular stores of Ret^{ON} neurons in the DRGs, albeit the relative increase was less pronounced than in proprioceptive neurons (Fig. 2.6C, D). These experiments showed that EES also recruits Aβ-LTMR feedback circuits. Contrary to proprioceptive feedback circuits, the contribution of Aβ-LTMR feedback circuits to the production of locomotion is less understood. As a first step towards this understanding, we incorporated Aβ-LTMR afferents innervating cutaneous receptors of the plantar surface of the paw within a previously validated neurobiomechanical computer model (Moraud et al., 2016) of the interactions between locomotor-related afferent feedback circuits and EES.

The model suggested that Aβ-LTMR afferent fibers innervating the plantar surface of the paw only fired transiently during the gait cycle, which contrasted with the continuous modulation of proprioceptive afferents (Bourane et al., 2015; Leem et al., 1993) (Fig. 2.6E, F). EES homogenously enhanced the mean firing rate of proprioceptive afferents without altering the encoding of proprioceptive information. Instead, EES disrupted the encoding of cutaneous information, even producing Aβ-LTMR afferent firing during gait phases when these afferents are normally quiescent.

2.3.5 Noradrenergic innervation of proprioceptive and Aβ-LTMR feedback circuits

We then reasoned that upregulating the gain of proprioceptive feedback circuits while down-regulating the contribution of Aβ-LTMR feedback circuits would potentiate the ability of EES to enable locomotion.

We sought to develop a clinically realistic approach to implement this sensory gating strategy in conjunction with EES. Noradrenergic $\alpha 2$ pathways exert a strong influence on the gain of sensory feedback circuits (Barbeau et al., 1987; Dietz et al., 1995; Musienko et al., 2009; Riddell et al., 1993). Indeed, noradrenergic drugs are used clinically to modulate tactile and proprioceptive information in order to alleviate pain and spasticity (Maupas et al., 2004; Nance et al., 1985; Pertovaara, 2006). We thus asked whether the differential expression pattern of $\alpha 2$ receptor subtypes in proprioceptive and Aβ-LTMR feedback circuits could support this sensory gating strategy.

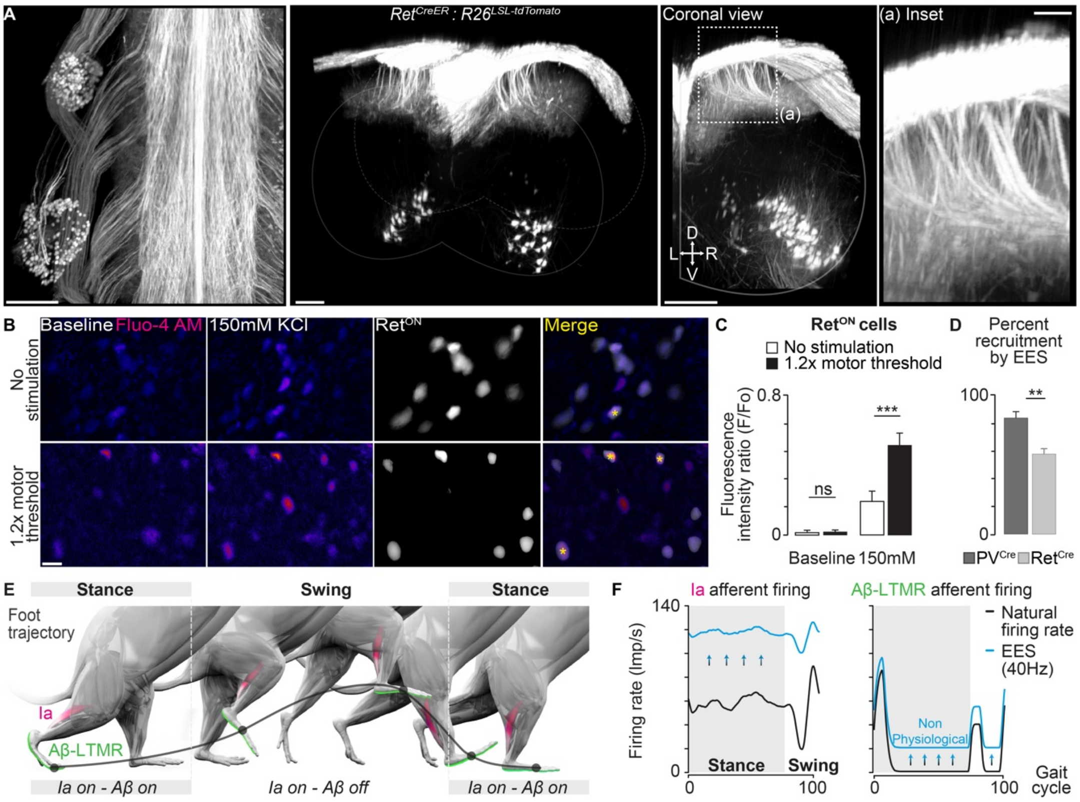
A
Ret^{CreER} : $R26^{LSL\text{-}tdTomato}$
Coronal view
(a) Inset
(a)
D
L
R
V
B
Baseline Fluo-4 AM
150mM KCl
Ret^{ON}
Merge
No stimulation
1.2x motor threshold
C
Ret^{ON} cells
☐ No stimulation
■ 1.2x motor threshold
Fluorescence intensity ratio (F/Fo)
0.8
0
ns
***
Baseline
150mM
D
Percent recruitment by EES
100
0
**
■ PV^{Cre} ■ Ret^{Cre}
E
Stance
Swing
Stance
Foot trajectory
Ia
Aβ-LTMR
Ia on - Aβ on
Ia on - Aβ off
Ia on - Aβ on
F
Ia afferent firing
Aβ-LTMR afferent firing
140
Firing rate (Imp/s)
0
Stance
Swing
0
100
Natural firing rate
EES (40Hz)
Non Physiological
0
100
Gait cycle

Figure 2.6: EES recruits LTMR neurons in the DRG (A) Cleared lumbosacral spinal cord with attached DRGs of a RetCreER : R26LSL-tdTomato mouse. Insets highlight the curvilinear trajectory of LTMR afferent fibers and neurons in the spinal cord and DRGs. Scale bars, 500µm (overview), 200µm, 200µm (coronal view) and 50µm for the insets, respectively. (B) Representative images of intracellular calcium release in L2 DRGs. Calcium imaging was conducted on RetCreER : R26LSL-tdTomato mice for two experimental conditions: no stimulation (n=5) and EES at 1.2x motor threshold (n=5). Asterisks highlight the released intracellular calcium in RetON neurons. Scale bar, 50µm. (C) Bar plot reporting calcium release in L2 DRGs for each experimental condition. EES at 1.2x motor threshold led to an increase in calcium release in RetON neurons. ***P < 0.001 (D) Bar plot reporting the relative percentage of PVON and RetON DRG neurons activated by EES. **P < 0.01. Non-paired Student's t-test. (E) Neurobiomechanical model of the hindlimbs in rats, including group-Ia afferents innervating the gastrocnemius muscle, and Aβ-LTMR innervating the foot sole. (F) Plots showing the firing rates of group-Ia and Aβ-LTMR afferents over the course of an entire gait cycle without and with EES. Arrows highlight the increased firing rates elicited by EES.

The $\alpha 2$ receptor family is subdivided into $\alpha 2$a, $\alpha 2$b and $\alpha 2$c subtypes (Fig. 2.7A), but only $\alpha 2$a and $\alpha 2$c receptors are robustly expressed in the spinal cord and DRGs (Nicholas et al., 1996). We thus studied the distribution of $\alpha 2$a and $\alpha 2$c receptors in $\alpha 2a^{GFP}$ and $\alpha 2c^{GFP}$ mouse lines (Gong et al., 2003) (Fig. 2.7B). First, we ensured that the GFP expression recapitulated the endogenous expression of α2a and α2c genes. We designed *in-situ* hybridization probes that confirmed the co-expression of GFP and mRNA for both receptors (Fig. 2.7B and Fig. 2.8). Second, we verified that the distribution of neurons expressing α2a and α2c receptors reproduced the topologies previously documented in the brain and brainstem (Fig. 2.8) (Scheinin et al., 1994).

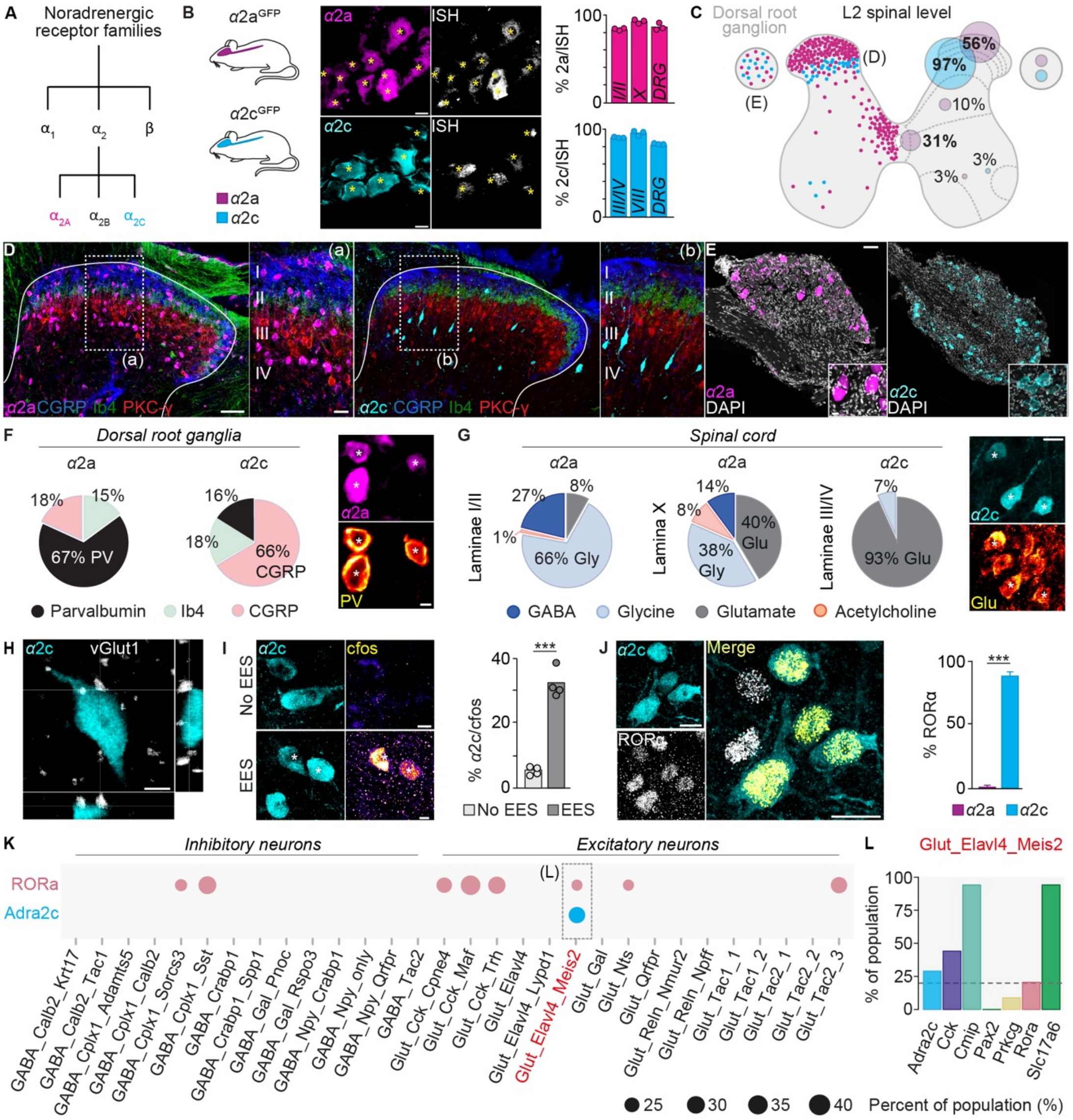
A
Noradrenergic receptor families
α1
α2
β
α2A
α2B
α2C
B
α2a^GFP
α2c^GFP
α2a
α2c
ISH
% 2a/ISH
% 2c/ISH
100
0
I/II
X
DRG
III/IV
VIII
C
Dorsal root ganglion
L2 spinal level
(D)
(E)
56%
97%
10%
31%
3%
3%
D
(a)
(b)
I
II
III
IV
α2a CGRP Ib4 PKC-γ
α2c CGRP Ib4 PKC-γ
E
α2a DAPI
α2c DAPI
F
Dorsal root ganglia
α2a
α2c
18%
15%
67% PV
16%
18%
66% CGRP
Parvalbumin
Ib4
CGRP
PV
G
Spinal cord
α2a
α2c
Laminae I/II
27%
8%
1%
66% Gly
Lamina X
14%
8%
40% Glu
38% Gly
Laminae III/IV
7%
93% Glu
GABA
Glycine
Glutamate
Acetylcholine
Glu
H
α2c
vGlut1
I
No EES
EES
cfos
% α2c/cfos
40
20
0
***
No EES
EES
J
α2c
Merge
RORα
% RORα
100
50
0
***
α2a
α2c
K
Inhibitory neurons
Excitatory neurons
RORa
Adra2c
(L)
GABA_Calb2_Krt17
GABA_Calb2_Tac1
GABA_Cplx1_Adamts5
GABA_Cplx1_Calb2
GABA_Cplx1_Sorcs3
GABA_Cplx1_Sst
GABA_Crabp1
GABA_Crabp1_Spp1
GABA_Gal_Pnoc
GABA_Gal_Rspo3
GABA_Npy_Crabp1
GABA_Npy_only
GABA_Npy_Qrfpr
GABA_Tac2
Glut_Cck_Cpne4
Glut_Cck_Maf
Glut_Cck_Trh
Glut_Elavl4
Glut_Elavl4_Lypd1
Glut_Elavl4_Meis2
Glut_Gal
Glut_Nts
Glut_Qrfpr
Glut_Reln_Nmur2
Glut_Reln_Npff
Glut_Tac1_1
Glut_Tac1_2
Glut_Tac2_1
Glut_Tac2_2
Glut_Tac2_3
25
30
35
40
Percent of population (%)
L
Glut_Elavl4_Meis2
% of population
100
75
50
25
0
Adra2c
Cck
Cmip
Pax2
Prkcg
Rora
Slc17a6

Figure 2.7: Noradrenergic α2a and α2c receptors are located on circuits activated by EES. (A) Noradrenergic receptor families.

Figure 2.7: (Continued) (B) Images showing α2aON and α2cON neurons in the DRGs of transgenic mice counterstained with an α2a and α2c in-situ hybridization probe (n=3 mice per line). Asterisks indicate double-labelled cells. Scale bars 20µm. Bar plots report that GFP reporter for both receptors are largely co-expressed with the α2a and α2c mRNA signal for all the studied regions of the spinal cord and DRGs. (C) Overview showing the location of cells expressing α2a (magenta) or α2c (cyan) receptor subtypes in the spinal cord and DRGs. (D) Representative images of GFP, PKC-γ, CGRP and Ib4 labelled dorsal horns displaying the distinct laminar location of α2aON and α2cON neurons. Scale bar 50µm for the overview, 25µm for the insets. (E) Images showing the expression of α2a and α2c receptor subtypes in DRGs. Scale bar 100µm for the overview, 20µm for the insets. (F) Polar plots displaying the phenotype of neurons expressing α2a or α2c in the DRGs. The picture shows α2aGFP and PV co-localization in the DRG, as highlighted with asterisks. Scale bar 10µm. (G) Polar plots displaying the phenotype of neurons expressing α2a or α2c in the various lamina of the spinal cord. The picture shows α2c-GFP and PV co-localization in neurons of laminae III/IV, as highlighted with asterisks. Scale bar 10µm. (H) Images showing vGlut1ON synapses from LTMR afferents that establish close appositions with an alpha2cON interneuron located laminae III/IV. (I) Images showing alpha2c and cfos co-localization in neurons located in laminae III/IV after 30 min of EES, as highlighted. (H) Images showing vGlut1ON synapses from LTMR afferents that establish close appositions with an α2cON interneuron located laminae III/IV. (I) Images showing α2c and cfos co-localization in neurons located in laminae III/IV after 30 min of EES, as highlighted with asterisks. Scale bars 5µm. Bar plot reporting the percentage of α2cON neurons co-localizing with cfos after EES versus no EES. ***P < 0.0001. Non-paired Student's t-test. (J) Images showing co-localization of α2c and RORα in interneurons located in laminae III/IV. Scale bars 10µm. Bar plot reporting the percentage of RORαON interneurons expressing α2a or α2c. ***P < 0.001. Non-paired Student's t-test. (K) Single-cell RNA sequencing experiment confirming the co-expression of α2c and RORα in a specific population of excitatory neurons (Glut_Elavl4_Meis2) located in the dorsal horn of the spinal cord. (L) Key molecular markers defining neurons (Glut_Elavl4_Meis2) expressing α2c and RORα.

Spinal neurons expressing α2a receptors were mostly found within laminae I/II and lamina X of the spinal cord grey matter. In contrast, neurons expressing α2c receptors were concentrated within laminae III/IV (Fig. 2.7C, D). Additionally, neurons expressing α2a and α2c receptors were found abundantly in DRGs (Fig. 2.7C, E).

α2a^{ON} and α2c^{ON} neurons exhibited remarkably distinct phenotypes, both in the spinal cord and DRGs (Stone et al., 1998). In DRGs, the α2a receptor subtype was predominantly expressed in PV^{ON} neurons (67%). Instead, α2c^{ON} neurons mainly expressed markers of nociception, including peptidergic (CGRP, 66%) and non-peptidergic (Ib4, 18%) neurons (Fig. 2.7F and Fig. 2.9).

Within laminae I/II, α2a receptors were mainly expressed in inhibitory glycinergic (66%) and GABAergic (27%) interneurons (Fig. 2.7G and Fig. 2.9). These interneurons are richly innervated by small-diameter, non-myelinated afferent fibers involved in the transmission of nociceptive information (Lallemend & Ernfors, 2012), making their recruitment with EES unlikely (Fig. 2.2C). Around the central canal (lamina X), α2a receptors were expressed in glutamatergic, glycinergic and cholinergic interneurons (Fig. 2.7G and Fig. 2.9). In contrast, α2c receptors were near-exclusively expressed in excitatory glutamatergic interneurons located in laminae III/IV of the spinal cord (93%, Fig. 2.7G and Fig. 2.9). These interneurons are involved in the transmission of innocuous Aβ-LTMR information (Bourane et al., 2015).

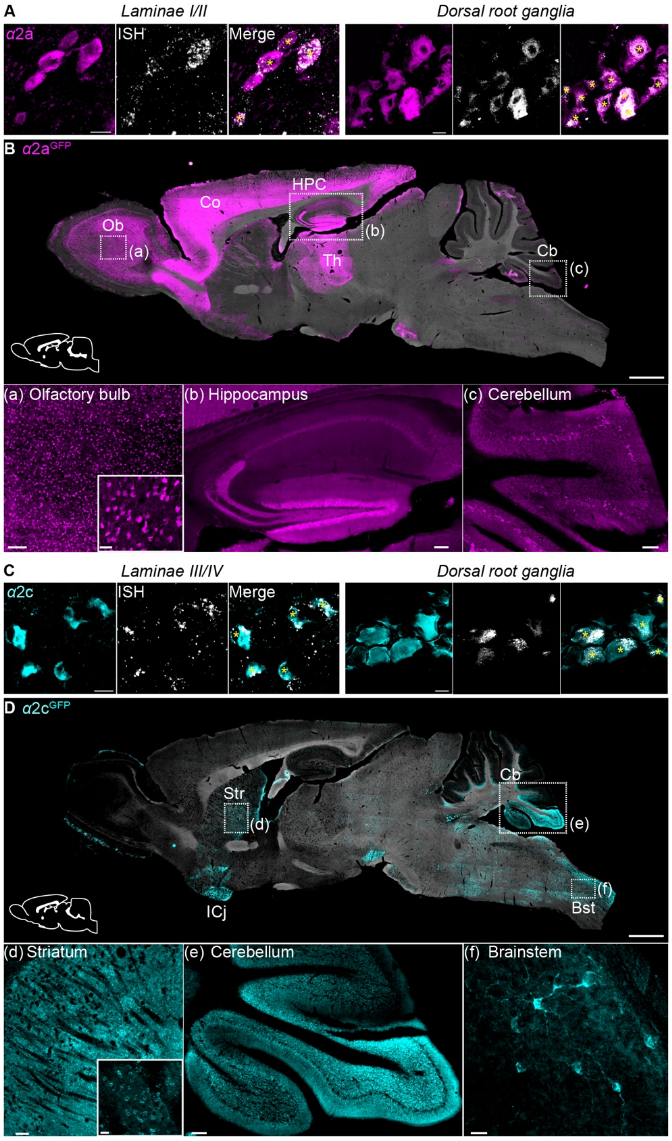
A
Laminae I/II
Dorsal root ganglia
α2a
ISH
Merge
B α2aGFP
Ob
(a)
Co
HPC
(b)
Th
Cb
(c)
(a) Olfactory bulb
(b) Hippocampus
(c) Cerebellum
C
Laminae III/IV
Dorsal root ganglia
α2c
ISH
Merge
D α2cGFP
Str
(d)
Cb
(e)
ICj
(f)
Bst
(d) Striatum
(e) Cerebellum
(f) Brainstem

Figure 2.8: Verification of the α2a and α2c GFP signals. (A) α2aON neurons counterstained with an α2a in-situ hybridization probe in laminae I/II and DRGs. Asterisks indicate double-labelling. Scale bars 10µm.

Figure 2.8: (Continued) (B) α2aON neurons in the brain and brainstem. Neurons expressing α2a receptors reproduced the previously documented topologies observed in the olfactory bulbs (Ob), cortex, hippocampus (HPC), thalamus and cerebellum (Cb). Scale bars, 1mm (overview), 100µm and 20µm (inset) (a), 100µm (b) and 100µm. (c) for the insets, respectively. (C) α2cON neurons counterstained with an α2c in-situ hybridization probe in laminae III/IV and DRGs. Asterisks indicate double-labelling. Scale bars 10µm. (D) α2cON neurons in the brain and brainstem. Neurons expressing α2c receptors reproduced the previously documented topologies observed in striatum (Str), islands of Calleja (ICj), cerebellum (Cb) and brainstem (Bst). Scale bars, 1mm (overview), 100µm and 20µm (inset) (a), 100µm (b) and 20µm (c) for the insets, respectively.

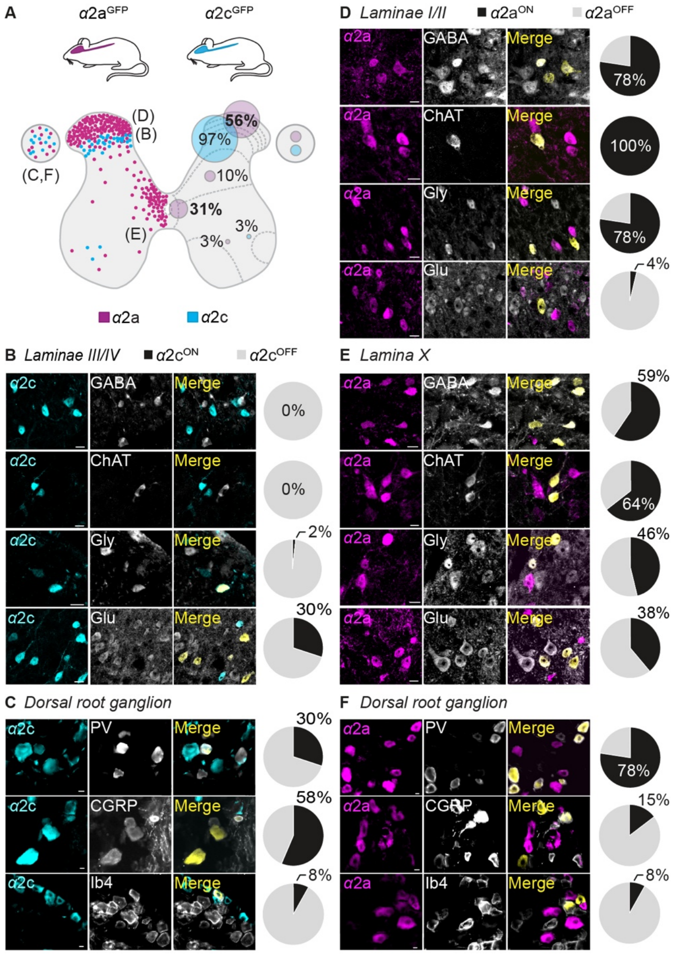
A
α2aGFP
α2cGFP
(D)
(B)
(C,F)
(E)
56%
97%
10%
31%
3%
3%
■α2a
■α2c
B Laminae III/IV
■α2cON
■α2cOFF
α2c
GABA
ChAT
Gly
Glu
Merge
0%
0%
2%
30%
C Dorsal root ganglion
PV
CGRP
Ib4
30%
58%
8%
D Laminae I/II
■α2aON
■α2aOFF
α2a
78%
100%
78%
4%
E Lamina X
59%
64%
46%
38%
F Dorsal root ganglion
78%
15%
8%

Figure 2.9: Phenotype of α2aON and α2cON neurons in the spinal cord and DRGs. (A) Overview showing the location of cells expressing α2a (magenta) or α2c (cyan) receptor subtypes in spinal cord and DRGs. (B) Images showing labelling of α2cON neurons in laminae III/IV and various neurotransmitters, scale bars 10µm. Pie charts indicate the percentage of α2aON neurons for each neurotransmitter in the respective area.

Figure 2.9: (Continued) (C) Labelling of α2cON neurons and various markers for sensory afferents in DRGs. Scale bars 10µm (D) Images showing labelling of α2aON neurons in laminae I/II and various neurotransmitters. Pie charts indicate the percentage of α2aON neurons for each neurotransmitter in the respective area. Scale bars 10µm (E) Images showing labelling of α2aON neurons in lamina X and various neurotransmitters. Scale bars 10µm (F) Labelling of α2aON neurons and various markers for sensory afferents in DRGs. Scale bars 10µm.

To confirm that $\alpha 2c^{ON}$ interneurons located in laminae III/IV receive synaptic inputs from Aβ-LTMR afferents, we immunolabelled their synapses with antibodies against vGlut1 in mice with complete SCI. $\alpha 2c^{ON}$ interneurons located in laminae III/IV were densely innervated by vGlut1^{ON} synapses (Fig. 2.7H). These interneurons were recruited by EES, since they expressed the activity-dependent marker cfos following 30 min of EES in the absence of limb movements compared to non-stimulated mice ($P<0.001$, Fig. 2.7I).

The phenotype and spatial distribution of $\alpha 2c^{ON}$ interneurons resembled the characteristics of neurons expressing the nuclear orphan receptor RORα (Bourane et al., 2015). Double-labelling experiments confirmed that nearly all these glutamatergic $\alpha 2c^{ON}$ interneurons express RORα (90%, Fig. 2.7J). RORα^{ON} interneurons receive direct Aβ-LTMR inputs and are essential for processing and transmitting light touch information involved in fine motor control (Bourane et al., 2015)). We confirmed this result in a single-cell RNA sequencing atlas of the mouse dorsal horn (Fig. 2.7K) (Häring et al., 2018). We found that only one excitatory cell type (*Glut_Elavl4_Meis2*) expressed both *RORα* and *Adra2c (α2c)*, consistent with our hypothesis that this combination of gene expression represents a unique and distinct cell type within the spinal cord. Several glutamatergic (*Slc17a6)* or classical markers including *Cck* and *Cmip* co-localized with *RORα*. In contrast, we found that these neurons expressed very low to negligible levels of *Pkcg* or *Pax2*, consistent with previous work (Bourane et al., 2015) (Fig. 2.7L).

These results established a remarkably distinct distribution and phenotype of neurons expressing $\alpha 2a$ or $\alpha 2c$ receptors within the spinal cord and DRG, including $\alpha 2a^{ON}$ PV^{ON} neurons in DRGs and glutamatergic $\alpha 2c^{ON}$ RORα^{ON} interneurons in the spinal cord that convey Aβ-LTMR information downstream and are strongly activated by EES.

2.3.6 Targeted pharmacotherapies potentiating the therapeutic efficacy of EES

We then leveraged this differential expression to test the basic concepts underlying our sensory gating strategy. The activation of $\alpha 2$ receptors induces a G-protein mediated decrease of neuronal activity (Pertovaara, 2006; Shen et al., 1992; Surprenant & North, 1988). We thus predicted that the activation of $\alpha 2a$ receptors would downregulate proprioceptive feedback circuits, thus suppressing locomotion enabled by EES. Instead, we anticipated that the activation of $\alpha 2c$ receptors would downregulate Aβ-LTMR feedback circuits, which would improve locomotion enabled by EES. To test these hypotheses, we administered the broad $\alpha 2$ agonist Clonidine in mice with complete SCI lacking $\alpha 2a$ or $\alpha 2c$ receptors (Altman et al., 1999; Philipp

& Hein, 2004) (Fig. 2.10A).

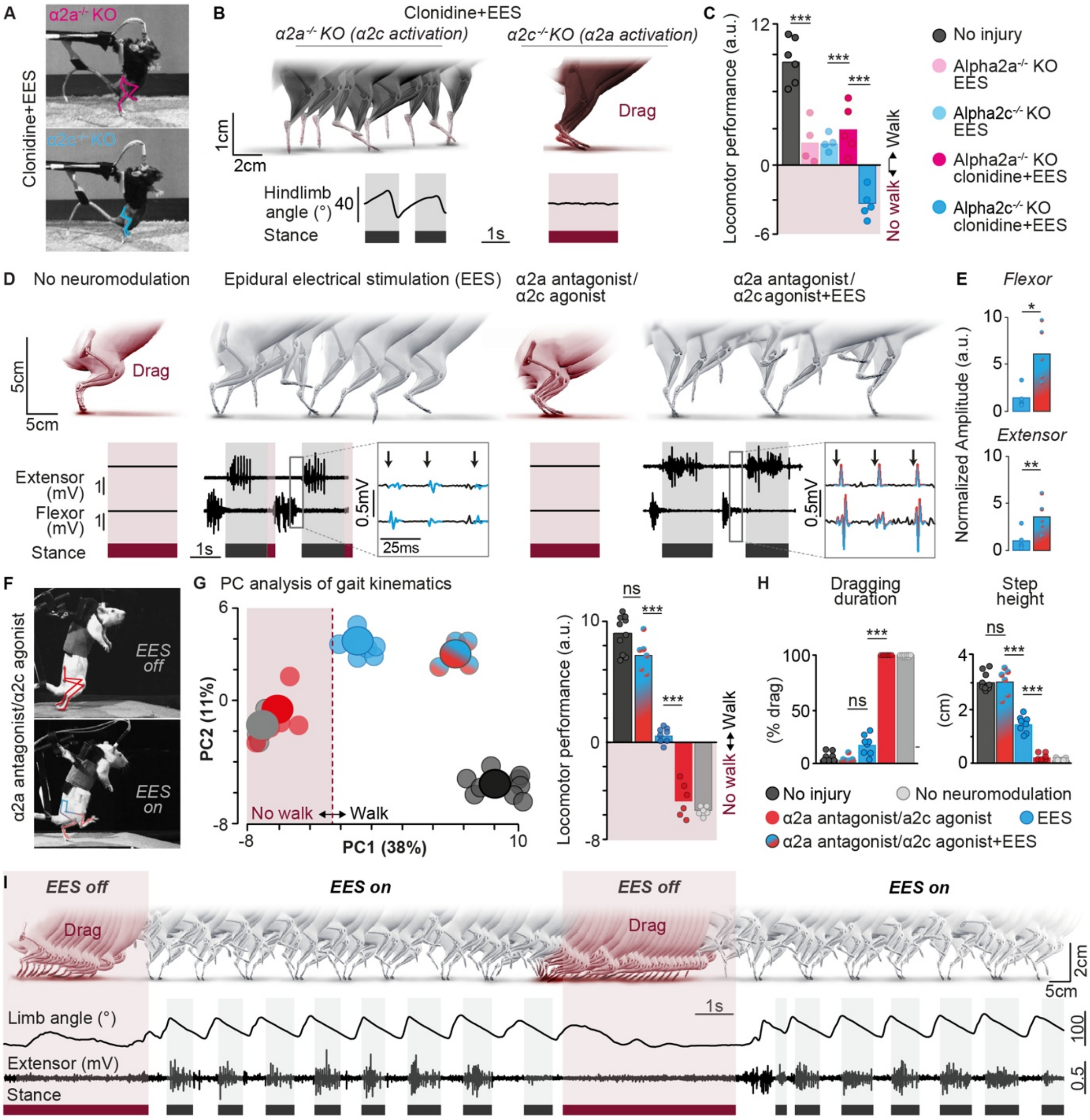

Figure 2.10: Targeted modulation of α2aON and α2cON circuits augments EES efficacy. (A) Effects of Clonidine and EES on stepping in α2a-/- and α2c-/- knockout mice with complete SCI. (B) Snapshots showing plantar stepping in α2a KO mice while α2c KO mice display complete paralysis. (C) Bar plot reporting average scores on PC1 for α2a (n=5) and α2c KO mice (n=5) compared to uninjured mice (n=6). ***P < 0.0001. Two-way ANOVA followed by Tukey's post-hoc test. (D) Effects of dual α2a antagonist/ α2c agonist and EES on stepping in rats with complete SCI. Conventions as in Fig. 2.4F. (E) Plots reporting the mean values of peak-to-peak amplitudes of muscle responses to EES (n = 5 rats). (F) Snapshots showing complete paralysis after administration of the dual α2a antagonist/ α2c agonist. Powerful stepping started as soon as EES was switched on.

Figure 2.10: (Continued) (G) PC analysis applied on 129 gait parameters. Small circles report mean values for each rat and condition, while the large circles correspond to the average for all rats. Bar plot reporting average scores on PC1 (n=6 injured rats and 10 non-injured rats). ***P < 0.0001. One-way ANOVA followed by Tukey's post-hoc test. (H) Bar plots showing average values of dragging duration and step height. ***P < 0.0001. One-way ANOVA followed by Tukey's post-hoc test. (I) Sequence showing hindlimb movements when turning EES on/off after the administration of the dual α2a antagonist/ α2c agonist.

The selective activation of α2a receptors completely blocked the ability of EES to enable locomotion (Fig. 2.10A-C). This failure was not due to a defect in spinal circuits, since EES promoted robust locomotion when the same mice received 5HT agonists (Fig. 2.11). On the contrary, activation of α2c receptors mediated an improvement of locomotion enabled by EES alone (Fig. 2.10A-C).

These results confirmed our hypotheses, establishing the prerequisite to test our sensory gating strategy in clinically relevant animal models. For this, we repurposed a selective dual α2a antagonist/α2c agonist agent (Delaunois et al., 2013; Jnoff et al., 2012) that we tested in rats with complete SCI. EES immediately enabled stepping of the otherwise paralyzed rats (Fig. 2.10D), but the effects of EES were insufficient to promote plantar foot placements and high levels of weight-bearing. The dual α2a antagonist/ α2c agonist alone exerted no visible influence on locomotor performance. Without EES, all the rats displayed complete paralysis. Turning on EES triggered the immediate production of plantar, weight-bearing locomotor movements (Fig. 2.10D). This facilitation was associated with an increase in EMG activity caused by a significant potentiation of muscle responses elicited by each pulse of EES ($p < 0.05$, Fig. 2.10E). Locomotion arrested immediately when EES was switched off, but resumed as soon as EES was reintroduced (Fig. 2.10I). Quantification of locomotor performance using PC analysis confirmed these behavioral observations (Fig. 2.10F-H).

These results identify a new targeted noradrenergic pharmacotherapy that aims to regulate the gain in proprioceptive and Aβ-LTMR feedback circuits in order to potentiate the ability of EES to enable walking after paralysis.

2.3.7 Circuit-level mechanisms underlying the potentiation of EES

We next aimed to expose the specific role of proprioceptive and Aβ-LTMR feedback circuits in the potentiation of EES when administrating the dual α2a antagonist/α2c agonist.

We first tested the necessity of proprioceptive feedback circuits. We performed these experiments in Egr3 mutant mice, which lack functional muscle spindle feedback circuits (Fig. 2.12A) (Takeoka et al., 2014). In the presence of the dual α2a antagonist/α2c agonist, EES failed to enable any stepping movement in Egr3 mutant mice with complete SCI, whereas wild-type mice exhibited coordinated locomotion (Fig. 2.12B, C). This failure contrasted with the locomotor movements observed after the administration of 5HT agonists, indicating that the lack of muscle spindle feedback circuits per se was not responsible for the complete paralysis ((Fig.

2.14)). Importantly, EES did not improve locomotion enabled by 5HT agonists alone in these mice (Fig. 2.12C).

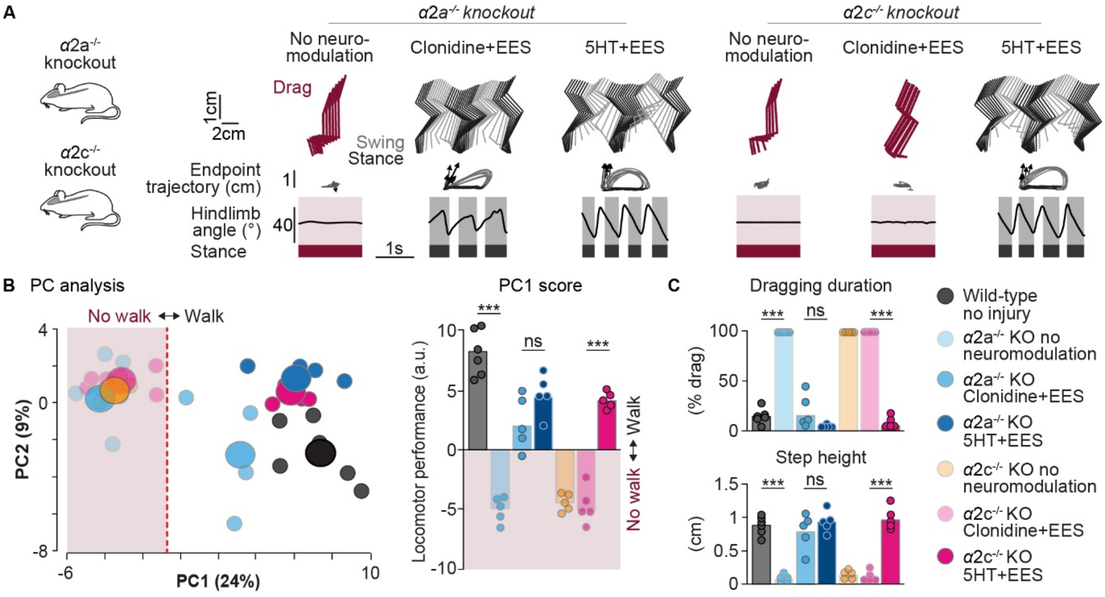

Figure 2.11: Effect of Clonidine or 5HT agonists and EES on locomotor performance of mice with a complete SCI and lacking α2a or α2c receptors (A) Functional experiments were performed in α2a-/- and α2c-/- knockout mice with complete SCI. Stick diagram decompositions of right leg movements are shown for all the experimental conditions, indicated above each sequence. 5HT refers to a combination of an agonist to 5HT2A receptors (Quipazine) and antagonist to 5HT1A/7 receptors (8-OHDPAT). (B) PC analysis applied on 104 gait parameters averaged for each mouse and condition (small circle). Large circles represent the average per group. Bar plot showing the average scores on PC1 (locomotor performance) of α2a (n=5) and α2c (n=5) knockout mice compared to non-injured mice (n=6). ***P < 0.0001. Two-way ANOVA followed by Tukey's post-hoc test. (C) Bar plots showing average values of classic gait parameters with high factor loadings on PC1. ***P < 0.001. Two-way ANOVA followed by Bonferroni's post-hoc test.

We then sought to dissect the Aβ-LTMR feedback circuits that could explain the potentiation of EES when administrating the dual α2a antagonist/α2c agonist. To guide this identification, we combined the finite element model (Fig. 2.2A) with a spiking neural network model that emulated mono- and di-synaptic connections of proprioceptive neurons onto motoneurons, and Ia-reciprocal inhibitory interneurons projecting to the antagonist pool of motoneurons (Formento et al., 2018). We expanded this computational model with the previously documented connectome of RORα^{ON} Aβ-LTMR feedback circuits (Bourane et al., 2015) (Fig. 2.12F). Contrary to the increase in amplitude of muscle responses observed *in-vivo* under the dual α2a antagonist/α2c agonist (Fig. 2.12D, E), this model predicted a decrease of muscle responses (Fig. 2.12F). Therefore, the documented connectome of RORα^{ON} Aβ-LTMR circuits could not explain the electrophysiological responses observed *in-vivo* (Fig. 2.12D). We hypothesized that this discrepancy could be explained by the previously suggested presence of an inhibitory interneuron intercalated between RORα^{ON} interneurons and motoneurons (Bourane et al., 2015) (Fig. 2.12G). Consequently, we modelled Aβ-LTMR feedback circuits with RORα^{ON} interneurons linked to both excitatory and inhibitory premotor interneurons. This model reproduced the strong increase in muscle response observed *in-vivo* (Fig. 2.12G).

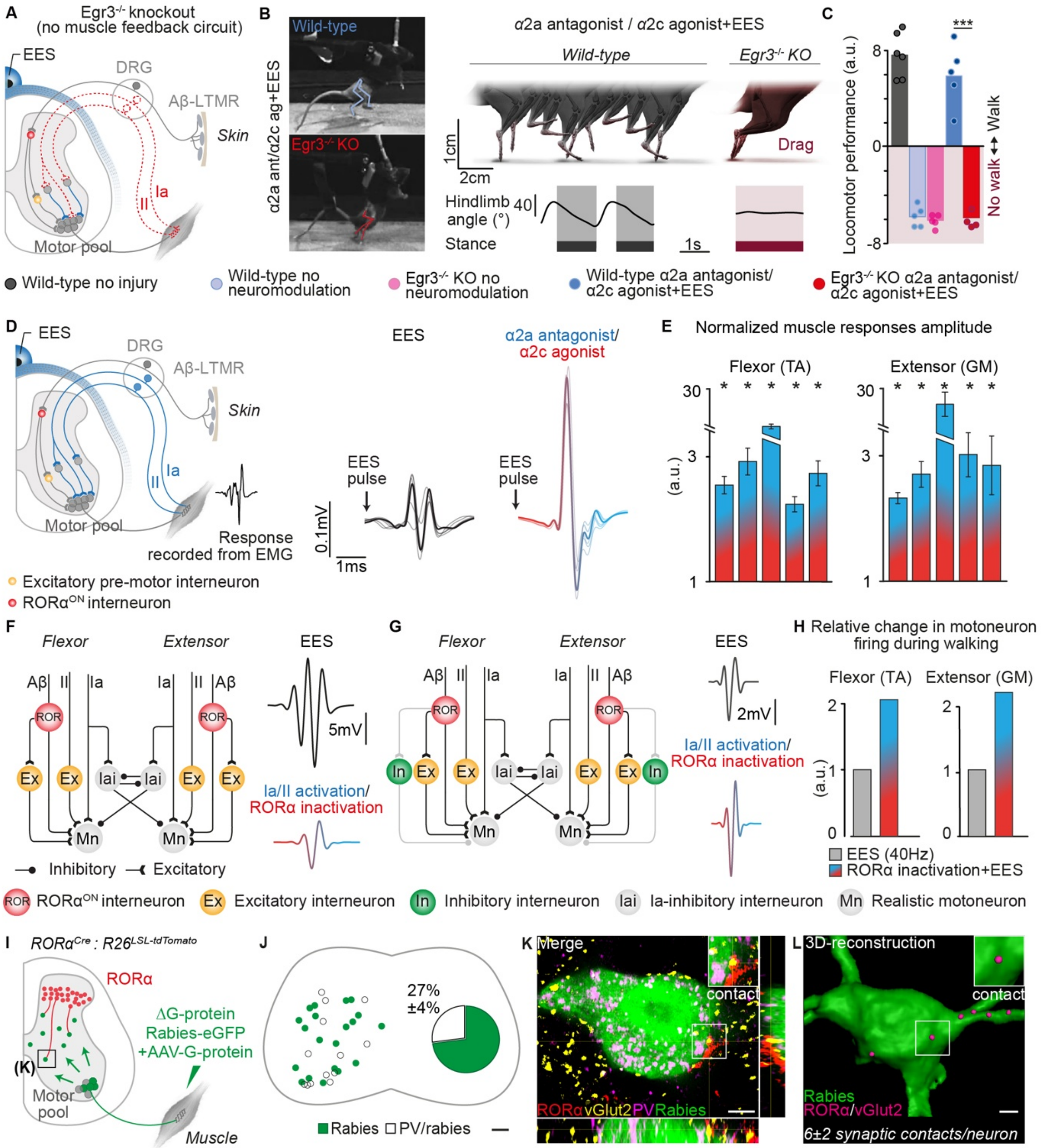
A
Egr3-/- knockout
(no muscle feedback circuit)
EES
DRG
Aβ-LTMR
Skin
Ia
II
Motor pool
B
Wild-type
Egr3-/- KO
α2a ant/α2c ag+EES
α2a antagonist / α2c agonist+EES
Wild-type
Egr3-/- KO
1cm
2cm
Drag
Hindlimb angle (°)
40
Stance
1s
C
Locomotor performance (a.u.)
8
0
-8
***
Walk
No walk
Wild-type no injury
Wild-type no neuromodulation
Egr3-/- KO no neuromodulation
Wild-type α2a antagonist/ α2c agonist+EES
Egr3-/- KO α2a antagonist/ α2c agonist+EES
D
EES
DRG
Aβ-LTMR
Skin
Ia
II
Motor pool
Response recorded from EMG
EES
EES pulse
0.1mV
1ms
α2a antagonist/
α2c agonist
EES pulse
Excitatory pre-motor interneuron
RORα^ON interneuron
E
Normalized muscle responses amplitude
Flexor (TA)
Extensor (GM)
(a.u.)
30
3
1
* * * * *
F
Flexor
Extensor
EES
Aβ
II
Ia
ROR
Ex
Iai
Mn
5mV
Ia/II activation/
RORα inactivation
Inhibitory
Excitatory
G
Flexor
Extensor
EES
In
Ex
Iai
Mn
2mV
Ia/II activation/
RORα inactivation
H
Relative change in motoneuron firing during walking
Flexor (TA)
Extensor (GM)
(a.u.)
2
1
0
EES (40Hz)
RORα inactivation+EES
ROR RORα^ON interneuron
Ex Excitatory interneuron
In Inhibitory interneuron
Iai Ia-inhibitory interneuron
Mn Realistic motoneuron
I
RORα^Cre : R26^LSL-tdTomato
RORα
ΔG-protein
Rabies-eGFP
+AAV-G-protein
(K)
Motor pool
Muscle
J
27%
±4%
Rabies
PV/rabies
K
Merge
contact
RORα vGlut2 PV Rabies
L
3D-reconstruction
contact
Rabies
RORα/vGlut2
6±2 synaptic contacts/neuron

Figure 2.12: Circuits potentiating EES with the dual α2a antagonist/α2c agonist. (A) Effects of the dual α2a antagonist/α2c agonist and EES on stepping in wild-type and Egr3-/- knockout mice with complete SCI. (B) EES fails to produce movements in mice lacking functional muscle spindles, in contrast to wild-type mice.

Figure 2.12: (Continued) (C) Bar plot reporting the average scores on PC1 (n=5 wild-type and n=4 Egr3KO (n=4) injured mice and n=5 non-injured mice. ***P < 0.0001. One-way ANOVA followed by Tukey's post-hoc test. (D) Effect of the dual α2a antagonist/α2c agonist on the muscle responses evoked by one pulse of EES. (E) Bar plots reporting the relative increase in the amplitude of muscle responses after the administration of the dual α2a antagonist/α2c agonist for each of the 5 tested rats. *P < 0.05, bootstrapping, two-sided. (F) Neuronal network used for simulations. Muscle responses to EES are shown without and with the activation of group-Ia/II afferents and inactivation of RoRα interneurons. (G) Adapted neuronal network wherein an inhibitory premotor interneuron has been interposed between RORα interneurons and motoneurons. Muscle responses shown in (F) are displayed for this adapted network. (H) Bar plots reporting the relative change in motoneuron firing during walking when RoRα interneurons are downregulated in the presence of EES. See neurobiomechanical simulations in Fig. S7. (I) Scheme summarizing monosynaptically-restricted tracing experiments to visualize inhibitory premotor interneurons receiving synaptic contacts from RORα interneurons. (J) Reconstruction showing the location of inhibitory PVON premotor interneurons in the spinal cord. (K) Image showing a rabiesON premotor interneuron co-localizing with PV in intermediate spinal cord lamina and receiving synaptic vGlut2ON synapses from RORαON interneurons. Scale bar 4μm. (L) 3D reconstruction of the interneuron shown in (J), including vGlut2ON synaptic contacts from RORαON interneurons. RabiesON/PVON neuron receives 6±2 synaptic contacts from RORαON interneurons. Scale bar 4μm.

We then sought to verify this anatomical prediction. We injected ΔG protein Rab–eGFP intramuscularly together with an AAV expressing rabies glycoprotein (AAV-oG) in $ROR\alpha^{Cre}$: $R26^{LSL-tdTomato}$ mice at post-natal day 2 (Fig. 2.12H). Inhibitory interneurons were identified by the marker ParValbumin (PV), which characterizes a group of inhibitory interneurons in intermediate and ventral spinal cord laminae (Arber, 2012; Molgaard et al., 2014). We found that 27 ± 4% of rabies^{ON} premotor interneurons co-labelled with PV (Fig. 2.12I). In intermediate laminae, vGlut2^{ON} synapses from RORα^{ON} interneurons were found in close contact to rabies^{ON}/PV^{ON} premotor interneurons (Fig. 2.12J, K).

We finally performed neurobiomechanical simulations to gain insights into the mechanisms that potentiate the efficacy of EES when α2c^{ON}/Aβ-LTMR/RORα^{ON} feedback circuits are downregulated. Simulations indicated that this downregulation led to a substantial increase in EES-induced recruitment of both flexor and extensor motoneurons (Fig. 2.12D, G), as observed *in-vivo* (Fig. 2.10E). This increase involved an unexpected mechanism. Due to the cancellation of inputs from RORα^{ON} interneurons, the resulting reduction of inhibitory post-synaptic potentials from downstream interneurons primed the membrane of motoneurons to respond vigorously to EES-induced excitatory inputs from proprioceptive afferents. Consequently, EES mediated a sustained and prolonged activity of motoneurons during their active phase, in particular in extensor motoneurons throughout the stance phase of gait (Fig. 2.13).

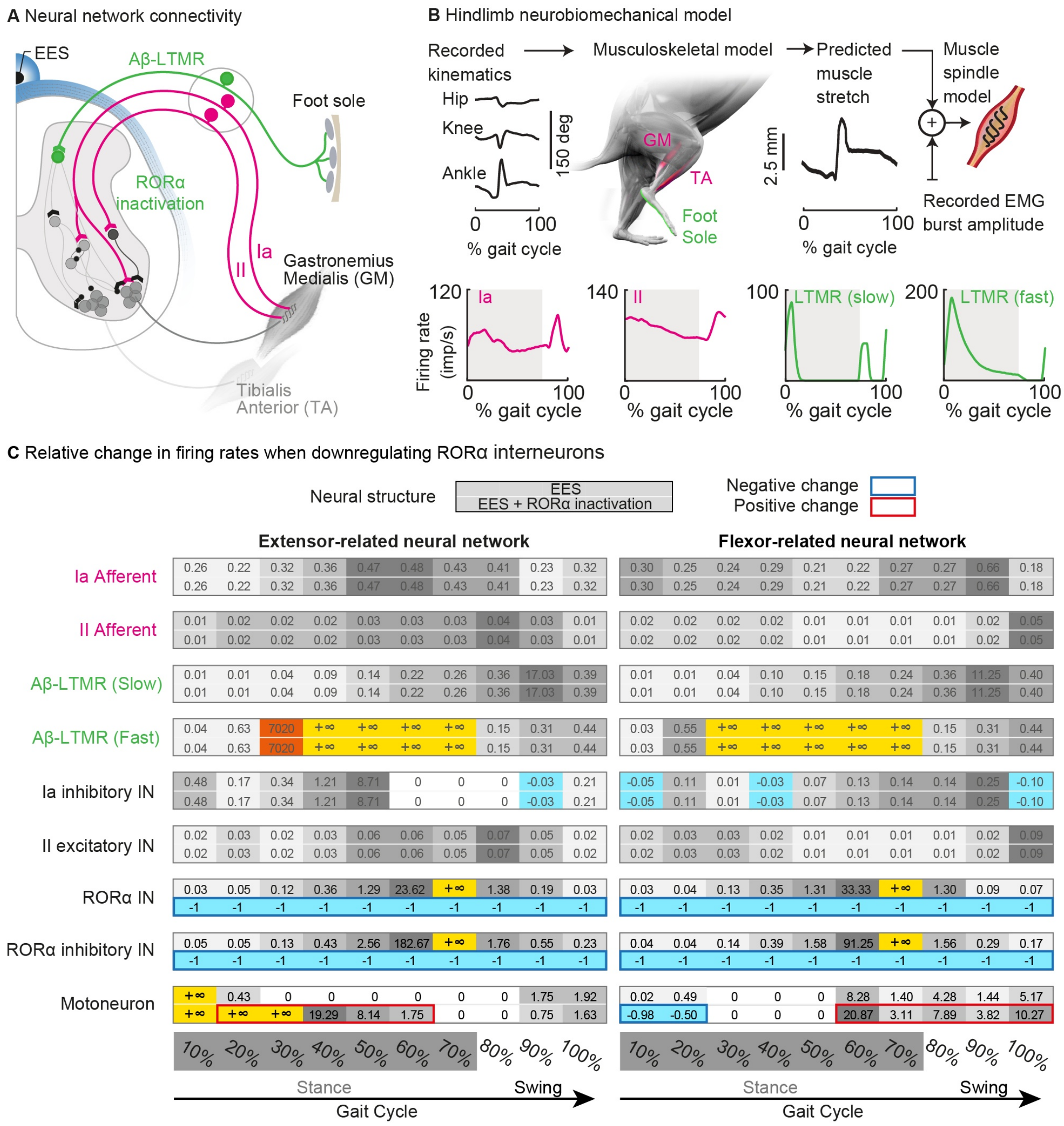
A Neural network connectivity
EES
Aβ-LTMR
Foot sole
RORα inactivation
Ia
II
Gastronemius Medialis (GM)
Tibialis Anterior (TA)
B Hindlimb neurobiomechanical model
Recorded kinematics
Hip
Knee
Ankle
150 deg
0
100
% gait cycle
Musculoskeletal model
GM
TA
Foot Sole
Predicted muscle stretch
2.5 mm
0
100
% gait cycle
Muscle spindle model
+
Recorded EMG burst amplitude
Firing rate (imp/s)
120
Ia
140
II
100
LTMR (slow)
200
LTMR (fast)
0
100
% gait cycle
C Relative change in firing rates when downregulating RORα interneurons
Neural structure
EES
EES + RORα inactivation
Negative change
Positive change
Stance
Swing
Gait Cycle

Extensor-related neural network

Neural structure		10%	20%	30%	40%	50%	60%	70%	80%	90%	100%
Ia Afferent	EES	0.26	0.22	0.32	0.36	0.47	0.48	0.43	0.41	0.23	0.32
	EES + RORα inactivation	0.26	0.22	0.32	0.36	0.47	0.48	0.43	0.41	0.23	0.32
II Afferent	EES	0.01	0.02	0.02	0.02	0.03	0.03	0.03	0.04	0.03	0.01
	EES + RORα inactivation	0.01	0.02	0.02	0.02	0.03	0.03	0.03	0.04	0.03	0.01
Aβ-LTMR (Slow)	EES	0.01	0.01	0.04	0.09	0.14	0.22	0.26	0.36	17.03	0.39
	EES + RORα inactivation	0.01	0.01	0.04	0.09	0.14	0.22	0.26	0.36	17.03	0.39
Aβ-LTMR (Fast)	EES	0.04	0.63	7020	+∞	+∞	+∞	+∞	0.15	0.31	0.44
	EES + RORα inactivation	0.04	0.63	7020	+∞	+∞	+∞	+∞	0.15	0.31	0.44
Ia inhibitory IN	EES	0.48	0.17	0.34	1.21	8.71	0	0	0	-0.03	0.21
	EES + RORα inactivation	0.48	0.17	0.34	1.21	8.71	0	0	0	-0.03	0.21
II excitatory IN	EES	0.02	0.03	0.02	0.03	0.06	0.06	0.05	0.07	0.05	0.02
	EES + RORα inactivation	0.02	0.03	0.02	0.03	0.06	0.06	0.05	0.07	0.05	0.02
RORα IN	EES	0.03	0.05	0.12	0.36	1.29	23.62	+∞	1.38	0.19	0.03
	EES + RORα inactivation	-1	-1	-1	-1	-1	-1	-1	-1	-1	-1
RORα inhibitory IN	EES	0.05	0.05	0.13	0.43	2.56	182.67	+∞	1.76	0.55	0.23
	EES + RORα inactivation	-1	-1	-1	-1	-1	-1	-1	-1	-1	-1
Motoneuron	EES	+∞	0.43	0	0	0	0	0	0	1.75	1.92
	EES + RORα inactivation	+∞	+∞	+∞	19.29	8.14	1.75	0	0	0.75	1.63

Flexor-related neural network

Neural structure		10%	20%	30%	40%	50%	60%	70%	80%	90%	100%
Ia Afferent	EES	0.30	0.25	0.24	0.29	0.21	0.22	0.27	0.27	0.66	0.18
	EES + RORα inactivation	0.30	0.25	0.24	0.29	0.21	0.22	0.27	0.27	0.66	0.18
II Afferent	EES	0.02	0.02	0.02	0.02	0.01	0.01	0.01	0.01	0.02	0.05
	EES + RORα inactivation	0.02	0.02	0.02	0.02	0.01	0.01	0.01	0.01	0.02	0.05
Aβ-LTMR (Slow)	EES	0.01	0.01	0.04	0.10	0.15	0.18	0.24	0.36	11.25	0.40
	EES + RORα inactivation	0.01	0.01	0.04	0.10	0.15	0.18	0.24	0.36	11.25	0.40
Aβ-LTMR (Fast)	EES	0.03	0.55	+∞	+∞	+∞	+∞	+∞	0.15	0.31	0.44
	EES + RORα inactivation	0.03	0.55	+∞	+∞	+∞	+∞	+∞	0.15	0.31	0.44
Ia inhibitory IN	EES	-0.05	0.11	0.01	-0.03	0.07	0.13	0.14	0.14	0.25	-0.10
	EES + RORα inactivation	-0.05	0.11	0.01	-0.03	0.07	0.13	0.14	0.14	0.25	-0.10
II excitatory IN	EES	0.02	0.03	0.03	0.02	0.01	0.01	0.01	0.01	0.02	0.09
	EES + RORα inactivation	0.02	0.03	0.03	0.02	0.01	0.01	0.01	0.01	0.02	0.09
RORα IN	EES	0.03	0.04	0.13	0.35	1.31	33.33	+∞	1.30	0.09	0.07
	EES + RORα inactivation	-1	-1	-1	-1	-1	-1	-1	-1	-1	-1
RORα inhibitory IN	EES	0.04	0.04	0.14	0.39	1.58	91.25	+∞	1.56	0.29	0.17
	EES + RORα inactivation	-1	-1	-1	-1	-1	-1	-1	-1	-1	-1
Motoneuron	EES	0.02	0.49	0	0	0	8.28	1.40	4.28	1.44	5.17
	EES + RORα inactivation	-0.98	-0.50	0	0	0	20.87	3.11	7.89	3.82	10.27

Figure 2.13: Effects of RORα inactivation on in-silico electrophysiological recordings during locomotion with EES. (A) Schematic overview depicting the neural network connectivity of the modeled proprioceptive feedback circuits related to extensor (medial gastrocnemius) and flexor (tibialis anterior) muscles, and Aβ-LTMR feedback circuits related to the foot sole. (B) Realistic neurobiomechanical model of the rat hindlimb. Afferent firing profiles of group Ia and group-II afferents are calculated using muscle spindle models combined with recordings of leg kinematics and muscle activity (EMG) in rats. The firing profile of rapidly-adapting and slowly-adapting Aβ-LTMR afferent fibers innervating the foot sole are calculated based on in vivo recordings of Aβ-LTMR afferent during walking.

Figure 2.13: (Continued) (C) Relative difference of the neuronal firing rates for all the modelled cells and afferent populations under the conditions EES and EES + RORα inactivation over the course of the gait cycle. Results are expressed as a relative increase or decrease with respect to the natural firing rates during locomotion of healthy rats. The value 1 indicates a change of 100%. The color coding is adjusted for each neural element in order to facilitate the understanding of the amplitude of the changes. In particular the red and blue boxes highlight the more relevant changes following inactivation of RORα interneuron inactivation.

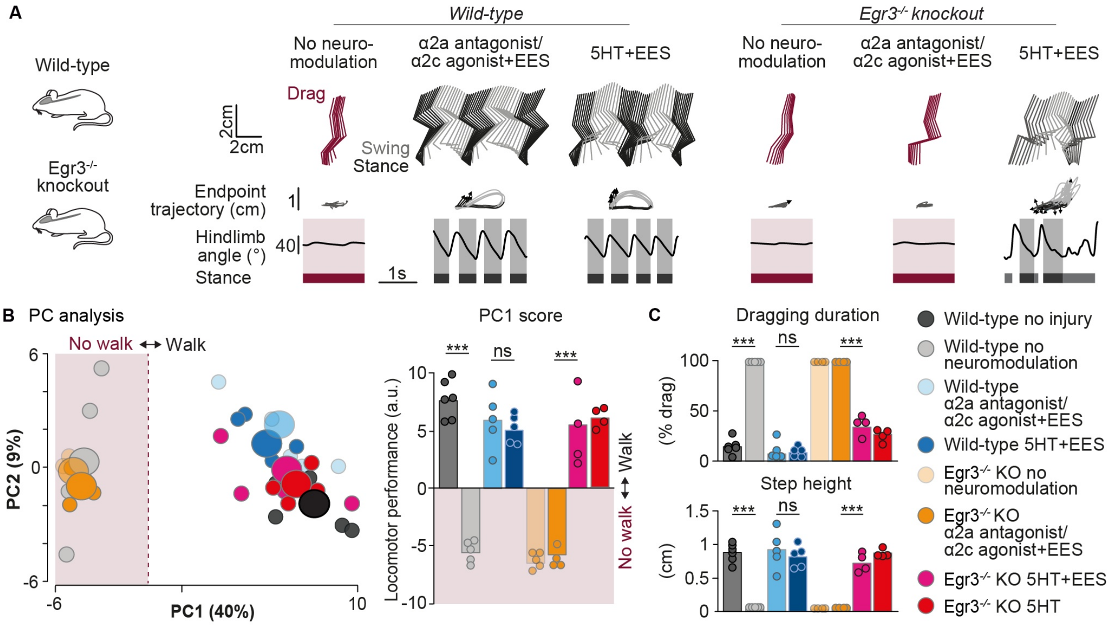

Figure 2.14: Potentiation of EES with the dual α2a antagonist/ α2c agonist requires functional proprioceptive feedback circuits (A) Functional experiments conducted in wild-type mice and in Egr3-/- knockout mice, which lacks functional muscle feedback circuits. Mice received a complete mid-thoracic SCI spindles and as under the dual α2a antagonist/ α2c agonist and EES. Stick diagram decompositions of right leg movements showing the functional outcomes for wild-type and Egr3 knockout mice under different experimental conditions. (B) PC analysis applied on 104 gait parameters averaged for each mouse and condition (small circle). Large circles represent the average per group. Bar plot showing the average scores on PC1 (locomotor performance) of injured wild-type (n=5) and Egr3KO (n=4) mice under the different experimental conditions compared to uninjured mice (n=5). ***$P < 0.0001$. One-way ANOVA followed by Tukey's post-hoc test. (C) Bar plots reporting average values of classical gait parameters with high factor loading on PC1. ***$P < 0.0001$ for dragging duration, ***$P = 0.0001$ for step height. Two-way ANOVA followed by Bonferroni's post-hoc test.

2.3.8 Voluntary control of walking in a preclinical model of severe SCI

Finally, we asked whether the combination of EES and dual α2a antagonist/α2c agonist could reestablish supraspinal control of locomotion after a clinically-relevant severe contusion SCI in adult rats. We delivered a robotically controlled impact (250 kdyn) onto thoracic segments (T8/T9) that spared as little as 8.7 ± 1.2% of intact cross-sectional tissue (Fig. 2.15A).

We sought to assess whether this contusion interrupted noradrenaline delivery below the injury. Locomotor-related descending noradrenergic pathways primarily originate from neurons expressing tyrosine hydroxylase (TH) in the Rostral VentroLateral Medulla (RVLM) (Jordan et al., 2008). To visualize the axons and synapses of these neurons, we performed stereotaxic infusions of AAV-DJ-hSyn-flex-mGFP-2A-Synaptophysin-mRuby into the RVLM of TH^{Cre} rats (Fig. 2.15A-D). CLARITY-optimized light-sheet microscopy of TH^{ON} fibers revealed that noradrenergic pathways extended within the lateral white matter, from where bundles of fibers projected into the spinal cord grey matter at regular intervals along the neuroaxis (Fig. 2.15D). The SCI interrupted the majority of noradrenergic projections, only sparing a subset of synapses arborizing from spared fibers located in the ventral white matter (Fig. 2.15E). This visualization revealed the pronounced depletion of noradrenaline in the lumbosacral spinal cord of injured rats.

To evaluate supraspinal (*voluntary*) control of leg movements, rats were positioned bipedally in a robotic body weight support that provided personalized assistance against gravity during overground locomotion (Fig. 2.15G) (Dominici et al., 2012). The systemic (i.p.) delivery of the dual α2a antagonist/α2c agonist combined with EES failed to enable locomotion in all tested rats (Fig. 2.15G-I). This failure contrasted with the ability of the rats to initiate and sustain locomotion when delivering EES and 5HT agonists.

We previously demonstrated that the recovery of locomotion after this type of SCI relies on the activation of glutamatergic neurons located in the ventral gigantocellular nucleus. These neurons relay the cortical commands to the lumbar spinal cord (Asboth et al., 2018). We found that α2c receptors are prominently expressed on glutamatergic neurons located in the ventral gigantocellular nucleus (Fig. 2.15F). We thus surmised that the systemic drug administration activated α2c receptors on these neurons, thus preventing the transmission of the supraspinal command to the lumbar spinal cord.

To test this hypothesis, we administered the dual α2a antagonist/α2c agonist to the lumbar spinal cord intrathecally. Under these conditions, all tested rats produced leg movements that allowed them to cross the entire extent of the runway (Fig. 2.15G-J)

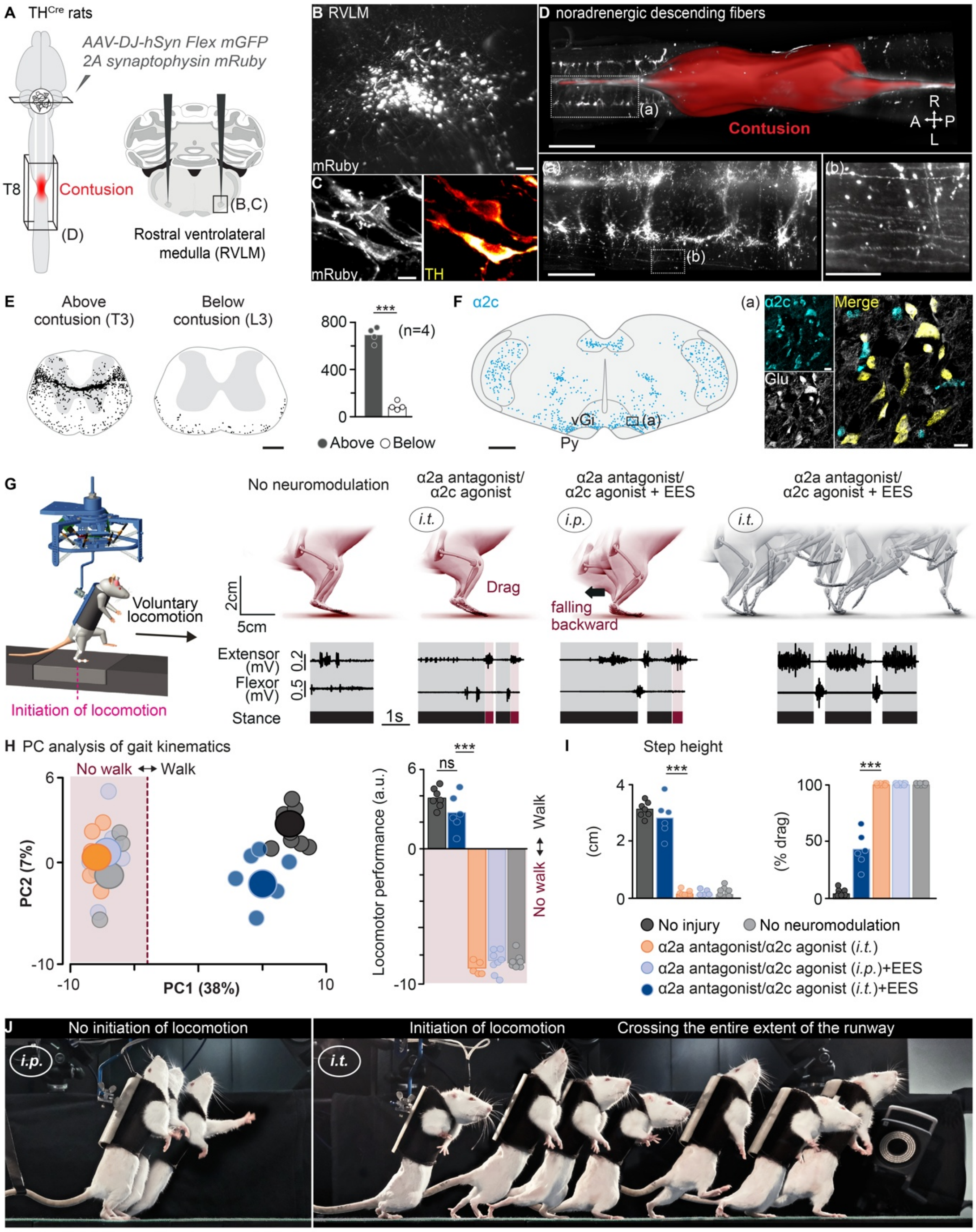
A THCre rats
AAV-DJ-hSyn Flex mGFP 2A synaptophysin mRuby
T8
Contusion
(D)
(B,C)
Rostral ventrolateral medulla (RVLM)
B RVLM
mRuby
C
mRuby
TH
D noradrenergic descending fibers
(a)
Contusion
R
A
P
L
(a)
(b)
(b)
E
Above contusion (T3)
Below contusion (L3)
***
800
400
0
(n=4)
Above
Below
F α2c
vGi
(a)
Py
(a) α2c
Merge
Glu
G
No neuromodulation
α2a antagonist/ α2c agonist
α2a antagonist/ α2c agonist + EES
α2a antagonist/ α2c agonist + EES
i.t.
i.p.
i.t.
Voluntary locomotion
2cm
5cm
Drag
falling backward
Initiation of locomotion
Extensor (mV) 0.2
Flexor (mV) 0.5
Stance
1s
H PC analysis of gait kinematics
No walk ↔ Walk
6
0
-10
PC2 (7%)
-10
PC1 (38%)
10
Locomotor performance (a.u.)
***
ns
6
0
-10
Walk
No walk
I
Step height
***
4
2
0
(cm)
***
100
50
0
(% drag)
No injury
No neuromodulation
α2a antagonist/α2c agonist (i.t.)
α2a antagonist/α2c agonist (i.p.)+EES
α2a antagonist/α2c agonist (i.t.)+EES
J
No initiation of locomotion
Initiation of locomotion
Crossing the entire extent of the runway
i.p.
i.t.

Figure 2.15: Voluntary control of locomotion in rats with a severe contusion SCI (A) Scheme illustrating tracing strategy to label descending noradrenergic axons and synapses in THCre rats. (B) 3D image showing the injection site in the Rostral VentroLateral Medulla (RVLM). Scale bar 300µm. (C) Images showing virus-infected neurons co-localizing with TH in the RVLM. Scale bar 10µm. (D) 3D rendering showing the interruption of noradrenergic descending fibers by the contusion. Scale bar 1.5mm, and 3D insets taken from above the contusion. Scale bars 500µm and 300µm, respectively.

Figure 2.15: (Continued) (E) Reconstructions of noradrenergic fibers above (T3) and below (L3) the contusion. Bar plot reports the count of noradrenergic fibers (n= 4 rats). Scale bar 500µm. ***P < 0.0001, paired Student's t-test. (F) Reconstruction of α2cON cells in the brainstem. Scale bar 500µm. Images showing α2cON neurons co-localizing with glutamate in the ventral gigantocellular nucleus (vGi). Scale bars 20µm. (G) Effects of EES and intrathecal versus systemic administration of the dual α2a antagonist/α2c agonist on voluntary control of overground locomotion in rats with contusion SCI. Convention as in Fig. 2.4F. (H) PC analysis of gait kinematics. Conventions as in Fig. 2.10G (n=6 injured and n=7 non-injured rats). ***P < 0.0001. One-way ANOVA followed by Tukey's post-hoc test. (I) Bar plots showing average values of step height and dragging duration. ***P < 0.0001. One-way ANOVA followed by Tukey's post-hoc test. (J) Chronophotography showing a rat unable to initiate locomotion after systemic (i.p.) injection of the dual α2a antagonist/α2c agonist and EES. Intrathecal (i.t.) injection of the same pharmacological agent resulted in powerful locomotion and the ability to cross the entire extent of the runway.

2.4 Discussion

We demonstrate that EES enables walking after SCI using proprioceptive feedback circuits as a gateway to motoneuron pools. Unexpectedly, EES also interferes with the encoding of cutaneous information in Aβ-LTMR/RORα^{ON} feedback circuits, which reduces the facilitation of walking with EES. We found that noradrenergic α2a and α2c receptors are distinctly expressed along proprioceptive versus Aβ-LTMR/RORα^{ON} feedback circuits. This differential expression enabled the design of a sensory gating pharmacotherapy targeting these circuits to potentiate the ability of EES to enable walking. Here, we emphasize the crucial role of proprioceptive feedback circuits to restore walking with EES, discuss our current understanding of Aβ-LTMR circuits engaged by EES, and consider the application of this knowledge for clinical therapies.

2.4.1 Proprioceptive gateways to spinal motor systems

It has been long assumed that the recruitment of proprioceptive afferents with EES is the main mechanism through which EES enables walking after SCI (Capogrosso et al., 2013; Edgerton et al., 2006; Y. P. Gerasimenko et al., 2006; Rattay et al., 2000). Here, we demonstrate that the location, topology, myelin content and diameter of proprioceptive afferent fibers impose their preferential activation when delivering EES over the dura mater of the lumbosacral spinal cord. We also demonstrate that proprioceptive feedback circuits are necessary for EES to enable walking, and that, in turn, augmenting the gain in these circuits improve the beneficial impact of EES on the production of gait. We thus establish that the modulation of proprioceptive feedback circuits is the main circuit-level mechanism enabling motor pattern formation when applying EES to the lumbosacral spinal cord after paralysis.

We propose that the recruitment of proprioceptive afferents with EES engages several key mechanisms of motor control and neuroplasticity. First, the diffuse projection patterns of proprioceptive afferents within the spinal cord raise the excitability of motor networks below the injury. This global enhancement of excitability augments the ability of spinal circuits to respond to sensory information and to residual synaptic inputs from anatomically spared yet functionally silent or weakened descending pathways (S. Harkema et al., 2011; Wagner et al., 2018). For example, optogenetic activation of glutamatergic reticulospinal neurons in mice with severe contusion SCI evokes responses in leg muscles, but only when EES increases the excitability of the lumbar spinal cord (Asboth et al., 2018). Second, the recruitment of proprioceptive feedback circuits generates direct and indirect excitatory drive to motoneurons, which provoke muscle contractions (Minassian et al., 2015; Sayenko et al., 2014; Wenger et al., 2014). Third, proprioceptive afferents modulate Ia reciprocal inhibitory interneurons, which coordinate the alternative recruitment of extensor and flexor motor pools (Kiehn, 2016; Prochazka, 1996; J. Zhang et al., 2014). The natural sensory information tunes the balance between excitation and inhibition in this circuity, which gates the excitatory drive induced by EES toward functionally relevant pathways (Moraud et al., 2016). Consequently, task-specific sensory information modulates the amplitude of muscle responses to EES, enabling the production of motor patterns that continuously meet the requirements of the ongoing motor execution.

In our model, we only represented afferents innervating muscle spindles. However, our results indicate that EES also recruits afferent transmitting information about the tension applied to tendons. Electrophysiological and modeling data predicted that group-Ia and group-Ib proprioceptive afferents exert a similar influence on motoneuron activity, suggesting that the impact of EES on the modulation of these two feedback circuits would be comparable (Kiehn, 2016; K. G. Pearson, 1995; Prochazka, 1996; Stienen et al., 2007). However, further experiments are necessary to dissect their specific contribution.

Augmentation of neuroplasticity is the fourth mechanism that is likely engaged by the recruitment of proprioceptive feedback circuits with EES. Mounting evidence indicates that proprioceptive information is essential to promote the reorganization of descending pathways that restores walking after SCI (Takeoka & Arber, 2019; Takeoka et al., 2014). Therefore, we hypothesize that their recruitment during gait rehabilitation with EES is a key mechanism restoring volitional control over previously paralyzed muscles in humans, even when EES is switched off (Rejc et al., 2017; Wagner et al., 2018). For example, we showed that gait rehabilitation enabled by EES promotes the directed growth of reticulospinal pathways into specific regions of the spinal cord that receive dense synaptic projections from proprioceptive afferents (Asboth et al., 2018).

Further studies are necessary to identify the specific molecular and epigenetic mechanisms augmenting neuroplasticity when recruiting proprioceptive neurons after SCI. For example, we found that the overactivation of proprioceptive neurons elicits a Creb-binding protein-mediated histone acetylation that triggers the expression of genes associated with regenerative programs (Hutson et al., 2019). After a SCI, this epigenetic reprogramming induces a pronounced sprouting of proprioceptive afferents into the spinal cord below injury, and enables the regeneration of ascending proprioceptive fibers across the site of injury. The identification of these mechanisms may uncover new targets to enhance recovery in response to

EES-supported rehabilitation programs.

2.4.2 Role of Aβ-LTMR feedback circuits

Cutaneous receptors located in the foot sole act as a tactile retina that captures the gravitational forces generated throughout stance (Kavounoudias et al., 1998). This information is encoded in the firing rate of Aβ-LTMRs afferents (Abraira & Ginty, 2013). Despite the importance of Aβ-LTMR feedback circuits to produce and correct locomotion, their anatomical and functional connectome is not fully characterized (Abraira et al., 2017; Bourane et al., 2015; Bui et al., 2016; Li et al., 2011; Panek et al., 2014). Recent studies identified a specific population of interneurons located in laminae III/IV and expressing RORα that receive innervations from Aβ-LTMR afferents and establish direct synaptic contacts onto V0c and V2a premotor interneurons, as well as motoneurons (Bourane et al., 2015). RORα interneurons integrate light touch and motor control information from the cortex and cerebellum to coordinate corrective movements during walking on challenging terrains. Here, we found that EES recruits Aβ-LTMR afferents, which leads to the activation of RORα interneurons. We also identified inhibitory interneurons interposed between RORα interneurons and motoneurons. These interneurons possess the profile of Ia reciprocal inhibitory interneurons (Alvarez et al., 2005; Bourane et al., 2015), which are critical to gate the excitatory drive elicited by EES (Moraud et al., 2016). Since Aβ-LTMRs are only transitorily recruited during walking, the continuous activation of Aβ-LTMRs with EES logically interferes with the encoding of touch by these afferents. Simulations suggested that this out-of-phase recruitment of Aβ-LTMRs engenders undesired inhibitory inputs to motoneurons, which prevent the development of a sustained activity in muscles. Indeed, phase-dependent modulation of cutaneous afferent circuits is crucial to produce well-coordinated movements (R. B. Stein & Capaday, 1988). For example, previous studies described supraspinal pathways that down-regulate tactile information during specific phases of movement execution in order to tune their contribution to the modulation of motoneuron activity (Duysens et al., 1990; Liu et al., 2018; Seki et al., 2003). After SCI, supraspinal pathways can no longer regulate the gain in sensory feedback circuits.

Here, we aimed to restore an advantageous modulation of sensory feedback circuits to support walking enabled by EES. We repurposed a dual selective noradrenergic agent that acts as an agonist to α2c receptors and an antagonist to α2a receptors (Delaunois et al., 2013). The remarkably distinct expression profiles of α2a receptors in proprioceptive neurons and α2c receptors in RORα interneurons offered a therapeutic window for the opposite modulation of proprioceptive and Aβ-LTMRs feedback circuits with this agent. Neurobiomechanical simulations suggested that the inactivation of RORα interneurons primed the membrane of motoneurons to respond to the otherwise enhanced excitatory drive from proprioceptive afferents. These synergistic mechanisms led to a robust increase in the amplitude of muscle responses to EES, which augmented the ability of EES to enable walking in rats with complete and clinically-relevant contusion SCI.

The expression pattern of α2 receptors was not limited to proprioceptive and Aβ-LTMRs. For example, α2c receptors were profusely expressed in nociceptive fibers. However, computer simulations indicated that the small diameter of these afferents is not compatible with their depolarization within the range of EES amplitudes used therapeutically. Similarly, a plethora of interneurons located in lamina I-III expressed α2a receptors. Yet, computer simulations showed that the rapid decline in the intensity of the electrical field elicited by EES combined with the electrical and anatomical properties of these small interneurons reduce the likelihood of their depolarization with EES to negligible levels. Moreover, these interneurons are innervated by afferent fibers of small diameters, which are unlikely recruited by EES. These considerations suggest that the modulations of proprioceptive and Aβ-LTMRs feedback circuits were the main mechanisms underlying the potentiation of the effects of EES when delivering the noradrenergic agent.

2.4.3 Implications for clinical applications

Our results reveal that the anatomical and biophysical properties of the nervous system transform the apparently unspecific electrical stimulation of the spinal cord into a therapeutic tool to modulate specific circuits involved in the control of movement. This understanding opens various opportunities to optimize the technologies and methods to deliver EES in humans with SCI.

Since EES targets proprioceptive afferents within individual posterior roots, it is critical to design personalized clinical leads with electrode configurations that target individual posterior roots with the maximal specificity for each patient (Capogrosso et al., 2018; Mendez et al., 2020; Wenger et al., 2016). These leads will support more precise stimulation programs, in particular dynamic stimulation protocols that aim to reinstate the natural dynamic of spinal circuits though the spatiotemporal modulation of individual posterior roots (Wagner et al., 2018; Wenger et al., 2016). These stimulation protocols are remarkably more efficacious than continuous EES to enable walking, cycling and other leg motor activities in humans with paralysis (Wagner et al., 2018; Wenger et al., 2016).

The detrimental recruitment of Aβ-LTMRs feedback circuits with EES stresses the importance of conceiving new stimulation protocols that mitigate this negative influence of EES. One strategy may involve the delivery of low amplitude / high-frequency bursts that primarily recruit proprioceptive afferents with the largest diameters, thus avoiding the recruitment of the relatively smaller LTMR afferents (Formento et al., 2018).

We and others exposed robust synergies between electrical spinal cord stimulation and serotonergic drugs (Courtine et al., 2009; Freyvert et al., 2018; Musienko et al., 2011), but these agents exert an unspecific influence over a board range of spinal circuits with very different functions. This lack of precise targets may preclude their therapeutic use in humans (Volpi-Abadie et al., 2013). Here, we repurposed a noradrenergic agent that increased the gain in functionally beneficial proprioceptive feedback circuits while gating the detrimental recruitment of Aβ-LTMR/RORα feedback circuits with EES. Consequently, this agent exerted no visible effect on motor performance in the absence of EES, but it primed sensory feedback circuits to respond to EES. Rats with clinically-relevant contusion SCI immediately regained supraspinal control of weight-bearing locomotion. These results provide a framework to design circuit-based strategies that augment the ability of EES to enable motor control and boost neuroplasticity in humans with SCI.

2.5 Materials and methods

2.5.1 Experimental model and subject details

Experiments were conducted on adult female Lewis rats (~220 g body weight), adult Long evans rats (~240 g body weight) and adult C57BL/6 mice (20-30 g body weight). PV^{Cre} (Jackson Laboratory, JAX# 017320), RORα^{Cre} (Bourane et al., 2015) α2a^{GFP} (MMRRC, MMRRC:014248-UCD), α2c^{GFP} (MMRRC, MMRRC:030098-UCD), α2a$^{-/-}$ knockout (Lähdesmäki et al., 2002), α2c$^{-/-}$ knockout (Hein et al., 1999), Egr3$^{-/-}$ knockout (Takeoka et al., 2014), *Ret*^{CreER} (Luo et al., 2009) and *R26*$^{LSL-tdTomato}$ (Jackson Laboratory, #007909) transgenic mouse strains were used and maintained on a mixed genetic background (129/C57BL/6). PV^{Cre} (RRRC, 773) and TH^{Cre} (Horizon discovery, TGRA8400) rat lines were maintained similarly. Experimental animals used were of both sexes. Housing, surgery, behavioral experiments and euthanasia were performed in compliance with the Swiss Veterinary Law guidelines. Animal care, including manual bladder voiding, was performed twice daily for the first 3 weeks after injury, and once daily for the remaining post-injury period. All procedures and surgeries were approved by the Veterinary Office of the canton of Vaud or Geneva in Switzerland.

2.5.2 Surgical procedures and post-surgical care

General surgical procedures used have been described previously (Asboth et al., 2018; van den Brand et al., 2012). All interventions were performed under general anesthesia and aseptic conditions. Analgesia (buprenorphine Temgesic, ESSEX Chemie AG, Switzerland, 0.01-0.05 mg per kg, s.c.) and antibiotics (Baytril 2,5%, Bayer Health Care AG, Germany, 5-10 mg per kg, s.c.) were provided for 3 and 5 days post-surgery, respectively.

Spinal cord injuries
Wildtype and transgenic rats received either a complete thoracic (T8) SCI or a severe contusion injury (250 kdyn; 1 dyn=10 N) using a force-controlled spinal cord impactor (IH-0400 Impactor, Precision Systems and Instrumentation LLC, USA). The spinal cord displacement induced by the impact was measured for each animal and the extent and location of each lesion was verified postmortem. All the tested mice received a complete thoracic lesion (T8).

Epidural electrical stimulation (EES) implants
EES electrodes were created by removing a small part (~400 μm notch) of insulation from Teflon-coated stainless-steel wires (AS632, Cooner Wire, USA), which were subsequently secured over the midline of the targeted spinal cord segment by suturing the wires to the dura. A common ground wire (~1cm of Teflon removed at the distal end) was inserted subcutaneously

over the right shoulder.

Electromyographic (EMG) implants

Bipolar intramuscular electrodes (Cooner Wire; AS632 and AS632-1 for rats and mice, respectively) were inserted bilaterally in the medial gastrocnemius (MG, ankle extensor, in rats) or vastus lateralis (VL, knee extensor, in mice) and tibialis anterior (TA, ankle flexor) muscles to record EMG activity. All the wires were connected to a percutaneous amphenol connector (Omnetics Connector Corporation, USA) cemented onto the skull of the animals.

2.5.3 Ex-vivo calcium imaging in mouse DRGs

Calcium imaging experiments were performed as described previously (Hutson et al., 2019). PV^{Cre}:$R26^{LSL-tdTomato}$ and Ret^{CreER}: $R26^{LSL-tdTomato}$ mice were anesthetized using urethane (0.5 - 0.6mg/kg bodyweight, dilution with saline). A laminectomy over the L2 spinal cord level was performed and EES was applied via acutely implanted electrodes for 30 minutes. The following experimental conditions were tested (1) no electrical stimulation; (2) 1.2x motor threshold EES and (3) supra-threshold EES (3x motor threshold). After stimulation, L1-L3 dorsal root ganglia (DRG) were dissected and prepared for calcium imaging experiments as previously described. Briefly, Fluo-4 AM (50µg, ThermoFisher, Cat.F14201) was re-suspend in 50µl DMSO (Sigma, Cat. D2650), diluted in 10 ml of HBSS without Ca^{2+} and Mg^{2+} (ThermoFisher, Cat. 14175095), supplemented with 10 mM Hepes (ThermoFisher, Cat. 15630080) and then stored in the dark at -20^{o}C. After acute stimulation experiments, DRGs were extracted and immediately suspended in Fluo-4-AM (10 µM) dissolved in HBSS supplemented with 10 mM Hepes for 1 hour at 37^{o}C, 5% CO_2. The Fluo-4-AM solution was then replaced with HBSS with 10 mM Hepes and the DRGs were washed for 1 hour at 37^{o}C, 5% $CO_{2.}$ The DRGs were placed into a video-microscopy chamber at 37^{o}C, 5% CO_2 and suspended in HBSS with 10 mM Hepes. Time-lapse recordings were taken with images acquired every second for 5 minutes. Imaging was done on an Olympus XCellence microscope (Olympus, Japan) equipped with a Hamamatsu camera (*ORCA 03G, Japan)* at 20X magnification. After 1 minute of baseline recording, increasing concentrations (50 mM, 100 mM and 150mM) of KCL (Sigma, Cat. P3911, USA) were added to the DRG to elicit depolarization and induce intracellular Ca^{2+} release. Quantification was done using the FiJi-ImageJ plug-in *Time series analyser,* where the soma of at least 20 neurons per DRG were analyzed. To determine the fold-change in Fluo-4 AM intensity after KCL addition, the Fluo-4-AM intensity ratio “F/Fo” was calculated by dividing the average fluorescence intensity after KCL addition “F” with the average intensity of baseline fluorescence “Fo”.

2.5.4 Behavioral testing and neurorehabilitation procedures

Bipedal locomotion on a treadmill

Starting 7 days after SCI, animals were trained 5 days per week for 20-30 min per day on the treadmill (11 cm/s for rats; 9 cm/s for mice) with adjustable robotic bodyweight support against the direction of gravity (Robomedica, USA). To reactivate the lumbar spinal cord during training, we administered a serotoninergic replacement therapy and EES (Courtine et al., 2009). Five minutes prior to training, the rodents received a systemic (i.p.) administration of quipazine (5-HT$_{2A/C}$, 0.2 - 0.3 mg/kg) and 8-OH-DPAT (5-HT$_{1A/7}$, 0.05 - 0.2 mg/kg) that was adjusted daily based on locomotor performance. Animals were trained until they showed plantar stepping enabled by EES only (2-3 weeks of training). Bipedal locomotor performance was then evaluated on the treadmill in different testing conditions.

Neurorehabilitation procedures

A subset of contused rats followed a rehabilitation program during 2 months, starting 7 days after SCI, as previously described in details (van den Brand et al., 2012). Briefly, rats were trained 5 days per week for 30 min per day. Five minutes prior to training, the rats received a systemic (i.p.) administration of quipazine (5-HT$_{2A/C}$, 0.2 - 0.3 mg/kg) and 8-OH-DPAT (5-HT$_{1A/7}$, 0.05 - 0.2 mg/kg) that was adjusted daily based on locomotor performance. During training, continuous EES (0.2ms, 100-300A, 40Hz) was delivered through L2 and S1 electrodes. Training was conducted bipedally on a treadmill (11 cm/s) with adjustable robotic bodyweight support against the direction of gravity (Robomedica, USA). Starting 2 weeks after injury, contused rats were additionally trained overground with the robotic bodyweight support system. The robotic bodyweight support provided optimal vertical and mediolateral support to the bipedally positioned animals (Dominici et al., 2012).

Leg motor control was evaluated along a straight runway with robotic assistance. All animals participated in behavioral evaluation 9 weeks post-injury. They were tested without neuromodulation, with EES, and with EES plus 5HT agonists. Experiments with mice did not involve rehabilitation procedures.

Kinematic, kinetic and muscle activity recordings

All procedures used have been detailed previously (Dominici et al., 2012; van den Brand et al., 2012). Bilateral leg kinematics were captured using the high-speed motion capture system Vicon (Vicon Motion Systems, UK), consisting of 12 infrared cameras (T-10, 200 Hz). Reflective markers were attached bilaterally at the iliac crest, the greater trochanter (hip joint), the lateral condyle (knee joint), the lateral malleolus (ankle), the distal end of the fifth metatarsophalangeal (mtp) joint and, for the rats, the tip of the fourth toe was added. The body was modeled as an interconnected chain of rigid segments, and joint angles were generated accordingly. EMG signals (2 kHz) were amplified, filtered (10-1000 Hz bandpass), stored and analyzed offline to compute the amplitude, duration and timing of individual bursts. For both the left and right legs, 10 successive step cycles were extracted over several trials on the runway for each rat under each experimental condition and time point. A 20 second interval was used when no or minimal leg movements were observed. To generate sequences of hindlimb movements, we projected the calculated coordinates of individual joints from kinematic recordings onto a 3-D rat model (Turbosquid.com, USA). We rendered the animated model using Maya (Autodesk Maya, USA). Final image composition was performed in Photoshop (Adobe Photoshop, USA). EMG signals were recorded concomitantly to video acquisition.

Analysis of kinematic, kinetic and muscle activity

A total of 104 (mice) and 129 (rats) parameters quantifying kinematics and muscle activity features were computed for each leg and gait/stroke cycle according to methods described in detail previously (Dominici et al., 2012; van den Brand et al., 2012). To evaluate differences between experimental conditions and groups, as well as the most relevant parameters to explain these differences, we implemented a multi-step statistical procedure based on PC analysis. All the details can be found in previous publications (Dominici et al., 2012; van den Brand et al., 2012).

2.5.5 Electrophysiological experiments

EES-evoked motor responses

Muscle responses elicited by single pulses of EES were recorded in ankle flexor (TA) and extensor (MG) muscles. Rectangular pulses (0.5 ms duration) were delivered at 0.2 Hz through the implanted EES electrodes. The intensity of EES was applied over a defined range of amplitudes, starting from threshold level. Evaluations were conducted during awake conditions. EMG signals (12.207 kHz) were amplified, filtered (1–5000 Hz bandpass), and stored for off-line analysis. Signals with movement artefacts were excluded. The onset latency and peak amplitude of the muscle responses different were quantified off-line using a custom-made software in Matlab (MathWorks).

Analysis of EMG bursts during walking

EMG recordings during locomotion was filtered using a band-pass filter (10-400 Hz) before passing a moving average window to obtain of an EMG envelope. This enveloppe was discretized into bins and the peak-to-peak amplitude of muscle responses in each bin was calculated.

Electrophysiological and Pharmacological experiments

Electrophysiological experiments were performed as described above. The following pharmacological agents were tested: (1) quipazine (5-HT2A/C, 0.2 - 0.3mg/kg) and 8-OH-DPAT (5-HT1A/7, 0.05 - 0.2mg/kg); (2) clonidine (NA2 agonist, 0.4 - 0.6mg/kg); (3) compound A08 (dual a2a antagonist/a2c agonist, 25 - 35mg/kg). All pharmacological agents were injected systemically (i.p.), with the exception of compound A08 that was also administered intrathecally (i.t.). These i.t. injections were performed according to methods described previously (la Calle & Paino, 2002; Mestre et al., 1994). Rats were securely held in position while a 30G needle was inserted into the tissues between the dorsal aspects of L5 and L6, perpendicular to the vertebral column. When the needle entered the subarachnoidal space, a sudden lateral movement of the tail was observed. This 'tail-flick' reflex was used as an indication of successful needle insertion. For each pharmacological agent tested, a volume of 0.05mL was injected. After injection, the syringe was held in position for a few seconds and progressively removed to avoid any liquid backflow. During the whole procedure, no sign of distress or pain was observed in all experimental animals.

2.5.6 Chemogenetics

To modulate the activity of proprioceptive afferent neurons in DRGs, we targeted PV^{ON} neurons using viral-mediated expression of DREADDs in transgenic rats. A total of 2.5µL of AAV2/5-hSyn-DIO-hm4Di-mCherry (titer 1.12^{E}13 VG/ml, Addgene, Plasmid #44362) or AAV2/5-hSyn-DIO-hm3Dq-mCherry (titer 1.0^{E}13 VG/ml, Addgene, Plasmid #44361) was injected into both left and right sciatic nerves of PV^{Cre} rats (n=4 for each virus). A 5µL Hamilton syringe was inserted into the nerve and used to slowly deliver the virus over the course of 90 seconds. The syringe was left in position for 2 minutes following injection to minimize any backflow. One week after virus injection, EES electrodes were implanted over the midline of spinal segment L4, which receives the more pronounced innervation from the sciatic nerve. In the same surgery, the rats received EMG electrodes and a severe contusion SCI, as explained above. Starting 7 days after SCI, all rats underwent the rehabilitation procedure described above. After 2 to 3 weeks of training, behavioral experiments were performed during EES applied at L4, before and after systemic (i.p.) injection of CNO (5 mg/kg body weight, dilution with saline). For both control (wildtype) and PV^{Cre} rats, functional testing was performed before and over the course of 45-60min after CNO-injection. Reflex measurements were performed during anesthesia with urethane (0.5 - 0.6 mg/kg bodyweight, dilution with saline). Muscle responses to EES were recorded as detailed above.

2.5.7 Genetic labelling of low-threshold mechanoreceptor neurons

To label the axons of Aβ-LTMR neurons, *Ret*^{CreER} mice were crossed with *R26*$^{LSL-tdTomato}$ (Luo et al., 2009). To induce the expression of Cre, tamoxifen (2mg) was delivered to the pregnant female mice via oral gavage for embryonic treatment at E10.5 and E11, as described previously (Abraira et al., 2017). For all timepoints, the morning after coitus and the appearance of a plug of the pregnant female was designated as E0.5 and the day of birth as P0. At E19.5 c-section and cross fostering was performed. For this, the pregnant female was anesthetized with isoflurane (4%) and a cervical dislocation was performed. The belly was then opened to expose the uterus. Using forceps to tear the uterus, each individual pup was exposed and rubbed with tissue paper until the skin was of pink colour. Pups were then placed in the cage of a female wild-type foster mouse.

2.5.8 Virus production

AAV constructs used for DREADD experiments were acquired at Addgene (hM4Di: Addgene plasmid N°44362 and hM3Dq: Addgene plasmid N°44361). AAV2/5 production was carried out in 293AAV HEK cells following standard procedures, yielding vector suspension with titers >1^{E}13 VG/ml.

The following vectors or constructs were obtained commercially: AAV-DJ-hSyn Flex mGFP 2A synaptophysin mRuby (Stanford vector core facility, reference AAV DJ GVVC-AAV-100), AAV2/6-G (The Boston Children's Hospital Viral Core) and Rabies-eGFP (Gene Transfer, Targeting and Therapeutics Core at the Salk Institute). The vectors were used at the concentration indicated for each injection procedures. All flexed AAV vectors used in the present study showed transgene expression only upon Cre-mediated recombination.

2.5.9 Virus and tracer delivery procedures

Spinal cord and brain targeted tracer or viral delivery were performed through stereotaxic injections using high precision instruments (David Kopf Instruments) under isoflurane anesthesia.

Monosynaptic-restricted rabies virus tracings were performed in RORα^{Cre}:R26$^{LSL-tdTomato}$ neonate mice according to protocols described previously (Gu et al., 2017). A virus mixture containing equal volumes of AAV2/6-G (1 x 10^{14} GC/ml, The Boston Children's Hospital Viral Core) and Rab-eGFP (1 x 10^{9} TU/ml, Gene Transfer, Targeting and Therapeutics Core at the Salk Institute) was injected unilaterally into the TA muscle of neonate mice (P2). 3μl of virus mixture was injected into each muscle.

Anterograde tract-tracing of axons from rostro ventrolateral medulla (RVLM) projection neurons was performed in four TH^{Cre} rats. A craniotomy was performed bilaterally over the brainstem medulla oblongata and AAV-DJ-hSyn-FLEX-mGFP-2A-Synaptophysin-mRuby (titer 1.15^{14} GC/ml, Stanford University, USA) was injected bilaterally into both RVLM. Four injections (250 nl per injection) at two different rostrocaudal locations at two depths were made. Coordinates used for targeting this nucleus were -12.12 to -12.62 mm anteroposterior from Bregma, 2 mm lateral and 8 to 8.3 mm ventral from the surface of the cerebellum.

Injections were performed using either a glass pipette driven with the Nanoliter pump (Nanoliter 2010 injector, *World Precision Instruments*) or using the Hamilton injection system (for brainstem injections in rats). The virus was injected at 3nl/s and the needle was held in place for 2 minutes before being slowly retracted.

Animals were deeply anesthetized by an i.p. injection of 0.5ml Pentobarbital-Na (50mg/mL) and transcardially perfused after a survival time of 8 (mice) to 18 (rats) days.

2.5.10 Perfusion protocol

Animals were anesthetized by an i.p. injection of 0.5ml Pentobarbital-Na (50 mg/mL; PBS) and transcardially perfused with approximately 80ml Ringer's solution containing 100'000IU/L heparin (Liquemin, Roche, Switzerland) and 0.25% NaNO2 followed by 300ml of cold 4% phosphate buffered paraformaldehyde, pH 7.4. The tissue was removed and postfixed in the same fixative before they were transferred to 30% sucrose in phosphate buffer (PB) for cryoprotection, or placed in PBC prior to tissue clearing. Prior to cryosectioning tissue was embedded in Tissue Tek O.C.T (Sakura Finetek Europe B.V., The Netherlands), frozen at -40°C and stored at -80°C until use.

2.5.11 Immunohistochemistry

Mounted or free-floating sections (30µm) were washed 3 times in 0.1M PBS and blocked in 5% normal goat serum containing 0.3% Triton (Sigma, USA). Sections were then incubated in primary antibody diluted in the blocking solution overnight at 4°C (CGRP, parvalbumin) or room temperature (GFP, Ib4, PKC-gamma, ChAT, RORα, vGlut1, vGlut2), or 3 nights at room temperature (Glutamate, Glycine, GABA). Primary antibodies used were rabbit anti-Glutamate (1:1000, Sigma, USA), rabbit anti-GABA (1:1000, Millipore, USA), rabbit anti-PKC-gamma (1:500, Santa Cruz Biotechnology, USA), rabbit anti-cfos (1:500, Santa Cruz Biotechnology, USA), rabbit anti-Parvalbumin (1:2000, Swant, Switzerland), rabbit anti-GFAP (1:1000, Dako, USA), rabbit anti-RFP (1:1000, Rockland, USA), chicken anti-GFP (1:500, Life Technologies, USA), goat anti-ChAT (1:500, Chemicon, USA), goat anti-RORα (1:500, Santa Cruz Biotechnology, USA), guinea-pig anti-vGlut1 (1:2000, Millipore, USA), mouse anti-vGlut2 (1:2000, Millipore, USA), mouse anti-CGRP (1:1000, Abcam, UK), mouse anti-TH (1:500, Millipore, USA) and rat anti-glycine (1:200, Immunosolution, Australia). Sections were again washed 3 times in 0.1M PBS and incubated with the appropriate secondary antibody (Alexa fluor 405, Alexa fluor 488, Alexa fluor 555 or Alexa fluor 647; Molecular Probes, Life Technologies, USA) in blocking solution. DAPI (Life Technologies, USA) was used as a counterstain at a dilution of 1:1000 in 0.1M PBS for 20 minutes. Slides were washed, air-dried and cover slipped with Mowiol (Calbiochem, USA).

2.5.12 Fluorescent in-situ hybridization

To label the mRNA of PV^{ON}, α2a^{ON} and α2c^{ON} interneurons in the spinal cord and DRG, an RNA labelling kit from Molecular instruments (Molecular instruments, USA) was used. After perfusion, tissues were fixed in 4% phosphate buffered paraformaldehyde for 3 hours at 4°C before they were transferred to 30% sucrose in phosphate buffer (PB) for cryoprotection at 4°C for 2 nights. RNA *in situ* hybridization was performed on 40µm spinal cord sections according to a standard protocol. Briefly, samples were placed in 5x SSCT (20x SSC buffer, Invitrogen, USA; 10% Tween 20, Applichem, Germany) for 10min and then pre-hybridized in 30% probe hybridization buffer (Molecular instruments, USA) for 30min at 37°C. Samples were hybridized overnight at 2µM probe concentration in 30% probe hybridization buffer at 37°C. Following hybridization, samples were washed in a solution of 30% probe wash buffer (Molecular instruments, USA) and 5x SSCT four times 15 minutes. Sections were then incubated in an amplification buffer (Molecular instruments, USA) for 30min at room temperature. In the meantime, fluorophore-labeled HCR hairpins (Molecular instruments, USA) were snap-cooled (heating at 95°C for 90sec) and cooled down to room temperature. Amplification was performed overnight at room temperature at a concentration of 120nM per hairpin in the amplification buffer. Following amplification, samples were washed in 5x SSCT for at least 2 times 30min to remove unbound hairpins. Lastly, sections were air-dried and coverslipped using Mowiol (Calbiochem, USA).

2.5.13 Neuromorphological evaluations

Evaluation of contusion SCI
The extent and location of spinal cord damage was evaluated in each experimental animal. The lesion cavity was cut in serial coronal sections (40 µm) that were stained using GFAP antibodies. For each lesion, we calculated the spared spinal cord surface with respect to the distance from the epicenter of the lesion, the spared area at the epicenter, and the total volume of damaged spinal cord tissue. The percentage of spared tissue at the epicenter was calculated using Fiji and normalized using the mean surface of sections rostral and caudal to the contusion, taking into account spinal cord compression.

Co-labeling quantifications
The percentage of double-labelled α2a^{GFP} and α2c^{GFP} neurons and various neurotransmitters (GABA, Glycine, Glutamate, and Acetylcholine) and sensory afferent markers (Parvalbumin, Ib4, CGRP) was quantified using 5 confocal image stacks per mouse at the L2 spinal cord level or in dorsal root ganglia. Images were acquired with standard imaging settings. Image acquisition was performed using a Leica TCS SPE or SP8 laser confocal scanning microscope (Leica Microsystems, Germany). Images were analyzed manually for double-labelling using the LAS AF interface (Leica Microsystems, Germany).

Quantification of synaptic contacts
For $ROR\alpha^{Cre} : R26^{LSL-tdTomato}$ mice injected with G-deleted rabies virus, the spinal cords were cut in coronal sections of 40m. Images were acquired with standard imaging settings, using a ZEISS LSM880 airyscan microscope (Zeiss, Germany). The number of RORα^{ON}/vGlut2^{ON} synaptic contacts onto inhibitory pre-motor interneurons were counted manually using the Fiji 3D object counter. Synaptic contacts were quantified on 3 confocal image stacks per mouse. Neurons and synaptic contacts were reconstructed offline using the Imaris software (Bitplane, USA).

2.5.14 Single-cell sequencing data processing

For single-cell sequencing data of the mouse spinal cord, we queried the gene expression omnibus. For this, three studies were identified. Two out of the three studies used droplet-based methodology with relatively low sequencing depth (~50,000 per cell), while the third study sequenced up to ~200,000 reads per cell. We retrieved the data from the gene expression omnibus (GSE103840, GSE103892) or the processed loom files available at mousebrain.org. Initial examination of the data revealed that the expression of markers of interest (*Rora, Adra2c*) were only robustly expressed with deeper sequencing, so only one dataset was used for further analysis.

Cells were classified according to the 30 global excitatory (glutamatergic) and inhibitory (GABAergic) phenotypes as described in the publication. In a first step, the relative expression of the key marker genes *Rora* and *Adra2c* across all cell types were examined. Cells were defined as expressing the gene if the read count was non-zero. We considered a gene robustly expressed if more than 20% of cells in that subtype showed non-zero expression, similar to previous work (Zeisel et al., 2018).

2.5.15 Dissection of mouse spinal cord with attached DRGs

PV^{Cre} : $R26^{LSL-tdTomato}$ and Ret^{CreER} : $R26^{LSL-tdTomato}$ mice were deeply anesthetized with an i.p. injection of pentobarbital and perfused with 4% PFA. Given the fragile nature of the DRGs and dorsal roots, the entire spinal column including spinal cord, dorsal roots and DRGs was dissected in a first step. The dorsal aspect of the vertebral column was then removed by performing laminectomies along the whole length of the spinal cord, while leaving the rest of the vertebral canal intact for DRG and dorsal root preservation. Tissue was then post-fixed in 4% PFA overnight at 4°C. Using fine scissors, the ventral aspect of the vertebral canal was carefully cut open along the midline over the whole length of the spinal cord which allowed a better access to the DRGs and dorsal roots. Each individual DRG was dissected under the microscope by carefully cutting and removing surrounding bone and connective tissue. Once all DRGs were dissected the meninges were removed as much as possible without damaging the attached nerve roots and DRGs. Tissue was then prepared for passive clearing.

2.5.16 Tissue clearing and 3D image acquisition

Clearing of mouse spinal cord with attached dorsal root ganglia (DRG)
Tissue was cleared using a passive CLARITY process (Chung and Deisseroth, 2013). For this, the sample was incubated in a hydrogel solution as above for 24 hours at 4°C with nutation. The tubes were then flushed with nitrogen (N_2) gas for 3 minutes and immediately closed to remove oxygen. Polymerization was then performed by incubating the hydrogel solution with the sample for 2 hours in a water bath at 37°C. Excess gel was removed and the sample washed in 0.001 M PBS at room temperature with shaking. The tissue was immersed in a falcon tube with clearing solution and placed in an incubator at 37°C shaking at 40 RPM. Clearing solution was exchanged every 24 hours with new solution for the first three days then every other day until the sample was clear (approximately 7 days). After clearing, the samples were placed in PBST with shaking at room temperature for 24 hours. Prior to imaging, samples were placed in RIMS (40 g Histodenz in 30 mL of 0.02M PBS for a total volume of 48.75 mL, pH 7.5, 0.01% sodium azide, refractive index: 1.465) for 24 hours.

Clearing of rat brainstem and spinal cord
Tissue was cleared using active CLARITY (E. Lee et al., 2016). Animals were deeply anesthetized with an i.p. injection of pentobarbital and perfused with 4% PFA. Rat brain and spinal cord tissue were dissected and post-fixed overnight in 4% PFA at 4°C. The meninges were removed from brain and spinal cord segments and incubated in a hydrogel solution composed of 4% acrylamide, 0.25% VA-044 initiator (Wako Pure Chemical Industries, Ltd., Osaka, Japan), and 0.001 M PBS for 24 hours at 4°C with nutation. The tubes were then flushed with nitrogen

(N_2) gas for 3 minutes and immediately closed to remove all oxygen. Polymerization was then performed by incubating the hydrogel solution with the sample for 2 hours in a water bath at 37°C. Polymerization resulted in a viscous gel that was not solidified, as previously described. Excess gel was carefully removed, and tissues were washed in 0.001M PBS for 5 minutes at room temperature with shaking. The tissue was placed in the X-CLARITY Clearing System (Logos Biosystems Inc., South Korea) and immersed in clearing solution (40 g sodium dodecyl sulfate, 200 mM boric acid, dH2O up to 1 L of solution, pH 8.5) and cleared with the following settings: 37°C, 100 RPM, and 1.2 A of current. A clearing solution was continually circulating through the clearing chamber. The clarification process lasted 10-15 hours for the spinal cord and about 30 hours for brainstem tissue. After clearing, the samples were placed in PBST (1x PBS, 0.1% (v/v) Triton-X, 0.02% (w/v) sodium azide) with shaking at room temperature for 24 hours. Prior to imaging, samples were placed in RIMS (40 g Histodenz in 30 mL of 0.02M PBS for a total volume of 48.75 mL, pH 7.5, 0.01% sodium azide, refractive index: 1.465) for 24 hours.

3D-imaging of cleared samples

Imaging was performed at the Advanced Light sheet Imaging Center (Wyss Center, Geneva, Switzerland) using a custom-built COLM system (Tomer et al., 2014) in combination with a customized MesoSPIM lightsheet microscope (Voigt et al., 2019) depending on the sample. We used a customized sample holder to immerse the spinal cord, brain, or paw in a chamber filled up with RIMS for CLARITY cleared samples. Images were acquired with 4x and 10x objectives with two lightsheets (left and the right sides) when using the COLM (spinal cord and brain) and a 2x objective when using the MesoSPIM (spinal cord). At 4x and 10x magnifications on the COLM, pixel resolutions were 1.4 μm by 1.4 μm by 5 m and 0.48 x 0.48 x 3 μm in x-, y-, and z-direction, respectively. At 2x magnification on the MesoSPIM, the pixel resolution was 3.26 x 3.26 x 3 μm in x-, y-, and z-direction. Image acquisition generated 16-bit TIFF files, and stitching of files was performed using TeraStitcher for COLM-acquired images and arivis Vision4D (arivis AG, Munich, Germany) for MesoSPIM-acquired images. Imaris (Bitplane, v.9.0.0) and arivis Vision4D (arivis AG, Munich, Germany) were both used to generate 3D reconstructions and optical sections of the raw images. The lesion volume was reconstructed using Imaris (Bitplane, USA).

2.5.17 Hybrid computational model

We designed a hybrid computational model combining (1) a 3D Finite Element Method (FEM) to characterize the electric potential and currents generated by EES, (2) a geometrically realistic biophysical model of spinal sensorimotor circuits to identify the type of neurons, fibers, and circuits recruited by EES-induced electrical fields and currents, (3) a spiking neural network reproducing proprioceptive and cutaneous feedback circuits associated with a pair of antagonist hindlimb muscles, (4) a muscle spindle and Aβ-LTMR model and (5) a musculoskeletal model of the rat hindlimb.

3D Finite Element Model

We developed an anatomically and electrically realistic volume conductor model of the rat lumbosacral spinal cord. For this, we acquired high-resolution MRI data in a rat between the spinal vertebrae T1 and S4 in order to visualize the different tissues located in the spinal canal. The rodent's spinal cord was imaged post-mortem in a 9.4T horizontal MRI system (Magnex Scientific, Abingdon, UK), equipped with a 12 cm internal diameter gradient coil insert and interfaced to a DirectDrive console (Varian, Palo Alto, CA) using a custom-made radio frequency coil. We segmented the vertebral bone, epidural fat, cerebrospinal fluid (CSF), white matter, grey matter and spinal roots from this dataset using the iSeg software developed by ZMT (www.zurichmedtech.com). We then imported the segmentation into Sim4Life, a software developed by ZMT (www.zurichmedtech.com).

EES was delivered through microwire electrodes, which we modeled as active sites of 1 mm in length as they have been described previously for functional experiments in rats (Courtine et al., 2009). EES electrodes were positioned on the dorsal aspect of the spinal segments L2, L4 and S1, which have been the primary sites shown to facilitate movement execution in rats (Musienko et al., 2009) and humans (Wagner et al., 2018) after SCI. The electrodes were placed over the spinal cord midline within the epidural space.

Simulation of EES in the FEM Model

The electrical potential was obtained by means of quasi-static approximation of the Maxwell equations. The corresponding simulation has already been predefined and is available in Sim4Life. A Dirichlet Boundary condition of $V(\delta\Omega_{electrode}) = 1V$ simulating a biphasic stimulation pulse of 40 µs duration was applied at the ventral surface of the active electrode site ($\delta\Omega_{electrode}$) to model the stimulation. Dirichlet boundary conditions of $V(\delta\Omega_{saline}) = 0V$ were set at the outermost boundaries of the model, where $\delta\Omega_{saline}$ is the outermost surface of the saline conductor. Conductivity values were taken from a previously published modelling study (Capogrosso et al., 2013). Similar to previous studies, we did not include the thin dura mater in our computational model (Ladenbauer et al., 2010).

Evaluation of Fiber and Cell Recruitment

We used the inbuilt Neuron 4.4 solver of Sim4Life to develop a computational model of group $A\alpha$-, $A\beta$-, $A\delta$- and C-fibers in the dorsal roots and motor axons in the ventral horn to characterize the percentage of recruited nervous structures with increasing EES amplitudes obtained from the FEM-simulation. 50 Neurons were simulated for each spinal cord segment and root. Fiber trajectories were obtained by initializing homogenously distributed streamlines following a diffusion tensor from the caudal end of each root to their termination end at the dorsal or ventral horn of the spinal grey matter. Neurons were simulated using the inbuilt Sweeney compartmental cable model of Sim4Life. Diameters of nerve fibers were modeled as log-norm functions with the following parameters: $A\alpha$: $\mu = 8.74$ µm, $\sigma = 0.2$ µm; $A\beta$: $\mu = 4.52$ µm, $\sigma = 0.31$ µm; $A\delta$: $\mu = 2.77$ µm, $\sigma = 0.21$ µm; $C = \mu = 1.08$ µm, $\sigma = 0.20$ µm; MN: $\mu = 11.52$ µm, $\sigma = 0.07$ µm. Recruitment curves for increasing EES amplitudes were simulated for each type of fiber.

Spiking neural network

The anatomically realistic spinal sensorimotor circuits were implemented as a spiking neural network in NEURON (Hines & Carnevale, 1997) using a parallel multi-threaded structure. The rat model of proprioceptive feedback circuits was elaborated from previously validated models (Formento et al., 2018; Moraud et al., 2016). Briefly, the spiking neural network includes populations of group Ia and group II afferent fibers, Ia-inhibitory interneurons, group-II excitatory interneurons and pools of α motoneurons. The number of cells, the number and the strength of the synapses contacting the different populations of neurons, and the characteristics of the cell models are described in previous publications (Capogrosso et al., 2013; Formento et al., 2018; Moraud et al., 2016).

Besides proprioceptive afferent inputs, we included inputs from cutaneous Aβ-LTMRs in our model. A total of 60 Aβ-LTMR cells located in laminae III/IV were implemented for rapidly adapting (RA) and slowly adapting (SA) afferent cells for each motor pool. Each Aβ-LTMR interneuron is synaptically connected to an excitatory pre-motor interneuron or motoneuron, as previously described for RORα^{ON} cells. These interneurons, which integrate LTMR inputs, have been shown to form excitatory connections to the homonymous motoneurons as well as to several classes of excitatory pre-motor interneurons. Besides the existence of excitatory connections from RORα^{ON} cells onto the motor system, the same study also suggested connections from RORα^{ON} interneurons onto inhibitory V2b^{ON} pre-motor interneurons. Therefore, besides the described excitatory connections, we also implemented an inhibitory di-synaptic pathway from RORα^{ON} interneurons onto motoneurons. Due to the absence of experimental measurements and values for those intraspinal RORα^{ON} circuits, we took over the synaptic strength of those networks from type II afferent cells or from similar populations of interneurons described in previous models (Formento et al., 2018; Moraud et al., 2016). Additionally, we added a baseline firing to each interneuron population as a Poisson point process with a firing rate of 30 Hz to simulate the resting state activity from other circuits.

Afferent firing rates

Musculoskeletal (Johnson et al., 2008) and muscle spindle (Prochazka & Gorassini, 1998a, 1998b) models were used to calculate the firing rate profiles of group-Ia and group-II afferent fibers innervating the flexor (tibialis anterior) and extensor (gastrocnemius medialis) muscles of the ankle during locomotion. For this purpose, we steered the musculoskeletal model with previously obtained recordings of rat hindlimb kinematics during locomotion to estimate the ankle muscle stretch profiles through inverse kinematics. We then used the muscle spindle model to compute firing rate profiles. To mimic the alpha–gamma linkage, muscle stretch and stretch velocity were linked to the envelope of EMG activity from the homonymous muscle. The estimated afferent firing rate profiles drove the activity of the modeled proprioceptive afferents.

Similarly, we developed a model of the Aβ-LTMR afferent firing as Poisson point processes with average firing rates fitted to experimental activity of Aβ-LTMR cells and 20% noise level. Their activity is encapsulated into the equations below. The firing was triggered by the foot strike obtained from the same rat hindlimb kinematics described above.

$$fr_{RA_{Swing}} = 250 * \exp(-55.29 * t) \tag{2.1}$$

$$fr_{RA_{Stance}} = 250 * \exp(-27.64 * t) \tag{2.2}$$

$$fr_{SA_{Swing}} = 0 \tag{2.3}$$

$$fr_{SA_{Stance}} = 10 * (23.47 * \exp(-6.24 * t) \ + 1.53) \tag{2.4}$$

2.5.18 Statistical procedures

All data are reported as mean values ± s.e.m. Behavioral assays were replicated several times (3 to 10 times depending on the experiments) and averaged per animal. Statistics were then performed over the mean of animals. Statistical analysis was performed in GraphPad Prism (USA) using two-sided paired or unpaired Student's t-tests, one-way ANOVA for neuromorphological evaluations with more than two groups, and one- or two-way repeated-measures ANOVA for functional assessments, when data were distributed normally. Post hoc Tukey's or Bonferroni test was applied when appropriate. The significance level was set as $p < 0.05$. The nonparametric Mann-Whitney or Wilcoxon signed-rank tests were used in comparisons of <5 rats or mice.

3 Inter-species differences necessitate the adaption of EES-protocols to improve activity-based therapies in a clinical setting

In the previous chapter, I provided evidence that EES recruits proprioceptive and cutaneous afferents. The results suggest that targeted modulation of proprioceptive neurons enable the emergence of motor pattern formation. Instead, continuous recruitment of cutaneous afferents seem to deteriorate EES by activating sensory feedback circuits out of phase. Hence, transient recruitment of sensory afferents may be necessary to retain the overall pattern of sensory firing activity.

In fact, retaining natural sensory firing actvity patterns during EES-enabled locomotion may be even more important as EES likely triggers Action Potentials (APs) that travel in both directions along the recruited fiber and may thus erase important natural sensory information by means of antidromic collision (Buonocore et al., 2008; Hunter & Ashby, 1994; Su et al., 1992). In this context, antidromic collision refers to erasure of sensory information by EES-evoked antidromic APs interacting with orthodromically-travelling APs elicited by sensory organs during movement.

Here, I present a work, that aimed to validate the erasure of natural sensory feedback with EES and suggest stimulation paradigms for enabling locomotion in rats and humans. We leveraged the musculoskeletal model described in the last chapter, to suggest that, due to inter-species differences of physiological parameters, EES applied with parameters commonly used for clinical research may abolish natural proprioceptive information in humans, but not in rats. We validated these results with electrophysiological evaluations, psychophysics tests and behavioral experiments. Instead, computer simulations suggested that spatiotemporal stimulation strategies and high-frequency, low-amplitude bursts of stimulation may mitigate the disruption of natural proprioceptive sensory activity, thus improving the formation of motor patterns with EES.

Related publication and personal contributions

The content of this chapter is adapted - with permission of the co-authors - from the following manuscript: Emanuele Formento, Karen Minassian, Fabien Wagner, Jean-Baptiste Mignardot, Camille Le Goff, **Andreas Rowald**, Jocelyne Bloch, Silvestro Micera‡, Marco Capogrosso‡ & Grégoire Courtine‡, "**Electrical spinal cord stimulation must preserve proprioception to enable locomotion in humans with spinal cord injury**", **Nature Neuroscience** (2018).
‡ contributed equally to this work

Personal contributions: Performed computer simulations, Designed experiments in rats, data analysis, figures preparation.

3.1 Abstract

Epidural Electrical Stimulation (EES) of the spinal cord reversed leg paralysis in animal models of Spinal Cord Injury (SCI) but has yet to reach similar efficacy in humans. Here, we hypothesized that this inter-species discrepancy is due to interferences between EES and proprioceptive information in humans. Computational simulations and preclinical / clinical experiments revealed that EES erases proprioceptive information in humans, but not in rats. This transient deafferentation prevents the modulation of reciprocal inhibitory networks critically involved in locomotion and abolishes the conscious perception of leg position. Consequently, continuous EES can facilitate locomotion within a narrow range of parameters that are insufficient to enable meaningful improvements in humans. Simulations showed that burst stimulation and spatiotemporal stimulation profiles mitigate the cancellation of proprioceptive information, enabling robust control over motoneuron activity. These results demonstrate the importance of delivering stimulation protocols that preserve proprioceptive information to facilitate walking with EES in humans.

3.2 Introduction

Spinal Cord Injury (SCI) has an immediate and devastating impact on the control of movement. These motor deficits result from the interruption of the communication between the brain and the spinal cord below the lesion, depriving the otherwise intact sensorimotor circuits from essential sources of modulation and excitation to produce movement (Kiehn, 2016). Due to the limited ability of the central nervous system for repair, the deficits are generally permanent. Currently, there is no medical treatment that significantly improves the recovery of motor control after SCI.

A variety of biological treatment paradigms showed promises to induce axon regeneration, reduce inflammation and scar formation, and reconstitute the spinal cord environment with neural progenitor grafts in experimental animal models (O’Shea et al., 2017). Complementary strategies have capitalized on our understanding of motor physiology to improve functional recovery (Barbeau et al., 1987; M. R. Dimitrijevic et al., 1998; Edgerton et al., 2008; Herman et al., 2002; Hofstoetter et al., 2015; Lovely et al., 1986; Minassian et al., 2016; Mushahwar et al., 2007; Wernig & Müller, 1992). These engineering strategies tap into spared circuits and residual neural pathways to modulate and augment the ability of the central nervous system to produce movement.

Amongst all these biological and technological strategies, Epidural Electrical Stimulation (EES) of the lumbar spinal cord showed the most striking preclinical outcomes. This treatment paradigm restored a broad range of adaptive motor behaviors in rodent, feline, and nonhuman primate models of leg paralysis (Capogrosso et al., 2016; Musienko et al., 2012; van den Brand et al., 2012; Wenger et al., 2014).

EES has also been applied to the human spinal cord for several decades but has yet to promote the same degree of therapeutic efficacy as in animal models. EES induced rhythmic movements of the legs in people with complete paralysis (M. R. Dimitrijevic et al., 1998; Minassian et al., 2004), and improved walking capacities when delivered during rehabilitation in two individuals with incomplete SCI (Herman et al., 2002; Huang et al., 2006). Moreover, this stimulation enabled the volitional activation of paralyzed muscles to initiate isolated movements of the leg in five individuals with motor complete paralysis (Angeli et al., 2014; Grahn et al., 2017; S. Harkema et al., 2011). These studies increased our understanding of spinal cord physiology, and draw attention to the potential of EES to improve motor control after SCI. However, EES failed to restore independent, weight-bearing locomotion in humans with severe SCI, despite the repetitive successes reported in animal models.

Currently, the mechanisms underlying species-specific responses to EES remain enigmatic. The identification of these mechanisms is not only essential for comparative spinal cord physiology, but also for guiding the development of evidence-based approaches that fulfil the potential of EES to improve recovery after SCI.

Computational models (Capogrosso et al., 2013; Ladenbauer et al., 2010; Rattay et al., 2000) and experimental studies (Y. P. Gerasimenko et al., 2006; Hofstoetter et al., 2018; Minassian et al., 2007; Moraud et al., 2016) conducted in both animal models and humans have provided evidence suggesting that EES recruits afferent fibers conveying proprioceptive information. The recruitment of these afferent fibers leads to the activation of motoneurons through monosynaptic and polysynaptic proprioceptive circuits, and to an increase in the excitability of the lumbar spinal cord through the broad integration of these afferent inputs within the spinal motor system. This modulation enhances the responsiveness of spinal circuits to residual descending signals and sensory feedback. In turn, task-specific sensory information modulates the reciprocal inhibitory networks in the spinal cord that gate the excitatory drive produced by EES towards functionally relevant pathways. This mechanism enables the generation of well-organized and adaptive patterns of muscle activation in animal models of paralysis (Moraud et al., 2016).

This conceptual framework implies that task-specific sensory information plays a central role in the formation of motor patterns in response to EES after SCI. However, this model has not considered the possibility that the recruitment of proprioceptive fibers during EES may interfere with the natural flow of task-specific proprioceptive information travelling along the very same fibers.

Electrical stimulation likely triggers action potentials that travel in both directions along the recruited fiber. EES would thus elicit both orthodromic action potentials that are conveyed to the spinal cord, and antidromic action potentials that travel towards sensory organs (Buonocore et al., 2008; Hunter & Ashby, 1994; Su et al., 1992). Consequently, antidromic action potentials may collide with action potentials conveying proprioceptive information, thus preventing the propagation of this information to spinal execution centers. The probability of these detrimental interactions is proportional to the stimulation frequency, the natural firing rate of sensory afferents, and the propagation time required by an action potential to travel along the entire length of the afferent fiber. These physiological parameters diverge dramatically between rats and humans. Indeed, the travelling time of action potentials along proprioceptive fibers is markedly longer in humans compared to rats. Moreover, the firing rates of proprioceptive afferents is relatively lower in humans (Prochazka, 1996). The resulting higher probability of collisions between natural and antidromic action potentials in humans may disrupt task-specific sensory information to unexpected levels. Here, we hypothesized that this phenomenon may explain the limited therapeutic efficacy of EES in paraplegic individuals compared to rats.

Using computer simulations, electrophysiological evaluations, psychophysics tests and behavioral experiments, we show that antidromic collisions abolish the natural proprioceptive information in humans, but not in rats. These detrimental effects of EES restrict the range of stimulation frequencies and amplitudes that can facilitate locomotion in humans with SCI. Computer simulations identified strategies that mitigate this issue. For example, encoding the natural proprioceptive information in the spatiotemporal structure of EES stimulation protocols may maximize the range of useful EES parameters. These results demonstrate that EES must preserve proprioception to facilitate walking in humans with SCI.

3.3 Results

3.3.1 The probability of antidromic collisions during EES is higher in humans compared to rats

We first studied the occurrence probability of antidromic collisions along proprioceptive afferent fibers when delivering continuous EES to the lumbar spinal cord. For both rats and humans, we developed computational models of proprioceptive afferent fibers that take into account the length of axons innervating proximal and distal muscles, as well as the propagation times of action potentials along these axons. We modelled realistic interactions between the natural firing along proprioceptive afferents and the action potentials elicited by EES (Fig. 3.1A). We used these computational models to calculate the probability of antidromic collisions in muscle spindle afferents as a function of EES frequency and natural firing rate.

The model indicated that the occurrence probability of antidromic collisions was extremely low in rats, regardless of the tested EES frequencies and natural firing rates of muscle spindles (Fig. 3.1B). While delivering EES at the frequency commonly used to enable locomotion in paralyzed rats (40 Hz (Courtine et al., 2009; van den Brand et al., 2012)) , this probability remained approximatively 20% across the entire range of physiological afferent firing rates.

The results of the simulations were dramatically different in humans. Due to the increase in action potential propagation times along human proprioceptive afferents, even relatively low frequencies of EES canceled the majority of the natural proprioceptive information. For distal muscles, the occurrence probability of antidromic collisions reached nearly 100% for natural afferent firing rates of 30 impulses per second with an EES frequency of 30 Hz (Fig. 3.1C). Logically, the disruption of natural proprioceptive information depends upon the distance of proprioceptive organs from the spinal cord. The occurrence probability of antidromic collisions was markedly higher along afferents innervating proprioceptors located in distal muscles compared to proximal muscles (Fig. 3.1C).

These results suggest that continuous EES may disrupt the natural proprioceptive information in humans, but not in rats. To confirm this prediction, we conducted a series of electrophysiological and psychophysical experiments.

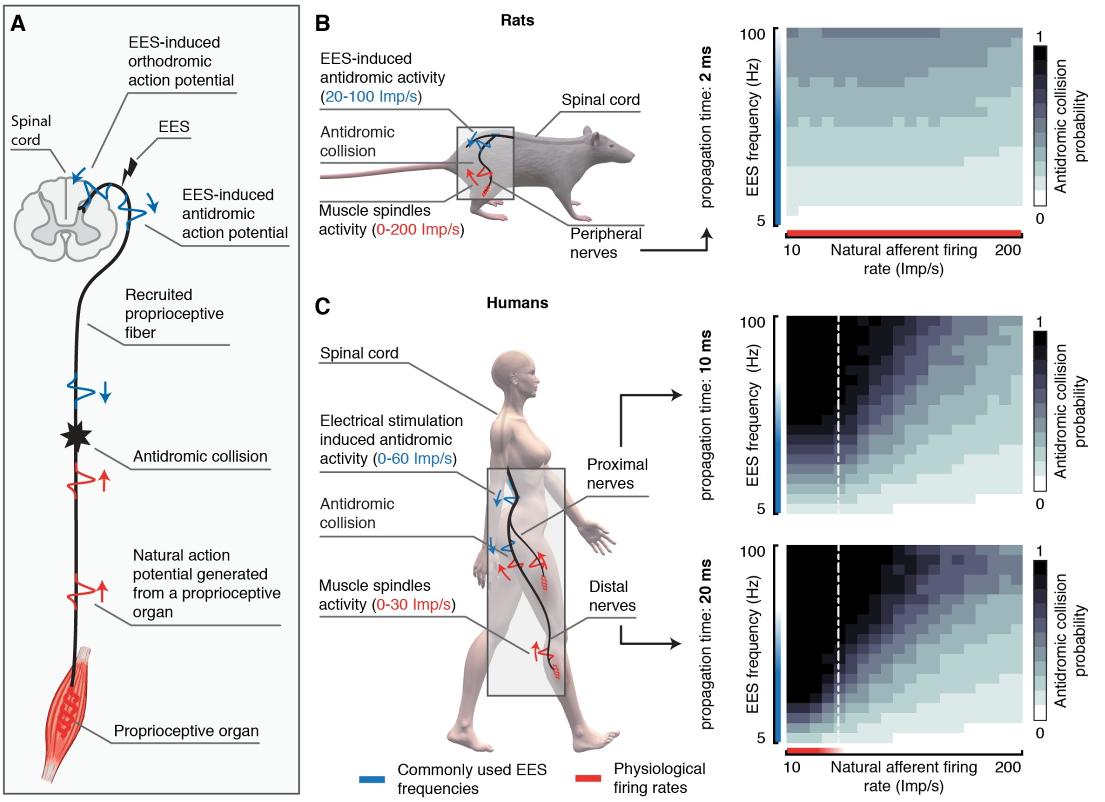

Figure 3.1: Probability of antidromic collisions during EES in rats and humans. A, Schematic illustration of antidromic collisions between EES-induced antidromic action potentials and natural action potentials traveling along the recruited proprioceptive afferent fibers. B,C, Probability for a natural action potential to collide with EES-induced antidromic action potential in the proprioceptive afferent fibers of rats (B; action potential propagation time along the entire length of the fiber: 2 ms) and in the proximal and distal proprioceptive afferent fibers of humans (C; action potential propagation time along the entire length of the fiber: 10 and 20 ms, respectively). The probability is calculated as a function of EES frequency and natural firing rate along afferent fibers. EES frequencies that are commonly used to facilitate locomotion in rats (Courtine et al., 2009; Moraud et al., 2016; van den Brand et al., 2012; Wenger et al., 2014) and humans (Angeli et al., 2014; S. Harkema et al., 2011; Huang et al., 2006; Minassian et al., 2004) are highlighted in blue. Physiological proprioceptive firing rates reported in rats (Hnk & lessler, 1973; Prochazka, 1999) and humans (Albert et al., 2006; Prochazka, 1996) are highlighted in red. Imp, impulse.

Experimental evidence 1: EES induces antidromic activity along human afferents

We first verified whether EES produces antidromic activity along the recruited afferent fibers. We conducted concurrent recordings of the proximal and distal branches of the tibial nerve (mixed nerve), the sural nerve (sensory nerve), and the soleus muscle during continuous EES of the lumbar spinal cord in two individuals with a chronic incomplete SCI (Fig. 3.2A; Subject #2 and #3 in Table 3.1).

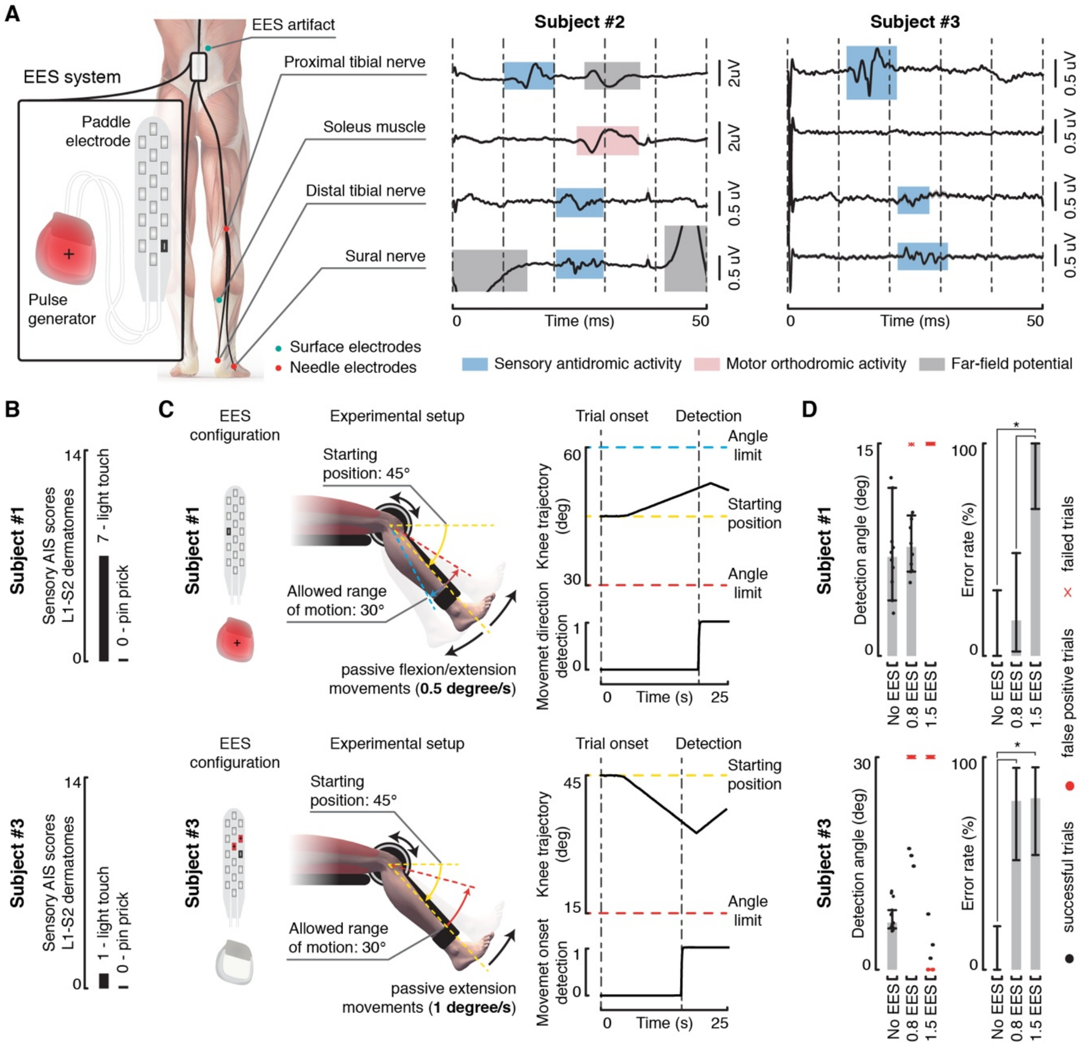

Figure 3.2: EES induces antidromic activity along proprioceptive afferents and disrupts proprioception. A, Recordings of antidromic activity from sensory nerves during EES. Needle and surface electrodes were inserted in peripheral nerves and over muscles, respectively, as depicted in the scheme. Continuous EES (20 Hz, monopolar pulses, black cathode and red anode) was delivered for approximatively one minute. Averaged evoked potentials (±SEM, n 1200) are shown for subject 1 and subject 3. Evoked potentials highlighted in blue, red and grey were respectively classified as antidromic afferent volleys, efferent orthodromic activity, and far-field potentials (e.g. electromyographic activity of nearby muscles). B, Sensory AIS scores relative to the L1-S2 dermatomes for the two subjects that performed the Threshold To Detection of Passive Movement (TTDPM) test.

Figure 3.2: (Continued) C, Setup of the TTDPM test. Randomly selected flexion or extension movements were imposed to the knee joint of subject 1 (top). A movement speed of 0.5 degree per second and a maximum allowed range of motion of 15 degrees was used. Subject 3 (bottom) was not able to perceive movement direction. Hence, only the ability to detect extension movements was assessed. A movement speed of 1 degree per second and a maximum allowed range of motion of 30 degrees was used. EES configurations used to target knee flexor and extensor muscles are reported. D, Bar plots reporting the detection angle (median ± 95% CI) and error rate (percentage correct trials ± 95% CI) on the TTDPM test performance without EES and when delivering continuous EES (50 Hz) at 0.8 and 1.5 times motor response threshold amplitudes. Black dots report the detection angle for successful trials, while red dots and red crosses indicate false positive and failure to detect movement within the allowed range of motion, respectively. The detection angle statistic (median ± 95% CI) was only computed when the subjects successfully completed 10 trials. *, $P < 0.05$, Clopper-Pearson interval.

We selected a site of EES that recruited the soleus muscle and adjusted the stimulation amplitude in order to elicit a sensation of tingling in the corresponding dermatome. EES frequency was fixed at 20 Hz. In subject #2, each pulse of EES elicited a response in the soleus muscle with a latency of 25 ms. This response has been associated with the recruitment of motoneurons through the activation of group-Ia afferents (Capogrosso et al., 2013; Hofstoetter et al., 2018; Minassian et al., 2007). Concurrently, we detected two responses in the proximal branch of the tibial nerve, with latencies of 12.5 and 26.5 ms. Only one response (latency, 21 ms) was recorded in the distal branch of this nerve (Fig. 3.2A). The responses induced in the proximal (12.5 ms) and distal (21 ms) branches of the tibial nerve (Fig. 3.2A), blue windows) likely resulted from the same neural volley propagating from the site of stimulation to the periphery. Since the responses recorded in the distal branch occurred prior to any motor response, they cannot be attributed to orthodromic efferent activity. In this scenario, the response in the distal branch of the tibial nerve should have emerged after the motor response elicited in the more proximal soleus muscle. Therefore, we conclude that these responses likely corresponded to antidromic afferent volleys resulting from the recruitment of the dorsal roots. The response with a latency of 22 ms recorded in the exclusively sensory sural nerve is also compatible with this conclusion. Indeed, due to the lack of motor fibers, the antidromic recruitment of Aβ afferents is the most probable explanation for this response. Finally, the second response recorded in the proximal branch of the tibial nerve (latency, 26.5 ms) is compatible with a far-field potential induced by the orthodromic recruitment of the soleus muscle. Similar results were achieved in subject #3. Each pulse of EES elicited a distinct response in both the proximal and distal branch of the tibial nerve (latencies, 12.5 and 22 ms respectively) and a response in the sural nerve (latency, 22.5ms). However, no motor responses were detected in the soleus muscle at this stimulation intensity.

These results support the hypothesis that EES elicits antidromic activity along both proprioceptive afferent fibers, opening the possibility that this stimulation interferes with the natural flow of sensory information in humans.

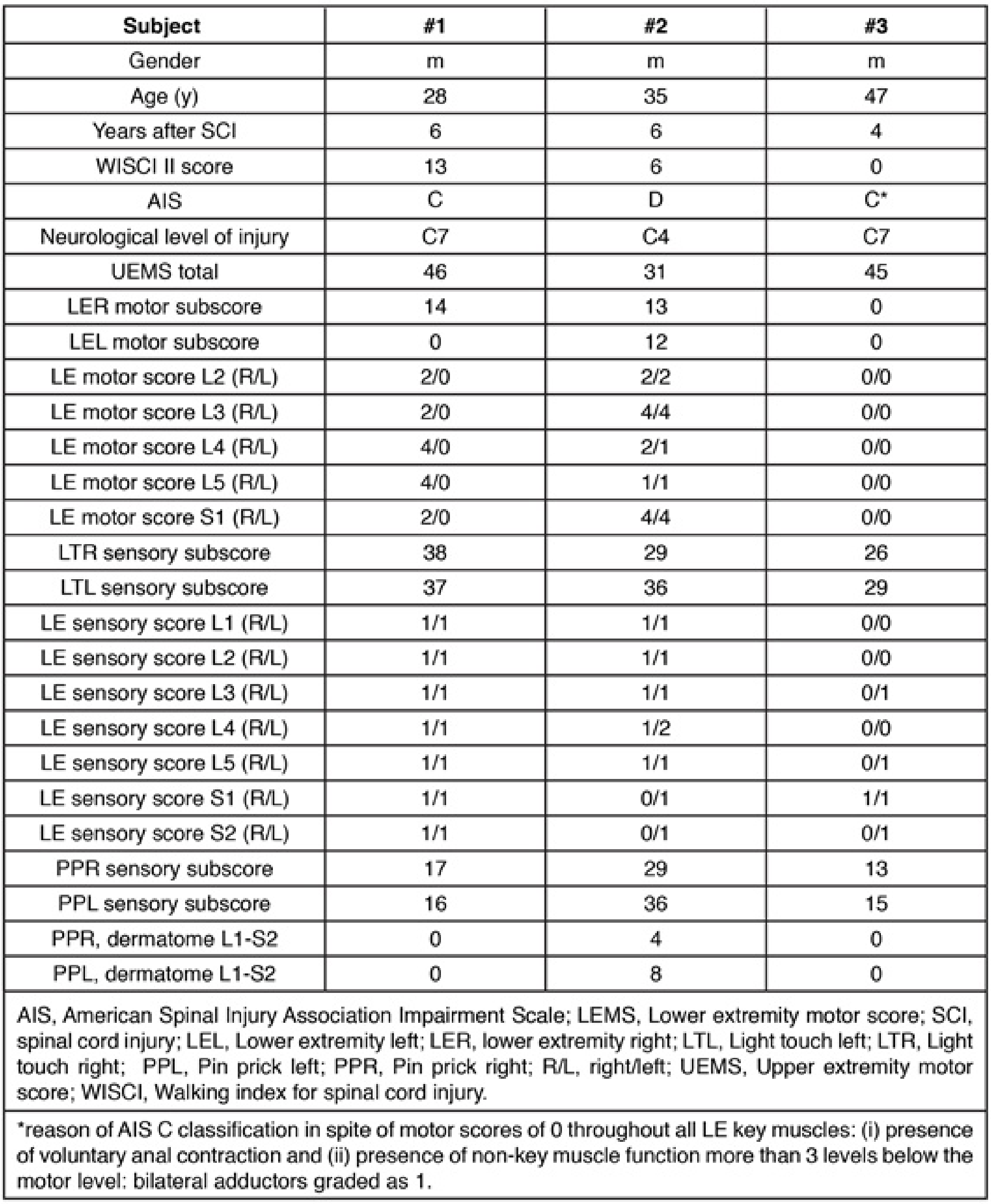

Subject	#1	#2	#3
Gender	m	m	m
Age (y)	28	35	47
Years after SCI	6	6	4
WISCI II score	13	6	0
AIS	C	D	C*
Neurological level of injury	C7	C4	C7
UEMS total	46	31	45
LER motor subscore	14	13	0
LEL motor subscore	0	12	0
LE motor score L2 (R/L)	2/0	2/2	0/0
LE motor score L3 (R/L)	2/0	4/4	0/0
LE motor score L4 (R/L)	4/0	2/1	0/0
LE motor score L5 (R/L)	4/0	1/1	0/0
LE motor score S1 (R/L)	2/0	4/4	0/0
LTR sensory subscore	38	29	26
LTL sensory subscore	37	36	29
LE sensory score L1 (R/L)	1/1	1/1	0/0
LE sensory score L2 (R/L)	1/1	1/1	0/0
LE sensory score L3 (R/L)	1/1	1/1	0/1
LE sensory score L4 (R/L)	1/1	1/2	0/0
LE sensory score L5 (R/L)	1/1	1/1	0/1
LE sensory score S1 (R/L)	1/1	0/1	1/1
LE sensory score S2 (R/L)	1/1	0/1	0/1
PPR sensory subscore	17	29	13
PPL sensory subscore	16	36	15
PPR, dermatome L1-S2	0	4	0
PPL, dermatome L1-S2	0	8	0

AIS, American Spinal Injury Association Impairment Scale; LEMS, Lower extremity motor score; SCI, spinal cord injury; LEL, Lower extremity left; LER, lower extremity right; LTL, Light touch left; LTR, Light touch right; PPL, Pin prick left; PPR, Pin prick right; R/L, right/left; UEMS, Upper extremity motor score; WISCI, Walking index for spinal cord injury.

*reason of AIS C classification in spite of motor scores of 0 throughout all LE key muscles: (i) presence of voluntary anal contraction and (ii) presence of non-key muscle function more than 3 levels below the motor level: bilateral adductors graded as 1.

Table 3.1: Subjects' data and neurological status according to the International Standards for Neurological Classification of Spinal Cord Injury.

Experimental evidence 2: EES disrupts kinesthesia in humans

Cancellation of sensory information due to antidromic collision should result in a reduced or altered conscious perception of joint position and movement velocity. We thus predicted that continuous EES would affect the perception of passive leg movements. To test this hypothesis, we exposed three individuals with a chronic incomplete SCI (Table 3.1) to a threshold to detection of passive movement (TTDPM) test (Han et al., 2016). Only subject #1 and subject #3 could complete the task without EES (Fig. 3.2B).

Participants were sitting in a robotic system that imposed a passive isokinetic leg movement at the knee from a neutral resting position (Fig. 3.2C). The participants were requested to detect the direction of the movement as soon as they were able to perceive it, but before the knee joint angle had reached a predefined amplitude. Detection angle and trials error rate were used as measurements of performance.

Without EES, subject #1 was able to detect the extension and flexion of the knee with a 100% success rate (median detection angle: 7 deg, 95% CI: 3.9-11.9 deg). Subject #3 was able to detect the onset of knee movements but failed to detect their direction. Consequently, we increased the range and speed of the movement, and limited the movement to extension. Without stimulation, subject #3 successfully detected movement onset with a 100% success rate (median detection angle: 6.7 deg, 95% CI: 5.8-8.4 deg).

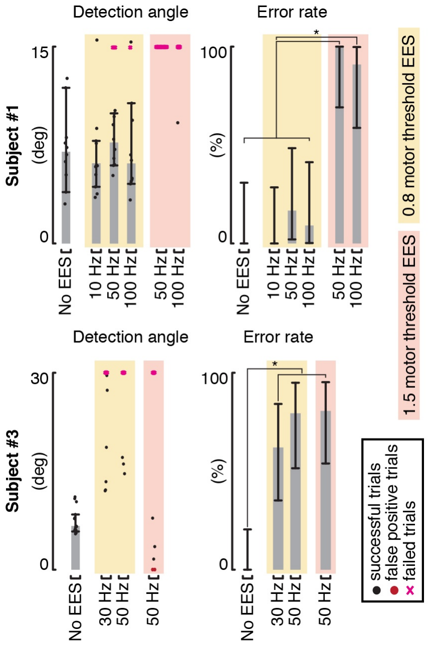

Figure 3.3: Impact of continuous EES on the threshold to detection of passive movement test performance. Bar plots reporting the detection angle (median ± 95% CI) and error rate (percentage correct trials ± 95% CI) on the TTDPM test performance without EES and when delivering continuous EES at 0.8 and 1.5 times motor response threshold amplitudes and a range of EES frequencies. Different EES frequencies were tested on subject 1 (10 Hz, 50 Hz, 100 Hz) and subject 3 (30 Hz, 50 Hz). At 1.5 motor response threshold amplitude, EES frequencies below 50 Hz induced spasms in the muscles and were thus not tested. Black dots report the detection angle for successful trials, while red dots and red crosses indicate false positive and failure to detect movement within the allowed range of motion, respectively. The detection angle statistic (median ± 95% CI) was only computed when the subjects successfully completed 10 trials. *, $P < 0.05$, Clopper-Pearson interval.

We then selected electrode configurations that targeted both extensor and flexor muscles of the knee, as verified from motor responses elicited in vastus lateralis and semitendinosus muscles. We first set the intensity that elicited a tingling sensation in the knee without producing motor responses (x 0.8 motor response threshold). At this intensity and over a broad range of frequencies, continuous EES did not alter performance of subject #1, while it disrupted the ability of subject #3 to detect movement onset (error rate higher than 60%) (Fig. 3.2D and Fig. 3.3). At higher stimulation intensities (x 1.5 motor response threshold), EES abolished the ability of both participants to carry out the experiment (error rate higher than 80%). The participants reported a complete loss of awareness about the position and movement of their leg.

These psychophysical experiments corroborate our hypothesis that continuous EES disrupts and may even block the natural proprioceptive information in humans. This disruption occurred at intensities and frequencies that are commonly used in clinical applications (Angeli et al., 2014; S. Harkema et al., 2011; Huang et al., 2006; Minassian et al., 2004).

Experimental evidence 3: continuous EES alters afferent modulation of spinal circuits in humans but not in rats

Sensory signals are known to alter the excitability of sensorimotor circuits. For example, the modulation of proprioceptive information during movement affects the amplitude of reflex responses induced by peripheral nerve stimulation (Capaday & Stein, 1986; Courtine et al., 2007; Dy et al., 2010; Knikou et al., 2008). These observations imply that the cancellation of proprioceptive information would affect the modulation of reflex responses elicited by EES. Consequently, the cancellation of proprioceptive information during EES in humans would reduce the modulation of motor responses proportionally to the intensity and frequency of stimulation in humans, but not in rats.

To test this hypothesis, we studied the modulation of reflex responses elicited by various EES frequencies (5 to 60 Hz) during passive oscillations of the ankle or knee joint. The same participants with chronic SCI were seated in a robotic system that imposed passive rhythmic extension / flexion movements of the ankle or knee at a fixed speed and amplitude (Fig. 3.4A). Simultaneously, we delivered continuous EES with electrode configurations and stimulation intensities that induced consistent reflex responses in flexor and extensor muscles of the targeted joint (Fig. 3.4A).

In all participants, the cyclic oscillations of the joint induced a significant phase-dependent modulation of the reflex responses elicited by EES in the mobilized muscles (normalized modulation depth superior to 0.3; $p < 0.05$ for every frequency; Fig. 3.4B-D). However, the amplitude of this modulation strongly depended on the frequency of stimulation. Quantification of angle-dependent motor responses revealed a pronounced monotonic decrease of the normalized modulation depth with EES frequency increments (Fig. 3.4D).

We performed the same experiments in four anesthetized rats with a chronic contusion SCI that were surgically implanted with a stimulating electrode over the lumbosacral spinal cord (Fig. 3.4E,F). As observed in humans, robot-controlled oscillations of the ankle induced a robust modulation of motor responses (normalized modulation depth superior to 0.18 ($p < 0.05$) for every frequency). However, we did not detect systematic relationships between EES frequencies and normalized modulation depth (Fig. 3.4E). Modulation of motor responses was still present at frequencies as high as 100 Hz (Fig. 3.4F). A linear fit of the median values yielded a slope close to 0 in all rats (median = 0.0003 with the 2.5^{th} and 97.5^{th} percentiles respectively of -0.0056 and 0.0015), suggesting a lack of linear dependency between modulation depth and EES frequency.

Together, these experiments provide compelling evidence that continuous EES with stimulation features typically used for facilitating movement leads to a considerable cancellation of proprioceptive information in humans, but not in rats. Moreover, this disruption alters the ability of proprioceptive information to modulate the motor output elicited by EES. These mechanisms may explain the limited therapeutic efficacy of EES in people with SCI compared to rodent models.

3.3.2 Computational models of proprioceptive feedback circuits during locomotion

To address this question, we sought to assess the impact of EES on the natural dynamics of proprioceptive feedback circuits during locomotion. Since these interactions cannot be studied in vivo, we synthetized EES properties, proprioceptive feedback circuits, and leg biomechanics into species-specific computational models (Fig. 3.5A). Specifically, we adapted a previously validated dynamic computational model (Moraud et al., 2016) to the specific anatomical features of rats and humans. The model includes the minimal proprioceptive neural network responsible for reciprocal activation of antagonist muscles (Fig. 3.5B). We steered this network with proprioceptive afferent activity. For this, we used a validated biomechanical model of the rat and human lower limbs to estimate the stretch velocity profile of ankle antagonist muscles during locomotion. We exploited this information to estimate the firing rates of proprioceptive afferent fibers through species-specific muscle spindle models (Fig. 3.5C). The model of proprioceptive afferent fibers also took into account the occurrence of orthodromic activity and antidromic collisions elicited by EES.

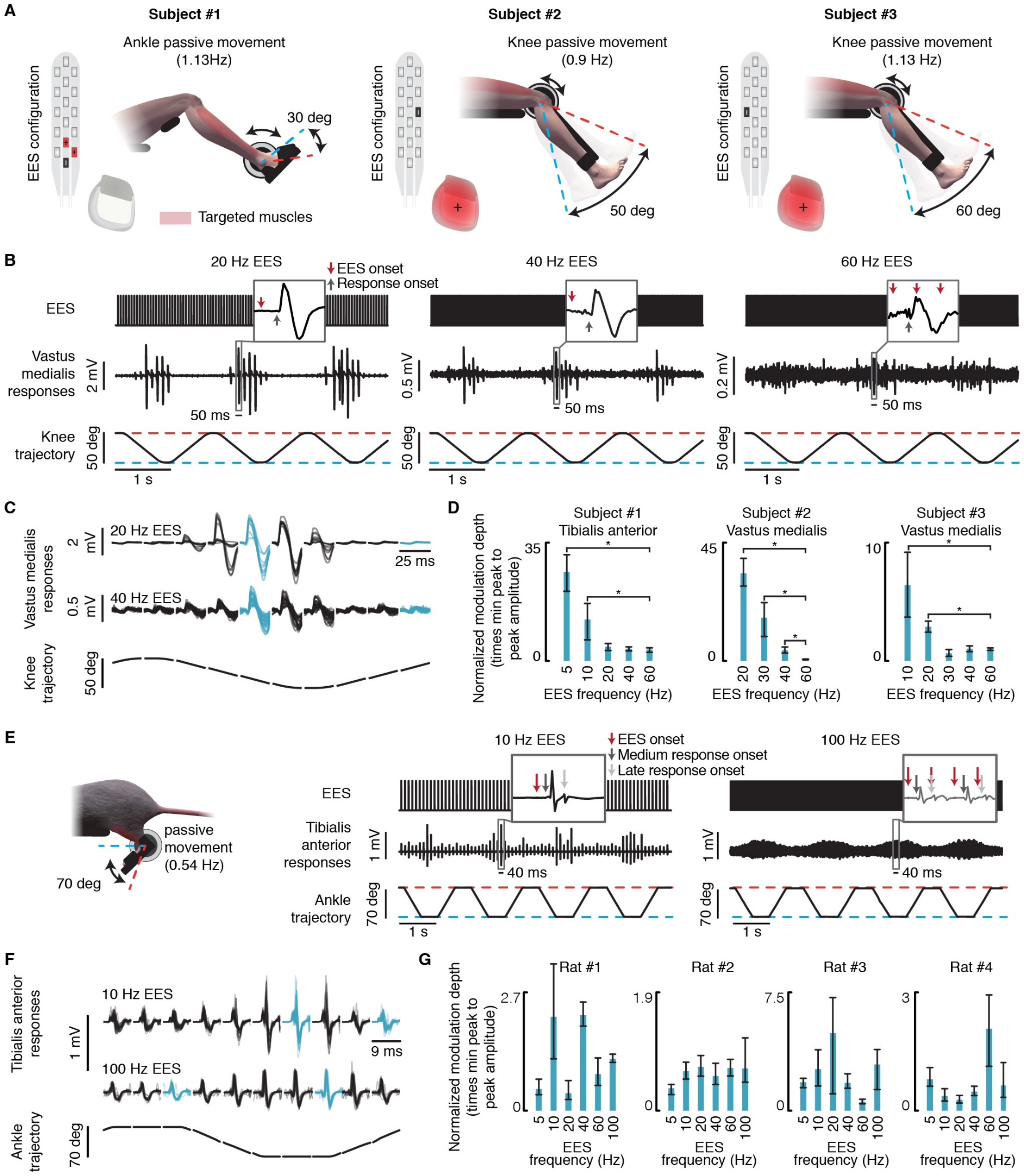

Figure 3.4: Effect of EES on the natural modulation of proprioceptive circuits during passive movements. A, Configuration of the experimental setup for humans. The subjects were secured in a robotic system that moved the ankle or knee joint passively within the reported range of motion. EES electrodes were configured to target a muscle mobilized during the selected joint movement, as highlighted in red for each subject. B, Plots showing EES pulses, EMG activity of the tibialis anterior, and changes in knee joint angle during passive oscillations of the knee for three different EES frequencies (20, 40 and 60 Hz) in subject 2. The rectangular windows highlight muscle responses induced by a single pulse of EES. Red and grey arrows depict the onset of the stimulation pulse and of the muscle response, respectively.

Figure 3.4: (Continued) C, The cycle of joint oscillation was divided into 10 bins of equal durations during which muscle responses were extracted and regrouped. Superimposed muscle responses are displayed for each bin for two EES frequencies (subject 2). Muscle responses used to compute the normalized modulation depth are depicted in light blue. D, Bar plots reporting the median and 95% CI of the normalized modulation depth, for every EES condition tested and for the different subjects. Low frequencies of stimulation often induced spasms in the muscles. Consequently, subjects 2 and 3 could not be tested with EES frequencies below 20 and 10 Hz, respectively. *, $P < 0.05$, bootstrap. E-G, Configuration of the experimental setup for rats with severe contusion SCI (250 kdyn).) and results following the same conventions as in (B-D) for humans.

We first studied the impact of EES amplitude and frequency on the activity of proprioceptive afferent activity during locomotion. To model increments in EES amplitude and frequency, we scaled up the number of recruited afferent fibers and the rates of both orthodromic and antidromic induced activities, respectively. In rats, EES did not alter the modulation depth of proprioceptive information. The percentage of antidromic collisions remained low across a broad range of amplitude and frequency (Fig. 3.5D). In striking contrast, the same parameters of EES dramatically disrupted the modulation of proprioceptive information in humans. Increase in stimulation frequency augmented the firing rate of the recruited fibers. With frequencies as low as 40 Hz, antidromic action potentials abolished the sensory information conveyed by each of the electrically stimulated fibers. The residual modulation of proprioceptive information solely resulted from the activity of non-recruited afferent fibers. Because increase in stimulation amplitude led to a higher number of recruited fibers, the percentage of erased proprioceptive information scaled up proportionally (Fig. 3.5D).

We then evaluated the impact of this cancellation on the ability of EES to steer the reciprocal activation of motoneurons innervating antagonist muscles during locomotion. Continuous EES delivered excitation to Ia-inhibitory interneurons and motoneurons. In rats, the modulation of Ia-inhibitory interneurons driven by the natural proprioceptive information led to a reciprocal activation of antagonist motoneurons that was coherent with the stance and swing phases of gait (Fig. 3.6A). As expected, increase in stimulation frequency or amplitude scaled up the firing rates of motoneurons. This increase was restricted to the phase of gait during which each pool of motoneurons was active.

The occurrence of antidromic collisions in the human model dramatically disrupted the dynamics of the neural network (Fig. 3.6B). At low frequency and low amplitude, EES steered the reciprocal activation of antagonist motoneurons, as observed in rats. With higher stimulation parameters, the cancellation of proprioceptive information prevented phase-dependent modulation of Ia-inhibitory interneurons. The resulting unbalance between antagonist pools of Ia-inhibitory interneurons led to a profound asymmetry in the excitatory drive delivered to motoneurons. Concretely, one of the motor pools became over active while the antagonist one received strong inhibition (Fig. 3.6B).

These results suggest that only a narrow range of EES parameters could be exploited to enhance the excitability of the human spinal cord after SCI without compromising the critical role of proprioceptive information in the production of locomotion.

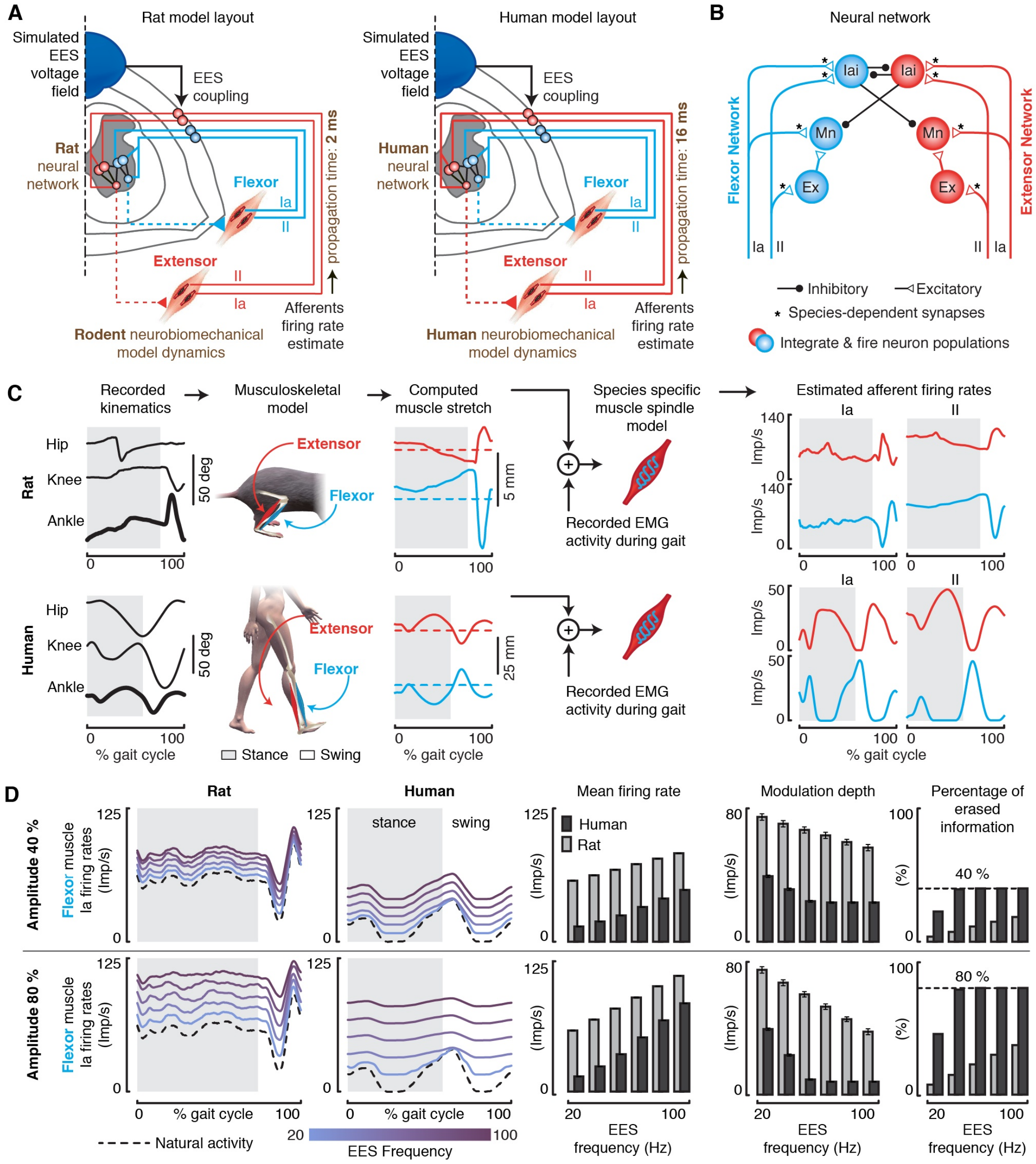

Figure 3.5: Impact of continuous EES on proprioceptive afferent firings during locomotion in rats and humans. A, Layout of the computational models built for rats and humans. The components highlighted in brown are tuned to match the anatomical and physiological features of rats versus humans. B, Spiking neural network model of muscle spindle feedback circuits for a pair of antagonist muscles. Mn, motoneuron. Ex, excitatory interneurons. Iai, Ia-inhibitory interneurons. The synapses highlighted with an asterisk (*) are tuned to match the known properties of humans and rats.

Figure 3.5: (Continued) C, Estimated stretch profiles and afferent firing rates of ankle flexor and extensor muscles over an entire gait cycle in rats (top) and humans (bottom). D, Impact of EES on the natural firing rate profiles of group-Ia afferents innervating a flexor muscle of the ankle during locomotion in rats (left) and humans (right). From left to right: averaged firing rate profiles of the simulated population of afferent fibers over one gait cycle, mean afferent firing rate (± SEM, n = 10 gait cycles), modulation depth of afferents firing rate profiles (mean ± SEM, n=10 gait cycles), and total amount of sensory information erased by EES. Results are reported over a range of EES frequencies. Top and bottom panels reports the results for EES amplitudes recruiting 40% (top) or 80% (bottom) of the entire population of modelled group-Ia afferents.

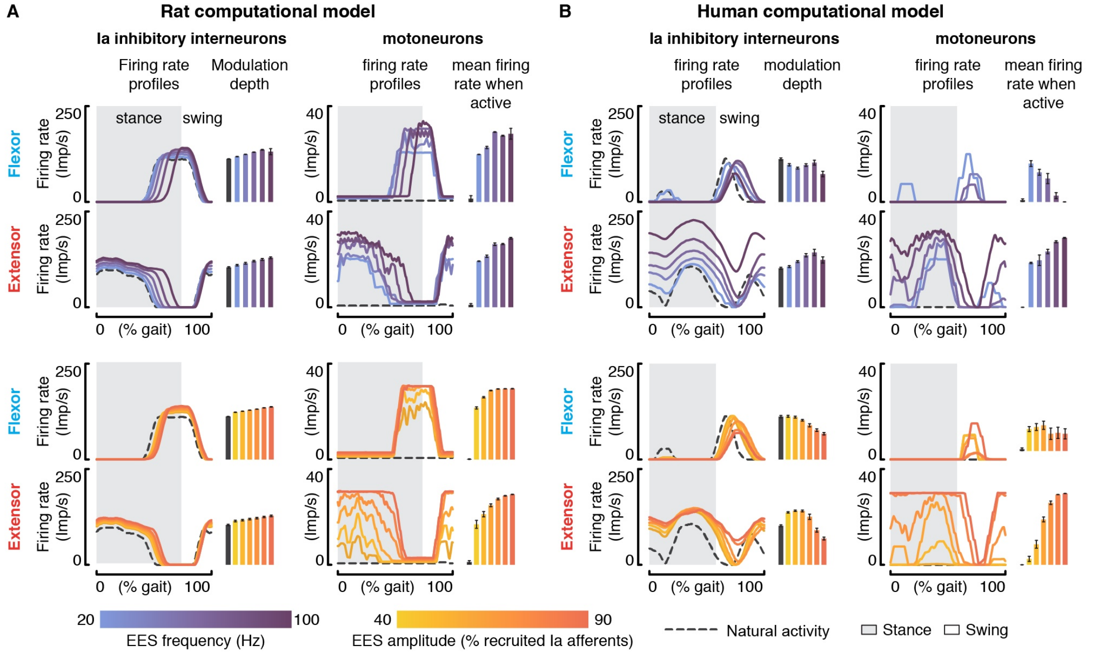

Figure 3.6: Interactions between EES and muscle spindle feedback circuits during locomotion in rats and humans. A,B, Impact of EES on the natural activity of Ia-inhibitory interneurons and on the activation of motoneurons during locomotion in rats and humans. Left, average firing rate profiles and modulation depth of the Ia-inhibitory interneuron populations embedded in the flexor or the extensor neural network (mean ± SEM., n = 10 gait cycles). Right, average firing rate profiles and mean firing rate during the active phase for motoneurons embedded in the flexor or the extensor neural network (mean ± SEM., n = 10 gait cycles. The impact of EES frequencies and amplitudes are reported in the top and bottom panels, respectively. EES amplitude was set to a value recruiting 60% of the modelled Ia afferents when EES frequency was modulated, while EES frequency was set to 60 Hz when the amplitude was modulated.

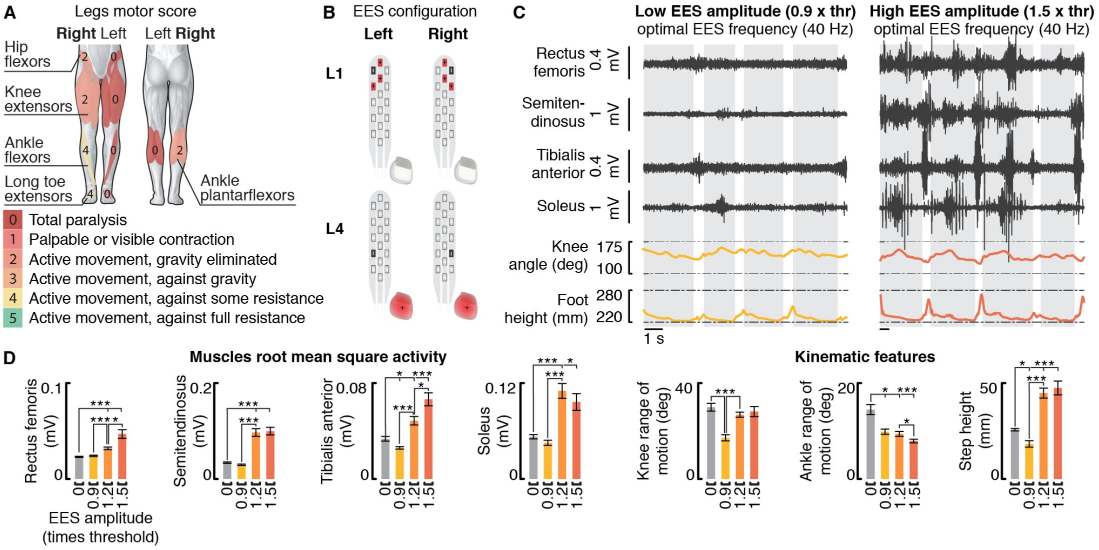

Figure 3.7: Impact of EES amplitude on muscle activity and leg kinematics during locomotion on a treadmill — Subject 1. A, AIS leg motor score. B, Configuration of electrodes targeting the left and right posterior roots projecting to the L1 and L4 segments. Continuous EES was delivered through these electrodes to facilitate locomotion. C, EMG activity of flexor (semitendinosus/tibialis anterior) and extensor (rectus femoris/soleus) muscles spanning the right knee and ankle joints, together with the changes in the knee ankle and foot height trajectories over four gait cycles without EES and with EES delivered at 0.9, 1.2 and 1.5 motor response threshold amplitude. EES frequency was set to 40Hz. D, Bar plots reporting the averaged root mean square activity of the recorded muscles, the averaged range of motion of the knee and ankle angles, and the average step height (mean ± SEM). *, $P < 0.05$, ***, $P < 0.001$, Wilcoxon rank-sum test.

3.3.3 The range of EES parameters facilitating locomotion is limited in humans compared to rats

We then evaluated the impact of tuning EES frequency and amplitude on the modulation of leg muscle activity during locomotion in rats and humans.

We tested rats with clinically relevant contusion of the mid-thoracic spinal cord (250 kdyn) that were implanted with a pair of stimulating electrodes over L2 and L4 spinal segments (n = 4 rats). Rats were positioned bipedally in robotic bodyweight support system over a treadmill (Fig. 3.8A). Continuous EES (40 Hz) delivered through both electrodes induced a robust facilitation of leg muscle activity without disrupting the alternation between antagonist muscles. As previously reported (Moraud et al., 2016; Wenger et al., 2016; Wenger et al., 2014), increase in EES frequency (20-80 Hz) led to a linear modulation of leg muscle activity, which resulted in a graded tuning of kinematic features such as the step height (Fig. 3.8B,C).

The three participants with SCI were provided with a gravity-assist (Mignardot et al., 2017) that delivered personalized upward and forward forces to the trunk in order to facilitate walking over a treadmill (Fig. 3.8D). With the help of the handlebars located on each side of the treadmill, subject #1 (60 % body weight support) and subject #2 (70 % body weight support) were able to produce alternating activation of antagonist leg muscles without EES. However, this muscle activity did not translate into functional movements, as both feet essentially dragged along the treadmill belt while the amplitude of leg movements remained limited. The delivery of continuous EES through manually-optimized electrode configurations (large electrical fields) and parameters (40 Hz, 3 to 9 mA) facilitated leg muscle activity and kinematic features (Fig. 3.8E,F and Fig. 3.7 and Fig. 3.9). Contrary to rats, however, the extent of this facilitation was insufficient to enable coordinated, weight-bearing locomotion. Subject #3 exhibited flaccid paralysis of all leg muscles in both legs. In this participant, continuous EES failed to produce consistent modulation of leg muscle activity (Fig. 3.10). All participants reported a complete loss of limb position awareness during EES, which affected their ability to coordinate the timing of their locomotor movements.

Consequently, we explored the possibility to augment the motor output with modulation of EES frequency or amplitude. From optimal EES parameters, increase in frequency or in amplitude did not translate into improved facilitation of walking. Typically, the amplitude of EMG activity scaled up in flexor muscles, but this increase was associated with a concomitant decrease in extensor muscles, even leading to a complete suppression of extensor muscle activity in some instances (Fig. 3.8E,F and Fig. 3.7 and Fig. 3.9). Moreover, the modulation of EES parameters led to a co-activation of antagonist muscles, with the occurrence of abnormal bursting activity in flexor muscles during the stance phase of gait. These experimental results are consistent with the predictions of our simulations, suggesting that only a narrow range of EES parameters can facilitate muscle activity without disrupting the natural modulation of reciprocal inhibitory networks due to the antidromic cancellation of proprioceptive feedback information.

These results confirm the predictions of the simulations, showing the limited efficacy of continuous EES for facilitating locomotion in humans with SCI compared to rats and thus providing a plausible explanation for this inter-species difference.

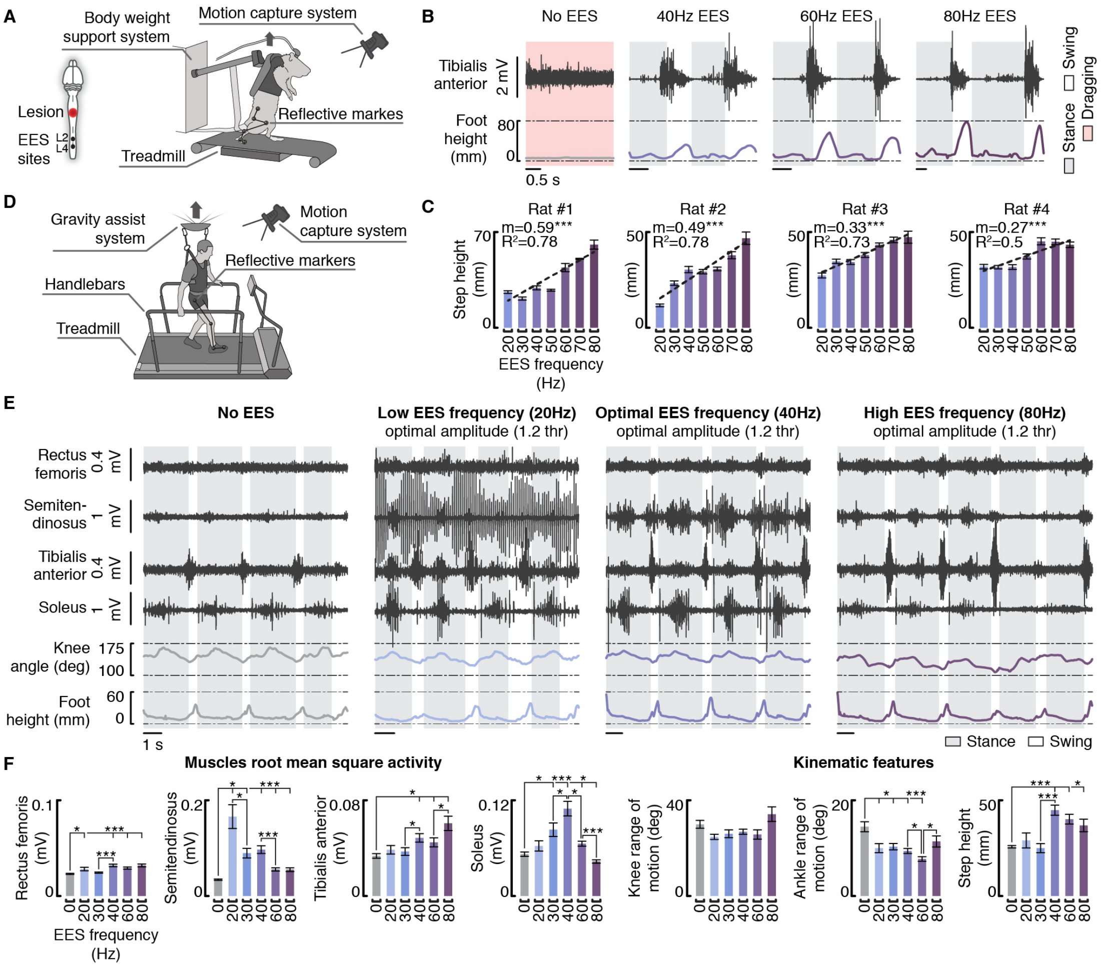

Figure 3.8: Impact of EES frequencies on muscle activity and leg kinematics during locomotion in rats and humans. A, Experimental setup in rats. Rats with a severe contusion SCI were positioned a robotic body weight support system located above a treadmill. Continuous EES was applied over L4 and L2 segments through chronically implanted electrodes secured over the midline of the dorsal spinal cord. B, EMG activity of the tibialis anterior muscle and foot height trajectory over two gait cycles without EES and with EES delivered at 40 Hz, 60 Hz and 80 Hz. C, Bar plots reporting the mean step height (± SEM) for the different tested EES frequencies. Dashed lines report the linear regression between the EES frequency and the step height. Slope (m) and R2 are reported. ***, $P < 0.001$ t-test slope > 0. D, Experimental setup in humans. Subjects were positioned in a robotic support system that provided personalized forward and upward forces to the trunk. Subjects were asked to step on the treadmill while holding the handlebars, since they were not able to step independently with the hands free. E, EMG activity of flexor (semitendinosus/tibialis anterior) and extensor (rectus femoris/soleus) muscles spanning the right knee and ankle joints, together with the changes in the knee ankle and foot height trajectories over four gait cycles without EES and with EES delivered at 20 Hz, 40 Hz and 80 Hz in subject 1. EES amplitude was set to 1.2 times the motor response threshold. Notice the opposite modulation of EMG activity in extensor and flexor muscles with increase in frequencies together with the co-activation of flexor muscles with extensor muscles.

Figure 3.8: (Continued) F, Bar plots reporting the averaged root mean square activity of the recorded muscles, the averaged range of motion of the knee and ankle angles, and the average step height (mean ± SEM) for subject 1. *, P < 0.05, ***, P < 0.001, Wilcoxon rank-sum test. The same results are reported for subjects 2 and 3 in Fig. 3.9 and 3.10.

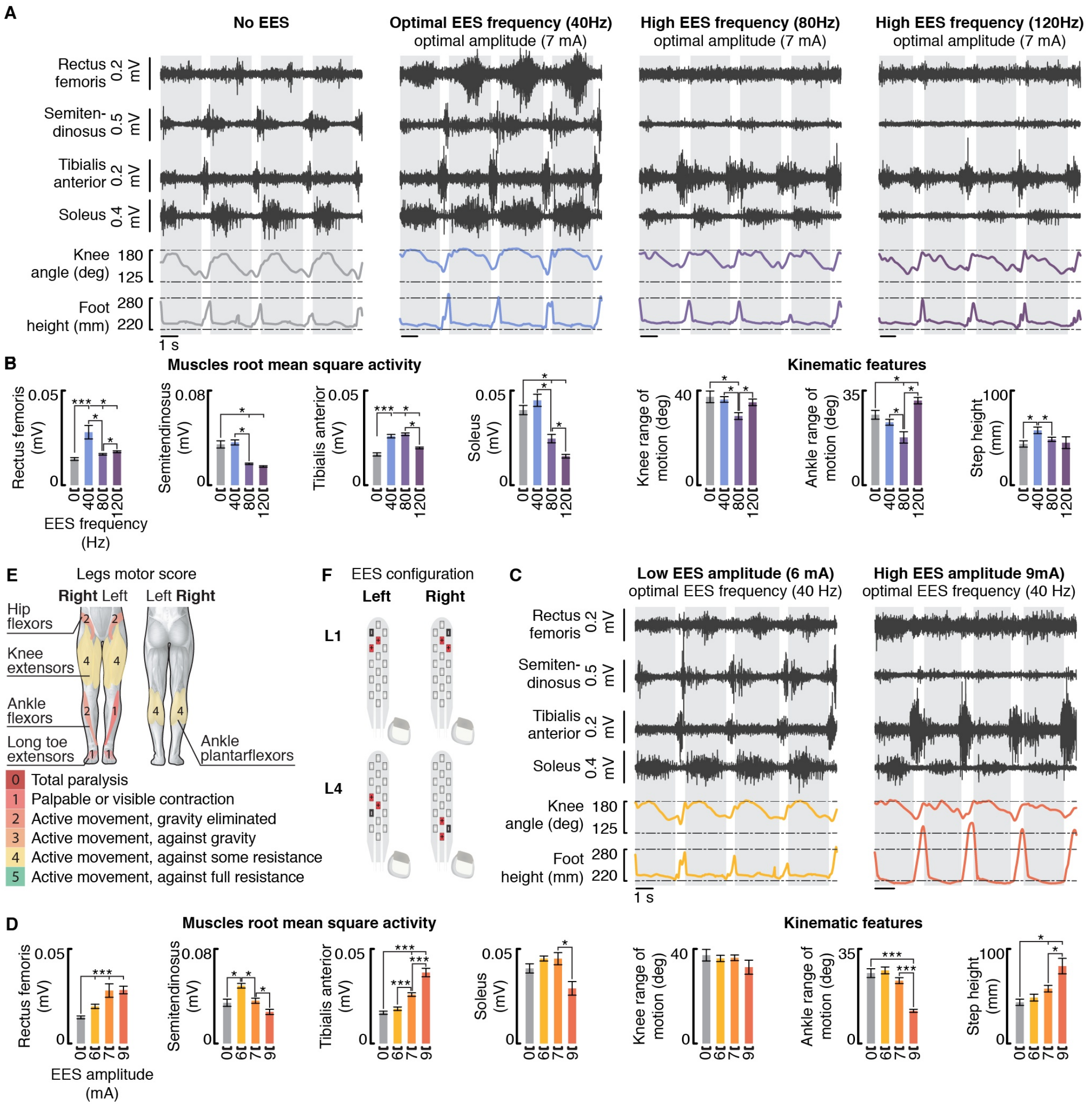

Figure 3.9: Impact of EES frequency and amplitude on muscle activity and leg kinematics during locomotion on a treadmill — Subject 2. The results displayed in Fig. 3.8 and Fig. 3.10 for subject 1 are reported for subject 2 using the same conventions.

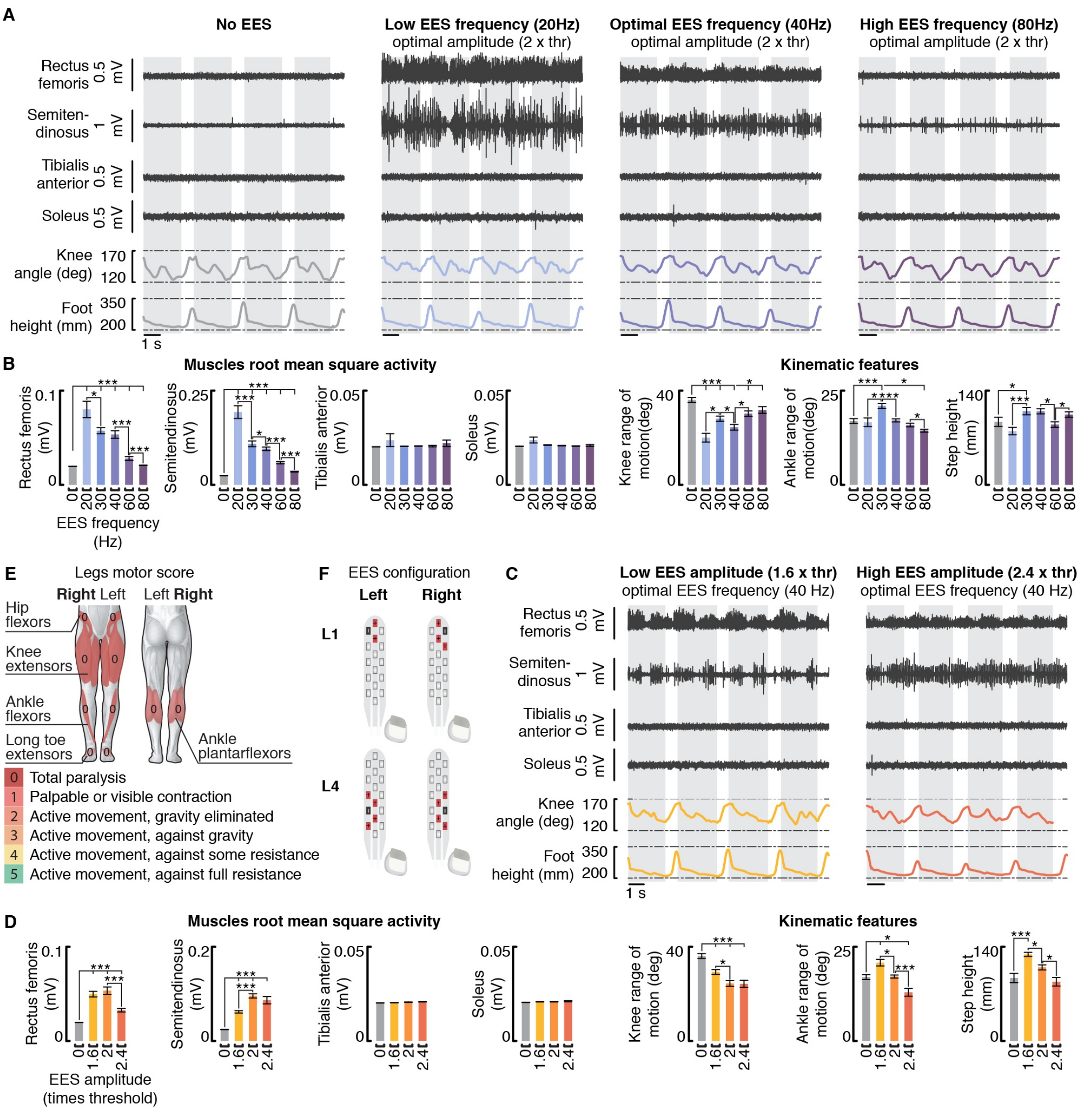

Figure 3.10: Impact of EES frequency and amplitude on muscle activity and leg kinematics during locomotion on a treadmill — Subject 3. The results displayed in Fig. 3.8 and Fig. 3.9 for subject 1 are reported for subject 3 using the same conventions.

3.3.4 Spatiotemporal EES protocols may remedy the limitations of continuous EES

We next sought to exploit our computational model to identify stimulation strategies that may remedy the disruption of reciprocal inhibitory networks observed during continuous EES. We reasoned that, to avoid this disruption, the temporal and spatial structure of the stimulation should encode the profile of proprioceptive feedback information. Specifically, we surmised that the amplitude / frequency of the stimulation targeting a specific muscle should be proportional to the instantaneous firing rate of the proprioceptive afferents originating from the sensory organs located in this muscle. Due to the continuous match between the proprioceptive afferent activity and the stimulation profile, EES would augment the overall excitation delivered to the targeted motor pool without compromising the information conveyed by the proprioceptive afferents. Targeting antagonist motor pools with their specific stimulation profile would contribute to maintaining the modulation of reciprocal inhibitory networks that is necessary to facilitate walking with EES. In turn, we hypothesized that the degree of excitation delivered to motor pools could then be controlled by scaling the range of EES amplitudes and frequencies used to configure the stimulation profiles.

We implemented this stimulation strategy in the human dynamic computational model. The spatiotemporal profile of the stimulation delivered to motor pools innervating flexor and extensor muscles of the ankle followed the natural modulation of their respective primary and secondary proprioceptive afferents (Fig. 3.11A,B). We did not explicitly model Golgi tendon organs, although Ib-afferents are also recruited with EES. Previous studies reported close correlations between the firing of Ib-afferents and the activity of the homonymous muscle (Prochazka, 1999). We thus used the EMG envelope as a surrogate for the firing profile of Ib-afferents.

Simulations revealed that this stimulation strategy erased the natural proprioceptive information to a similar extent as continuous stimulation (Fig. 3.11C). Due to the continuous match between the natural proprioception and stimulation profile, however, the proprioceptive signals reaching the spinal cord contained the same amount of information. While the percentage of erased information steadily increased with the stimulation amplitude (Fig. 3.11C), the depth of proprioceptive afferent modulation remained preserved, or even increased for higher stimulation amplitudes. Consequently, the stimulation artificially drove the reciprocal modulation of Ia-inhibitory interneurons, as would the natural proprioception during walking (Fig. 3.11C). Scaling up the range of EES amplitudes with this stimulation strategy proportionally augmented the mean firing rates of proprioceptive afferents, which led to a linear increase in the excitation delivered to motoneurons. Since this excitation was restricted to the active phase of each motoneuron pool, increasing the amplitude or frequency of EES enabled a graded modulation of the firing rate of both extensor and flexor motoneurons (Fig. 3.11C). These results suggest that encoding the profile of proprioceptive afferent activity into the spatiotemporal structure of EES protocols may expand and refine the control over the amplitude of motoneuron activity while also reinforcing the modulation of reciprocal inhibitory networks, thereby enhancing the facilitation of walking compared to continuous EES.

3.3.5 High frequency, low amplitude EES alleviates the disruptive effects of continuous EES

Reproducing the profile of proprioceptive afferent activity may prove difficult in clinical settings. We thus explored whether alternative strategies based on continuous EES could alleviate the cancellation of proprioception with EES.

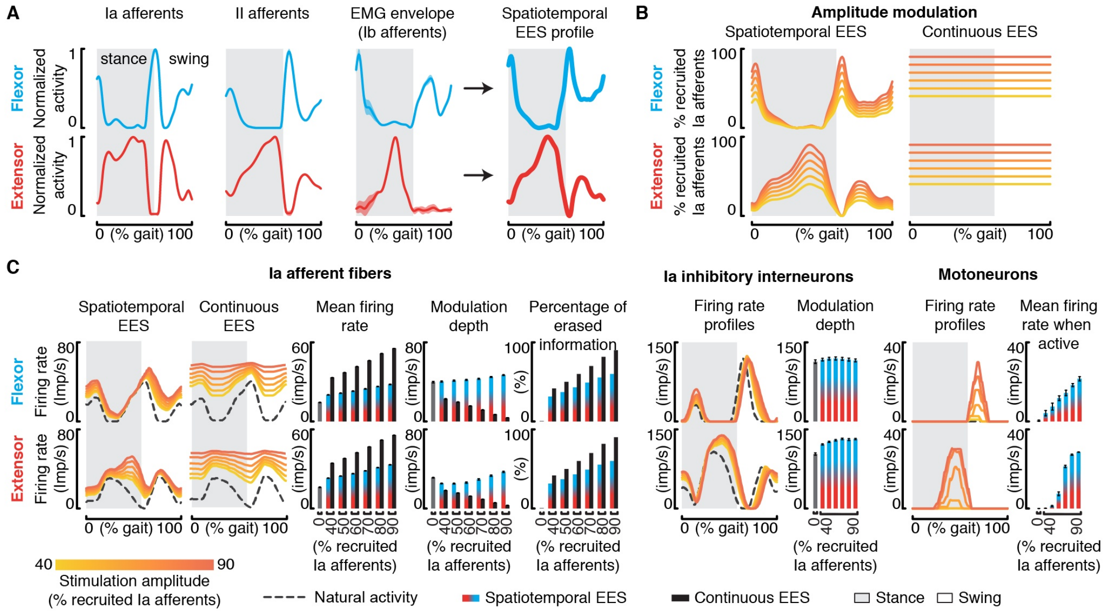

Figure 3.11: Spatiotemporal EES protocols encoding proprioceptive sensory information. A, Estimation of spatiotemporal stimulation profiles that match the natural flow of proprioceptive information generated from flexor and extensor muscles of the ankle during gait. From left to right: estimated averaged firing rate profiles of group-Ia, group-II and group-Ib (equivalent to the muscle activity) afferents over a gait cycle, and the sum of these profiles that yielded the estimated stimulation profiles. B, Percentage of primary afferents that are recruited when applying the estimated spatiotemporal stimulation profile and during continuous stimulation. C, Impact of the estimated spatiotemporal stimulation profile on the modulation of muscle spindle feedback circuits from flexor and extensor muscles, including from left to right: group-Ia afferents firings, bar plots reporting the averaged mean firing rate and modulation depth of primary afferents (mean ± SEM., n = 10 gait cycles), overall percentage of sensory information erased by EES, modulation of Ia-inhibitory interneurons, and motoneuron activity. For comparison, the impact of continuous EES on the group-Ia afferent firings is also reported. Results of simulations are shown for a range of EES amplitudes. Conventions are the same as in Fig. 3.6.

We sought to design a stimulation strategy that minimizes the amount of erased proprioceptive information during continuous EES while providing high excitation to motoneurons. Each Ia-afferent synapses onto every single motoneuron that innervates the homonymous muscle (Mendell & Henneman, 1971; Segev et al., 1990). Moreover, electrophysiological studies showed that high-frequency stimulation of nerve afferents leads to a temporal summation of Excitatory Post-Synaptic Potentials (EPSP) delivered to the targeted cell (Bawa & Chalmers, 2008; Collins et al., 1984; Koerber & Mendell, 1991). Therefore, the recruitment of a limited number of Ia-afferents with a stimulation burst of low amplitude but high frequency could theoretically deliver the same excitation to motoneurons that the recruitment of a large number of Ia-afferents with single pulses of high amplitude. We thus hypothesized that each pulse of EES could be replaced by a high-frequency / low amplitude burst of EES that would provide the same overall excitation to motoneurons while reducing the amount of erased proprioceptive information due to the limited number of recruited afferent fibers. In turn, the excitation delivered to motor pools could then be controlled by adjusting the frequency between each burst of EES.

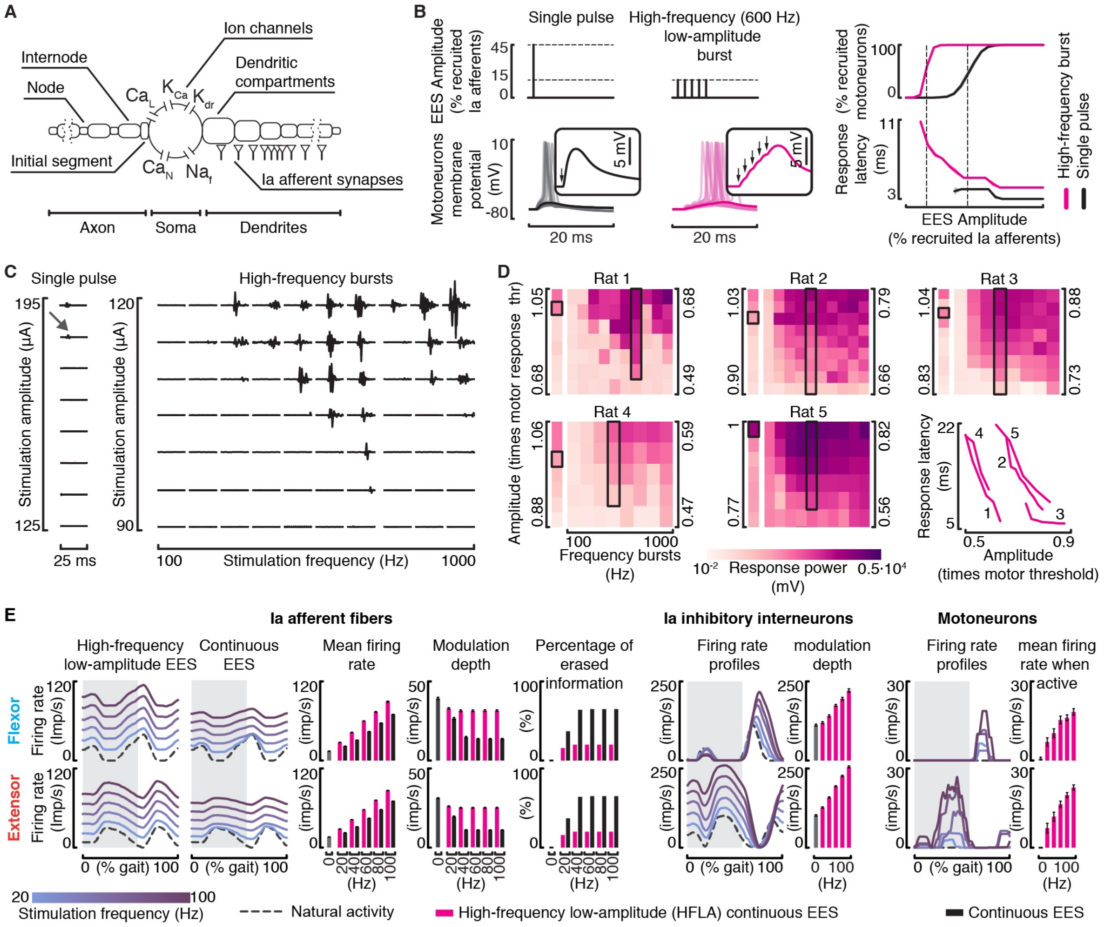

Figure 3.12: High-frequency low-amplitude EES protocols preserve proprioceptive information. A, Realistic models of alpha motoneurons and of the strength and distribution of group-Ia synaptic contacts. B, Simulations showing the response of motoneurons to a singe pulse of EES at an amplitude recruiting 45% of the afferent population, and to a high-frequency bursts (5 pulses, 600 Hz) at an amplitude recruiting 15% of the afferent population. Windows show a zoomed view of the motoneuron membrane potential depolarizations in response to the pulses of EES (arrows). Right: plots showing the percentage of recruited motoneurons and the average (mean ± SEM) latency before the onset of an action potential.

Figure 3.12: (Continued) C, Responses recorded from the tibialis anterior muscle following a single pulse of EES (left) and high-frequency bursts of EES (right) applied to the lumbar (L2) spinal cord of rats with severe contusion SCI over a range of amplitudes and burst frequencies. The grey arrow indicates the responses induced by a single pulse of EES at the motor response threshold amplitude, emphasizing the need to deliver high amplitudes to elicit responses with single pulses compared to high-frequency bursts. D, Heatmaps representing the power of the motor response to single pulses (column on the left) and high-frequency bursts (matrix on the right) of EES over a range of EES amplitudes and bursts frequencies, for 5 rats. EES amplitude is reported as a multiple of motor response threshold, amplitude corresponding to the response highlighted by the black box. The highlighted column corresponds to the bursts with a frequency inducing the largest motor responses. Right, latencies of motor responses elicited by EES bursts with the frequency highlighted in the black boxes, at increasing amplitudes. E, Impact of continuous high-frequency low-amplitude EES protocols (600 Hz, 20% recruited afferents) on the modulation of the muscle spindle feedback circuits, following the same conventions as in Fig. 3.6. For comparison, the impact of continuous EES on the group-Ia afferent firings is also reported.

We tested the hypotheses underlying this stimulation strategy using computer simulations with realistic motoneuron models and realistic distribution of Ia-afferent synaptic contacts (Fig. 3.12A). As predicted, the temporal summation of EPSPs elicited by high frequency / low amplitude bursts of stimulation enabled recruiting the same number of motoneurons as single pulses of high amplitude EES (Fig. 3.12B).

To validate these results experimentally, we conducted electrophysiological experiments in four rats. Fig. 3.12C shows representative motor responses recorded in the tibialis anterior when delivering single pulses of EES and single bursts of EES (25 ms duration with frequencies ranging from 100 to 1000 Hz) at increasing amplitudes. Compared to single pulses, high-frequency burst stimulation decreased the threshold to elicit a motor response by 39.8% (SEM: ± 4.4%). The largest reductions were obtained towards 500 Hz (SEM: ± 54.8 Hz). For a given frequency, a decrease in burst amplitude led to an increase in the latency of motor responses, suggesting that a higher number of pulses was necessary to recruit motoneurons through the temporal summation of EPSPs (Fig. 3.12D).

We finally implemented this stimulation strategy into our human computational model. In the simulation, we delivered EES bursts consisting of 5 pulses at 500 Hz with a stimulation amplitude recruiting 25% of all primary afferent fibers. Compared to continuous EES, this stimulation reduced the amount of erased proprioceptive information (Fig. 3.12E). Decreasing the duration between each EES burst led to a proportional increase in the excitability delivered to motoneurons.

These computational and experimental results suggest that high frequency / low amplitude stimulation protocols may alleviate the detrimental impact of continuous EES on the modulation of proprioceptive feedback circuits in humans.

3.4 Discussion

Our results show that EES erases proprioceptive information in humans. Computer simulations suggest that this cancellation of proprioceptive information disrupts the natural activity of reciprocal inhibitory networks that are essential to produce alternating recruitment of antagonist motor pools during locomotion. Consequently, only a narrow range of EES parameters can facilitate walking in people with SCI, which is insufficient to mediate clinically meaningful improvements of locomotion without rehabilitation. Computer simulations guided the design of EES protocols that not only preserve proprioceptive information but also enable a robust control over motoneuron activity. Here, we discuss the significance of these results, stress the dramatic consequences of the transient proprioceptive deafferentation during EES, and envision the avenues for translating these new stimulation protocols into clinical settings.

3.4.1 EES erases proprioceptive information in humans, but not in rats

Mounting evidence indicates that EES primarily recruits the large afferent fibers at their entrance in the spinal cord through the posterior roots (Capogrosso et al., 2013; Y. P. Gerasimenko et al., 2006; Hofstoetter et al., 2018; Hofstoetter et al., 2015; Ladenbauer et al., 2010; Rattay et al., 2000). These afferent fibers mainly innervate proprioceptive organs, which sense changes in muscle length and tension, and to a lesser extent, mechanoreceptors within the skin. EES elicits orthodromic action potentials along the recruited afferent fibers that mediate the therapeutic effects of the stimulation through the modulation of proprioceptive feedback circuits (Moraud et al., 2016). However, we show that EES also induces antidromic action potentials that travel in the opposite direction. Indeed, recordings of peripheral nerve activity identified antidromic volleys propagating toward sensory organs in response to EES in humans. Previous studies documented the presence of antidromic action potentials traveling along the sensory fibers of the sciatic, peroneal and sural nerves in rats, dogs, nonhuman primates and humans in response to EES applied to thoracic segments (Buonocore et al., 2008; Hunter & Ashby, 1994; Su et al., 1992). Here, we establish the high occurrence of antidromic action potentials when EES targets the posterior roots of lumbar segments.

We reasoned that EES-induced antidromic action potentials may collide with the action potentials conveying the natural proprioceptive information. The annihilation of action potentials following these collisions is due to the refractory period of Ranvier's nodes. Computer simulations predicted a high occurrence probability of these collisions along the recruited afferent fibers when EES is delivered at frequencies commonly used to facilitate movements after SCI. Due to the increased propagation time of action potentials along proprioceptive afferent fibers in humans, the incidence of these collisions is considerably higher than in rats. These results suggested that EES may partially cancel the natural proprioceptive information in humans.

To assess this possibility, we conducted experiments that highlighted the dramatic consequences of these collisions on the integration of proprioceptive information in the brain and spinal cord of humans with SCI. First, we found that the delivery of continuous EES abolishes the conscious perception of joint position and displacement. Second, we showed that proprioceptive information drives the modulation of spinal circuits during movement, and consequently, that the cancellation of proprioceptive information during continuous EES disrupts this modulation.

During the past two decades, numerous studies applied EES to the human spinal cord for improving motor functions after SCI (Angeli et al., 2014; Carhart et al., 2004; Grahn et al., 2017; S. Harkema et al., 2011; Herman et al., 2002; Huang et al., 2006; Minassian et al., 2004). The vast majority of the involved participants exhibited no or limited sensations in the legs, which may explain why this unexpected cancellation of proprioception information remained unnoticed. However, this phenomenon has far-reaching implications for the development of a therapy based on EES. Indeed, this transient proprioceptive deafferentation not only alters the conscious control of movement and the modulation of spinal circuits with EES, but may also compromise the reorganization of residual descending pathways during rehabilitation enabled by EES, as we discuss below.

3.4.2 Proprioceptive information must be preserved to enable locomotion with EES

Bipedal locomotion requires the integration of information from a multiplicity of sensory modalities. Proprioception may be the most important of these modalities. Proprioceptive information gives rise to a conscious perception of limb positions that play a critical role during walking (Dietz, 2002; Tuthill & Azim, 2018). For example, the sudden loss of proprioception induces severe gait deficits (Cole, 1995; Sanes et al., 1985). Individuals with a chronic loss of proprioception can learn to compensate for this loss with other sensory modalities, especially vision (Cole, 1995). While this adaptation enables them to walk again, the cognitive load associated with this execution obliged them to rely on a wheelchair in their daily life. All the human subjects involved in our study reported a loss of limb position awareness during EES. Consequently, this disruption of proprioception strongly limits the clinical relevance of continuous EES to support locomotor functions during daily living activities in people with SCI.

In addition to their integration in the brain, the information derived from proprioceptive organs is broadcasted throughout the spinal cord via a dense network of afferent feedback circuits that directly activate motoneurons and shape motor pattern formation during locomotion. Signals from muscle spindles and Golgi tendon organs determine the timing of phase transitions, contribute substantially to the recruitment of leg muscles, and coordinate the adaptions of leg movements to unpredictable perturbations and task-specific requirements (Dietz & Duysens, 2000; Hultborn & Nielsen, 2007; Rossignol et al., 2006). Our results suggest that these key mechanisms of motor control are obstructed during continuous EES. Moreover, the interruption of descending pathways reinforces the critical role of these proprioceptive feedback circuits, which then become the primary source of control for motor pattern formation (Edgerton et al., 2004). For example, the integration of proprioceptive information enables the spinal cord to coordinate locomotion across a broad range of speeds, loads and directions in animal models of complete SCI (Courtine et al., 2009). The disruption of proprioceptive information during EES would severely deteriorate this ability of the spinal cord to coordinate motor pattern formation after SCI.

We previously documented some of the mechanisms through which EES facilitates locomotion in rats. In particular, we showed that the modulation of reciprocal inhibitory circuits via proprioceptive feedback during each phase of gait directs the excitatory drive elicited by EES towards the motor pools that are functionally relevant at this specific time (Moraud et al., 2016). This mechanism transforms the unspecific excitatory drive into a spatially and temporally specific pattern of excitation delivered to antagonist motor pools. The spinal cord thus acts as an elegant filter that endows EES with the necessary specificity for therapeutic applications. Due to the cancellation of proprioceptive information in humans, only narrow ranges of EES frequencies and amplitudes are able to take advantage of this mechanism. As soon as the stimulation elicits responses in muscles, computer simulations indicate that EES disrupts movement-related modulation of reciprocal inhibitory circuits. The resulting destabilization of the network leads to an unbalance in the excitation delivered to antagonist motor pools, favoring one motor pool over the other. Consequently, the modulation of EES parameters failed to enable the graded control over motoneuron activity that was observed in the rodent computational model. Experimental recordings confirmed these results, both in rodents and humans with SCI. We previously showed that this controllability enables targeting lesion-specific gait deficits and mediating task-specific adjustments of leg movements through closed-loop controllers and brain-spine interfaces in rats and nonhuman primates (Capogrosso et al., 2016; Moraud et al., 2016; Wenger et al., 2014). These features may be essential to facilitate the complex postural and propulsive requirements underlying the bipedal gait of humans.

Finally, input from proprioceptive organs plays a determinant role in steering the reorganization of residual descending pathways that restores locomotion after SCI. Mice lacking functional proprioceptive circuits display defective rearrangements of descending projections after SCI, which abolish the extensive recovery occurring spontaneously in wild-type mice after the same injury (Takeoka et al., 2014). Similarly, clinical studies reported that the preservation of proprioceptive information is a key predictor of recovery after neurotrauma (S.-W. Park et al., 2008), suggesting that this specific sensory channel may also contribute to steering the reorganization of residual neuronal pathways in humans. Therefore, the disruption of natural proprioception may reduce the ability of EES to augment neuroplasticity and recovery when delivered during rehabilitation.

The multifaceted roles of proprioceptive information for coordinating locomotor functions and steering functional recovery after SCI emphasize the critical importance of identifying EES protocols that preserve proprioceptive information in order to fulfill the therapeutic potential of this treatment paradigm for clinical applications.

3.4.3 EES strategies that replace or preserve proprioceptive information

We exploited this new understanding to design sensory-compliant EES protocols that circumvent the cancellation of natural proprioception during EES and may therefore augment the therapeutic efficacy of EES in humans. We identified two protocols, which we discuss below.

We first conceptualized a strategy that aims to replace the cancelled proprioceptive information with a spatiotemporal stimulation profile that encodes the natural firing rates of proprioceptive afferents from each muscle during locomotion. Computer simulations confirmed that this EES protocol not only preserves proprioceptive information but also augments the degree of control over motoneuron activity while preserving the alternation between antagonist muscles. Realistically, the afferents originating from a single muscle cannot be targeted specifically with current stimulation technologies. However, these stimulation protocols could be approximated with EES bursts delivered over spatially–selective spinal cord regions using a temporal sequence that coincides with the firing profile of the proprioceptive afferents innervating these specific spinal cord regions. This approach is comparable to the EES protocols that encode the spatiotemporal sequence of motoneuron activation during locomotion (Wenger et al., 2016). Compared to continuous EES, this targeted stimulation strategy enables a markedly higher degree of control over motoneuron activity in rodent and nonhuman primate models of SCI (Capogrosso et al., 2016; Wenger et al., 2016). Incidentally, the alternation of spatially-selective bursts also preserves the natural proprioceptive information flowing in the dorsal roots that are not engaged by the stimulation. Our simulations suggest that the delivery of EES bursts coinciding with the profile of proprioceptive afferent firing, as opposed to motoneurons, would further enhance the control over motoneuron activity, while additionally maximising the amount of preserved proprioceptive information.

We found that the delivery of EES bursts with a low amplitude, but high frequency may be an alternative or even complementary stimulation strategies to circumvent the cancellation of proprioceptive information. Due to the low amplitude, the stimulation recruits a limited number of afferents. Each proprioceptive afferent establishes synapses onto all the homonymous motoneurons (Mendell & Henneman, 1971; Segev et al., 1990). Consequently, the repeated recruitment of these afferents with EES bursts at high-frequency leads to a summation of excitatory post-synaptic potentials in motoneurons, which receive an overall amount of excitation that is equivalent to that induced by continuous EES at high amplitude and low frequency. However, all the non-recruited afferents continue providing essential information about the change in length and tension in the muscles. These results have general implications for EES protocols. First, the modulation of EES bursts allows to augment the amount of excitation delivered to motoneurons without the need to increase the stimulation amplitude. Second, the lower amplitude requirements would improve the spatial selectivity of the stimulation.

These novel stimulation protocols require dedicated implantable pulse generators that allow the delivery of EES bursts with high-frequency resolution through independent current sources whose temporal and spatial parameters are controllable independently in real-time. Various companies are developing next-generation implantable pulse generators that partially meet these requirements. In parallel, we are conducting a clinical study using a commercially available stimulator with a modified firmware in order to obtain proof-of-concept data on the relevance of these novel stimulation protocols (https://clinicaltrials.gov/show/NCT02936453).

While the efficacy of the stimulation protocols derived from the present results remains to be established, our findings stress the necessity of identifying strategies that preserve proprioception in order to facilitate motor control and steer plasticity with EES in humans.

3.5 Materials and Methods

3.5.1 Computer simulations

Computer simulations were performed in python 2.7 using the NEURON (Hines & Carnevale, 1997) simulation environment to run the spiking neural network models and OpenSim (S. L. Delp et al., 2007) for the biomechanical model of rats and humans. The network model code is available at https://github.com/FormentoEmanuele/MuscleSpindleCircuitsModel.

Model of a proprioceptive afferent fiber recruited by EES

The afferent fiber model was characterized by two parameters: (i) the propagation time required by an action potential to travel the whole length of the fiber, and (ii) the firing rate at which action potentials are generated at the level of the sensory organ. These parameters were adjusted to meet the properties of all the modelled afferent fibers. For each Action Potential (AP), we simulated the propagation from the sensory organ of origin to the spinal cord and the refractory dynamics (mean refractory period ± standard deviation: 1.6 ± 0.16 ms) along the fiber. We modeled EES as a periodic event recruiting the most proximal portion of the fiber. The recruitment only occurred when the fiber was not under refractory period. When a fiber was electrically activated, an antidromic AP propagated towards the distal end of the fiber. The encounter of this antidromic AP with a sensory AP traveling towards the spinal cord led to an antidromic collision that cancelled both spikes.

Estimation of antidromic collisions probability

The developed fiber model was used to assess the probability of antidromic collisions based on EES frequency, the firing rate of the sensory organs, and the propagation time required by an AP to travel along the whole length of the fiber. Propagation times were limited to 2 ms in rat afferents. Due to the extended length of axons in humans, we modelled human afferents innervating proximal (10 ms) and distal (20 ms) muscles. Antidromic collision probability was defined as the probability of a natural sensory AP to collide with an EES-induced antidromic AP within a single fiber. For every tested model parameters and stimulation frequencies, we integrated the dynamic of the fiber over 60 seconds and evaluated the number of antidromic collisions occurring within this time window. To estimate antidromic collisions probability, we averaged the results of 50 simulations initialized with EES onset delays varying between 0 and 10 ms.

Rat model of proprioceptive feedback circuits

The rat model of proprioceptive feedback circuits was elaborated from a previously validated model (Moraud et al., 2016), which we modified to integrate a simpler and faster model of the motoneurons and the new model of proprioceptive afferents, including the occurrence of antidromic collisions.

Briefly, this model is composed of four components: (i) a spiking neural network reproducing the proprioceptive feedback circuits associated with a pair of antagonist muscles, (ii) a muscle spindle model, (iii) a musculoskeletal model of the rat hindlimb, and (iv) a finite element method model of EES of the rat lumbar spinal cord (Fig. 3.5A).

The spiking neural network includes populations of group-Ia and group-II afferent fibers, Ia-inhibitory interneurons, group-II excitatory interneurons, and pools of alpha motoneurons. The number of cells, the number and the strength of the synapses contacting the different populations of neurons, and the characteristics of the cell models are described in our previous work (Moraud et al., 2016). To speed up the simulation time, we replaced our previous realistic motoneuron model with an integrate and fire cell model designed to reproduce the realistic membrane response dynamics to excitatory and inhibitory stimuli (Burke, 1968; Harrison & Taylor, 1981; McIntyre & Grill, 2002; Munson et al., 1980). Specifically, we set the refractory period to 20 ± 1 ms and the membrane time constant $\tau_{membrane}$ to 6 ± 0.3 ms. Excitatory synapses were modelled as instantaneous changes in current exponentially decaying with time constant $\tau_{excitatory}$ 0.25 ms. Inhibitory synapses were modelled as alpha functions with a rise time constant $\tau_{inhibitory\_1}$ of 2 ms, and a decay time constant $\tau_{inhibitory\_2}$ of 4.5 ms (Fig. 3.13A). We adjusted the motoneurons synaptic weights to match experimental Excitatory and Inhibitory Post-Synaptic Potentials (EPSPs/IPSPs). For this, we normalized experimental EPSPs (Harrison & Taylor, 1981; Munson et al., 1980) and IPSPs (McIntyre & Grill, 2002) to the minimum depolarization necessary to induce an AP in our realistic model (Fig. 3.13B,C). Afferent fibers were modeled with an AP propagation time of 2 ms. This parameter was estimated to represent rat afferent fibers innervating the antagonist muscles of the ankle.

The musculoskeletal (Johnson et al., 2011; Johnson et al., 2008) and muscle spindle (Prochazka, 1999) models were used to calculate the firing rate profiles of group-Ia and group-II afferent fibers innervating the flexor (tibialis anterior) and extensor (gastrocnemius medialis) muscles of the ankle during locomotion. For this purpose, we mobilized the musculoskeletal model with the recordings of the rat hindlimb kinematics during locomotion to estimate the ankle muscles stretch profiles through inverse kinematics. We then used the muscle spindle model to compute the firing rate profiles. To mimic the alpha-gamma linkage, muscles stretch and stretch velocity were linked to the envelope of EMG activity from the homonymous muscle (Eqn. 3.1 and 3.2 (Prochazka, 1999)). The estimated afferent firing rate profiles drove the activity of the modelled proprioceptive afferents.

A validated finite element method model of EES of the lumbar spinal cord (Capogrosso et al., 2013) was finally used to estimate the proportion of afferent and efferent fibers recruited at a given stimulation amplitude. Realistic interactions between EES and the natural sensory activity along the modelled afferent fibers were integrated using the developed proprioceptive afferent model.

$$Ia_{firingrate} = 50 + 2 \cdot stretch + 4.3 \cdot sign(stretch_{Velocity}) \cdot |stretch_{Velocity}|^{0.6} + 50 \cdot EMG_{env} \tag{3.1}$$

$$f_{firingrate} = 80 + 13.5 \cdot stretch + 20 \cdot EMG_{env}(t) \tag{3.2}$$

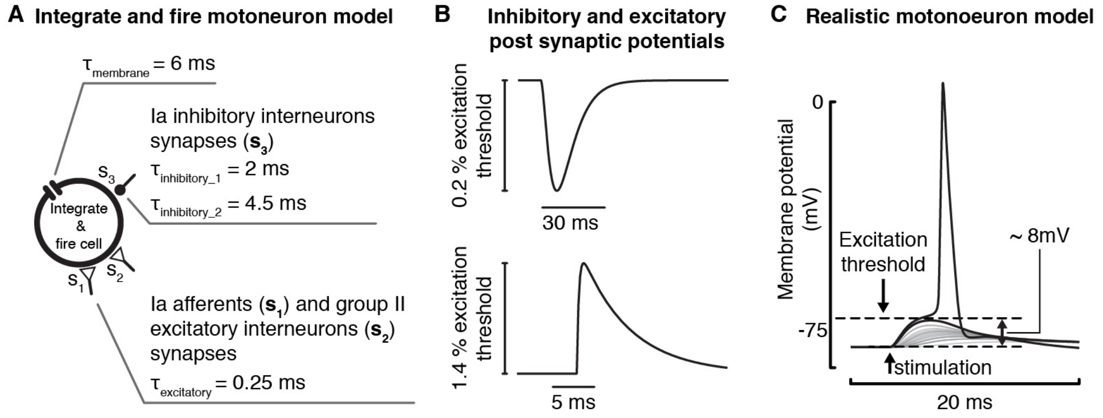
A Integrate and fire motoneuron model
$\tau_{membrane}$ = 6 ms
Ia inhibitory interneurons synapses (s_3)
$\tau_{inhibitory\_1}$ = 2 ms
$\tau_{inhibitory\_2}$ = 4.5 ms
s_3
Integrate & fire cell
s_1
s_2
Ia afferents (s_1) and group II excitatory interneurons (s_2) synapses
$\tau_{excitatory}$ = 0.25 ms
B Inhibitory and excitatory post synaptic potentials
0.2 % excitation threshold
30 ms
1.4 % excitation threshold
5 ms
C Realistic motonoeuron model
0
Membrane potential (mV)
Excitation threshold
~ 8mV
-75
stimulation
20 ms

D

	s_1	s_2	s_3
Number of synapses	60	116	232
Experimental IPSP/EPSP	52 / 212 μV	~ 0.33·s_1 EPSP	~ -0.13 μV
Integrate and fire IPSP/EPSP	1.4% excitation threshold	0.7% excitation threshold	-0.2% excitation threshold

Figure 3.13: Integrate and fire motoneuron model. A, Schematic of the integrate and fire model and of the different synapses contacting this cell. B, Simulated Inhibitory and Excitatory Post-Synaptic Potentials (IPSPs/EPSPs) induced by the activation of a single Ia-inhibitory interneuron or a single group-Ia afferent fiber, respectively. C, Excitation threshold of our realistic alpha motoneuron model (Moraud et al., 2016). D, Number and amplitude of experimental (Harrison & Taylor, 1981; McIntyre & Grill, 2002; Munson et al., 1980) and modelled EPSP/IPSPs induced from the synaptic contacts originating from group-Ia afferents (s1), group-II excitatory interneurons (s2), and Ia-inhibitory interneurons (s3).

Human model of proprioceptive feedback circuits

The layout of the rat model served as a basis to build the human model of proprioceptive feedback circuits. To take into account the specific anatomical and physiological features of humans, we adapted the musculoskeletal model, the muscle spindle model, the weights of the synapses in the network, the length of the modelled afferent fibers, and the output of the finite element method model of EES (Fig. 3.5A).

To estimate the stretch of flexor (tibialis anterior) and extensor (soleus) muscles spanning the ankle joints, we used the 3DGaitModel2392 OpenSim lower limb model (S. Delp et al., 1990) and kinematic data of healthy subjects during locomotion on a treadmill (Mignardot et al., 2017; Wojtusch & von Stryk, 2015). We tuned the muscle spindle model to account for the lower firing rates of human proprioceptive afferents compared to those of rodents (Hnk

& lessler, 1973; Prochazka, 1996). Specifically, we scaled Eqn. 3.1 and 3.2 down by 0.2 and 0.25, respectively, to produce firing rates that remained within the range of values generally observed in humans (rarely exceeding 30 Imp/s (Albert et al., 2006; Prochazka, 1996, 1999)). The envelopes of EMG activity were extracted from the same subjects from whom we also extracted the kinematic data (Mignardot et al., 2017; Wojtusch & von Stryk, 2015).

We assumed that if the occurrence probability of antidromic collisions would be the same in humans and rodents, the human model should reproduce results that are qualitatively similar to the simulations obtained in rats. Hence, we optimized the weight of the synaptic connections between the afferent fibers and their target spinal neurons by driving the network with the estimated human afferent firings but without modifying the propagation time required by sensory APs to reach the spinal cord — a parameter proportional to the occurrence probability of antidromic collisions (Fig. 3.14A). To this purpose we performed a systematic search by progressively increasing the synaptic weights of connections from afferent fibers. EES frequency and percentage of Ia-afferents recruited by EES were set to 60 Hz and to 60%, respectively. We defined a set of fitness functions and relative minimum scores to define the range of synaptic weights that produce the desired behavior of the network (Eqn. 3.3) and selected one set of weights for further simulations (Fig. 3.14B,C).

$$\begin{cases} \text{percentile\_90}(\boldsymbol{MotoneuronsFR_{ext}}) > 5 Imp/s \\ \text{percentile\_90}(\boldsymbol{MotoneuronsFR_{flex}}) > 5 Imp/s \\ \text{1-mean}(\boldsymbol{MotoneuronsFR_{flex}} \cdot \boldsymbol{MotoneuronsFR_{ext}}) > 0.9 \end{cases} \tag{3.3}$$

We then modified the AP propagation time parameter of the afferent fiber models to 16 ms, which is a representative value for the proprioceptive afferents innervating ankle muscles in humans (Hofstoetter et al., 2018).

We assumed that the ratio between the amount of primary and secondary afferent fibers recruited by EES while increasing the stimulation amplitude is similar in rats and humans. We thus used the finite element method model of the rat spinal cord to estimate the percentage of primary and secondary afferents recruited by the stimulation. However, to take into account the considerably larger distance of the ventral roots from the epidural electrodes, we did not simulate the direct recruitment of motor axons. This phenomenon commonly occurs in rats but is limited in humans (Capogrosso et al., 2013; Rattay et al., 2000).

Spatiotemporal stimulation profiles

Spatiotemporal EES profiles encoding the natural proprioceptive information originating from a pair of antagonist muscles spanning the ankle joint were estimated in two steps. First, we computed the normalized average firing rate profiles of group-Ia, group-II and group-Ib afferents over a gait cycle. Second, these three profiles were averaged to produce a stimulation profile that encodes the global proprioceptive information (Fig. 3.11A). Since group-Ib afferent firing is closely correlated to the activity of the muscle along which the associated Golgi tendon organ is connected (Prochazka, 1999), we approximated the firing rates of group-Ib afferents with the envelope of the EMG activity from the homonymous muscle during gait. Simulations were conducted using the estimated stimulation profile for each muscle. EES amplitude was adjusted proportionally to the changes in the estimated stimulation profile while the length of the stimulation profile was adjusted based on the duration of each gait cycle.

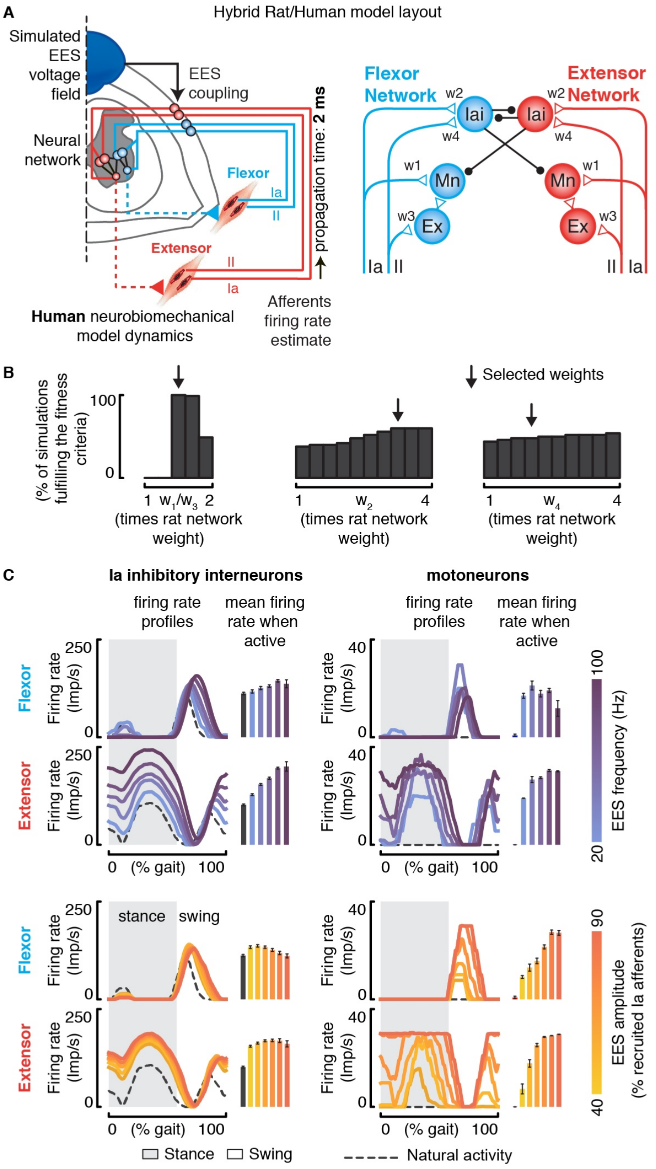
A
Hybrid Rat/Human model layout
Simulated EES voltage field
EES coupling
Neural network
propagation time: 2 ms
Flexor
Ia
II
Extensor
II
Ia
Human neurobiomechanical model dynamics
Afferents firing rate estimate
Flexor Network
Extensor Network
Iai
Iai
Mn
Mn
Ex
Ex
w1
w2
w3
w4
Ia
II
B
Selected weights
(% of simulations fulfilling the fitness criteria)
100
0
1 w1/w3 2
(times rat network weight)
1 w2 4
(times rat network weight)
1 w4 4
(times rat network weight)
C
Ia inhibitory interneurons
motoneurons
firing rate profiles
mean firing rate when active
Flexor
Extensor
Firing rate (Imp/s)
250
40
0
0 (% gait) 100
EES frequency (Hz)
20
100
stance
swing
EES amplitude (% recruited Ia afferents)
40
90
Stance
Swing
Natural activity

Figure 3.14: Adaptation of the rat neural network to humans.

Figure 3.14: (Continued) A, Model layout of the hybrid rat-human computational model used to tune the human neural network weights. W1, w2, w3 and w4 represent the weights of the neural network connections that have been modified to adapt the rat neural network to the human one. B, Systematic search results. W1 and w3 were ranged together between 1 and 2 times the weight used in the rat network, while w2 and w4 were ranged between 1 and 4 times. Bar plots report the percentage of simulations that fulfilled the defined fitness criteria. Selected weights that have been used for further simulations are highlighted with an arrow. C, Effect of EES on the natural activity of Ia-inhibitory interneurons and on the production of motor patterns during locomotion, in the hybrid rat-human model for the selected set of synaptic weights. Panels on the left report the average firing rate profiles of the Ia-inhibitory interneuron populations associated to either the flexor or the extensor network, as well as their modulation depth (mean ± SEM, n = 10 gait cycles). Similarly, right-most panels represent the average firing rate profiles of motoneurons and their mean firing rate activity during the phase in which they are active (mean ± SEM, n = 10 gait cycles). Effects of different EES frequencies and amplitudes are reported on the top and bottom panels, respectively.

High-frequency low-amplitude EES model

To assess the effect of high-frequency low-amplitude EES on the membrane potentials of motoneurons, we used our previously validated conductance-based motoneuron model that integrates realistic synaptic boutons from group-Ia afferents (Moraud et al., 2016) (Fig. 3.12A,B). However, simulations on the effect of high-frequency low-amplitude EES on the muscle spindle feedback circuits were still performed using the simplified integrate and fire motoneuron model (Fig. 3.12E). The realistic conductance-based model was used in order to obtain a more precise estimate of motoneurons' soma responses to high-frequency bursts of EES.

3.5.2 Experimental procedures in humans

Spinal cord stimulation system implanted in human subjects with SCI

Experiments conducted in human subjects with SCI were carried out within the framework of an ongoing clinical study that has been approved by Swiss authorities (Swissethics protocol number 04/2014 ProjectID: PB_2016-00886, Swissmedic protocol 2016-MD-0002). The study is conducted at the Lausanne University Hospital (CHUV). All subjects signed written inform consent prior to their participation. The subjects were surgically implanted with a spinal cord stimulation system comprising an implantable pulse generator (Activa^{TM} RC, Medtronic plc, Fridley, Minnesota, SA) connected to a 16-electrode paddle array (Medtronic Specify^{TM} 5-6-5 surgical lead) that was placed over the lumbosacral segments of the spinal cord. Subject related data and details on their neurological status, evaluated according to the International Standards for Neurological Classification of Spinal Cord Injury, are provided in Table 3.1.

Recording of EES-induced antidromic activity along human afferents

Recordings of the neural activity induced by EES were performed with the NIM Eclipse system (Medtronic plc, Fridley, Minnesota, USA). The activity of the soleus muscle was recorded with surface EMG electrodes (Ambu Neuroline 715, Ambu Sarl, Bordeaux, France), while the activity of the sural and of the proximal and distal branches of the tibial nerve were recorded using percutaneous disposable needle electrodes (Ambu Neuroline Twisted Pair Subdermal 12 x 0.4 mm, Ambu Sarl, Bordeaux, France). The proximal branch of the tibial nerve was recorded at the level of the popliteal fossa (Fig. 3.2A). The electrode insertion point was defined by searching for the site that elicited an H-reflex at the lowest stimulation amplitude. The distal branch of the tibial nerve was recorded at the level of the medial malleolus (Fig. 3.2A). The recording electrode position was determined by applying electrical stimulation to this site and by verifying the evoked potentials at the level of the proximal branch of the tibial nerve. The sural nerve was recorded at the level of the lateral malleolus. The specific location of the electrode was defined following the same procedure as for the distal branch of the tibial nerve. Neural and EMG signals were sampled at 10000 Hz, amplified, and online band-pass filtered (30-1000 Hz). For the entire duration of the experiment, participants remained relaxed in a supine position. EES was delivered at 20 Hz for 60 seconds in order to collect a total of approximately 1200 pulses. We selected EES sites that mainly recruited the posterior root innervating the S1 spinal segment, as verified in the presence of motor responses in the soleus muscle following each pulse of EES. For the experiment, the stimulation amplitude was reduced to just-below the motor response threshold in order to avoid contaminating neural recordings with electromyographic activity or movement artifacts. To verify that the stimulation amplitude was sufficient to recruit afferent fibers in the recorded nerves, we controlled that the stimulation elicited a sensation of tingling in the corresponding dermatome. We recorded EES artifacts with surface electrodes positioned in the vicinity of the implanted paddle array. The artifacts were used as triggers to extract and average the evoked potentials.

Assessment of proprioceptive function during EES

The threshold to detection of passive movement test33 was performed with the Humac Norm Cybex system (Computer Sports Medicine Inc., Stoughton, US). Subjects were first tested without EES and then during continuous EES. Throughout the experiment, participants' tactile, visual, and aural information were occluded by using foam cushions, blindfolds, and headphones with pink noise. The experimental protocol was tailored for each participant, since each of them presented distinct levels of proprioceptive functions. At the beginning of each trial, the participant's knee joint was moved to 45 degrees. The participant was informed with a tap on the shoulder that a new trial was about to start. The trial was then started after a randomised time delay to assess false positive detections. In subject #1, we imposed movements of knee extension or knee flexion at the constant speed of 0.5 degrees per second. Flexion and extension were delivered randomly. The participant was instructed to report the movement direction, as soon as he became aware of it, by pushing a button. A maximum displacement of 15 degrees was allowed (Fig. 3.2B). Button-triggered digital signal and joint kinematics were recorded at a sampling frequency of 5000 Hz. The trial was considered successful if the direction of the movement was correctly identified. A trial was considered unsuccessful when the movement was either misclassified or not perceived at all. Subject #3 was not able to detect the direction of the imposed movement, even in the absence of continuous EES. To simplify the task, we limited the movement to knee extension, increased the movement speed to 1 degree per second, and allowed a maximum displacement of 30 degrees (Fig. 3.2B). A trial was considered successful if the movement was detected within the allowed range of movement. Subject #2 was not able to perceive the imposed movements and was thus excluded from this experiment.

A total number of 15 repetitions or 10 successful repetitions were performed to complete an assessment for a given EES condition. In case of 10 successful detections, we bootstrapped the median and the 95% confidence interval of the knee angle at which the participant detected the movement. The proportion between successful and unsuccessful trials was used to compute participants' error rate and 95% confidence interval by using the Clopper-Pearson interval method based on Beta distribution.

We adjusted the configuration of EES electrodes to target both flexor and extensor muscles of the knee. Recordings of the EMG activity from the vastus lateralis and semitendinosus muscles allowed the identification of the minimum stimulation amplitude necessary to recruit these muscles. We then assessed the proprioceptive functions of the subjects during continuous EES that was delivered with amplitudes below (0.8 times) and above (1.5 times) the motor response threshold. For both amplitudes, we tested a range of frequencies : 10, 30, 50 and 100 Hz. At 1.5 the motor threshold amplitude frequencies below 50 Hz induced spastic contractions, and were thus not tested.

Assessment of EES-induced responses during passive joint movements

The Humac Norm Cybex was used to impose passive joint movements with a sinusoidal profile of fixed amplitude and frequency, while continuous EES was delivered to produce motor responses in the muscles spanning this joint. The subjects were asked to relax, neither to resist, follow, nor facilitate the movements. Muscle responses and EES artifacts were recorded with wireless surface EMG electrodes (Myon 320, Myon AG, Schwarzenberg, Switzerland) at a sampling frequency of 5000 Hz. Joint kinematic was recorded with the Cybex system at 5000 Hz. EES parameters, as well as the targeted joint, the speed and the amplitude of the movement were set depending on subject-specific constraints (Fig. 3.4A). In subject #1, the Cybex system was used to produce flexion and extension movements of the ankle joint at a frequency of 1.13 Hz and a range of motion of 30 degrees. These parameters were chosen to be as large as possible in order to maximize the amount of proprioceptive signals generated from the targeted muscles while minimizing discomfort. EES electrodes were configured in order to recruit the targeted muscles. EES was delivered with frequencies ranging from 5 to 60 Hz. The stimulation amplitude was set to induce consistent muscle responses across the range of tested frequencies, corresponded to 1.25 times the motor response threshold. For every tested condition, a minimum of 1 minute of recording was performed. Recording duration was extended to 2 minutes when EES was delivered at 5 Hz. In subject #2 and #3, we could not find electrode configurations that recruited the targeted muscles without causing discomfort at the required EES amplitudes and frequencies. Therefore, we adapted the experiment and targeted the knee joint instead of the ankle joint. Moreover, we limited the range of tested frequencies. Specifically, for subject #3 we kept an oscillation frequency of 1.13 Hz, set a movement range of 60 degrees, and limited the range of EES frequencies from 10 to 60 Hz. These settings also led to spastic contractions in subject #2. Consequently, we reduced the movement range and frequency to 50 degrees and 0.9 Hz, respectively, and limited the range of EES frequencies between 20 and 60 Hz.

To quantify the modulation of muscle responses during the passive movements, we extracted the timing of every EES pulse with the recorded stimulation artifacts. We then extracted the muscles responses and grouped them according to the phase of the cyclic movement (n = 10 bins) (Fig. 3.4B). When more than one EES pulse occurred within a given bin, only the response with highest amplitude was selected. We bootstrapped the normalized modulation depth median and 95% confidence interval (Eqn. 3.4) by computing the median peak to peak amplitudes (*mP2Ps*) of the responses occurred in the different bins. Normalization was performed in order to account for frequency-dependent depression of EES-induced muscle responses (Calancie et al., 1993; Ishikawa et al., 1966; Schindler-Ivens & Shields, 2000).

$$NormalizedModulationDepth = \frac{[\max(mP2Ps) - \min(mP2Ps)]}{min(mP2Ps)} \tag{3.4}$$

Continuous EES during locomotion on a treadmill

The FLOAT robotic suspension system (Lutz Medical Engineering AG, Rudlingen, Switzerland) was used to provide the participants with personalized upward and forward forces to the trunk during locomotion a treadmill (Mignardot et al., 2017; Vallery et al., 2013). EES was delivered using four configurations of electrodes. Each configuration involved one or multiple anodes and cathodes. We configured these electrode combinations to target the left and right posterior roots projecting to the L1 and L4 segments. For this purpose, we searched the electrode configurations that activated preferentially the iliopsoas and the tibialis anterior. These motor pools spanned the L1/L2 segments and L4/L5 segments, respectively. The amplitude and frequency of these four electrode configurations were optimized by visual inspection of the induced EMG activity and facilitation of kinematics when subjects were asked to step on the treadmill. EMG recordings were performed with wireless surface electrodes (Myon 320, Myon AG, Schwarzenberg, Switzerland) and recorded at 1000 Hz. Leg kinematics was recorded using the Vicon motion capture system (Vicon Motion Systems, Oxford, UK) at 100 Hz. Subjects were not able to step on the treadmill without assistance. We therefore allowed them to assist their leg movements using their arms that were resting on the handrail of the treadmill. Analysis of EMG activity and kinematics was conducted using methods reported in details previously (Mignardot et al., 2017).

3.5.3 Experimental procedures in rats

Animal husbandry

All procedures and surgeries were approved by the Veterinary Office of the canton of Geneva in Switzerland. The experiments were conducted in 9 adult female Lewis rats (~220 g body weight) and 4 Long-Evans rats (~240 g body weight). Rats were housed separately with a light/dark cycle of 12 hours.

Surgical procedures

Surgical procedures have been described in detail previously (Courtine et al., 2009; van den Brand et al., 2012). All the interventions were performed in aseptic conditions and under general anesthesia. Briefly, rats received a severe thoracic (T8) contusion SCI (250 kdyn) by using a force-controlled spinal cord impactor (IH-0400 Impactor, Precision Systems and Instrumentation LLC, USA). During the same surgery, EES electrodes were sutured to the dura overlying the midline of S1 and L2 spinal segments in Lewis rats, and of L4 and L2 spinal segments in Long-Evans rats. Electrodes were created by removing a small part of insulation (~400 µm) from Teflon-coated stainless-steel wires (AS632, Cooner Wire, USA). A common ground wire electrode (~1 cm of active site) was placed subcutaneously over the right shoulder. Finally, bipolar electrodes (same type as used for EES) were implanted bilaterally in the left and right tibialis anterior muscles to record the EMG activity.

Assessment of EES induced responses during passive joint movements

Lewis rats (n=4) were positioned in a prone position within a support system that let the hindlimbs hanging freely. The right paw was secured within a 3D printed pedal connected to a stepper motor (QSH4218-51-10-049, Trinamic Motion Control GmbH, Waterloohain, Germany). We used this robotic platform to impose cyclic movements of the ankle with a fixed amplitude (70 degrees) and frequency (0.54 Hz), while continuous EES was delivered to evoke motor responses in the tibialis anterior muscle (Fig. 3.4D). EES was delivered using an IZ2H Stimulator controlled by a RZ2 BioAmp Processor (Tucker-Davis Technologies, Alachua, US). EES amplitude was set to approximately 1.2 times the motor response threshold. We tested a range of EES frequencies. 5 to 100 Hz. EMG activity of the tibialis anterior was amplified with a PZ3 Low Impedance Amplifier (Tucker-Davis Technologies, Alachua, US) and recorded with the RZ2 BioAmp Processor at a sampling frequency of 24414 Hz. Ankle kinematic was record with the Vicon motion capture system at sampling frequency of 200 Hz. For every tested EES condition a minimum of 1 minute of recording was performed. To analyze the modulation of the muscle responses, we used the same procedures that we adopted in the equivalent experiment carried out in human subjects.

Electrophysiological recordings of high-frequency low-amplitude EES

We tested the impact of high-frequency low-amplitude EES in 5 Lewis rats. EES and EMG recordings were performed with the setup used for assessing the modulation of muscle responses during passive movements. The motor response threshold was measured using single pulses of EES that were delivered at amplitudes close to this threshold, thus allowing to obtain a precise value. High-frequency bursts were then delivered at amplitudes below the identified motor response threshold. The aim was to evaluate whether high-frequency stimulation was able to recruit motoneurons at lower amplitudes than single pulses. For each amplitude, we tested burst frequencies ranging from 100 to 1000 Hz. The duration of each burst was kept constant at 25 ms. During the experiments, the rats were hold in a resting position with the hindlimbs hanging freely.

Continuous EES during locomotion on a treadmill

Behavioural experiments during locomotion were performed in 4 Long-Evans rats. Following one to two weeks of rehabilitation using previously described procedures (Courtine et al., 2009; van den Brand et al., 2012), we evaluated the impact of different EES frequencies on the modulation of muscle activity and hindlimb kinematics during bipedal locomotion on a treadmill. Locomotion was recorded without EES and with EES at frequencies ranging from 20 to 80 Hz. EES amplitude was kept fixed at the optimal value found during training. For each experimental condition, a minimum of 10 steps or 20 seconds of minimal leg movements were recorded.

Hindlimb kinematics was recorded with the Vicon motion capture system (Vicon Motion Systems, Oxford, UK) at a sampling frequency of 200 Hz. EMG signals were amplified and filtered online (10–10000 Hz band-pass) by a Differential AC Amplifier (A-M System, Sequim, US) and recorded at 2000 kHz with the Vicon system.

3.5.4 Statistics

Data are reported as mean ± standard error of the mean (SEM.) or median values ± 95% confidence interval (CI.). Confidence intervals and significance were analyzed using the non-parametric Wilcoxon rank-sum test, student's t-test, the Clopper-Pearson interval based on Beta distribution method, or a bootstrapping approach based on the Monte Carlo algorithm resampling scheme (n=10'000 iterations).

4 A technological framework to restore walking in paralyzed individuals with epidural electrical stimulation

EES applied over the lumbosacral spinal cord has the capacity to restore locomotion in animal models of SCI. However, the rehabilitative efficacy of EES is greatly diminished in humans. In the previous chapter, we demonstrated that this inter-species discrepancy is partially a result of interference between EES and natural sensory activity of proprioceptive afferents during locomotion. We leveraged computational simulations to highlight that this undesirable interaction can be minimized through the use of high-frequency, low-amplitude bursts of stimulation and spatiotemporal stimulation profiles, that preserve proprioceptive information, while reawakening their underlying spinal circuitry.

In this chapter, I describe how these spatiotemporal stimulation paradigms were used to enable activity-based training in humans with SCI. Here, I describe a technological framework that has the capacity to restore walking in paralyzed individuals. One key aspect of this framework is the targeted recruitment of individual dorsal roots to emulate the migration of motor pool activity in the spinal cord during locomotion (Capogrosso et al., 2016; Cappellini et al., 2010; Wenger et al., 2016; Wenger et al., 2014). However, the human spinal cord exhibits a large degree of anatomical variability between subjects (Frostell et al., 2016; Ko et al., 2004; Mendez et al., 2020; Toossi et al., 2020), rendering the selective targeting of individual spinal roots challenging and thus disrupting the clinical implementation of spatiotemporal stimulation paradigms. For this purpose, I generated semi-personalized computational models for preoperative treatment planning of EES in three participants with incomplete SCI. We demonstrate that spatiotemporal spinal cord stimulation enables activity-based training of these individuals, while continuous stimulation fails to facilitate locomotor movements.

Related publication and personal contributions

The content of this chapter is adapted - with permission of the co-authors - from the following manuscript: Fabien Wagner*, Jean-Baptiste Mignardot*, Camille Mignardot*, Robin Demesmaeker†, Salif Komi†, Marco Capogrosso†, **Andreas Rowald**, Ismael Seáñez-González, Miroslav Caban, Elvira Pirondini, Molywan Vat, Laura McCracken, Roman Heimgartner, Isabelle Fodor, Anne Watrin, Perinne Seguin, Katrien Van Den Keybus, Gregoire Eberle, Brigitte Schurch, Etienne Pralong, Fabio Becce, John Prior, Nik Buse, Rik Buschman, Stefano Carda, Joachim von Zitzewitz, Vincent Delattre, Tim Denison, Hendrik Lambert, Armin Curt, Karen Minassian‡ & Jocelyne Bloch‡ & Grégoire Courtine‡, "**Targeted Neurotechnologies restore walking in humans with spinal cord injury**", **Nature** (2018).
*, †, ‡ contributed equally to this work

Personal contributions: Conceived and developed the computational framework, adapted medical imaging protocols, collected and analyzed medical imaging datasets, developed the computational models, performed computer simulations, figures preparation.

4.1 Abstract

Spinal cord injury leads to severe locomotor deficits or even complete leg paralysis. Here we introduce targeted spinal cord stimulation neurotechnologies that enabled voluntary control of walking in individuals who had sustained a spinal cord injury more than four years ago and presented with permanent motor deficits or complete paralysis despite extensive rehabilitation. Using an implanted pulse generator with real-time triggering capabilities, we delivered trains of spatially selective stimulation to the lumbosacral spinal cord with timing that coincided with the intended movement. Within one week, this spatiotemporal stimulation had re-established adaptive control of paralysed muscles during overground walking. Locomotor performance improved during rehabilitation. After a few months, participants regained voluntary control over previously paralysed muscles without stimulation and could walk or cycle in ecological settings during spatiotemporal stimulation. These results establish a technological framework for improving neurological recovery and supporting the activities of daily living after spinal cord injury.

4.2 Introduction

Spinal Cord Injury (SCI) disrupts communication within the nervous system, leading to the loss of essential neurological functions. At present, activity-based therapies are the only medical practices that can be used to enhance recovery (Behrman et al., 2017; Field-Fote et al., 2005; Jones et al., 2014). The volitional production of active movements during training promotes reorganization of neuronal pathways and thereby augments recovery (Côté et al., 2017; Edgerton et al., 2008). However, the most affected patients who fail to produce active movements voluntarily, experience minimal benefits from these therapies (Behrman et al., 2017).

This situation has prompted the development of multifaceted neurotechnologies (Borton et al., 2013), such as lower limb exoskeletons, bodyweight support systems, functional electrical stimulation of muscles, and spinal cord neuromodulation therapies, all of which share the same goal: to enable patients to sustain active movements during training to enhance the reorganization of neuronal pathways (Edgerton et al., 2008). Three decades of clinical research using these neurotechnologies suggested that Epidural Electrical Stimulation (EES) of the spinal cord may be pivotal to achieve this goal (Angeli et al., 2018; Field-Fote & Roach, 2011; M. L. Gill et al., 2018; Minassian et al., 2016). EES not only enables the brain to exploit spared but functionally silent descending pathways in order to produce movements of paralysed limbs (Angeli et al., 2014; Barolat et al., 1986), but also improves the ability of the spinal cord to translate task–specific sensory information into the muscle activity that underlies standing and walking (Angeli et al., 2018; Angeli et al., 2014; Carhart et al., 2004; Danner et al., 2015; M. L. Gill et al., 2018; Grahn et al., 2017; Minassian et al., 2004).

To harness the therapeutic potential of EES, we studied its underlying mechanisms. We found that EES activates motor neurons by recruiting proprioceptive circuits within the posterior roots of the spinal cord (Capogrosso et al., 2013; Y. Gerasimenko et al., 2008; Moraud et al., 2018; Rattay et al., 2000). This understanding translated into EES protocols that target individual posterior roots to access the motor neuron pools located in the spinal cord segment innervated by each root (Wenger et al., 2016). To engage motor neurons at the appropriate time, spatially selective EES trains are delivered with timing that coincides with the intended movement. Compared to empirical stimulation protocols, spatiotemporal EES enhances the potency of leg movements, which enabled weight-bearing locomotion in animal models of leg paralysis (Capogrosso et al., 2016; Wenger et al., 2016; Wenger et al., 2014). When combined with overground locomotor training enabled by a gravity-assist device (Dominici et al., 2012), this stimulation promotes extensive reorganization of residual neural pathways that improves locomotion with and even without stimulation (Asboth et al., 2018; van den Brand et al., 2012; Wenger et al., 2016).

Here, we report the development of targeted neurotechnologies for delivering spatiotemporal EES during overground locomotor training with a gravity-assist device in humans (Mignardot et al., 2017). We hypothesized that spatiotemporal EES would immediately enable voluntary locomotion despite chronic paralysis, and that the ability to sustain active movements during training would promote meaningful functional improvements with and even without stimulation.

4.3 Results

4.3.1 Targeted neurotechnologies to deliver spatiotemporal stimulation during walking

We developed a wireless environment that allows real–time control over temporal sequences of independently–adjusted EES trains to the lumbosacral spinal cord of humans during unconstrained walking within a large and safe workspace (Fig. 4.2b). To enable overground walking, we used a robotic suspension system that applies personalized upward, forward and mediolateral forces to the trunk through a dedicated harness (Fig. 4.1a). A gravity–assist algorithm configures these forces to meet the specific needs of each participant (Mignardot et al., 2017). We integrated this system within a recording platform allowing real-time processing of forces applied to the trunk, whole–body kinematics, ground reaction forces, electromyographic (EMG) activity of leg muscles and foot movement dynamics using accelerometers and gyroscopes (Fig. 4.1a). To deliver stimulation, we endowed an implantable pulse generator commonly used for deep brain stimulation therapies with wireless communication modules (Capogrosso et al., 2016) that enabled real–time control over the spatial and temporal parameters of EES with a latency of about 100 ms (Fig. 4.2b). EES sequences could be pre–programmed in open-loop or adjusted in closed-loop based on external signals, notably the spatiotemporal trajectory of the feet (Wenger et al., 2016; Wenger et al., 2014). The posterior roots innervating the lumbosacral spinal cord were targeted using a 16-electrode paddle array commonly used for pain therapies.

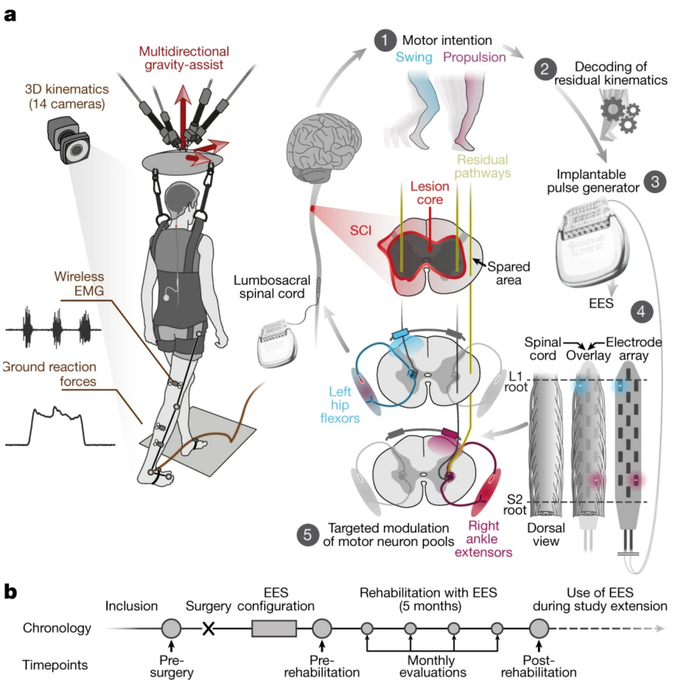
a
Multidirectional gravity-assist
3D kinematics (14 cameras)
Wireless EMG
Ground reaction forces
Lumbosacral spinal cord
1 Motor intention
Swing
Propulsion
2 Decoding of residual kinematics
Residual pathways
Lesion core
SCI
Spared area
Implantable pulse generator 3
EES 4
Spinal cord
Overlay
Electrode array
L1 root
Left hip flexors
S2 root
5 Targeted modulation of motor neuron pools
Right ankle extensors
Dorsal view
b
Chronology
Timepoints
Inclusion
Surgery
EES configuration
Rehabilitation with EES (5 months)
Use of EES during study extension
Pre-surgery
Pre-rehabilitation
Monthly evaluations
Post-rehabilitation

Figure 4.1: Technology and study design. a, Targeted neurotechnologies enable walking after SCI. Multidirectional assistance of trunk movements during overground locomotion while 3D kinematics, ground reaction forces and EMG activity are recorded wirelessly. An implantable pulse generator connected to a 16-electrode paddle array was used to target the posterior roots projecting to specific motor neuron pools, illustrated for hip flexors and ankle extensors. Real-time processing of residual kinematics ensures that targeted EES coincides with movement intent. b, Study timeline

4.3.2 Targeted surgical implantation of individuals with a chronic cervical SCI

We enrolled three males who suffered a traumatic cervical SCI more than 4 years prior to the beginning of the study. While they exhibited varying sensory and motor deficits in the upper and lower extremities, they all displayed low motor scores in the lower limbs or complete motor paralysis, which bound them to a wheel chair (Table 4.1).

We aimed at targeting the posterior roots entering the lumbar and upper sacral segments (Fig. 4.1) that contain the motoneuron pools innervating leg muscles (Fig. 4.3a). For this purpose, we developed a stereotyped surgical protocol including pre–operative imaging as well as intraoperative electrophysiological and radiological assessments that guided the targeted placement of the paddle array over the spinal cord (Fig. 4.2a).

4.3.3 Targeting spatially selective regions of the spinal cord

We established a practical procedure to identify electrode configurations that target the posterior roots projecting to the spinal cord regions embedding the motoneurons involved in mobilizing each joint of the legs in healthy subjects. Our objective was to activate these regions while the participants with SCI attempted to execute these movements.

We first established a reference atlas of motoneuron activation maps associated with the flexion or extension of the hip, knee or ankle joints in healthy individuals, which we derived from EMG recordings using well-established methods (Cappellini et al., 2010; Yakovenko et al., 2002). We obtained reproducible motoneuron activation maps for each movement.

For example, a hip flexion involved the activation of upper lumbar segments, while an ankle extension (plantar flexion) activated motoneuron pools restricted to upper sacral segments (Fig. 4.3b). The activation was logically restricted to the hemicord ipsilateral to the movement.

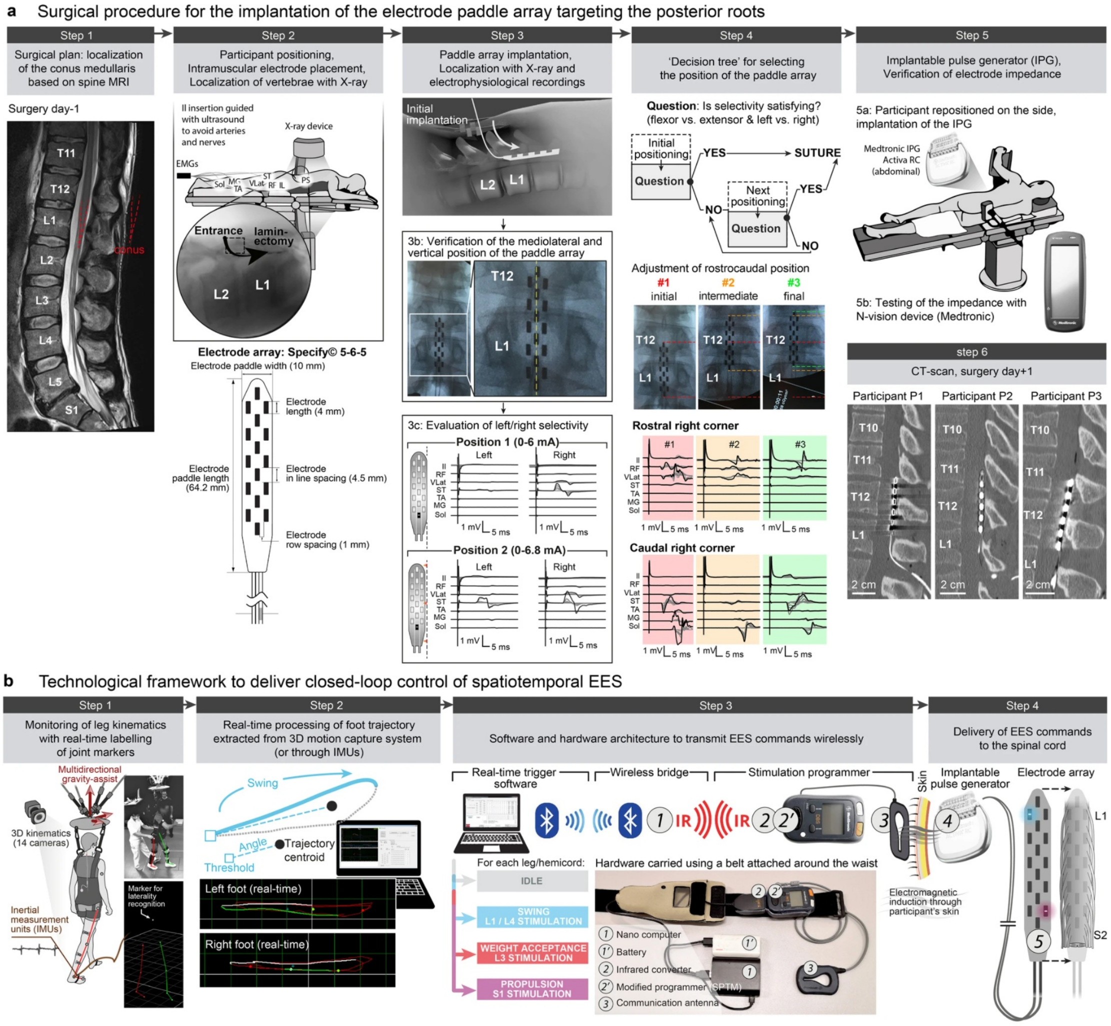
a Surgical procedure for the implantation of the electrode paddle array targeting the posterior roots
Step 1
Surgical plan: localization of the conus medullaris based on spine MRI
Surgery day-1
T11
T12
L1
L2
L3
L4
L5
S1
conus
Step 2
Participant positioning, Intramuscular electrode placement, Localization of vertebrae with X-ray
Il insertion guided with ultrasound to avoid arteries and nerves
X-ray device
EMGs
Sol
MG
TA
VLat
ST
RF
IL
PS
Entrance
lamin-ectomy
L2
L1
Electrode array: Specify© 5-6-5
Electrode paddle width (10 mm)
Electrode length (4 mm)
Electrode paddle length (64.2 mm)
Electrode in line spacing (4.5 mm)
Electrode row spacing (1 mm)
Step 3
Paddle array implantation, Localization with X-ray and electrophysiological recordings
Initial implantation
L2
L1
3b: Verification of the mediolateral and vertical position of the paddle array
T12
L1
3c: Evaluation of left/right selectivity
Position 1 (0-6 mA)
Left
Right
Il
RF
VLat
ST
TA
MG
Sol
1 mV
5 ms
Position 2 (0-6.8 mA)
Step 4
'Decision tree' for selecting the position of the paddle array
Question: Is selectivity satisfying? (flexor vs. extensor & left vs. right)
Initial positioning
Question
YES
SUTURE
NO
Next positioning
Question
YES
NO
Adjustment of rostrocaudal position
#1 initial
#2 intermediate
#3 final
T12
L1
Rostral right corner
#1
#2
#3
Caudal right corner
Step 5
Implantable pulse generator (IPG), Verification of electrode impedance
5a: Participant repositioned on the side, implantation of the IPG
Medtronic IPG Activa RC (abdominal)
5b: Testing of the impedance with N-vision device (Medtronic)
step 6
CT-scan, surgery day+1
Participant P1
Participant P2
Participant P3
T10
T11
T12
L1
2 cm
b Technological framework to deliver closed-loop control of spatiotemporal EES
Step 1
Monitoring of leg kinematics with real-time labelling of joint markers
Multidirectional gravity-assist
3D kinematics (14 cameras)
Inertial measurement units (IMUs)
Marker for laterality recognition
Step 2
Real-time processing of foot trajectory extracted from 3D motion capture system (or through IMUs)
Swing
Angle
Trajectory centroid
Threshold
Left foot (real-time)
Right foot (real-time)
Step 3
Software and hardware architecture to transmit EES commands wirelessly
Real-time trigger software
Wireless bridge
Stimulation programmer
For each leg/hemicord:
IDLE
SWING L1 / L4 STIMULATION
WEIGHT ACCEPTANCE L3 STIMULATION
PROPULSION S1 STIMULATION
1
IR
IR
2
2′
3
Hardware carried using a belt attached around the waist
1 Nano computer
1′ Battery
2 Infrared converter
2′ Modified programmer (SPTM)
3 Communication antenna
Skin
Electromagnetic induction through participant's skin
Step 4
Delivery of EES commands to the spinal cord
Implantable pulse generator
4
Electrode array
5
L1
S2

Figure 4.2: Surgical procedure and technological framework. a, Surgery. Step 1: high-resolution MRI for pre-surgical planning. The entry point into the epidural space is based on the position of the conus. Step 2: placement of subdermal and intramuscular needle EMG electrodes for key leg muscles and paraspinal (PS) muscles. A subdermal needle is inserted over the sacrum and used as a return electrode for stimulation. Bottom, schematic of the 16-electrode paddle array. Step 3: surgical openings based on pre-surgical planning, typically between the L1 and L2 vertebrae, which are identified through intraoperative X-ray. The mediolateral positions of the paddle array are evaluated with X-ray and recordings of EMG responses following single pulses of EES delivered to the most rostral or most caudal midline electrodes.

Figure 4.2: (Continued) Step 4: the rostrocaudal position of the paddle array is optimized using EMG responses to single-pulse EES delivered to the electrodes located at each corner of the paddle array. The aim is to obtain strong ipsilateral responses in hip flexors with the most rostral electrodes and strong ipsilateral responses in ankle extensors with the most caudal electrodes. Step 5: implantable pulse generator (IPG) placed within the abdomen. Once connected to the paddle array, the impedance of the electrodes is evaluated to verify that all the components are properly connected. Step 6: post-surgical CT scan showing the location of the paddle array with respect to the vertebrae in each participant. b, Technological framework and surgical procedure. Step 1: participants wear reflective markers that are monitored using infrared cameras. An algorithm assigns the markers to the joints in real-time. Step 2: the spatiotemporal trajectory of the foot around a calculated centre of rotation (centroid, updated every 3 s) is converted into angular coordinates that trigger and terminate EES protocols when a user-defined threshold is crossed. Step 3: EES commands are transmitted to the IPG via Bluetooth (1) to a module that converts them into infrared signals (2), which are then transferred to the stimulation programmer device (2). Step 4: the stimulation programmer transmits EES commands into the IPG (4) via induction telemetry, using an antenna (3) taped to the skin and aligned to the IPG. EES is delivered through the paddle array (5).

We then sought to identify the electrode locations that could target the posterior roots projecting to spinal cord regions underlying these motoneuron activation maps. To guide this process, we developed hybrid computational models (Capogrosso et al., 2013) that we personalized for each participant using high-resolution radiological imaging and advanced modelling software. We performed simulations that estimated the degree of recruitment of each posterior root with each electrode. We thus identified the electrode locations that presented the highest probability of recruiting the posterior roots projecting to each of the targeted spinal cord regions (Fig. 4.3c).

We then implemented a systematic procedure to identify the relevant electrode configurations and optimal stimulation amplitudes (Fig. 4.4). We delivered monopolar pulses of EES at increasing intensities through the subset of electrodes with the highest probability to activate the targeted posterior roots. We projected the amplitude of the muscle responses elicited in each leg into synthetic circular plots that provide a qualitative overview of the spatial selectivity of the stimulation at each intensity (Fig. 4.3d). To quantify this spatial selectivity, we elaborated an algorithm that calculates the relative activation for each of the targeted spinal cord regions. If the selectivity was insufficient, we devised multipolar electrode configurations that steered the electrical field towards the posterior roots projecting to the targeted spinal cord region.

For the three participants, this procedure led to the identification of electrode configurations that targeted the spinal cord regions involved in mobilizing the hip, knee and ankle joints from both legs (Fig. 4.5). Computer simulations confirmed the high correlations between the identified electrode configurations and the recruitment of the posterior roots projecting to each of the targeted spinal cord regions (Fig. 4.5).

Participant	**P1**		**P2**		**P3**	
Gender	m		m		m	
Age (y)	28		35		47	
Years after SCI	6		6		4	
Assessments at study enrollment (Pre) and after rehabilitation period (Post)	Pre	Post	Pre	Post	Pre	Post
Walking index for spinal cord injury (WISCI II score; max. 20)	13	16	6	13	0	0
American Spinal Injury Association Impairment Scale (AIS)	C	D	D	D	C*	C
Neurological level of injury	C7	C8	C4	C4	C7	C7
Upper Extremity Motor Scores:						
C5, elbow flexors (right | left)	5 | 5	5 | 5	5 | 5	5 | 5	5 | 5	5 | 5
C6, wrist extensors (right | left)	5 | 5	5 | 5	5 | 4	4 | 4	5 | 5	5 | 5
C7, elbow extensors (right | left)	5 | 5	5 | 5	4 | 4	4 | 4	5 | 4	5 | 5
C8, finger flexors (right | left)	4 | 4	5 | 4	1 | 0	3 | 1	4 | 4	4 | 5
T1, finger abductors (right | left)	4 | 4	4 | 4	3 | 0	3 | 0	4 | 4	4 | 4
(max. 5 per side)						
Total (max. 50)	46	47	31	33	45	47
Lower Extremity Motor Scores:						
L2, hip flexors (right | left)	2 | 0	4 | 2	2 | 2	3 | 2	0 | 0	0 | 1
L3, knee extensors (right | left)	2 | 0	4 | 3	4 | 4	4 | 4	0 | 0	1 | 0
L4, ankle dorsiflexors (right | left)	4 | 0	4 | 1	2 | 1	4 | 4	0 | 0	0 | 1
L5, long toe extensors (right | left)	4 | 0	4 | 2	1 | 1	2 | 4	0 | 0	0 | 1
S1, ankle plantar flexors (right | left)	2 | 0	4 | 2	4 | 4	5 | 4	0 | 0	0 | 0
(max. 5 per side)						
Total (max. 50)	14	30	25	36	0	4
Light Touch Sensory Scores:						
L1-S2 dermatomes subscore (right | left)	7 | 7	7 | 7	5 | 8	2 | 10	1 | 4	2 | 5
(max. 14 per side)						
Total (max. 112)	75	76	65	71	55	57
Pin Prick Sensory Scores:						
L1-S2 dermatomes subscore (right | left)	0 | 0	0 | 0	4 | 8	1 | 13	0 | 0	0 | 0
(max. 14 per side)						
Total (max. 112)	33	30	65	86	28	28

Table 4.1: Subjects' neurological status according to the International Standards for Neurological Classification of Spinal Cord Injury at study entry and after completion of the five-month training program. *Reason for AIS C classification in spite of motor scores of 0 throughout all lower extremity key muscles is the presence of voluntary anal contraction.

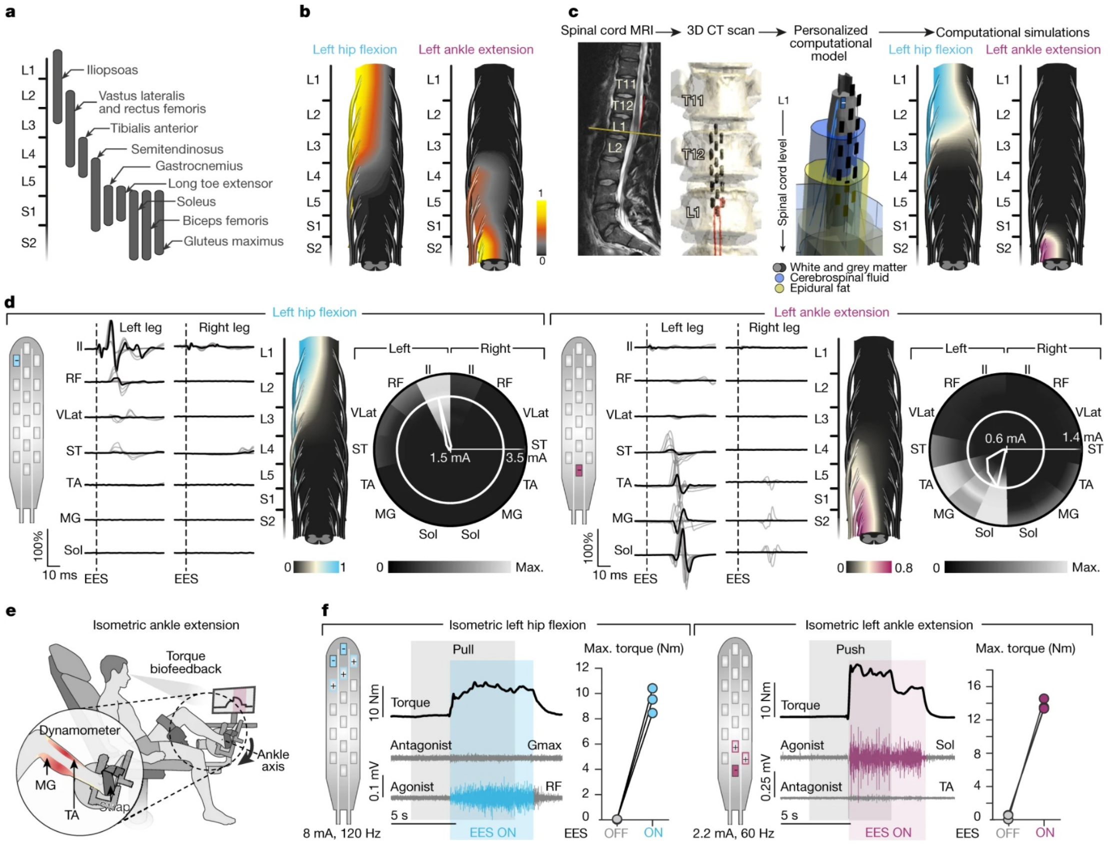

Figure 4.3: Configuration of targeted EES. a, Distribution of motor neuron pools within the spinal cord (Sharrard, 1964). b, Map of motor neuron activation underlying isometric torque production in a healthy subject (consistent across three repetitions and subjects). c, Personalized computational model of EES. Simulated map of motor neuron activation following EES targeting the L1 and S2 posterior roots. d, Electrophysiological experiments were used to determine optimal electrodes and amplitudes for targeting specific spinal cord regions. EMG responses when delivering single-pulse EES at increasing amplitudes are shown (grey traces). Motor neuron activation maps correspond to optimal amplitudes (black traces). Circular plots report EMG amplitude (in grey scale) at increasing amplitudes (radial axis). White circles show optimal amplitudes; polygons quantify selectivity at this amplitude. e, Instrumented chair used to measure single-joint torques. f, Targeted EES enables voluntary force production by paralysed muscles. Isometric torque and EMG activity while delivering targeted EES, including quantification (n = 3 repetitions, P1). Gmax, gluteus maximus; Il, iliopsoas; MG, medial gastrocnemius; RF, rectus femoris; Sol, soleus; ST, semitendinosus; TA, tibialis anterior; VLat, vastus lateralis.

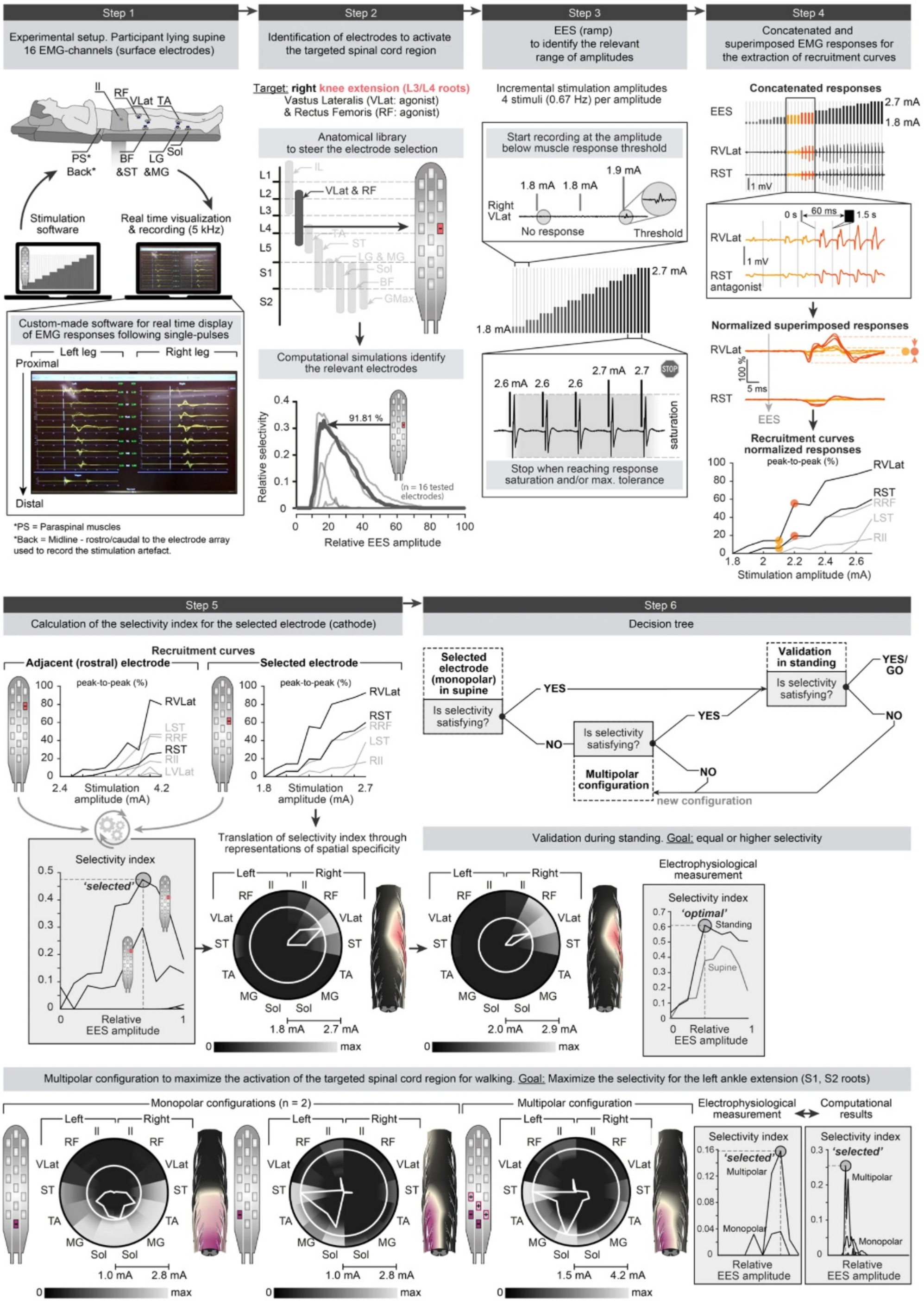
Step 1
Experimental setup. Participant lying supine
16 EMG-channels (surface electrodes)
Il
RF
VLat
TA
PS*
Back*
BF
&ST
LG
&MG
Sol
Stimulation software
Real time visualization & recording (5 kHz)
Custom-made software for real time display of EMG responses following single-pulses
Left leg
Right leg
Proximal
Distal
*PS = Paraspinal muscles
*Back = Midline - rostro/caudal to the electrode array used to record the stimulation artefact.
Step 2
Identification of electrodes to activate the targeted spinal cord region
Target: right knee extension (L3/L4 roots)
Vastus Lateralis (VLat: agonist)
& Rectus Femoris (RF: agonist)
Anatomical library to steer the electrode selection
L1
L2
L3
L4
L5
S1
S2
IL
VLat & RF
TA
ST
LG & MG
Sol
BF
GMax
Computational simulations identify the relevant electrodes
Relative selectivity
0.4
0.3
0.2
0.1
0
91.81 %
(n = 16 tested electrodes)
0
20
40
60
80
100
Relative EES amplitude
Step 3
EES (ramp) to identify the relevant range of amplitudes
Incremental stimulation amplitudes
4 stimuli (0.67 Hz) per amplitude
Start recording at the amplitude below muscle response threshold
1.8 mA
1.8 mA
1.9 mA
Right VLat
No response
Threshold
2.7 mA
1.8 mA
2.6 mA
2.6
2.6
2.7 mA
2.7
STOP
saturation
Stop when reaching response saturation and/or max. tolerance
Step 4
Concatenated and superimposed EMG responses for the extraction of recruitment curves
Concatenated responses
EES
2.7 mA
1.8 mA
RVLat
RST
1 mV
0 s
60 ms
1.5 s
RVLat
1 mV
RST antagonist
Normalized superimposed responses
RVLat
100 %
5 ms
RST
EES
Recruitment curves normalized responses
peak-to-peak (%)
100
80
60
40
20
0
RVLat
RST
RRF
LST
RII
1.8
2
2.2
2.4
2.6
Stimulation amplitude (mA)
Step 5
Calculation of the selectivity index for the selected electrode (cathode)
Recruitment curves
Adjacent (rostral) electrode
Selected electrode
peak-to-peak (%)
100
80
60
40
20
0
RVLat
LST
RRF
RST
RII
LVLat
2.4
Stimulation amplitude (mA)
4.2
RVLat
RST
RRF
LST
RII
1.8
Stimulation amplitude (mA)
2.7
Selectivity index
0.5
0.4
0.3
0.2
0.1
0
'selected'
0
Relative EES amplitude
1
Translation of selectivity index through representations of spatial specificity
Left
Right
Il
Il
RF
RF
VLat
VLat
ST
ST
TA
TA
MG
MG
Sol
Sol
1.8 mA
2.7 mA
0
max
Step 6
Decision tree
Selected electrode (monopolar) in supine
Is selectivity satisfying?
YES
NO
Is selectivity satisfying?
YES
NO
Multipolar configuration
new configuration
Validation in standing
Is selectivity satisfying?
YES/ GO
NO
Validation during standing. Goal: equal or higher selectivity
2.0 mA
2.9 mA
0
max
Electrophysiological measurement
Selectivity index
0.7
0.6
0.5
0.4
0.3
0.2
0.1
0
'optimal'
Standing
Supine
0
Relative EES amplitude
1
Multipolar configuration to maximize the activation of the targeted spinal cord region for walking. Goal: Maximize the selectivity for the left ankle extension (S1, S2 roots)
Monopolar configurations (n = 2)
1.0 mA
2.8 mA
0
max
1.0 mA
2.8 mA
0
max
Multipolar configuration
1.5 mA
4.2 mA
0
max
Electrophysiological measurement
Computational results
Selectivity index
0.16
0.12
0.08
0.04
0
'selected'
Multipolar
Monopolar
Relative EES amplitude
Selectivity index
0.3
0.2
0.1
0
'selected'
Multipolar
Monopolar
Relative EES amplitude

Figure 4.4: Identification of electrode configurations to target selected posterior roots.

Figure 4.4: (Continued) Step 1: single-pulse EES and EMG recording setup. Step 2: Motoneuron pools are located in specific segments, which informs on the relative recruitment of each posterior root with EES. For example, electrodes targeting the L3/L4 posterior roots will elicit the strongest EMG responses in the knee extensors. A personalized computational model of EES allows the performance of simulations that evaluate the relative activation of a given posterior root with a given electrode over the entire range of amplitude. Each curve corresponds to an electrode. The highlighted curve corresponds to selected electrode after Step 3-5. Step 3: Single pulses of EES are delivered through the subset of electrodes identified with simulations. The EMG responses are recorded over a broad range of EES amplitude. Step 4: The EMG responses are concatenated, averaged for each EMG amplitude, and the peak-to-peak amplitude of the average responses calculated to elaborate a recruitment curve for each recorded leg muscles (black traces: targeted muscles). Step 5: The polar plots display the normalized EMG responses (greyscale) when delivering single–pulse EES at increasing amplitudes (radial axis), where the white circle highlights the optimal EES amplitude and the polygon quantifies the relative muscular selectivity at this amplitude. The motoneuron activation maps are shown for the optimal amplitudes. Step 6: Decision tree to validate or optimize electrode configurations. The selected electrode is tested during standing since the position of the paddle array with respect to the spinal cord can change between supine and standing. In this example, the selectivity improves during standing. When the selectivity is not deemed sufficient, the current is steered toward the targeted posterior roots using multipolar configurations. The example shows the increased selectivity of a multipolar configuration with 2 cathodes surrounded by 3 anodes, compared to the 2 corresponding monopolar configurations. These results are verified experimentally and with computer simulations.

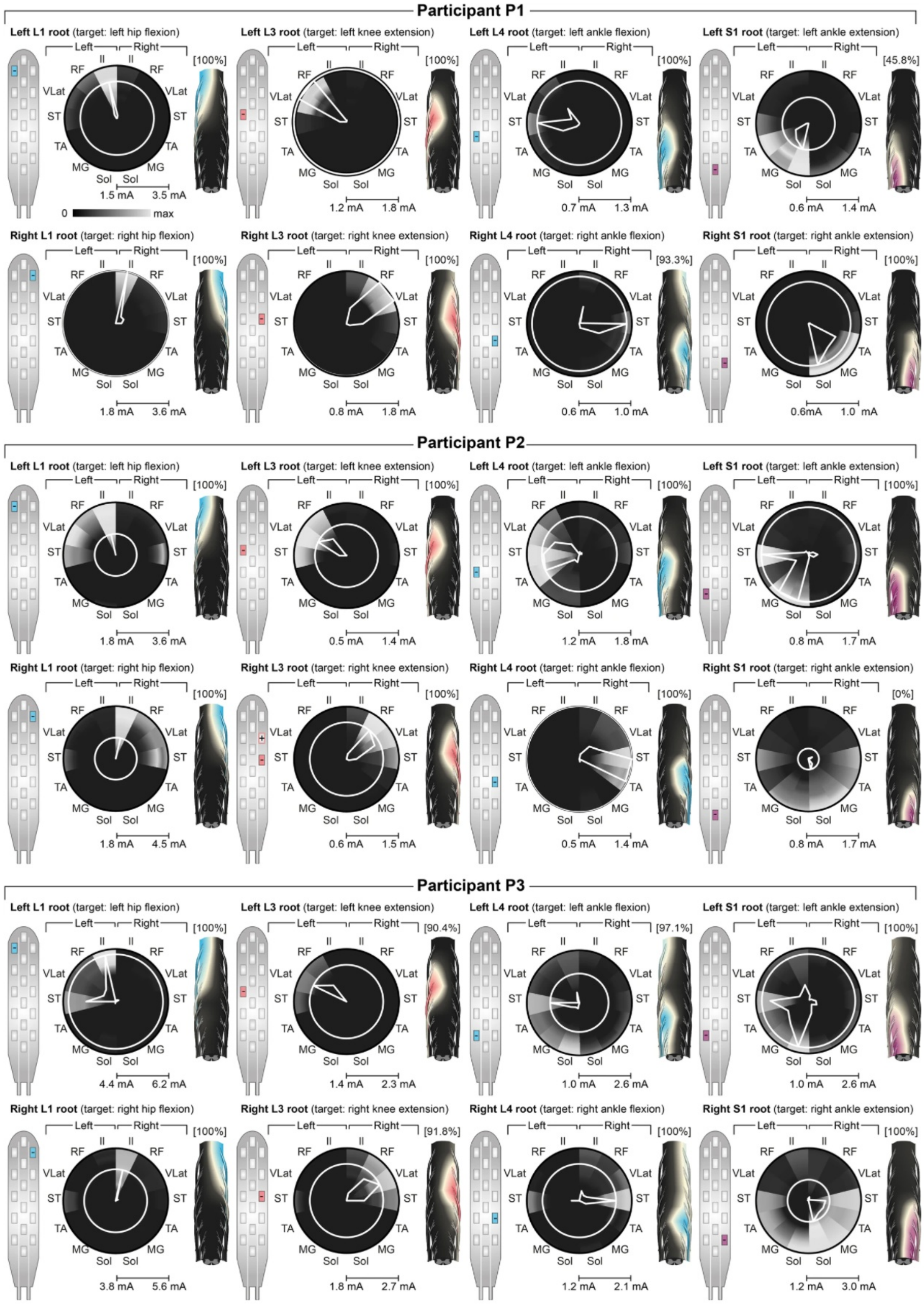

Figure 4.5: Spatial selectivity of targeted electrode configurations.

Figure 4.5: (Continued) Monopolar configurations (shown on paddle array schematics) experimentally selected to target the left and right posterior roots associated with hip flexion (L1), knee extension (L3), ankle flexion (L4) and ankle extension (S1) for the three participants. The circular plots and motor neuron activation maps use the same conventions as in Fig. 4.3 and Fig. 4.4 (median of n = 4 pulses). The normalized selectivity index is reported above each motor neuron activation map. This index represents the percentage of posterior root selectivity for the electrode configuration selected experimentally, with respect to the maximum posterior root selectivity that can be achieved among all monopolar configurations (all selectivity indices obtained from computational simulations). Note that in P2, the electrode selected experimentally to target the right S1 root was located on the midline and resulted in bilateral activation within computational.

4.3.4 Targeted electrical stimulation enables control over the movement of single joints

We next tested whether the delivery of EES through the identified electrode configurations mediated the expected facilitation of the intended leg movements.

While seated in a standardized position, participants were required to produce an isometric force restricted to a single joint (Fig. 4.3e). Fig. 4.3f shows attempts to produce hip flexion and ankle extension torques with the left leg in participant P1 who could not activate any muscles of this leg without stimulation. EES immediately enabled voluntary activation of the targeted muscles without undesired coactivation of other muscles, which produced a substantial torque at the targeted joint.

Without voluntary attempts to activate muscles, EES induced minimal muscle contraction. With the selected amplitudes, EES augmented the excitability of the targeted motoneuron pools, which enabled residual yet dormant descending inputs to activate the muscles and thus perform the intended movements.

The same results were obtained for all the targeted joints in all the participants. However, the facilitation was variable across joints and participants, as expected based on the highly variable neurological deficits (Fig. 4.6).

4.3.5 EES modulates cortical processes involved in producing movement

These results opened the possibility that the recruitment of sensory pathways with EES directly modulates cortical excitability, which may facilitate the production of movement (Asanuma & Mackel, 1989).

To study this hypothesis, we recorded ElectroEncephaloGraphic (EEG) activity when the participants attempted to produce a knee extension torque without and with EES. Between 90 and 140 ms after the onset of EES, the sensorimotor cortex displayed a robust response (Fig. 4.9a), which likely resulted from the recruitment of sensory afferents (Berić et al., 1986).

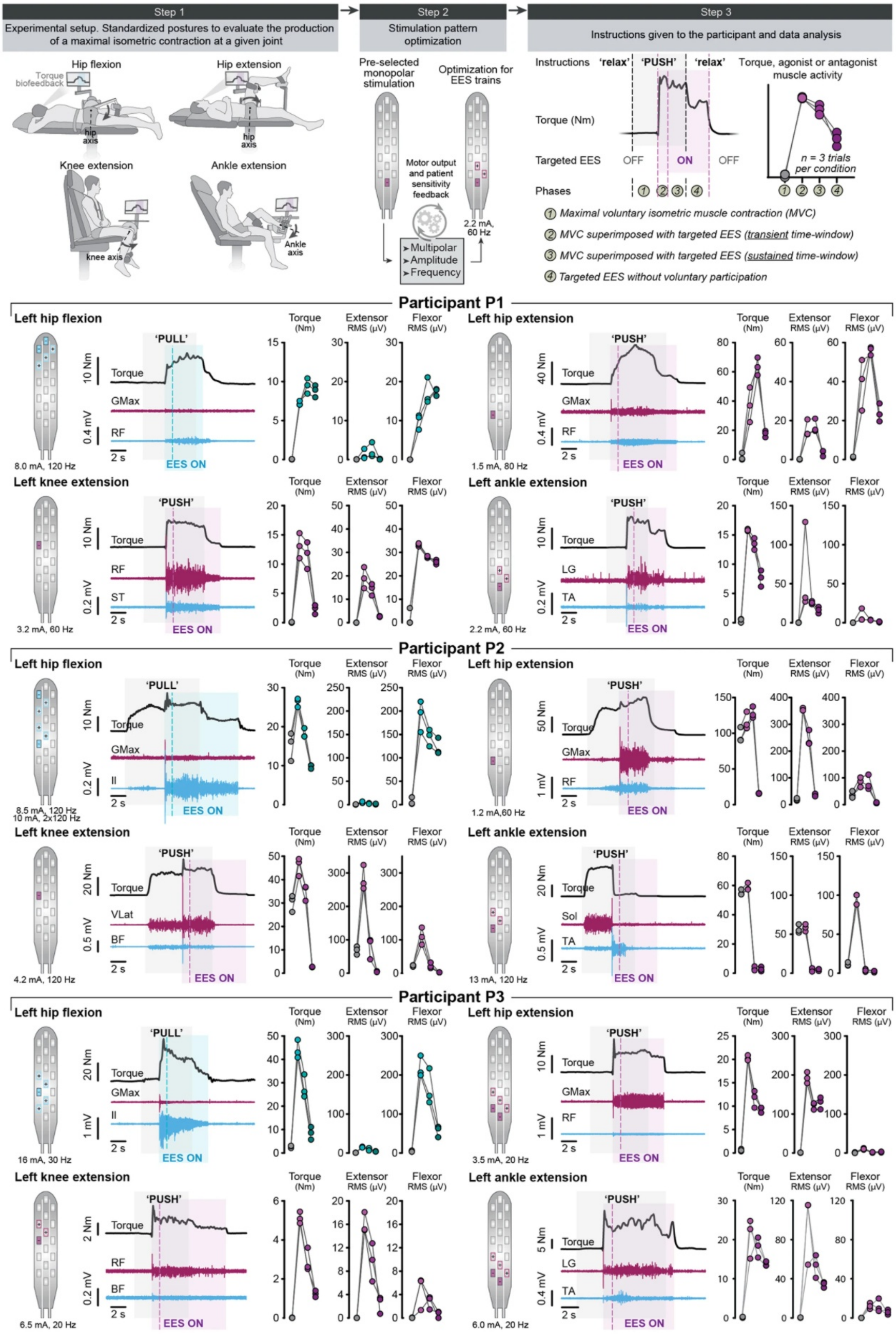

Figure 4.6: Single-joint movements enabled by targeted EES.

Figure 4.6: (Continued) Step 1: participants are placed in standardized positions to allow assessment of voluntary torque production at a single joint (isometric contractions) without and with targeted EES. Step 2: EES protocols elaborated from single-pulse experiments (Figs. 4.3, 4.7) are optimized for each task using multipolar configurations and adjustments of EES amplitude and frequency. Step 3: sequence of each trial. Participants were asked to produce a maximal voluntary contribution, but failed in most cases, as evidenced by the absence of EMG activity during this period. While they continued trying to activate the targeted muscle, EES was switched on. After a few seconds, participants were instructed to stop their voluntary contribution. After a short delay, EES was switched off. For each sequence, the produced torque and EMG activity of the key agonist and antagonist muscles acting at the targeted joint were calculated over the four indicated phases of the trial. Plots report the measured torques and EMG activity during the various phase of the trial for the left legs of all participants for the four tested joints (cyan, flexor; magenta, extensor), together with EES parameters and electrode configurations. All measurements were performed before rehabilitation, except for hip extension in P1 and P2 (not tested before), and ankle extension in P3 (no capacity before rehabilitation), which were carried out after rehabilitation. Targeted EES enabled or augmented the specific recruitment of the targeted muscle, which resulted in the production of the desired torque at the targeted joint, except for ankle extension of P2. Plots show quantification of the EMG activity and torque for n = 3 trials per condition. Note that hip flexion can be enabled or augmented with EES targeting L1 and/or L4 posterior.

Both without and with EES, attempts to activate right knee extensor muscles led to an Event–Related Desynchronization (ERD) of the left sensorimotor cortex in β–band frequencies. This cortical activity has been linked to movement execution, and is normally followed by an Event–Related reSynchronization (ERS) immediately after movement termination (Gourab & Schmit, 2010). The amplitude of ERS decreases proportionally to SCI severity (Gourab & Schmit, 2010). When regaining the ability to active leg muscles voluntarily with EES, the three participants displayed an increase in ERS amplitude that scaled up with their neurological deficits (Fig. 4.9b).

While the mechanisms underlying this sudden change in cortical dynamics requires further investigation, these results suggest that EES enhances cortical excitability in a way that allows a more natural dynamics during movement execution.

4.3.6 Spatiotemporal stimulation restores the sequence of motoneuron activation for walking

In healthy individuals, walking involves reproducible sequences of muscle activation (Fig. 4.7a). The projection of this EMG activity onto the spinal cord yielded spatiotemporal maps of motoneuron activity that revealed the successive activation of three well-defined hotspots located in specific regions of the spinal cord. The migration of these hotspots reflect body mechanics (Cappellini et al., 2010), successively ensuring weight acceptance, propulsion and swing (Fig. 4.7b).

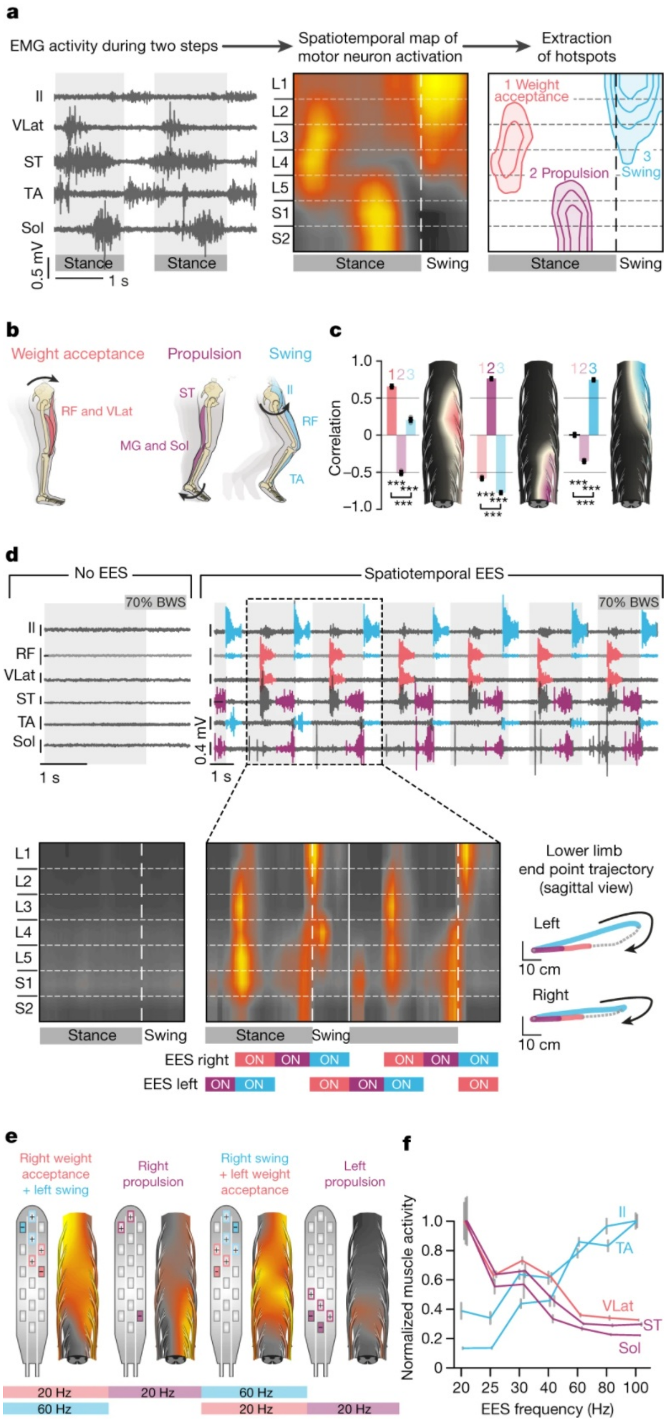

Figure 4.7: Configuration of spatiotemporal EES for walking. a, EMG activity during walking in healthy individuals. Spatiotemporal map of motor neuron activation highlights hotspots (mean, n = 12 gait cycles, representative subject). Equipotential lines represent 45–75% activation. b, Functional target of each hotspot. c, Map of motor neuron activation following 500-ms bursts of targeted EES during standing. Bar plots show Pearson's correlations for each hotspot (mean ± s.e.m., n = 12 bursts, ***P < 0.001; one-way ANOVA, post hoc Tukey's Honest Significant Difference (HSD) test). d, EMG activity and map of motor neuron activation during EES or without EES after a motor complete SCI while stepping on a treadmill with support and assistance (P3). EES timing is indicated along foot trajectories (bottom right; n = 73 steps) and below motor neuron activation maps. e, Spatiotemporal EES sequence for data shown in d. f, Mean (± s.e.m.) modulation of EMG amplitude in flexor and extensor muscles during walking with increasing EES frequencies (n = 20, 15, 16, 17, 15, 16, 15 gait cycles for 20, 25, 30, 40, 60, 80, 100 Hz, respectively; P3).

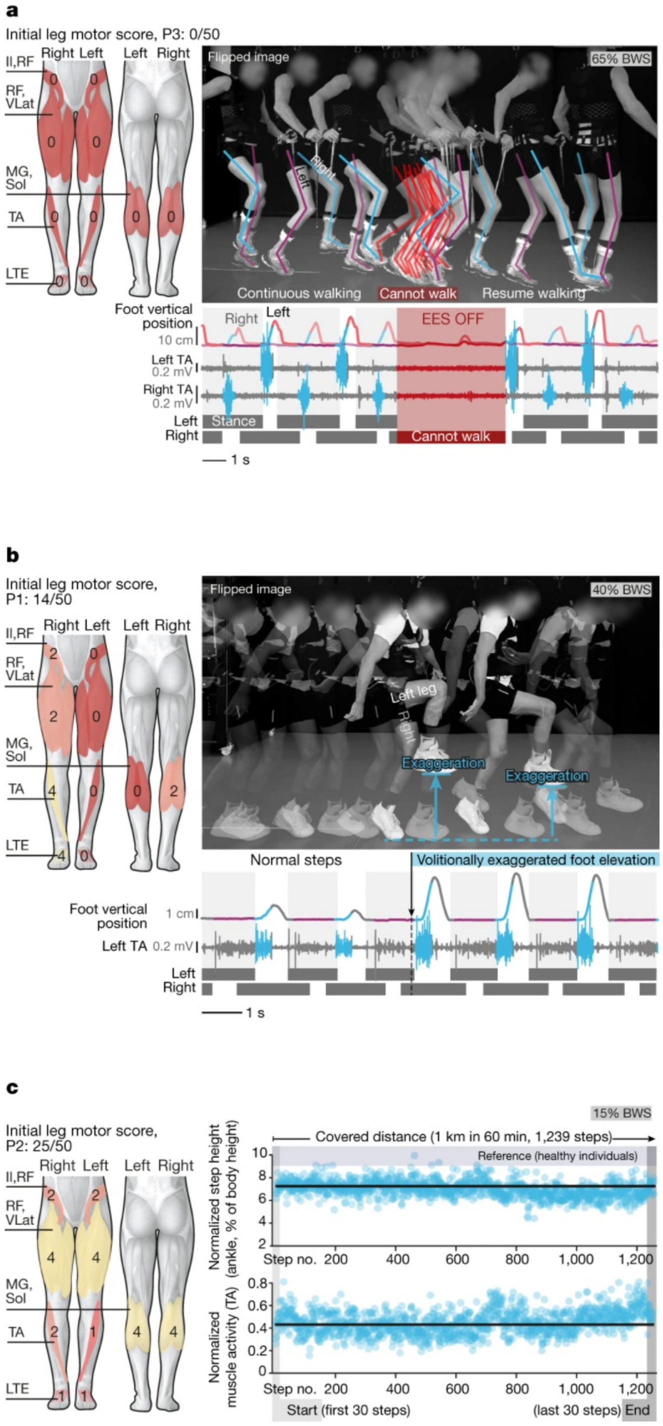

Figure 4.8: Voluntary control of adaptive and sustained locomotion. a, Spatiotemporal EES enables voluntary control of overground walking. Chronophotography, tibialis anterior (TA) EMG activity and foot vertical position during overground walking with gravity-assist and sticks while EES is switched on, then off, then on. Leg motor scores shown on muscles in diagrams: 0, total paralysis; 1, palpable or visible contraction; 2, active movement, gravity eliminated; 3, active movement against gravity; 4, active movement against some resistance; 5, active movement against full resistance. b, Spatiotemporal EES enables voluntary control of leg kinematics. Overground walking when participants were requested to perform steps with normal heights and then exaggerated step elevations. c, Spatiotemporal EES enables sustained walking. Consecutive values of step height and EMG activity over 60 min of walking with EES (P1: 1.2 km; P2, P3: 1 km). Experiments in a, b were repeated at least five times; the experiment in c was performed once, but participants routinely walked for 60 min during training. BWS, bodyweight support.

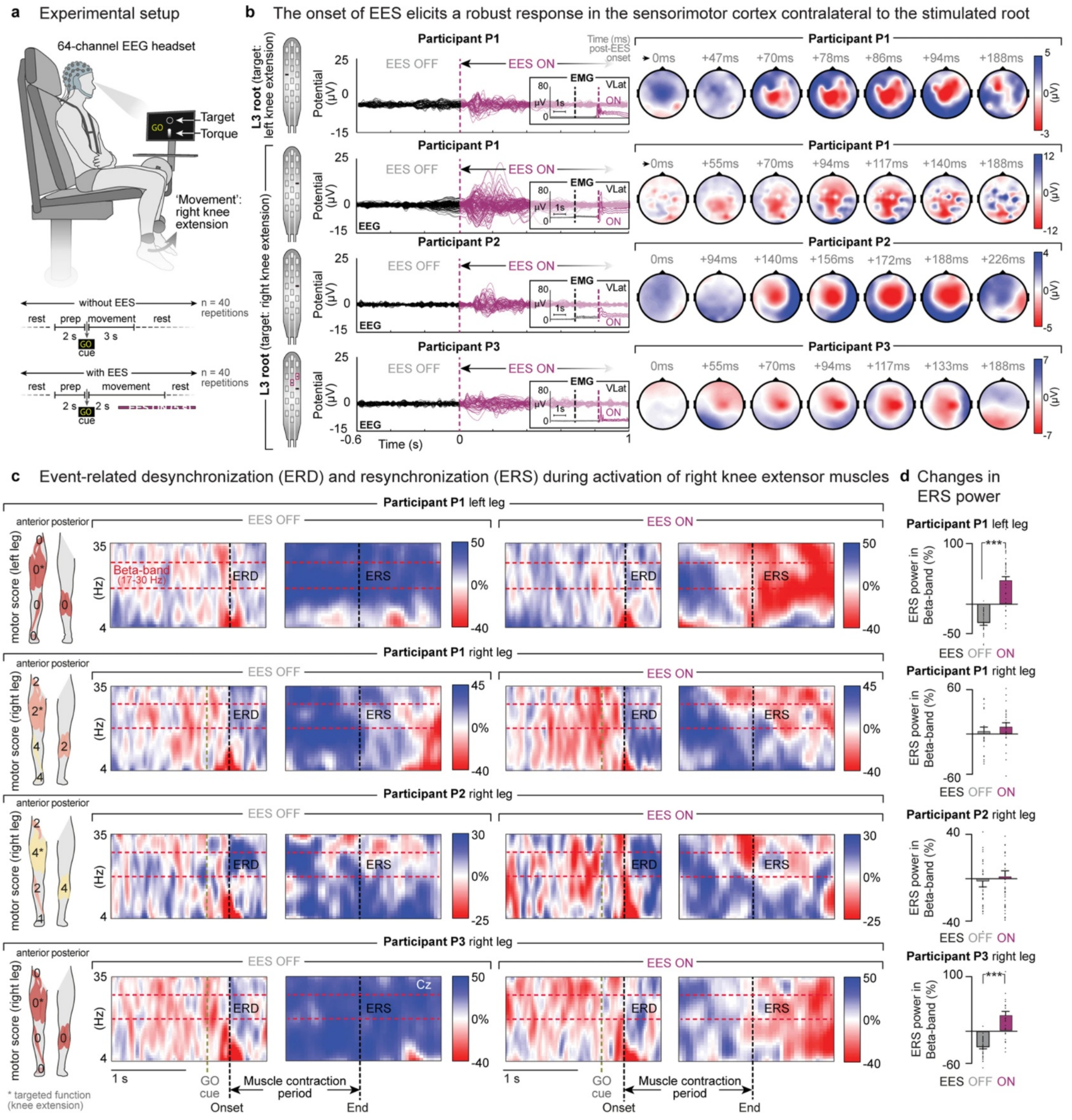

Figure 4.9: Modulation of EEG activity during volitional contraction of leg muscles without and with EES. a, Recordings of EEG activity while participants were asked to produce an isometric torque at the knee joint without and with continuous EES targeting motor neuron pools innervating knee extensors, as shown in b. b, Superimposed EEG responses (n = 40 repetitions) and temporal changes in the topography of average activity over the cortical surface after the onset of EES, as indicated above each map. The onset was calculated from the onset of EMG responses in the targeted vastus lateralis muscle (insets). The stimulation elicited a robust event-related response over the left sensorimotor cortex with a latency of 90 ± 40 ms for P1 and P3, and of 170 ± 40 ms for P2 (full range of the peaks and middle of this range indicated). c, Average normalized time–frequency plots (n = 40 trials) showing ERD and ERS over the Cz electrode (central top electrode) for each individual during the voluntary activation of knee extensor muscles without and with EES. Schematic drawings (left) indicate the motor scores of the tested legs, including the targeted muscles (*), at the time of enrolment in the study. Both legs were tested in P1 owing to his asymmetric deficits.

Figure 4.9: (Continued) d, Normalized average power (mean ± s.e.m.) of the β-band over the Cz electrode during ERS from 0 to 500 ms after termination of contraction without and with continuous EES (n = 40 repetitions for each condition, individual data points shown except for outliers more than 3 median absolute deviations away from the median). ***P < 0.001 (permutation tests, see Methods).

To reproduce this sequence of hotspot activation, we selected the electrode configurations that targeted these specific regions. We found high correlations between each hotspot and the activated spinal cord region with targeted EES (Fig. 4.7c).

To optimize the sequence over which EES trains are delivered to facilitate walking (Fig. 4.7d-e), we fine-tuned the timing of each train using a closed–loop controller that triggered stimulation based on foot trajectory (Wenger et al., 2016; Wenger et al., 2014). We thus adjusted the onset and duration of each train to approach the spatiotemporal sequence of motoneuron activation underlying walking in healthy individuals (Fig. 4.10).

To tune the relative activation of muscles, we adjusted the amplitude and frequency of each stimulation train (Fig. 4.10). As previously reported in animal models (Wenger et al., 2016; Wenger et al., 2014), we found a linear relationship between the stimulation frequency and amplitude of flexor muscle activity (Fig. 4.7f), such that increasing the frequency enhanced whole-limb flexion proportionally (Fig. 4.10). Unexpectedly, extensor motoneuron pools responded oppositely to increases in frequency. Proprioceptive afferents establish profuse direct synaptic contacts onto extensor motoneurons, whereas these afferents primarily recruit flexor motoneurons through interneurons (Pierrot-Desseilligny & Burke, 2012; Schieppati, 1987). Monosynaptic projections onto motoneurons are highly sensitive to low-frequency depression (Schindler-Ivens & Shields, 2000), which may explain the negative response of extensor motoneurons to increases in frequency.

Within less than 5 days and despite more than four years of muscle paralysis, this procedure led to spatiotemporal stimulation sequences (Fig. 4.7e) that enabled EMG activity underlying locomotion in otherwise quiescent (Fig. 4.7d) or poorly active leg muscles during stepping on a treadmill (Fig. 4.11). The corresponding spatiotemporal maps of motoneuron activation resembled those of healthy individuals. Analysis of EMG signals in the three participants confirmed that each train of EES induced the activation of, or a significant increase in, the activity of the targeted muscles during the targeted temporal window (Fig. 4.11).

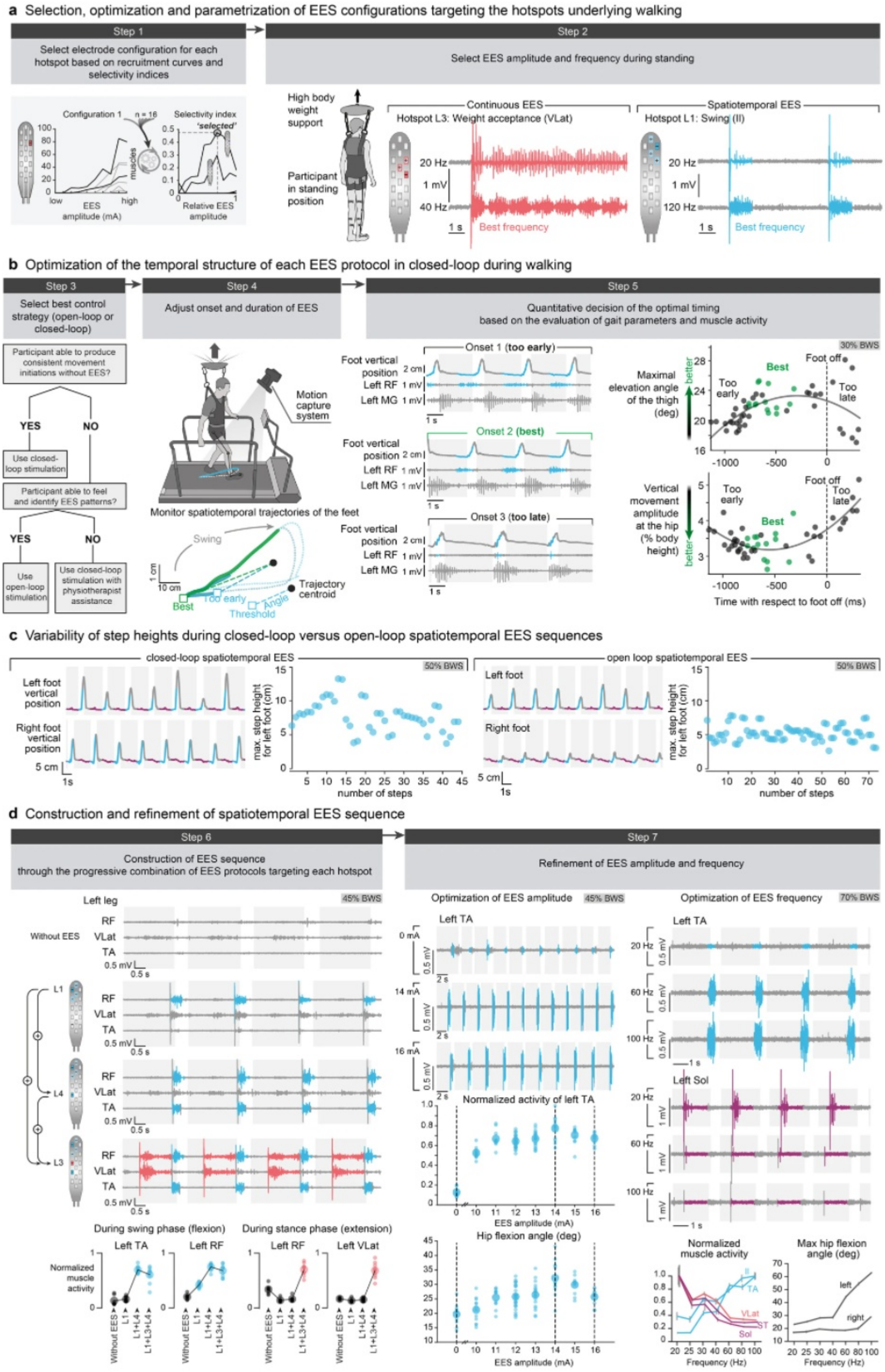

Figure 4.10: Configuration of spatiotemporal EES to enable walking.

Figure 4.10: (Continued) a, Spatial configuration. Step 1: select electrode configurations from single-pulse experiments to target the three hotspots underlying the production of walking in healthy individuals (weight acceptance: L3; propulsion: S1; swing: L1/L4). Step 2: optimize EES amplitude and frequency while delivering EES during standing. Multipolar configurations can be used to refine selectivity of EES protocols. Example shows continuous EES targeting the right L3 posterior root to facilitate right knee extension during standing, and trains (500 ms) of EES targeting the right L1 posterior root stimulation to facilitate hip flexion. Two EES frequencies are shown (P3). b, Temporal configuration. Step 3: decision tree to select the best strategy to configure the temporal structure of EES protocols. If the participant is able to initiate leg movements consistently, use closedloop EES based on real-time processing of foot trajectory. If the participant is not able to initiate consistent leg movements but can feel when EES is applied, use open-loop EES. If the participant is not able to generate movement and cannot feel EES, use closed-loop EES combined with physiotherapist assistance to move the legs. Step 4: real-time monitoring of the spatiotemporal trajectory of the feet. The trajectory is modelled as a foot rotating in space around the centroid of the movement (updated every 3 s). Angular thresholds determine the onset and end of EES protocols. Step 5: example showing the effect of three different angular thresholds on the onset of EES and resulting kinematics and EMG activity, including the quantification of kinematics for each step and condition that enables selecting the optimal onset of EES trains (P1). The same approach is used to optimize the duration of each train. c, Comparisons between closed-loop and open-loop EES. Plots show the vertical displacements of the left and right feet and successive step heights during walking with spatiotemporal EES delivered in closed loop versus open loop, showing the reduced variability of step height during pre-programmed EES sequences (P1). d, Resulting EMG patterns. Step 6: example of the progressive addition of EES protocols targeting specific hotspots. Plots show the quantification of EMG activity for the displayed muscles (n = 7 gait cycles for no EES and n = 9 gait cycles for each stimulation condition, P2). Step 7: EES amplitudes and frequencies are adjusted to avoid detrimental interactions between the different EES protocols and thus obtain the desired kinematic and EMG activity. Plots report the modulation of EMG activity and kinematics with increases in EES amplitude and frequency (mean ± s.e.m.; amplitude data: n = 10, 12, 12, 30, 19, 12, 11, 10 gait cycles for amplitudes in increasing order, P2; frequency data: n = 20, 15, 16, 17, 15, 16, 15 gait cycles for frequencies in increasing order, P3).

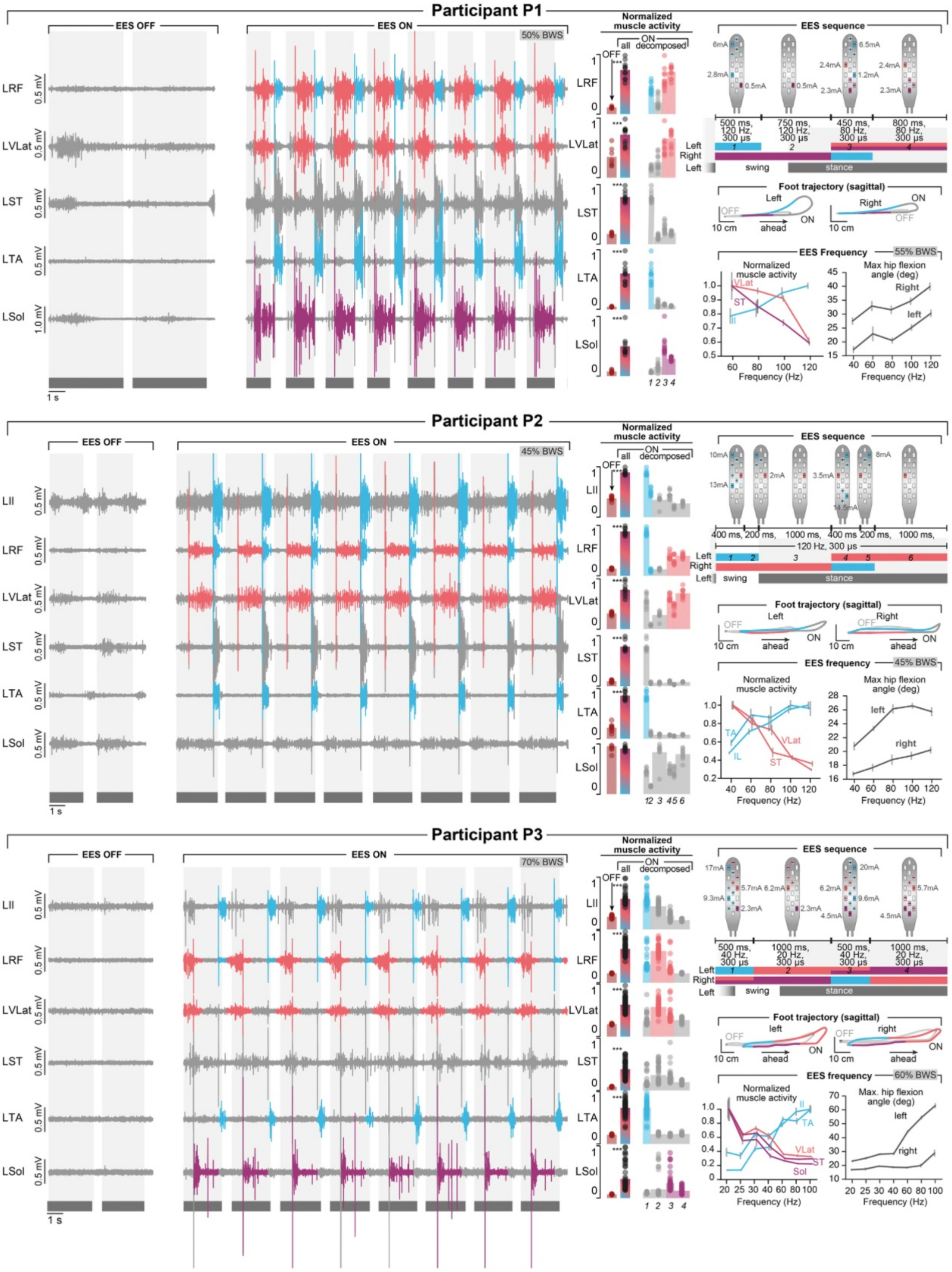

Figure 4.11: Targeted modulation of muscle activity during walking.

Figure 4.11: (Continued) Each panel reports the same representative data and quantification for one participant. Left, EMG activity of leg muscles during walking on a treadmill without EES (EES OFF) and with spatiotemporal EES (EES ON) while applying 50%, 45% and 70% body weight support for participants P1, P2 and P3, respectively. Stance and swing phases are indicated by grey and white backgrounds, respectively. The personalized spatiotemporal EES sequence (open loop) is schematized at the top right. The colours of each EES protocol refer to the targeted hotspots: weight acceptance (salmon), propulsion (magenta) and swing (cyan). These colours are used in the EMG traces to indicate the temporal window over which each targeted EES protocol is active. The bar plots report the amplitude of muscle activity without EES and with spatiotemporal EES, for which the quantification was performed over the entire burst of EMG activity and during each temporal window with targeted EES. The temporal windows are labelled with a number that refers to the spatiotemporal EES sequence. These results show the pronounced increase in the EMG activity of the targeted muscles (P1, no EES: n = 7 gait cycles, EES: n = 11 gait cycles; P2, no EES: n = 9 gait cycles, EES: n = 9 gait cycles; P3, no EES: n = 10 gait cycles, EES: n = 57 gait cycles). The average spatiotemporal trajectories of both feet with respect to the hip in the sagittal plane are shown for walking without EES and with spatiotemporal EES. The presence of targeted EES is indicated with the same colour code. Plots at bottom right show the relationships between EES frequency and the modulation of the EMG activity of flexor (blue) and extensor (magenta or salmon) muscles and maximum amplitude of hip movements during walking (mean ± s.e.m.; P1: n = 14, 17, 15, 19 gait cycles for increasing frequencies; P2: n = 13, 16, 10, 17, 12 gait cycles for increasing frequencies; P3: n = 20, 15, 16, 17, 15, 16, 15 gait cycles for increasing frequencies). ***P < 0.001. Student's t-test.

4.3.7 Voluntary control of adaptive and sustained locomotor movements overground

We next evaluated the functional impact of these spatiotemporal stimulation sequences on the ability of the three participants to walk actively overground, produce task-specific adaptations of leg movements and sustain locomotion over extensive periods of time. The active production of sustained, task-specific movements constitutes the fundamental principle of activity–based physical therapies.

Participants were asked to walk overground with the gravity-assist and spatiotemporal stimulation. The stimulation enabled all three participants to walk voluntarily until the stimulation was stopped, which arrested locomotion immediately. They resumed locomotion upon their will as soon as the stimulation was reintroduced (Fig. 4.8a , Fig. 4.12).

We next investigated their ability to produce voluntary adjustments of leg movements. We used two paradigms. First, we asked the participants to produce exaggerated step elevations during locomotion. Those who failed to walk without stimulation were able to enhance their step elevation three to fivefold compared to regular steps during otherwise constant spatiotemporal EES parameters (Fig. 4.8b and Fig. 4.12). Second, we asked them to walk on a treadmill over a range of speeds while delivering spatiotemporal EES with a constant rhythm. Not only were the participants able to adjust their stride length to the current speed, but they also could stop and stand despite the treadmill belt motion and ongoing stimulation (Fig. 4.12).

Finally, we asked them to walk on a treadmill for one hour. All three participants sustained more than 1200 steps during this period, without showing exhaustion of muscle activity or impairments in locomotor performance over time (Fig. 4.8c and Fig. 4.12).

These combined results show that spatiotemporal EES not only enabled completely or partially paralyzed individuals to walk overground, but also allowed them to produce voluntary adjustments of leg movements that supported standing and walking over a range of speeds for durations as long as one hour.

4.3.8 Continuous stimulation failed to facilitate locomotor movements

Previous studies showed that continuous EES of the spinal cord induces rhythmic patterns of leg muscle activity when therapists manually assist leg movements on a moving treadmill belt (Angeli et al., 2014; Barolat et al., 1986; Schieppati, 1987). However, this activity did not translate into overground walking.

We found similar results in our participants. Continuous widespread EES enhanced muscle activity during assisted stepping on a treadmill, but this stimulation poorly facilitated voluntary locomotion overground. Moreover, all the participants reported a loss of limb position awareness combined with unpleasant sensations and functionally detrimental co-activation across muscles, which was confirmed in EMG recordings (Fig. 4.14).

4.3.9 Rehabilitation improves walking capabilities with stimulation

The participants followed a rehabilitation program four to five times per week for five months, combining stepping on a treadmill, walking overground, strengthening of individual muscles and standing—each enabled by task–specific EES sequences (Fig. 4.15a).

During EES, all three participants increased their overground walking capacities. Improvements followed a reproducible chronology: the non–ambulatory participants initially necessitated crutches and the gravity-assist to walk overground (Fig. 4.15b). After one to three months, they could walk hand–free when provided with hip movement assistance in the gravity-assist. Eventually, P1 and P2 regained independent walking while 35% of their bodyweight was supported against gravity (Fig. 4.15c). P3 necessitated a walker to progress freely overground with EES and the gravity-assist for safety only (Fig. 4.13a).

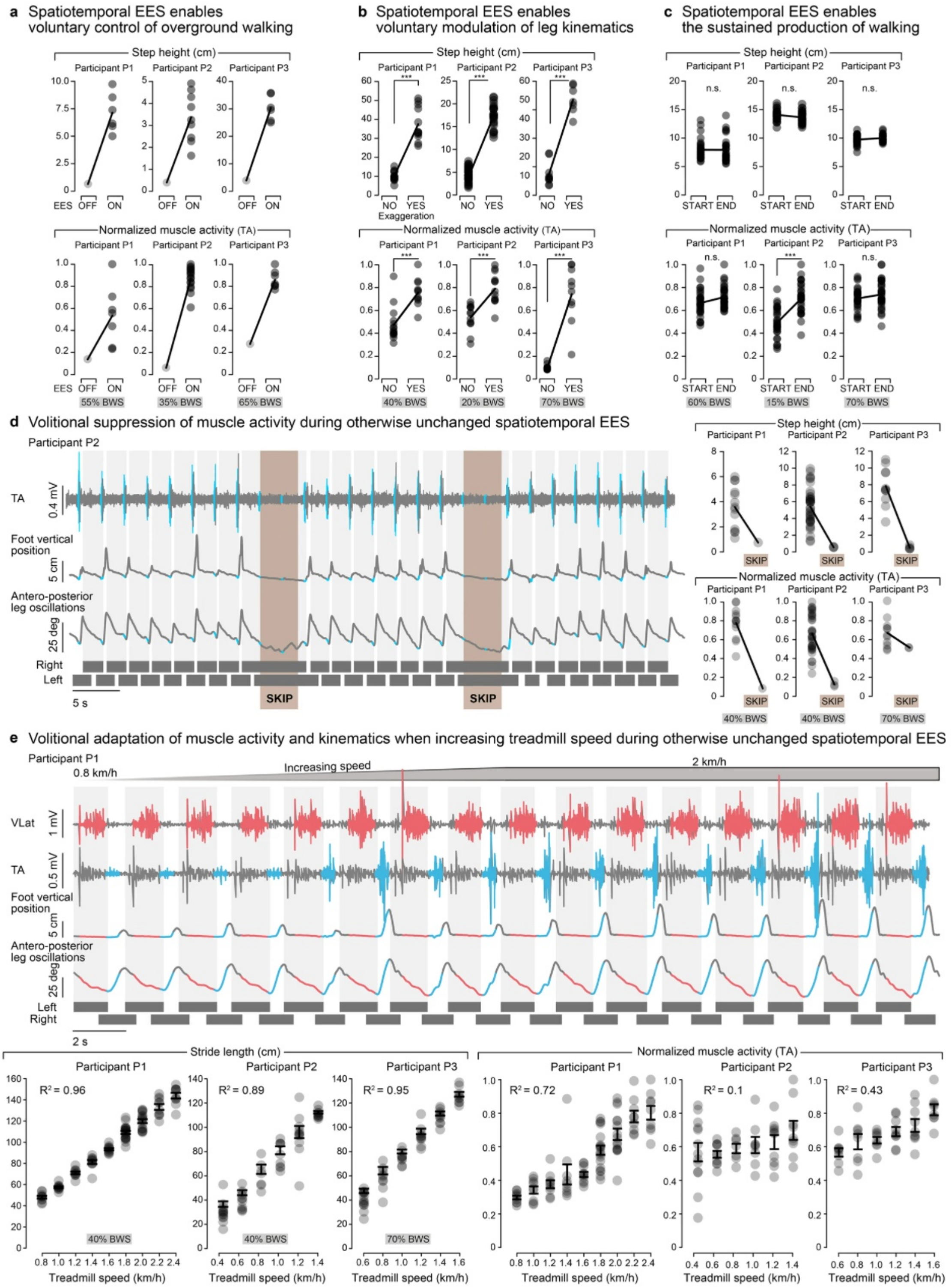

Figure 4.12: Volitional adaptations of walking during otherwise unchanged spatiotemporal EES.

Figure 4.12: (Continued) a–c, Quantifications of experiments shown in Fig. 4.8a–c for each participant. a, Step height and TA EMG activity with and without EES during overground walking (P1, EES ON: n = 7 gait cycles; P2, EES ON: n = 16 gait cycles; P3, EES ON, n = 7 gait cycles). b, Step height and TA EMG activity during normal steps and when participants were requested to perform exaggerated step elevations during overground walking (P1, n = 15 normal gait cycles, n = 11 exaggerated gait cycles; P2, n = 31 normal gait cycles, n = 23 exaggerated gait cycles; P3, n = 14 normal gait cycles, n = 10 exaggerated gait cycles). c, Step height and TA EMG activity during the first and last 30 steps extracted from a sequence of 1 h of locomotion on a treadmill (n = 30 gait cycles for all conditions). ***$P < 0.001$; n.s., non-significant; Student's t-test. d, EMG activity of representative leg muscles, vertical displacements of the foot and anteroposterior oscillations of the leg (virtual limb joining the hip to the foot) while P2 was walking continuously on the treadmill with spatiotemporal EES (open loop). The participant was asked to suppress the effects of EES and stand during one cycle of open-loop spatiotemporal EES sequence, highlighted in brown (SKIP), whereas he actively contributed to the production of movement the rest of the time. Plots report the quantification of step height and TA EMG activity during walking and when skipping steps for each participant (P1, n = 13 normal gait cycles, n = 1 skipped cycles; P2, n = 36 normal gait cycles, n = 3 skipped gait cycles; P3, n = 11 normal gait cycles, n = 2 skipped cycles). e, EMG activity of two representative muscles, vertical displacements of the foot and anteroposterior oscillations of the leg while P1 was walking on the treadmill and the speed of the belt increased progressively from 0.8 to 2 km h–1. Plots show relationships between treadmill speed and mean stride length and TA EMG activity in all participants (P1: n = 9, 9, 9, 9, 10, 18, 15, 9, 9 gait cycles for increasing speeds; P2: n = 13, 10, 7, 8, 10, 9 gait cycles for increasing speeds; P3: n = 8, 8, 10, 9, 9, 8 gait cycles for increasing speeds; s.e.m. shown). The range of tested speeds was adapted to the walking ability of each participant.

4.3.10 Rehabilitation promotes neurological recovery and restores walking without stimulation

Without EES, participants P1 and P2 regained the ability to transit from sitting to standing and walking with crutches (Fig. 4.13a), which increased their WISCI score from 13 to 16 and 6 to 13, respectively. P1 could even walk without assistive devices for several steps between parallel bars. This functional recovery translated into significant improvements in well–established clinical tests such as the ten–meter and six–minute walk tests without EES (Fig. 4.13b). Evaluations conducted several months after the end of the 5–month rehabilitation program showed that both participants, who continued practicing one or twice per week, maintained or further improved their performance.

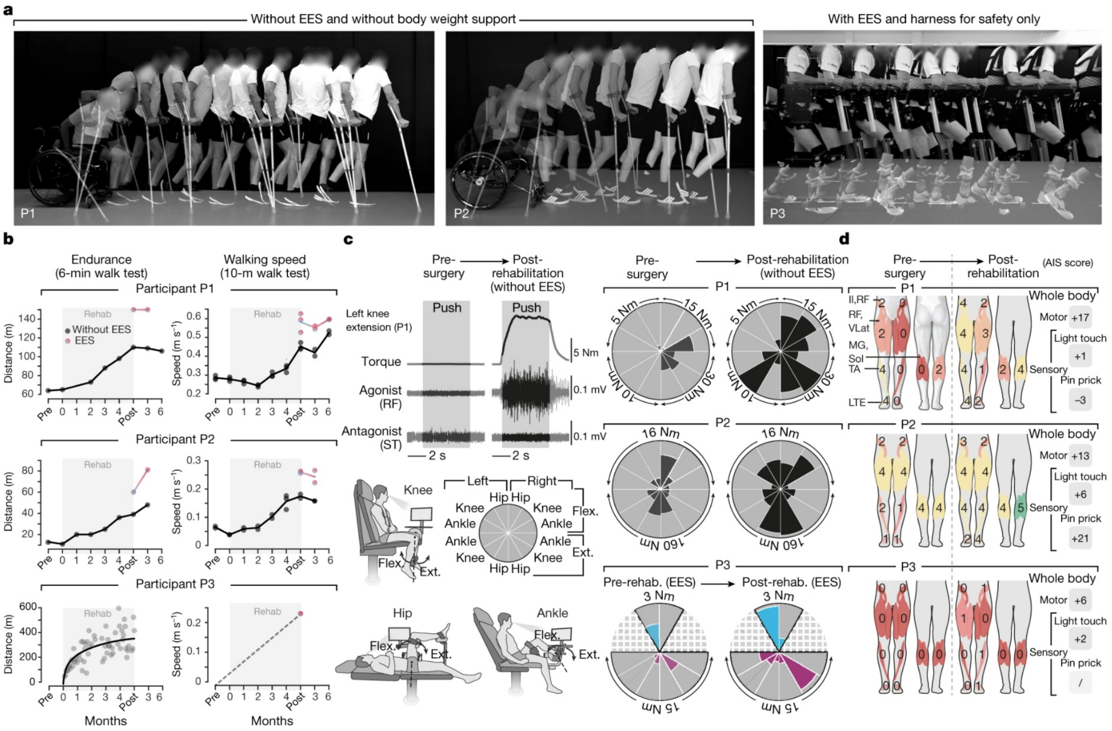

Figure 4.13: Rehabilitation mediates neurological recovery. a, Improved mobility after rehabilitation. Chronophotography shows P1 and P2 transiting from sitting to walking with crutches without EES; P3 progresses overground with a walker and EES; repeated at least three times on different days. b, Plots reporting changes in 6-min and 10-m walk tests for P1 and P2. Tests were performed without gravity-assist, following clinical guidance. For P3 plots report changes in walking distance during rehabilitation and walking speed with EES (with transparent body weight support). c, Evaluations of isometric torque production for each joint, quantified before surgery and after rehabilitation without EES for P1 and P2, and with EES for P3. d, Changes in lower limb motor and sensory scores after rehabilitation. Changes in motor and sensory scores on Abbreviated Injury Scale (AIS)

These improvements were accompanied by the recovery of voluntary leg movements without EES. For example, P1 regained the ability to sustain an extension of his previously paralyzed left leg against the direction of gravity (Fig 4.13c). Quantified measurements revealed that both P1 and P2 ameliorated their ability to produce a torque at each joint of both legs (Fig 4.13c). This recovery translated into an increase of 16 and 11 points in AIS lower limb motor scores, respectively (Fig 4.13d). These scores increased by 4 points in participant P3, but without EES this recovery was insufficient to produce measurable forces when seated in the chair. However, voluntary force production increased substantially during EES (Fig 4.13c). Moreover, he regained the ability to trigger robust movements of the legs against gravity without EES and showed a pronounced increase in the mass of thigh and trunk muscles (Fig 4.17). Unexpectedly, P1, P2 and P3 also ameliorated upper limb motor scores by 2, 4 and 2 points, respectively.

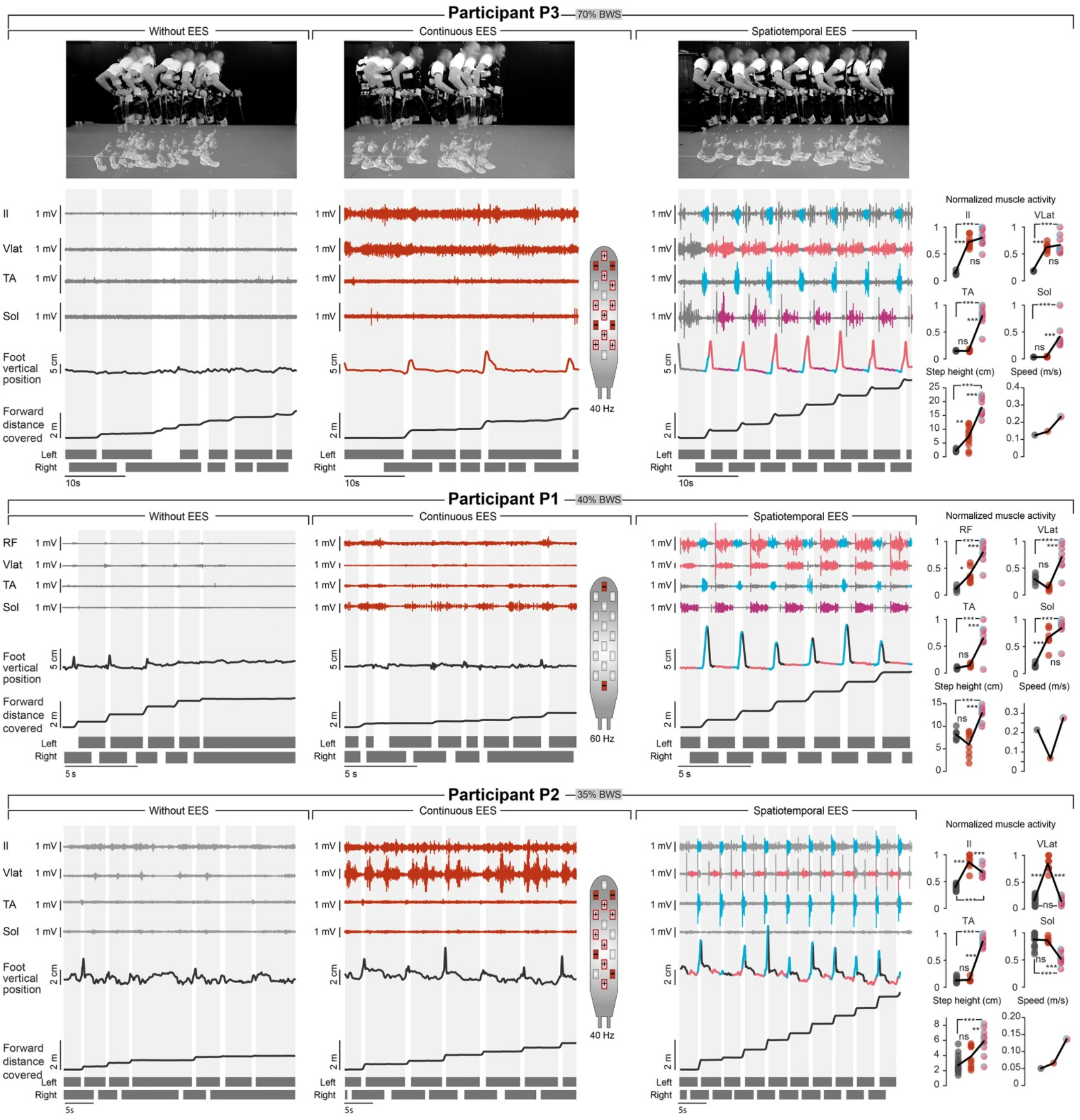

Figure 4.14: Comparison between continuous and spatiotemporal EES during overground walking. Each panel represents one participant who is attempting to walk overground with gravity-assist without EES (left), with continuous EES (middle) and with spatiotemporal EES (right). EMG activity of representative leg muscles, vertical position of the foot and distance covered by the foot in the forward direction are displayed for each experimental condition. Continuous EES is applied throughout the trial (red). For P2 and P3, we optimized EES protocols that targeted the posterior roots on both sides, whereas EES was applied over the most rostral and most caudal midline electrodes for P1, as shown next to each plot. Spatiotemporal EES is represented using the same colour scheme as in Fig. 4.7 and Fig. 4.11. The plots report quantification of EMG activity, step height and mean speed (based on distance covered) for the three experimental conditions (P1, n = 6, 7, 8 gait cycles for no EES, continuous EES and spatiotemporal EES; P2, n = 17, 7, 9 gait cycles for no EES, continuous EES and spatiotemporal EES; P3, n = 6, 10, 9 gait cycles for no EES, continuous EES and spatiotemporal EES). ***P < 0.001; **P < 0.01; n.s., non-significant. One-way ANOVA, post hoc Tukey's HSD. These recordings were repeated on at least three different days for each participant.

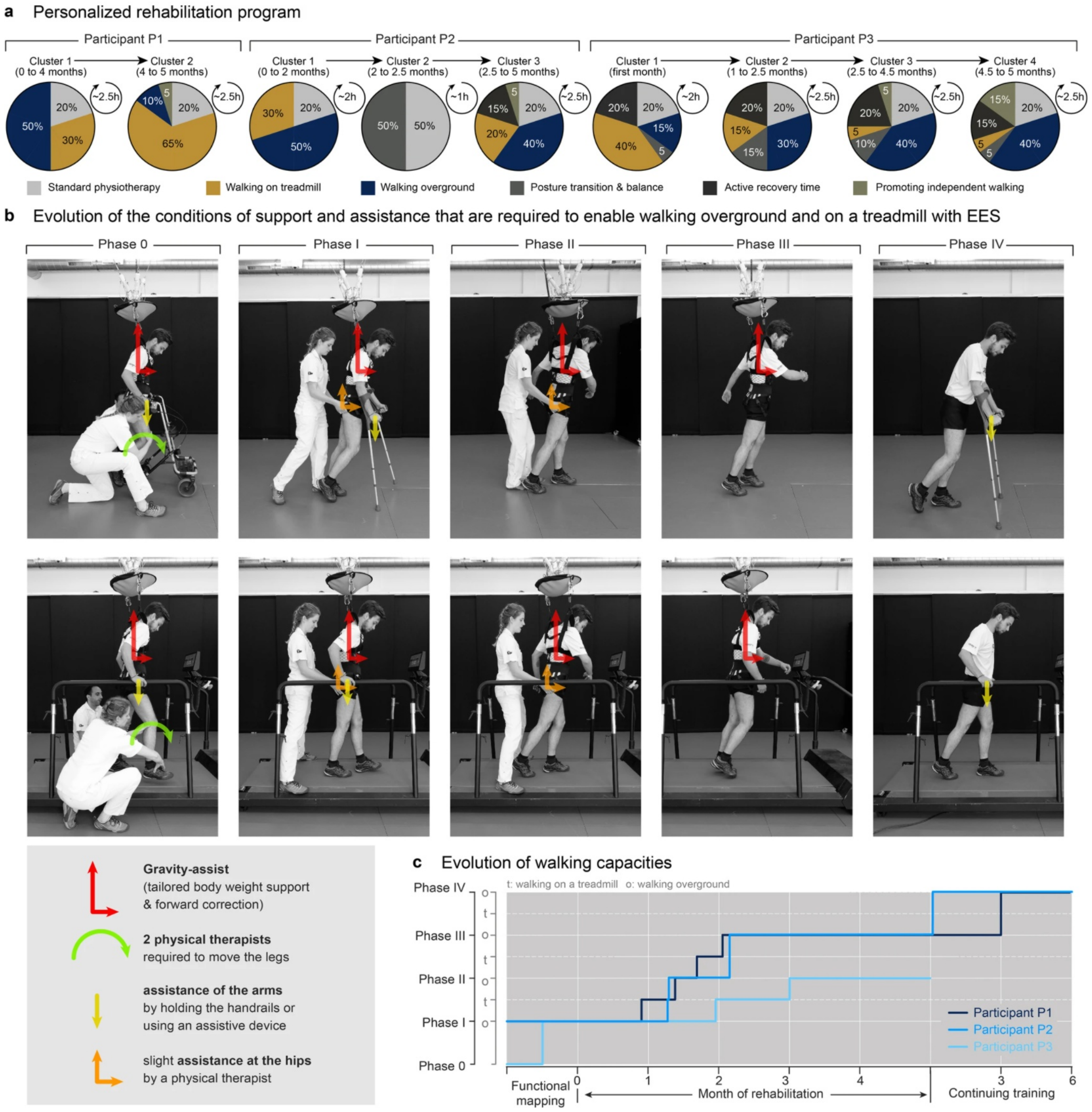

Figure 4.15: Rehabilitation program and evolution of walking capacity. a, Rehabilitation programs were continuously personalized on the basis of the current motor performance of participants. Walking capacities evolved in phases (b). For this reason, the relative percentage of training in the various tasks has been divided into clusters, which correspond to the evolution of walking capacities. To facilitate the sustained production of reproducible locomotor movements (Fig. 4.10c), EES was delivered in open-loop mode during gait rehabilitation. b, Walking capacities evolved through stereotypical phases that are illustrated in the snapshots. c, Plots showing the progression of the three participants along the phases of recovery during the rehabilitation program, and during the subsequent 6 months for P1 and P2. P3 had just completed the rehabilitation program at the time of submission of this study.

4.3.11 Targeted neurotechnologies supporting motor activities at home and in the community

All three participants learned to take advantage of spatiotemporal stimulation to execute functional leg movements, suggesting that practical stimulation technologies could support activities of daily living. For this purpose, we engineered an integrated solution based on a tablet enabling the configuration of task–specific stimulation sequences that are switched on and off with a personalized voice–controlled watch (Fig. 4.16a). To adapt stimulation sequences to movement intents, we conceived adaptive algorithms that trigger stimulation sequences in closed–loop based on real-time acquisition of signals from wearable inertial measurement units.

The robustness of triggering–event detections allowed the participants to transit from sitting to standing and walking freely in the community (Fig. 4.16b and Fig. 4.18a). The stimulation markedly improved their performance in the ten–meter and six–minute walk tests (Fig. 4.13b). A stimulation program specific for cycling permitted long rides in the forest with an adapted bike powered with the arms and legs (Fig. 4.18b).

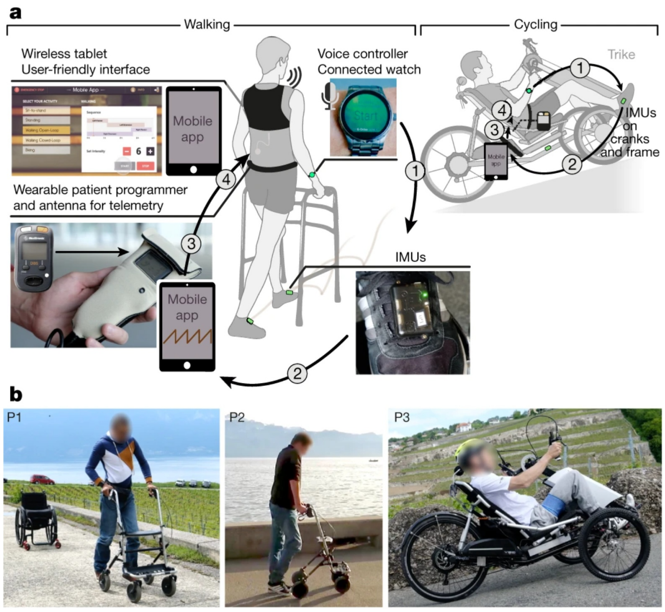
a
Walking
Cycling
Wireless tablet
User-friendly interface
Mobile app
Voice controller
Connected watch
Trike
IMUs on cranks and frame
Wearable patient programmer and antenna for telemetry
Mobile app
IMUs
1
2
3
4
b
P1
P2
P3

Figure 4.16: Spatiotemporal EES in ecological settings. a, System to support activities of daily living. Tablet featuring a mobile App allows participants to select EES sequences, delivered in open loop or closed loop based on Inertial Measurement Units (IMUs) located on both feet or attached onto the cranks and frame of a trike. 1. A personalized voice-controlled watch allows the user to switch EES on or off. 2. IMUs detect foot or crank motion during walking or cycling. 3. Controller sends commands to the patient programmer. 4. Spatiotemporal EES is adjusted in a closed loop. b, Walking and cycling activities in ecological settings are enabled by spatiotemporal EES.

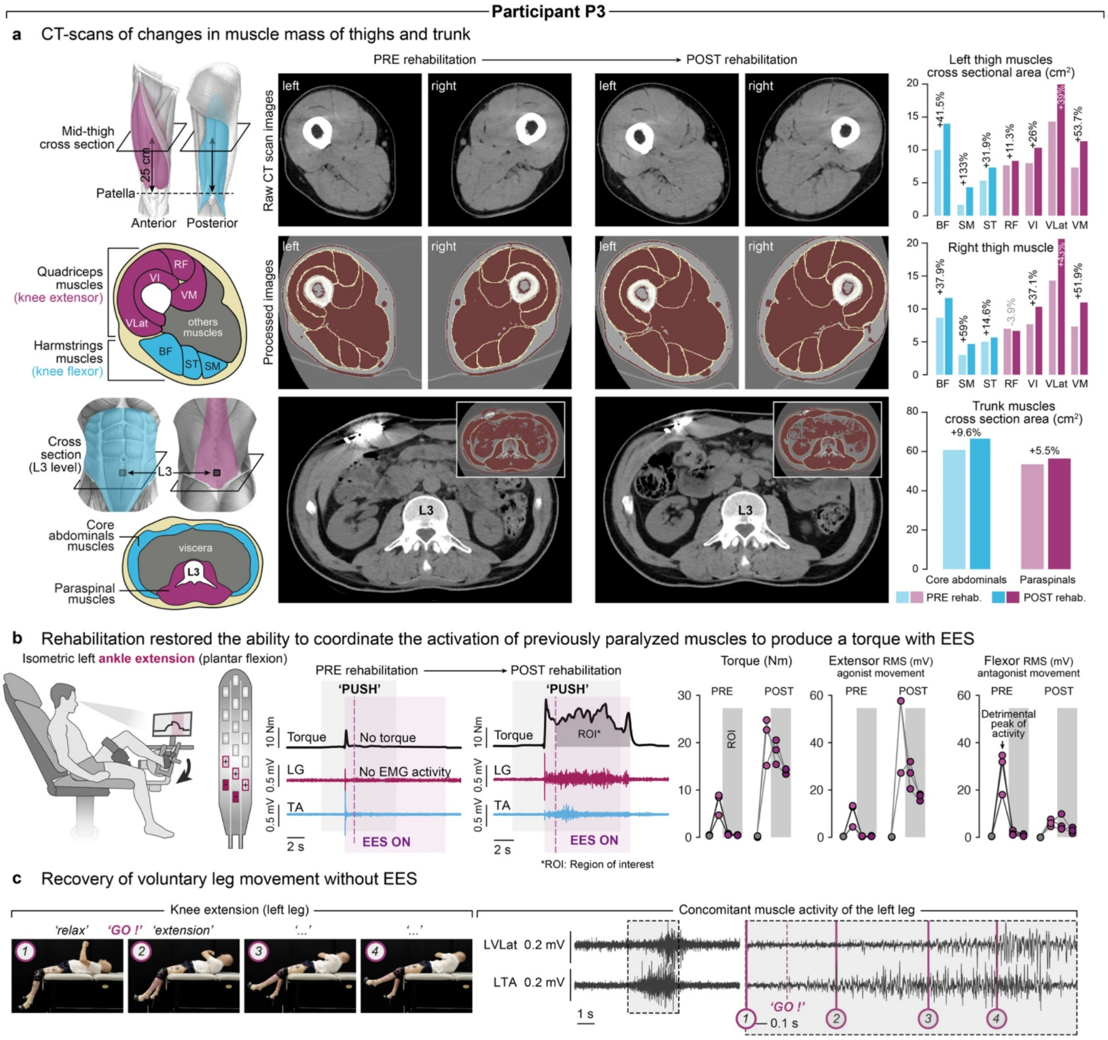
Participant P3
a CT-scans of changes in muscle mass of thighs and trunk
PRE rehabilitation
POST rehabilitation
Mid-thigh cross section
25 cm
Patella
Anterior Posterior
Raw CT scan images
left
right
Processed images
Quadriceps muscles (knee extensor)
RF
VI
VM
VLat
others muscles
Harmstrings muscles (knee flexor)
BF
ST
SM
Cross section (L3 level)
L3
Core abdominals muscles
viscera
Paraspinal muscles
Left thigh muscles cross sectional area (cm²)
+41.5%
+133%
+31.9%
+11.3%
+26%
+53.7%
Right thigh muscle
+37.9%
+59%
+14.6%
-3.9%
+37.1%
+51.9%
BF SM ST RF VI VLat VM
Trunk muscles cross section area (cm²)
+9.6%
+5.5%
Core abdominals
Paraspinals
PRE rehab.
POST rehab.
b Rehabilitation restored the ability to coordinate the activation of previously paralyzed muscles to produce a torque with EES
Isometric left ankle extension (plantar flexion)
'PUSH'
Torque
No torque
LG
No EMG activity
TA
10 Nm
0.5 mV
2 s
EES ON
ROI*
*ROI: Region of interest
Torque (Nm)
Extensor RMS (mV) agonist movement
Flexor RMS (mV) antagonist movement
PRE
POST
ROI
Detrimental peak of activity
c Recovery of voluntary leg movement without EES
Knee extension (left leg)
'relax' 'GO !' 'extension' '...' '...'
1 2 3 4
Concomitant muscle activity of the left leg
LVLat 0.2 mV
LTA 0.2 mV
1 s
'GO !'
0.1 s

Figure 4.17: Changes in muscle mass and quality and recovery of voluntary movements with and without EES in participant P3. a, Skeletal muscle mass and quality were assessed at the pre- and post-rehabilitation time points using X-ray attenuation from CT images obtained at the abdomen (L3 vertebra) and mid-thigh (25 cm above femorotibial joint space). Muscle mass was determined by measuring the Cross-Sectional Areas (CSAs) of muscle tissues, while muscle quality was reflected by CT attenuation numbers (in Hounsfield Units, HU) within the CSAs. Muscle segmentations were performed semi-automatically using ImageJ and muscle-specific HU thresholds (–29 to 150 HU). Plots report the substantial changes in muscle mass at mid-thigh, for both flexor and extensor muscles, and of trunk muscles. Muscle quality was also improved at both levels: total mid-thigh, left: 52.9 to 56.1 HU, right: 51.9 to 56.7 HU; total L3, 45.9 to 48.3 HU. This increase in CT attenuation numbers between the baseline CT scan and the follow-up imaging reflected the decrease in muscle fibre lipid content at the mid-thigh and abdomen. These evaluations were part of a protocol amendment obtained when enrolling P3. b, Assessment of voluntary torque production at the ankle (extension) with targeted EES before and after rehabilitation. Conventions are as in Fig. 4.6.

Figure 4.17: (Continued) c, Snapshots showing voluntary extension of the left leg against the direction of gravity together with the concomitant sequence of EMG activity in the extensor and flexor muscles of this leg. The zoomed window shows the relationship between the movement and the EMG activity, indicated with the numbers. This participant presented flaccid paralysis, and had thus no control over leg muscles before the surgery. This movement was observed repeatedly at the end of the rehabilitation period.

4.4 Discussion

We developed targeted spinal cord stimulation neurotechnologies that immediately restored voluntary control of walking in three individuals with severe or complete paralysis. The stimulation targets proprioceptive feedback circuits through the recruitment of selected posterior roots (Capogrosso et al., 2013; Moraud et al., 2016; Moraud et al., 2018; Rattay et al., 2000). This understanding was pivotal to enable the immediate control of volitional walking despite chronic paralysis. Within a few days, this framework guided the personalization of spatiotemporal EES sequences that continuously coincide with the intended movements. Consequently, the stimulation augments the excitability of the motoneuron pools that are concomitantly engaged by the natural flow of task–specific sensory information and residual supraspinal command. This spatiotemporal convergence enables a robust and more natural control of leg movements compared to other empirical stimulation paradigms (Angeli et al., 2014; Y. P. Gerasimenko et al., 2015; Grahn et al., 2017).
We hypothesize that this spatiotemporal convergence is also responsible for the unexpected neurological recovery observed in the three participants. Indeed, rehabilitation not only improved locomotor performance with EES, but also mediated a neurological recovery that restored voluntary leg movements without EES. We previously showed that mice lacking proprioceptive feedback circuits exhibit defective rearrangement of descending pathways after SCI, which abolishes locomotor recovery (Takeoka et al., 2014). Conversely, we propose that the repeated spatiotemporal contingence between the residual supraspinal command and the recruitment of proprioceptive feedback circuits with EES increases the strength and number of terminals from residual descending projections through bidirectional spike–timing–dependent plasticity (Holtmaat & Svoboda, 2009; Nishimura et al., 2013). Electrophysiological studies have documented such plasticity in humans with SCI (Perez et al., 2003; Urbin et al., 2017). This interpretation is consistent with the pronounced anatomical reorganization of residual cortico–reticulo–spinal circuits observed in rodents when EES enables robot–assisted gait training despite complete leg paralysis (Asboth et al., 2018; van den Brand et al., 2012). As in humans, rodents regained a motor cortex dependent control of leg movements that persisted without EES (Asboth et al., 2018), but only when rehabilitation commenced early after SCI. We therefore anticipate that this therapeutic strategy will be even more efficacious immediately after SCI, when the potential for plasticity is elevated and the neuromuscular system has not yet undergone the dramatic deteriorations consecutive to chronic paralysis (Dietz, 2010). These proofs–of–concepts stress the urgent need to develop a therapeutic platform that

take full advantage of targeted spinal cord stimulation to enable motor control after SCI and combines all the essential practical features to support rehabilitation in clinical settings and its use at home and in the community.

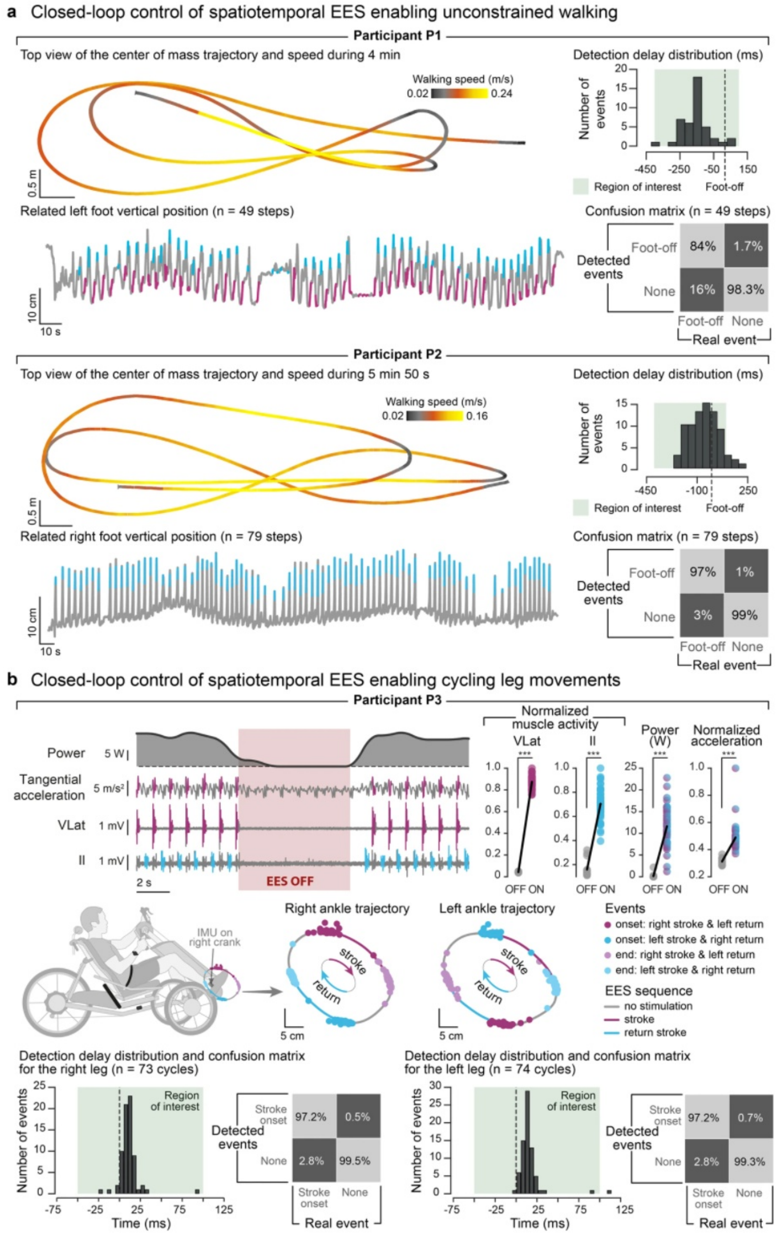

Figure 4.18: Performance of closed-loop spatiotemporal EES to enable walking and cycling outside the laboratory.

Figure 4.18: (Continued) a, P1 and P2 were asked to walk freely overground with a walker (no body weight support) for 6 min. The concomitant vertical displacements of the foot show the consistency of EES triggering events despite variable foot kinematics and voluntary breaks. The trajectory of the centre of mass is shown from a top view to illustrate the ability to steer locomotion along any desired path. EES protocols took into account the deficits of each participant (cyan, EES targeting hip flexion; magenta, EES targeting knee and ankle extension). Histograms indicate the number of detected foot-off events for the represented leg as a function of the latency with respect to real foot-off events. The confusion matrix associated with these detections is represented below, as a percentage of the real events that were correctly or incorrectly classified. Detections were considered valid if they occurred between 400 ms before and 100 ms after real foot-off events, as highlighted in green on histograms (P1, n = 49 gait cycles; P2, n = 79 gait cycles). b, Closed-loop spatiotemporal EES was delivered in P3 using an electric trike powered by hand and foot pedals. Traces show EMG activities of the targeted hip flexor and knee extensor muscles on one leg together with the tangential acceleration of the pedal and power generated at the foot pedal. Plots report the quantification of flexor and extensor EMG activities, peak tangential accelerations and generated power without and with EES. Successive ankle trajectories during cycling are shown together with the timing of EES protocols targeting the hip flexor and knee extensor muscles. The histograms and confusion matrices report the performance of the controller following the same conventions as in a, except that the correct detection window was restricted to 50 ms before and 100 ms after the desired crank position (P3: n = 73 pedalling cycles). ***P < 0.001. Student’s t-test.

4.5 Materials and methods

4.5.1 Clinical study and participants

Study design and objectives

All experiments were carried out as part of the ongoing clinical feasibility study STIMO (“Stimulation Movement Overground”), which investigates the effects of spatiotemporal EES combined with weight-supported overground locomotor training on the recovery of motor function after SCI. This study was approved by the Swiss ethical authorities (Swissethics protocol number 04/2014 ProjectID: PB_2016-00886, Swissmedic protocol 2016-MD-0002) and was conducted in accordance with the Declaration of Helsinki. All participants signed a written informed consent prior to their participation. More information at clinicaltrials.gov (NCT02936453).

All surgical and experimental procedures were performed at the Lausanne University Hospital (CHUV). The timeline of the study is reported in Fig. 4.1b. Briefly, the study involved assessments before surgery, the surgical implantation of the neurostimulation system, a one-month period during which EES protocols were configured, and a five-month rehabilitation period with physiotherapists taking place four to five times per week for one to three hours (Fig. 4.15a), including monthly assessments.

The rehabilitation program was personalized to the participants' improvements. Each session was typically segmented into three parts: (i) conventional physiotherapy (30 min), (ii) locomotor training with gravity-assist and EES (60 to 90 minutes), (iii) Recovery (stretching, massage). The physiotherapy sessions included muscle stretching and/or muscle strengthening, volitional control of movement and standing.

Based on improvements observed in P1 and P2, an optional three-year study extension was submitted and approved by the ethical authorities to allow the use of EES without body weight support outside the laboratory environment. This amendment included 9 sessions of training with gravity-assist, 3 times per week, which was performed by P3 only. There was no serious adverse event during the course of the study.

Study participants

Three individuals who had suffered a traumatic cervical SCI participated in the study. Their neurological status was evaluated according to the International Standards for Neurological Classification of Spinal Cord Injury (Kirshblum & Waring, 2014), and is reported in Table 4.1. At enrollment, participant P1 was 28 years old and was classified with a C7 lesion that occurred six years earlier during a gymnastics accident. His left leg was completely paralyzed while his right leg retained some residual functions (lower extremity motor scores left: 0/25, right: 14/25). He could ambulate with a walker with no braces and no physical assistance over ten meters (WISCI score: 13). He had followed an extensive rehabilitation program consisting of 262 sessions of Lokomat-assisted locomotor training over a period of three years, which led to very limited improvements of his overground walking capacities and failed to mediate any neurological improvement of his paralyzed left leg. Participant P2 was 35 years old and was classified with a C4 lesion that occurred six years earlier during a bicycle accident. His impairments were bilateral, with some residual functions in both legs (left: 12/25, right: 13/25). He could ambulate with a walker, braces and physical assistance of one person over ten meters (WISCI score: 6). A few months prior to his enrollment, he had terminated 50 rehabilitation sessions involving both stepping on a treadmill and overground locomotion. He had plateaued at a very low functional level (WISCI II score of 6). Participant P3 was 47 years old, classified with a C7 lesion that occurred four years earlier during a bicycle accident. He presented bilateral flaccid leg paralysis, with motor scores of 0 on all key leg muscles. He did not have any spasticity in his legs and could neither stand nor ambulate at all (WISCI score: 0), despite extensive participation in physical exercise with adapted devices for home use.

4.5.2 Surgical implantation

Investigational device

Participants were implanted in the posterior epidural space with a 16-electrode paddle array clinically approved for the treatment of chronic pain (Specify$^{\text{TM}}$ 5-6-5 surgical lead for participants P1 and P2, Specify® SureScan® MRI 5-6-5 for participant P3; Medtronic plc, Fridley, MN, USA). This paddle array was connected to an IPG (Medtronic Activa$^{\text{TM}}$ RC) standardly used for Deep-Brain Stimulation. These combined elements and associated firmware constitute an investigational device that was tested as part of this clinical study.

Pre-surgical planning
Pre-operative MRI allowed the identification of the conus medullaris. Average spinal cord anatomical dimensions (Canbay et al., 2014; Minassian et al., 2007) were then used to estimate the position of the targeted spinal cord segments (L1-S2) with respect to the vertebrae.

Laminectomy and paddle array insertion
The insertion level was identified under fluoroscopy. An approximately 5 cm midline skin incision was performed, the fascia opened and the muscles retracted bilaterally. Excision of the midline ligamentous structures and L1/L2 flavectomy enabled the insertion of the paddle array that was placed over the midline of the exposed dura and advanced rostrally to the target location.

Electrophysiological monitoring
Electrophysiological testing was conducted using the NIM Eclipse® monitoring and stimulation system (Medtronic Xomed Inc, Jacksonville, FL, USA) to optimize the medial and segmental position of the paddle array. EES was delivered at increasing amplitude (0.5 Hz) to elicit muscle responses that were recorded with subdermal (Neuroline Twisted Pair Subdermal, 12 x 0.4 mm, Ambu A/S, Ballerup, Denmark) or intramuscular needle electrodes (Ultra Sharp, 44 mm/27 g, Chalgren Enterprises, Inc. Gilroy, CA, USA), as explained in Fig. 4.2a. The final location of the paddle array overlaid lumbar and upper sacral segments in participant P1 and P3. Due to his height (192 cm), the paddle array was too short in P2, which imposed the selection of a position targeting the weak hip flexor muscles rather than ankle extensor muscles.

Pulse generator implantation
The Implantable Pulse Generator (IPG) was inserted into a subcutaneous pocket in the abdomen. An extension cable was then tunneled from one opening to the other and connected to the IPG.

4.5.3 Personalized computational model

Personalization
We personalized computational models to simulate the spread of electric potential and currents generated by single pulses of EES. The model is composed of an anatomically accurate volume conductor model including the human spinal cord that is coupled to a geometrically realistic biophysical model of human primary afferents. First, we elaborated an average human spinal cord model comprising white and grey matter compartments combining information

from the Paxinos human atlas and anatomical measurements of segments lengths and widths taken from 15 human cadaveric spinal cords (Watson et al., 2009). Second, for each participant we adapted the length of the white and grey matter compartments to patient-specific data extracted at the L1 vertebral level from pre-operative T2-weighted MRI images. The CerebroSpinal Fluid (CSF) dimensions were also segmented out of the pre-operative MRI-images. Anatomically realistic vertebral bones and discs were generated and fitted to post-operative CT-data for each patient and the epidural fat was initialized to fit the inner borders of the bone. Finally, the whole spinal model was placed in a saline conductor to represent the human body (Capogrosso et al., 2013). Isotropic dielectric coefficients for each compartment were taken from previous studies (Howell et al., 2014). We then estimated the precise position of each electrode by segmentation of post-implantation CT-data and registered it to the vertebral bone.

The model was discretized and Maxwell's equations were solved under quasi-static conditions with the Finite Element Method to determine an accurate representation of electric potentials and currents generated by single pulses of EES in each subject. Monopolar pulses were modelled as Dirichlet-boundary conditions of 1 V at the active electrode site with a duration of 500 µs. Dirichlet-boundary conditions of 0 V were initialized at the outermost boundaries of the model or at contacts selected as anodes in case of multipolar configurations. The models were all implemented in Sim4Life v3.4 (ZMT Zürich MedTech AG).

We used NEURON (Hines & Carnevale, 1997) in Sim4Life to model 50 myelinated Group-I afferent fibers per posterior root as a log-norm function with a mean fiber diameter of 16 µm and a standard deviation of 4 µm. An anatomically accurate trajectory of the afferent fibers was initialized and fitted around their entry and exit point determined by the anatomical parameters extracted from MRI and CT-data. A Sweeney model was used to describe the equation of the active membrane at the nodes of Ranvier and at the passive internodal segments. The electrical compartments were automatically initialized in Sim4Life. The resting potential was set to -80 mV. Recruitment of group-Ia afferents was evaluated by linearly scaling the extracellular voltage applied at each fiber's compartment until an action potential was generated.

Posterior root selectivity index for simulations

For a given electrode configuration and EES amplitude, computational simulations yielded the percentage of fibers activated in each posterior root. We derived a root selectivity index $SI_{computational}(r_i, I)$ for each root r_i and each stimulation amplitude I:

$$SI_{computational}(r_i, I) = \frac{A_{r_i}(I)}{1+\sum_{otheripsilateralroots} A_{r_j}(I)} \cdot f_+(\frac{A_{r_i}(I) - A_{r_{contralateral(i)}}(I)}{A_{r_i}(I) + A_{r_{contralateral(i)}}(I)}) \tag{4.1}$$

where $A_{r_i}(I)$ represents the percentage of fibers activated in root r_i, $r_{contralateral(i)}$ is root contralateral to root r_i and $f_+(x) = \begin{cases} x & \text{if } x > 0 \\ 0 & \text{if } x \leq 0 \end{cases}$. The first term of this selectivity index represents the rostrocaudal ipsilateral root selectivity, while the second term indicates the mediolateral selectivity and penalizes configurations that activate the root contralateral to the targeted one. If the contralateral root is more activated than the targeted root, the selectivity index is equal to 0. If only the targeted root is recruited, the selectivity equals 1. This selectivity index was calculated for a range of stimulation amplitudes (number of recruited afferent fibers) and the maximum was taken to characterize the overall selectivity of each electrode configuration.

Single-Pulse EES

Single-pulse EES was used to identify electrode configurations recruiting the targeted posterior roots (L1, L3, L4, S1). This identification was based on the recruitment order of lower-limb muscles with specific segmental innervations in response to single pulses of EES (300 µs pulse width) repeated every 1.5 s with increasing amplitudes.

Participants were lying relaxed in supine position on an examination table. EMG activity was recorded bilaterally from the Iliopsoas (Il), Rectus Femoris (RF), Vastus Lateralis (VLat), Semi-Tendinosus (ST), Tibialis Anterior (TA), Medial Gastrocnemius (MG), and Soleus (Sol) muscles with wireless bipolar surface electrodes (Myon 320, Myon AG, Schwarzenberg, Switzerland). Each electrode pair was placed centrally over the muscle with a longitudinal alignment and an inter-electrode distance of 3 cm. Abrasive paste (Nuprep, Weaver and Company, Aurora, CO) was used for skin preparation to reduce electrode-skin resistance and improve EMG signal quality. Stimulation artefacts required to display stimulus-triggered EMG activity were picked up by an additional pair of surface-EMG electrodes placed over the spine at the thoracolumbar junction. EMG signals were amplified with a gain of 500 and band-pass filtered between 20 and 450 Hz. Continuous EMG signals were sampled at 5 kHz and saved to a desktop computer. Stimulus-triggered EMGs were visualized in real-time as superimposed traces for each muscle within a 50-ms time window following each stimulus.

Recordings were performed with graded stimulation amplitudes in order to compute recruitment curves, which indicate the degree of recruitment of each muscle as the stimulation amplitude is increased. Specific electrode sites were tested according to the segmental organization of lower limb muscle innervation (Sharrard, 1964) and predictions from computer simulations. Each selected electrode was stimulated in monopolar configuration as the cathode, with the case of the implantable pulse generator set as the anode. First, low-amplitude stimulation was applied to identify the lowest response threshold across all recorded muscles. Then, EES amplitude was increased manually to identify the amplitudes at which the responses reached a plateau, limited to levels that did not cause discomfort to the participant. Finally, single-pulse EES at amplitudes ranging from response threshold to saturation was performed automatically, with four repetitions at each EES amplitude, and recorded EMG responses were used to compute recruitment curves and a functional selectivity index (see "Data processing" section).

This procedure was repeated to identify eight sites targeting the left and right L1 (hip flexion), L3 (knee extension), L4 (ankle flexion) and S1 (ankle extension) posterior roots. If the selectivity was not satisfactory, EES was refined with multipolar electrode configurations, using additional anodes and cathodes to steer the electrical field towards the targeted posterior roots.

Finally, the optimal electrode configurations for each targeted posterior root were validated during standing with body weight support.

4.5.4 Evaluation of single-joint torque production

Assessment of voluntary force production
Maximum torques produced at the knee, ankle and hip in flexion and extension were measured using the Humac Norm Cybex dynamometer system (Computer Sports Medicine Inc., Stoughton, MA). For measuring maximum isometric knee flexion and extension, the participant was seated in upright position, the knee placed in line with the dynamometer axis of rotation, and the lever arm pad of the system secured to the lower leg just above the ankle. Hip, knee, and ankle assumed angles of 90°, respectively. For ankle flexion and extension, the participant was seated reclined, with an angle of 120° between the trunk and the thigh of the leg under examination. The thigh was secured to a stabilization arm provided by the system, and the ankle was strapped to the foot platform attachment, with the joint aligned with the dynamometer axis of rotation. Knee and ankle were at angles of 90°. Hip flexion and extension were assessed in supine position, with the distal thigh strapped to the measuring lever arm, and hip and knee at 90° of flexion. For each single-joint task, the participants were asked to produce a progressive contraction from rest to maximum strength with real-time visual torque biofeedback, with three repetitions and at least a 1-minute resting period between each attempt. If spasticity was induced during the attempted task, the trial was repeated. The torques developed were measured at a sample frequency of 5 kHz, and in parallel, EMG was acquired from the main agonists and antagonists of the respective movement attempt, sampled at 5 kHz. This assessment was carried out at all the main and monthly intermediate time points, with identical settings of the dynamometer system for each participant.

Impact of EES on voluntary force production
A similar setup was used to study the interactions between targeted EES and voluntary attempts of single-joint movements. EES was applied with parameters optimized to facilitate hip flexion, hip extension, knee extension or ankle extension. Electrode configurations derived from single-pulse experiments were used to target the posterior roots projections to the spinal cord regions containing motoneurons associated with the intended movement. EES amplitude and frequency were adjusted manually. If necessary, EES was refined using multipolar electrode configurations. EES was applied with a delay following the onset of the voluntary motor task for a duration of a few seconds and was stopped 1-2 seconds after the participant had stopped the voluntary movement. This procedure was repeated three times for each of the studied tasks. The torques produced were assessed by dynamometry in the standardized positions as described above, except for the hip flexion which was assessed in prone position, with the hip at 10° of extension and the knee fully extended.

4.5.5 Technological framework

Gait analysis and rehabilitation environment
For assisting treadmill and overground locomotion, we used an overhead support system based on cable robot technology (FLOAT, Lutz Medical Engineering GmbH, Rüdlingen, Switzerland) that allows the application of forces to the trunk through a dedicated harness (Maine Anti-Gravity Systems, Inc. Portland, ME) in each of the Cartesian directions (van den Brand et al., 2012). The robotic interface was integrated within a gait analysis platform, which allowed acquisition of EMG activity, ground reaction forces and whole-body kinematics in real-time. EMG activity during walking was acquired bilaterally at 1 kHz using the 16-channel wireless Myon system, with bipolar surface electrodes placed over the from the Iliopsoas (Il), Rectus Femoris (RF), Vastus Lateralis (VLat), SemiTendinosus (ST), Biceps Femoris (BF), Tibialis Anterior (TA), Medial Gastrocnemius (MG), and Soleus (Sol) muscles. Kinematic recordings were obtained at a 100-Hz sampling rate using a 3D motion capture system (Vicon Motion Systems, Oxford, UK), consisting of 14 infrared cameras that covered a 12 x 4 x 2.5 m workspace. Head, trunk, and bilateral upper and lower extremity kinematics were captured by these infrared cameras and 34 small infrared-reflective markers (16 mm, Prophysics AG, Schaffhauserstrasse 121, Kloten, Switzerland) positioned over standardized anatomical landmarks. Two force plates (9260AA6, Kistler, Winterthur, Switzerland) were installed in the middle of the workspace to monitor ground reaction forces. We also captured chronophotographic images of participants using a high-definition camera (FUJIFILM X-T2, 5 images/s, ISO 6400, shutter speed 1/250 sec) and overlaid successive images offline for illustrative purposes.

Real-time gait event detection
To perform real-time gait event detection, we placed large infrared-reflective markers (46 mm, Prophysics AG, Schaffhauserstrasse 121, Kloten, Switzerland) on the main joints of the leg (greater trochanter, lateral femoral condyle and lateral malleolus) and an extra marker on the left arm to differentiate body sides. We developed a custom C++ based control software to detect gait events in real time based on kinematic information from the motion capture system and to send EES triggering commands to the neurostimulation system. This control software streamed the real-time 3D-positions of all the large kinematic markers detected. The labeling of these markers was then performed in the control software itself, based on their vertical position and additional geometrical constraints. Then, the control software computed the trajectory of the foot with respect to the hip and the centroid of this trajectory over the last few steps. An overlay of past trajectories and the current centroid were displayed as feedback for the user. The vector between the current point on the foot trajectory and the centroid was used to define an angular variable evolving monotonically throughout the gait cycle. A set of user-defined thresholds were applied on this angular variable to define the occurrence of desired gait events, such as foot off, foot strike, mid-swing or midstance. These events were used as triggers to start or stop specific spinal cord stimulation protocols.

Neurostimulation system

EES was delivered with an IPG (Medtronic Activa™ RC) that enabled monopolar and multipolar stimulation at constant current or constant voltage through one or a subset of the 16 electrodes of the paddle array or the case of the IPG (anode). The IPG was modified from its clinical version with an investigational firmware that enabled real-time communication with a software running on an external computer (NEUWalk Research Programmer Application NRPA, Model 09103, Medtronic). The NRPA acted as a relay between EES triggering commands sent by the control software described in the previous section and the IPG. It communicated wirelessly with the IPG through the following communication chain: the NRPA sent commands via a virtual COM port corresponding to a Bluetooth adapter, a custom wireless bridge consisting of a nano computer (Raspberry Pi) received this command and forwarded it to a virtual COM port corresponding to a USB adapter, a USB to infrared adapter (ACT-IR224UN-LN115-LE, ACTiSYS Corporation, Fremont, CA, USA) transformed this command into infrared signals that were then read by a modified Medtronic patient's programmer (Sensing Programmer Telemetry Module SPTM, Medtronic), which finally transmitted the command to the patient's IPG by electromagnetic induction through the skin (Fig. 4.2b). This constituted our overall investigational system: motion capture system, control software, NRPA relay software, wireless bridge, SPTM and IPG with modified firmware connected to the 16-electrode paddle array. This system allowed real-time triggering of stimulation protocols with a median latency of 110 ms (99th percentile, 135 ms).

4.5.6 Configuration of targeted EES

After approximately ten days of rest following the surgery, participants started a one-month period during which we configured EES protocols to enable single-joint movements and walking.

Single-joint movements

We delivered EES with electrode configuration targeting the posterior roots projecting to the spinal cord regions containing the motoneuron pools associated with the intended movement. Electrode configurations were selected using the selectivity index calculated from single-pulse EES experiments and optimized with multipolar configurations when necessary (Fig. 4.4).

Spatiotemporal EES during walking

These EES protocols were guided by the spatiotemporal maps of motoneuron activation reconstructed from EMG activity of healthy individuals during walking (Cappellini et al., 2010; Yakovenko et al., 2002) (see "Data processing" section). These spatiotemporal maps revealed that walking involved the successive activation of three hotpots restricted to specific spinal cord regions. EES protocols targeting the posterior roots projecting to these hotspots were selected from the selectivity index that was calculated during single-pulse EES experiments. The configuration, amplitude and frequency of EES were optimized during standing and refined during walking. The onset and duration of each EES protocol was optimized using the procedures described in Fig. 4.10. EES train durations could be pre-determined or terminated by a gait event (e.g. mid-swing).

Continuous EES during overground walking
Continuous EES was delivered using a variety of locations that covered the broad range of protocols employed in previous studies (Angeli et al., 2014; Barolat et al., 1986; Carhart et al., 2004), both on a treadmill and overground. We report the results from the most efficient protocols for each participant. In general, these protocols involved the widespread activation of the spinal cord through the recruitment of the L1 and S1 roots or L1 and L4 roots on both sides simultaneously, as employed in recent studies (M. L. Gill et al., 2018). EES pulses were interleaved with a 2 ms interval to avoid superposition of the electric fields generated by each configuration. EES amplitude and frequency were optimized visually.

EEG recordings
Subjects were asked to produce an isometric torque at the right knee without and with targeted EES (Fig. 4.9). The subjects seated on the Humac Norm Cybex dynamometer with the knee flexed at 90° and were instructed to follow a sequence displayed on a screen in front of them: movement preparation (auditory cue), GO cue around 2 s after movement preparation, movement execution (about 3 seconds). During trials with EES, 2 s after the initiation of the movement the stimulation was switched on for about 5 s. EEG data were continuously acquired using 64 channels in standard 10–20 configuration (ANT neuro) at a sampling rate of 1024 Hz.

4.5.7 Clinical evaluations

International Standards for Neurological Classification of Spinal Cord Injury (ISNCSCI)
Each participant's neurological status was assessed before surgery and after 5 months of rehabilitation based on the ISNCSCI, a comprehensive clinician-administered neurological examination of residual sensory and motor function quantifying SCI severity (Kirshblum & Waring, 2014).

WISCI II score
Functional walking ability was assessed by the WISCI II score (Dittuno & Dittuno Jr, 2001), which evaluates the amount of physical assistance, assistive devices or braces required to walk overground for ten meters.

Muscle mass and quality
Muscle mass and quality were quantified using CT images obtained at abdominal (L3 vertebra) and mid-thigh (25 cm above femorotibial joint space) levels, assessed before surgery and after rehabilitation. Muscle segmentations were performed semi-automatically using ImageJ and specific HU thresholds (Aubrey et al., 2014) (-29 to 150 HU) (Fig. 4.17a). Muscle quality

was assessed using CT attenuation numbers, which reflect lipid content in skeleton muscle (Goodpaster et al., 2000).

10-meter walk test
Walking speed was assessed by a timed 10-meter walk test without body weight support. Participants were instructed to walk with the preferred assistive device as fast as they could. Participants P1 and P2 performed the test with a standard 4-wheel walker. This test was also performed with spatiotemporal EES after rehabilitation and during follow-up after obtaining the authorization to use spatiotemporal EES without body weight support. Participant P3 performed the test only after rehabilitation using a 4-wheel walker with armrests, spatiotemporal EES, and the presence of the body weight support for safety.

6-minute walk test
Endurance was assessed by the distance covered overground within 6 minutes with the preferred assistive device. Participants P1 and P2 performed this test in the same conditions as the 10-meter walk test. Participant P3 was unable to perform this test.

4.5.8 Study extension and technologies for use in the community

Technological framework
The home-based system consists of a tablet (Surface Pro 4, Microsoft) containing personalized EES programs, each associated with a specific training activity. Custom software was developed in C to allow switching between EES protocols and loading them onto the IPG. A Graphical User Interface (GUI) allows the participant to change the amplitudes of EES protocols, and to start or stop an activity from the tablet or using a commercially available smartwatch (Fossil Q Marshal, Fossil Group, Inc., USA) connected to the tablet via bluetooth. Participants can either tap on the smartwatch screen or use a voice controller implemented using a keyword detection system (Snowboy Hotword Detection, non-commercial license, KITT.AI, Baidu, Inc., China) built on artificial neural networks.
Participants could select activities with EES delivered in open-loop or closed-loop. The controller of closed-loop EES used a pair of Inertial Measurement Units (IMUs, NGIMU, FW v.1.5 HW v1.6, x-io Technologies Limited, UK) connected to the tablet via WiFi, streaming data at 90 Hz.

Closed-loop walking
During closed-loop walking, the pitch angle of IMUs placed on the feet or tibia enabled gait event detection based on a Kalman filter combining the accelerations and angular velocities of IMU signals:

$$\begin{cases} \text{Noisy measurement from accelerometers:} & \text{if } \theta_{measured} = atan2(A_y, A_x) \\ \text{Kalman observation model:} & \text{if } \theta_{measured} = H \cdot (\frac{\theta_{real}}{\dot{\theta}}) + \omega_1 withH = (10) \\ \text{Kalman state-transition model:} & \text{if } (\frac{\theta_{real}}{\dot{\theta}})_{i+1} = A \cdot (\frac{\theta_{real}}{\dot{\theta}})_i + \omega_2 withA = \begin{bmatrix} 1 & 1/f_s \\ 0 & 1 \end{bmatrix} \end{cases}$$

where A_x and A_y represent the accelerations measured by the accelerometers in the plane of movement, $\dot{\theta}$ represents the angular velocity measured by the gyroscope around the axis of the joint (ankle or knee), $\theta_{measured}$ is an approximation of the pitch angle assuming that the IMU is static and that only gravity contributed to the accelerations, atan2 is the four-quadrant inverse tangent, θ_{real} is the real pitch angle that estimated by the Kalman filter, ω_1 and are ω_2 Gaussian noises. Gait events are detected when the pitch angle crosses a pre-defined threshold personalized for each participant.

Closed-loop biking
Gait event detection was based on one IMU placed on the crank and another IMU attached on the frame of the trike. These IMUs were used to measure the angle of the crank and the current slope on non-levelled terrains, respectively. Detections were based on the above described Kalman filter that first estimated the measured angle from the accelerometers:

$$\theta_{measured} = atan2(A_y, A_x - r \cdot \dot{\theta}^2) \tag{4.2}$$

Communication delays with the IPG could result in variability in EES timing as the angular velocity is varied. To avoid this issue, we estimated the angular velocity $\dot{\theta}$ over the last cycle and thresholded the crank angle at $\theta_{threshold} - \dot{\theta} \cdot \tau_{communication}$, where $\theta_{threshold}$ is the desired angular threshold and $\tau_{communication}$ is the communication delay (about 110 ms).
EES protocols promoted knee extension when the crank reached 90° (top) together with hip flexion of the contralateral leg. This system was mounted on a tricycle specially conceived for patients with motor impairments, combining foot and hand pedals and electrically-powered assistance (Trike, GBY SA, Vuisternens-en-Ogoz, Switzerland).

4.5.9 Data processing

Recruitment curves during single-pulse EES
EMG signals were band-passed filtered between 10 and 450 Hz (4th-order Butterworth filter). EES onset was determined using semi-automatic methods based on stimulation artefact recordings. The evoked responses were extracted and superimposed to isolate the monosynaptic components based on visual inspection by an experienced neurophysiologist. The temporal window of these responses started 10 to 20 ms after EES onset and lasted 40 to 50 ms, depending on the muscle and participant. For each EES amplitude, the responses were quantified as the peak-to-peak amplitude to generate recruitment curves that we displayed

in circular plots. Muscles are distributed at different angular positions, while the radial axis corresponds to EES amplitude (Fig. 4.3d, Fig. 4.4 and Fig. 4.5). A greyscale shading reports the normalized EMG activity. The white circle highlights the EES amplitude that corresponds to the highest selectivity index. The polygon describes the muscle selectivity at the optimal EES amplitude: the edges of the polygon represent the normalized EMG activity on the radial axis for a particular muscle, scaled so that the polygon fills the circle.

Selectivity index

We targeted the posterior roots projecting to L1, L3, L4 and S1 segments to modulate motoneurons associated with hip flexion, knee extension, ankle flexion and ankle extension. To identify the relevant electrodes, we computed a selectivity index $SI_{experimental}(g_i, I)$ for each targeted muscle group g_i and EES amplitude I. This selectivity index contains two terms, one indicating the selectivity on the targeted side, and one indicating the mediolateral selectivity for the targeted side s_i

$$SI_{experimental}(g_i, I) = SI_{targetedmuscles}(g_i, I) \cdot SI_{leftvsright}(s_i, I)$$
$$\begin{cases} \mathrm{SI}_{targetedmuscles}(g_i, I) = \frac{\sum_{muscles in g_i} \omega_{i,j} \cdot log(1+A_j(I))}{log 2} \\ \mathrm{SI}_{leftvsright}(s_i, I) = f_+(\frac{max_{ipsilateral_{s_i}}(A_j(I)) - max_{contralateral(s_i}(A_j(I))}{max_{ipsilateral_{s_i}}(A_j(I)) + max_{contralateral(s_i}(A_j(I))}) \\ \mathrm{f}_+ = \begin{cases} \mathrm{x\ if\ x} > 0 \\ 0 \mathrm{\ if\ x} \leq 0 \end{cases} \end{cases} \tag{4.3}$$

where $A_j(I)$ represents the normalized EMG activity of muscle j in response to EES amplitude I. $\omega_{i,j}$ is a weight associated with muscle j for the targeted muscle group g_i. For each targeted muscle group, weights of agonists (respectively antagonists) are positive (respectively negative), and the sum of weights over agonists (respectively antagonists) is equal to 1 (respectively -1). These weights were chosen empirically to capture the respective contributions of each muscle in the targeted muscle group:

	Ilio-psoas (Il)	Rectus femoris (RF)	Vastus lateralis (VLat)	Semi-tendi nosus (ST)	Tibialis anterior (TA)	Gastroc-nemius medialis (MG)	Soleus (Sol)
Hip flexion (L1)	0.8	0.2	-	-1	-	-	-
Knee extension (L3)	-0.5	0.2	0.8	-0.5	-	-	-
Ankle flexion (L4)	-	-	-	-	1	-0.2	-0.8
Ankle extension (S1)	-	-	-	-	-1	0.2	0.8

Table 4.2: Weights of agonist and antagonist muscle groups for the calculation of selectivity indices from EMG data.

Torque and EMG activity during voluntary contractions

The recorded torque was low-pass filtered below 5 Hz and EMG activities were band-pass filtered between 10 and 450 Hz (4th-order Butterworth filter). The Root Mean Square (RMS) of the EMG activity was calculated with a 500-ms centered running window. During maximum voluntary contractions without EES, the torque produced was quantified as the average within a 500-ms time window centered at the peak torque. EMG activities were quantified as their RMS value at the peak torque. During maximum voluntary contractions with EES, the task was divided into four time periods: onset of voluntary contribution, EES onset, end of voluntary contribution, EES end. Because the sudden onset of EES created a transient peak in the torque and EMG activities, we further split the analysis between the transient (EES onset to 1.1 s) and sustained effects after EES onset (Fig. 4.6).

EMG activity during walking

EMG activities were processed according to the SENIAM (Surface Electromyography for the Non-Invasive Assessment of Muscles) standards for EMG recordings. All displayed EMG activities during walking were band-pass filtered between 10 and 450 Hz (4th-order Butterworth filter). A moving average of the rectified EMG signal within a centered 250-ms time window was used to generate normalized EMG envelopes for quantification. With EES, the sudden EES onset created transient peaks of EMG activity that did not translate into sustained muscle contractions but nevertheless contributed to the computation of EMG envelopes. To avoid this issue, we systematically clipped EMG responses within a time window of 50 ms around the onset of EES trains.

Calculation of motoneuron activation maps

Motoneuron pools innervating hip flexors (Il, RF), knee extensors (VLat, RF), ankle flexors (TA) and ankle extensors (MG, Sol) are spatially distributed along the rostro-caudal axis of the lumbosacral spinal cord (Dietz, 2010). We modelled the activation of motoneuron pools in each spinal segment S_i as a linear combination of the normalized EMG activities of leg muscles M_j:

$$S_i = \frac{\sum_{muscles} W_{i,j} \cdot M_j}{\sum_{muscles} W_{i,j}} \tag{4.4}$$

If all muscles reach their maximum activity, the activation of each spinal segment is equal to 1. The coefficients $W_{i,j}$ represent how much each muscle reflects the underlying activity of a spinal segment (Cappellini et al., 2010). As an approximation, we took for $W_{i,j}$ the ratio of motoneurons innervating the muscle j and present in the spinal segment i, with respect to all motoneurons innervating the muscle j.
These coefficients were derived from anatomical studies (Sharrard, 1964).

	Iliopsoas (Il)	Rectus femoris (RF)	Vastus lateralis (VLat)	Semi-tendinosus (ST)	Tibialis anterior (TA)	Gastrocnemius medialis (MG)	Soleus (Sol)
L1	0.4	0	0	0	0	0	0
L2	0.4	0.12	0.12	0	0	0	0
L3	0.2	0.19	0.19	0	0	0	0
L4	0	0.19	0.19	0.12	0	0.77	0
L5	0	0	0	0.4	0.23	0.23	0.09
S1	0	0	0	0.4	0.77	0	0.45
S2	0	0	0	0.08	0	0	0.45

Table 4.3: Myotome of average population.

Motoneuron activation maps derived from single-pulse EES experiments were calculated from the peak-to-peak responses, while motoneuron activation maps during functional tasks were computed with the instantaneous or average value of EMG envelopes. Motoneuron activation maps were interpolated and superimposed onto a 3D illustration of the human spinal cord.

Extraction of hotspots underlying walking

Three hotspots were extracted from the spatiotemporal maps of motoneuron activation underlying walking of healthy individuals. Hotspots were extracted from the isopotential lines at 45, 55, 65 and 75 % of the maximum activation in the maps (Wenger et al., 2016). The correlations between each targeted hotspot and EES-induced EMG activity were calculated based on the average motoneuron activation maps of each hotspot ($S_{i,hotspot}$ and those obtained from the EMG activity induced by a 500 ms train of EES during standing ($S_{i,stim}$. The Pearson correlation coefficient was calculated as:

$$\rho_{stim,hotspot} = \frac{\sum_{segments}(S_{i,stim} - \overline{S_{stim}}) \cdot (S_{i,hotspot} - \overline{S_{hotspot}})}{\sqrt{\sum_{segments}(S_{i,stim} - \overline{S_{stim}})^2 \cdot (S_{i,hotspot} - \overline{S_{hotspot}})^2}} \tag{4.5}$$

where $\overline{S} = \frac{1}{N_{segments}} \cdot \sum_{segments} S_i$ and $N_{segments}$ is the number of segments.

Processing of EEG signals

Raw EEG signals were filtered (1-40 Hz, zero-phase IIR filters), down-sampled at 128 Hz, and re-referenced to a common average. ‘Eye blink’ and ‘eye movements’ artifacts were removed by Independent Component Analysis. EES evoked activity was computed by averaging EEG signals from -0.6 to 1 s after stimulation artifact. During volitional movements, epochs were extracted from -1.5 to 1 s after GO cue and from -500 to 500 ms after movement termination, defined as the torque reaching 2 % of the local maximum value. Time frequency spectra were calculated using sliding Hamming windows of 200 ms with time steps of 32 ms. Power spectra were normalized to the average values of the corresponding frequency bin. Beta (17-30Hz) power spectra over leg sensorimotor area (Cz) was calculated during Event Related reSynchronization (ERS), defined 0 to 500 ms after movement.

Statistics

All quantifications show the mean and standard error of the mean of the represented variables, in addition to all individual data. Normality of the data was confirmed using the Kolmogorov-Smirnov test. Comparisons between two conditions were performed using a two-tailed Student’s t-test. Comparisons involving more than two categories were performed using a 1-way ANOVA, followed post hoc by Tukey’s Honest Significance Difference tests. *, **, *** indicate a p-value smaller than 0.05, 0.01, 0.001 respectively. Significant differences for EEG data were obtained by randomly permuting single trial beta ERS values of the two conditions. The number of permutations was determined to reach $\alpha = 0.001$.

5 Enabling immediate recovery of trunk and leg motor functions after complete paralysis with dedicated epidural electrical stimulation paradigms

In chapter 3, I provided evidence that the artificial recruitment of proprioceptive afferents with continuous EES interferes with the natural firing of these recruited afferents during locomotion through antidromic collisions. I suggested that the use of spatiotemporal stimulation may mitigate the cancellation of proprioceptive information.

In chapter 4, I outlined a clinical trial in which spatiotemporal stimulation strategies were combined with activity-based training in individuals who had sustained a spinal cord injury more than four years ago and presented permanent motor deficits or complete paralysis. For this purpose, I improved the stimulation paradigm by one additional component. I developed semi-personalized hybrid computational models of each participant, composed of coupled 3D FEM and compartmental cable models of the lumbosacral spinal cord to guide the surgical implantation of the neurostimulation system. Through this procedure we gained the capacity to target individual posterior roots in large and diversified patient-cohorts. Hence, we referred to this approach as targeted spinal cord stimulation. We were able to enable voluntary control of walking in our participants. We observed an improvement of locomotor performance during rehabilitation that ultimately re-established voluntary control over previously paralysed muscles without stimulation.

These results established a technological framework that can aid activity-based therapies for the recovery of locomotion in paralysed subjects and support activity of daily living after spinal cord injury. However, the precise targeting of individual posterior roots remained challenging. This was due to two factors: 1. EES was applied over the lumbosacral spinal cord with multielectrode paddle leads that were not designed for this specific purpose; 2. My computational models were not fully personalized so that levels of unspecific activation of proprioceptive afferents persisted.

In this following chapter, I outline a rectification to these challenges. Firstly, I developed a computational framework to automatically generate fully personalized computational models from high-resolution medical imaging datasets, including critically-important realistic representations of rootlet structures. Secondly, I combined this computational framework with anatomical assessments to devise an arrangement of electrodes on a paddle lead to specifically target the posterior roots of the lumbosacral spinal cord in large and diversified patient-cohorts. Thirdly, we implanted three subjects with complete spinal cord injury with this neuromodulation system. For this purpose, I leveraged my computational framework to optimize the placement of the paddle lead on the lumbosacral spinal cord to gain control over key muscles in their legs. I demonstrate that this newly devised multielectrode paddle lead targets the ensemble of dorsal roots projecting to spinal segments embedding motoneurons innervating leg and lower-trunk muscles better than a commonly used lead that was originally designed to alleviate chronic pain. Finally, we show that individuals with complete sensorimotor SCI immediately regained the ability to stand, walk, cycle, swim, and control their trunk.

Related publication and personal contributions

The content of this chapter is adapted - with permission of the co-authors - from the following manuscript: **Andreas Rowald***, Salif Komi*, Robin Demesmaeker*, Edeny Baaklini†, Sergio Daniel Hernandez-Charpak†, Edoardo Paoles†, Hazael Montanaro, Antonino Cassara, Fabio Becce, Bryn Lloyd, Taylor Newton, Jimmy Ravier, Nawal Kinany, Marina D´Ercole, Aurélie Paley, Nicolas Hankov, Camille Varescon, Laura McCracken, Molywan Vat, Miroslav Caban, Anne Watrin, Charlotte Jacquet, Léa Bole-Feysot, Cathal Harte, Henri Lorach, Andrea Galvez, Manon Tschopp, Natacha Herrmann, Moïra Wacker, Lionel Geernaert, Isabelle Fodor, Valentin Radevich, Katrien Van Den Keybus, Grégoire Eberle, Etienne Pralong, Maxime Roulet, Jean-Baptiste Ledoux, Eleonora Fornari, Stefano Mandija, Loan Mattera, Roberto Martuzzi, Bruno Nazarian, Stefan Benkler, Simone Callegari, Nathan Greiner, Benjamin Fuhrer, Martijn Froeling, Nik Buse, Tim Denison, Rik Buschman, Damien Ganty, Jurriaan Bakker, Vincent Delattre, Hendrik Lambert, Karen Minassian, Cornelis A T van den Berg, Anne Kavounoudias, Silvestro Micera, Dimitri Van De Ville, Quentin Barraud, Erkan Kurt, Niels Kuster, Esra Neufeld, Marco Capogrosso, Leonie Asboth, Fabien B. Wagner‡ & Jocelyne Bloch‡ & Grégoire Courtine‡, "**Immediate recovery of trunk and leg motor functions after complete paralysis**", **Nature Medicine** (in review).
*, †, ‡ contributed equally to this work

Personal contributions: conceived and developed the computational framework, adapted medical imaging protocols, collected and analyzed medical imaging datasets, developed the computational models, performed computer simulations, performed behavioural and electrophysiological experiments, data analysis, figures preparation, manuscript writing.

5.1 Abstract

Epidural Electrical Stimulation (EES) targeting the dorsal roots of lumbosacral segments restored mobility in individuals with paralysis due to Spinal Cord Injury (SCI). However, EES was delivered with multielectrode paddle leads that were not designed to target the ensemble of dorsal roots involved in leg and trunk movements. Here, we hypothesized that an arrangement of electrodes targeting these roots specifically would result in superior efficacy, restoring more diverse motor activities after the most severe SCI. We established a personalizable computational framework to inform the arrangement of electrodes on a new paddle lead, guide its neurosurgical positioning, and configure activity-specific stimulation programs. We show that individuals with complete sensorimotor SCI immediately regained the ability to stand, walk, cycle, swim, and control their trunk.

5.2 Introduction

Three decades of preclinical (Asboth et al., 2018; Courtine et al., 2009; Ichiyama et al., 2008; van den Brand et al., 2012; Wenger et al., 2014) and clinical (Angeli et al., 2018; Barolat et al., 1986; Danner et al., 2015; Darrow et al., 2019; M. R. Dimitrijevic et al., 1998; Formento et al., 2018; M. L. Gill et al., 2018; S. Harkema et al., 2011; Herman et al., 2002; Wagner et al., 2018) research showed that EES applied over the lumbosacral spinal cord can restore standing and walking after SCI. A subset of the treated individuals with motor complete paralysis even regained the ability to walk overground with EES after many months of intense training assisted by multiple physical therapists (Angeli et al., 2018; M. L. Gill et al., 2018). However, translation of EES into a commonly available therapy requires a technological framework that not only enables immediate recovery of numerous motor activities with limited human resources, but also mediates this recovery in every treated individual. Here, we aim to address all these challenges.

Mounting evidence suggests that EES recruits large-diameter afferent fibers at their entrance in the spinal cord through the dorsal roots (Capogrosso et al., 2013; Formento et al., 2018; Y. P. Gerasimenko et al., 2006; Moraud et al., 2016; Rattay et al., 2003). The recruitment of large-diameter, myelinated afferent fibers primarily leads to the activation of motoneurons embedded in the spinal segment innervated by the root wherein these afferents reside (Wagner et al., 2018; Wenger et al., 2014). Therefore, targeting an individual dorsal root enables the modulation of specific motoneuron ensembles (Capogrosso et al., 2016; Wagner et al., 2018; Wenger et al., 2014). This biological principle guided the development of EES protocols (Capogrosso et al., 2016; Capogrosso et al., 2018; Minev et al., 2015; Wenger et al., 2014) that target the individual dorsal roots with a predefined timing to reproduce the natural spatiotemporal activation pattern (Cappellini et al., 2010; Yakovenko et al., 2002) of motoneurons during walking. Compared to continuous EES, these biomimetic stimulation protocols have mediated superior recovery of walking after SCI (Capogrosso et al., 2016; Formento et al., 2018; Wagner et al., 2018; Wenger et al., 2014).

Thus far, EES has been delivered using off-label neurotechnologies that were originally designed to alleviate chronic pain (Angeli et al., 2018; Barolat et al., 1986; Danner et al., 2015; Formento et al., 2018; M. L. Gill et al., 2018; S. Harkema et al., 2011; Herman et al., 2002; Wagner et al., 2018). These neurotechnologies include paddle leads with an arrangement of electrodes that target the dorsal column (Molnar & Barolat, 2014). Instead, the recovery of motor functions requires targeting the dorsal roots (Minassian et al., 2012). While the relative coverage of the paddle lead determines the efficacy of EES to enable volitional movements after paralysis (Mesbah et al., 2020; Wagner et al., 2018), the short length of existing paddle leads limits the number of dorsal roots that can be targeted with EES. Therefore, current neurotechnologies fail to leverage the biological principles through which EES restores movement after SCI.

Here, we designed and fabricated a new paddle lead with an arrangement of electrodes that aim to target the ensemble of dorsal roots projecting to spinal segments embedding motoneurons innervating leg and lower-trunk muscles. We also established a new, semi-automated personalizable computational framework combining high-resolution structural and functional imaging to optimize the surgical placement of this lead. Finally, we developed a purpose software with real-time displays of EES waveforms and physiological signals to support the rapid configuration of biomimetic stimulation programs that can be used independently by patients in the community.

We aimed to leverage this portfolio of new neurotechnologies to elaborate activity-dependent stimulation programs that address the deficits of individuals presenting with the most severe forms of SCI across a broad range of motor activities, including the critically-important control of the trunk (Angeli et al., 2018; M. Gill et al., 2020; Moraud et al., 2018).

5.3 Results

5.3.1 Variability of spinal cord topological organisation

Sacral (S1-S2), lumbar (L1-L5) and low-thoracic (T12) dorsal roots project to spinal segments containing motoneurons innervating leg and lower-trunk muscles (Fig. 5.1a). Therefore, we aimed to identify an arrangement of electrodes that would be suitable to target all of these roots across the human population. We first asked whether the inter-individual variability of spinal cord anatomy would be compatible with this aim.

Neuroanatomical quantification of 27 spinal cords exposed a pronounced variability of spinal segment lengths. In particular, we identified a disproportionately large degree of variability in the length of upper lumbar segments (Fig. 5.1b).

We previously showed that the tridimensional topology of a dorsal root determines the distribution of EES-induced electric potentials along this root, and consequently, the probability of recruiting afferent fibers embedded within this root (Greiner et al., 2021). Therefore, we complemented our neuroanatomical quantifications with an analysis of tridimensional dorsal root topology.

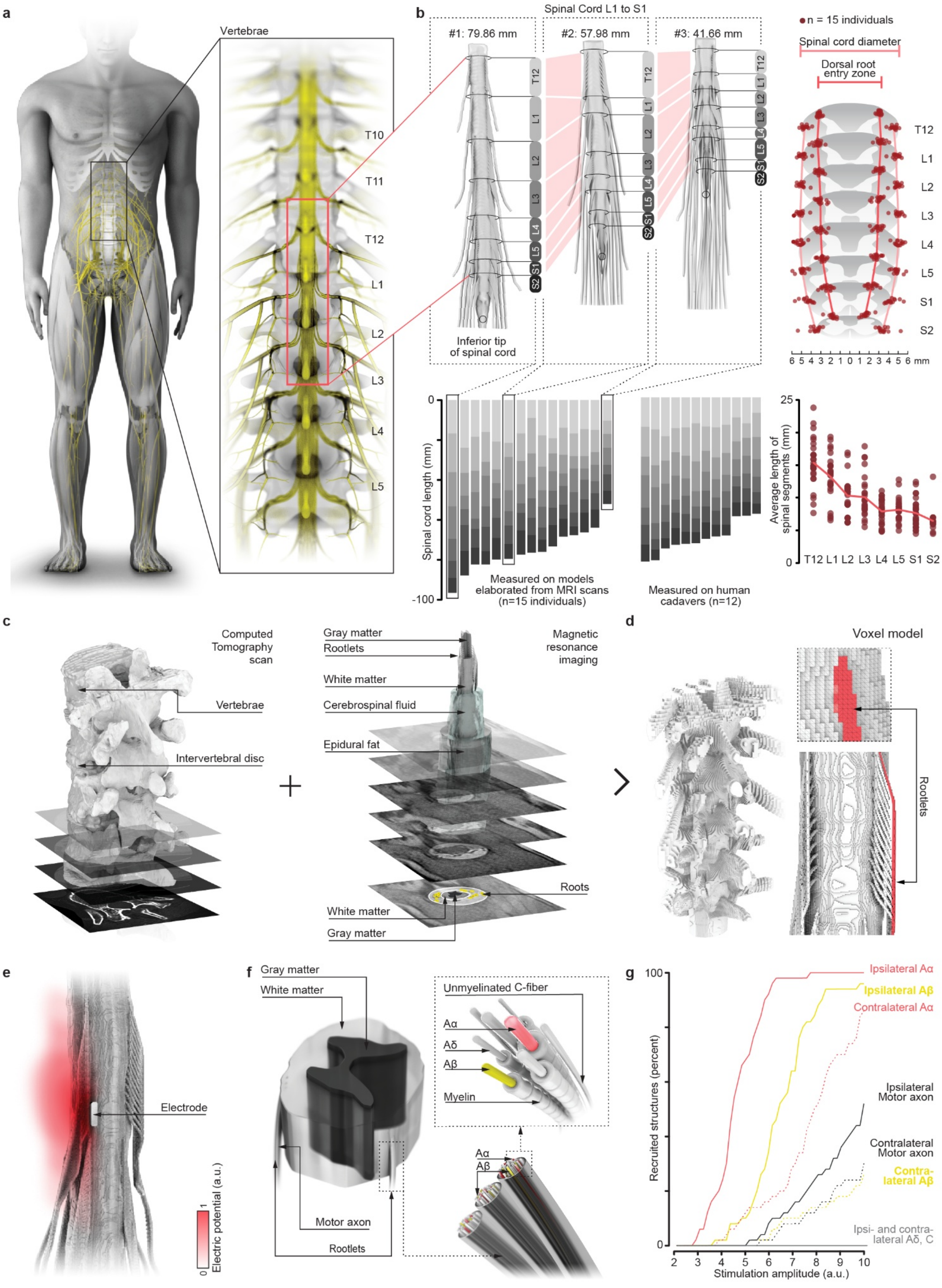
a
Vertebrae
T10
T11
T12
L1
L2
L3
L4
L5
b
Spinal Cord L1 to S1
#1: 79.86 mm
#2: 57.98 mm
#3: 41.66 mm
T12
L1
L2
L3
L4
L5
S1
S2
Inferior tip
of spinal cord
● n = 15 individuals
Spinal cord diameter
Dorsal root
entry zone
T12
L1
L2
L3
L4
L5
S1
S2
6 5 4 3 2 1 0 1 2 3 4 5 6 mm
0
Spinal cord length (mm)
-100
Measured on models
elaborated from MRI scans
(n=15 individuals)
Measured on human
cadavers (n=12)
25
Average length of
spinal segments (mm)
0
T12 L1 L2 L3 L4 L5 S1 S2
c
Computed
Tomography
scan
Vertebrae
Intervertebral disc
+
Gray matter
Rootlets
White matter
Cerebrospinal fluid
Epidural fat
Magnetic
resonance
imaging
Roots
White matter
Gray matter
d
Voxel model
Rootlets
e
Electrode
Electric potential (a.u.)
0
1
f
Gray matter
White matter
Unmyelinated C-fiber
Aα
Aδ
Aβ
Myelin
Aα
Aβ
Motor axon
Rootlets
g
100
Recruited structures (percent)
0
Ipsilateral Aα
Ipsilateral Aβ
Contralateral Aα
Ipsilateral
Motor axon
Contralateral
Motor axon
Contra-
lateral Aβ
Ipsi- and contra-
lateral Aδ, C
2 3 4 5 6 7 8 9 10
Stimulation amplitude (a.u.)

Figure 5.1: Anatomical quantification and personalizable computational models

Figure 5.1: (Continued) a, Human spinal cord, including a visualization of the targeted thoracic, lumbar and sacral dorsal roots. b, Spinal cord topology from 27 adult individuals were quantified from MRI/CT scans of 15 healthy volunteers and anatomical measurements of 12 cadavers. Each bar or dot reports measurements from one individual. Three complete anatomical models are shown from individuals with widely different topologies. c, Automated framework to elaborate anatomical models of spinal cord tissues from high-resolution MRI and CT images. d, Discretization of anatomical models as voxels using rectilinear (structured) gridding. e, Distribution of electric potential when delivering one pulse of EES. f, Compartmental cable models incorporating the entire range of afferents and efferents are initialized in the rootlets. g, Relative recruitment of afferents and efferents when delivering a single pulse of EES with increasing amplitude.

This analysis required visualizing the dorsal roots of humans in vivo, since postmortem loss of cerebrospinal fluid alters the topological organization of these roots in the spinal cord. To enable this visualization, we optimized structural Magnetic Resonance Imaging (MRI) sequences that increased the tridimensional spatial resolution while enhancing the contrast resolution between the cerebrospinal fluid and spinal cord tissues (Fig. 5.1c and 5.2). This contrast enabled the semi-automated segmentation of images to recognize the bones and joints, cerebrospinal fluid, soft tissues, spinal cord, and spinal root contours. We then converted the segmented images into realistic tridimensional anatomical models of the entire spine (Fig. 5.1d). We could thus analyze the topology of the dorsal roots in 15 healthy individuals. This analysis confirmed the pronounced variability in the rostrocaudal distribution of dorsal roots in humans (Fig. 5.1b). Instead, we found that the widths of the dorsal root entry zones were remarkably consistent across the 15 spinal cords (Fig. 5.1b and Fig. 5.4).

5.3.2 Atlas of computational spinal cord models

Our implantable pulse generator could accommodate a paddle lead with 16 electrodes. Therefore, our challenge was to identify an arrangement of 16 electrodes that can access the 16 targeted dorsal roots despite the highly variable topology of the human spinal cord. We posited that resolving this challenge would require tradeoffs, and that identifying these tradeoffs would be contingent on computational models.

We therefore established a pipeline to generate highly-realistic personalizable computational models of the interactions between EES and the spinal cord. This pipeline leverages the verified anatomical and biophysical models of the Sim4Life computational life-sciences simulation platform (Neufeld et al., 2013).

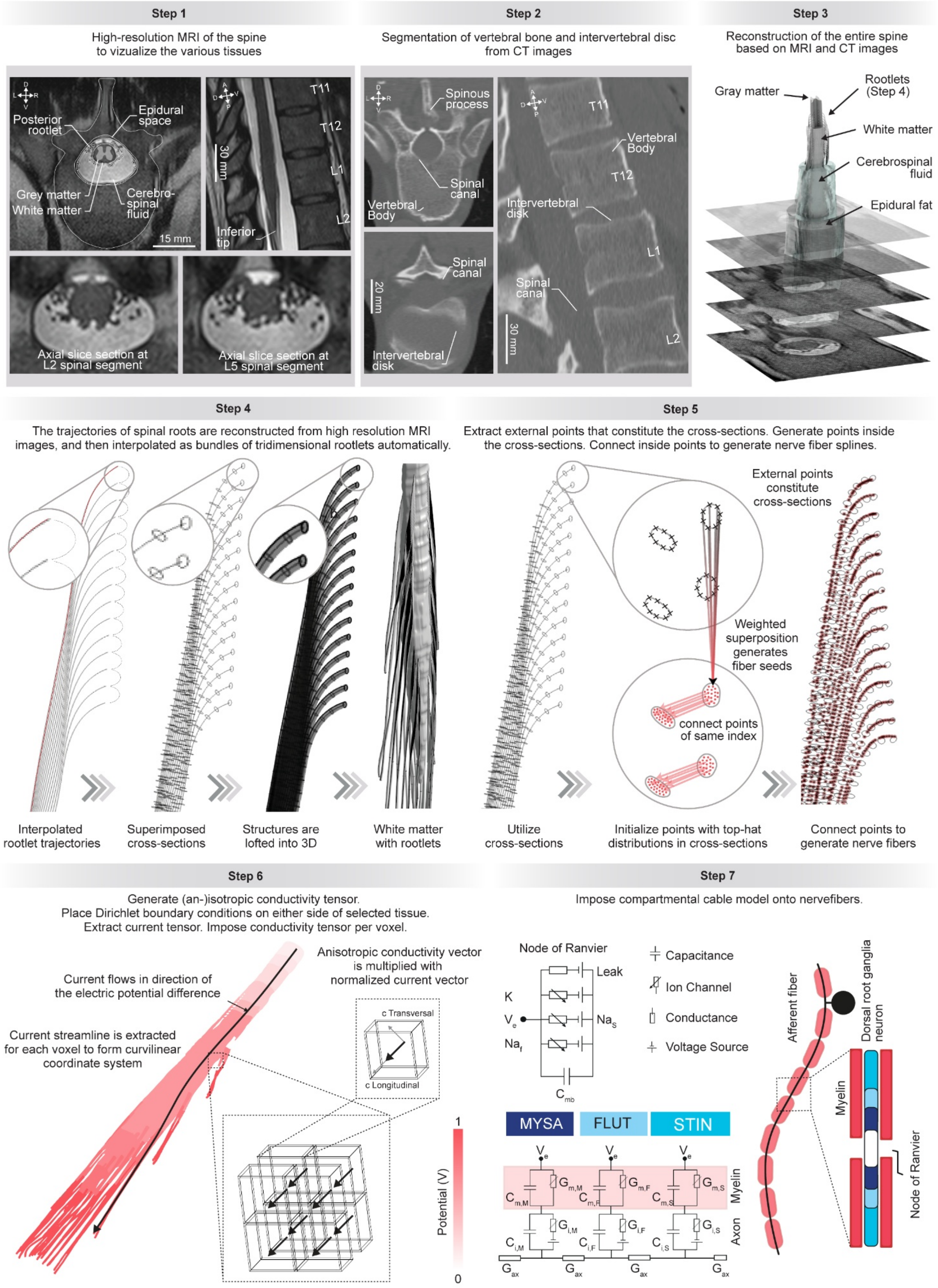
Step 1
High-resolution MRI of the spine to vizualize the various tissues
Posterior rootlet
Epidural space
Grey matter
White matter
Cerebro-spinal fluid
15 mm
T11
T12
L1
L2
30 mm
Inferior tip
Axial slice section at L2 spinal segment
Axial slice section at L5 spinal segment
Step 2
Segmentation of vertebral bone and intervertebral disc from CT images
Spinous process
Spinal canal
Vertebral Body
Spinal canal
20 mm
Intervertebral disk
T11
Vertebral Body
T12
Intervertebral disk
L1
Spinal canal
30 mm
L2
Step 3
Reconstruction of the entire spine based on MRI and CT images
Gray matter
Rootlets (Step 4)
White matter
Cerebrospinal fluid
Epidural fat
Step 4
The trajectories of spinal roots are reconstructed from high resolution MRI images, and then interpolated as bundles of tridimensional rootlets automatically.
Interpolated rootlet trajectories
Superimposed cross-sections
Structures are lofted into 3D
White matter with rootlets
Step 5
Extract external points that constitute the cross-sections. Generate points inside the cross-sections. Connect inside points to generate nerve fiber splines.
External points constitute cross-sections
Weighted superposition generates fiber seeds
connect points of same index
Utilize cross-sections
Initialize points with top-hat distributions in cross-sections
Connect points to generate nerve fibers
Step 6
Generate (an-)isotropic conductivity tensor.
Place Dirichlet boundary conditions on either side of selected tissue.
Extract current tensor. Impose conductivity tensor per voxel.
Current flows in direction of the electric potential difference
Current streamline is extracted for each voxel to form curvilinear coordinate system
Anisotropic conductivity vector is multiplied with normalized current vector
c Transversal
c Longitudinal
1
Potential (V)
0
Step 7
Impose compartmental cable model onto nervefibers.
Node of Ranvier
Leak
K
V_e
Na_S
Na_f
C_mb
Capacitance
Ion Channel
Conductance
Voltage Source
MYSA
FLUT
STIN
V_e
V_e
V_e
G_m,M
G_m,F
G_m,S
C_m,M
C_m,F
C_m,S
Myelin
G_i,M
G_i,F
G_i,S
C_i,M
C_i,F
C_i,S
Axon
G_ax
G_ax
G_ax
G_ax
Afferent fiber
Dorsal root ganglia neuron
Myelin
Node of Ranvier

Figure 5.2: Personalizable computational models of the interactions between EES and the spinal cord. Step 1, High-resolution MRI images enable clear-cut visualization of spinal tissues, including individual dorsal roots. Step 2, CT images enable reconstructing the tridimensional geometry of vertebral bodies.

Figure 5.2: (Continued) Step 3, Elaboration of highly realistic anatomical models from MRI and CT scans. Step 4, Automatic generation of rootlets based on the identification of the uppermost rootlet (shown in red) in high-resolution MRI acquisitions. Rootlet trajectories are interpolated from this rootlet, using the measured segment length as a reference. Step 5, Splines representing the nerve fibers are automatically generated inside the rootlets. For this purpose, points are initialized in each cross-section based on a weighted superposition of the points constituting the cross-section itself. These points are connected to generate splines. Step 6, Conductivity maps are imposed on each voxel of the discretized finite element models. The white matter and rootlets require an anisotropic conductivity map. Functionality has been implemented in Sim4Life for that purpose that generates anisotropic conductivity maps by solving a diffusion problem with suitable boundary conditions in the tissues of interest and locally aligning conductivity tensors with the gradient of the obtained solution. Step 7, Compartmental cable models are initialized along each spline to integrate the nerve fibers.

We configured Sim4Life to generate tridimensional finite element models of the lumbosacral spinal cord from the segmented images of MRI scans, and then assigned realistic biophysical properties to all the modeled tissues (Fig. 5.1 and 5.2). In addition, we developed an algorithm that creates models of rootlet bundles and their innervation patterns, since we found that the rootlets must be modeled explicitly to obtain accurate simulations (Fig. 5.4). Sim4Life then functionalized the anatomical geometry with populations of efferents and afferents fiber models (trajectories and biophysics) whose myelin contents and diameters correspond to Aα, Aβ, Aδ, and C fibers (Fig. 5.1f). These fiber models were implemented as compartmental cable models embedded within their corresponding ventral and dorsal roots. Finally, the physics and neuron electrophysiology solvers of the Sim4Life simulation platform predicted the probability of recruiting efferent and afferent fibers within each root when delivering EES. To illustrate the relevance of this computational pipeline, we asked whether EES applied over the human spinal cord primarily recruits large-diameter afferent fibers in the dorsal root, as we previously demonstrated in rats (Capogrosso et al., 2013). Simulations suggested that this preferential recruitment is even more pronounced in humans, since the majority of Aα fibers were recruited before the depolarisation of Aβ fibers in the model (Fig. 5.1g).
Using this pipeline, we generated a freely available atlas of 15 personalized computational models (see section 5.5.8) that provided an instrumental resource to analyse the influence of electrode arrangements on the relative recruitment of dorsal roots.

5.3.3 Optimized electrode arrangement

We reasoned that identifying tradeoffs for an optimal arrangement of 16 electrodes on the paddle lead would require circumscribing the analysis to the key anatomical features that determine the selectivity of EES. We thus restricted our analysis to four key features (Fig. 5.3a):
(**i**) **Rostrocaudal distributions:** We merged all the spinal cords of the atlas into a unified model that captured the averaged topology of the human spinal cord. We found that each

individual spinal cord displayed specific dorsal root distributions (Fig. 5.4), which would justify non-uniform distributions of electrodes along the rostrocaudal direction. However, the interactions between varying spinal cord lengths and distinct dorsal root distributions led to inconsistencies across individuals. Therefore, we anticipated that a uniform distribution of electrodes along the rostrocaudal direction would be more appropriate to circumvent the inherent variability in the distribution of the targeted dorsal roots (Fig. 5.3b).

(**ii**) **Lateral positions to maximize left-right selectivity:** Simulations indicated that positioning the electrode 2.3 mm lateral to the midline would maximize the selective recruitment of the ipsilateral dorsal root entry zone.. However, this selectivity declined by 50% when the electrode was moved by 1 mm toward the midline. Such mediolateral deviations are inevitable when a paddle lead is inserted into the irregular spinal canal. We concluded that the lateral positions of the electrodes must be optimized to mitigate the detrimental impact of these potential mediolateral deviations. Simulations indicated that placing the electrodes at 4.7 mm from the midline would meet this requirement (Fig. 5.3c).

(**iii**) **Midline positions to enable current steering:** The modulation of motoneurons with EES requires current amplitudes that vary substantially across the dorsal roots and between individuals. We anticipated that large amplitudes of EES would augment the spread of electric potentials over the spinal cord, and consequently, reduce the selectivity of the electrode. Indeed, simulations confirmed that increasing the amplitude of EES leads to a proportional recruitment of non-targeted dorsal roots, especially from the contralateral side (Fig. 5.3d). This result compelled us to identify strategies to attenuate the undesired recruitment of non-targeted roots with increasing amplitudes of EES. Simulations revealed that multipolar electrode configurations incorporating midline electrodes enable steering the current toward the targeted root while minimizing the recruitment of contralateral roots (Fig. 5.3d).

(**iv**) **Arrangement for the sacral region:** Biomimetic EES leverages the rostrocaudal organization of dorsal root entry zones to recruit the individual dorsal roots specifically. However, the agglutination of the lumbar rootlets around sacral segments is an impediment to the selective recruitment of the sacral root entry zones (Fig. 2e). Since the somatotopy of the lumbar dorsal rootlet bundles is maintained along the transverse axis of sacral segments, we reasoned that a transverse arrangement of electrodes would rescue this selectivity. We also anticipated that this arrangement would enable steering current toward the targeted sacral root entry zones while shielding the non-targeted lumbar dorsal rootlets. Simulations confirmed these considerations (Fig. 5.3e).

These computational experiments identified key tradeoffs to mitigate the impact of variable spinal cord topology on the design of the new paddle lead. We translated these tradeoffs into an arrangement of 16 electrodes that we accommodated on a new paddle lead fabricated with standard medical-grade processes (Fig. 5.3f). Extensive bench and in vivo testing was conducted to validate the mechanical, electrical and biocompatibility properties of the paddle lead, which led to the equivalent of an investigational device exemption from Swiss competent authorities.

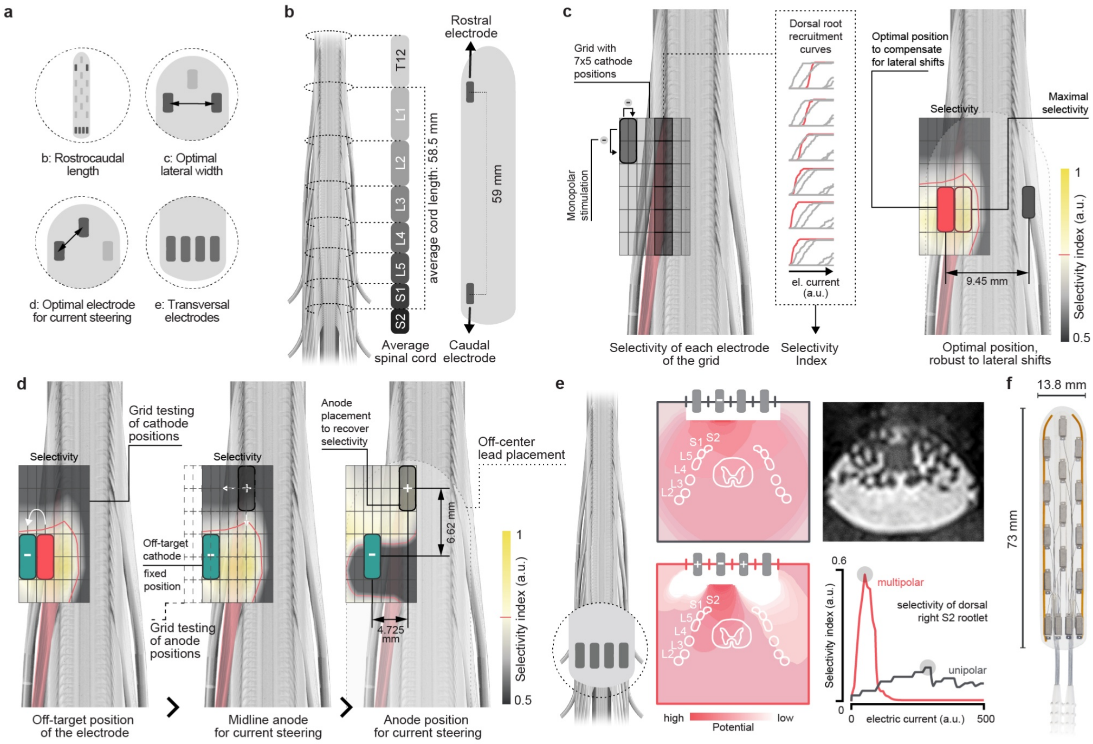
a
b: Rostrocaudal length
c: Optimal lateral width
d: Optimal electrode for current steering
e: Transversal electrodes
b
Rostral electrode
T12
L1
L2
L3
L4
L5
S1
S2
average cord length: 58.5 mm
59 mm
Average spinal cord
Caudal electrode
c
Grid with 7x5 cathode positions
Monopolar stimulation
Dorsal root recruitment curves
el. current (a.u.)
Selectivity of each electrode of the grid
Selectivity Index
Optimal position to compensate for lateral shifts
Selectivity
Maximal selectivity
9.45 mm
Optimal position, robust to lateral shifts
Selectivity index (a.u.)
1
0.5
d
Selectivity
Grid testing of cathode positions
Off-target cathode
fixed position
Grid testing of anode positions
Anode placement to recover selectivity
Off-center lead placement
6.62 mm
4.725 mm
Off-target position of the electrode
Midline anode for current steering
Anode position for current steering
Selectivity index (a.u.)
1
0.5
e
S1
S2
L5
L4
L3
L2
high
Potential
low
0.6
multipolar
selectivity of dorsal right S2 rootlet
unipolar
Selectivity index (a.u.)
0
0
electric current (a.u.)
500
f
13.8 mm
73 mm

Figure 5.3: Optimal arrangement of electrodes. a, Highlight of the four features that guided the positioning of the electrodes on the new paddle lead. These features were studied using computational experiments detailed in panels b, c, d, and e. b, Generalized model reconstructed from averaging all the spinal cords of the atlas. The length of the new paddle lead was calculated from this model. c, A grid of 7 x 5 electrodes was positioned over each targeted rootlet bundle, here shown for the L1 dorsal root. Simulations computed a selectivity index for each electrode of the grid to determine the distributions of the lateral electrodes (red rectangle). d, Due to the inherent variability of dorsal root distributions and putative deviations during surgical placement, the selectivity of the cathodes may require adjustments (e.g. simulated offset as blue rectangle). Simulations determined that lateral shifts of the cathodes compensate for deviations in the medial direction, while anodes located over the midline steer current with bipolar stimulation. e, Distribution of electrical potentials when delivering unipolar versus multipolar stimulation over the dorsal roots agglutinated within the thecal sac. The transverse arrangement of electrodes enables steering the current toward the targeted sacral dorsal roots. f, Arrangement of electrodes on the new paddle lead.

5.3.4 Precise preoperative planning

We then asked whether this arrangement of electrodes would enable the expected selective recruitment of all the targeted dorsal roots.

To answer this question, we quantified the selectivity of the new paddle lead for 15 spinal cords of the atlas. Performances differed across the individual models (Fig. 5.4), as expected from the mismatch between a fixed arrangement of electrodes and the large variability of human spinal cord anatomy.

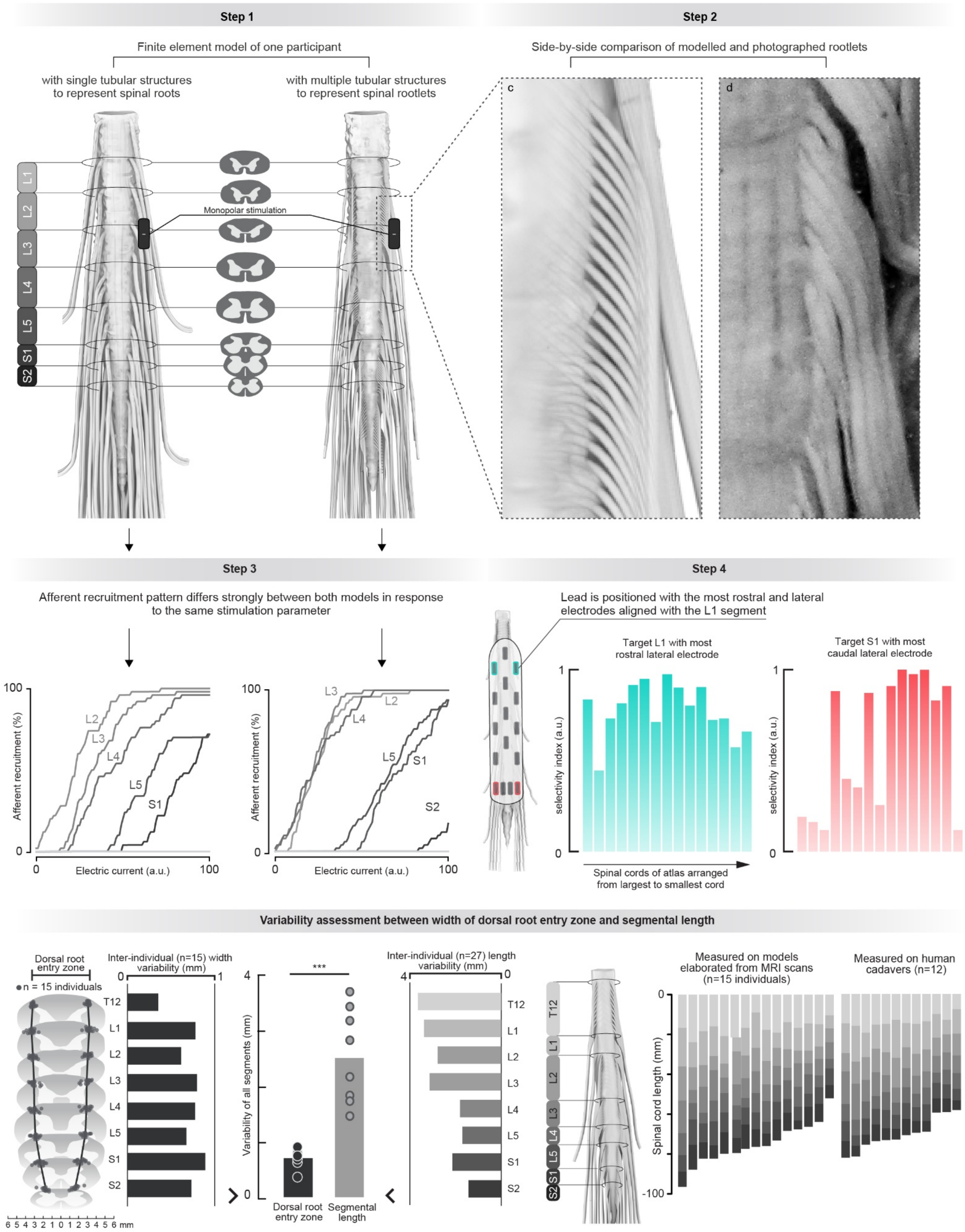

Figure 5.4: Importance of modeling rootlet bundles.

Figure 5.4: (Continued) Step 1, Models of the same spinal cord wherein the dorsal roots are modelled as single tubular structures (left) versus multiple tubular structures mimicking the topology of rootlet bundles observed in humans (right), as shown in Step 2, side by side comparison of the rootlet bundles in the model and in a real spinal cord. To create the model of the rootlets, we determined the entry point of the uppermost rootlet for each spinal segment, and then populated the space from the uppermost rootlet of a given dorsal root to the uppermost rootlet of the next dorsal root by distributing rootlets homogeneously across this space. Step 3, A pulse of EES was delivered with increasing intensities through the electrode depicted in Step 1, over the L3 dorsal root. The plots show the resulting recruitment curve of each dorsal root. The explicit models of rootlets led to pronounced differences in the recruitment curves of each dorsal root. Step 4, Performance of the new paddle lead evaluated in 15 computational models of the atlas. The top left electrode of the paddle lead was positioned over the dorsal root innervating the L1 spinal segment, as depicted in the model on the left. The plot on the left reports the selectivity of this electrode for each model, organized laterally based on the length of the spinal cord (as reported in Fig. 5.1). The plot on the right reports the selectivity of the bottom left electrode to recruit the dorsal root projecting to the S1 spinal segment. Lower Panel, Horizontal bar plots on the left report the variability of the width of the dorsal root entry zone (n = 15 healthy volunteers). Horizontal bar plots on the right report the variability of length of each spinal segment (n = 27 spinal cords). The bar plot between these two plots reports the variability of the width of the dorsal root entry zones and of the length of spinal segments. ***, $P < 0.0001$, t-test.

We concluded that leveraging the full potential of the new paddle lead for each participant would require precise intraoperative positioning. To guide this neurosurgical procedure, we developed a preoperative plan that aims to predict the optimal position of the paddle lead for each participant of the clinical study (Table 5.1).

We exploited our pipeline to generate a personalized computational model of the spinal cord for each participant (Fig. 5.5a). Since EES modulates motoneurons through the recruitment of large-diameter, myelinated afferent fibers, we presumed that localizing the predominant projectome of these fibers in the spinal cord would improve the personalization of the models, and thus the precision of simulations.

To expose this projectome, we monitored the Blood Oxygenation Level Dependent (BOLD) response in the spinal cord (Kinany et al., 2020) when activating proprioceptors, which are innervated by large-diameter afferent fibers. We employed two methods (Fig. 5.6). First, we mobilized each joint passively to elicit a proprioceptive message from the lengthened muscles. Second, we implemented a more precise method based on the application of a mechanical vibration to the tendon of a targeted muscle (Courtine et al., 2007; Landelle et al., 2020). Muscle tendon vibration induces the selective recruitment of muscle spindle afferents embedded in the muscle attached to the vibrated tendon (J.-P. Roll et al., 1989).

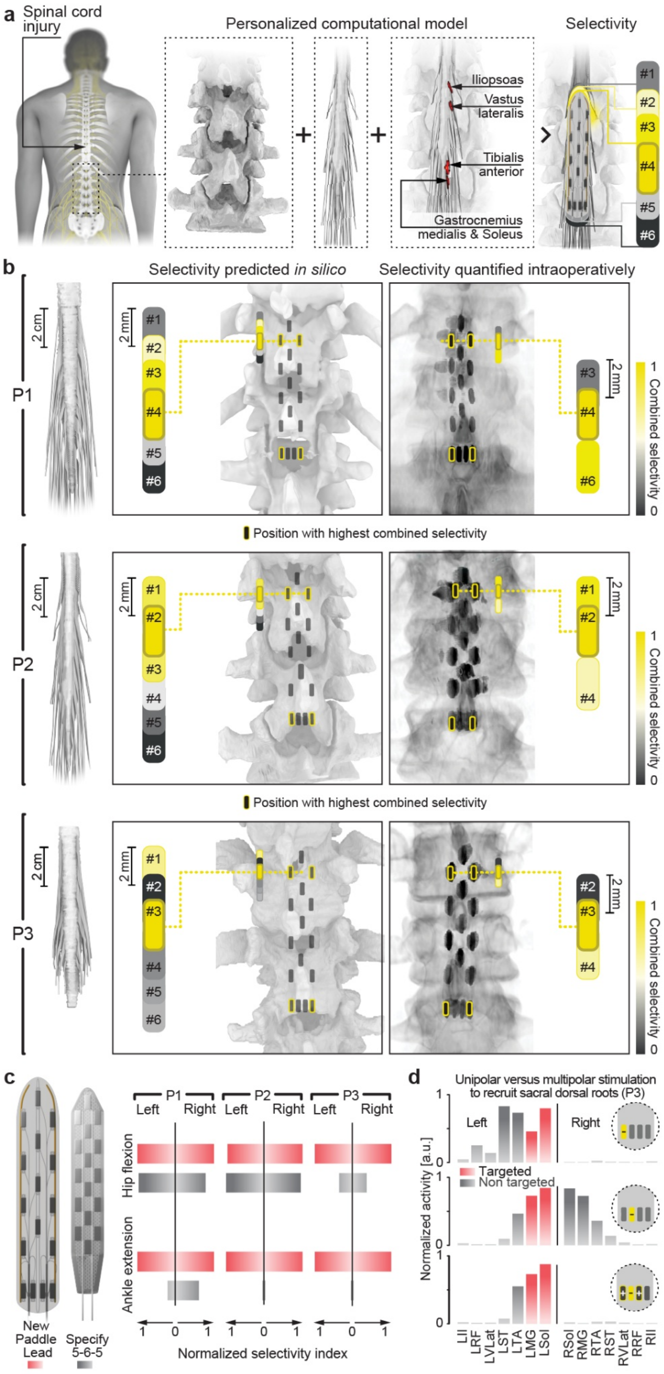
a
Spinal cord injury
Personalized computational model
Selectivity
Iliopsoas
Vastus lateralis
Tibialis anterior
Gastrocnemius medialis & Soleus
#1
#2
#3
#4
#5
#6
b
Selectivity predicted in silico
Selectivity quantified intraoperatively
P1
P2
P3
2 cm
2 mm
Combined selectivity
1
0
Position with highest combined selectivity
c
New Paddle Lead
Specify 5-6-5
P1
P2
P3
Left
Right
Hip flexion
Ankle extension
Normalized selectivity index
1
0
d
Unipolar versus multipolar stimulation to recruit sacral dorsal roots (P3)
Left
Right
Targeted
Non targeted
Normalized activity [a.u.]
LIl
LRF
LVLat
LST
LTA
LMG
LSol
RSol
RMG
RTA
RST
RVLat
RRF
RIl

Figure 5.5: Preoperative planning and intraoperative validation. a, CT scan combined with structural and functional MRI acquisitions enabled the personalization of computational models predicting the interactions between the location of EES and the recruitment of afferents in the dorsal roots. b, For each participant, simulations (left) calculated the relative selectivity of the paddle lead for 6 positions separated by 2 mm, as shown in the vertical bars positioned over the computational model, and their enlarged version next to each bar. The selectivity of electrodes located at each corner of the paddle lead is aggregated in a combined (color coded) selectivity index. The same procedure was conducted intraoperatively (right) for three positions of the paddle lead, including the optimal position predicted by the model. Representations are the same as in the computational simulations. The final surgical positioning of the paddle lead is displayed in the reconstructed CT images. c, Bar plots reporting the selectivity of electrodes from the new paddle lead (in red) and Specify 5-6-5 (in grey) to recruit muscles eliciting hip flexion and ankle extension. d, Bar plots reporting the amplitude of muscle responses when stimulating with monopolar versus multipolar electrode configurations, showing the ability of the transverse electrode arrangement to selectively recruit sacral roots despite the agglutination of all lumbar dorsal roots within the stimulated region.

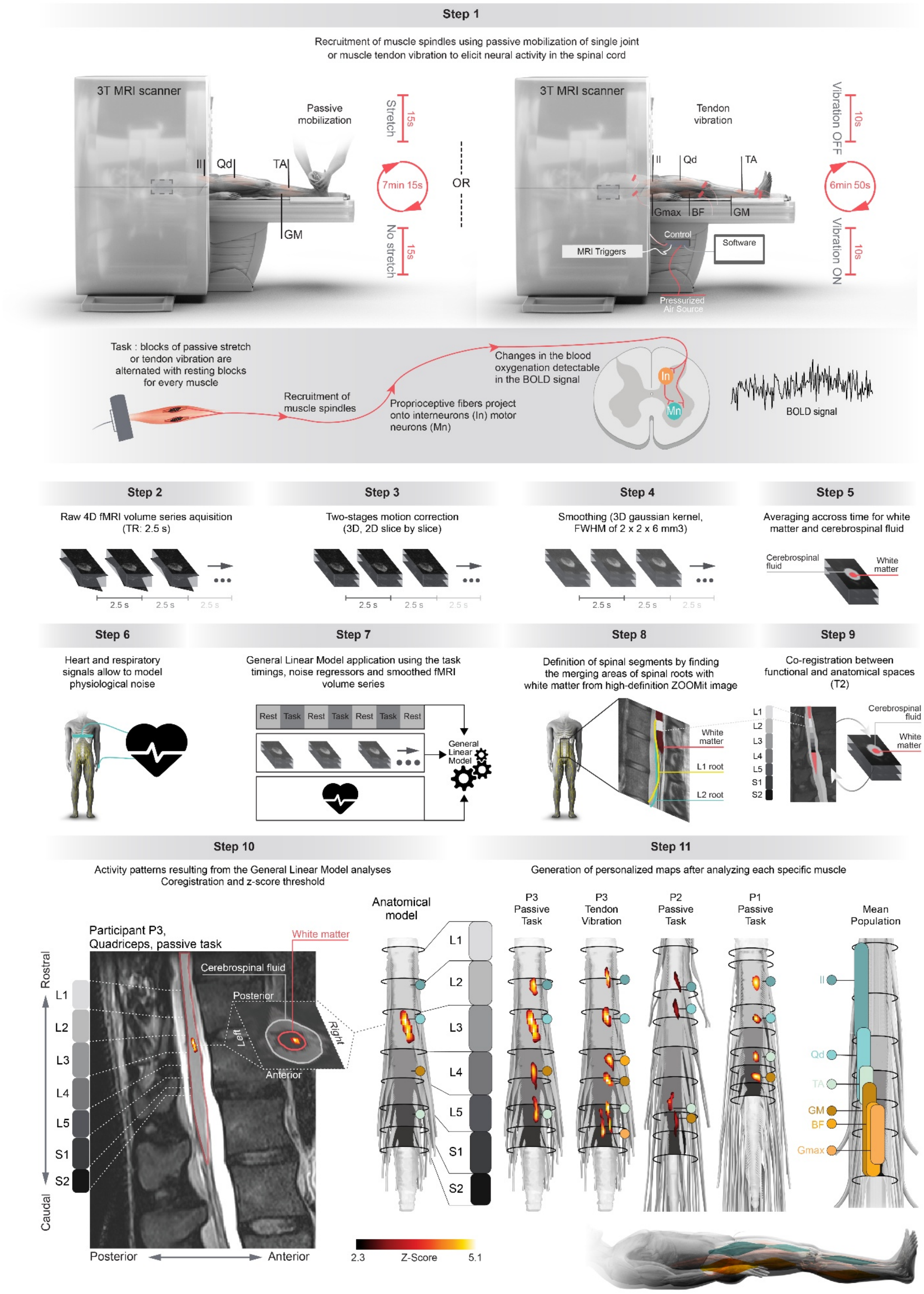
Step 1
Recruitment of muscle spindles using passive mobilization of single joint or muscle tendon vibration to elicit neural activity in the spinal cord
3T MRI scanner
Passive mobilization
Il
Qd
TA
GM
Stretch
15s
7min 15s
No stretch
15s
OR
3T MRI scanner
Tendon vibration
Il
Qd
TA
Gmax
BF
GM
Control
Software
MRI Triggers
Pressurized Air Source
Vibration OFF
10s
6min 50s
Vibration ON
10s
Task : blocks of passive stretch or tendon vibration are alternated with resting blocks for every muscle
Recruitment of muscle spindles
Proprioceptive fibers project onto interneurons (In) motor neurons (Mn)
Changes in the blood oxygenation detectable in the BOLD signal
In
Mn
BOLD signal
Step 2
Raw 4D fMRI volume series aquisition (TR: 2.5 s)
2.5 s
2.5 s
2.5 s
Step 3
Two-stages motion correction (3D, 2D slice by slice)
2.5 s
2.5 s
2.5 s
Step 4
Smoothing (3D gaussian kernel, FWHM of 2 x 2 x 6 mm3)
2.5 s
2.5 s
2.5 s
Step 5
Averaging accross time for white matter and cerebrospinal fluid
Cerebrospinal fluid
White matter
Step 6
Heart and respiratory signals allow to model physiological noise
Step 7
General Linear Model application using the task timings, noise regressors and smoothed fMRI volume series
Rest
Task
Rest
Task
Rest
Task
Rest
General Linear Model
Step 8
Definition of spinal segments by finding the merging areas of spinal roots with white matter from high-definition ZOOMit image
White matter
L1 root
L2 root
Step 9
Co-registration between functional and anatomical spaces (T2)
L1
L2
L3
L4
L5
S1
S2
Cerebrospinal fluid
White matter
Step 10
Activity patterns resulting from the General Linear Model analyses Coregistration and z-score threshold
Participant P3, Quadriceps, passive task
White matter
Cerebrospinal fluid
Posterior
Left
Right
Anterior
Rostral
Caudal
L1
L2
L3
L4
L5
S1
S2
Posterior
Anterior
Step 11
Generation of personalized maps after analyzing each specific muscle
Anatomical model
L1
L2
L3
L4
L5
S1
S2
P3 Passive Task
P3 Tendon Vibration
P2 Passive Task
P1 Passive Task
Mean Population
Il
Qd
TA
GM
BF
Gmax
2.3
Z-Score
5.1

Figure 5.6: Identification of the projectome from propriospinal neurons.

Figure 5.6: (Continued) Step 1, Acquisition of functional MRI from the spinal cord in response to the recruitment of proprioceptive afferents from specific leg muscles. The muscle spindles are recruited either by stretching the muscles in which they are embedded (the limb is mobilized by a physiotherapist, aided with audio cues), or by applying muscle tendon vibration using MR-compatible pneumatic vibrators (synchronized with MRI triggers). Two runs are acquired for each muscle. Only the right leg muscles are tested. In addition to the functional volume series, T2 anatomical images and physiological (heart rate, respiratory) signals are acquired. Step 2, Raw fMRI volume series are repeatedly acquired every 2.5 s (TR) in functional runs lasting about 7 minutes. Step 3, A two staged motion correction (3D and then 2D slice-by-slice) is applied for each run. First, the volumes are registered to their respective averaged-in-time image using 3D rigid body realignment. Secondly, taking as reference the averaged-in-time corrected volume, a slice-by-slice 2D realignment is applied thus accounting for the non rigid property of the spinal cord. Step 4, The motion corrected series are spatially smoothed, volume by volume with 3D gaussian kernel with Full Width at Half Maximum (FWHM) of 2x2x6mm^3. Step 5, The motion-corrected series are again averaged through time. The cerebrospinal fluid and white matter are segmented from this mean functional image. Step 6, Physiological signals (heart rate and respiratory) acquired concomitantly to the fMRI volumes are used to model physiological noise (RETROICOR based procedure). If no signals are available, noise regressors are built with component based noise extraction (aCompCor). Step 7, Acquisition timings corresponding to the task-design, pre-processed (motion corrected, smoothed) fMRI volume series and physiological noise regressors are submitted to a specific first level generalized linear model. A second level fixed effects analysis (subject level, task specific) is performed by combining the two runs. Whenever possible, multiple comparison corrections are performed ($Z > 2$, $p_{corr} < 0.05$). Step 8, Spinal segments are identified from high-definition T2-ZOOMit structural images that allow visualization of the dorsal roots. Spinal segments are then reported in the T2 anatomical image acquired in each run. Step 9, Using non-rigid transformations, the mean functional images are coregistered to the T2 anatomical image. Step 10, Thresholded activity patterns resulting from the generalized linear model are coregistered to the anatomical image. The projectome of proprioceptive neurons innervating the mobilized muscles are extracted and mapped to the anatomical model. Step 11, Projectomes from the three participants, and for comparison, averaged myotome distribution measured electrophysiologically in a large population of patients undergoing surgery. The color dots represent reconstructed projectome from key leg muscles. Vertical color bars represent mean population distribution of muscular motor hotpots. The projectomes differed across the participants. In particular, the projectome identified in P3 revealed an unexpected inversion of the projectome from ankle antagonists. This rostrocaudal inversion was confirmed electrophysiologically.

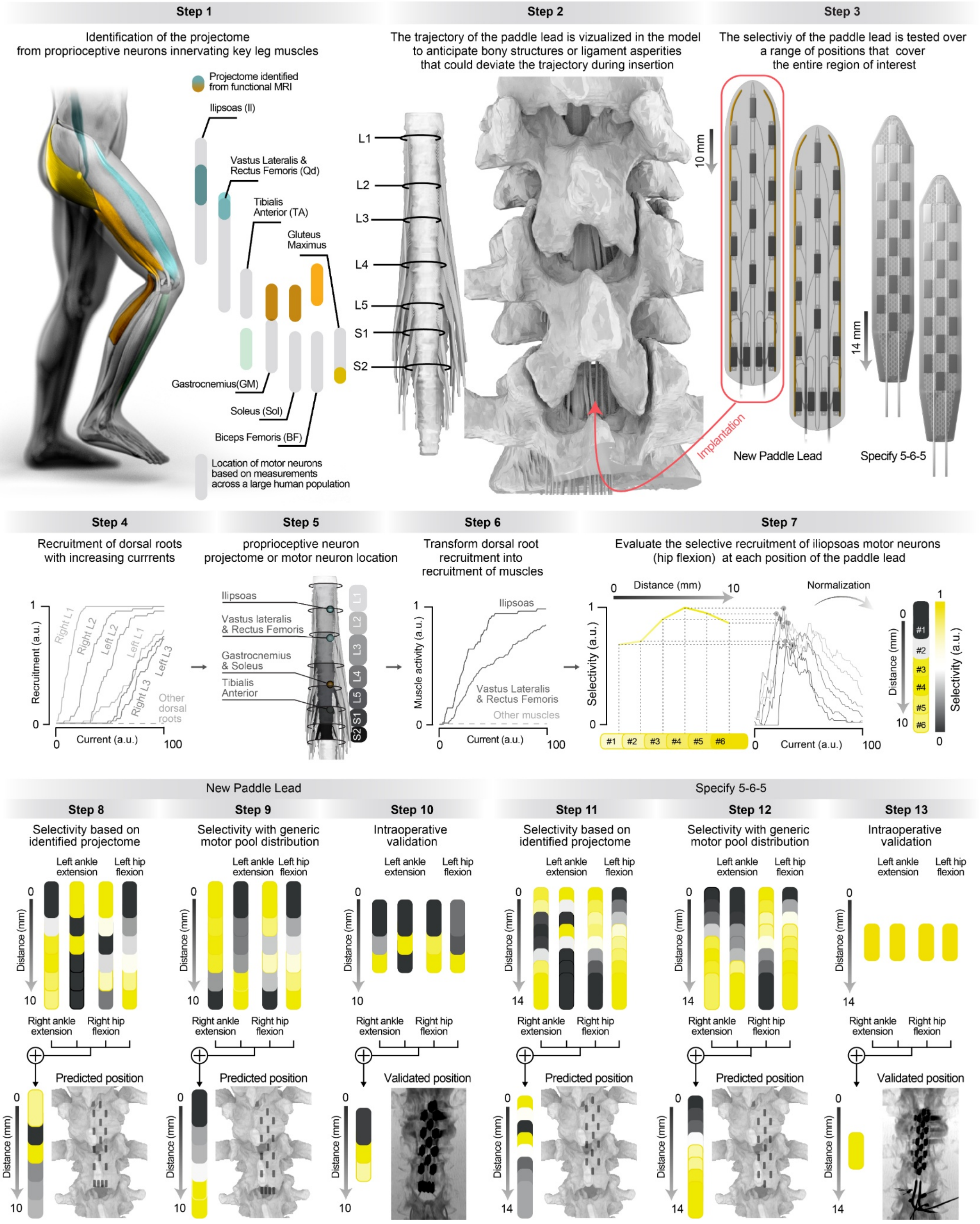
Step 1
Identification of the projectome from proprioceptive neurons innervating key leg muscles
Projectome identified from functional MRI
Ilipsoas (Il)
Vastus Lateralis & Rectus Femoris (Qd)
Tibialis Anterior (TA)
Gluteus Maximus
Gastrocnemius(GM)
Soleus (Sol)
Biceps Femoris (BF)
Location of motor neurons based on measurements across a large human population
Step 2
The trajectory of the paddle lead is vizualized in the model to anticipate bony structures or ligament asperities that could deviate the trajectory during insertion
L1
L2
L3
L4
L5
S1
S2
Step 3
The selectiviy of the paddle lead is tested over a range of positions that cover the entire region of interest
10 mm
14 mm
Implantation
New Paddle Lead
Specify 5-6-5
Step 4
Recruitment of dorsal roots with increasing currrents
Recruitment (a.u.)
Current (a.u.)
Right L1
Right L2
Left L2
Left L1
Left L3
Right L3
Other dorsal roots
Step 5
proprioceptive neuron projectome or motor neuron location
Ilipsoas
Vastus lateralis & Rectus Femoris
Gastrocnemius & Soleus
Tibialis Anterior
Step 6
Transform dorsal root recruitment into recruitment of muscles
Muscle activity (a.u.)
Vastus Lateralis & Rectus Femoris
Other muscles
Step 7
Evaluate the selective recruitment of iliopsoas motor neurons (hip flexion) at each position of the paddle lead
Distance (mm)
Normalization
Selectivity (a.u.)
#1 #2 #3 #4 #5 #6
New Paddle Lead
Specify 5-6-5
Step 8
Selectivity based on identified projectome
Step 9
Selectivity with generic motor pool distribution
Step 10
Intraoperative validation
Step 11
Selectivity based on identified projectome
Step 12
Selectivity with generic motor pool distribution
Step 13
Intraoperative validation
Left ankle extension
Left hip flexion
Right ankle extension
Right hip flexion
Distance (mm)
Predicted position
Validated position
0
10
14
1
100

Figure 5.7: Preoperative planning for optimal placement of the new paddle lead. Step 1, CT, MRI and fMRI acquisitions allow to personalize a computational model of the interactions between EES and the spinal cord for each participant. Step 2, The insertion of the new paddle lead within the spinal canal is visualized in the model to anticipate bony structures or ligaments that could deviate the trajectory. Step 3, The new paddle lead is positioned at 6 locations separated by 2 mm, thus covering the entire region of the spinal cord targeted by the therapy. The same procedure was applied to the Specify 5-6- 5 lead, except that 2 additional locations were necessary to cover the entire region since this lead is shorter than the new paddle lead.

Figure 5.7: (Continued) Step 4, The plot shows the recruitment of each dorsal root when simulating the delivery of EES at increasing intensities through the electrodes located at the corners of the paddle lead. Step 5, The recruitment of dorsal roots is translated into the recruitment of motor pools based on a transformation matrix that maps the recruitment of afferents to the recruitment of motor pools. The transformation matrix was either based on the averaged location of motor pools across the human population(Schirmer et al., 2011), or the projectome of proprioceptive neurons from key leg muscles identified from fMRI. Step 6, Applying the transformation matrix depicted in Step 5 allows to convert the predicted recruitment of dorsal roots shown in Step 4 into a prediction of motor pool recruitment. Step 7, For each position of the lead, the recruitment of the targeted motor pools compared to the non-targeted motor pools is measured to obtain a selectivity index. For each position of the paddle lead, the selectivity index for the tested electrode is color coded, and the selectivity between the tested locations interpolated to obtain a continuum. Step 8, The selectivity indices obtained for the electrodes located at each corner of the paddle lead (from left to right, targeting motoneurons eliciting hip flexion or ankle extension) are aggregated into a combined selectivity index that defines the performance of the paddle lead at the tested position. The optimal position for the paddle lead was defined as the position for which the highest combined selectivity index was obtained (most yellow rectangle). Step 9, Optimal position of the new paddle lead predicted based on a personalized computational model but a generic distribution of motoneuron locations. Step 10, Intraoperative quantification of the combined selectivity index, and thus identification of the optimal position of the new paddle lead. The predicted optimal position of the paddle lead based on a personalized model with the identified projectomes of proprioceptive neurons matched the optimal position validated intraoperatively, whereas simulations based on the averaged location of motor pools across the human population failed to predict the optimal position. Step 11-13, The procedures described in Steps 8-10 were repeated for the Specify 5-6-5 paddle lead. Note that the intraoperative validation of the optimal position of the Specify 5-6-5 was restricted to one position to minimize the duration of the surgical intervention.

While proprioceptive afferents project across several spinal segments adjacent to their entry zone, the recruitment of these afferents leads to the predominant activation of homonymous motoneurons (Pierrot-Desseilligny & Burke, 2012). Accordingly, the recruitment of proprioceptive afferents from muscles distributed at the ankle, knee and hip levels induced BOLD responses that remained confined within one or two spinal segments (Fig. 5.6). These responses thus exposed the predominant projectome of large-diameter afferents innervating the mobilized muscles, and therefore, a good approximation of the associated myotome. For each participant, we integrated the reconstructed projectome from key leg muscles into the personalized computational model (Fig. 5.7).

We finally selected the rostrocaudal position of the paddle lead that targeted motoneuron ensembles with the maximal possible selectivity. To quantify this selectivity, we implemented an algorithm that calculated the relative activation of the targeted muscles with respect to the non-targeted muscles (Wagner et al., 2018). The insertion of the paddle lead to this position was then simulated in the model to anticipate possible spinal canal obstructions that could impede or deviate the trajectory of the lead (Fig. 5.6).

5.3.5 Intraoperative validation of model predictions

We next aimed to validate the predictions of simulations, and the relevance of improving the precision of the models with personalized features to generate these predictions.
We conducted these experiments in the 3 participants of the clinical study who underwent a neurosurgical intervention to implant the new paddle lead over the spinal cord (Table 5.1). We first performed an intraoperative tridimensional CT scan to map the predicted optimal position of the paddle lead to the anatomy of each participant, and thus guide the insertion of the lead. Once the paddle lead was placed at the predicted position, we quantified the selectivity of the electrodes located at each corner of the lead. We delivered single-pulses of EES to elicit muscle responses that we monitored with electromyographic recordings. We quantified the selectivity of each electrode using the same algorithm as in simulations.
After this assessment, we studied whether alternative locations would permit superior selectivity. Moving the paddle lead by approximately 2 mm in the rostral or caudal directions resulted in lower selectivity, indicating that the predicted position achieved the highest performance (Fig. 5.5b).
We finally asked whether the personalized features of the models were important for predicting the optimal position of the paddle lead (Lempka et al., 2020). Simulations based on a generic computational model or theoretical myotome distributions failed to reach the same accuracy as the personalized computational models (Fig. 5.8).

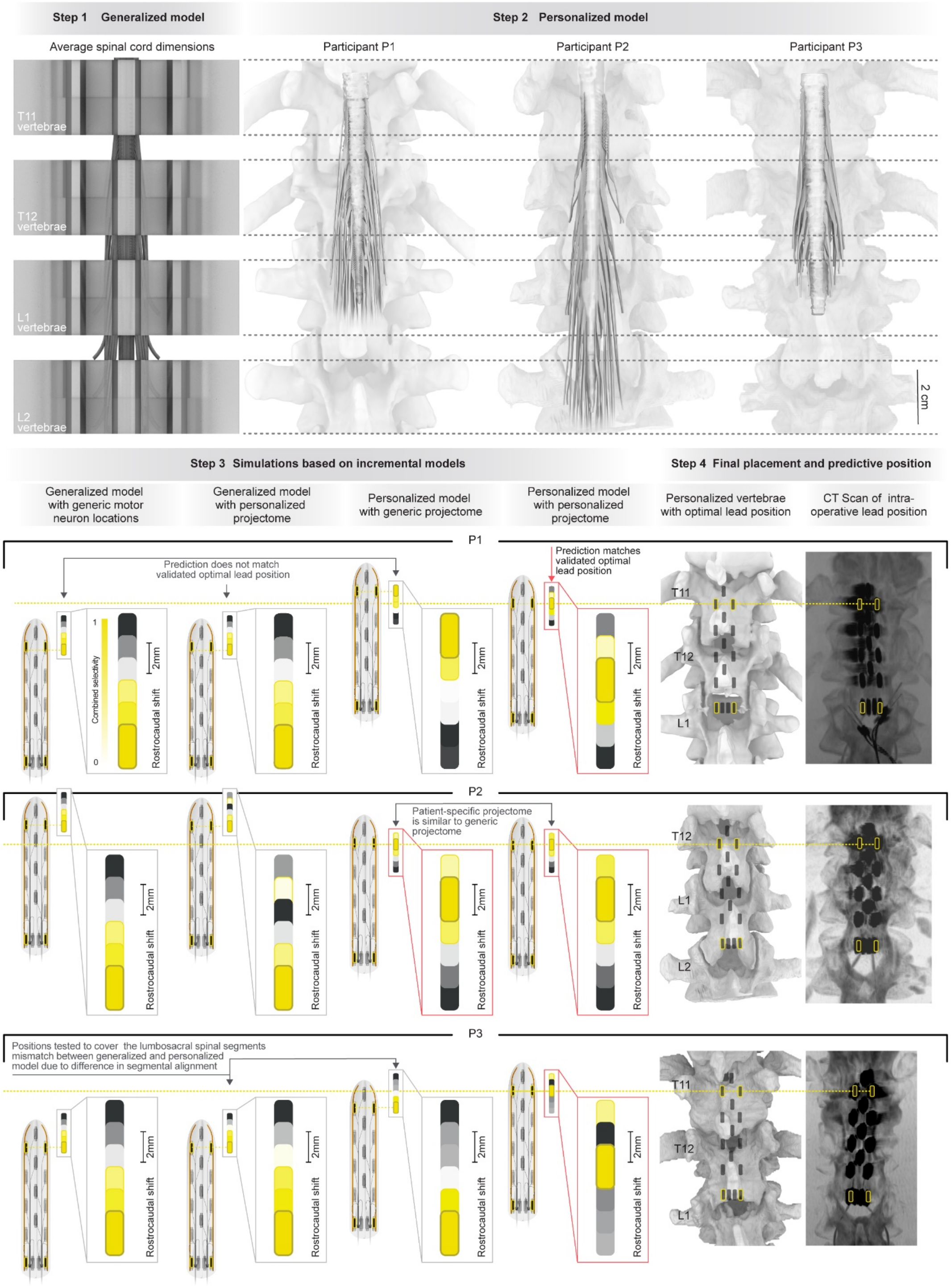
Step 1 Generalized model
Step 2 Personalized model
Average spinal cord dimensions
Participant P1
Participant P2
Participant P3
T11 vertebrae
T12 vertebrae
L1 vertebrae
L2 vertebrae
2 cm
Step 3 Simulations based on incremental models
Step 4 Final placement and predictive position
Generalized model with generic motor neuron locations
Generalized model with personalized projectome
Personalized model with generic projectome
Personalized model with personalized projectome
Personalized vertebrae with optimal lead position
CT Scan of intra-operative lead position
P1
Prediction does not match validated optimal lead position
Prediction matches validated optimal lead position
Combined selectivity
1
0
2mm
Rostrocaudal shift
T11
T12
L1
P2
Patient-specific projectome is similar to generic projectome
T12
L1
L2
P3
Positions tested to cover the lumbosacral spinal segments mismatch between generalized and personalized model due to difference in segmental alignment
T11
T12
L1

Figure 5.8: Impact of model abstractions to determine the optimal position of the paddle lead. Step 1, Generalized computational model of the interaction between EES and the spinal cord, including the location of motoneurons from key leg muscles. Step 2, Personalized computational model of the interaction between EES and the spinal cord for the three participants. The models are aligned with the generalized model depicted in Step 1.

Figure 5.8: (Continued) Step 3, Simulations predict the optimal position of the new paddle lead for each participant, following the procedures explained in Extended Data Figure 4, but based on various model abstractions, as explained in the boxes above each prediction. Step 4, The optimal position of the new paddle lead was validated intraoperatively, as explained in Fig. 5.7, and is shown on a CT scan reconstruction. The horizontal yellow line passing through the top electrodes of the paddle lead highlights the optimal position, thus allowing a direct comparison between the various predictions and the optimal position. The fully personalized models achieved the best performance.

5.3.6 Superior selectivity of the new electrode arrangement

We then sought to demonstrate that the new arrangement of electrodes enhanced the coverage and selectivity of EES compared to paddle leads that were originally designed for pain treatment. We selected the Specify 5-6-5, since this paddle lead has been the most commonly used to restore walking in humans with SCI (Angeli et al., 2018; M. L. Gill et al., 2018; S. Harkema et al., 2011; Wagner et al., 2018).

To enable a direct comparison, we performed an intraoperative assessment of the Specify 5-6-5 in the same participants. The rostrocaudal coverage of the Specify 5-6-5 is shorter than the new paddle lead by 18.8 mm. Accordingly, simulations predicted that the Specify 5-6-5 would not be able to target all the dorsal roots in these participants. Intraoperative electrophysiological measurements confirmed these predictions (Fig. 5.5c and Fig. 5.7).

Finally, we asked whether the arrangement of electrodes at the bottom of the paddle lead enables a more selective recruitment of dorsal roots agglutinated in the thecal sac. As expected, multipolar combinations of these electrodes enhanced the selective recruitment of the soleus and gastrocnemius medialis muscles, whose motoneurons are located in sacral segments (Fig. 5.5d).

5.3.7 Configuration and real-time control of stimulation

Biomimetic EES involves the delivery of concurrent stimulation waveforms with a precise timing and varying combinations of frequencies and amplitudes. Moreover, many motor activities necessitate adjustment of stimulation parameters in closed-loop via wireless links. To support these features, we upgraded an implantable pulse generator (IPG) commonly used for deep brain stimulation with wireless communication modules (Fig. 5.10). This neurostimulation platform supported real-time updates of EES frequency, amplitude and timing from up to 10 stimulation waveforms (Wagner et al., 2018). The new paddle lead was interfaced with the IPG, which was implanted in the abdomen.

Biomimetic EES requires the personalized configuration of activity-dependent stimulation programs (Fig. 5.9). To facilitate this configuration, we developed a new software that operates through touch-screen interfaces to configure electrode libraries, customize pre-established activity-specific stimulation programs, and update EES parameters. To simplify these operations, wireless recordings of limb kinematics and muscle activity are displayed in real-time, concomitantly to the occurence of EES waveforms (Fig. 5.10).

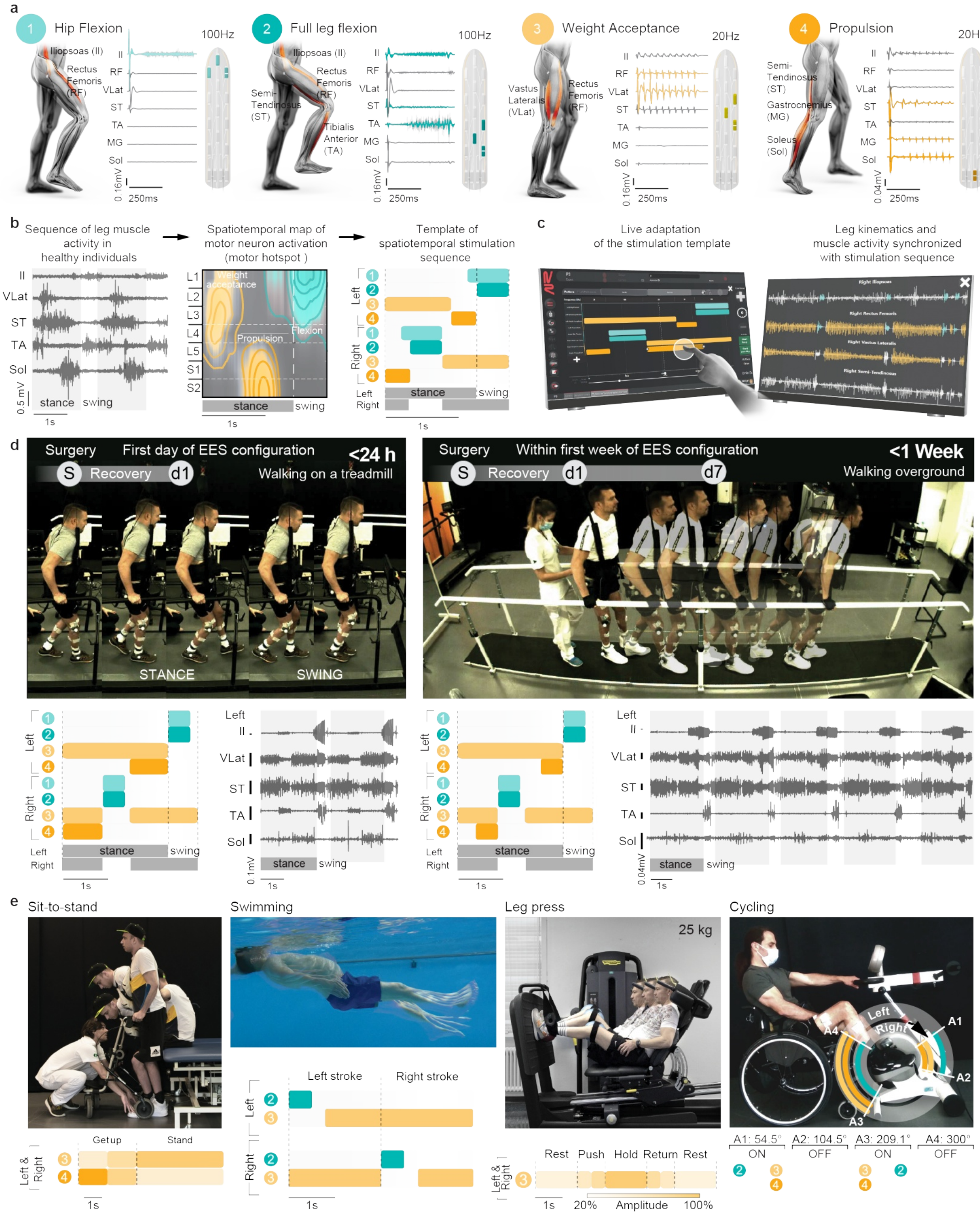
a
1 Hip Flexion
100Hz
Iliopsoas (Il)
Rectus Femoris (RF)
Il
RF
VLat
ST
TA
MG
Sol
0.16mV
250ms
2 Full leg flexion
100Hz
Semi-Tendinosus (ST)
Tibialis Anterior (TA)
3 Weight Acceptance
20Hz
Vastus Lateralis (VLat)
4 Propulsion
20Hz
Gastrocnemius (MG)
Soleus (Sol)
0.04mV
b
Sequence of leg muscle activity in healthy individuals
Spatiotemporal map of motor neuron activation (motor hotspot)
Template of spatiotemporal stimulation sequence
0.5 mV
stance
swing
1s
L1
L2
L3
L4
L5
S1
S2
Weight acceptance
Propulsion
Flexion
Left
Right
c
Live adaptation of the stimulation template
Leg kinematics and muscle activity synchronized with stimulation sequence
Right Iliopsoas
Right Rectus Femoris
Right Vastus Lateralis
Right Semi-Tendinosus
d
Surgery
First day of EES configuration
<24 h
S
Recovery
d1
Walking on a treadmill
STANCE
SWING
Within first week of EES configuration
<1 Week
d7
Walking overground
e
Sit-to-stand
Getup
Stand
Left & Right
Swimming
Left stroke
Right stroke
Leg press
25 kg
Rest Push Hold Return Rest
20%
Amplitude
100%
Cycling
Left
Right
A1
A2
A3
A4
A1: 54.5°
ON
A2: 104.5°
OFF
A3: 209.1°
ON
A4: 300°
OFF

Figure 5.9: Configuration of activity-dependent stimulation programs.

Figure 5.9: (Continued) a, Library of optimized anode and cathode configurations and stimulation frequencies to modulate motor pools associated with the key phases of gait, as highlighted with the color code. b, Sequence of muscle activity underlying walking in healthy people, converted into a spatiotemporal map of motoneuron activity that highlights the timing and location of motor hotspot activation; translated into a preprogrammed sequence of stimulation bursts (template) that aims to reproduce this activation pattern. Color code as in (a). The configurations of electrodes targeting each hotspot are derived from the library, and injected into this template. c, Software enabling live adjustments of stimulation patterns and parameters based on real-time feedback from muscle activity and kinematic sensors that are synchronized with stimulation sequences. d, Walking on a treadmill with stimulation after less than one hour of configuration, including sequence of stimulation and underlying muscle activity. e, Independent walking between parallel bars less than one week after the onset of the therapy. f, Chronophotography of sit-to-stand, swimming, leg-press and motomed exercises enabled by activity-specific stimulation programs, displayed at the bottom of each chronophotography.

5.3.8 Immediate recovery of walking after complete paralysis

Our next objective was to demonstrate the superior performance of the new paddle lead to restore walking after SCI. Previous studies showed that a subset of individuals with complete motor paralysis could regain independent stepping with EES following many months of training (M. L. Gill et al., 2018; Wagner et al., 2018). Here, we aimed to restore independent stepping on the first day of stimulation in all the participants.

Personalized configuration of EES programs started by assembling preoperative and intraoperative information into a library of cathode and anode configurations targeting individual dorsal roots (Fig. 5.13). Each configuration aimed to modulate a specific ensemble of motoneurons that are confined within specific regions of the spinal cord, termed motor hotspots (Fig. 5.9b). Each configuration was then optimized based on the responses elicited by EES. For this purpose, we delivered brief trains (500 ms) of stimulation in a supine position, since bursts elicited ample functional movements of the legs that identified potential undesired movements and thus facilitated the fine-tuning of anode-cathode combinations (Fig. 5.13). Pulse frequencies were adjusted for extensor (20 Hz) versus flexor (100 Hz) muscles, since the motoneurons innervating these muscles exhibit distinct preferential activation frequencies (Wagner et al., 2018) (Fig. 5.14).

The three participants presented noticeable differences in the topological organisation of their dorsal roots (Fig. 5.5). Yet, the arrangement of electrodes on the new paddle lead supported the optimization of multipolar configurations that enabled targeting all the motor hotspots involved in the production of walking with the necessary selectivity (Fig. 5.14). Elaborating this library did not last longer than one hour.

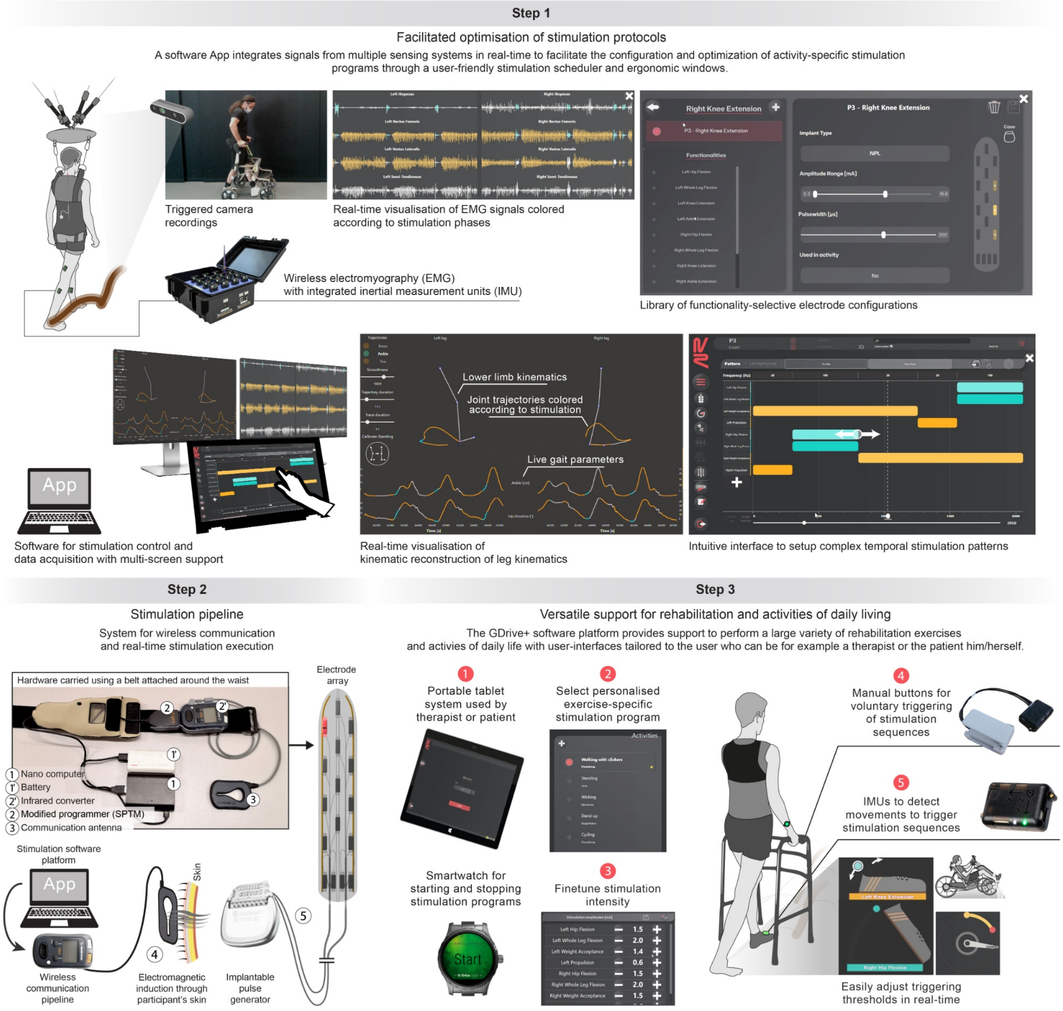

Step 1

Facilitated optimisation of stimulation protocols

A software App integrates signals from multiple sensing systems in real-time to facilitate the configuration and optimization of activity-specific stimulation programs through a user-friendly stimulation scheduler and ergonomic windows.

Step 2

Stimulation pipeline

System for wireless communication and real-time stimulation execution

Step 3

Versatile support for rehabilitation and activities of daily living

The GDrive+ software platform provides support to perform a large variety of rehabilitation exercises and activies of daily life with user-interfaces tailored to the user who can be for example a therapist or the patient him/herself.

Triggered camera recordings
Real-time visualisation of EMG signals colored according to stimulation phases
Wireless electromyography (EMG) with integrated inertial measurement units (IMU)
Library of functionality-selective electrode configurations
Right Knee Extension
P3 - Right Knee Extension
App
Software for stimulation control and data acquisition with multi-screen support
Lower limb kinematics
Joint trajectories colored according to stimulation
Live gait parameters
Real-time visualisation of kinematic reconstruction of leg kinematics
Intuitive interface to setup complex temporal stimulation patterns
Hardware carried using a belt attached around the waist
① Nano computer
1' Battery
2' Infrared converter
② Modified programmer (SPTM)
③ Communication antenna
Electrode array
Stimulation software platform
App
Skin
④
⑤
Wireless communication pipeline
Electromagnetic induction through participant's skin
Implantable pulse generator
① Portable tablet system used by therapist or patient
② Select personalised exercise-specific stimulation program
Activities
Smartwatch for starting and stopping stimulation programs
Start
③ Finetune stimulation intensity
Left Hip Flexion 1.5
Left Whole Leg Flexion 2.0
Left Weight Acceptance 1.4
Left Propulsion 0.6
Right Hip Flexion 1.5
Right Whole Leg Flexion 2.0
Right Weight Acceptance 1.5
④ Manual buttons for voluntary triggering of stimulation sequences
⑤ IMUs to detect movements to trigger stimulation sequences
Easily adjust triggering thresholds in real-time

Figure 5.10: Purpose software for configuration, optimisation, evaluation and implementation of activity. Step 1, A custom-built software named GDrive+ integrates signals from video cameras, sensors of muscle activity, and inertial measurement units (accelerometers and gyroscopes) in real-time and wirelessly. Each configuration of electrodes targeting a given hotspot/muscle group is color-coded in the interface, and is visualized onto the kinematic and physiological signals when EES is turned on. This synchronized visualization provides direct feedback to configure and optimize activity-specific stimulation programs. This configuration is performed via dedicated graphical interfaces that allow to change the timing and parameters of stimulation directly onto a stimulation scheduler and ergonomic windows, including touch screens. This software allows the configuration and personalization of activity-dependent stimulation programs in less than one hour.

Figure 5.10: (Continued) Step 2, EES commands are transmitted to the Implantable Pulse Generator (IPG) via Bluetooth (1) to a module that converts them into infrared signals (2), which are then transferred to the stimulation programmer device (2). The stimulation programmer transmits EES commands into the IPG via induction telemetry (4), using an antenna (3) taped to the skin and aligned to the IPG. EES is delivered through the paddle array (5). This communication chain allows the control of up to 4 concomitant stimulation waveforms in real-time, with a response latency of approximately 120 ms. Step 3, A handheld tablet and connected smartwatch (1) running our custom-made software App provide user-friendly interfaces for therapists and participants to select activity-specific stimulation programs (2) and to adapt relevant stimulation parameters of these programs (3) to perform rehabilitation exercises or support activities of daily living. Custom-built ergonomic clickers (4) or inertial measurement units (5) are placed on the body or assistive devices to ensure that the stimulation is delivered with a timing corresponding to the intended movement.

Once the library of electrode configurations was established, the temporal sequence of EES pulses was optimized for each participant. Walking involves stereotypical spatiotemporal patterns of motor hotspot activation that directly reflect changes in body mechanics (Cappellini et al., 2010; Yakovenko et al., 2002) (Fig. 5.9a,b). Therefore, the next step of the procedure consisted of injecting the electrode configurations targeting specific motor hotspots into pre-established sequences of EES pulses that aimed to reproduce the natural spatiotemporal patterns of motor hotspot activation during walking (Capogrosso et al., 2016; Capogrosso et al., 2018; Wagner et al., 2018; Wenger et al., 2016) (Fig. 5.9b). Finally, EES parameters were fine-tuned through a stimulation scheduler displayed on the software. This fine-tuning involved interactions with the physical therapist and participant who was attempting to walk (Fig. 5.9c). This procedure allowed the configuration of EES programs for walking within one hour.

All three participants with chronic SCI exhibited complete sensorimotor paralysis of both legs (Table 5.1). They were unable to stand nor take any step and exhibited no muscle activity in leg muscles during these attempts (Fig. 5.15). On the very first day of stimulation, all the participants could step independently on a treadmill, although gait patterns exhibited poor extension components. Consequently, substantial amounts of body weight support were necessary (Fig. 5.9d). After one to three additional days of optimizations, gait patterns were sufficiently optimized to enable the three participants to ambulate independently overground while supported in a multidirectional body weight support system (Mignardot et al., 2017) (Fig. 5.9e). This recovery involved the production of substantial activity in leg muscles with a timing that coincided with pronounced excursions of hip, knee and ankle joints (Fig. 5.9b and Fig. 5.15).

Two out of the three participants could modulate the amplitude of leg movements when asked to increase their step length voluntarily (Fig. 5.15). Contrary to the fatigue that rapidly occurs with direct neuromuscular stimulation (Shokur et al., 2021), the participants could produce up to 300 hundred independent steps as early as the very first day of stimulation (Fig. 5.15).

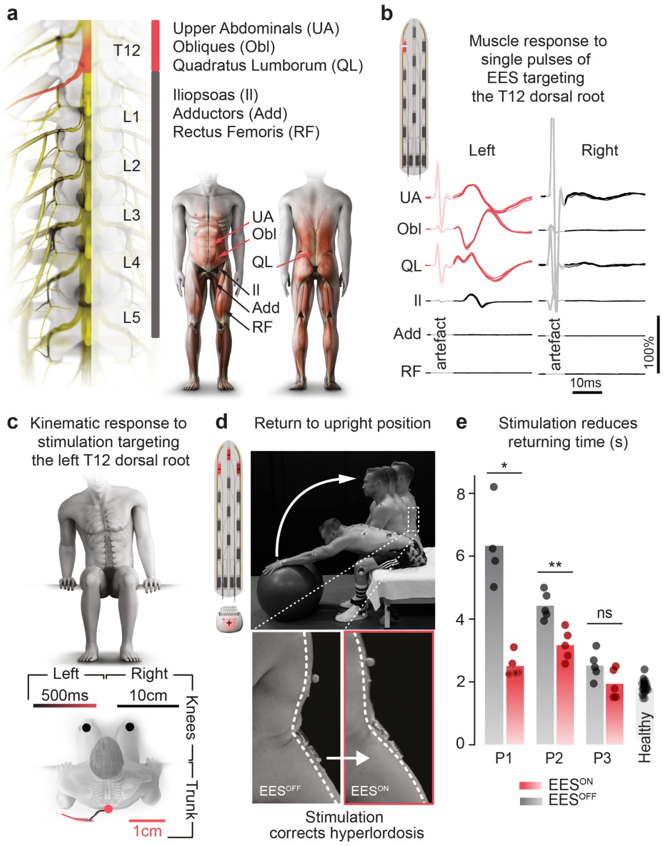

Figure 5.11: Configuration of trunk-specific stimulation programs. a, Stimulation of the dorsal root projections to the T12 spinal segment modulates trunk and abdominal muscles, b, as shown in muscle responses. c, Temporal course (color-coded) of coronal plane trunk trajectory elicited by side-specific stimulation. d, Chronophotography of a sequence of trunk flexion and extension. The onsets highlight trunk posture at rest without and with a stimulation program optimized for modulation of motor pools innervating trunk muscles. e, Bar plots reporting the time necessary to complete the return phase (extension) of the flexion / extension sequence of trunk movements for the 3 participants, compared to 5 healthy individuals (Mann- Whitney test, *, p<0.05; **, p<0.01).

5.3.9 Extension to other motor activities

We reasoned that the biological principles through which EES restores walking could support the configuration of EES programs to enable other motor activities.

To test this possibility, we exploited our software that allows the rapid configuration of activity-specific stimulation programs. We thus configured EES programs that enabled the 3 participants to use their legs to swim in the water or pedal actively on a motorized bike (Fig. 5.9f). EES programs also allowed the performance of various rehabilitation exercises such as squats or leg press with variable loads (Fig. 5.9f).

We next applied the same principles to target trunk muscles with the aim to improve the control of the trunk (Fig. 5.16). Indeed, the three participants showed various impairments in the stabilization and control of trunk postures (Fig. 5.17). EES programs targeting trunk muscles normalized trunk postures (Fig. 5.11a). Moreover, EES immediately improved the control of the trunk. For example, participants who exhibited difficulties to regain an upright trunk posture from a fully flexed position performed this task with ease, as captured in the marked increase in the speed of these executions (Fig. 5.11b).

5.3.10 Recovery of independence in ecological settings

Activity-dependent stimulation programs enabled the immediate recovery of trunk and leg motor functions in people with complete paralysis. While weight bearing capacities and overall performances remain limited at this stage, this recovery provided the opportunity to engage the otherwise dormant neuromuscular system into sustained and active training sessions. We thus asked whether performance would improve with practice, and whether these improvements would be sufficient to regain some independence in ecological settings. The three participants underwent a 5-month program during which EES enabled them to stand, walk and perform a broad range of exercises 4 to 5 times per week, lasting between one to two hours. We developed a simplified interface of the software that allowed participants and physical therapists to switch between activity-dependent stimulation programs and to fine-tune key parameters of these programs. We also equipped the assistive devices with ergonomic clickers that trigger EES programs upon desire. For example, they could easily switch between standing and walking, or between the swing and stance phases of gait (Fig. 5.10). Participants could select several modes of stimulation, including pre-programmed EES sequences that were executed in open-loop or triggered with clickers, or closed-loop control of EES sequences based on video recordings or wearable sensors (Fig. 5.10).

Performance with EES improved dramatically. All three participants progressively regained full-weight bearing capacities (Fig. 5.12b), which translated into the ability to stand independently in community settings. Improvement of gait patterns and weight bearing capacities also allowed them to walk independently with the help of a front-wheel walker for stability, which enabled the performance of the 10-meter and 6 min walk test without any assistance (Fig. 5.12c). One of the participants even regained the ability to climb a staircase and to progress over complex terrains. Participants could also ride a recumbent trike powered with the arms and legs (Fig. 5.12). Finally, improved control of trunk postures allowed the practice of leisure activities such as boxing, enjoying a drink while standing at a bar, or paddling a canoe on a lake (Fig. 5.12).

The recovery of full weight-bearing capacities and improved trunk control over the course of 6 months coincided with a substantial increase in the mass of leg and trunk muscles (Fig. 5.12c). Moreover, two of the participants recovered the ability to activate proximal muscles voluntarily in the absence of EES (Fig. 5.18).

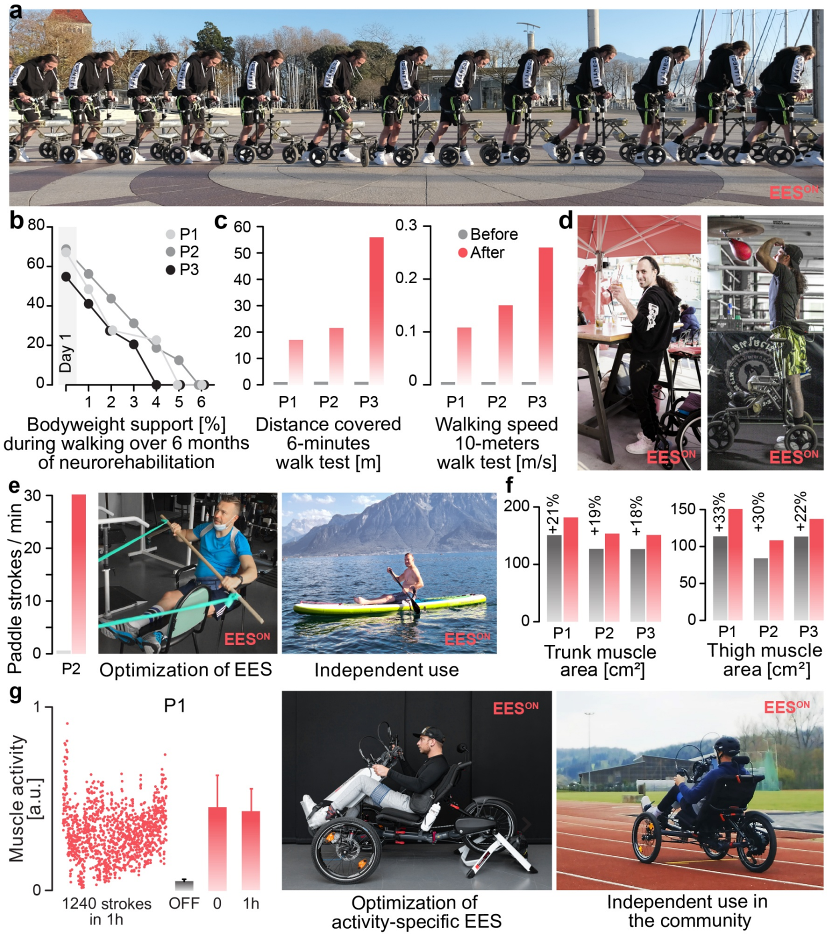

Figure 5.12: Recovery of independence in the community. a, Chronophotography of independent walking outdoors after 6 months of practice with activity-specific programs. b, Progressive recovery of weight bearing capacity during walking over the course of the 6 months of practice. c, Bar plots reporting performance in the six-minute walk test and ten-meter walk test before and after neurorehabilitation with activity-specific stimulation programs. No assistance was provided during these tests. d, Standing for extensive periods of time for boxing or enjoying a drink at a high table of a bar. e, Stimulation programs for trunk stability while paddling were developed in the lab, and then used to support paddling activity on a lake. Bar plots report the number of paddle strokes per minute with and without EES. f, Bar plots reporting changes in thigh and trunk muscle mass, quantified as total/specific cross-sectional area. g, Amplitude of muscle activity for each of 1240 strokes performed over one hour. Bar plots report the mean amplitude of muscle activity without EES (gray), and calculated during the 100 first and 100 last cycles (red). Photographs illustrate the setting for the development of cycling stimulation, and its use community settings.

5.4 Discussion

Only one study previously reported the case of an individual with complete sensorimotor paralysis (M. L. Gill et al., 2018) who regained over-ground walking during continuous EES, but only when assisted by two physical therapists. Another study described the effects of continuous EES in two individuals with complete sensorimotor paralysis and two individuals with complete motor paralysis but sparing of leg sensory function (Angeli et al., 2018). One of the individuals with incomplete SCI regained independent overground walking while the other one was able to perform steps between parallel bars held by physical therapists. The two individuals with complete sensorimotor paralysis never recovered overground walking. In these two studies, the recovery of independent stepping during continuous EES required nearly one year of intense rehabilitation.

Here, we show that biomimetic EES enabled the immediate recovery of standing, walking, cycling, swimming and trunk control in all three individuals with complete sensorimotor paralysis. After a few months of neurorehabilitation, these individuals were able to leverage biomimetic EES to support various motor activities in the community. Central to this radically increased efficacy was an arrangement of electrodes that targeted the ensemble of sacral, lumbar and low-thoracic dorsal roots involved in the production of leg and trunk movements, combined with a purpose software that renders the configuration of activity-dependent biomimetic stimulation programs rapid, simple and predictable.

While the three participants could ambulate independently, it is important to point out that they did not regain the fluid gait that characterizes natural walking in humans. Yet, this recovery was sufficient to perform various motor activities for extensive periods of time, and thus to undergo active neurorehabilitation. Moreover, two participants were able to diminish or augment the extent of leg movements during EES, suggesting that the stimulation boosted signals from residual descending pathways. The recovery of volitional muscle activation without EES following neurorehabilitation reinforced this interpretation. Preclinical studies showed that this recovery is mediated by the sprouting of residual fibers from descending pathways (Asboth et al., 2018; van den Brand et al., 2012). We thus surmised that a small number of nerve fibers had survived the injury, but that these nerve fibers had remained functionally silent due to the low level of activity below the injury (Edgerton & Harkema, 2011).

We previously showed that neurorehabilitation supported by EES restored a more natural gait pattern and more extensive volitional movements without EES in individuals with incomplete SCI, emphasizing the logical importance of residual pathways to mediate recovery. Therefore, the development of biological repair interventions that preserve or reestablished neural pathways remains critical to enhance the potential for recovery with neurorehabilitation supported by EES (Courtine & Sofroniew, 2019; Morse et al., 2021). Biomimetic EES may also support the immediate production of active and sustained movements in the early phase after SCI, which may enable taking full advantage of the window of enhanced neuroplasticity post-injury to augment neurological recovery.

The development of the paddle lead required a number of tradeoffs to circumvent the considerable variability in the topology of the dorsal roots across the human population. While this new paddle lead allowed us to validate our therapeutic concepts, the fixed coverage and uniform distribution of electrodes along the rostrocaudal direction were inevitably suboptimal. Similarly, we positioned the electrodes as lateral as possible to avoid undesirable activation of dorsal roots from the contralateral side, but simulations predicted that a personalized location of electrodes in the mediolateral direction would improve the selective recruitment of dorsal root entry zones. Therefore, we anticipate that delivering this therapy across the human population may require a library of paddle leads or even personalized leads. While current regulations for medical devices are not compatible with the possibility to tune electrode configurations within silicone-based paddle leads, microfabrication processes may provide a realistic path for personalized leads (Barra et al., 2020; Schiavone et al., 2020). In turn, our personalizable computational framework enables selecting the optimal paddle lead for each patient, and planning its surgical positioning for optimal selectivity. With a large choice of leads or increased number of electrodes, the preoperative planning may also be greatly simplified since the ability to recruit all of the targeted dorsal roots would eliminate the need to localize projectomes precisely with fMRI acquisitions. High-density electrode arrays are under development, but the challenge may reside in the availability of implantable pulse generators that can deliver concurrent stimulation waveforms controlled wirelessly and in real-time. Indeed, taking full advantage of biomimetic EES will require neurostimulation platforms designed for closed-loop operations, combining ultrafast and reliable wireless communication with the ability to process large volumes of data from wearable sensors or even neurosensors interfaced with the brain (Benabid et al., 2019; Bonizzato et al., 2018; Capogrosso et al., 2016).

We only targeted the dorsal roots projecting to the low thoracic segment. However, the selective modulation of specific trunk and abdominal muscles suggest that targeting additional thoracic dorsal roots with relevant temporal sequences (Moraud et al., 2018) will further improve control over trunk movements (Chen et al., 2003; M. Gill et al., 2020).

These therapeutic concepts are relevant to address other neurological functions that are critical for people with SCI (Anderson, 2004). Preliminary studies showed that EES can regulate neural circuits involved in the regulation of bladder and bowel functions (Herrity et al., 2018), hemodynamics (Legg Ditterline et al., 2020; Squair et al., 2021), and arm/hand movements (Greiner et al., 2021). These circuits are located in specific regions of the spinal cord. Therefore, neurotechnologies targeting the dorsal roots projecting to these specific regions will likely enhance the ability of EES to regulate these neurological functions after SCI. Targeting some of these functions may require highly-specific stimulation of certain dorsal roots, which could be achieved with the direct neuromodulation of dorsal root ganglia (Soloukey et al., 2020).

Implementation of this therapy across clinical centers worldwide will require automated computational pipelines and AI assistants to support the selection, positioning and configuration of paddle leads. Advances in machine-learning algorithms and cloud-based computing for medical applications established the technological landscape to realize this transition and scale up this therapy.

Biomimetic EES enabled the immediate recovery of trunk and leg motor functions in three participants with complete sensorimotor paralysis, which allowed them to undergo neurorehabilitation and regained some independence in ecological settings. This recovery combined with our previous findings in people with incomplete SCI (Wagner et al., 2018) is opening a realistic pathway to deploy a therapy that will mediate clinically meaningful improvements in people presenting with a broad range of SCI severities.

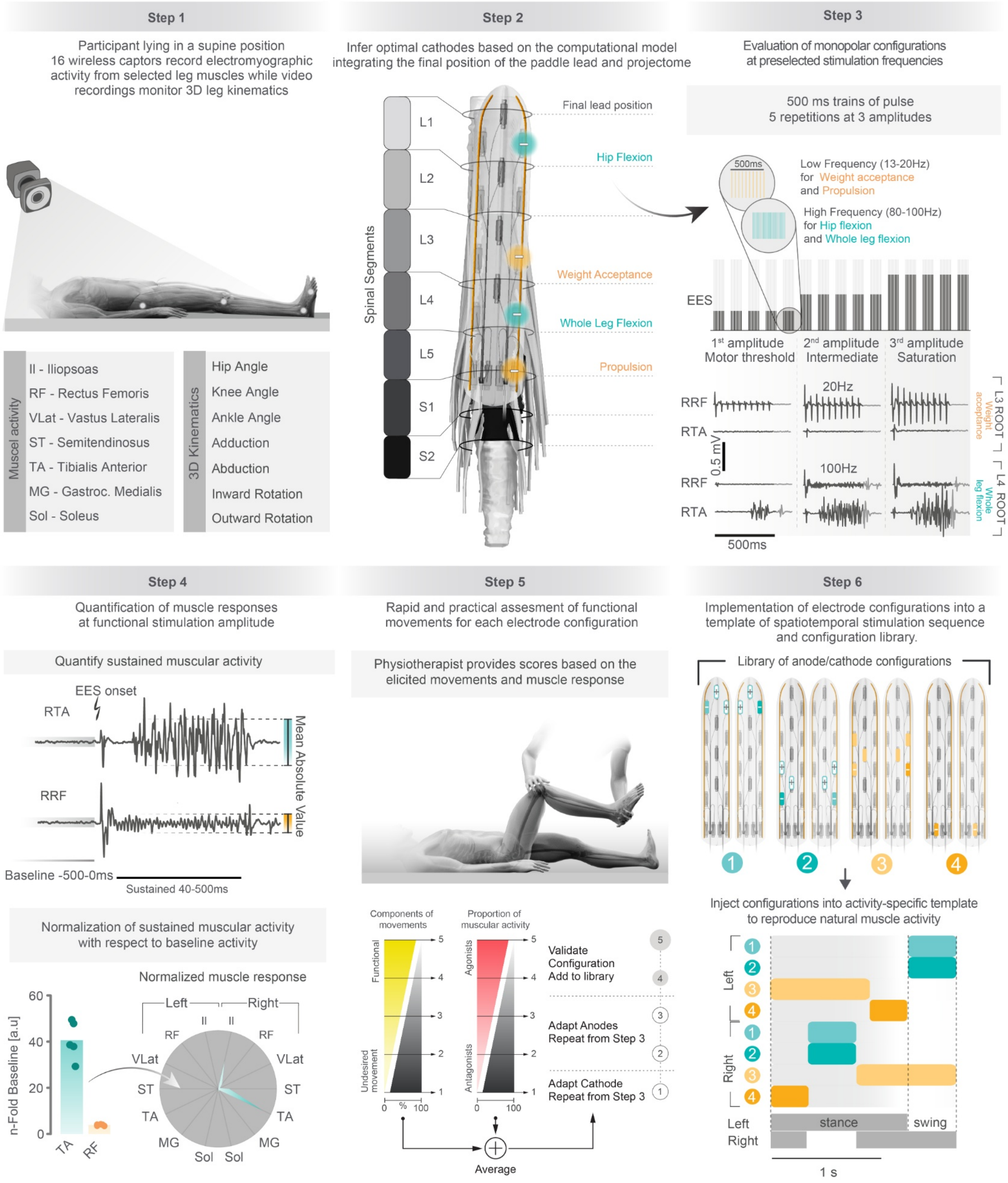
Step 1
Participant lying in a supine position
16 wireless captors record electromyographic activity from selected leg muscles while video recordings monitor 3D leg kinematics
Muscel activity
Il - Iliopsoas
RF - Rectus Femoris
VLat - Vastus Lateralis
ST - Semitendinosus
TA - Tibialis Anterior
MG - Gastroc. Medialis
Sol - Soleus
3D Kinematics
Hip Angle
Knee Angle
Ankle Angle
Adduction
Abduction
Inward Rotation
Outward Rotation
Step 2
Infer optimal cathodes based on the computational model integrating the final position of the paddle lead and projectome
Spinal Segments
L1
L2
L3
L4
L5
S1
S2
Final lead position
Hip Flexion
Weight Acceptance
Whole Leg Flexion
Propulsion
Step 3
Evaluation of monopolar configurations at preselected stimulation frequencies
500 ms trains of pulse
5 repetitions at 3 amplitudes
500ms
Low Frequency (13-20Hz)
for Weight acceptance
and Propulsion
High Frequency (80-100Hz)
for Hip flexion
and Whole leg flexion
EES
1st amplitude
Motor threshold
2nd amplitude
Intermediate
3rd amplitude
Saturation
20Hz
100Hz
RRF
RTA
RRF
RTA
0.5 mV
500ms
L3 ROOT
Weight acceptance
L4 ROOT
Whole leg flexion
Step 4
Quantification of muscle responses at functional stimulation amplitude
Quantify sustained muscular activity
EES onset
RTA
RRF
Mean Absolute Value
Baseline -500-0ms
Sustained 40-500ms
Normalization of sustained muscular activity with respect to baseline activity
Normalized muscle response
n-Fold Baseline [a.u]
60
40
20
0
TA
RF
Left
Right
Il
Il
RF
RF
VLat
VLat
ST
ST
TA
TA
MG
MG
Sol
Sol
Step 5
Rapid and practical assesment of functional movements for each electrode configuration
Physiotherapist provides scores based on the elicited movements and muscle response
Components of movements
Functional
Undesired movement
Proportion of muscular activity
Agonists
Antagonists
5
4
3
2
1
0
%
100
Average
Validate Configuration Add to library
Adapt Anodes Repeat from Step 3
Adapt Cathode Repeat from Step 3
Step 6
Implementation of electrode configurations into a template of spatiotemporal stimulation sequence and configuration library.
Library of anode/cathode configurations
1
2
3
4
Inject configurations into activity-specific template to reproduce natural muscle activity
Left
Right
Left
Right
stance
swing
1 s

Figure 5.13: Configuration of activity-specific stimulation protocols. Step 1, The participant is lying supine in a relaxed posture. Wireless sensors are positioned over selected leg muscles to monitor electromyographic signals in conjunction with leg kinematics using an optical 3D motion capture system. Step 2, Intraoperative imaging of the final paddle lead position guides the realignment of the paddle lead with respect to the personalized model of the interactions between EES and the spinal cord. The optimal cathode to target specific motoneurons are inferred based on the location of the electrodes with respect to the dorsal roots and location of motoneurons identified from fMRI measurements. Step 3, The performance of the preselected optimal cathode is assessed using trains of pulses delivered with predefined frequency ranges that are optimal for the targeted motoneurons.

Figure 5.13: (Continued) Step 4, The muscle responses are quantified from 40 to 500 ms after stimulation onset, and then normalized with respect to a baseline window selected 500ms before stimulation onset. The relative amplitudes of muscle responses are represented in a polar plot that allows to appreciate the relative recruitment of each muscle. Step 5, A physiotherapist grades the precision of the elicited movements and muscle activity based on a simple clinical scale that enables the quick adjustment of anode and cathode configurations to achieve the most optimal selectivity. Step 6, This procedure enables the rapid elaboration of a library of anode and cathodes targeting specific muscles and motor hotspots, which are then implemented in preprogrammed stimulation templates that aim to reproduce the natural activation of muscles during the desired activity.

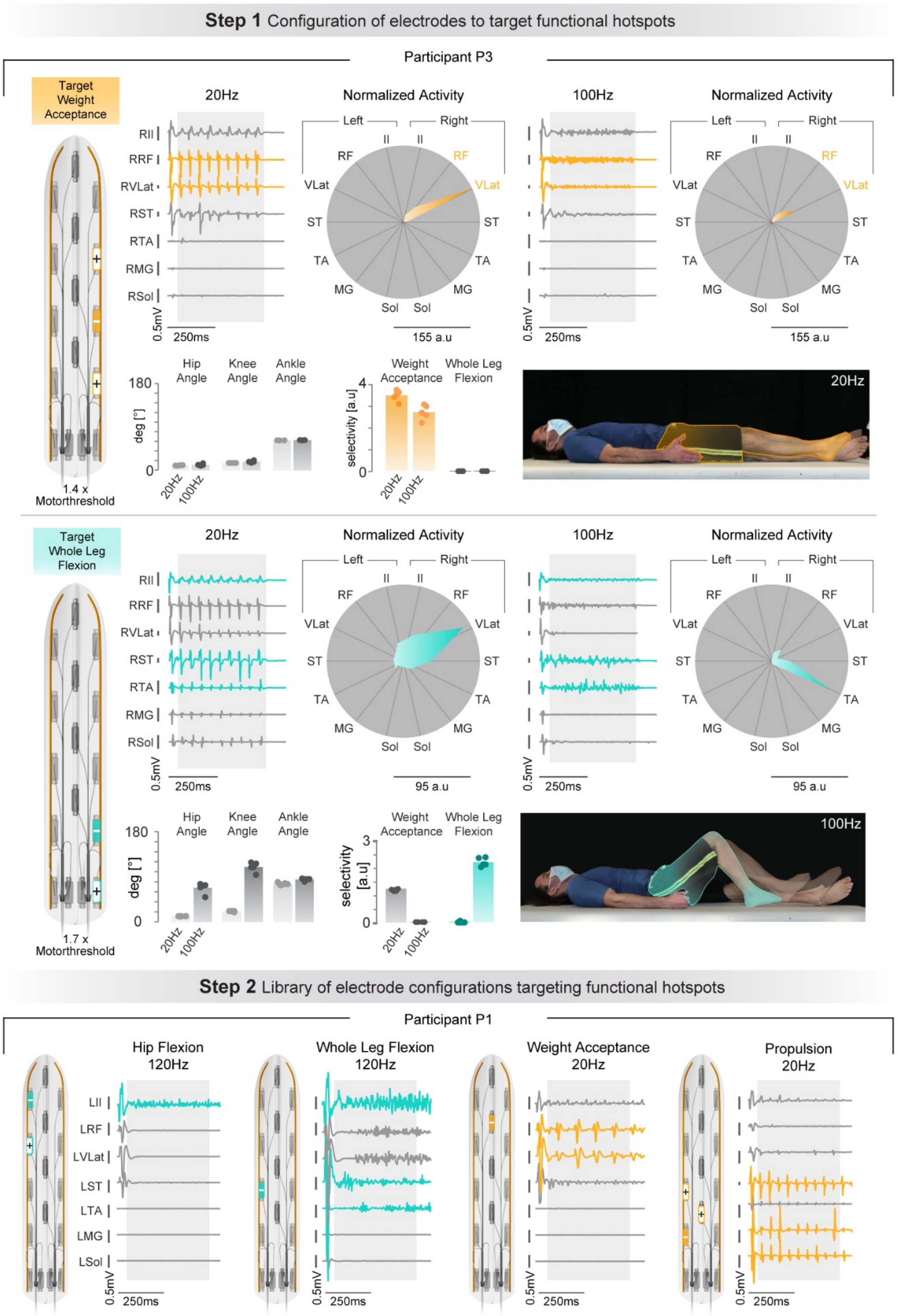

Figure 5.14: Configuration of frequency-specific EES trains to elicit functional muscular and kinematic activity.

Figure 5.14: (Continued) Step 1, Configuration of electrodes to target the hotspots associated with weight acceptance (top) and whole-leg flexion (bottom). Example from participant P3. EES bursts are delivered at 20 Hz. (weight acceptance, optimal frequency for motoneurons innervating extensor muscles) and 100 Hz (whole-leg flexion, optimal frequency for motoneurons innervating flexor muscles) to elicit muscle responses, recorded from the Iliopsoas (Il), Rectus Femoris (RF), Vastus Lateralis (VLat), Semitendinosus (ST), Tibialis Anterior (TA), Gastrocnemius Medialis (MG), and Soleus (Sol) muscles (mean response, n=5 repetitions). The muscles associated with the targeted hotspot are color-coded. Polar plots report the normalized muscle responses, using the same convention as in Fig. 5.13. Polar plot units are normalized with respect to the baseline (n-fold). Bar plots report the amplitude of associated kinematic responses from each joint, and the selectivity indexes for targeted and non-targeted muscles. Step 2, Similar representations are shown for participant P1.

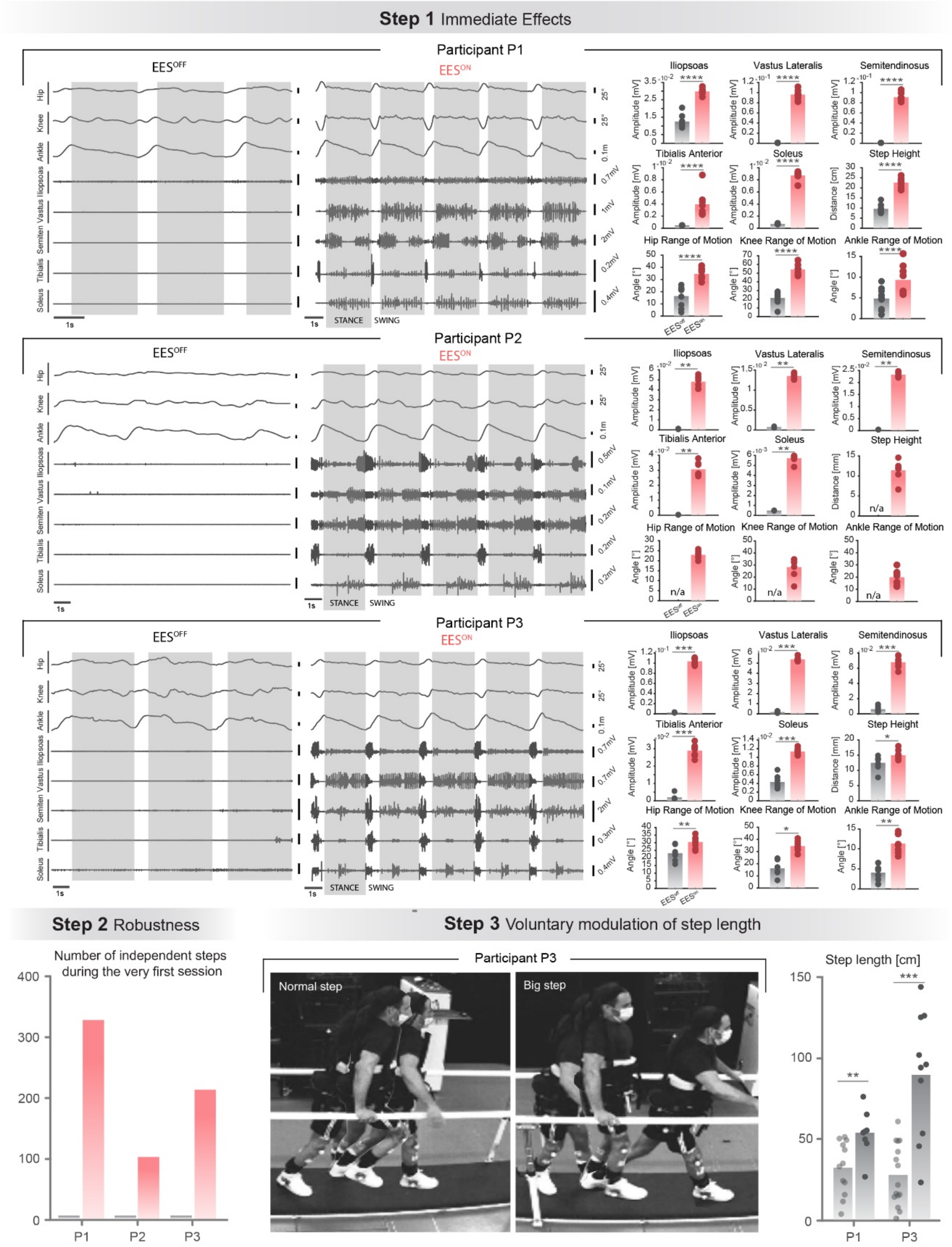

Figure 5.15: Immediate recovery of independent stepping with EES. Step 1, Kinematic and muscle activity underlying stepping on a treadmill without and with EES on the very first day of stimulation for the 3 participants. Bar plots report quantification of the muscle activity, and the range of motion for the hip, knee and ankle in both conditions. Muscular activities are quantified as Mean Absolute Value over their expected phase of activity. Step 2, Number of independent steps performed during the very first day of stimulation.

Figure 5.15: (Continued) Step 3, Chronophotographies showing normal and voluntarily exaggerated steps while stimulation parameters remain otherwise unchanged. Bar plots report the mean step length quantified during normal and exaggerated steps (Mann-Whitney test, *, p<0.05; **, p<0.01; ***, p<0.001,****, p<0.0001).

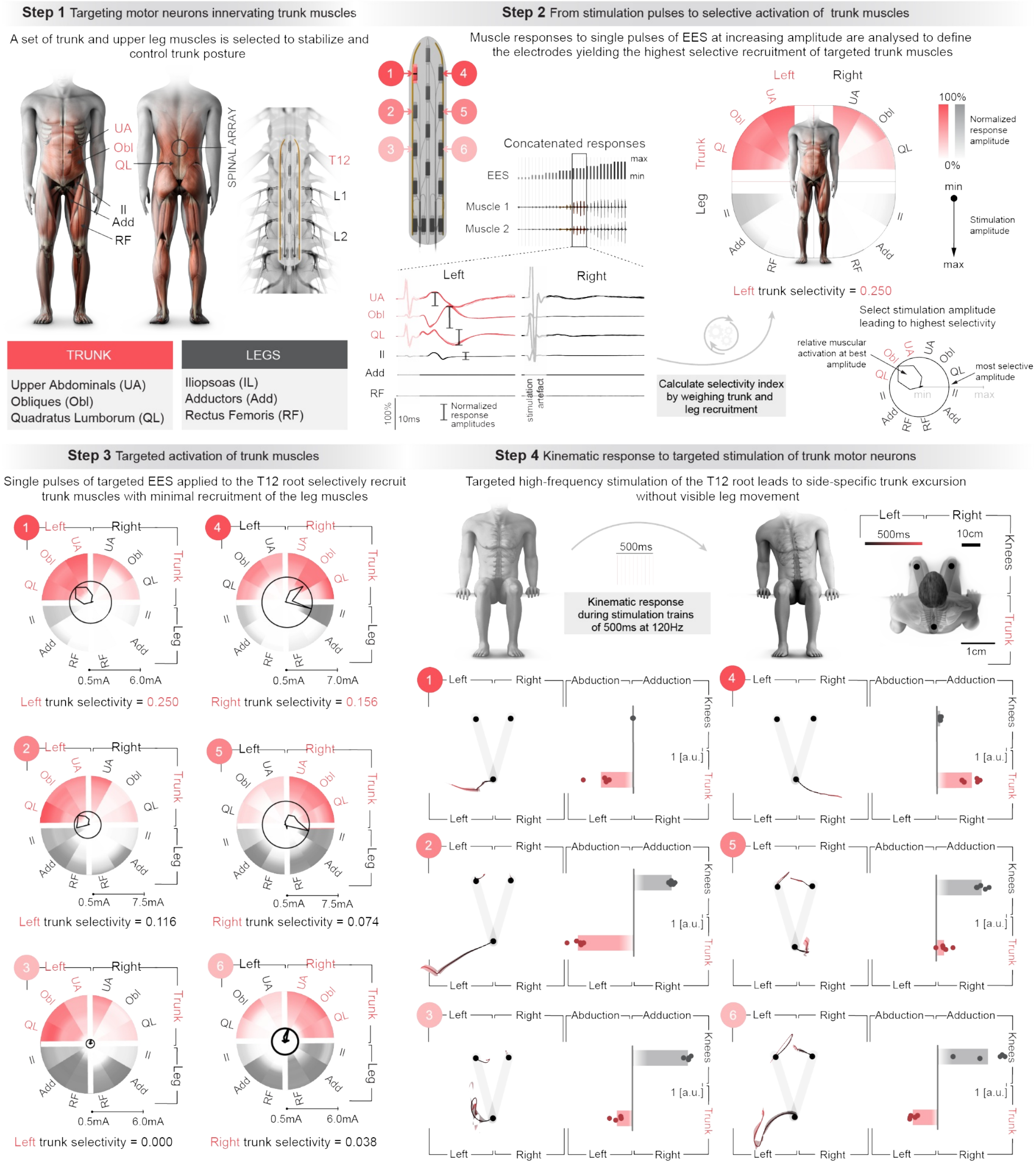
Step 1 Targeting motor neurons innervating trunk muscles
A set of trunk and upper leg muscles is selected to stabilize and control trunk posture
UA
Obl
QL
Il
Add
RF
SPINAL ARRAY
T12
L1
L2
TRUNK
Upper Abdominals (UA)
Obliques (Obl)
Quadratus Lumborum (QL)
LEGS
Iliopsoas (IL)
Adductors (Add)
Rectus Femoris (RF)
Step 2 From stimulation pulses to selective activation of trunk muscles
Muscle responses to single pulses of EES at increasing amplitude are analysed to define the electrodes yielding the highest selective recruitment of targeted trunk muscles
1
2
3
4
5
6
Concatenated responses
EES
max
min
Muscle 1
Muscle 2
Left
Right
UA
Obl
QL
Il
Add
RF
100%
10ms
Normalized response amplitudes
stimulation artefact
Trunk
Leg
100%
0%
Normalized response amplitude
min
max
Stimulation amplitude
Left trunk selectivity = 0.250
Select stimulation amplitude leading to highest selectivity
Calculate selectivity index by weighing trunk and leg recruitment
relative muscular activation at best amplitude
most selective amplitude
min
max
Step 3 Targeted activation of trunk muscles
Single pulses of targeted EES applied to the T12 root selectively recruit trunk muscles with minimal recruitment of the leg muscles
1
0.5mA 6.0mA
Left trunk selectivity = 0.250
4
0.5mA 7.0mA
Right trunk selectivity = 0.156
2
0.5mA 7.5mA
Left trunk selectivity = 0.116
5
0.5mA 7.5mA
Right trunk selectivity = 0.074
3
0.5mA 6.0mA
Left trunk selectivity = 0.000
6
0.5mA 6.0mA
Right trunk selectivity = 0.038
Step 4 Kinematic response to targeted stimulation of trunk motor neurons
Targeted high-frequency stimulation of the T12 root leads to side-specific trunk excursion without visible leg movement
500ms
Kinematic response during stimulation trains of 500ms at 120Hz
Left
Right
500ms
10cm
1cm
Knees
Trunk
Abduction
Adduction
1 [a.u.]

Figure 5.16: Selective recruitment of trunk muscles. Step 1, Trunk and abdominal muscles are primarily innervated by motoneurons located in the thoracic region of the spinal cord. The new paddle array enables targeting the dorsal roots projecting to the T12 spinal segment, allowing the recruitment of trunk and abdominal muscles.

Figure 5.16: (Continued) Step 2, Single pulses of EES at increasing amplitude are delivered over electrodes to evaluate their ability to recruit trunk and abdominal muscles. Muscle responses are calculated, normalized, and then represented in a polar plot. The selectivity of trunk/abdominal versus leg muscle activation is calculated with a selectivity index formula. Side-specific recruitment of trunk and abdominal muscles is obtained with the upper electrodes of the new paddle lead. Step 3, Polar plots reporting the activation of trunk/abdominal muscles versus leg muscles when delivering EES through various electrodes of the new paddle lead, as indicated by the number referring to the electrodes depicted in step 2. Step 4, Trains of EES are delivered through the same electrodes as in Step 2 to elicit kinematic responses. For each tested electrode, the panels depict the mean time-dependent trajectory of trunk and knee movements in the plane perpendicular to the direction of gravity, and bar plots reporting the mean amplitude of trunk and knee movement in abduction or adduction. Electrodes 1 and 4, which are located over the top row of the new paddle lead, elicited side-specific trunk movement without disturbing knee movements.

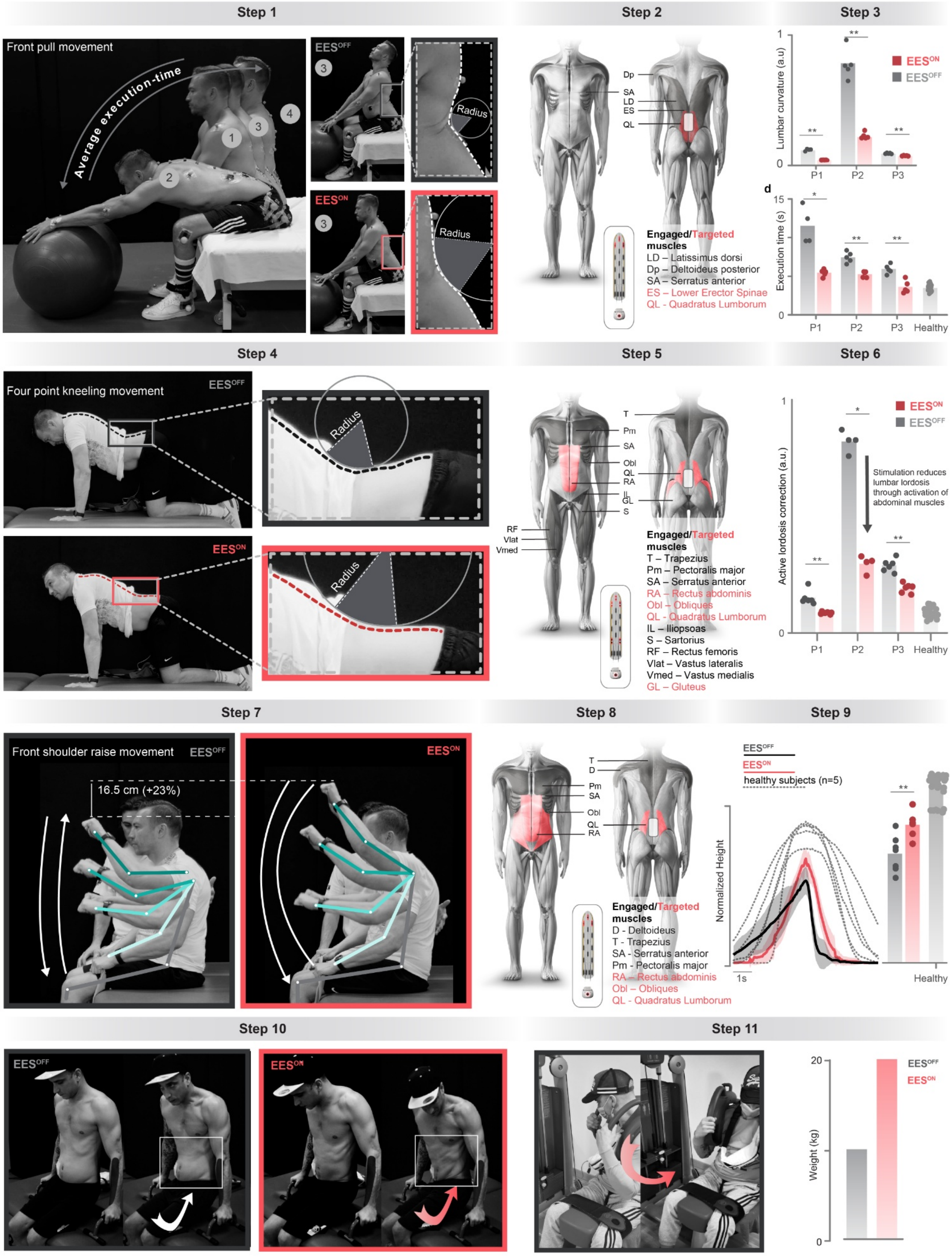
Step 1
Front pull movement
Average execution-time
1
2
3
4
EES^OFF
EES^ON
Radius
Step 2
Dp
SA
LD
ES
QL
Engaged/Targeted muscles
LD – Latissimus dorsi
Dp – Deltoideus posterior
SA – Serratus anterior
ES – Lower Erector Spinae
QL - Quadratus Lumborum
Step 3
Lumbar curvature (a.u)
1
0
**
P1
P2
P3
EES^ON
EES^OFF
d
Execution time (s)
15
5
0
*
P1
P2
P3
Healthy
Step 4
Four point kneeling movement
EES^OFF
EES^ON
Radius
Step 5
T
Pm
SA
Obl
QL
RA
IL
GL
S
RF
Vlat
Vmed
Engaged/Targeted muscles
T – Trapezius
Pm – Pectoralis major
SA – Serratus anterior
RA – Rectus abdominis
Obl – Obliques
QL – Quadratus Lumborum
IL – Iliopsoas
S – Sartorius
RF – Rectus femoris
Vlat – Vastus lateralis
Vmed – Vastus medialis
GL – Gluteus
Step 6
Active lordosis correction (a.u.)
1
0
EES^ON
EES^OFF
Stimulation reduces lumbar lordosis through activation of abdominal muscles
P1
P2
P3
Healthy
Step 7
Front shoulder raise movement
EES^OFF
16.5 cm (+23%)
EES^ON
Step 8
T
D
Pm
SA
Obl
QL
RA
Engaged/Targeted muscles
D - Deltoideus
T - Trapezius
SA - Serratus anterior
Pm - Pectoralis major
RA – Rectus abdominis
Obl – Obliques
QL - Quadratus Lumborum
Step 9
EES^OFF
EES^ON
healthy subjects (n=5)
Normalized Height
1s
**
Healthy
Step 10
EES^OFF
EES^ON
Step 11
Weight (kg)
20
0
EES^OFF
EES^ON

Figure 5.17: Immediate recovery of trunk control. Step 1, Participant P2 performing repeated front pull movement on a medicine ball without stimulation (black/EES OFF) and with EES targeting the T12 dorsal root (red/EES ON). Radius of curvature of the lumbar region is measured at position 3, which is the most difficult position for the participants to stabilize. Exercises were repeated 4-5 times in each condition (EES OFF/ON).

Figure 5.17: (Continued) Step 2, Representation of the trunk muscles engaged in the execution of the task (grey) and EES targeted muscles (red), together with the electrode configuration to target the subset of these muscles affected by the SCI. Step 3, Bar plots reporting the radius of curvature of the lumbar region at position 3 and the execution time of the whole exercise for each participant (Mann-Whitney test, *, $p<0.05$; **, $p<0.01$). Step 4, Participant P2 performing repeated lumbar lordosis correction in four-point kneeling position in the absence of stimulation (black/EES OFF) and with a stimulation program that targeted trunk, abdominal and gluteus muscles to stabilize the four-point kneeling position (red/EES ON). Radius of curvature of the lumbar region is measured at the time of maximal contraction and maximal relaxation of the lower back. Exercises were repeated 4-5 times in each condition (EES OFF/ON). Step 5, Same as Step 2. Step 6, Bar plots reporting the lumbar curvature without and with stimulation. Step 7, Participant P2 performing repeated front shoulder raise in the absence of stimulation (black/EES OFF) and with EES (red/EES ON). Exercises were repeated 4-5 times in each condition (EES OFF/ON). Step 8, Same as Step 2. Step 9, Changes in position of the wrist in the vertical plane during the front shoulder raise movement, showing improved symmetry and range of motion with EES turned on. The bar plot reports the execution time of this task with and without EES, and in healthy individuals for comparison. Step 10, Dips lifting hip. In the absence of stimulation, the participant (P1) is able to lift his own body-weight but is not able to lift his pelvis (black). With EES, he is able to activate his lower abdominal and oblique muscles to lift his pelvis on both sides. Step 11, The participant (P1) is using a torso rotation machine at the gym. In the absence of stimulation, he is able to rotate to both sides lifting 10kg. EES enables him to perform this exercise with twice this weight as represented on the bar plot.

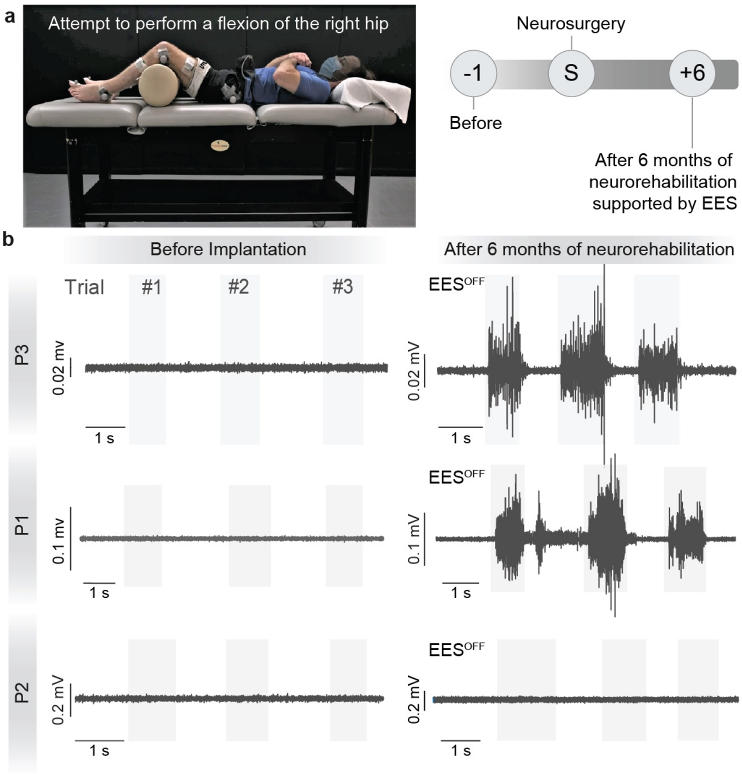

Figure 5.18: Volitional activation of muscles. a, While lying in a supine position, participants were requested to attempt to perform three successive flexions of the right hip without EES and in the absence of any facilitation manoeuvres. Data is shown before the neurosurgical implantation and after 6 months of neurorehabilitation supported by EES. b, EMG activity was recorded from the right Iliopsoas. Two out of 3 participants with complete sensorimotor paralysis recovered volitional activation of the Iliopsoas muscle with EES turned off.

Participant	**P1**		**P2**		**P3**	
Gender	m		m		m	
Age at study enrolment (y)	32		41		29	
Years after SCI at study enrolment	8 years and 11 months		1 year and 3 months		2 years and 10 months	
Assessment at study enrolment (Pre) and after rehabilitation period (Post)	Pre	Post	Pre	Post	Pre	Post
American Spinal Injury Association Impairment Scale (AIS)	A	A	A	A	B	C
Neurological level of injury	T4	T3	T3	T3	T7	T7
Lower Extremity Motor Score						
L2, hip flexors (right | left)	0 | 0	0 | 0	0 | 0	0 | 0	0 | 0	1 | 2
L3, knee extensors (right | left)	0 | 0	0 | 0	0 | 0	0 | 0	0 | 0	1 | 1
L4, ankle dorsiflexors (right | left)	0 | 0	0 | 0	0 | 0	0 | 0	0 | 0	0 | 1
L5, long toe extensors (right | left)	0 | 0	0 | 0	0 | 0	0 | 0	0 | 0	0 | 0
S1, ankle plantar flexors (right | left) (max. 5 per side)	0 | 0	0 | 0	0 | 0	0 | 0	0 | 0	0 | 0
Total (max. 25 | 25)	0 | 0	0 | 0	0 | 0	0 | 0	0 | 0	2 | 4
Deep anal pressure (DAP)	No	No	No	No	Yes	Yes
Voluntary anal contraction (VAC)	No	No	No	No	No	No
Light-Touch Sensory score						
L1-S2 dermatomes subscore (right | left)	0 | 0	0 | 0	0 | 0	0 | 0	0 | 0	0 | 0
Total (max. 112)	23 | 23	22 | 22	23 | 23	21 | 22	32 | 31	30 | 31
Pin Prick Sensory Scores						
L1-S2 dermatomes subscore (right | left)	0 | 0	0 | 0	0 | 0	0 | 0	0 | 0	0 | 0
Total (max. 56 | 56)	22 | 22	21 | 22	24 | 24	21 | 21	30 | 28	30 | 30

Table 5.1: Demographic and neurological status of participants

5.5 Materials and Methods

5.5.1 Study design and objectives

All experiments were carried out as part of the ongoing clinical feasibility study STIMO ("Stimulation Movement Overground"), which investigates the effects of spatiotemporal EES combined with weight-supported overground locomotor training on the recovery of motor function after SCI. This study was approved by the Swiss ethical authorities (Swissethics protocol number 04/2014 ProjectID: PB_2016-00886, Swissmedic protocol 2016-MD-0002) and was conducted in accordance with the Declaration of Helsinki. All participants signed a written informed consent prior to their participation. More information at clinicaltrials.gov (NCT02936453). All surgical and experimental procedures were performed at the Lausanne University Hospital (CHUV). The study involved assessments before surgery, the surgical implantation of the neurostimulation system, a one-month period during which EES protocols were configured, and a five-month rehabilitation period with physiotherapists taking place four to five times per week for one to three hours. The rehabilitation program was personalized based on the participants' improvements. At the end of the rehabilitation period, the participants were given the opportunity to be enrolled in a study extension phase during which they could continue using the neurostimulation system at home. They are currently followed-up on a regular basis by the study team for up to 6 years.

5.5.2 Study participants

Three individuals who had suffered a traumatic thoracic SCI participated in the study. Their neurological status was evaluated according to the International Standards for Neurological Classification of Spinal Cord Injury (Kirshblum & Waring, 2014), and is reported in Table 5.1. At enrollment, participant P1 was 32 years old and was classified with a motor and sensory complete (AIS-A), T4 lesion that occurred nine years earlier during a motor bike accident. He presented with bilateral leg paralysis, with motor scores of 0 on all key leg muscles. He could neither stand nor ambulate at all (WISCI score: 0), despite extensive participation in physical exercise with adapted devices for home use. Participant P2 was 41 years old and was classified with a motor and sensory complete (AIS-A) T6/T7 lesion that occurred one year earlier during a motor bike accident. He presented with bilateral flaccid leg paralysis, with motor scores of 0 on all key leg muscles. He did not have any spasticity in his legs and could neither stand nor ambulate at all (WISCI score: 0), despite extensive participation in physical exercise with adapted devices for home use. Participant P3 was 29 years old, classified with a motor complete (AIS-B) T5/T6 lesion that occurred three years earlier during a motor bike accident. He presented with bilateral spastic leg paralysis, with motor scores of 0 on all key leg muscles.

5.5.3 Cadaver analysis

Formalin-fixated human spinal cords (n=12) were immersed in PBS 0,1M. The dura was carefully dissected using appropriate surgical tools to identify and expose the lumbosacral spinal segments. The roots were pinned individually using a specific color-code at their entry point to the cord. The length of each lumbosacral spinal segments was measured using a caliper. The length of each spinal segment was defined as the root attachment length plus the lower inter-root length. The measurements were averaged over the total number of dissected cords.

5.5.4 Healthy volunteer MRI Data

MRI acquisitions on healthy volunteers were performed on a 3T Philips Ingenia system (Philips Healthcare, Best, The Netherlands) in supine position. For these acquisitions, we used the torso anterior receiver coil and the posterior receiver coil (embedded in Table 5.2). The following sequences were acquired:

1. T2-weighted MRI sequence; Multi-Slice Cartesian Fast-Field-Echo (FFE); field-of-view (anterior-posterior/feet-head/ right-left): 180x480x92 mm^3; acquired resolution: 1x1x3 mm^3; reconstructed resolution: 0.75x0.75x3 mm^3; slice orientation: sagittal; repetition time/echo time: 334/8.1 ms; flip angle: 25; number of signal averages: 3; acquisition time: 5 min 20 sec.

2. T1-weighted MRI sequence; Multi-Slice Cartesian Fast-Field-Echo (FFE); field-of-view (anterior-posterior/feet-head/ right-left): 180x480x92 mm^3; acquired resolution: 1x1x3 mm^3; reconstructed resolution: 0.75x0.75x3 mm^3; slice orientation: sagittal; repetition time/echo time: 140/4.6 ms; flip angle: 80; number of signal averages: 2; acquisition time: 5 min 20 sec.

3. Gray/white matter contract (butterfly) sequence; Multi-Slice Multi-Echo Cartesian Fast-Field-Echo (FFE); field-of-view (anterior-posterior/feet-head/ right-left): 80x135x200 mm^3; acquired resolution: 0.8x0.8x4 mm^3; reconstructed resolution: 0.5x0.5x4 mm^3; slice orientation: transverse; repetition time/echo time/delta echo time: 993/4.6/6.1 ms; Number of echoes = 4; flip angle: 65; number of signal averages: 1; acquisition time: 5 min 15 sec.

4. A 3D Fast-Field-Echo (FFE) balanced-Steady-State-Free-Precession sequence (bSSFP) was developed to visualize the nerve roots inside the spinal canal. This sequence is T1/T2*-weighted, thus the nerve roots appear with negative contrast against CereBroSpinal Fluid (CSF). It has an almost isotropic resolution allowing Multi-Planar-Reconstruction (MPR) with negligible loss of details. Furthermore, it is fully balanced, thus allowing high SNR, and intrinsically flow compensated. Hence, CSF flow artifacts affecting standard clinical sequences are minimized. The following imaging parameters were used: field-of-view (right-left/anterior-posterior/feet-head): 250x40x350 mm^3; acquired resolution: 0.6x0.6x1 mm^3; reconstructed resolution: 0.35x0.35x0.35 mm^3; slice orientation: coronal; repetition time/echo time: 7/3.5 ms; Flip angle: 55; acceleration factor: 1.2 feet-head direction; number of signal averages: 1; acquisition time: 4 min 30 sec.

Technical parameter	**T2-weighted turbo spin-echo**	**T2-weighted SPACE with ZOOMit**	**T2-weighted TrueFISP**
Plane	Sagittal	Axial	Coronal
No. of sections	21	160	80
Section thickness (mm)	3	0.5	0.6
Section gap (mm)	0.3	0	0
Field of view (mm)	290 × 333	300 × 105	250 × 250
Acquisition matrix	448 × 314	512 × 512	448 × 224
Voxel size (mm^3)	0.6 × 0.6 × 3	0.3 × 0.3 × 0.5*	0.3 × 0.3 × 0.6*
K-space sampling	Cartesian	Spiral	Cartesian
Phase-encoding direction	Head to feet	Anterior to posterior	Feet to head
Repetition time (ms)	4560	3080	6.04
Echo time (ms)	98	106	3.02
Turbo factor	19	270	N/A
No. of signal averages	2	1.4	1
Flip angle (degrees)	127	100	52
Bandwidth (Hz/pixel)	228	574	558
Acquisition time (min:sec)	2:41	10:11	6:55

* after interpolation

Table 5.2: Acquisition parameters for MR pulse sequences to image thoracolumbar spine.

5.5.5 Structural MRI of the Thoracolumbar Spine

Each subject underwent structural MRI of the thoracolumbar spine on a 3T MR scanner (Magnetom Prisma^{fit}, Siemens Healthineers) with 16-channel body and 32-channel spine array coils. Participants were positioned supine with arms at their side. Prior to MR image acquisition, shim boxes were applied to correct for magnetic field inhomogeneities. The standard MRI protocol comprised the following three pulse sequences, all used without gadolinium-based contrast agent administration: a) 2D sagittal T2-weighted turbo spin-echo (repetition time (TR), 3080 msec; echo time (TE), 98 msec; voxel size, $0.6\times0.6\times3$ mm^3); b) 3D axial T2-weighted SPACE (Sampling Perfection with Application-optimized Contrasts using different flip angle Evolution) with ZOOMit (dynamic excitation pulses to achieve selective/zoomed field-of-view) software (TR, 2500 msec; TE, 106 msec; interpolated voxel size, $0.3\times0.3\times0.5$ mm^3); and c) 3D coronal T2-weighted TrueFISP (True Fast Imaging with Steady state Precession) (TR, 6.04 msec; TE, 3.02 msec; interpolated voxel size, $0.3\times0.3\times0.6$ mm^3). The total scan time was <25 min overall. Detailed acquisition parameters for the three MR pulse sequences used to image the medullary cone and nerve roots of the participants' thoracolumbar spine:

5.5.6 Spinal cord fMRI

We performed lumbosacral spinal cord functional magnetic imaging (fMRI) to visualize the projectome of proprioceptive neurons innervating specific muscles. Muscle spindle afferents, which sense the length and change in length of the muscle wherein they are embedded, were recruited by passive muscle stretch (three participants) and muscle tendon vibrations (one participant). The fMRI pre-processing, processing and analysis pipeline were based on recent cervical spinal cord fMRI studies (Kinany et al., 2019; Kinany et al., 2020; K. A. Weber et al., 2020; K. A. Weber et al., 2016a, 2016b). We tailored this pipeline to image the lumbar spinal cord.

fMRI data acquisition
Participants were comfortably installed in the scanner (Siemens Prisma 3 Tesla, Erlangen, Germany) in a supine position. Spine and body coils (Siemens, Erlangen, Germany) were used. The participants were instructed to relax, to remain still and to breathe normally. All three participants underwent at least one experimental recording, involving passive limb mobilization to stretch specific groups of muscles. Participants P3 was involved in an additional acquisition during which muscle tendon vibrations were applied to selected muscles (see below).Functional acquisitions were performed using a gradient-echo echo-planar sequence with a ZOOmit field-of-view imaging, with repetition time (TR) = 2.5 s, echo time (TE) = 34 ms, FOV = 48x144 mm, flip angle = 80°, in plane resolution = 1.1 mm x 1.1 mm, and slice thickness = 3 mm. 27 axial slices were acquired per volume. The first slice rostrocaudally is placed slightly above the L1 segment. Manual shimming adjustments focused on the spinal cord were done to adjust field homogeneity. Physiological data (respiratory and cardiac signals) were directly acquired using MRI compatible photoplethysmography and respiratory belt (Siemens, Erlangen, Germany). A T2-weighted high-resolution anatomical image (sequence SPACE with a resolution of 0.4 mm x 0.4 mm x 0.8 mm, TR = 1.5 s, TE = 135 ms) was also acquired for registration and normalization purposes.

Mechanical vibration
MRI-compatible pneumatic vibrators were used to stimulate muscle spindle afferents. Small

amplitude (0.5 mm peak to peak) and constant frequency (70 Hz) vibrations were delivered using a SMC ITV2050 air-pressure regulator driving the rotation of eccentric ceramic spherical masses embedded in the vibrator turbine. The stimulation parameters were selected based on the fact that small amplitude vibration activates preferentially primary muscle spindle endings, with responses linearly proportional to the vibration frequency up to 70-80 Hz (J. P. Roll & Vedel, 1982). A custom software implemented in the LabVIEW environment (National Instruments) allowed to synchronize the vibratory stimulations with the MRI acquisitions. This device did not produce artefacts in the fMRI scans, nor modified the Signal-to-Noise Ratio (SNR), as already reported in previous studies during which vibrations were applied during brain fMRI acquisitions (Kavounoudias et al., 2008; Landelle et al., 2018).

Six pneumatic vibrators were attached to the subject's right leg using elastic bands on the tendons of each pair of agonist/antagonist (extensor/flexor) muscles at the ankle, knee and hip levels. The aim was to target the Gastrocnemius Medialis/Soleus, Tibialis Anterior, Quadriceps, Iliopsoas, Gluteus and Biceps Femoris muscles. The protocol was divided in 2 runs for each pair of agonist/antagonist muscles per joint. In each run, two vibrators, one located on the flexor muscle and the other on the extensor muscle, were alternatively activated in blocks of 10 s. One run consisted of 18 alternate vibration blocks. To avoid any bias, the order of the 6 runs was randomized.

fMRI data Processing

The fMRI pre-processing was carried out using the FMRIB Software Library (FSL) v5.0 (Jenkinson et al., 2012) and the Spinal Cord Toolbox (SCT) v4.3 (De Leener et al., 2017).

A two-phase motion correction procedure was performed using FMRIB's Linear Image Registration Tool (Jenkinson et al., 2002). First, the volumes of each run were averaged into a mean image. The centerline of the spinal cord was automatically extracted (Gros et al., 2018). A cylindrical mask of diameter 30 mm was drawn along it and used to exclude the regions outside the spinal cord. Within each run, all volumes were registered to the mean image using three-dimensional rigid body realignment (spline interpolation and least square cost function). To consider that the spinal cord is a non-rigid structure, a two-dimensional slice-wise realignment (spline interpolation and least square cost function) was conducted, taking as reference the mean image of the corrected volumes (Cohen-Adad et al., 2009; K. Weber et al., 2014). Finally, all runs corresponding to the same session in the scanner were aligned to the first run of the session using three-dimensional rigid body realignment (spline interpolation and least square cost function). All images were inspected to ensure that any artefacts or bottom slices with insufficient signal were cropped out. Two slices were in general removed per run. Motion scrubbing was also performed with FSL's tool to identify outliers volumes, using DVARS (the root mean square of the difference of intensity between consecutive volumes) metric in the spinal cord, with a box-plot cut-off (75th percentile + 1.5 x the interquartile range) (Power et al., 2014).

Both the cerebrospinal fluid and the spinal cord were automatically segmented (with manual corrections when necessary) using the Spinal Cord Toolbox (SCT) (Gros et al., 2019) from the mean functional and the T2 anatomical images.

Nuisance regressors were built using FSL's physiological noise modelling tool on the acquired cardiac and respiratory signals, using an approach based on the RETROICOR procedure (Eippert et al., 2017). Low and high order Fourier expansions were used to model the physiological signals (Brooks et al., 2008; Kong et al., 2012). This resulted in 32 noise regressors, to which an additional cerebrospinal fluid regressor was included (10 % most variable cerebrospinal fluid voxels). When no physiological signals were available, regressors based on anatomical priors were determined using component-based noise extraction (aCompCor (Behzadi et al., 2007)) through the PhysIO Toolbox (Kasper et al., 2017). The motion corrected volumes were masked with the segmented cerebrospinal fluid mask. The first five principal components, as well as the mean of these time series were extracted and kept as noise regressors.

Coregistration was performed within each subject (functional-to-anatomical). Using the Spinal Cord Toolbox, functional images were coregistered to the T2 anatomical image with non-rigid transformations.

The motion corrected functional volumes were spatially smoothed, volume by volume, using a 3D Gaussian kernel (with FWHM of 2 x 2 x 6 mm^3, along the centerline of the spinal cord, to preserve consistency at the anatomical level.

Spinal segments L1 to S2 were identified using the high-resolution structural MRI. The L1 dorsal root was identified from its entry region in the spinal canal (entering just below the L1 vertebra) until the region where it innervates the spinal cord, which defines the L1 spinal segment. The more caudal segments (L2 - S2) were identified by following the dorsal roots along the rostrocaudal axis.

fMRI data analysis

Using the pre-processed functional volumes (motion corrected, smoothed) and the noise regressors (physiological and motion outliers), for each run, a first-level statistical analysis was performed using FMRIB's Improved Linear Model with local auto-correlation correction (Woolrich et al., 2001). As explanatory variables, the timings of the task (block design) were convolved with the three optimal basis functions using FMRIB's Linear Optimal Basis Set (Woolrich et al., 2004), with the second and third waveforms orthogonal to the first waveform. The resulting parameter estimates for the two runs were passed through a fixed-effects model to obtain the second level analysis (subject level and task specific) activation maps. To account for multiple comparisons, the Z statistic images were set to ($Z > 2$, $p < 0.05$) whenever possible. These results were then registered to the respective anatomical image to assess their spatial distribution with respect to spinal segments.

5.5.7 Personalized hybrid computational models

We designed a computational framework that supports the semi-automated creation of personalized, geometrically and neurofunctionally realistic hybrid neurophysical volume conductor models of the lower thoracic and lumbosacral spinal cord from high-resolution MRI and CT data. These models combine a 3D Finite Element Method (FEM) to characterize the electric potential and currents generated by EES with compartmental cable models to estimate the recruitment profile of individual nerve fibers.

Semi-automatic segmentation of anatomical tissues from MRI and CT data
Segmentation of MRI and CT data was performed using iSeg, a software developed by ZMT (www.zurichmedtech.com). We augmented this software with two plugins that accelerate the segmentation process. First, a Kalman-filter based plugin called *Root tracer* was implemented. *Root Tracer* utilizes the same algorithm as iSeg's *Auto-Tube Tracer* plugin to label the spinal roots semi-automatically. In each algorithm step, the current image slice is transformed into a label map which contains all identified roots. Each root is represented by a distinct label object. The plugin enables the user to manually correct missing or falsely identified spinal roots. The plugin then predicts the position of the successive roots in the consecutive slice by considering (a) the distance between the given root and all roots in the previous slice, (b) the difference in parameters between the given root and all roots in the previous slice (for more information on considered parameters see itk::ShapeLabelObject) and (c) a unique Kalman filter for each root that utilizes the position of all occurrences of the given root in the previous slices to predict its next position. The probability of root x from the current slice being root a from the previous slice is defined as:

$$P(x=a) = \frac{e^{-(w_d \times D_{x\to a} + w_p \times \Delta P_{x\to a} + w_k \times \Delta K_{x\to a})}}{\sum_i^N e^{-(w_d \times D_{x\to i} + w_p \times \Delta P_{x\to i} + w_k \times \Delta K_{x\to i})}} \tag{5.1}$$

Where $D_{x\to a}$ is the physical difference on the image between root x and a. $\Delta P_{x\to a}$ is the difference in parameters between root x and a. $\Delta K_{x\to a}$ is the difference between the Kalman filter's prediction between root x and a. W_d, w_p and w_k are user-defined weights relating to these parameters.
A second plugin, named *CT Auto-Bone,* enables the automated segmentation of vertebral bones from CT data. This plugin leverages a method based on enhancing the sheetness appearance of the cortical bone (Krčah et al., 2011), i.e. the brighter CT pixel layer corresponding to bone boundaries. The sheetness measure is computed from the eigenvalues of the local Hessian (second derivatives of image intensities) and is used as the boundary term for an automatic graph-cut segmentation. The implementation uses the Graph Cut combinatorial optimization library (https://github.com/odanek/gc) and is available as a plugin in medical image segmentation tool set iSEG (https://github.com/ITISFoundation/osparc-iseg).

Generation of spinal cord 3D models
All relevant anatomical tissues were segmented in iSeg v 3.10.43.78. The procedure consisted of implementing the *CT Auto-Bone* plugin to segment the vertebral bone from the CT data. The space between the vertebral bodies was then filled with vertebral discs when possible, by means of thresholding, manual segmentation and interpolation. Similarly, the vertebral bone, cerebrospinal fluid and white matter were extracted from high-resolution MRI images.

The *Root Tracer* plugin was applied to the same MRI images to identify the spinal roots. The epidural space was filled with another tissue named epidural fat by means of boolean subtraction between an enlarged cerebrospinal fluid and vertebral bone. The grey matter was placed to scale inside of the white matter, using contours generated from anatomical data (Sengul, 2013). The segmented images were then imported in Sim4Life v6.0.0.3176 (ZMT. www.zurichmedtech.com) and transformed into a 3D model using the *Surface Extraction* tool. The coordinates of the spinal roots were extracted as x-y-z coordinates. We developed a custom-made algorithm to generate a continuum of rootlets for each spinal root. This algorithm was based on the assumptions that each rootlet has a fixed diameter and that the lower thoracic and lumbosacral spinal cord exhibit a continuum of rootlets with only minor empty spaces in between the roots along the rostrocaudal direction. Concretely, the centerlines of two roots were extracted and the tridimensional coordinates at the entry point into the white matter were used to interpolate the trajectories of the rootlets. The number of rootlets was determined by the distance between the entry-points under the assumption that each rootlet has a fixed diameter. Rootlet diameters were assigned based on anatomical observations (Liu et al., 2015). Elliptical cross-sections were placed along the trajectories with their normal vector parallel to the tangent vector of the trajectory. Finally, the contours that defined the rootlets were imported in Sim4Life and lofted together using the *SkinWire* function.

Model of the paddle leads

We created a model of the new paddle lead and of the Specify 5-6-5. These models were composed of tridimensional orthopes with rounded edges to depict the electrodes. The electrodes were placed inside another tridimensional orthope with rounded edges that modelled the paddle lead. The models of the paddle leads were positioned at distinct locations within the epidural space to study the interactions between the location of the stimulation and the recruitment of afferent fibers.

Finite element models

Due to the variability in the topological organization of the spinal cord amongst the studied human population, we discretized the models as voxels using the robust rectilinear (structured) gridding engine provided by Sim4Life. Region-specific grid resolution thresholds were imposed: maximum 2 mm for vertebral bone and discs, 1 mm for the epidural fat and cerebrospinal fluid, 0.6 mm for the paddle lead of the spinal cord stimulator, 0.3 mm for the grey and white matter, as well as any electrodes and 0.1 mm for the rootlets. The entire model was submerged in a large conducting material to simulate the human body. This material is referred to as saline conductor (-10 mm grid resolution threshold). We applied conductivity maps for each tissue. Conductivity values were taken from a previously published study (Capogrosso et al., 2013). Similar to previous studies, we did not include the thin dura mater in our model (Ladenbauer et al., 2010). To model the anisotropic conductivity of the white matter and rootlets, we expanded the capability of Sim4Life to enable the automatic calculation of anisotropic and inhomogeneous conductivity maps from helper simulations. These helpers solve the Laplace Equation ($\Delta V = 0$) with the following Dirichlet and Neumann boundary conditions: V($\delta\Omega_{rostral}$) = 1 at the rostral surface of the white matter, V($\delta\Omega_{caudal}$) = 0 at the caudal end of each rootlet and the inferior tip of the white matter, and isolating ($|\nabla V| = 0$). We solved the electro-quasistatic approximation of the Maxwell equations using the Sim4Life solver ($\nabla\sigma\nabla\varphi = 0$, with σ the conductivity and the permittivity), while assigning a constant σ throughout the computational domain, which comprised white matter and rootlets. The resulting E-fields (proportional to the potential gradients), were then used to define the local orientation of the principal conduction components of the anisotropic tissue conductivity. The tensor was computed according to the following equation:

$$\sigma(x) = \sigma_{longitudinal} \times P(x) + \sigma_{transversal} \times (I_3 - P(x)) \tag{5.2}$$

, where , $P(x) = E(X) \otimes (\frac{E(X)}{E(X)^2})$.

Simulation of EES in the Model

The electrical potential induced by EES was obtained by solving the electro-quasistatic approximation of the Maxwell equations. The corresponding simulation has already been predefined and is available in Sim4Life. A Dirichlet Boundary condition of V($\delta\Omega_{electrode}$) = 1V simulating a biphasic stimulation pulse of 500 µs duration was applied at the active electrode site ($\delta\Omega_{electrode}$) to model the stimulation commonly occurring throughout this study. Dirichlet boundary conditions of V($\delta\Omega_{saline}$) = -1V were set at the location of a return electrode within the saline conductor to simulate the position of the implantable pulse generator. Von Neumann conditions with $\frac{\partial V}{\partial x} = 0$ were applied at the outermost surface of the saline conductor. Convergence tolerance were set to the predefined value high.

Modeling and recruitment of nerve fibers

We used the integrated NEURON 4.4 (Hines & Carnevale, 2001) solver of Sim4Life to develop a computational model of group Aα-, Aβ-, Aδ- and C-fibers that we positioned within the dorsal roots, and of α-motor axons that we positioned in the ventral roots. Fifty fibers per fiber population were simulated for each spinal cord segment. The trajectories of the fibers were automatically generated, by uniformly distributing 50 points $P_{i,n}$ in each Contour C_n and connecting those that have the same index i. To ensure that nerve fibers remain similarly positioned relative to each other inside each rootlet (i.e., the fibers are not meandering), we use a single set of weights $w_{i,l}$ according to:

$$P_{i,n} = \sum_{l=1}^{N} w_{i,l} \times \begin{pmatrix} X_{ln} \\ Y_{ln} \\ Z_{ln} \end{pmatrix}$$

where $(X_{ln}, Y_{ln}, Z_{ln},)$ are the coordinates of the N points composing C_n. The weights w_l are sampled uniformly at random in the unit simplex. This was possible as the C_n were defined with similar topologies, namely that they posses the same number of points N with equal indexes which are isomorphic. Finally, the trajectories of these splines were interpolated to smooth their trajectories and imported in Sim4Life. Compartmental cable models were then applied to these trajectories. We designed Sensory MRG model (Gaines et al., 2018) that we integrated into Sim4Life to simulate Aα- and Aβ-fibers with arbitrary diameters. We also integrated Motor MRG models (Gaines et al., 2018) with arbitrary diameters for the α-motor axons. Finally, we simulated Aδ-fibers with Sweeney Models (Sweeney et al., 1987) and C-fibers with Sundt-Models (Sundt et al., 2015). Diameters of nerve fibers were stochastically assigned according to log-norm distributions with the following parameters: Aα: µ = 16.5 µm, σ = 2 µm; Aβ: µ = 10,5 µm, σ = 2 µm; Aδ: µ = 3 µm, σ = 1 µm; C = µ = 0.85 µm, σ = 0.5 µm; MN: µ = 11.52 µm, σ = 0.07 µm. For each amplitude of EES, we calculated the recruitment curve of each population of fibers for increasing EES amplitudes.

Dorsal root selectivity index

For a given electrode configuration and EES amplitude, computational simulations yielded the percentage of fibers activated in each dorsal root. We derived a root selectivity index $SI_{computational}(r_i,\ I)$ for each root r_i and each stimulation amplitude I:

$$SI_{computational}(r_i,\ I) = \frac{A_{r_i}(I)}{1+\sum_{other\ ipsilateral\ roots} A_{r_j}(I)} . f_+\left(\frac{A_{r_i}(I) - A_{r_{contralateral(i)}}(I)}{A_{r_i}(I) + A_{r_{contralateral(i)}}(I)}\right) \quad (5.3)$$

where $A_{r_i}(I)$ represents the percentage of fibers activated in root r_i, $r_{contralateral(i)}$ is the root contratateral to root r_i , and $f_+(x) = \begin{matrix} x\ if\ x > 0 \\ 0\ if\ x \leq 0 \end{matrix}$.

The first term of this selectivity index represents the rostrocaudal ipsilateral root selectivity, while the second term indicates the medio-lateral selectivity and penalizes configurations that activate the root contralateral to the targeted one. If the contralateral root is more activated than the targeted root, the selectivity index is equal to 0. If only the targeted root is recruited, the selectivity equals 1. This selectivity index was calculated for a range of stimulation amplitudes and the maximum was taken to characterize the overall selectivity of each electrode configuration.

Preoperative placement optimization

To optimize the intraoperative placement of the paddle leads, we performed simulations based on the personalized model of each participant. We manually placed a model of the new paddle lead and Specify 5-6-5 in the epidural space. Since simulations revealed that Aα fibers are nearly all activated before the recruitment of the other fiber populations (Fig. 5.1), we only considered Aα-fibers in the dorsal rootlets, thus allowing to optimize computational resources. We computed the electric potential scaling required to recruit each fiber. We then calculated the percentage of fibers recruited within each spinal segment at each electric potential scaling I and interpolated this recruitment profile to 10'000 datapoints over the entire electric potential scaling required to activate each fiber in the model with each electrode at each position of the paddle lead. We then elaborated transformation matrices to translate this afferent recruitment profile to an estimation of the recruitment of motoneurons and thus muscle activity $A_j(I)$, where *j* denoted the muscle. Two transformation matrices were used. First, we built a transformation matrix for each patient based on the projectome of proprioceptive neurons from key leg muscles identified from fMRI acquisitions. Second, we built a generic transformation matrix based on the distribution of myotomes measured electrophysiologically in a large population of patients undergoing surgery (Schirmer et al., 2011). These matrices can be found in Table 5.3 and Table 5.4.

To identify the optimal placement of the paddle lead, we computed a selectivity index

$$SI_{functionality}(g_i, I)$$

that quantified the performance of an electrode to target a muscle group g_i with respect to non-targeted muscles. This selectivity index contains two terms, one indicating the selectivity on the targeted side, and one indicating the mediolateral selectivity for the targeted side s_i:

$$SI_{functionality}(g_i, I) = SI_{targetedmuscles}(g_i, I) \cdot SI_{leftvsright}(s_i, I)$$

$$\begin{cases} \mathrm{SI}_{targetedmuscles}(g_i, I) = f_+\left(\frac{\sum_{musclesing_i} \omega_{i,j} \cdot log(1+A_j(I))}{log2}\right) \\ \mathrm{SI}_{leftvsright}(s_i, I) = f_+\left(\frac{max_{ipsilateral_{s_i}}(A_j(I)) - max_{contralateral(s_i}(A_j(I))}{max_{ipsilateral_{s_i}}(A_j(I)) + max_{contralateral(s_i}(A_j(I))}\right) \\ \mathrm{f}_+ = \begin{cases} \mathrm{x \text{ if } x > 0} \\ \mathrm{0 \text{ if } x \leq 0} \end{cases} \end{cases} \tag{5.4}$$

where $A_j(I)$ represents the normalized activity of the muscle *j* in response to EES delivered at the amplitude *I*. $\omega_{i,j}$ is a weight associated with the muscle *j* for the targeted muscle group g_i and is summarized in the table below. For each targeted muscle group, weights of agonists (respectively antagonists) are positive (respectively negative), and the sum of weights over agonists (respectively antagonists) is equal to 1 (respectively -1). These weights were chosen empirically to capture the respective contributions of each muscle in the targeted muscle group. We then chose the maximum selectivity index for each targeted muscle group among all selectivity indices computed for each electrode in a given position of the paddle lead. We then calculated the average of these selectivity indices for each targeted muscle group at each location of the paddle lead, while penalizing the performance when a targeted muscle group was theoretically not reachable:$SI_{average} = \frac{1}{4}\sum_i SI_i$ Where $SI_i = \begin{matrix} SI_{functionality} \; of \; functionality \; i \\ 0.5 \times SI_{functionality} \; of \; functionality \; i \end{matrix}$ and $i \in lefthipflexion, righthipflexion, leftankleextension, rightankleextension.$

Patient P1	Iliopsoas	Rectus Femoris/ Vastus Lateralis	Semi-Tendinosis	Tibialis Anterior	Gastrocnemius Medialis/ Soleus
L1	0	0	0	0	0
L2	1	0	0	0	0
L3	0	1	0.07	0	0
L4	0	0	0.23	0	0
L5	0	0	0.4	1	0
S1	0	0	0.3	0	0.5
S2	0	0	0	0	0.5

Patient P2	Iliopsoas	Rectus Femoris/ Vastus Lateralis	Semi-tendinosis	Tibialis Anterior	Gastrocnemius Medialis/ Soleus
L1	0.7	0.1	0	0	0
L2	0.3	0.6	0	0	0
L3	0	0.3	0.07	0	0
L4	0	0	0.23	0.4	0
L5	0	0	0.4	0.5	0.4
S1	0	0	0.3	0.1	0.5
S2	0	0	0	0	0.1

Patient P3	Iliopsoas	Rectus Femoris/ Vastus Lateralis	Semi-tendinosis	Tibialis Anterior	Gastrocnemius Medialis/ Soleus
L1	0.5	0	0	0	0
L2	0.5	0	0	0	0
L3	0	1	0	0	0
L4	0	0	0	0	0.5
L5	0	0	1	0	0.5
S1	0	0	0	1	0
S2	0	0	0	0	0

Table 5.3: Normalized patient-specific projectome as obtained from fMRI.

Literature	Iliopsoas	Rectus Femoris/ Vastus Lateralis	Semi-Tendinosus	Tibialis Anterior	Gastrocnemius Medialis/ Soleus
L1	0.45	0.12	0	0	0
L2	0.3	0.27	0	0	0
L3	0.17	0.37	0.07	0.04	0.01
L4	0.06	0.24	0.23	0.34	0.08
L5	0.01	0	0.4	0.43	0.17
S1	0.01	0	0.3	0.19	0.38
S2	0	0	0	0	0.36

Table 5.4: Myotome of average population. Taken from (Wagner et al., 2018).

	Iliopsoas	Rectus Femoris/ Vastus Lateralis	Semi-Tendinosus	Tibialis Anterior	Gastrocnemius Medialis/ Soleus
Hip flexion (L1)	0.8	0.2	-1	-	-
Ankle extension (S1)	-	-	-	-1	1

Table 5.5: Weights of agonist and antagonist muscle groups in the legs for the calculation of selectivity indices for preoperative treatment planning.

5.5.8 Atlas of computational spinal cord models

Using our computational pipeline, we generated a freely available atlas of 15 personalized computational models from healthy volunteers. These models provided an instrumental resource to analyze the influence of electrode arrangements on the relative recruitment of dorsal roots. We also generated personalized computational models of our study participants. These models enabled precise preoperative planning that guided the neurosurgical procedure. In order to easily inspect the anatomy of the spinal cord, the distribution of electric fields within the anatomy, and the consequent neural activity following a common pulse of epidural electrical stimulation we provide access to an online resource on https://osparc.io/. For access, please contact the author of this thesis directly.

5.5.9 Neurosurgical intervention

Laminectomy and paddle lead insertion
A intraoperative tridimensional CT scan was performed to map the predicted optimal position of the paddle lead to the anatomy of each participant, and thus guide the insertion of the lead at this position. An approximately 5 cm midline skin incision was performed, the fascia opened and the muscles retracted bilaterally. Excision of the midline ligamentous structures and laminectomy between L1 and L2 spinal segments enabled the insertion of the paddle array that was placed over the midline of the exposed dura and advanced rostrally to the target location.

Electrophysiological monitoring
Electrophysiological recordings were conducted using the NIM Eclipse monitoring and stimulation system (Medtronic Xomed Inc, Jacksonville, FL, USA). Single-pulses of EES (0.5 Hz) were delivered at increasing amplitude to elicit muscle responses that were recorded from subdermal (Neuroline Twisted Pair Subdermal, 12 x 0.4 mm, Ambu A/S, Ballerup, Denmark) or intramuscular needle electrodes (Ultra Sharp, 44 mm/27 g, Chalgren Enterprises, Inc. Gilroy, CA, USA).

Intraoperative comparison of the paddle leads
During the surgical intervention, the Specify 5-6-5 paddle lead (Specify 5-6-5, Medtronic Inc, Minneapolis, MN, USA) was inserted before the new paddle lead. Electrophysiological monitoring of muscle responses guided the placement to an optimal position to recruit the iliopsoas muscle (L1 dorsal root). Recordings were obtained at 3 different positions apart from 2 mm, centered around the optimal position. Then, the new paddle lead (Onward medical) was inserted through the same opening. The same procedure was then repeated. Since the new paddle lead displayed superior selectivity compared to the Specify 5-6-5, the new paddle lead was implanted chronically.

Pulse generator implantation.

An Implantable Pulse Generator (IPG) (Medtronic Activa^{TM} RC, Medtronic Inc, Minneapolis, MN, USA) commonly used for Deep-Brain Stimulation therapies was inserted into a subcutaneous pocket in the participant's abdomen. The paddle array cables were then tunneled between both openings and connected to the implantable pulse generator.

5.5.10 Configuration of activity-specific stimulation programs

After approximately ten days of rest following the surgery, participants started a one-month period during which we configured activity-specific stimulation programs to support the performance of motor activities involving leg and trunk musculatures.

Electrode configurations
We delivered EES with electrode configurations targeting the dorsal roots projecting to the spinal cord regions containing the motoneuron pools associated with the intended movement-These spinal cord regions were derived from the projectome of proprioceptive neurons innervating the homonymous motoneurons, as identified with fMRI recordings. The cathodes were selected based on intraoperative recordings at the final position of the paddle lead. Additional anode configurations completed the cathodes to increase the selectivity when necessary. The procedure to elaborate the library of anodes and cathodes is described in Fig. 5.13. EES pulse width was fixed at 300µs. The amplitude and frequencies of EES were optimized for each electrode configuration, as described in Fig. 5.14.

Spatiotemporal stimulation sequences to support walking
Sequences of EES pulses to support walking were derived from the spatiotemporal maps of motoneuron activation reconstructed from muscle activity of healthy individuals during walking (Wagner et al., 2018). These spatiotemporal maps revealed that walking involves the successive activation of three hotpots restricted to specific spinal cord regions. We thus created a template of spatiotemporal stimulation sequences that aim to reproduce the spatiotemporal activation pattern of these hotspots during walking in healthy individuals. For each targeted hotspot, we selected an appropriate anode/cathode configuration from the library and updated the template with these configurations. The parameters (frequency, amplitude), onset and duration of each train of EES was optimized during walking on treadmill and overground and by inspecting the synchronicity of the muscular activity and kinematics with EES trains, and by integrating the feedback from the physical therapist and participant, as detailed in Fig. 5.14.

Spatiotemporal stimulation sequences to support other motor activities
We then configured activity-specific stimulation programs to support other motor activities such as standing, cycling, sit-to-stand, leg press and swimming. For this purpose, we exploited the same framework as for elaborating the stimulation template for walking. We thus conceived spatiotemporal sequences that reproduce the natural activation of motor hotpots / muscle groups during each motor activity. We also developed EES program that targeted the

motoneurons innervating the trunk and abdominal musculatures to facilitate trunk postures and the execution of trunk exercises. This procedure is described in Fig. 5.16.

5.5.11 Clinical evaluations

International Standards for Neurological Classification of Spinal Cord Injury (ISNCSCI)
Participant's neurological status was assessed based on the ISNCSCI, a comprehensive clinician-administered neurological examination of residual sensory and motor function quantifying SCI severity (Kirshblum & Waring, 2014).

Six-minute walk test
Endurance was assessed by the distance covered overground within 6 minutes with a standard 4-wheel walker and spatiotemporal EES turned on. This test was performed at the beginning and at the end of the 5-months of rehabilitation.

Quantification of muscle mass
Muscle mass was quantified from non-contrast CT images obtained with a 64-detector row CT scanner (Discovery CT750 HD, GE Healthcare) at the abdominal (L3 vertebra) and mid-thigh (25 cm cranial to the tibiofemoral joint space) levels, acquired prior to surgery and after the period of 5-month of rehabilitation. Muscle segmentations were performed semi-automatedly in ImageJ by applying specific CT number thresholds (in Hounsfield unit, HU) for the identification of muscle (from -29 to +150 HU) and adipose (from -190 to -30 HU) tissues (Gomez-Perez et al., 2016). Muscle mass and skeletal muscle area are reported in cm^2 for specific abdominal and thigh muscles or muscle compartments.

Rehabilitation program
Participants followed a rehabilitation program four to five times per week for five months. The rehabilitation program was personalized to participants' performance. This period of rehabilitation comprised walking on a treadmill and overground with multiple assistive devices, sit-to-stand, standing, leg and trunk muscle exercises, swimming and cycling. Activity-specific stimulation programs were delivered to enable the practice of these activities.

5.5.12 Technological framework

Rehabilitation and movement analysis environment
When necessary, a tailored amount of body weight support was provided to the participants using an overhead support system based on cable robot technology (Rysen, Motek Medical BV). This robotic system allows the application of tailored forces to the trunk through a dedicated harness along the vertical and anteroposterior directions.
Electromyographic activity of selected muscles was acquired at a 2kHz sample rate using the 16-channel wireless Delsys system, with bipolar surface electrodes placed over the following muscles of the lower limbs (Iliopsoas (Il), Rectus Femoris (RF), Adductors (Add), Vastus Lat-

eralis (VLat), SemiTendinosus (ST), Tibialis Anterior (TA), Medial Gastrocnemius (MG), and Soleus (Sol)) and/or trunk muscles (Abdominal Muscles (Abs), Quadratus Lomborum (QL) and Obliques (Obl)). Kinematic recordings were obtained at a 100-Hz sampling rate using a 3D motion capture system (Vicon Motion Systems, Oxford, UK), consisting of 14 infrared cameras that covered a 12 x 4 x 2.5 m workspace. Body kinematics were captured by these infrared cameras through the use of infrared-reflective markers positioned over standardized anatomical landmarks. We also captured chronophotographic images of participants using a high-definition camera (FUJIFILM X-T2, 5 images/s, ISO 6400, shutter speed 1/250 sec). Successive snapshots were overlaid offline to illustrate the dynamic of movements.

Neurostimulation system

EES was delivered with an implantable pulse generator (IPG, Medtronic Activa$^{\text{TM}}$ RC) that enabled monopolar and multipolar stimulation at constant current or constant voltage through one or a subset of the 16 electrodes of the paddle lead or the case of the IPG (anode). The IPG was modified from its clinical version with an investigational firmware that enabled real-time communication with a software running on an external computer (NEUWalk Research Programmer Application or NRPA, Model 09103, Medtronic). The NRPA acted as a relay between EES triggering commands sent by the control software called G-Drive Plus (described below) and the IPG. The NRPA communicated wirelessly with the IPG through the following communication chain: the NRPA sent commands via a virtual COM port corresponding to a Bluetooth adapter, a custom wireless bridge consisting of a nano computer (Raspberry Pi) received this command and forwarded it to a virtual COM port 6 corresponding to a USB adapter, a USB to infrared adapter (ACT-IR224UN-LN115-LE, ACTiSYS Corporation, Fremont, CA, USA) transformed this command into infrared signals that were then read by a modified Medtronic patient's programmer (Sensing Programmer Telemetry Module SPTM, Medtronic), which finally transmitted the command to the patient's IPG by electromagnetic induction through the skin (Fig. 5.10).

Software App for configuration, optimization and evaluation of neurostimulation

A custom software App was built to configure, optimize and evaluate the effects of EES. The C# App runs on a desktop computer, laptop or tablet and interfaces with the stimulation system (through the NRPA application) and sensor systems for data acquisition and closed-loop stimulation. The App includes a user-friendly stimulation scheduler that enables the rapid personalization of spatiotemporal stimulation sequences from preprogrammed templates. The user can choose to loop a sequence automatically, to switch between different motor activities with one click, or to link stimulation sequences to specific events detected by the sensors. These events can be triggered by detecting movement-specific changes detected through inertial measurement units (NGIMU, x-io Technologies Limited) placed on the participant's body or by clicking on custom-built ergonomic buttons mounted on an assistive device. The App provides real-time visualization (SciChart WPF library, SciChart Ltd) of the muscular activity and leg kinematics based on wireless sensors that measures the electromyographic activity and inertial measurement units placed on the participant's body (Delsys Trigno system, Delsys Incorporated). The App also triggers acquisition from video cameras. The muscular and kinematic data are synchronized with the stimulation sequences and color-coded with respect to the targeted motor hotspots. This color-coded visualization allows the immediate assessment of the effects of the stimulation on muscle activity and whole-body kinematics. All the acquired data, including the information about EES stimulation patterns, are saved for offline analysis.

The App provides graphical interfaces tailored to the needs of the different user types, i.e. stimulation experts, physical therapists and study participants. Concretly, the same App can be used by stimulation experts on a multi-screen desktop system to configure and optimize stimulation parameters, by therapists to select and modulate rehabilitation exercises on a handheld tablet, or by study participants to start and stop activity-dependent stimulation programs to support activities of daily living through a smartwatch.

5.5.13 Data processing

Analysis of intraoperative muscle activity

Intraoperative recordings of muscle activity were band-pass filtered between 10 and 450 Hz (4th -order Butterworth filter). The peak-to-peak amplitudes of the monosynaptic components of muscle responses were extracted and normalized with respect to the maximal value obtained during the recordings.

Lower limb selectivity index

To quantify the performance of the paddle leads to target specific dorsal roots, we computed a selectivity index $SI_{experimental}\left(g_i\ I\right)$ for each targeted muscle group g_i and EES amplitude This selectivity index contains two terms, one indicating the selectivity on the targeted side, and one indicating the mediolateral selectivity for the targeted side s_i:

$$SI_{experimental}(g_i, I) = SI_{targetedmuscles}(g_i, I) \cdot SI_{leftvsright}(s_i, I)$$

$$\begin{cases} \mathrm{SI}_{targetedmuscles}(g_i, I) = f_+\left(\frac{\sum_{musclesing_i} \omega_{i,j} \cdot log(1+A_j(I))}{log2}\right) \\ \mathrm{SI}_{leftvsright}(s_i, I) = f_+\left(\frac{max_{ipsilateral_{s_i}}(A_j(I)) - max_{contralateral(s_i}(A_j(I))}{max_{ipsilateral_{s_i}}(A_j(I)) + max_{contralateral(s_i}(A_j(I))}\right) \\ \mathrm{f}_+ = \begin{cases} \mathrm{x\ if\ x} > 0 \\ 0 \mathrm{\ if\ x} \leq 0 \end{cases} \end{cases} \tag{5.5}$$

where $A_j(I)$ represents the normalized muscle response when delivering a single pulse of EES at the amplitude I. $\omega_{i,j}$ is a weight associated with the muscle j for the targeted muscle group g_i. For each targeted muscle group, weights of agonists (respectively antagonists) are positive (respectively negative), and the sum of weights over agonists (respectively antagonists) is equal to 1 (respectively -1). These weights were chosen to capture the respective contributions of

	Ilio-psoas	Rectus Femoris	Vastus Lateralis	Semi-Tendinosus	Tibialis Anterior	Gastrocnemius Medialis	Soleus
Hip flexion (L1)	0.8	0.2	-	-1	-	-	-
Ankle extension (S1)	-	-	-	-	-1	0.2	0.8
Weight Acceptance	-0.3	0.2	0.8-	-0.5			-0.2
Whole Leg Flexion	0.4	-	-0.45		0.6	-0.1	-0.45
Propulsion	-0.5			0.5	-0.5	0.1	0.4

Table 5.6: Weights of agonist and antagonist muscle groups in the legs for the calculation of selectivity indices from EMG data.

each muscle in the targeted hotspot:

We then chose the maximum selectivity index for each targeted dorsal root among all selectivity indices computed for each tested electrode at a given position of the paddle lead. We then calculated the average of these selectivity indices for targeted dorsal root at each lead location:

$$SI_{average} = \frac{1}{4}\sum_i SI_i$$

Where $SI_i = \begin{array}{l} SI_{functionality}\ of\ functionality\ i \\ 0.5 \times SI_{functionality}\ of\ functionality\ i \end{array}$
and $i \in lefthipflexion, righthipflexion, leftankleextension, rightankleextension.$

Analysis of lower limb muscle activity
The electromyographic activity from lower limb muscles was processed according to the SENIAM (Surface Electromyography for the Non-Invasive Assessment of Muscles) standards for electromyographic recordings. All displayed electromyographic activities during walking were band-pass filtered between 10 and 450 Hz (4th -order Butterworth filter). A moving average of the rectified electromyographic signal within a centered 250-ms time window was used to generate normalized electromyographic envelopes for quantification.

Recruitment of trunk and abdominal muscles during single-pulse EES
Electromyographic signals from trunk abdominal muscles were band-passed filtered between 10 and 450 Hz (4th -order Butterworth filter. EES onset was determined using semi-automatic methods based on recordings of stimulation artefacts. The temporal window of muscle responses was defined within a 40 or 50 ms starting 10 ms after EES onset, depending on the muscle. For each amplitude of EES, muscle responses were quantified as the peak-to-peak amplitude. These values were translated into recruitment curves that we displayed in circular

plots. In these circular plots, muscles are distributed at different angular positions. The radial axis corresponds to EES amplitude (Fig. 5.15). A color shading reports the normalized amplitude of muscle activity. The black circle highlights the EES amplitude that corresponds to the highest selectivity index. The polygon describes the muscle selectivity at the optimal EES amplitude: the edges of the polygon represent the normalized muscle activity on the radial axis for a particular muscle, scaled so that the polygon fills the circle.

Trunk selectivity index

To quantify the relative selectivity of trunk recruitment compared to the recruitment of lower limb muscles, the lower-limb selectivity index was adapted with the following weights:

	Upper Abdominals	Obliques	Quadratus Lomborum	Iliopsoas	Adductors	Rectus Femoris
Trunk	0.33	0.33	0.33	-0.33	-0.33	-0.33

Table 5.7: Weights of agonist and antagonist muscle groups of the trunk muscles for the calculation of selectivity indices from EMG data.

Analysis of trunk kinematics

Reflective markers were secured to the spine at T10 and L5, and on both knees to record trunk and leg kinematics. The responses were analyzed over the window of 500ms that followed the onset of the stimulation. Kinematic data was low-pass filtered (4th-order Butterworth filter) with a cut-off at 10Hz.

Analysis of trunk posture and kinematics during exercises

Trunk exercises were recorded with a FujiFilm XT-2 camera. Video-based kinematic analysis of the lumbar curvature was performed through a semi-automated detection of the body segments and by an expert visually fitting circles to calculate the lumbar curvature.

5.5.14 Statistics

All quantifications show the mean and all individual data. Comparisons between two conditions were performed using a two-tailed Student's t-test, when normality was confirmed or a non-parametric Mann-Whitney rank sum test otherwise. Comparisons involving more than two categories were performed using a 1-way ANOVA, followed by the post-hoc Tukey's Honest Significance Difference tests. *, **, *** indicate a p-value smaller than 0.05, 0.01, 0.001 respectively.

6 Application of personalizable computational models for the restoration of other neurological functions and development of novel neuromodulation paradigms

In chapters 2 and 3, I described a computational approach to study the interactions between EES and proprioceptive and cutaneous feedback circuits in the lumbosacral spinal cord. I outlined how these mechanistic insights motivated stimulation strategies to recover locomotion after SCI. Thereafter, I explained in chapters 4 and 5, a technological framework to enable activity-based therapies in individuals with SCI that leverages these stimulation strategies. For this purpose, I developed a computational framework that enables the rapid generation of highly realistic, personalizable, hybrid computational models for implant design and preoperative treatment planning. The insights and innovations, that were a direct result of the work described in the previous chapters, ultimately culminated in enabling various motor functions, including locomotion, in three individuals with incomplete SCI and three individuals with complete SCI.

These results inspired me to test, whether the computational approach I described in the previous chapters, could be useful when translated to the treatment of other neurological impairments, the development of novel neuromodulation paradigms or aid in the design of spinal cord implants for translational research. In this chapter, I describe three use-cases I was fortunate enough to be able to contribute to.

I contributed to a work that aimed to control hemodynamic instability after SCI. In this context, I leveraged a combination of hybrid computational modeling and circuit-level modeling to suggest that EES has the capacity to control hemodynamics by recruiting large-diameter, myelinated afferent fibers in the low-thoracic spinal cord of rats. Moreover, I was able to suggest electrode configurations to target these hemodynamic hotspots in an individual presenting orthostatic hypotension due to a chronic, clinically complete, cervical SCI that was implanted with a paddle electrode array. Indeed, these stimulation parameters induced robust pressor responses in this individual.

Thus far, I have described my development of volume conductor models that accurately depict the anatomy of rats and humans. Here, I also report my development of volume conductor models of mice and Non-Human Primates (NHPs). The former I leveraged within a work, that aimed to develop a novel optoelectronic system with the purpose to enable precise manipulation of targeted neurons and pathways across the spinal cord in mice. For this purpose, I evaluated safety and efficacy of this device by performing heat diffusion and light propagation simulations in the mouse spinal cord model. First, I wanted to evaluate, where a Light-Emitting Diode (LED) needed to be placed mediolaterally over the spinal cord to enable efficient photostimulation of afferent fibers and spinal interneurons. My results suggest that positioning a LED above each dorsal horn yields deeper light penetration than a single LED positioned above the midline of the spinal cord. Second, I proposed that red light can efficiently penetrate the entire dorsoventral spinal cord, while blue light fails to do so, within the range of tested power densities. Third, I estimated the heat diffusion in the spinal cord within the range of tested power densities. My results indicate that there are serious constraints on the useage of red light with this optoelectronic system due to overheating of the spinal tissues.

I have also leveraged my mouse volume conductor model to provide estimates of suitable dimensions for the optoelectronic dimension to comfortably fit within the epidural space of the mouse spinal cord. Furthermore, similar to this approach, I leveraged my NHP model to provide estimations on spinal cord dimensions for implants that are to be utilized in translational research. The dimensions given in this thesis may hopefully inform the design of spinal implants for future research.

Related publication and personal contributions

The content of this chapter is adapted - with permission of the co-authors - from the following manuscripts:
Jordan W. Squair, Matthieu Gautier[†], Lois Mahe[†], Jan Elaine Soriano[†], **Andreas Rowald**[†], Arnaud Bichat, Newton Cho, Mark A. Anderson, Nicholas D. James, Jerome Gandar, Anthony V. Incognito, Giuseppe Schiavone, Zoe K. Sarafis, Achilleas Laskaratos, Kay Bartholdi, Robin Demesmaeker, Salif Komi, Charlotte Moerman, Bita Vaseghi, Berkeley Scott, Ryan Rosentreter, Claudia Kathe, Jimmy Ravier, Laura McCracken, Xiaoyang Kang, Nicolas Vachicouras, Florian Fallegger, Ileana Jelescu, YunLong Cheng, Qin Li, Rik Buschman, Nicolas Buse, Tim Denison, Sean Dukelow, Rebecca Charbonneau, Ian Rigby, Steven K. Boyd, Philip J. Millar, Eduardo Martin Moraud, Marco Capogrosso, Fabien B. Wagner, Quentin Barraud, Erwan Bezard, Stéphanie P. Lacour, Jocelyne Bloch, Grégoire Courtine[‡] & Aaron A. Phillips[‡], "**Neuroprosthetic baroreflex controls hemodynamics after spinal cord injury**", **Nature** (2021).
[†], [‡] contributed equally to this work

Personal contributions: Designed and developed the computational model, performed computer simulations, designed experiments in rats, data analysis, figures preparation.

Claudia Kathe[*], Frédéric Michoud[*], Philipp Schönle[*], **Andreas Rowald**, Noé Brun, Jimmy Ravier, Ivan Furfaro, Valentina Paggi, Kyungjin Kim, Sadaf Soloukey, Leonie Asboth, Thomas H. Hutson, Ileana Jelescu, Antoine Philippides, Noaf Alwahab, Jérôme Gandar, Daniel Huber, Chris I. De Zeeuw, Quentin Barraud, Qiuting Huang, Stéphanie P. Lacour[‡] & Grégoire Courtine[‡], "**Wireless closed-loop optogenetics across the entire dorsoventral spinal cord in ecological environments**", **Nature Biotechnology** (Accepted).
[*], [‡] contributed equally to this work

Personal contributions: Designed and developed the computational model, performed computer simulations, acquired high-resolution MRI/CT datasets, figures preparation.

Giuseppe Schiavone, Florian Fallegger, Xiaoyang Kang, Beatrice Barra, Nicolas Vachicouras, Evgenia Roussinova, Ivan Furfaro, Sébastien Jiguet, Ismael Seáñez, Simon Borgognon, **Andreas Rowald**, Qin Li, Chuan Qin, Erwan Bézard, Jocelyne Bloch, Grégoire Courtine[‡], Marco Capogrosso[‡] & Stéphanie P. Lacour, "**Soft, Implantable Bioelectronic Interfaces for Translational Research**", **Advanced Materials** (2020).
[‡] contributed equally to this work

Personal contributions: Designed and developed the computational model, figures preparation.

6.1 Hemodynamics can be controlled with EES in preclinical animal models and humans after SCI

Spinal Cord Injury (SCI) induces hemodynamic instability that threatens survival (Inoue et al., 2014; Readdy et al., 2015; Squair et al., 2016), impairs neurological recovery (Squair et al., 2019; Squair et al., 2017), increases the risk of cardiovascular disease (Cragg et al., 2013; Wu et al., 2012), and reduces quality of life (Carlozzi et al., 2013; Illman et al., 2000). Hemodynamic instability in this context is due to the interruption of supraspinal efferent commands to sympathetic circuits located in the spinal cord (Furlan et al., 2003). This prevents the natural baroreflex from controlling these circuits to adjust peripheral vascular resistance. Clinical studies in individuals with SCI suggested that Epidural Electrical Stimulation (EES) applied over lumbosacral segments can also transiently increase blood pressure (Darrow et al., 2019; S. J. Harkema, Ditterline, et al., 2018; S. J. Harkema, Wang, et al., 2018; West et al., 2018). However, lumbosacral segments contain few sympathetic efferent neurons, casting doubt that this approach harnesses the full potential of EES to activate sympathetic circuits and achieve hemodynamic stability after SCI.

In the associated publication, **Neuroprosthetic baroreflex controls hemodynamics after spinal cord injury** (Squair et al., 2021), we investigated the topology and dynamics of the sympathetic circuits enganged by EES in a preclinical model. We developed a stimulation protocol to regulate hemodynamics in closed-loop and tested this stimulation strategy in rodents, non-human primates and humans after both acute and chronic SCI. We demonstrated that hemodynamics can be controlled for extended periods of time in all tested models.

Here, I highlight how I leveraged computational modeling to contribute to the understanding of hemodynamic control with EES and the identification of efficient and robust EES strategies. Unlike previous chapters, I only briefly discuss technological innovations and experimental results, as the purpose of this chapter is only to highlight the translational aspect of my computational approach from enabling locomotion to the control of hemodynamics.

6.1.1 EES engages sympathetic circuitry in low thoracic segments to control hemodynamics

We demonstrated that the change of blood pressure in response to EES follows a Gaussian distribution along the T6 to L1 spinal segments that peaks around the low thoracic segments in rodent models (Squair et al., 2021). These pressor responses linearly correlate with the anatomical distribution of sympathetic pre-ganglionic neurons in the spinal cord, suggesting that the recruitment of T11-T13 sympathetic pre-ganglionic neurons cause blood pressure increases with EES (Squair et al., 2021).

To investigate which neural substrate triggers the pressor response when recruited by EES, I utilized the computational models of a rat spinal cord described in chapter 2. I replicated the experimental setup in rodent models by placing cathodes at the dorsal root entry zone of the T11-T13 segments (Fig. 6.1a), simulating the electric field in response to EES (Fig. 6.1c) and calculating the resulting recruitment profile (Fig. 6.1b). The simulation results suggested that EES primarily recruits large-diameter, myelinated afferent fibers located in the dorsal roots (Fig. 6.1b). We validated this hypothesis by progressively ablating these spinal roots in an experimental rat model (Squair et al., 2021). Interestingly, this result is in line with the estimated recruitment pattern of EES in the lumbosacral spinal cord of rats (Capogrosso et al., 2013) (see chapter 2 and chapter 3).

Previous clinical studies reported pressor responses when stimulating rostral lumbar segments (Darrow et al., 2019; S. J. Harkema, Ditterline, et al., 2018; S. J. Harkema, Wang, et al., 2018; West et al., 2018), which contrasts with our finding that pressor responses elicited by EES require the recruitment of the dorsal roots projecting to the caudal thoracic segments (Fig. 6.1b). Close examination of the trajectory of spinal roots in my volume conductor model revealed that the L2 segment can be found at the T12 vertebrae. At the position of the inter-vertebral foramen of the T12 vertebrae, the T12 dorsal root bends significantly to exit the vertebral canal. Previous computational investigations described that the activity of the axon depends on the second space derivative of the extracellular medium in response to an electrical stimulus (Rattay, 1986). I therefore reasoned, that the T12 dorsal root may be recruited at the L2 segment due to its bending at the inter-vertebral foramen and that this may be a contributing factor towards the pressor responses reported in previous clinical studies (Darrow et al., 2019; S. J. Harkema, Ditterline, et al., 2018; S. J. Harkema, Wang, et al., 2018; West et al., 2018). However, it is also well established that the recruitment order of the spinal roots is highly related to the cathode level (Rattay et al., 2000). Hence, I proposed that mediolateral shifts in cathode positioning at the L2 segment may recruit large-diameter, myelinated afferent fibers in the caudal thoracic dorsal roots, where they bend and pass through the inter-vertebral foramen. In order to investigate this hypothesis, I placed an electrode at the midline of the spinal cord and gradually shifted its position laterally towards the inter-vertebral foramen. The resulting recruitment profile suggests that a cathode positioned over the midline of the spinal cord recruits a significant amount of large-diameter, myelinated afferent fibers in the L2 dorsal root prior to recruiting any afferents in the T12 dorsal root (Fig. 6.1f). However, shifting the cathode position towards the inter-vertebral foramen, closes the distance between the recruitment profiles of the T12 and L2 dorsal root (Fig. 6.1f). Indeed, at the lateral edge of the epidural space, afferents of the T12 dorsal root are recruited prior to afferents of the L2 dorsal root (Fig. 6.1f). We validated these results by ablating the T12 dorsal root in experimental rat models (Fig. 6.1f). In fact, this procedure significantly blunted the pressor response elicited by EES applied at L2 spinal segment (Fig. 6.1f). This suggests, that the recruitment of afferents in the T12 dorsal root play at least a partial role in the induction of pressor responses when stimulating rostral lumbar segments.

These and other experimental results suggest that EES activates splanchnic sympathetic neurons through the depolarization of afferent fibers in the dorsal roots (Squair et al., 2021). However, the exact connectivity between large-diameter, myelinated afferent fibers and splanchnic sympathetic neurons are unknown. Labelling afferent projections revealed an absence of afferent axons and synapses within the intermediolateral column that contains the vast majority of sympathetic pre-ganglionic neurons (Squair et al., 2021; Strack et al., 1988). Immunolabelling and pseudorabies-mediated tracing experiments suggested the existence of either direct excitatory, direct inhibitory or indirect excitatory connections between afferent fibers and sympathetic pre-ganglionic neurons (Squair et al., 2021). To reject a subset of the functional necessity of these connectivities, I built a network model with direct and indirect excitatory and indirect inhibitory connections to sympathetic pre-ganglionic neurons (Fig. 6.1e). These simulations suggest that indirect inhibitory connections are superfluous to elicit activity in sympathetic pre-ganglionic neurons in the absence of other network connections (Fig. 6.1e). It is important to note, however, that this circuit model is extremely limited as it does not take into account higher order mechanisms, such as complex network architectures. For this reason, I encourage more detailed exploration of circuit-level interactions in future works.

6.1.2 Enabling clinical implementation with personalized computational models of the low thoracic spinal cord

We finally aimed to validate the key features of the neuroprosthetic baroreflex in an individual presenting with a chronic, clinically complete (American Spinal Injury Association Impairment Scale A) cervical SCI that led to debilitating, medically refractory orthostatic hypotension (Squair et al., 2021). This individual was previously implanted with a commercially-available electrode lead below the T10 and T11 vertebral bodies (Squair et al., 2021). My aim was to confirm an electrode configuration that enabled the selective recruitment of the low thoracic spinal segments. I segmented out the position of the paddle lead relative to the vertebral bodies from post-operative CT-scans. I identified the paddle lead to be implanted between the T10 and T12 spinal segments. Hence, most electrode configurations would already target the low thoracic segments. Simulations suggested that the electrode configuration visualized in Fig. 6.1g, would yield a selective recruitment of the T11 dorsal root. As the T12 spinal segment has been found to raise blood pressure more than the T11 or T13 dorsal root in rodent models (Squair et al., 2021) and since rodents have one additional thoracic spinal segment when compared to humans, I reasoned that this electrode configuration should elicit a pronounced pressor response. Indeed, testing this configuration in the individual induced robust pressor responses (Fig. 6.1h). Here, it is important to note, that other stimulation paradigms can be imagined that could further increase the pressor response. However, within this thesis, my intention was solely to confirm that this electrode configuration would yield robust recruitment of the T11 dorsal root.

6.1.3 Outlook on personalized computational modeling for hemodynamic control with EES

EES can control hemodynamics after SCI (Darrow et al., 2019; S. J. Harkema, Ditterline, et al., 2018; S. J. Harkema, Wang, et al., 2018; Squair et al., 2021; West et al., 2018). Although the mechanisms underlying this phenomenon have been explored, they remain largely unknown (Squair et al., 2021). For this purpose, I highlight here key features in the computational modeling that limit the understanding of circuit-level interactions that can explain hemodynamic control with EES.

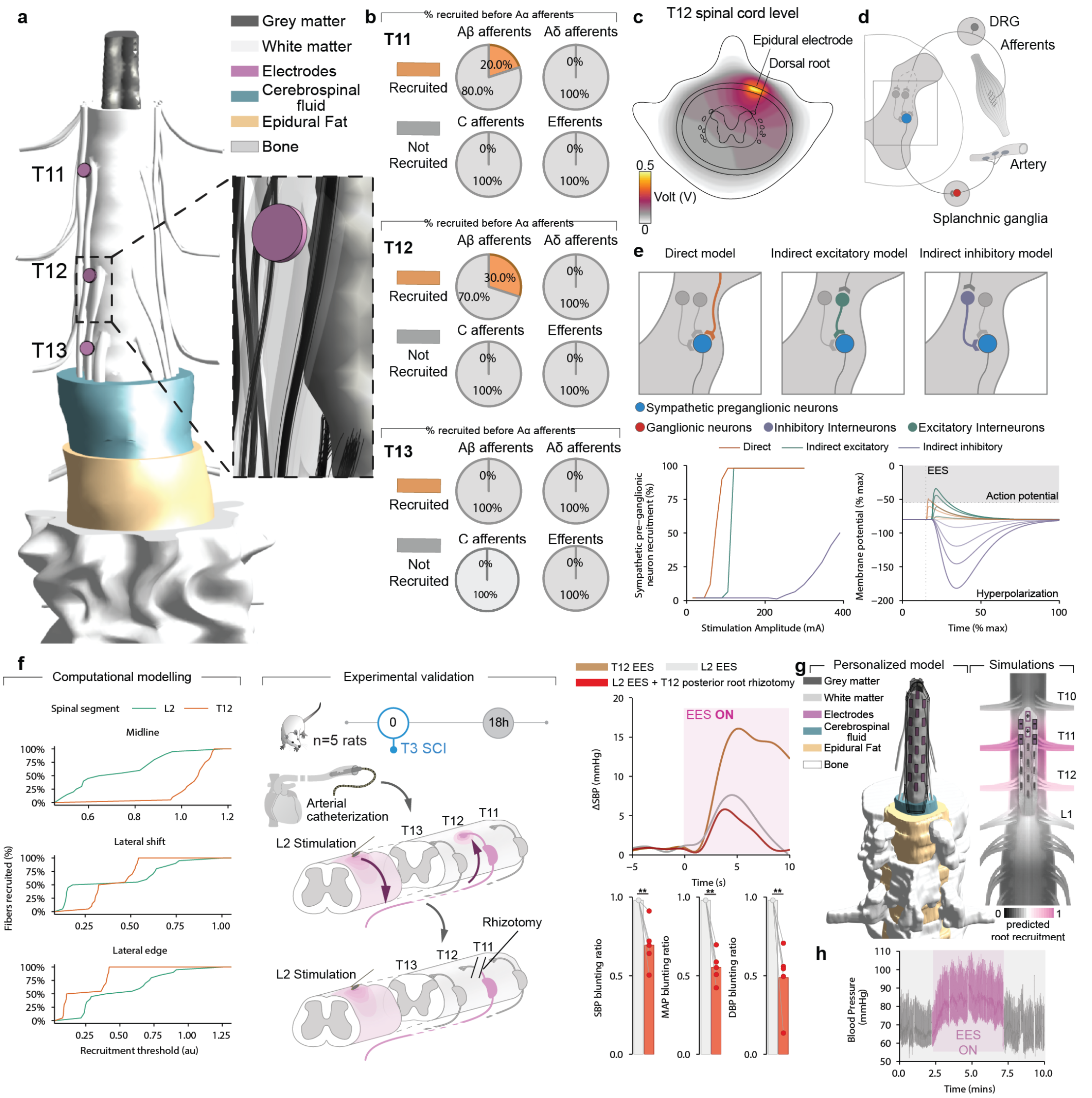

Figure 6.1: Overview of computational models developed for hemodynamic control with EES. a. Hybrid computational model of low thoracic and lumbar rat spinal cord. b. Recruitment profiles from cathodic stimuli applied over electrodes mapped out in a. c. Sketch of the electric field as a result of a FEM approach in model a. c. Hypothesized circuitries underlying hemodynamic control with the recruitment of large-diameter, myelinated afferent fibers. e. Results of circuit-level modeling of proposed circuitries in d. f. Recruitment profile of simulation and experimental validation of mediolateral shifts in cathodic origin of stimulation applied at L2 segment. g. Personalized hybrid compuational model of an individual with SCI to confirm stimulation strategy in-silico. h. Blood pressure change in-vivo in response to stimulation outlined in g.

Firstly, in the associated publication we demonstrated experimentally, that EES applied over the low-thoracic spinal cord yields pronounced blood pressor responses in preclinical models and humans with SCI. My computational efforts suggest that EES applied over the low-thoracic spinal cord primarily recruits large-diameter, myelinated afferent fibers (Fig. 6.1b). However, this does not necessarily indicate that this recruitment is the primary mechanism underlying hemodynamic control with EES. In fact, other circuit-level interactions can be imagined. For example, EES may also influence extracellular membrane potentials of other neural substrates at these segments. Moreover, it is unclear at this point how the recruitment of large-diameter, myelinated afferent fibers could result in increases of blood pressor. A first, but unfortunately still very limited step, towards understanding hemodynamic control with EES has been proposed in this chapter. I built a very rudimentary circuit-level model that received recruitment profiles from a hybrid computational model of EES applied over the low-thoracic spinal cord of rats. This circuit-level model only takes into account mono- and disynaptic connections that have been identified by immunolabelling and virus-tracing experiments carried out in the associated publication (Squair et al., 2021). Obviously, the results of this network model are as limited as the datasets that underlie its constructions. Indeed, further research into network connectivity is necessary to draw any conclusions on circuit-level interactions. Furthermore, the initiated cell populations have been assumed to not be affected by EES beyond its recruitment of afferent fibers. In order to characterize the effect of EES on these circuits, I recommend manipulating their extracellular membrane potential in line with the electric fields calculated by the hybrid computational model. Lastly, direct comparison between simulated and experimental results are difficult to draw in the absence of some kind of gauge between cell activity and blood pressor response. This limitation may be ameliorated by taking into account the biophysical response of EES on the vascular system in future research.

Another important question to be addressed is the optimal positioning of cathodes along the spinal cord to elicit pressor responses. Previous clinical studies suggested that EES applied at rostral lumbar segments can increase blood pressure (Darrow et al., 2019; S. J. Harkema, Ditterline, et al., 2018; S. J. Harkema, Wang, et al., 2018; West et al., 2018). In contrast, we report that EES elevates blood pressure when targeting the low-thoracic spinal segments (Squair et al., 2021). In order to rectify this mismatch between our work and previous results, I suggested that mediolateral shifts in cathode positioning might explain why blood pressure responses were observed when EES was applied to rostral lumbar segments. For this purpose, I performed computer simulations of varying mediolateral cathode positions across the L2 segment. The results suggest that EES at this spinal segment may recruit afferents of the T12 spinal root in rats, when the cathode was shifted laterally from the midline, to a significant degree. However, the underlying computational simulations are limited by missing MRI-data that accurately describe the trajectory of spinal roots outside the vertebral canal. In fact, I estimated the bending of the spinal roots beyond the point where they exit the vertebral canal to be minimal in order to minimize their recruitment beyond this points (Rattay, 1986). However, I approximated their curvature at the inter-vertebral foramen to be almost 90°. This might overestimate the recruitment of afferents in the T12 root (Rattay, 1986). Adjusting root trajectory in my hybrid computational model with supplementary MRI-data may enable future works to explore this effect further.

Hopefully, my work provides a good starting ground for future research in the mechanisms underlying hemodynamic control with EES. This future research might enable the definition of clinical protocols for hemodynamic control after SCI with EES. This would open the avenue for personalized computational modeling to futher improve the efficacy of EES paradigms for hemodynamic control. Currently, there is no commercially-available electrode lead to control hemodynamics after SCI. As such, a similar approach as described in chapter 5 may be taken to use an atlas of thoracic spinal cord models to design a neuromodulation device for this particular purpose. Similarly, the need to specifically target specific neural substrates in the spinal cord may necessitate treatment planning tools in the same fashion as described in chapter 5. I presented a first attempt for such a treatment planning tool in this chapter (see Fig. 6.1g). However, this approach was very rudimentary in nature. Indeed, I merely confirmed electrode configurations for hemodynamic control after a spinal cord stimulator has already been implanted. Instead, I encourage the use of pre-operative treatment optimization by leveraging personalized computational models.

6.1.4 Computational modeling methods for hemodynamic control

Hybrid computational model of the rat spinal cord

I previously described a model of EES of the lumbar and sacral regions of the rat spinal cord (see chapter 2). I extended this effort to create a hybrid computational model of the lower thoracic and upper lumbar segments of the rat spinal cord. For this purpose, I acquired high-resolution MRI datasets of the rat spinal cord and manually segmented the white matter, spinal roots, CerebroSpinal Fluid (CSF) and vertebral bone to create a realistic tridimensional reconstruction of the thoracic and lumbar spinal cord of a rat. I artificially filled the epidural space between the bone and CSF and assigned it as the material epidural fat. In addition, I used tracings of the grey matter of rats and scaled them to the size of the white matter to create this material. I then placed this model in a large saline conductor to represent the remaining body of the rat. I assigned the same conductivity values as described in chapter 2 to this model and calculated the electric fields elicited by electrical spinal cord stimulation using a finite element approach. The models were all implemented in Sim4Life v3.4 (ZMT Zürich MedTech AG) (Neufeld et al., 2013).

Furthermore, I combined these solutions with anatomically and biophysically realistic neural structures to derive the type of fibers and neurons activated by the stimulation (McIntyre & Grill, 2002; Sundt et al., 2015). I then coupled these activation maps with a purely hypothetical network model composed of integrate-and-fire neurons. Three network architectures were tested. The connection was mediated through either monosynaptic, disynaptic excitatory, or disynaptic inhibitory pathways. Electrophysiological parameters were recorded in-silico at all neuron populations.

Hybrid computational model of the human spinal cord

I repeated the same procedure as in ‘Hybrid computational model of the rat spinal cord’ with MRI and computed tomography datasets of a human patient implanted with the Specify 5-6-5 array.

6.2 Evaluation of safety and efficacy of a novel optoelectronic system to manipulate neural substrates in the spinal cord of mice

The common theme across all preceding chapters is that EES predominantly activates large-diameter, myelinated afferent fibers in the dorsal roots. I further optimized this selective recruitment pattern for enabling locomotion in preclinical models and individuals with SCI (see chapters 3, 4 and 5). However, this specific recruitment pattern makes EES undesirable for mechanistic studies of neuronal subtypes, sensory pathways and supraspinal projections during control of neurological functions compared to other neuromodulation therapies. In particular, optogenetics has opened up unprecedented possibilities for controlling targeted cells and pathways of the nervous system with high spatiotemporal precision (Deisseroth, 2010; Roy et al., 2016; Won et al., 2020). However, I am unaware of any optoelectronic system that can target neurons in the spinal cord at this date.

In the associated publication, **Wireless closed-loop optogenetics across the entire dorsoventral spinal cord in ecological environments**, we introduced a wireless system that enables ultrafast closed-loop manipulation of any targeted neurons and pathways across the entire dorsoventral spinal cord in untethered mice behaving freely within ecological environments. This system uses micro-Light-Emitting Diodes (LEDs), integrated within thin stretchable carriers capable to conform to the dura matter of the spinal cord. However, since the light rapidly scatters when penetrating spinal tissues, targeting deep intraspinal neurons with epidural light-emitting sources requires irradiances that are substantially higher than those required for photostimulation in the vicinity of targeted neurons or pathways. Such high irradiance leads to local heating of tissue due to light absorption, which may alter neuronal responses or damage tissues (Owen et al., 2019).

Here, I propose a hybrid computational model to assess the attenuation of photostimulation through spinal tissues while simultaneously evaluating heat diffusion of optoelectronic systems implanted in the epidural space of the lumbar spinal cord of mice. Similar to the last section, I only briefly discuss technological innovations and experimental results, as the purpose of this chapter is merely to highlight the translational aspect of my computational approach from the design of EES strategies to the development of novel neuromodulation paradigms.

6.2.1 A computational model of the mouse lumbar spine to provide estimates of suitable dimensions for spinal implants

Firstly, the dimensions of the optoelectronic implant needed to be conformed to the anatomical requirements of the lumbar spinal cord of mice. For this purpose, I acquired high-resolution Magnetic Resonance Imaging (MRI) and Computerized Tomography (CT) datasets to generate a tridimensional anatomical model of the mouse spinal cord and vertebral column

(Fig. 6.2a, b). I constructed a 3D model of the mouse spinal cord from these imaging datasets (Fig. 6.2c). This 3D model outlined the suitable length (18 mm), width (2.5 mm) and thickness (< 100 µm) of the implant to cover the rostrocaudal and mediolateral extents of the lumbar spinal cord and served as the basis of the Finite Element Method (FEM) model in the coming sections.

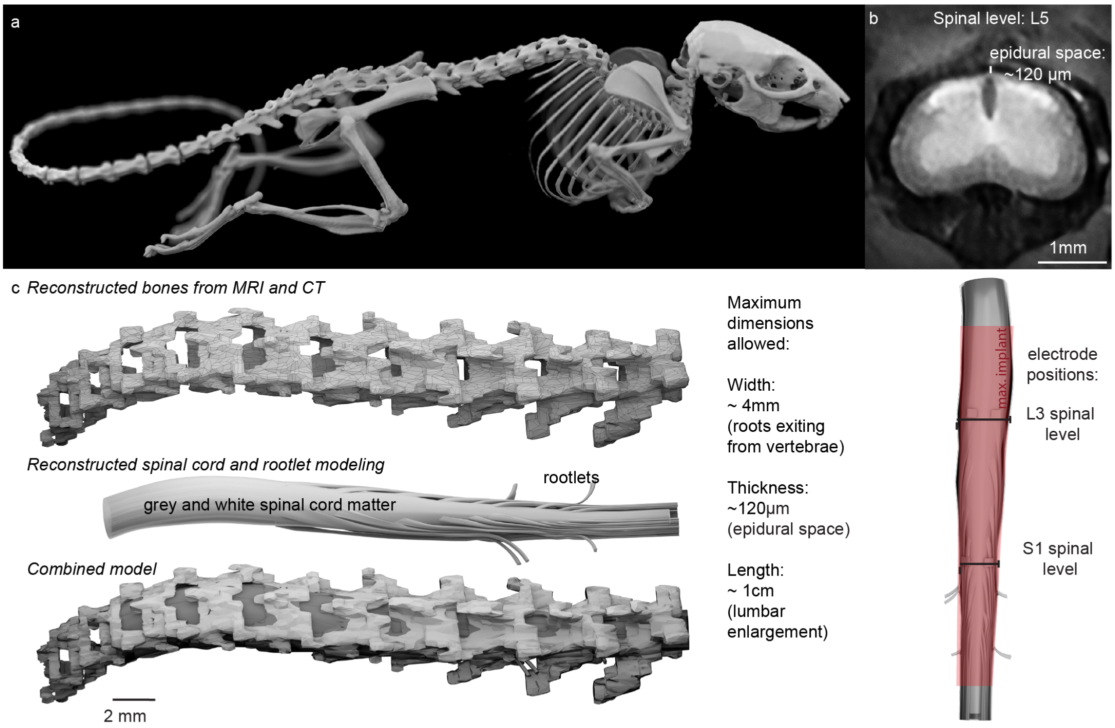
a
b
Spinal level: L5
epidural space:
~120 µm
1mm
c Reconstructed bones from MRI and CT
Reconstructed spinal cord and rootlet modeling
rootlets
grey and white spinal cord matter
Combined model
2 mm
Maximum dimensions allowed:
Width:
~ 4mm
(roots exiting from vertebrae)
Thickness:
~120µm
(epidural space)
Length:
~ 1cm
(lumbar enlargement)
max. implant
electrode positions:
L3 spinal level
S1 spinal level

Figure 6.2: 3D volume of mouse spinal cord. a. CT-reconstruction of skeletal system. b. Transverse crosssection of MRI images. c. Reconstruction of lumbar spinal cord outlines suitable dimensions of implant.

6.2.2 A computational model of light penetration in the spinal cord of mice

The rapidly evolving library of experimental opsins is offering a broad repertoire of tools to target cellular mechanisms (Deisseroth, 2015; F. Zhang et al., 2011). These opsins are activated by specific wavelengths spanning the entire spectrum of light. In the course of the associated study, we focussed on the question whether our micro-LED array could activate red-shifted or blue-shifted opsins.

Firstly, physiological constraints needed to be taken into account to design the protocol for light application in the spinal cord. The grey and white matter of the spinal cord present with dramatically different contents of light-diffracting lipid-rich myelin. Consequently, spinal tissues exhibit region-specific light penetration properties, suggesting that the position of the light-emitting dies may play an important role in the efficiency of photostimulation, especially to reach deeply located regions. I addressed this possibility with computer simulations of blue light by solving Helmhotz equations in a FEM model (see section 6.2.5). I complemented my anatomical model with a FEM approach to light penetration within the spinal cord (Fig. 6.3). I prepared two different simulations. The first utilized a single micro-LED placed medially over the midline of the spinal cord. In the second setup I placed a micro-LED over each dorsal horn on either side of the spinal cord. I simulated light penetration with increasing levels of power density between 50 $\frac{mW}{mm^2}$ and 150 $\frac{mW}{mm^2}$. The results indicated that positioning the micro-LEDs above the dorsal horns would result in deeper light penetration across the spinal cord than a single micro-LED placed centrally over the spinal cord (Fig. 6.3a).

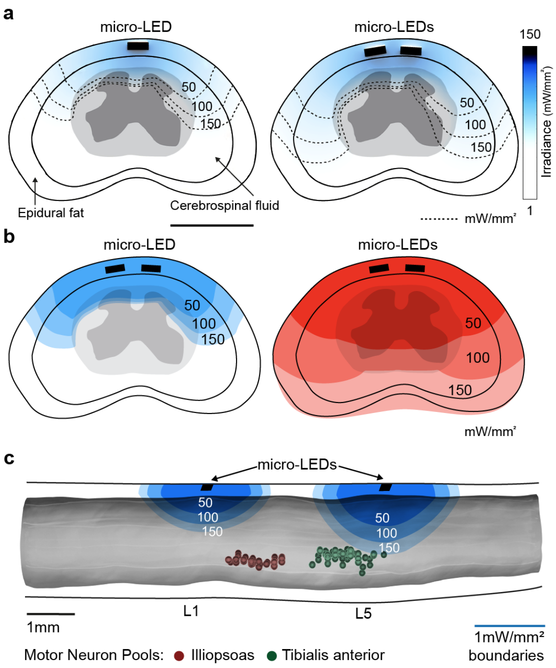

Figure 6.3: Simulations showing the penetration of light through spinal tissues with various power densities. a. Transverse crosssection of blue-light (wavelength 600 nm) penetration. b. Transverse crosssection of blue and red-light (wavelength 470 nm) penetration. c. Sagital view of blue-light penetration.

Secondly, I wanted to assess whether positioning two micro-LEDS would be sufficient to target interneurons located in the intermediate lamina with red or blue light. Simulations revealed that red-shifted light could penetrate the entire depth of the spinal cord, whereas blue light extinguished rapidly when entering these tissues (Fig. 6.3b).

Lastly, I aimed to assess whether the penetration depth would vary significantly if light were to be applied at different locations along the rostrocaudal axis of the lumbar spinal cord. Since red-light seemed to easily penetrate the entire spinal cord, I focussed on studying light penetration in the context of blue-light. I applied blue-light just below the L1 and L5 segment with two micro-LEDs placed over the dorsal horns. While neither location was fully penetrable with blue-light within the range of tested power densities, light was able to reach the ventral horn of the spinal cord just below the L5 segment (Fig. 6.3c). These results suggest, that blue-light may not be able to reach the motoneuron pools of the ilipsoas around the L2 segments, but may extend to the motoneuron pools of the tibialis anterior around the L5 segment.

6.2.3 A computational model of heat diffusion with photostimulation protocols in mice

The reliable activation of opsins that drive hyperpolarization in neurons requires the delivery of sustained photostimulation. Duty cycles with extended stimulation-ON times can lead to tissue heating, which alters neuronal responses (Owen et al., 2019). To assess these thermal constraints I simulated the heat diffusion with a duty cycle of 25% and 100% within the mouse spinal cord (Fig. 6.4). Simulations indicate that a duty cycle of 25% exhibit minimal heating in the spinal cord at amplitudes of 6 mA (corresponding to power density of 50 $\frac{mW}{mm^2}$ of blue light). However, already at 12 mA (corresponding to power density of 100 $\frac{mW}{mm^2}$ of blue light), these simulations suggest that the temperature rises to over 40°C in the epidural space. Fortunately, neither the white nor the grey matter are being significantly heated up. On the other hand, application of 18 mA (corresponding to power density of 100 $\frac{mW}{mm^2}$ of blue light) already heats the dorsal aspect of the white matter by approximately 1°C. In turn, a duty cycle of 100% shows significant heating of white and grey matter across tested currents.

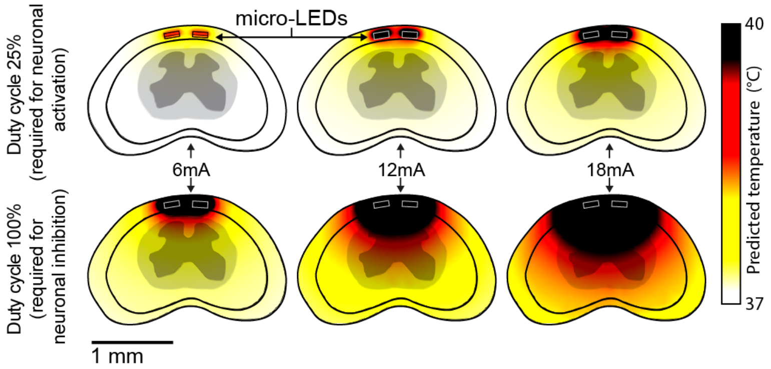

Figure 6.4: Transverse crosssection of heat diffusion in the spinal cord with 6mA (50 $\frac{mW}{mm^2}$), 12mA (100 $\frac{mW}{mm^2}$), 18mA (150 $\frac{mW}{mm^2}$)

6.2.4 Limitations and outlook of light propagation and heat diffusion simulations in the mouse spinal cord

Here, I presented a computational model that aided in the design of an optoelectronic system that enables precise manipulation of targeted neurons and pathways throughout the brain in untethered conditions. For this purpose, I reconstructed the tridimensional geometry of the mouse spinal cord from high-resolution MRI- and CT-datasets to provide estimates of suitable dimensions for spinal implants in mice. This procedure may be important for translational research to design spinal implants for varying species (see section 6.3).

I also proposed a computational approach for evaluating the efficacy of penetration depths of varying light-application methods on the basis of solving Helmholtz equations in a FEM model of the mouse spinal cord (see section 6.2.5). However, due to the extremely small size of the mouse spinal cord, all spinal tissues had to be discretized into a very fine mesh. This approach was computationally expensive and thus I opted to exclude various spinal tissues, such as the meninges. This might affect the interpretability of the presented results. Hence, I encourage the inclusion of more realistic anatomical representations for future research.

Lastly, I evaluated the heat diffusion within the mouse spinal cord due to application of light with micro-LEDs. This approach might be useful to establish guidelines for efficient yet safe spinal cord photostimulation. However, within my FEM approach, not only did I exclude various spinal tissues but I also neglected the hydrodynamics taking place in the vertebral canal. It is well established that the CSF, flows around the spinal cord and therefore transports heat within the vertebral canal. Therefore, I consider all the heat diffusion results in this chapter to overestimate the temperature changes in the vertebral canal. This was sufficient for my purpose, as I wanted to establish safe photostimulation thresholds. For future research, I suggest the inclusion of these tissues and physical phenomena to establish more reliable guidelines for spinal cord photostimulation.

6.2.5 Computational modeling methods for safety and efficacy evaluations of optoelectronic devices in the spinal cord

Computerized tomography

Perfused mice were placed in a 50 ml Falcon tube. The mouse was scanned in a micro-CT Quantum GX (Perkin Elmer, Waltham, MA, USA) with a FOV of 25 mm at 90 kV and 80 mA over 360° (Angle 0.45°) using the high-resolution 14-min protocol. The projections obtained were then reconstructed at a voxel size of 50 µm or 20 µm using the Quantum GX software. Segmentation was performed with Analyze 12.0 (AnalyzeDirect, Inc., USA).

Magnetic resonance imaging

The mice were placed in a Falcon tube which was filled with Galden® (Fluorochem, Hadfield, UK) to match the tissue magnetic susceptibility and improve magnetic field homogeneity around the cord. Mouse cords were scanned on a 9.4T MR system (Varian Medical Systems, Palo Alto, CA, USA) equipped with 400 mT/m gradients, using a 3.5-mm diameter birdcage coil for radiofrequency transmission and reception. High-resolution axial anatomical images were acquired using a fast spin-echo sequence (in-plane resolution: 47 x 47 μm^2, FOV: 12x12 mm^2, matrix size: 192x192 zero-filled to 256x256, slice thickness: 0.5 mm, 20 slices, TE/TR = 13/5000 ms, echo train length: 4, TEeff = 13 ms, 24 averages, scan time = 1h36min).

Computational model

An anatomically accurate 3D finite element model of the mouse spinal cord was generated. First, sagittal sections of the grey and white matter were extracted from an atlas of the spinal cord (Watson et al., 2009). Secondly, these sections were placed and scaled manually to fit the collected MRI data. In turn, the cerebrospinal fluid and epidural fat were first segmented from the same datasets, then sections were extracted and smoothed. All sections were lofted together to generated 3D volumes (Sim4Life by ZMT) (Neufeld et al., 2013). The LEDs were approximated as three-layer rectangular structure consisting of Polyisobuthylene, Polydimethylsiloxane and silicon carbide. The entire geometry was encapsulated into a cylindrical volume to approximate the surrounding tissues as saline. All volumes were imported into COMSOL and discretized into a tetrahedral mesh with extremely fine element size (COMSOL Multiphysics® v. 5.3. www.comsol.com. COMSOL AB, Stockholm, Sweden). Physics-based simulations of the bioheat transfer and the light penetration were applied. For the former the bioheat transfer equations of COMSOL were utilized for which thermal conductivity, density and heat capacity values were exported from an atlas of such values in Sim4Life. Dirichlet boundary conditions were applied at the outermost surface of the saline volume. A heat source was applied at the appropriate layer for each simulation. The light penetration was calculated with the Helmholtz equations. Scattering and absorption coefficients were taken from various prior publications (Bashkatov et al., 2000; Mignon et al., 2018; Yaroslavsky et al., 2002). Dirichlet boundary conditions were implemented for the LED contacts and the outermost surface of the saline volume. A parametric sweep was applied for the power density with the irradiance with values of 50, 100 and 150 $\frac{mW}{mm^2}$.

6.3 Guiding implant design for translational research

The convergence of materials science, electronics, and biology, namely bioelectronic interfaces, leads novel and precise communication with biological tissue, particularly with the nervous system. However, the translation of lab-based innovation toward clinical use calls for further advances in materials, manufacturing and characterization paradigms, and design rules. In the associated publication **Soft, Implantable Bioelectronic Interfaces for Translational Research** we presented a translational framework engineered to accelerate the deployment of microfabricated interfaces for translational research (Schiavone et al., 2020).

A key element in the design of implants for translational research is the inspection of variations of anatomical features across species. As such, my computational framework can play an important role in the assessment of these features due to its capacity to rapidly create tridimensional volume models of key species. In this thesis, I have already described anatomically-realistic tridimensional models of mice, rats and humans. These models enabled the anatomical analysis of key features of the vertebral canal, that can aid in the development of spinal implants across these species. However, the translation of neuromodulation paradigms from preclinical research into a clinical setting often requires testing in Non-Human Primates (NHPs). Anatomical computer models of NHPs may be valuable in the design of spinal implants for translational research. In the context of this thesis, tridimensional models have been largely generated from high-resolution MRI- and CT-datasets. In particular, the critically important MRI-data is difficult to acquire for NHPs, as their small stature requires the usage of research scanners that enable the acquisition of high-resolution MRI-datasets. Unfortunately, these scanners are often constructed with bores to fit only smaller species. Here, I present a reconstruction of a macaca fascicularis NHP, from MRI-datasets acquired with a clinically-relevant MRI scanner and supplemented with CT-datasets of the vertebral bodies (Fig 6.5). Although the resolution of these scans was not sufficient to extract the trajectory of the spinal roots, the segmentation clearly highlights the anatomical dimensions of key anatomical features. In particular, measurements of the epidural space have proven valuable in the design and testing of spinal implants (Schiavone et al., 2020).

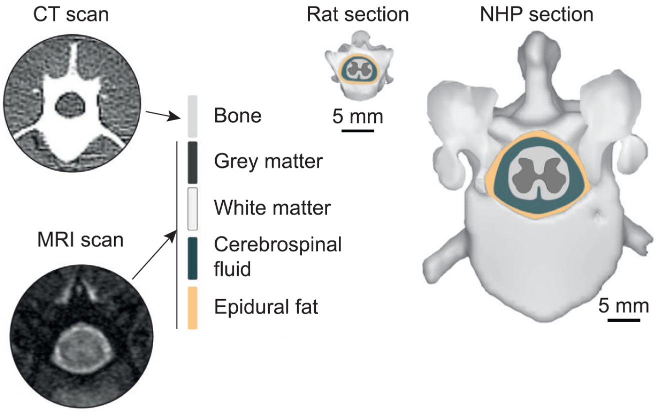

Figure 6.5: Segmentation of high-resolution MRI and CT images enables a 3D reconstruction of the spinal cord in Non-Human Primates (NHPs) and rats.

7 Conclusions and perspectives

In this thesis, I used a hypothesis-driven approach to aid in the restoration of neural functioning after neurological disorders. I focused primarily on the recovery of locomotion after SCI with EES. For this purpose, I leveraged computational modeling to study the mechanisms underlying the formation of motor patterns in preclinical animal models and humans with EES, develop personalizable EES strategies to enable activity-based therapies after SCI and design spinal cord stimulation electrode arrays. Lastly, I translated my computational approach for treatment of other neurological disorders and the development of novel neuromodulation paradigms.

Mechanisms underlying the formation of motor patterns in animal models and humans with EES after SCI

The exact interactions between EES and the nervous system remain largely unknown. In particular computational efforts suggested that EES recuits large-diameter, myelinated (i.e. proprioceptive and cutaneous) afferent fibers in the dorsal roots, while only minimally interacting with interneurons, motoneurons and smaller-diameter and/or unmyelinated afferent fibers (Capogrosso et al., 2013; Minassian et al., 2007; Rattay et al., 2000). Unfortunately, these claims remain large unsubstantiated due to lack of experimental evidence. Be that as it may, it is well established that proprioceptive feedback circuits play a major role in the formation of motor patterns with EES after SCI (Kiehn, 2016; Moraud et al., 2016; Takeoka et al., 2014). Unfortunately, the interactions between EES and cutaneous afferents remain largely unexplored. Moreover, little attention has been given to the interactions between these artificially induced activity patterns and natural firing patterns of sensorimotor circuits with EES thus far.

In this thesis, I aimed to provide direct and indirect evidence for the recruitment of proprioceptive and ctuaneous afferent fibers in the dorsal roots. Moreover, I studied the role of cutaneous afferents in the formation of motor patterns with EES after SCI. Lastly, I focused on dissecting the interactions between artificially induced firing patterns in proprioceptive feedback circuits and their natural activity during locomotion.

Development of personalizable EES strategies to enable activity-based therapies after SCI

The lack of mechanistic understanding in the past had a significant impact on the development of EES strategies to enable activity-based therapies after SCI. EES paradigms have largely been thought of by inductive reasoning from empirical observations. This approach is necessarily suboptimal given the large space of parameters surrounding EES-supported activity-based therapies. In the absence of clear mechanistic understanding of this technology, clinical implementations fail to personalize their treatment to each subject and thus are unable to account for variabilities between individuals. As such, a significant discrepancy in the efficacy and robustness of enabling locomotion with EES can be seen both between species and between subjects (Angeli et al., 2018; Angeli et al., 2014; Carhart et al., 2004; Courtine et al., 2009; M. L. Gill et al., 2018; S. Harkema et al., 2011).

In this thesis, I used a deductive approach on the basis of computational simulations and hypothesis-driven behavioral, electrophysiological and psychophysical experiments to develop personalizable EES strategies that are efficacious and robust in large and diversified patient-cohorts.

Design of spinal cord stimulation electrode arrays

Thus far, EES has been delivered using off-label neurotechnologies that were originally designed to alleviate chronic pain (Angeli et al., 2018; Barolat et al., 1986; Danner et al., 2015; Formento et al., 2018; M. L. Gill et al., 2018; S. Harkema et al., 2011; Herman et al., 2002; Wagner et al., 2018). At the center of these neurotechnologies are paddle leads designed to target the dorsal column (Molnar & Barolat, 2014). Instead, as discussed above, the recovery of motor functions requires targeting large-diameter, myelinated afferent fibers within the dorsal roots (Capogrosso et al., 2013; Minassian et al., 2007; Minassian et al., 2012; Rattay et al., 2000).

In this thesis, I used computational modeling and anatomical analysis to inform the design of paddle leads that aim to enable locomotion after SCI.

Application of personalizable computational models for the treatment of other neurological disorders and the development of novel neuromodulation paradigms.

Beyond locomotion, a hypothesis-driven approach may aid in the treatment of a wide range of neurological impairments and the development of novel neuromodulation paradigms. In this thesis, I briefly summarize how I leveraged personalizable computational modeling in three use-cases. These are hemodynamic control with EES after SCI, optoelectronic manipulation of neurons and pathways across the dorsoventral spinal cord in mice and implant design for translational research.

In this chapter, I first briefly summarize the main findings of this thesis. I then discuss my perspective on how the work presented in my thesis may influence the development of neuromodulation strategies that enable activity-based therapies after SCI.

7.1 Summary of the main findings

In **chapter 2**, I presented a combined effort of finite element modeling, neuromusculoskeletal modeling as well as a series of anatomical, electrophysiological and behavioral experiments in transgenic rats and mice to study the mechanisms underlying the formation of motor patterns in rodents with EES after SCI. I outlined a combination of finite element modeling and neuron-specific calcium imaging of dorsal root ganglia in rodents to demonstrate that EES recruits both proprioceptive (Aα/Aβ) and cutaneous LTMR (Aβ-LTMR) afferents. I provided chemogenetic evidence that there may exist a causal relationship between the recruitment of proprioceptive feedback circuits and the formation of motor patterns during EES. In contrast, I utilized neuromusculoskeletal modeling to suggest that the continuous recruitment of Aβ-LTMR afferents disrupts the production of locomotion. I reasoned that tuning the gain of proprioceptive and Aβ-LTMR feedback circuits in opposite directions would potentiate the therapeutic efficacy of EES. Leveraging noradrenergic pharmacotherapies that target the $\alpha 2$ receptors, I provided experimental evidence for this hypothesis in rodent models. Indeed, repurposing a dual $\alpha 2$a antagonist / $\alpha 2$c agonist, that upregulates the gain in proprioceptive feedback circuits while downregulating the gain in Aβ-LTMR feedback circuits, I observed robust locomotion in preclinical models of complete SCI and severe contusion SCI.

Unfortunately, the pharmacological intervention proposed in chapter 2 is not available for use in humans yet. Therefore, I aimed in **chapter 3** to investigate the species-specific effects of the recruitment of proprioceptive afferent fibers with EES. Neuromusculoskeletal modeling in humans and rodents revealed that in humans, unlike in rodents, EES applied with amplitudes and frequencies commonly used for therapeutic avenues, disrupts natural sensory feedback by means of antidromic collision. A battery of experiments in rats and humans with SCI confirmed this hypothesis. Instead, I outlined stimulation paradigms that preserve natural afferent activity by recruiting specific proprioceptive afferents by emulating their natural firing pattern during locomotion with low-amplitude, high-frequency bursts of stimulation.

This particular stimulation paradigm could have vast clinical implications, if successfully implemented in a clinical context. For this purpose, I outlined in **chapter 4** a technological framework to enable activity-based therapies in people with chronic, incomplete SCI with EES. The proposed stimulation strategies in chapter 3 rely on the appropriate spatiotemporal activation of proprioceptive afferent fibers in the dorsal roots, effectively reproducing the migration of motoneuron pools during locomotion. Unfortunately, as discussed in chapter 1.1.5, the human spinal cord exhibits a large degree of anatomical variability in large and diversified patient-cohorts. For this reason, I developed a computational framework capable of rapidly generating personalized hybrid computational models for pre-operative treatment planning. In chapter 4, I provide evidence that spatiotemporal spinal cord stimulation enables activity-based training of these individuals, while continuous stimulation did not promote locomotor movements to the same degree in the participants.

At the core of the technological framework in chapter 4 stands a commercially-available paddle lead, conceived to alleviate pain by targeting the dorsal column (Molnar & Barolat, 2014). In turn, enabling locomotion with EES requires the recruitment of large-diameter, myelinated afferent fibers within the dorsal roots (Capogrosso et al., 2013; Minassian et al., 2007; Minassian et al., 2012; Rattay et al., 2000). In **chapter 5**, I reasoned that using computational modeling, I could develop an arrangement of electrodes on a paddle lead more suitable to enable locomotion with EES. I outlined how I advanced my computational framework to generate anatomically and functionally realistic hybrid computational models from medical imaging datasets. I generated an atlas of personalized hybrid computational models. In combination with anatomical assessments of human cadavers, this atlas aided me in designing an arrangement of electrodes on a paddle lead for the generation of locomotion in humans with SCI. I leveraged my computational framework for pre-operative treatment planning and validated the efficacy of my computational framework and the new paddle lead in-silico and in-vivo through intraoperative electrophysiological assessments in three human participants with chronic and complete SCI. I demonstrate that this neurotechnology enabled the rapid elaboration of activity-dependent stimulation programs that address the deficits of three human participants with chronic and complete SCI over a broad range of motor activities.

In chapters 2, 3, 4 and 5, I outlined how to leverage personalizable computational modeling to study the mechanisms underlying the formation of motor patterns in animal models and humans with EES, develop EES strategies to enable activity-based therapies after SCI and design spinal cord stimulation electrode arrays. This was my original goal. In the following **chapter 6**, I tested the viability of my computational framework to be translated for use in other neurological disorders and the development of novel neuromodulation paradigms. For this purpose, I defined three new subgoals. Fistly, I wanted to aid in the translation of EES to new use-cases. As an example I picked the control of hemodynamics. I leveraged a similar approach to what has been described in the previous chapters. I was able to demonstrate that EES can control hemodynamics by recruiting large-diameter, myelinated afferent fibers in the low-thoracic spinal cord. I also confirmed the necessary stimulation paradigms to control hemodynamics in an individual with hemodynamic instability due to SCI. Secondly, I aimed at testing hypothesis-driven development of neurmodulation therapies by evaluating the safety and efficacy of an optoelectronic system to enable locomotion in pre-clinical models. I developed light-propagation and heat diffusion models in the mouse lumbar spinal cord. Finally, I tested the usability of my framework in supporting translational research by inspection of variations of anatomical features across species.

I believe, that all the results outlined in these chapters highlight the important role personalizable computational models can play in the development and testing of neuromodulation therapies for the recovery of nervous function after neurological disorders.

7.2 Perspectives

The work proposed in this thesis highlights the importance of hypothesis-driven engineering to develop neuromodulation therapies. In particular, I outlined the important role computational modeling can play to increase the efficacy, robustness and safety of neuromodulation therapies. I paid particular attention to demonstrate the use-case of personalizable computational models for EES to enable locomotion after SCI. Here, I present my perspective on how these technologies should be improved and utilized in the future.

7.2.1 Towards personalized treatment planning of neuromodulation therapies

It is a well known, yet seldomly adressed fact, that medical interventions of any kind are often ineffective. Percentages of patients for whom common treatments of varying conditions are ineffective range from 38-75 % (Spear et al., 2001). A major cause is inter-subject variability of various physiological parameters that may affect the treatment. The natural question to ask is, whether there is a method that enables the treatment process to focus on the actual patient at hand. In the case of neuromodulation therapies, that often ultimately focus on the application of electrical stimulation to various areas of the nervous system, the natural candidate for this kind of procedure is computational modeling.

Indeed, computational models of deep brain stimulation have proven to be an invaluable tool for clinical decision support. In particular, incorporating patient anatomy and electrode location into computational simulations have shown to enable clinical staff to select stimulation parameters that are vastly superior to standard clinical procedures (Frankemolle et al., 2010). This patient-specific approach to computational modeling may very well be beneficial to translate to other neuromodulation therapies. However, this necessitates that the targets of the neuromodulation therapy are clearly identified. Various computational studies, including this thesis suggest that EES enables the formation of motor patterns by recruiting large-diameter, myelinated afferent fibers in the dorsal roots (Capogrosso et al., 2013; Minassian et al., 2007; Rattay et al., 2000) (see chapter 2 and chapter 3). The dorsal roots have been difficult to visualize in the past, but mounting technological advancements in the field of medical imaging, including the advancements presented in this thesis, suggest that the spinal roots are visualizable with commercially-available technologies commonly found in medical centers (Ranger et al., 2008) (see chapter 4 and chapter 5).

Once medical imaging datasets are collected that accurately illustrate the anatomy of the spinal cord, a patient-specific volume conductor model can be constructed. However, a clinically-limiting factor is the time-intensive segmentation procedure to reconstruct the subjects anatomy. Luckily the field of computer vision has been growing rapidly in the past years. Indeed, already today, there are already tools available that enable the automatic reconstruction of the spinal cord from MRI datasets (De Leener et al., 2017). These tools, however, are yet to be adapted to include the critically important information of the spinal roots. With only limited available datasets that visualize the spinal roots at this date, more medical imaging datasets will have to be collected. This effort might very well also necessitate the need to pool together resources from multiple centers to enable the robust segmentation across scanners of various types and vendors.

Given that the segmentation problem has been solved, the next issue at hand will be streamlining the modeling process. Indeed, this highly complex venture necessitates not only a high degree of knowledge in the fields of physics, neuroscience and computer science but also requires access to expensive computational resources. One solution would be to include a staff of medical physicists, that, equipped with sufficient training and the necessary hard- and software, could prepare the treatment planning at each center. However, the costs of this venture would be enormous. Instead, I believe that this issue requires the development of user-friendly and cloud-based services with pre-programmed workflows. In fact, as I outlined in chapter 1.4, the procedure surrounding the development of hybrid computational models is largely linear. Hence, the necessary steps could be automated. With the additional inclusion of automated segmentation procedures and pre-defined analysis modes a service can be imagined that fully automates the treatment planning to support activity-based therapies with EES in a pre-operative fashion. In fact, similar developments are already in place by the U.S. National Institutes of Health (NIH)-funded Open Platform for Online Simulations for Stimulating Peripheral Activity to Relieve Conditions - o2S2PARC project.

By no means is the procedure discussed above limited to treatment planning to enable locomotion with EES. In fact, even for other applications or other neuromodulation therapies are the targets well defined. An example is discussed in chapter 6, where I suggest that the control of hemodynamics requires targeting the low-thoracic dorsal roots with EES. Hence, the exact same procedure as for treatment planning to enable locomotion with EES can be applied, with only the notable exception of changing the target from the lumbosacral spinal cord to the low-thoracic region. Similarly, this procedure is also not limited to a pre-operative context. Indeed, incorporating post-operative imaging datasets to localize implant location in the spinal cord could enable further optimization of clinically relevant stimulation parameters such as amplitude or frequency to increase specificity.

7.2.2 Leveraging in-silico assessments for the design of neuromodulation technologies

Another important aspect of neuromodulation technologies is the design of the actual devices utilized to interact with the nervous system. These designs are often based on inductive analysis of empirical observations. This procedure is necessarily suboptimal as it fails to address the underlying mechanisms at play. Computational models on the other hand offer a great opportunity to replicate and abstract out the mechanisms in the absence of noisy experimental acquisition and processing methods. Additionally, the time from conceiving an experimental protocol to receiving the results is primarily limited by computational hardware rather than collection of study participants, ethical considerations, data collection and data processing. Ultimately, this means computational modeling enables faster data generation than experimental protocols. In conjunction with the generation of personalized models, technologies can be tested and optimized in large and diversified patient-cohorts faster with computational optimization than with experimental data collection.

I have outlined an attempt to establish this procedure in chapter 5. However, this approach is neither limited to the use-case of enabling locomotion after SCI in humans, nor is this attempt optimal. In fact, in chapter 5 I merely confirmed rudimentary hypothesis regarding electrode locations in extremely limited stimulation configurations in an averaged spinal cord model. While I fundamentally believe this approach to be optimal, I would suggest future works to include the use of optimization algorithms to define electrode locations by simultaneously exploring all possible parameters including electrode size, location and shape with not just limited stimulation configurations of these electric contacts but while enabling any superposition of electric currents imaginable. While this procedure might be extremely computationally expensive, the implementation of optimization routines such as genetic algorithms should massively reduce computational costs. Lastly, this optimization procedure should not be limited to a single averaged representation of the subsystem that is to be studied but should include personalized computational representations of diverse cohorts of individuals. Ultimately, I believe this procedure to yield more efficient neuromodulation technologies that are robust across individuals

7.2.3 Optimizing EES-based rehabilitation strategies with in-silico investigations of neural adaptation mechanisms

Thus far, I have always talked about optimizing the capacity of EES to recruit large-diameter, myelinated afferent fibers linked to the activation of muscles necessary to produce locomotion. However, ultimately the goal of EES in the context of locomotion is to enable activity-based therapies that may hopefully recover the capacity of the individual to produce the formation of motor patterns. In recent years, several experimental studies demonstrated recovery of locomotion by combining EES with intense physical training in individuals with SCI (Angeli et al., 2018; M. L. Gill et al., 2018; Wagner et al., 2018). This tremendous achievement is a first step towards a clinical solution for SCI patients. Nonetheless, there is currently only limited consensus on the definition of clinically meaningful protocols.

Experimental evidence in animal models suggest that reinforced inputs to the nervous systems can improve performance of a trained task (Thompson et al., 2013; Thompson et al., 2017). This may indicate the viability of EES as a long-term rehabilitation tool. Yet, performance in related tasks can remain unchanged, improve or even decrease (Girgis et al., 2007; Krajacic et al., 2009; Starkey et al., 2011). The latter case is referred to as task-dependent recovery. This phenomenon is particularly disruptive to the potential therapeutic benefits of neuromodulation therapies. Indeed, regaining the capacity to walk at the cost of loosing the capacity to stand is a real possibility.

It is therefore necessary to disentangle the circuit-level adaptations taking place as a consequence of EES-enabled activity-based therapies. This includes both the adaptations taking place as a consequence of reinforced inputs from artificially recruiting nervous structures with EES and the reinforced stimuli taking place as a result of the applied training protocols. In chapter 5, I have outlined how hybrid computational models can be utilized to realistically estimate the recruitment patterns taking place as a result of a particular stimulation protocol in an individual. I have also explained in chapters 2 and 3 how neuromusculoskeletal modeling can decipher circuit-level mechanisms taking place during EES-enabled locomotion. Hence, understanding circuit-level adaptions as a consequence of EES-enabled activity-based therapies could be achieved by coupling both together and extending the circuit-level model with learning rules emulating neural plasticity. In fact, thinking one step further into the future, including the generation of personalized volume conductor models could enable a first step towards personalized EES-enabled activity-based therapies.

7.3 General conclusion

In this thesis, I leveraged computational modeling to study the mechanisms underlying the formation of motor patterns in animal models and humans with EES, developed personalizable EES strategies to enable activity-based therapies after SCI and designed spinal cord stimulation electrode arrays. Firstly, I provided evidence that EES recruits large-diameter, myelinated afferent fibers in the dorsal roots that transmit information of proprioceptive and cutaneous sensory organs. I studied the mechanisms of the underlying sensorimotor circuits innervated by these proprioceptive and cutaneous afferent fibers. I suggested that while EES enables the formation of motor patterns through the recruitment of proprioceptive feedback circuits, the continuous recruitment of cutaneous afferents may disrupt the production of locomotion. Secondly, I investigated interspecies differences of EES. I suggested that EES-parameters such as amplitude and frequency in ranges commonly used for therapeutic avenues may disrupt natural sensory feedback by means of antidromic collision. Instead, I suggested stimulation paradigms that preserve natural afferent activity by recruiting specific proprioceptive afferents by emulating their natural firing pattern during locomotion with low-amplitude, high-frequency bursts of stimulation. Third, I described a technological framework that warrants the application of such stimulation paradigms to enable activity-based therapies in people with SCI. I outlined how personalized hybrid computational models can be used for treatment planning in the context of this technological framework. Fourth, I advanced the realism of these personalized hybrid computational models, validated their efficacy in treatment planning over standard clinical practice and leveraged them to inform the arrangements of electrodes on a paddle lead, specifically designed to target large-diameter, myelinated afferent fibers in the dorsal roots. Lastly, I outlined how I translated personalizable computational modeling for use in other neurological disorders and the development of novel neuromodulation paradigms. I suggested that EES can control hemodynamics by recruiting large-diameter, myelinated afferent fibers in the low-thoracic spinal cord and confirmed stimulation paradigms to control hemodynamics in an individual with hemodynamic instability due to SCI. I evaluated safety and efficacy of a novel optoelectronic system with the capacity to enable locomotion in pre-clinical models and proposed how personalizable computational modeling may be efficacious in supporting translational research.

Bibliography

Abraira, V. E., & Ginty, D. D. (2013). The sensory neurons of touch. *Neuron, 79*(4), 618–639. https://doi.org/10.1016/j.neuron.2013.07.051

Abraira, V. E., Kuehn, E. D., Chirila, A. M., Springel, M. W., Toliver, A. A., Zimmerman, A. L., Orefice, L. L., Boyle, K. A., Bai, L., Song, B. J., Bashista, K. A., O'Neill, T. G., Zhuo, J., Tsan, C., Hoynoski, J., Rutlin, M., Kus, L., Niederkofler, V., Watanabe, M., … Ginty, D. D. (2017). The cellular and synaptic architecture of the mechanosensory dorsal horn. *Cell, 168*(1-2), 295–310.e19. https://doi.org/10.1016/j.cell.2016.12.010

Ahuja, C. S., & Fehlings, M. (2016). Concise review: bridging the gap: novel neuroregenerative and neuroprotective strategies in spinal cord injury. *STEM CELLS Translational Medicine, 5*(7), 914–924. https://doi.org/10.5966/sctm.2015-0381

Albert, F., Bergenheim, M., Ribot-Ciscar, E., & Roll, J.-P. (2006). The ia afferent feedback of a given movement evokes the illusion of the same movement when returned to the subject via muscle tendon vibration. *Experimental Brain Research, 172*(2), 163–174. https://doi.org/10.1007/s00221-005-0325-2

Alexeeva, N., & Calancie, B. (2014). Efficacy of QuadroPulse rTMS for improving motor function after spinal cord injury: three case studies. *The Journal of Spinal Cord Medicine, 39*(1), 50–57. https://doi.org/10.1179/2045772314y.0000000279

Alizadeh, A., Dyck, S. M., & Karimi-Abdolrezaee, S. (2019). Traumatic spinal cord injury: an overview of pathophysiology, models and acute injury mechanisms. *Frontiers in Neurology, 10*. https://doi.org/10.3389/fneur.2019.00282

Altman, J. D., Trendelenburg, A. U., MacMillan, L., Bernstein, D., Limbird, L., Starke, K., Kobilka, B. K., & Hein, L. (1999). Abnormal regulation of the sympathetic nervous system in α2a-adrenergic receptor knockout mice. *Molecular Pharmacology, 56*(1), 154–161. https://doi.org/10.1124/mol.56.1.154

Alvarez, F. J., Jonas, P. C., Sapir, T., Hartley, R., Berrocal, M. C., Geiman, E. J., Todd, A. J., & Goulding, M. (2005). Postnatal phenotype and localization of spinal cord v1 derived interneurons. *The Journal of Comparative Neurology, 493*(2), 177–192. https://doi.org/10.1002/cne.20711

Amos, A., Armstrong, D., & Marple-Horvat, D. (1990). Changes in the discharge patterns of motor cortical neurones associated with volitional changes in stepping in the cat. *Neuroscience Letters, 109*(1-2), 107–112. https://doi.org/10.1016/0304-3940(90)90546-l

Anderson, K. D. (2004). Targeting recovery: priorities of the spinal cord-injured population [PMID: 15672628]. *Journal of Neurotrauma*, *21*(10), 1371–1383. https://doi.org/10.1089/neu.2004.21.1371

Andujar, J.-É., Lajoie, K., & Drew, T. (2010). A contribution of area 5 of the posterior parietal cortex to the planning of visually guided locomotion: limb-specific and limb-independent effects. *Journal of Neurophysiology*, *103*(2), 986–1006. https://doi.org/10.1152/jn.00912.2009

Angeli, C. A., Boakye, M., Morton, R. A., Vogt, J., Benton, K., Chen, Y., Ferreira, C. K., & Harkema, S. J. (2018). Recovery of over-ground walking after chronic motor complete spinal cord injury [PMID: 30247091]. *New England Journal of Medicine*, *379*(13), 1244–1250. https://doi.org/10.1056/NEJMoa1803588

Angeli, C. A., Edgerton, V. R., Gerasimenko, Y. P., & Harkema, S. J. (2014). Altering spinal cord excitability enables voluntary movements after chronic complete paralysis in humans. *Brain*, *137*(5), 1394–1409. https://doi.org/10.1093/brain/awu038

Arber, S. (2012). Motor circuits in action: specification, connectivity, and function. *Neuron*, *74*(6), 975–989. https://doi.org/10.1016/j.neuron.2012.05.011

Arber, S., Ladle, D. R., Lin, J. H., Frank, E., & Jessell, T. M. (2000). ETS gene er81 controls the formation of functional connections between group ia sensory afferents and motor neurons. *Cell*, *101*(5), 485–498. https://doi.org/10.1016/s0092-8674(00)80859-4

Asanuma, H., & Mackel, R. (1989). Direct and indirect sensory input pathways to the motor cortex; its structure and function in relation to learning of motor skills. *The Japanese Journal of Physiology*, *39*(1), 1–19. https://doi.org/10.2170/jjphysiol.39.1

Asboth, L., Friedli, L., Beauparlant, J., Martinez-Gonzalez, C., Anil, S., Rey, E., Baud, L., Pidpruzhnykova, G., Anderson, M. A., Shkorbatova, P., Batti, L., Pagès, S., Kreider, J., Schneider, B. L., Barraud, Q., & Courtine, G. (2018). Cortico–reticulo–spinal circuit reorganization enables functional recovery after severe spinal cord contusion. *Nature Neuroscience*, *21*(4), 576–588. https://doi.org/10.1038/s41593-018-0093-5

Aubrey, J., Esfandiari, N., Baracos, V. E., Buteau, F. A., Frenette, J., Putman, C. T., & Mazurak, V. C. (2014). Measurement of skeletal muscle radiation attenuation and basis of its biological variation [PMC4309522[pmcid]]. *Acta physiologica (Oxford, England)*, *210*(3), 489–497. https://doi.org/10.1111/apha.12224

Bachmann, L. C., Matis, A., Lindau, N. T., Felder, P., Gullo, M., & Schwab, M. E. (2013). Deep brain stimulation of the midbrain locomotor region improves paretic hindlimb function after spinal cord injury in rats. *Science Translational Medicine*, *5*(208), 208ra146–208ra146. https://doi.org/10.1126/scitranslmed.3005972

Barbeau, H., Julien, C., & Rossignol, S. (1987). The effects of clonidine and yohimbine on locomotion and cutaneous reflexes in the adult chronic spinal cat. *Brain Research*, *437*(1), 83–96. https://doi.org/10.1016/0006-8993(87)91529-0

Barbeau, H., & Rossignol, S. (1990). The effects of serotonergic drugs on the locomotor pattern and on cutaneous reflexes of the adult chronic spinal cat. *Brain Research*, *514*(1), 55–67. https://doi.org/10.1016/0006-8993(90)90435-e

Barolat, G., Myklebust, J. B., & Wenninger, W. (1986). Enhancement of voluntary motor function following spinal cord stimulation - case study. *Stereotactic and Functional Neurosurgery*, *49*(6), 307–314. https://doi.org/10.1159/000100160

Barolat, G. (1988). Surgical management of spasticity and spasms in spinal cord injury: an overview. *The Journal of The American Paraplegia Society*, *11*(1), 9–13. https://doi.org/10.1080/01952307.1988.11735787

Barra, B., Conti, S., Perich, M., Zhuang, K., Schiavone, G., Fallegger, F., Galan, K., James, N. D., Barraud, Q., Delacombaz, M., Kaeser, M., Rouiller, E. M., Milekovic, T., Lacour, S., Bloch, J., Courtine, G., & Capogrosso, M. (2020). Epidural electrical stimulation of the cervical dorsal roots restores voluntary arm control in paralyzed monkeys. https://doi.org/10.1101/2020.11.13.379750

Bashkatov, A. N., Genina, E. A., Kochubey, V. I., Sinichkin, Y. P., Korobov, A. A., Lakodina, N. A., & Tuchin, V. V. (2000). In-vitro study of control of human dura mater optical properties by acting of osmotical liquids. In V. V. Tuchin (Ed.), *Controlling tissue optical properties: applications in clinical study*. SPIE. https://doi.org/10.1117/12.405939

Bawa, P., & Chalmers, G. (2008). Responses of human motoneurons to high-frequency stimulation of ia afferents. *Muscle & Nerve*, *38*(6), 1604–1615. https://doi.org/10.1002/mus.21184

Behrman, A. L., Ardolino, E. M., & Harkema, S. J. (2017). Activity-based therapy: from basic science to clinical application for recovery after spinal cord injury [01253086-201707001-00007[PII]]. *Journal of neurologic physical therapy : JNPT*, *41 Suppl 3*(Suppl 3 IV STEP Spec Iss), S39–S45. https://doi.org/10.1097/NPT.0000000000000184

Behzadi, Y., Restom, K., Liau, J., & Liu, T. T. (2007). A component based noise correction method (compcor) for bold and perfusion based fmri. *NeuroImage*, *37*(1), 90–101. https://doi.org/https://doi.org/10.1016/j.neuroimage.2007.04.042

Belanger, M., Drew, T., Provencher, J., & Rossignol, S. (1996). A comparison of treadmill locomotion in adult cats before and after spinal transection. *Journal of Neurophysiology*, *76*(1), 471–491. https://doi.org/10.1152/jn.1996.76.1.471

Beloozerova, I. N., & Sirota, M. G. (1993). The role of the motor cortex in the control of accuracy of locomotor movements in the cat. *The Journal of Physiology*, *461*(1), 1–25. https://doi.org/10.1113/jphysiol.1993.sp019498

Beloozerova, I. N., & Sirota, M. G. (2003). Integration of motor and visual information in the parietal area 5 during locomotion. *Journal of Neurophysiology*, *90*(2), 961–971. https://doi.org/10.1152/jn.01147.2002

Benabid, A. L., Costecalde, T., Eliseyev, A., Charvet, G., Verney, A., Karakas, S., Foerster, M., Lambert, A., Morinière, B., Abroug, N., Schaeffer, M.-C., Moly, A., Sauter-Starace, F., Ratel, D., Moro, C., Torres-Martinez, N., Langar, L., Oddoux, M., Polosan, M., … Chabardes, S. (2019). An exoskeleton controlled by an epidural wireless brain–machine interface in a tetraplegic patient: a proof-of-concept demonstration. *The Lancet Neurology*, *18*(12), 1112–1122. https://doi.org/10.1016/s1474-4422(19)30321-7

Berić, A., Dimitrijević, M., Sharkey, P., & Sherwood, A. (1986). Cortical potentials evoked by epidural stimulation of the cervical and thoracic spinal cord in man. *Electroen-*

cephalography and Clinical Neurophysiology/Evoked Potentials Section, *65*(2), 102–110. https://doi.org/https://doi.org/10.1016/0168-5597(86)90042-0

Bocci, T., Marceglia, S., Vergari, M., Cognetto, V., Cogiamanian, F., Sartucci, F., & Priori, A. (2015). Transcutaneous spinal direct current stimulation modulates human corticospinal system excitability. *Journal of Neurophysiology*, *114*(1), 440–446. https://doi.org/10.1152/jn.00490.2014

Bocci, T., Vannini, B., Torzini, A., Mazzatenta, A., Vergari, M., Cogiamanian, F., Priori, A., & Sartucci, F. (2014). Cathodal transcutaneous spinal direct current stimulation (tsDCS) improves motor unit recruitment in healthy subjects. *Neuroscience Letters*, *578*, 75–79. https://doi.org/10.1016/j.neulet.2014.06.037

Bonizzato, M., Pidpruzhnykova, G., DiGiovanna, J., Shkorbatova, P., Pavlova, N., Micera, S., & Courtine, G. (2018). Brain-controlled modulation of spinal circuits improves recovery from spinal cord injury. *Nature Communications*, *9*(1). https://doi.org/10.1038/s41467-018-05282-6

Bonnot, A., Whelan, P. J., Mentis, G. Z., & O'Donovan, M. J. (2002). Locomotor-like activity generated by the neonatal mouse spinal cord [The Segerfalk symposium on Principles of Spinal Cord Function, Plasticity and Repair]. *Brain Research Reviews*, *40*(1), 141–151. https://doi.org/https://doi.org/10.1016/S0165-0173(02)00197-2

Borton, D., Micera, S., Millán, J. d. R., & Courtine, G. (2013). Personalized neuroprosthetics. *Science Translational Medicine*, *5*(210), 210rv2–210rv2. https://doi.org/10.1126/scitranslmed.3005968

Bossetti, C. A., Birdno, M. J., & Grill, W. M. (2007). Analysis of the quasi-static approximation for calculating potentials generated by neural stimulation. *Journal of Neural Engineering*, *5*(1), 44–53. https://doi.org/10.1088/1741-2560/5/1/005

Bourane, S., Grossmann, K. S., Britz, O., Dalet, A., Del Barrio, M. G., Stam, F. J., Garcia-Campmany, L., Koch, S., & Goulding, M. (2015). Identification of a spinal circuit for light touch and fine motor control. *Cell*, *160*(3), 503–515. https://doi.org/10.1016/j.cell.2015.01.011

Bouton, C. E., Shaikhouni, A., Annetta, N. V., Bockbrader, M. A., Friedenberg, D. A., Nielson, D. M., Sharma, G., Sederberg, P. B., Glenn, B. C., Mysiw, W. J., Morgan, A. G., Deogaonkar, M., & Rezai, A. R. (2016). Restoring cortical control of functional movement in a human with quadriplegia. *Nature*, *533*(7602), 247–250. https://doi.org/10.1038/nature17435

Bouyer, L., & Rossignol, S. (2003a). Contribution of cutaneous inputs from the hindpaw to the control of locomotion. II. spinal cats. *Journal of Neurophysiology*, *90*(6), 3640–3653. https://doi.org/10.1152/jn.00497.2003

Bouyer, L., & Rossignol, S. (2003b). Contribution of cutaneous inputs from the hindpaw to the control of locomotion. II. spinal cats. *Journal of Neurophysiology*, *90*(6), 3640–3653. https://doi.org/10.1152/jn.00497.2003

Bracci, E., Ballerini, L., & Nistri, A. (1996). Spontaneous rhythmic bursts induced by pharmacological block of inhibition in lumbar motoneurons of the neonatal rat spinal cord

[PMID: 8714641]. *Journal of Neurophysiology*, *75*(2), 640–647. https://doi.org/10.1152/jn.1996.75.2.640

Brooks, J. C., Beckmann, C. F., Miller, K. L., Wise, R. G., Porro, C. A., Tracey, I., & Jenkinson, M. (2008). Physiological noise modelling for spinal functional magnetic resonance imaging studies. *NeuroImage*, *39*(2), 680–692. https://doi.org/https://doi.org/10.1016/j.neuroimage.2007.09.018

Brown, T. G. (1914). On the nature of the fundamental activity of the nervous centres; together with an analysis of the conditioning of rhythmic activity in progression, and a theory of the evolution of function in the nervous system [PMC1420503[pmcid]]. *The Journal of physiology*, *48*(1), 18–46. https://doi.org/10.1113/jphysiol.1914.sp001646

Brown, T. G., & Sherrington, C. S. (1911). The intrinsic factors in the act of progression in the mammal. *Proceedings of the Royal Society of London. Series B, Containing Papers of a Biological Character*, *84*(572), 308–319. https://doi.org/10.1098/rspb.1911.0077

Brown, T. G., & Sherrington, C. S. (1912). The factors in rhythmic activity of the nervous system. *Proceedings of the Royal Society of London. Series B, Containing Papers of a Biological Character*, *85*(579), 278–289. https://doi.org/10.1098/rspb.1912.0051

Buchanan, T., Lloyd, D., Manal, K., & Besier, T. (2004). Neuromusculoskeletal modeling: estimation of muscle forces and joint moments and movements from measurements of neural command. *Journal of applied biomechanics*, *20 4*, 367–95.

Bui, T. V., Stifani, N., Akay, T., & Brownstone, R. M. (2016). Spinal microcircuits comprising dI3 interneurons are necessary for motor functional recovery following spinal cord transection. *eLife*, *5*. https://doi.org/10.7554/elife.21715

Buonocore, M., Bonezzi, C., & Barolat, G. (2008). Neurophysiological evidence of antidromic activation of large myelinated fibres in lower limbs during spinal cord stimulation. *Spine*, *33*(4), E90–E93. https://doi.org/10.1097/brs.0b013e3181642a97

Burke, R. E. (1968). Group ia synaptic input to fast and slow twitch motor units of cat triceps surae. *The Journal of Physiology*, *196*(3), 605–630. https://doi.org/10.1113/jphysiol.1968.sp008526

Burkitt, A. N. (2006). A review of the integrate-and-fire neuron model: II. inhomogeneous synaptic input and network properties. *Biological Cybernetics*, *95*(2), 97–112. https://doi.org/10.1007/s00422-006-0082-8

Butt, S. J., & Kiehn, O. (2003). Functional identification of interneurons responsible for left-right coordination of hindlimbs in mammals. *Neuron*, *38*(6), 953–963. https://doi.org/10.1016/s0896-6273(03)00353-2

Cadotte, D., Cadotte, A., Cohen-Adad, J., Fleet, D., Livne, M., Wilson, J., Mikulis, D., Nugaeva, N., & Fehlings, M. (2014). Characterizing the location of spinal and vertebral levels in the human cervical spinal cord. *American Journal of Neuroradiology*, *36*(4), 803–810. https://doi.org/10.3174/ajnr.a4192

Calancie, B., Broton, J. G., Klose, K. J., Traad, M., Difini, J., & Ayyar, D. R. (1993). Evidence that alterations in presynaptic inhibition contribute to segmental hypo- and hyperexcitability after spinal cord injury in man. *Electroencephalography and Clinical Neuro-*

physiology/Evoked Potentials Section, *89*(3), 177–186. https://doi.org/10.1016/0168-5597(93)90131-8

Canbay, S., Gürer, B., Bozkurt, M., Comert, A., Izci, Y., & Başkaya, M. K. (2014). Anatomical relationship and positions of the lumbar and sacral segments of the spinal cord according to the vertebral bodies and the spinal roots. *Clinical Anatomy*, *27*(2), 227–233. https://doi.org/https://doi.org/10.1002/ca.22253

Cangiano, L., & Grillner, S. (2003). Fast and slow locomotor burst generation in the hemispinal cord of the lamprey [PMID: 12611971]. *Journal of Neurophysiology*, *89*(6), 2931–2942. https://doi.org/10.1152/jn.01100.2002

Cangiano, L., & Grillner, S. (2005). Mechanisms of rhythm generation in a spinal locomotor network deprived of crossed connections: the lamprey hemicord. *Journal of Neuroscience*, *25*(4), 923–935. https://doi.org/10.1523/JNEUROSCI.2301-04.2005

Capaday, C., & Stein, R. (1986). Amplitude modulation of the soleus h-reflex in the human during walking and standing. *The Journal of Neuroscience*, *6*(5), 1308–1313. https://doi.org/10.1523/jneurosci.06-05-01308.1986

Capogrosso, M., & Lempka, S. F. (2020). A computational outlook on neurostimulation. *Bioelectronic Medicine*, *6*(1). https://doi.org/10.1186/s42234-020-00047-3

Capogrosso, M., Milekovic, T., Borton, D., Wagner, F., Moraud, E. M., Mignardot, J.-B., Buse, N., Gandar, J., Barraud, Q., Xing, D., Rey, E., Duis, S., Jianzhong, Y., Ko, W. K. D., Li, Q., Detemple, P., Denison, T., Micera, S., Bezard, E., … Courtine, G. (2016). A brain–spine interface alleviating gait deficits after spinal cord injury in primates. *Nature*, *539*(7628), 284–288. https://doi.org/10.1038/nature20118

Capogrosso, M., Wagner, F. B., Gandar, J., Moraud, E. M., Wenger, N., Milekovic, T., Shkorbatova, P., Pavlova, N., Musienko, P., Bezard, E., Bloch, J., & Courtine, G. (2018). Configuration of electrical spinal cord stimulation through real-time processing of gait kinematics. *Nature Protocols*, *13*(9), 2031–2061. https://doi.org/10.1038/s41596-018-0030-9

Capogrosso, M., Wenger, N., Raspopovic, S., Musienko, P., Beauparlant, J., Bassi Luciani, L., Courtine, G., & Micera, S. (2013). A computational model for epidural electrical stimulation of spinal sensorimotor circuits. *Journal of Neuroscience*, *33*(49), 19326–19340. https://doi.org/10.1523/JNEUROSCI.1688-13.2013

Cappellini, G., Ivanenko, Y. P., Dominici, N., Poppele, R. E., & Lacquaniti, F. (2010). Migration of motor pool activity in the spinal cord reflects body mechanics in human locomotion [PMID: 20881204]. *Journal of Neurophysiology*, *104*(6), 3064–3073. https://doi.org/10.1152/jn.00318.2010

Carhart, M. R., Jiping He, Herman, R., D'Luzansky, S., & Willis, W. T. (2004). Epidural spinal-cord stimulation facilitates recovery of functional walking following incomplete spinal-cord injury. *IEEE Transactions on Neural Systems and Rehabilitation Engineering*, *12*(1), 32–42. https://doi.org/10.1109/TNSRE.2003.822763

Carlozzi, N. E., Fyffe, D., Morin, K. G., Byrne, R., Tulsky, D. S., Victorson, D., Lai, J.-S., & Wecht, J. M. (2013). Impact of blood pressure dysregulation on health-related quality of life in persons with spinal cord injury: development of a conceptual model. *Archives of*

Physical Medicine and Rehabilitation, *94*(9), 1721–1730. https://doi.org/10.1016/j.apmr.2013.02.024

Chapleau, M. W., Li, Z., Meyrelles, S. S., Ma, X., & Abboud, F. M. (2006). Mechanisms determining sensitivity of baroreceptor afferents in health and disease. *Annals of the New York Academy of Sciences*, *940*(1), 1–19. https://doi.org/10.1111/j.1749-6632.2001.tb03662.x

Chau, C., Barbeau, H., & Rossignol, S. (1998). Early locomotor training with clonidine in spinal cats. *Journal of Neurophysiology*, *79*(1), 392–409. https://doi.org/10.1152/jn.1998.79.1.392

Chen, C.-L., Yeung, K.-T., Bih, L.-I., Wang, C.-H., Chen, M.-I., & Chien, J.-C. (2003). The relationship between sitting stability and functional performance in patients with paraplegia11no commercial party having a direct financial interest in the results of the research supporting this article has or will confer a benefit upon the author(s) or upon any organization with which the author(s) is/are associated. *Archives of Physical Medicine and Rehabilitation*, *84*(9), 1276–1281. https://doi.org/https://doi.org/10.1016/S0003-9993(03)00200-4

Coburn, B. (1985). A theoretical study of epidural electrical stimulation of the spinal cord - part II: effects on long myelinated fibers. *IEEE Transactions on Biomedical Engineering*, *BME-32*(11), 978–986. https://doi.org/10.1109/tbme.1985.325649

Coburn, B., & Sin, W. K. (1985). A theoretical study of epidural electrical stimulation of the spinal cord part i: finite element analysis of stimulus fields. *IEEE Transactions on Biomedical Engineering*, *BME-32*(11), 971–977. https://doi.org/10.1109/tbme.1985.325648

Cohen-Adad, J., Gauthier, C., Brooks, J., Leblond, H., Fisher, J., Beaumont, E., Dubeau, S., Lesage, F., Doyon, J., Benali, H., & Rossignol, S. (2009). Venous effect in spinal cord fmri: insights from intrinsic optical imaging and laser speckle. *Neuroimage*, *47*. https://doi.org/10.1016/S1053-8119(09)72063-4

Cole, J. (1995). *Pride and a daily marathon* (1st MIT Press ed). MIT Press.

Collins, W. F., Honig, M. G., & Mendell, L. M. (1984). Heterogeneity of group ia synapses on homonymous alpha-motoneurons as revealed by high-frequency stimulation of ia afferent fibers. *Journal of Neurophysiology*, *52*(5), 980–993. https://doi.org/10.1152/jn.1984.52.5.980

Cook, A. W. (1976). Electrical stimulation in multiple sclerosis. *Hospital Practice*, *11*(4), 51–58. https://doi.org/10.1080/21548331.1976.11706516

Côté, M.-P., Murray, M., & Lemay, M. A. (2017). Rehabilitation strategies after spinal cord injury: inquiry into the mechanisms of success and failure [PMID: 27762657]. *Journal of Neurotrauma*, *34*(10), 1841–1857. https://doi.org/10.1089/neu.2016.4577

Courtine, G., De Nunzio, A. M., Schmid, M., Beretta, M. V., & Schieppati, M. (2007). Stance- and locomotion-dependent processing of vibration-induced proprioceptive inflow from multiple muscles in humans [PMID: 17065250]. *Journal of Neurophysiology*, *97*(1), 772–779. https://doi.org/10.1152/jn.00764.2006

Courtine, G., Gerasimenko, Y., van den Brand, R., Yew, A., Musienko, P., Zhong, H., Song, B., Ao, Y., Ichiyama, R. M., Lavrov, I., Roy, R. R., Sofroniew, M. V., & Edgerton, V. R. (2009).

Transformation of nonfunctional spinal circuits into functional states after the loss of brain input (2009/09/20) [nn.2401[PII]]. *Nature neuroscience*, *12*(10), 1333–1342. https://doi.org/10.1038/nn.2401

Courtine, G., & Sofroniew, M. V. (2019). Spinal cord repair: advances in biology and technology. *Nature Medicine*, *25*(6), 898–908. https://doi.org/10.1038/s41591-019-0475-6

Cragg, J. J., Noonan, V. K., Krassioukov, A., & Borisoff, J. (2013). Cardiovascular disease and spinal cord injury: results from a national population health survey. *Neurology*, *81*(8), 723–728. https://doi.org/10.1212/wnl.0b013e3182a1aa68

Danner, S. M., Hofstoetter, U. S., Freundl, B., Binder, H., Mayr, W., Rattay, F., & Minassian, K. (2015). Human spinal locomotor control is based on flexibly organized burst generators. *Brain*, *138*(3), 577–588. https://doi.org/10.1093/brain/awu372

Darrow, D., Balser, D., Netoff, T. I., Krassioukov, A., Phillips, A., Parr, A., & Samadani, U. (2019). Epidural spinal cord stimulation facilitates immediate restoration of dormant motor and autonomic supraspinal pathways after chronic neurologically complete spinal cord injury. *Journal of Neurotrauma*, *36*(15), 2325–2336. https://doi.org/10.1089/neu.2018.6006

De Leener, B., Lévy, S., Dupont, S. M., Fonov, V. S., Stikov, N., Louis Collins, D., Callot, V., & Cohen-Adad, J. (2017). Sct: spinal cord toolbox, an open-source software for processing spinal cord mri data. *NeuroImage*, *145*, 24–43. https://doi.org/https://doi.org/10.1016/j.neuroimage.2016.10.009

Deer, T. R., Mekhail, N., Provenzano, D., Pope, J., Krames, E., Leong, M., Levy, R. M., Abejon, D., Buchser, E., Burton, A., Buvanendran, A., Candido, K., Caraway, D., Cousins, M., DeJongste, M., Diwan, S., Eldabe, S., Gatzinsky, K., Foreman, R. D., … North, R. (2014). The appropriate use of neurostimulation of the spinal cord and peripheral nervous system for the treatment of chronic pain and ischemic diseases: the neuromodulation appropriateness consensus committee. *Neuromodulation: Technology at the Neural Interface*, *17*(6), 515–550. https://doi.org/10.1111/ner.12208

Deisseroth, K. (2010). Optogenetics. *Nature Methods*, *8*(1), 26–29. https://doi.org/10.1038/nmeth.f.324

Deisseroth, K. (2015). Optogenetics: 10 years of microbial opsins in neuroscience. *Nature Neuroscience*, *18*(9), 1213–1225. https://doi.org/10.1038/nn.4091

Delaunois, A., Ron, P. D., Dedoncker, P., Rosseels, M.-L., Cornet, M., Jnoff, E., Hanon, E., Guyaux, M., & Depelchin, B. O. (2013). Advantageous safety profile of a dual selective alpha2cagonist/alpha2aantagonist antinociceptive agent. *Fundamental & Clinical Pharmacology*, *28*(4), 423–438. https://doi.org/10.1111/fcp.12047

de Leon, R. D., Tamaki, H., Hodgson, J. A., Roy, R. R., & Edgerton, V. R. (1999). Hindlimb locomotor and postural training modulates glycinergic inhibition in the spinal cord of the adult spinal cat. *Journal of Neurophysiology*, *82*(1), 359–369. https://doi.org/10.1152/jn.1999.82.1.359

Delp, S. L., Anderson, F. C., Arnold, A. S., Loan, P., Habib, A., John, C. T., Guendelman, E., & Thelen, D. G. (2007). OpenSim: open-source software to create and analyze dynamic simulations of movement. *IEEE Transactions on Biomedical Engineering*, *54*(11), 1940–1950. https://doi.org/10.1109/tbme.2007.901024

Delp, S., Loan, J., Hoy, M., Zajac, F., Topp, E., & Rosen, J. (1990). An interactive graphics-based model of the lower extremity to study orthopaedic surgical procedures. *IEEE Transactions on Biomedical Engineering*, *37*(8), 757–767. https://doi.org/10.1109/10.102791

Dietz, V. (2003). Spinal cord pattern generators for locomotion. *Clinical Neurophysiology*, *114*(8), 1379–1389. https://doi.org/https://doi.org/10.1016/S1388-2457(03)00120-2

Dietz, V., Colombo, G., Jensen, L., & Baumgartner, L. (1995). Locomotor capacity of spinal cord in paraplegic patients. *Annals of Neurology*, *37*(5), 574–582. https://doi.org/10.1002/ana.410370506

Dietz, V. (2002). Proprioception and locomotor disorders. *Nature Reviews Neuroscience*, *3*(10), 781–790. https://doi.org/10.1038/nrn939

Dietz, V. (2010). Behavior of spinal neurons deprived of supraspinal input. *Nature Reviews Neurology*, *6*(3), 167–174. https://doi.org/10.1038/nrneurol.2009.227

Dietz, V., & Duysens, J. (2000). Significance of load receptor input during locomotion: a review. *Gait & Posture*, *11*(2), 102–110. https://doi.org/10.1016/s0966-6362(99)00052-1

Dimitrijevic, M. R., Gerasimenko, Y., & Pinter, M. M. (1998). Evidence for a spinal central pattern generator in humansa. *Annals of the New York Academy of Sciences*, *860*(1), 360–376. https://doi.org/https://doi.org/10.1111/j.1749-6632.1998.tb09062.x

Dimitrijevic, M., Dimitrijevic, M., Illis, L., Nakajima, K., Sharkey, P., & Sherwood, A. (1986). Spinal cord stimulation for the control of spasticity in patients with chronic spinal cord injury: i. clinical observations. *Central Nervous System Trauma*, *3*(2), 129–143. https://doi.org/10.1089/cns.1986.3.129

Dittuno, P. L., & Dittuno Jr, J. F. (2001). Walking index for spinal cord injury (wisci ii): scale revision. *Spinal Cord*, *39*(12), 654–656. https://doi.org/10.1038/sj.sc.3101223

Dominici, N., Ivanenko, Y. P., Cappellini, G., d'Avella, A., Mondı, V., Cicchese, M., Fabiano, A., Silei, T., Di Paolo, A., Giannini, C., Poppele, R. E., & Lacquaniti, F. (2011). Locomotor primitives in newborn babies and their development. *Science*, *334*(6058), 997–999. https://doi.org/10.1126/science.1210617

Dominici, N., Keller, U., Vallery, H., Friedli, L., van den Brand, R., Starkey, M. L., Musienko, P., Riener, R., & Courtine, G. (2012). Versatile robotic interface to evaluate, enable and train locomotion and balance after neuromotor disorders. *Nature Medicine*, *18*(7), 1142–1147. https://doi.org/10.1038/nm.2845

Drew, T. (1993). Motor cortical activity during voluntary gait modifications in the cat. i. cells related to the forelimbs. *Journal of Neurophysiology*, *70*(1), 179–199. https://doi.org/10.1152/jn.1993.70.1.179

Drew, T., Jiang, W., Kably, B., & Lavoie, S. (1996). Role of the motor cortex in the control of visually triggered gait modifications. *Canadian Journal of Physiology and Pharmacology*, *74*(4), 426–442. https://doi.org/10.1139/y96-043

Drew, T., Andujar, J.-E., Lajoie, K., & Yakovenko, S. (2008). Cortical mechanisms involved in visuomotor coordination during precision walking. *Brain Research Reviews*, *57*(1), 199–211. https://doi.org/10.1016/j.brainresrev.2007.07.017

Drew, T., & Marigold, D. S. (2015). Taking the next step: cortical contributions to the control of locomotion [Motor circuits and action]. *Current Opinion in Neurobiology*, *33*, 25–33. https://doi.org/https://doi.org/10.1016/j.conb.2015.01.011

Dubuc, R., Brocard, F., Antri, M., Fénelon, K., Gariépy, J.-F., Smetana, R., Ménard, A., Le Ray, D., Viana Di Prisco, G., Pearlstein, É., Sirota, M. G., Derjean, D., St-Pierre, M., Zielinski, B., Auclair, F., & Veilleux, D. (2008). Initiation of locomotion in lampreys [Networks in Motion]. *Brain Research Reviews*, *57*(1), 172–182. https://doi.org/https://doi.org/10.1016/j.brainresrev.2007.07.016

Duffell, L. D., & de Neufvillle Donaldson, N. (2020). A comparison of FES and SCS for neuroplastic recovery after SCI: historical perspectives and future directions. *Frontiers in Neurology*, *11*. https://doi.org/10.3389/fneur.2020.00607

Duysens, J., Tax, A., Nawijn, S., Berger, W., Prokop, T., & Altenmller, E. (1990). Gating of sensation and evoked potentials following foot stimulation during human gait. *Experimental Brain Research*, *105*(3). https://doi.org/10.1007/bf00233042

Dy, C. J., Gerasimenko, Y. P., Edgerton, V. R., Dyhre-Poulsen, P., Courtine, G., & Harkema, S. J. (2010). Phase-dependent modulation of percutaneously elicited multisegmental muscle responses after spinal cord injury. *Journal of Neurophysiology*, *103*(5), 2808–2820. https://doi.org/10.1152/jn.00316.2009

Edgerton, V. R., Courtine, G., Gerasimenko, Y. P., Lavrov, I., Ichiyama, R. M., Fong, A. J., Cai, L. L., Otoshi, C. K., Tillakaratne, N. J., Burdick, J. W., & Roy, R. R. (2008). Training locomotor networks. *Brain Research Reviews*, *57*(1), 241–254. https://doi.org/10.1016/j.brainresrev.2007.09.002

Edgerton, V. R., Kim, S. J., Ichiyama, R. M., Gerasimenko, Y. P., & Roy, R. R. (2006). Rehabilitative therapies after spinal cord injury. *Journal of Neurotrauma*, *23*(3-4), 560–570. https://doi.org/10.1089/neu.2006.23.560

Edgerton, V. R., Tillakaratne, N. J., Bigbee, A. J., de Leon, R. D., & Roy, R. R. (2004). PLASTICITY OF THE SPINAL NEURAL CIRCUITRY AFTER INJURY. *Annual Review of Neuroscience*, *27*(1), 145–167. https://doi.org/10.1146/annurev.neuro.27.070203.144308

Edgerton, V. R., & Harkema, S. (2011). Epidural stimulation of the spinal cord in spinal cord injury: current status and future challenges [PMC3361963[pmcid]]. *Expert review of neurotherapeutics*, *11*(10), 1351–1353. https://doi.org/10.1586/ern.11.129

Eippert, F., Kong, Y., Jenkinson, M., Tracey, I., & Brooks, J. C. (2017). Denoising spinal cord fmri data: approaches to acquisition and analysis [Cleaning up the fMRI time series: Mitigating noise with advanced acquisition and correction strategies]. *NeuroImage*, *154*, 255–266. https://doi.org/https://doi.org/10.1016/j.neuroimage.2016.09.065

Famm, K., Litt, B., Tracey, K. J., Boyden, E. S., & Slaoui, M. (2013). A jump-start for electroceuticals. *Nature*, *496*(7444), 159–161. https://doi.org/10.1038/496159a

Field-Fote, E. C., Lindley, S. D., & Sherman, A. L. (2005). Locomotor training approaches for individuals with spinal cord injury: a preliminary report of walking-related outcomes.

Journal of neurologic physical therapy : JNPT, *29*(3), 127–137. https://doi.org/10.1097/01.npt.0000282245.31158.09

Field-Fote, E. C., & Roach, K. E. (2011). Influence of a locomotor training approach on walking speed and distance in people with chronic spinal cord injury: a randomized clinical trial (2010/11/04) [ptj.20090359[PII]]. *Physical therapy*, *91*(1), 48–60. https://doi.org/10.2522/ptj.20090359

Fleshman, J., Lev-Tov, A., & Burke, R. (1984). Peripheral and central control of flexor digitorum longus and flexor hallucis longus motoneurons: the synaptic basis of functional diversity. *Experimental Brain Research*, *54*(1). https://doi.org/10.1007/bf00235825

Formento, E., Minassian, K., Wagner, F., Mignardot, J. B., Le Goff-Mignardot, C. G., Rowald, A., Bloch, J., Micera, S., Capogrosso, M., & Courtine, G. (2018). Electrical spinal cord stimulation must preserve proprioception to enable locomotion in humans with spinal cord injury. *Nature Neuroscience*, *21*(12), 1728–1741. https://doi.org/10.1038/s41593-018-0262-6

Forssberg, H., & Grillner, S. (1973). The locomotion of the acute spinal cat injected with clonidine i.v. *Brain Research*, *50*(1), 184–186. https://doi.org/10.1016/0006-8993(73)90606-9

Frankemolle, A. M. M., Wu, J., Noecker, A. M., Voelcker-Rehage, C., Ho, J. C., Vitek, J. L., McIntyre, C. C., & Alberts, J. L. (2010). Reversing cognitive–motor impairments in parkinson's disease patients using a computational modelling approach to deep brain stimulation programming. *Brain*, *133*(3), 746–761. https://doi.org/10.1093/brain/awp315

Frey, H. (1930). Zur frage der variationen der wirbelsäule als ursache klinischer erscheinungen [cited By 1]. *Zbl. Chir.*, *57*, 2898–2903.

Freyvert, Y., Yong, N. A., Morikawa, E., Zdunowski, S., Sarino, M. E., Gerasimenko, Y., Edgerton, V. R., & Lu, D. C. (2018). Engaging cervical spinal circuitry with non-invasive spinal stimulation and buspirone to restore hand function in chronic motor complete patients. *Scientific Reports*, *8*(1). https://doi.org/10.1038/s41598-018-33123-5

Frostell, A., Hakim, R., Thelin, E. P., Mattsson, P., & Svensson, M. (2016). A review of the segmental diameter of the healthy human spinal cord. *Frontiers in Neurology*, *7*. https://doi.org/10.3389/fneur.2016.00238

Furlan, J. C., Fehlings, M. G., Shannon, P., Norenberg, M. D., & Krassioukov, A. V. (2003). Descending vasomotor pathways in humans: correlation between axonal preservation and cardiovascular dysfunction after spinal cord injury. *Journal of Neurotrauma*, *20*(12), 1351–1363. https://doi.org/10.1089/089771503322686148

Gaines, J. L., Finn, K. E., Slopsema, J. P., Heyboer, L. A., & Polasek, K. H. (2018). A model of motor and sensory axon activation in the median nerve using surface electrical stimulation. *Journal of Computational Neuroscience*, *45*(1), 29–43. https://doi.org/10.1007/s10827-018-0689-5

Gerasimenko, Y., Roy, R. R., & Edgerton, V. R. (2008). Epidural stimulation: comparison of the spinal circuits that generate and control locomotion in rats, cats and humans

(2007/08/01) [S0014-4886(07)00292-0[PII]]. *Experimental neurology*, *209*(2), 417–425. https://doi.org/10.1016/j.expneurol.2007.07.015

Gerasimenko, Y. P., Lavrov, I. A., Courtine, G., Ichiyama, R. M., Dy, C. J., Zhong, H., Roy, R. R., & Edgerton, V. R. (2006). Spinal cord reflexes induced by epidural spinal cord stimulation in normal awake rats. *Journal of Neuroscience Methods*, *157*(2), 253–263. https://doi.org/https://doi.org/10.1016/j.jneumeth.2006.05.004

Gerasimenko, Y. P., Lu, D. C., Modaber, M., Zdunowski, S., Gad, P., Sayenko, D. G., Morikawa, E., Haakana, P., Ferguson, A. R., Roy, R. R., & Edgerton, V. R. (2015). Noninvasive reactivation of motor descending control after paralysis [PMID: 26077679]. *Journal of Neurotrauma*, *32*(24), 1968–1980. https://doi.org/10.1089/neu.2015.4008

Gill, M., Linde, M., Fautsch, K., Hale, R., Lopez, C., Veith, D., Calvert, J., Beck, L., Garlanger, K., Edgerton, R., Sayenko, D., Lavrov, I., Thoreson, A., Grahn, P., & Zhao, K. (2020). Epidural electrical stimulation of the lumbosacral spinal cord improves trunk stability during seated reaching in two humans with severe thoracic spinal cord injury. *Frontiers in Systems Neuroscience*, *14*, 79. https://doi.org/10.3389/fnsys.2020.569337

Gill, M. L., Grahn, P. J., Calvert, J. S., Linde, M. B., Lavrov, I. A., Strommen, J. A., Beck, L. A., Sayenko, D. G., Van Straaten, M. G., Drubach, D. I., Veith, D. D., Thoreson, A. R., Lopez, C., Gerasimenko, Y. P., Edgerton, V. R., Lee, K. H., & Zhao, K. D. (2018). Neuromodulation of lumbosacral spinal networks enables independent stepping after complete paraplegia. *Nature Medicine*, *24*(11), 1677–1682. https://doi.org/10.1038/s41591-018-0175-7

Girgis, J., Merrett, D., Kirkland, S., Metz, G. A. S., Verge, V., & Fouad, K. (2007). Reaching training in rats with spinal cord injury promotes plasticity and task specific recovery. *Brain*, *130*(11), 2993–3003. https://doi.org/10.1093/brain/awm245

Goldberger, M. E. (1977). Locomotor recovery after unilateral hindlimb deafferentation in cats. *Brain Research*, *123*(1), 59–74. https://doi.org/10.1016/0006-8993(77)90643-6

Gomes-Osman, J., & Field-Fote, E. C. (2013). Bihemispheric anodal corticomotor stimulation using transcranial direct current stimulation improves bimanual typing task performance. *Journal of Motor Behavior*, *45*(4), 361–367. https://doi.org/10.1080/00222895.2013.808604

Gomes-Osman, J., & Field-Fote, E. C. (2015). Improvements in hand function in adults with chronic tetraplegia following a multiday 10-hz repetitive transcranial magnetic stimulation intervention combined with repetitive task practice. *Journal of Neurologic Physical Therapy*, *39*(1), 23–30. https://doi.org/10.1097/npt.0000000000000062

Gomez-Perez, S. L., Haus, J. M., Sheean, P., Patel, B., Mar, W., Chaudhry, V., McKeever, L., & Braunschweig, C. (2016). Measuring abdominal circumference and skeletal muscle from a single cross-sectional computed tomography image. *Journal of Parenteral and Enteral Nutrition*, *40*(3), 308–318. https://doi.org/https://doi.org/10.1177/0148607115604149

Gong, S., Zheng, C., Doughty, M. L., Losos, K., Didkovsky, N., Schambra, U. B., Nowak, N. J., Joyner, A., Leblanc, G., Hatten, M. E., & Heintz, N. (2003). A gene expression atlas of the central nervous system based on bacterial artificial chromosomes. *Nature*, *425*(6961), 917–925. https://doi.org/10.1038/nature02033

Goodpaster, B. H., Kelley, D. E., Thaete, F. L., He, J., & Ross, R. (2000). Skeletal muscle attenuation determined by computed tomography is associated with skeletal muscle lipid content [PMID: 10904041]. *Journal of Applied Physiology*, *89*(1), 104–110. https://doi.org/10.1152/jappl.2000.89.1.104

Goulding, M. (2009). Circuits controlling vertebrate locomotion: moving in a new direction. *Nature Reviews Neuroscience*, *10*(7), 507–518. https://doi.org/10.1038/nrn2608

Gourab, K., & Schmit, B. D. (2010). Changes in movement-related β-band eeg signals in human spinal cord injury. *Clinical Neurophysiology*, *121*(12), 2017–2023. https://doi.org/https://doi.org/10.1016/j.clinph.2010.05.012

Grahn, P. J., Lavrov, I. A., Sayenko, D. G., Van Straaten, M. G., Gill, M. L., Strommen, J. A., Calvert, J. S., Drubach, D. I., Beck, L. A., Linde, M. B., Thoreson, A. R., Lopez, C., Mendez, A. A., Gad, P. N., Gerasimenko, Y. P., Edgerton, V. R., Zhao, K. D., & Lee, K. H. (2017). Enabling task-specific volitional motor functions via spinal cord neuromodulation in a human with paraplegia. *Mayo Clinic Proceedings*, *92*(4), 544–554. https://doi.org/https://doi.org/10.1016/j.mayocp.2017.02.014

Greiner, N., Barra, B., Schiavone, G., Lorach, H., James, N., Conti, S., Kaeser, M., Fallegger, F., Borgognon, S., Lacour, S., Bloch, J., Courtine, G., & Capogrosso, M. (2021). Recruitment of upper-limb motoneurons with epidural electrical stimulation of the cervical spinal cord. *Nature Communications*, *12*(1), 435. https://doi.org/10.1038/s41467-020-20703-1

Grillner, S. (1981). Control of locomotion in bipeds, tetrapods, and fish. https://doi.org/10.1002/cphy.cp010226

Grillner, S. (2003). The motor infrastructure: from ion channels to neuronal networks. *Nature Reviews Neuroscience*, *4*(7), 573–586. https://doi.org/10.1038/nrn1137

Grillner, S. (2011). Human locomotor circuits conform. *Science*, *334*(6058), 912–913. https://doi.org/10.1126/science.1214778

Grillner, S., & Robertson, B. (2015). The basal ganglia downstream control of brainstem motor centres—an evolutionarily conserved strategy [Motor circuits and action]. *Current Opinion in Neurobiology*, *33*, 47–52. https://doi.org/https://doi.org/10.1016/j.conb.2015.01.019

Gros, C., De Leener, B., Badji, A., Maranzano, J., Eden, D., Dupont, S. M., Talbott, J., Zhuoquiong, R., Liu, Y., Granberg, T., Ouellette, R., Tachibana, Y., Hori, M., Kamiya, K., Chougar, L., Stawiarz, L., Hillert, J., Bannier, E., Kerbrat, A., … Cohen-Adad, J. (2019). Automatic segmentation of the spinal cord and intramedullary multiple sclerosis lesions with convolutional neural networks. *NeuroImage*, *184*, 901–915. https://doi.org/https://doi.org/10.1016/j.neuroimage.2018.09.081

Gros, C., De Leener, B., Dupont, S. M., Martin, A. R., Fehlings, M. G., Bakshi, R., Tummala, S., Auclair, V., McLaren, D. G., Callot, V., Cohen-Adad, J., & Sdika, M. (2018). Automatic spinal cord localization, robust to mri contrasts using global curve optimization.

Medical Image Analysis, *44*, 215–227. https://doi.org/https://doi.org/10.1016/j.media.2017.12.001

Grossmann, K. S., Giraudin, A., Britz, O., Zhang, J., & Goulding, M. (2010). Genetic dissection of rhythmic motor networks in mice. *Breathe, walk and chew: the neural challenge: part i* (pp. 19–37). Elsevier. https://doi.org/10.1016/b978-0-444-53613-6.00002-2

Gu, Z., Kalambogias, J., Yoshioka, S., Han, W., Li, Z., Kawasawa, Y. I., Pochareddy, S., Li, Z., Liu, F., Xu, X., Wijeratne, H. R. S., Ueno, M., Blatz, E., Salomone, J., Kumanogoh, A., Rasin, M.-R., Gebelein, B., Weirauch, M. T., Sestan, N., … Yoshida, Y. (2017). Control of species-dependent cortico-motoneuronal connections underlying manual dexterity. *Science*, *357*(6349), 400–404. https://doi.org/10.1126/science.aan3721

Hägglund, M., Borgius, L., Dougherty, K. J., & Kiehn, O. (2010). Activation of groups of excitatory neurons in the mammalian spinal cord or hindbrain evokes locomotion. *Nature Neuroscience*, *13*(2), 246–252. https://doi.org/10.1038/nn.2482

Hägglund, M., Dougherty, K. J., Borgius, L., Itohara, S., Iwasato, T., & Kiehn, O. (2013). Optogenetic dissection reveals multiple rhythmogenic modules underlying locomotion. *Proceedings of the National Academy of Sciences*, *110*(28), 11589–11594. https://doi.org/10.1073/pnas.1304365110

Han, J., Waddington, G., Adams, R., Anson, J., & Liu, Y. (2016). Assessing proprioception: a critical review of methods. *Journal of Sport and Health Science*, *5*(1), 80–90. https://doi.org/10.1016/j.jshs.2014.10.004

Handbook of physiology : a critical, comprehensive presentation of physiological knowledge and concepts. (1977). American Physiological Society Distributed by Williams & Wilkins.

Häring, M., Zeisel, A., Hochgerner, H., Rinwa, P., Jakobsson, J. E. T., Lönnerberg, P., Manno, G. L., Sharma, N., Borgius, L., Kiehn, O., Lagerström, M. C., Linnarsson, S., & Ernfors, P. (2018). Neuronal atlas of the dorsal horn defines its architecture and links sensory input to transcriptional cell types. *Nature Neuroscience*, *21*(6), 869–880. https://doi.org/10.1038/s41593-018-0141-1

Harkema, S., Gerasimenko, Y., Hodes, J., Burdick, J., Angeli, C., Chen, Y., Ferreira, C., Willhite, A., Rejc, E., Grossman, R. G., & Edgerton, V. R. (2011). Effect of epidural stimulation of the lumbosacral spinal cord on voluntary movement, standing, and assisted stepping after motor complete paraplegia: a case study. *The Lancet*, *377*(9781), 1938–1947. https://doi.org/10.1016/S0140-6736(11)60547-3

Harkema, S. J., Ditterline, B. L., Wang, S., Aslan, S., Angeli, C. A., Ovechkin, A., & Hirsch, G. A. (2018). Epidural spinal cord stimulation training and sustained recovery of cardiovascular function in individuals with chronic cervical spinal cord injury. *JAMA Neurology*, *75*(12), 1569. https://doi.org/10.1001/jamaneurol.2018.2617

Harkema, S. J., Schmidt-Read, M., Lorenz, D. J., Edgerton, V. R., & Behrman, A. L. (2012). Balance and ambulation improvements in individuals with chronic incomplete spinal cord injury using locomotor training–based rehabilitation. *Archives of Physical Medicine and Rehabilitation*, *93*(9), 1508–1517. https://doi.org/10.1016/j.apmr.2011.01.024

Harkema, S. J., Wang, S., Angeli, C. A., Chen, Y., Boakye, M., Ugiliweneza, B., & Hirsch, G. A. (2018). Normalization of blood pressure with spinal cord epidural stimulation after severe spinal cord injury. *Frontiers in Human Neuroscience, 12.* https://doi.org/10.3389/fnhum.2018.00083

Harrison, P. J., & Taylor, A. (1981). Individual excitatory post-synaptic potentials due to muscle spindle ia afferents in cat triceps surae motoneurones. *The Journal of Physiology, 312*(1), 455–470. https://doi.org/10.1113/jphysiol.1981.sp013638

Hay, M., Thomas, D. W., Craighead, J. L., Economides, C., & Rosenthal, J. (2014). Clinical development success rates for investigational drugs. *Nature Biotechnology, 32*(1), 40–51. https://doi.org/10.1038/nbt.2786

Hein, L., Altman, J. D., & Kobilka, B. K. (1999). Two functionally distinct α2-adrenergic receptors regulate sympathetic neurotransmission. *Nature, 402*(6758), 181–184. https://doi.org/10.1038/46040

Hentall, I. D., & Gonzalez, M. M. C. (2011). Promotion of recovery from thoracic spinal cord contusion in rats by stimulation of medullary raphe or its midbrain input. *Neurorehabilitation and Neural Repair, 26*(4), 374–384. https://doi.org/10.1177/1545968311425178

Herman, R., He, J., D'Luzansky, S., Willis, W., & Dilli, S. (2002). Spinal cord stimulation facilitates functional walking in a chronic, incomplete spinal cord injured. *Spinal Cord, 40*(2), 65–68. https://doi.org/10.1038/sj.sc.3101263

Herrity, A. N., Williams, C. S., Angeli, C. A., Harkema, S. J., & Hubscher, C. H. (2018). Lumbosacral spinal cord epidural stimulation improves voiding function after human spinal cord injury [PMC5989228[pmcid]]. *Scientific reports, 8*(1), 8688–8688. https://doi.org/10.1038/s41598-018-26602-2

Hines, M. L., & Carnevale, N. T. (1997). The NEURON Simulation Environment. *Neural Computation, 9*(6), 1179–1209. https://doi.org/10.1162/neco.1997.9.6.1179

Hines, M. L., & Carnevale, N. T. (2001). Neuron: a tool for neuroscientists [PMID: 11496923]. *The Neuroscientist, 7*(2), 123–135. https://doi.org/10.1177/107385840100700207

Hnk, P., & lessler, M. J. (1973). Changes in muscle spindle activity of the chronically de-efferented gastrocnemius of the rat. *Pflgers Archiv European Journal of Physiology, 341*(2), 155–170. https://doi.org/10.1007/bf00587322

Ho, C. H., Triolo, R. J., Elias, A. L., Kilgore, K. L., DiMarco, A. F., Bogie, K., Vette, A. H., Audu, M. L., Kobetic, R., Chang, S. R., Chan, K. M., Dukelow, S., Bourbeau, D. J., Brose, S. W., Gustafson, K. J., Kiss, Z. H., & Mushahwar, V. K. (2014). Functional electrical stimulation and spinal cord injury. *Physical Medicine and Rehabilitation Clinics of North America, 25*(3), 631–654. https://doi.org/10.1016/j.pmr.2014.05.001

Hofstoetter, U. S., Freundl, B., Binder, H., & Minassian, K. (2018). Common neural structures activated by epidural and transcutaneous lumbar spinal cord stimulation: elicitation of posterior root-muscle reflexes (N. Weidner, Ed.). *PLOS ONE, 13*(1), e0192013. https://doi.org/10.1371/journal.pone.0192013

Hofstoetter, U. S., Krenn, M., Danner, S. M., Hofer, C., Kern, H., McKay, W. B., Mayr, W., & Minassian, K. (2015). Augmentation of voluntary locomotor activity by transcutaneous spinal cord stimulation in motor-incomplete spinal cord-injured individuals. *Artificial Organs, 39*(10), E176–E186. https://doi.org/10.1111/aor.12615

Holsheimer, J. (2002). Which neuronal elements are activated directly by spinal cord stimulation. *Neuromodulation: Technology at the Neural Interface*, *5*(1), 25–31. https://doi.org/10.1046/j.1525-1403.2002._2005.x

Holtmaat, A., & Svoboda, K. (2009). Experience-dependent structural synaptic plasticity in the mammalian brain. *Nature Reviews Neuroscience*, *10*(9), 647–658. https://doi.org/10.1038/nrn2699

Howell, B., Lad, S. P., & Grill, W. M. (2014). Evaluation of intradural stimulation efficiency and selectivity in a computational model of spinal cord stimulation. *PLOS ONE*, *9*(12), 1–25. https://doi.org/10.1371/journal.pone.0114938

Howells, D. W., Sena, E. S., & Macleod, M. R. (2013). Bringing rigour to translational medicine. *Nature Reviews Neurology*, *10*(1), 37–43. https://doi.org/10.1038/nrneurol.2013.232

Howells, J., Trevillion, L., Bostock, H., & Burke, D. (2012). The voltage dependence ofIhin human myelinated axons. *The Journal of Physiology*, *590*(7), 1625–1640. https://doi.org/10.1113/jphysiol.2011.225573

Huang, H., He, J., Herman, R., & Carhart, M. (2006). Modulation effects of epidural spinal cord stimulation on muscle activities during walking. *IEEE Transactions on Neural Systems and Rehabilitation Engineering*, *14*(1), 14–23. https://doi.org/10.1109/tnsre.2005.862694

Hultborn, H. (1976). Transmission in the pathway of reciprocal ia inhibition to motoneurones and its control during the tonic stretch reflex. *Progress in brain research* (pp. 235–255). Elsevier. https://doi.org/10.1016/s0079-6123(08)60736-0

Hultborn, H., Jankowska, E., & Lindström, S. (1971). Recurrent inhibition of interneurones monosynaptically activated from group ia afferents. *The Journal of Physiology*, *215*(3), 613–636. https://doi.org/10.1113/jphysiol.1971.sp009488

Hultborn, H., & Nielsen, J. B. (2007). Spinal control of locomotion ? from cat to man. *Acta Physiologica*, *189*(2), 111–121. https://doi.org/10.1111/j.1748-1716.2006.01651.x

Hultborn, H. (2003). Changes in neuronal properties and spinal reflexes during development of spasticity following spinal cord lesions and stroke: studies in animal models and patients. *Journal of Rehabilitation Medicine*, *35*(0), 46–55. https://doi.org/10.1080/16501960310010142

Hunter, J. P., & Ashby, P. (1994). Segmental effects of epidural spinal cord stimulation in humans. *The Journal of Physiology*, *474*(3), 407–419. https://doi.org/10.1113/jphysiol.1994.sp020032

Hutson, T. H., Kathe, C., Palmisano, I., Bartholdi, K., Hervera, A., Virgiliis, F. D., McLachlan, E., Zhou, L., Kong, G., Barraud, Q., Danzi, M. C., Medrano-Fernandez, A., Lopez-Atalaya, J. P., Boutillier, A. L., Sinha, S. H., Singh, A. K., Chaturbedy, P., Moon, L. D. F., Kundu, T. K., … Giovanni, S. D. (2019). Cbp-dependent histone acetylation mediates axon regeneration induced by environmental enrichment in rodent spinal cord injury models. *Science Translational Medicine*, *11*(487), eaaw2064. https://doi.org/10.1126/scitranslmed.aaw2064

Ichiyama, R. M., Courtine, G., Gerasimenko, Y. P., Yang, G. J., van den Brand, R., Lavrov, I. A., Zhong, H., Roy, R. R., & Edgerton, V. R. (2008). Step training reinforces specific spinal locomotor circuitry in adult spinal rats. *Journal of Neuroscience*, *28*(29), 7370–7375. https://doi.org/10.1523/JNEUROSCI.1881-08.2008

Illman, A., Stiller, K., & Williams, M. (2000). The prevalence of orthostatic hypotension during physiotherapy treatment in patients with an acute spinal cord injury. *Spinal Cord*, *38*(12), 741–747. https://doi.org/10.1038/sj.sc.3101089

Inanici, F., Samejima, S., Gad, P., Edgerton, V. R., Hofstetter, C. P., & Moritz, C. T. (2018). Transcutaneous electrical spinal stimulation promotes long-term recovery of upper extremity function in chronic tetraplegia. *IEEE Transactions on Neural Systems and Rehabilitation Engineering*, *26*(6), 1272–1278. https://doi.org/10.1109/tnsre.2018.2834339

Inoue, T., Manley, G. T., Patel, N., & Whetstone, W. D. (2014). Medical and surgical management after spinal cord injury: vasopressor usage, early surgerys, and complications. *Journal of Neurotrauma*, *31*(3), 284–291. https://doi.org/10.1089/neu.2013.3061

Ishikawa, K., Ott, K., Porter, R. W., & Stuart, D. (1966). Low frequency depression of the h wave in normal and spinal man. *Experimental Neurology*, *15*(1), 140–156. https://doi.org/10.1016/0014-4886(66)90039-2

Jackson, A., & Zimmermann, J. B. (2012). Neural interfaces for the brain and spinal cord—restoring motor function. *Nature Reviews Neurology*, *8*(12), 690–699. https://doi.org/10.1038/nrneurol.2012.219

James, N. D., McMahon, S. B., Field-Fote, E. C., & Bradbury, E. J. (2018). Neuromodulation in the restoration of function after spinal cord injury. *The Lancet Neurology*, *17*(10), 905–917. https://doi.org/10.1016/s1474-4422(18)30287-4

Jankowska, E., Krutki, P., & Matsuyama, K. (2005). Relative contribution of ia inhibitory interneurones to inhibition of feline contralateral motoneurones evoked via commissural interneurones. *The Journal of Physiology*, *568*(2), 617–628. https://doi.org/10.1113/jphysiol.2005.088351

Jankowska, E. (2008). Spinal interneuronal networks in the cat: elementary components. *Brain Research Reviews*, *57*(1), 46–55. https://doi.org/10.1016/j.brainresrev.2007.06.022

Jenkinson, M., Bannister, P., Brady, M., & Smith, S. (2002). Improved optimization for the robust and accurate linear registration and motion correction of brain images. *NeuroImage*, *17*(2), 825–841. https://doi.org/https://doi.org/10.1006/nimg.2002.1132

Jenkinson, M., Beckmann, C. F., Behrens, T. E., Woolrich, M. W., & Smith, S. M. (2012). Fsl [20 YEARS OF fMRI]. *NeuroImage*, *62*(2), 782–790. https://doi.org/https://doi.org/10.1016/j.neuroimage.2011.09.015

Jnoff, E., Christophe, B., Collart, P., Coloretti, F., Debeuckelaere, A., DeRyck, M., Fuks, B., Genicot, C., Gillard, M., Guyaux, M., Price, N., Vandergeten, M.-C., & Vermeiren, C. (2012). Discovery of selective alpha2cadrenergic receptor agonists. *ChemMedChem*, *7*(3), 385–390. https://doi.org/10.1002/cmdc.201100528

Johnson, W. L., Jindrich, D. L., Zhong, H., Roy, R. R., & Edgerton, V. R. (2011). Application of a rat hindlimb model: a prediction of force spaces reachable through stimulation of nerve fascicles. *IEEE Transactions on Biomedical Engineering*, *58*(12), 3328–3338. https://doi.org/10.1109/tbme.2011.2106784

Johnson, W. L., Jindrich, D. L., Roy, R. R., & Edgerton, V. R. (2008). A three-dimensional model of the rat hindlimb: musculoskeletal geometry and muscle moment arms. *Journal of Biomechanics*, *41*(3), 610–619. https://doi.org/10.1016/j.jbiomech.2007.10.004

Jones, M. L., Evans, N., Tefertiller, C., Backus, D., Sweatman, M., Tansey, K., & Morrison, S. (2014). Activity-based therapy for recovery of walking in individuals with chronic spinal cord injury: results from a randomized clinical trial. *Archives of Physical Medicine and Rehabilitation*, *95*(12), 2239–2246.e2. https://doi.org/10.1016/j.apmr.2014.07.400

Jordan, L. M., Liu, J., Hedlund, P. B., Akay, T., & Pearson, K. G. (2008). Descending command systems for the initiation of locomotion in mammals. *Brain Research Reviews*, *57*(1), 183–191. https://doi.org/10.1016/j.brainresrev.2007.07.019

Kalaska, J. F. (2009). From intention to action: motor cortex and the control of reaching movements. *Advances in experimental medicine and biology* (pp. 139–178). Springer US. https://doi.org/10.1007/978-0-387-77064-2_8

Kandel, E. R. (Ed.). (2013). *Principles of neural science* (5th ed). McGraw-Hill.

Kasper, L., Bollmann, S., Diaconescu, A. O., Hutton, C., Heinzle, J., Iglesias, S., Hauser, T. U., Sebold, M., Manjaly, Z.-M., Pruessmann, K. P., & Stephan, K. E. (2017). The physio toolbox for modeling physiological noise in fmri data. *Journal of Neuroscience Methods*, *276*, 56–72. https://doi.org/https://doi.org/10.1016/j.jneumeth.2016.10.019

Kato, M. (1987). Motoneuronal activity of cat lumbar spinal cord following separation from descending or contralateral impulses. *Central Nervous System Trauma*, *4*(4), 239–248. https://doi.org/10.1089/cns.1987.4.239

Kavounoudias, A., Roll, J., Anton, J., Nazarian, B., Roth, M., & Roll, R. (2008). Proprio-tactile integration for kinesthetic perception: an fmri study. *Neuropsychologia*, *46*(2), 567–575. https://doi.org/https://doi.org/10.1016/j.neuropsychologia.2007.10.002

Kavounoudias, A., Roll, R., & Roll, J.-P. (1998). The plantar sole is a ‘dynamometric map’ for human balance control. *NeuroReport*, *9*(14), 3247–3252. https://doi.org/10.1097/00001756-199810050-00021

Kiehn, O. (2006). Locomotor circuits in the mammalian spinal cord [PMID: 16776587]. *Annual Review of Neuroscience*, *29*(1), 279–306. https://doi.org/10.1146/annurev.neuro.29.051605.112910

Kiehn, O. (2016). Decoding the organization of spinal circuits that control locomotion. *Nature Reviews Neuroscience*, *17*(4), 224–238. https://doi.org/10.1038/nrn.2016.9

Kinany, N., Pirondini, E., Martuzzi, R., Mattera, L., Micera, S., & Van de Ville, D. (2019). Functional imaging of rostrocaudal spinal activity during upper limb motor tasks. *NeuroImage*, *200*, 590–600. https://doi.org/https://doi.org/10.1016/j.neuroimage.2019.05.036

Kinany, N., Pirondini, E., Micera, S., & Van De Ville, D. (2020). Dynamic functional connectivity of resting-state spinal cord fmri reveals fine-grained intrinsic architecture. *Neuron*, *108*(3), 424–435.e4. https://doi.org/https://doi.org/10.1016/j.neuron.2020.07.024

Kirshblum, S., & Waring, W. (2014). Updates for the international standards for neurological classification of spinal cord injury [Spinal Cord Injury Rehabilitation]. *Physical Medicine and Rehabilitation Clinics of North America*, *25*(3), 505–517. https://doi.org/https://doi.org/10.1016/j.pmr.2014.04.001

Kjaerulff, O., & Kiehn, O. (1997). Crossed rhythmic synaptic input to motoneurons during selective activation of the contralateral spinal locomotor network. *Journal of Neuroscience*, *17*(24), 9433–9447. https://doi.org/10.1523/JNEUROSCI.17-24-09433.1997

Knikou, M., Angeli, C. A., Ferreira, C. K., & Harkema, S. J. (2008). Soleus h-reflex modulation during body weight support treadmill walking in spinal cord intact and injured subjects. *Experimental Brain Research*, *193*(3), 397–407. https://doi.org/10.1007/s00221-008-1636-x

Ko, H.-Y., Park, J. H., Shin, Y. B., & Baek, S. Y. (2004). Gross quantitative measurements of spinal cord segments in human. *Spinal Cord*, *42*(1), 35–40. https://doi.org/10.1038/sj.sc.3101538

Koerber, H. R., & Mendell, L. M. (1991). Modulation of synaptic transmission at ia-afferent connections on motoneurons during high-frequency afferent stimulation: dependence on motor task. *Journal of Neurophysiology*, *65*(6), 1313–1320. https://doi.org/10.1152/jn.1991.65.6.1313

Kong, Y., Jenkinson, M., Andersson, J., Tracey, I., & Brooks, J. C. (2012). Assessment of physiological noise modelling methods for functional imaging of the spinal cord. *NeuroImage*, *60*(2), 1538–1549. https://doi.org/https://doi.org/10.1016/j.neuroimage.2011.11.077

Krajacic, A., Ghosh, M., Puentes, R., Pearse, D., & Fouad, K. (2009). Advantages of delaying the onset of rehabilitative reaching training in rats with incomplete spinal cord injury. *European Journal of Neuroscience*, *29*(3), 641–651. https://doi.org/10.1111/j.1460-9568.2008.06600.x

Krčah, M., Székely, G., & Blanc, R. (2011). Fully automatic and fast segmentation of the femur bone from 3d-ct images with no shape prior. *2011 IEEE International Symposium on Biomedical Imaging: From Nano to Macro*, 2087–2090. https://doi.org/10.1109/ISBI.2011.5872823

Kremer, E., & Lev-Tov, A. (1997). Localization of the spinal network associated with generation of hindlimb locomotion in the neonatal rat and organization of its transverse coupling system [PMID: 9084588]. *Journal of Neurophysiology*, *77*(3), 1155–1170. https://doi.org/10.1152/jn.1997.77.3.1155

Krucoff, M. O., Rahimpour, S., Slutzky, M. W., Edgerton, V. R., & Turner, D. A. (2016). Enhancing nervous system recovery through neurobiologics, neural interface training, and neurorehabilitation. *Frontiers in Neuroscience*, *10*. https://doi.org/10.3389/fnins.2016.00584

Kumru, H., Benito-Penalva, J., Valls-Sole, J., Murillo, N., Tormos, J. M., Flores, C., & Vidal, J. (2016). Placebo-controlled study of rTMS combined with lokomat® gait training for treatment in subjects with motor incomplete spinal cord injury. *Experimental Brain Research*, *234*(12), 3447–3455. https://doi.org/10.1007/s00221-016-4739-9

Kumru, H., Gunduz, A., Rothwell, J., & Vidal, J. (2017). Non-invasive brain stimulation to promote motor and functional recovery following spinal cord injury. *Neural Regeneration Research*, *12*(12), 1933. https://doi.org/10.4103/1673-5374.221143

la Calle, J. L. D., & Paino, C. L. (2002). A procedure for direct lumbar puncture in rats. *Brain Research Bulletin*, *59*(3), 245–250. https://doi.org/10.1016/s0361-9230(02)00866-3

Ladenbauer, J., Minassian, K., Hofstoetter, U. S., Dimitrijevic, M. R., & Rattay, F. (2010). Stimulation of the human lumbar spinal cord with implanted and surface electrodes: a computer simulation study. *IEEE Transactions on Neural Systems and Rehabilitation Engineering*, *18*(6), 637–645. https://doi.org/10.1109/TNSRE.2010.2054112

Lähdesmäki, J., Sallinen, J., MacDonald, E., Kobilka, B., Fagerholm, V., & Scheinin, M. (2002). Behavioral and neurochemical characterization of α2a-adrenergic receptor knockout mice. *Neuroscience*, *113*(2), 289–299. https://doi.org/10.1016/s0306-4522(02)00185-9

Lallemend, F., & Ernfors, P. (2012). Molecular interactions underlying the specification of sensory neurons. *Trends in Neurosciences*, *35*(6), 373–381. https://doi.org/10.1016/j.tins.2012.03.006

Landelle, C., El Ahmadi, A., & Kavounoudias, A. (2018). Age-related impairment of hand movement perception based on muscle proprioception and touch. *Neuroscience*, *381*, 91–104. https://doi.org/https://doi.org/10.1016/j.neuroscience.2018.04.015

Landelle, C., Anton, J.-L., Nazarian, B., Sein, J., Gharbi, A., Felician, O., & Kavounoudias, A. (2020). Functional brain changes in the elderly for the perception of hand movements: a greater impairment occurs in proprioception than touch. *NeuroImage*, *220*, 117056. https://doi.org/https://doi.org/10.1016/j.neuroimage.2020.117056

Lee, B. B., Cripps, R. A., Fitzharris, M., & Wing, P. C. (2014). The global map for traumatic spinal cord injury epidemiology: update 2011, global incidence rate. *Spinal Cord*, *52*(2), 110–116. https://doi.org/10.1038/sc.2012.158

Lee, E., Choi, J., Jo, Y., Kim, J. Y., Jang, Y. J., Lee, H. M., Kim, S. Y., Lee, H.-J., Cho, K., Jung, N., Hur, E. M., Jeong, S. J., Moon, C., Choe, Y., Rhyu, I. J., Kim, H., & Sun, W. (2016). ACT-PRESTO: rapid and consistent tissue clearing and labeling method for 3-dimensional (3d) imaging. *Scientific Reports*, *6*(1). https://doi.org/10.1038/srep18631

Leem, J. W., Willis, W. D., & Chung, J. M. (1993). Cutaneous sensory receptors in the rat foot. *Journal of Neurophysiology*, *69*(5), 1684–1699. https://doi.org/10.1152/jn.1993.69.5.1684

Legg Ditterline, B. E., Wade, S., Ugiliweneza, B., Singam, N. S., Harkema, S. J., Stoddard, M. F., & Hirsch, G. A. (2020). Beneficial cardiac structural and functional adaptations after lumbosacral spinal cord epidural stimulation and task-specific interventions: a pilot study. *Frontiers in Neuroscience*, *14*, 1066. https://doi.org/10.3389/fnins.2020.554018

Lempka, S. F., & Patil, P. G. (2018). Innovations in spinal cord stimulation for pain. *Current Opinion in Biomedical Engineering*, *8*, 51–60. https://doi.org/10.1016/j.cobme.2018.10.005

Lempka, S. F., Zander, H. J., Anaya, C. J., Wyant, A., Ozinga IV, J. G., & Machado, A. G. (2020). Patient-specific analysis of neural activation during spinal cord stimulation for pain. *Neuromodulation: Technology at the Neural Interface*, *23*(5), 572–581. https://doi.org/https://doi.org/10.1111/ner.13037

Li, L., Rutlin, M., Abraira, V. E., Cassidy, C., Kus, L., Gong, S., Jankowski, M. P., Luo, W., Heintz, N., Koerber, H. R., Woodbury, C. J., & Ginty, D. D. (2011). The functional organization of cutaneous low-threshold mechanosensory neurons. *Cell*, *147*(7), 1615–1627. https://doi.org/10.1016/j.cell.2011.11.027

Limousin, P., Krack, P., Pollak, P., Benazzouz, A., Ardouin, C., Hoffmann, D., & Benabid, A.-L. (1998). Electrical stimulation of the subthalamic nucleus in advanced parkinson's disease. *New England Journal of Medicine*, *339*(16), 1105–1111. https://doi.org/10.1056/nejm199810153391603

Liu, Y., Zhou, X., Ma, J., Ge, Y., & Cao, X. (2015). The diameters and number of nerve fibers in spinal nerve roots (2014/03/07) [PMC4612209[pmcid]]. *The journal of spinal cord medicine*, *38*(4), 532–537. https://doi.org/10.1179/1079026814Z.000000000273

Liu, Y., Latremoliere, A., Li, X., Zhang, Z., Chen, M., Wang, X., Fang, C., Zhu, J., Alexandre, C., Gao, Z., Chen, B., Ding, X., Zhou, J.-Y., Zhang, Y., Chen, C., Wang, K. H., Woolf, C. J., & He, Z. (2018). Touch and tactile neuropathic pain sensitivity are set by corticospinal projections. *Nature*, *561*(7724), 547–550. https://doi.org/10.1038/s41586-018-0515-2

Lovely, R., Gregor, R., Roy, R., & Edgerton, V. (1986). Effects of training on the recovery of full-weight-bearing stepping in the adult spinal cat. *Experimental Neurology*, *92*(2), 421–435. https://doi.org/10.1016/0014-4886(86)90094-4

Luo, W., Enomoto, H., Rice, F. L., Milbrandt, J., & Ginty, D. D. (2009). Molecular identification of rapidly adapting mechanoreceptors and their developmental dependence on ret signaling. *Neuron*, *64*(6), 841–856. https://doi.org/10.1016/j.neuron.2009.11.003

Mahlknecht, P., Limousin, P., & Foltynie, T. (2015). Deep brain stimulation for movement disorders: update on recent discoveries and outlook on future developments. *Journal of Neurology*, *262*(11), 2583–2595. https://doi.org/10.1007/s00415-015-7790-8

Marigold, D. S., Andujar, J.-E., Lajoie, K., & Drew, T. (2011). Motor planning of locomotor adaptations on the basis of vision. *Progress in brain research* (pp. 83–100). Elsevier. https://doi.org/10.1016/b978-0-444-53825-3.00011-5

Markram, H., Muller, E., Ramaswamy, S., Reimann, M. W., Abdellah, M., Sanchez, C. A., Ailamaki, A., Alonso-Nanclares, L., Antille, N., Arsever, S., Kahou, G. A. A., Berger, T. K., Bilgili, A., Buncic, N., Chalimourda, A., Chindemi, G., Courcol, J.-D., Delalondre, F., Delattre, V., … Schürmann, F. (2015). Reconstruction and simulation of neocortical microcircuitry. *Cell*, *163*(2), 456–492. https://doi.org/10.1016/j.cell.2015.09.029

Martin, J. (2016). Harnessing neural activity to promote repair of the damaged corticospinal system after spinal cord injury. *Neural Regeneration Research*, *11*(9), 1389. https://doi.org/10.4103/1673-5374.191199

Matsuyama, K., Kobayashi, S., & Aoki, M. (2006). Projection patterns of lamina viii commissural neurons in the lumbar spinal cord of the adult cat: an anterograde neural tracing study. *Neuroscience*, *140*(1), 203–218. https://doi.org/https://doi.org/10.1016/j.neuroscience.2006.02.005

Matsuyama, K., & Drew, T. (1997). Organization of the projections from the pericruciate cortex to the pontomedullary brainstem of the cat: a study using the anterograde tracerPhaseolus vulgaris-leucoagglutinin. *The Journal of Comparative Neurology*, *389*(4), 617–641. https://doi.org/10.1002/(sici)1096-9861(19971229)389:4<617::aid-cne6>3.0.co;2-3

Maupas, E., Marque, P., Roques, C. F., & Simonetta-Moreau, M. (2004). Modulation of the transmission in group ii heteronymous pathways by tizanidine in spastic hemiplegic patients. *Journal of Neurology, Neurosurgery & Psychiatry*, *75*(1), 130–135. https://jnnp.bmj.com/content/75/1/130

Mayer, W. P., Murray, A. J., Brenner-Morton, S., Jessell, T. M., Tourtellotte, W. G., & Akay, T. (2018). Role of muscle spindle feedback in regulating muscle activity strength during walking at different speed in mice. *Journal of Neurophysiology*, *120*(5), 2484–2497. https://doi.org/10.1152/jn.00250.2018

McCrea, D. A., Pratt, C. A., & Jordan, L. M. (1980). Renshaw cell activity and recurrent effects on motoneurons during fictive locomotion. *Journal of Neurophysiology*, *44*(3), 475–488. https://doi.org/10.1152/jn.1980.44.3.475

Mcintyre, C. C., & Foutz, T. J. (2013). Computational modeling of deep brain stimulation. *Handbook of clinical neurology* (pp. 55–61). Elsevier. https://doi.org/10.1016/b978-0-444-53497-2.00005-x

McIntyre, C. C., & Grill, W. M. (2002). Extracellular stimulation of central neurons: influence of stimulus waveform and frequency on neuronal output. *Journal of Neurophysiology*, *88*(4), 1592–1604. https://doi.org/10.1152/jn.2002.88.4.1592

McIntyre, C. C., Richardson, A. G., & Grill, W. M. (2002). Modeling the excitability of mammalian nerve fibers: influence of afterpotentials on the recovery cycle. *Journal of Neurophysiology*, *87*(2), 995–1006. https://doi.org/10.1152/jn.00353.2001

Mendell, L. M., & Henneman, E. (1971). Terminals of single ia fibers: location, density, and distribution within a pool of 300 homonymous motoneurons. *Journal of Neurophysiology*, *34*(1), 171–187. https://doi.org/10.1152/jn.1971.34.1.171

Mendez, A., Islam, R., Latypov, T., Basa, P., Joseph, O. J., Knudsen, B., Siddiqui, A. M., Summer, P., Staehnke, L. J., Grahn, P. J., Lachman, N., Windebank, A. J., & Lavrov, I. A. (2020). Segment-specific orientation of the dorsal and ventral roots for precise therapeutic targeting of human spinal cord. https://doi.org/10.1101/2020.01.31.928804

Mesbah, S., Ball, T., Angeli, C., Rejc, E., Dietz, N., Ugiliweneza, B., Harkema, S., & Boakye, M. (2020). Predictors of volitional motor recovery with epidural stimulation in individuals with chronic spinal cord injury. *Brain*, *144*(2), 420–433. https://doi.org/10.1093/brain/awaa423

Mestre, C., Pélissier, T., Fialip, J., Wilcox, G., & Eschalier, A. (1994). A method to perform direct transcutaneous intrathecal injection in rats. *Journal of Pharmacological and Toxicological Methods*, *32*(4), 197–200. https://doi.org/10.1016/1056-8719(94)90087-6

Mignardot, J.-B., Le Goff, C. G., van den Brand, R., Capogrosso, M., Fumeaux, N., Vallery, H., Anil, S., Lanini, J., Fodor, I., Eberle, G., Ijspeert, A., Schurch, B., Curt, A., Carda, S., Bloch, J., von Zitzewitz, J., & Courtine, G. (2017). A multidirectional gravity-assist algorithm that enhances locomotor control in patients with stroke or spinal cord injury. *Science Translational Medicine*, *9*(399). https://doi.org/10.1126/scitranslmed.aah3621

Mignon, C., Tobin, D. J., Zeitouny, M., & Uzunbajakava, N. E. (2018). Shedding light on the variability of optical skin properties: finding a path towards more accurate prediction of light propagation in human cutaneous compartments. *Biomedical Optics Express*, *9*(2), 852. https://doi.org/10.1364/boe.9.000852

Minassian, K., Jilge, B., Rattay, F., Pinter, M. M., Binder, H., Gerstenbrand, F., & Dimitrijevic, M. R. (2004). Stepping-like movements in humans with complete spinal cord injury induced by epidural stimulation of the lumbar cord: electromyographic study of compound muscle action potentials. *Spinal Cord*, *42*(7), 401–416. https://doi.org/10.1038/sj.sc.3101615

Minassian, K., Persy, I., Rattay, F., Pinter, M., Kern, H., & Dimitrijevic, M. (2007). Human lumbar cord circuitries can be activated by extrinsic tonic input to generate locomotor-like activity [Second European Workshop on Human Movement Science]. *Human Movement Science*, *26*(2), 275–295. https://doi.org/https://doi.org/10.1016/j.humov.2007.01.005

Minassian, K., Hofstoetter, U., Tansey, K., & Mayr, W. (2012). Neuromodulation of lower limb motor control in restorative neurology [Restorative Neurology and Motor Control]. *Clinical Neurology and Neurosurgery*, *114*(5), 489–497. https://doi.org/https://doi.org/10.1016/j.clineuro.2012.03.013

Minassian, K., Hofstoetter, U. S., Danner, S. M., Mayr, W., Bruce, J. A., McKay, W. B., & Tansey, K. E. (2015). Spinal rhythm generation by step-induced feedback and transcutaneous posterior root stimulation in complete spinal cord–injured individuals. *Neurorehabilitation and Neural Repair*, *30*(3), 233–243. https://doi.org/10.1177/1545968315591706

Minassian, K., McKay, W. B., Binder, H., & Hofstoetter, U. S. (2016). Targeting lumbar spinal neural circuitry by epidural stimulation to restore motor function after spinal cord injury. *Neurotherapeutics*, *13*(2), 284–294. https://doi.org/10.1007/s13311-016-0421-y

Minev, I. R., Musienko, P., Hirsch, A., Barraud, Q., Wenger, N., Moraud, E. M., Gandar, J., Capogrosso, M., Milekovic, T., Asboth, L., Torres, R. F., Vachicouras, N., Liu, Q., Pavlova, N., Duis, S., Larmagnac, A., Vörös, J., Micera, S., Suo, Z., … Lacour, S. P. (2015). Electronic dura mater for long-term multimodal neural interfaces. *Science*, *347*(6218), 159–163. https://doi.org/10.1126/science.1260318

Molgaard, S., Ulrichsen, M., Boggild, S., Holm, M.-L., Vaegter, C., Nyengaard, J., & Glerup, S. (2014). Immunofluorescent visualization of mouse interneuron subtypes. *F1000Research*, *3*, 242. https://doi.org/10.12688/f1000research.5349.2

Molnar, G., & Barolat, G. (2014). Principles of cord activation during spinal cord stimulation. *Neuromodulation: Technology at the Neural Interface*, *17*(S1), 12–21. https://doi.org/https://doi.org/10.1111/ner.12171

Moraud, E. M., Capogrosso, M., Formento, E., Wenger, N., DiGiovanna, J., Courtine, G., & Micera, S. (2016). Mechanisms underlying the neuromodulation of spinal circuits for correcting gait and balance deficits after spinal cord injury. *Neuron*, *89*(4), 814–828. https://doi.org/10.1016/j.neuron.2016.01.009

Moraud, E. M., von Zitzewitz, J., Miehlbradt, J., Wurth, S., Formento, E., DiGiovanna, J., Capogrosso, M., Courtine, G., & Micera, S. (2018). Closed-loop control of trunk posture improves locomotion through the regulation of leg proprioceptive feedback after spinal cord injury. *Scientific Reports*, *8*(1), 76. https://doi.org/10.1038/s41598-017-18293-y

Mori, S. (1987). Integration of posture and locomotion in acute decerebrate cats and in awake, freely moving cats. *Progress in Neurobiology*, *28*(2), 161–195. https://doi.org/10.1016/0301-0082(87)90010-4

Mori, S., Matsui, T., Kuze, B., Asanome, M., Nakajima, K., & Matsuyama, K. (1999). Stimulation of a restricted region in the midline cerebellar white matter evokes coordinated quadrupedal locomotion in the decerebrate cat. *Journal of Neurophysiology*, *82*(1), 290–300. https://doi.org/10.1152/jn.1999.82.1.290

Morse, L. R., Field-Fote, E. C., Contreras-Vidal, J., Noble-Haeusslein, L. J., Rodreick, M., Shields, R. K., Sofroniew, M., Wudlick, R., Zanca, J. M., Anke, A., Anderson-Erisman, K. D., Basso, M., Boninger, M., Chen, Y., Chernesky, J., Coker, J., Collinger, J. L., Courtine, G., Dulin, J., … and, R. Z. (2021). Meeting proceedings for SCI 2020: launching a decade of disruption in spinal cord injury research. *Journal of Neurotrauma*, *38*(9), 1251–1266. https://doi.org/10.1089/neu.2020.7174

Munson, J. B., Fleshman, J. W., & Sypert, G. W. (1980). Properties of single-fiber spindle group II EPSPs in triceps surae motoneurons. *Journal of Neurophysiology*, *44*(4), 713–725. https://doi.org/10.1152/jn.1980.44.4.713

Murray, L. M., Edwards, D. J., Ruffini, G., Labar, D., Stampas, A., Pascual-Leone, A., & Cortes, M. (2015). Intensity dependent effects of transcranial direct current stimulation on corticospinal excitability in chronic spinal cord injury. *Archives of Physical Medicine and Rehabilitation*, *96*(4), S114–S121. https://doi.org/10.1016/j.apmr.2014.11.004

Mushahwar, V. K., Jacobs, P. L., Normann, R. A., Triolo, R. J., & Kleitman, N. (2007). New functional electrical stimulation approaches to standing and walking. *Journal of Neural Engineering*, *4*(3), S181–S197. https://doi.org/10.1088/1741-2560/4/3/s05

Musienko, P., van den Brand, R., Marzendorfer, O., Roy, R. R., Gerasimenko, Y., Edgerton, V. R., & Courtine, G. (2011). Controlling specific locomotor behaviors through multidimensional monoaminergic modulation of spinal circuitries. *Journal of Neuroscience*, *31*(25), 9264–9278. https://doi.org/10.1523/jneurosci.5796-10.2011

Musienko, P., Courtine, G., Tibbs, J. E., Kilimnik, V., Savochin, A., Garfinkel, A., Roy, R. R., Edgerton, V. R., & Gerasimenko, Y. (2012). Somatosensory control of balance during locomotion in decerebrated cat. *Journal of Neurophysiology*, *107*(8), 2072–2082. https://doi.org/10.1152/jn.00730.2011

Musienko, P., van den Brand, R., Maerzendorfer, O., Larmagnac, A., & Courtine, G. (2009). Combinatory electrical and pharmacological neuroprosthetic interfaces to regain motor function after spinal cord injury. *IEEE Transactions on Biomedical Engineering*, *56*(11), 2707–2711. https://doi.org/10.1109/tbme.2009.2027226

Nadeau, S., Jacquemin, G., Fournier, C., Lamarre, Y., & Rossignol, S. (2010). Spontaneous motor rhythms of the back and legs in a patient with a complete spinal cord transection [PMID: 20019383]. *Neurorehabilitation and Neural Repair*, *24*(4), 377–383. https://doi.org/10.1177/1545968309349945

Nance, P. W., Shears, A. H., & Nance, D. M. (1985). Clonidine in spinal cord injury [PMC1346067[pmcid]]. *Canadian Medical Association journal*, *133*(1), 41–42. https://pubmed.ncbi.nlm.nih.gov/2988731

Neufeld, E., Szczerba, D., Chavannes, N., & Kuster, N. (2013). A novel medical image data-based multi-physics simulation platform for computational life sciences. *Interface Focus*, *3*(2), 20120058. https://doi.org/10.1098/rsfs.2012.0058

Nicholas, A. P., Hökfely, T., & Pieribone, V. A. (1996). The distribution and significance of CNS adrenoceptors examined with in situ hybridization. *Trends in Pharmacological Sciences*, *17*(7), 245–255. https://doi.org/10.1016/0165-6147(96)10022-5

Nishimura, Y., Perlmutter, S. I., Eaton, R. W., & Fetz, E. E. (2013). Spike-timing-dependent plasticity in primate corticospinal connections induced during free behavior (2013/11/07) [S0896-6273(13)00762-9[PII]]. *Neuron*, *80*(5), 1301–1309. https://doi.org/10.1016/j.neuron.2013.08.028

Nissen, U. V., Mochida, H., & Glover, J. C. (2005). Development of projection-specific interneurons and projection neurons in the embryonic mouse and rat spinal cord. *Journal of Comparative Neurology*, *483*(1), 30–47. https://doi.org/https://doi.org/10.1002/cne.20435

Noga, B., Shefchyk, S., Jamal, J., & Jordan, L. (1987). The role of renshaw cells in locomotion: antagonism of their excitation from motor axon collaterals with intravenous mecamylamine. *Experimental Brain Research*, *66*(1). https://doi.org/10.1007/bf00236206

O'Shea, T. M., Burda, J. E., & Sofroniew, M. V. (2017). Cell biology of spinal cord injury and repair. *Journal of Clinical Investigation*, *127*(9), 3259–3270. https://doi.org/10.1172/jci90608

Owen, S. F., Liu, M. H., & Kreitzer, A. C. (2019). Thermal constraints on in vivo optogenetic manipulations. *Nature Neuroscience*, *22*(7), 1061–1065. https://doi.org/10.1038/s41593-019-0422-3

Panek, I., Bui, T., Wright, A. T. B., & Brownstone, R. M. (2014). Cutaneous afferent regulation of motor function. *Acta neurobiologiae experimentalis*, *74*(2), 158–171. http://europepmc.org/abstract/MED/24993626

Park, E., Kim, Y.-H., Chang, W. H., Kwon, T. G., & Shin, Y.-I. (2014). Interhemispheric modulation of dual-mode, noninvasive brain stimulation on motor function. *Annals of Rehabilitation Medicine*, *38*(3), 297. https://doi.org/10.5535/arm.2014.38.3.297

Park, S.-W., Wolf, S. L., Blanton, S., Winstein, C., & Nichols-Larsen, D. S. (2008). The EXCITE trial: predicting a clinically meaningful motor activity log outcome. *Neurorehabilitation and Neural Repair*, *22*(5), 486–493. https://doi.org/10.1177/1545968308316906

Pearson, K. G. (1995). Proprioceptive regulation of locomotion. *Current Opinion in Neurobiology*, *5*(6), 786–791. https://doi.org/10.1016/0959-4388(95)80107-3

Pearson, K. (2008). Role of sensory feedback in the control of stance duration in walking cats. *Brain Research Reviews*, *57*(1), 222–227. https://doi.org/10.1016/j.brainresrev.2007.06.014

Perez, M. A., Field-Fote, E. C., & Floeter, M. K. (2003). Patterned sensory stimulation induces plasticity in reciprocal ia inhibition in humans. *Journal of Neuroscience*, *23*(6), 2014–2018. https://doi.org/10.1523/JNEUROSCI.23-06-02014.2003

Pertovaara, A. (2006). Noradrenergic pain modulation. *Progress in Neurobiology*, *80*(2), 53–83. https://doi.org/10.1016/j.pneurobio.2006.08.001

Philipp, M., & Hein, L. (2004). Adrenergic receptor knockout mice: distinct functions of 9 receptor subtypes. *Pharmacology & Therapeutics*, *101*(1), 65–74. https://doi.org/10.1016/j.pharmthera.2003.10.004

Pierrot-Desseilligny, E., & Burke, D. (2012). *The circuitry of the human spinal cord.*

Plonsey, R., & Heppner, D. B. (1967). Considerations of quasi-stationarity in electrophysiological systems. *The Bulletin of Mathematical Biophysics*, *29*(4), 657–664. https://doi.org/10.1007/bf02476917

Power, J. D., Mitra, A., Laumann, T. O., Snyder, A. Z., Schlaggar, B. L., & Petersen, S. E. (2014). Methods to detect, characterize, and remove motion artifact in resting state fmri. *NeuroImage*, *84*, 320–341. https://doi.org/https://doi.org/10.1016/j.neuroimage.2013.08.048

Pratt, C. A., & Jordan, L. M. (1987). Ia inhibitory interneurons and renshaw cells as contributors to the spinal mechanisms of fictive locomotion. *Journal of Neurophysiology*, *57*(1), 56–71. https://doi.org/10.1152/jn.1987.57.1.56

Prochazka, A. (1996). Proprioceptive feedback and movement regulation. https://doi.org/10.1002/cphy.cp120103

Prochazka, A. (1999). Chapter 11 quantifying proprioception. *Progress in brain research* (pp. 133–142). Elsevier. https://doi.org/10.1016/s0079-6123(08)62850-2

Prochazka, A., & Gorassini, M. (1998a). Ensemble firing of muscle afferents recorded during normal locomotion in cats. *The Journal of Physiology*, *507*(1), 293–304. https://doi.org/10.1111/j.1469-7793.1998.293bu.x

Prochazka, A., & Gorassini, M. (1998b). Models of ensemble firing of muscle spindle afferents recorded during normal locomotion in cats. *The Journal of Physiology*, *507*(1), 277–291. https://doi.org/10.1111/j.1469-7793.1998.277bu.x

Quinlan, K. A., & Kiehn, O. (2007). Segmental, synaptic actions of commissural interneurons in the mouse spinal cord. *Journal of Neuroscience*, *27*(24), 6521–6530. https://doi.org/10.1523/JNEUROSCI.1618-07.2007

Ranger, M., Irwin, G., Bunbury, K., & Peutrell, J. (2008). Changing body position alters the location of the spinal cord within the vertebral canal: a magnetic resonance imaging study. *British Journal of Anaesthesia*, *101*(6), 804–809. https://doi.org/10.1093/bja/aen295

Rattay, F., Minassian, K., & Dimitrijevic, M. R. (2000). Epidural electrical stimulation of posterior structures of the human lumbosacral cord: 2. quantitative analysis by computer modeling. *Spinal Cord*, *38*(8), 473–489. https://doi.org/10.1038/sj.sc.3101039

Rattay, F., Resatz, S., Lutter, P., Minassian, K., Jilge, B., & Dimitrijevic, M. R. (2003). Mechanisms of electrical stimulation with neural prostheses. *Neuromodulation: Technology at the Neural Interface*, *6*(1), 42–56. https://doi.org/https://doi.org/10.1046/j.1525-1403.2003.03006.x

Rattay, F. (1986). Analysis of models for external stimulation of axons. *IEEE Transactions on Biomedical Engineering*, *BME-33*(10), 974–977. https://doi.org/10.1109/tbme.1986.325670

Ray, D. L., Juvin, L., Ryczko, D., & Dubuc, R. (2011). Supraspinal control of locomotion. *Progress in brain research* (pp. 51–70). Elsevier. https://doi.org/10.1016/b978-0-444-53825-3.00009-7

Readdy, W. J., Whetstone, W. D., Ferguson, A. R., Talbott, J. F., Inoue, T., Saigal, R., Bresnahan, J. C., Beattie, M. S., Pan, J. Z., Manley, G. T., & Dhall, S. S. (2015). Complications and outcomes of vasopressor usage in acute traumatic central cord syndrome. *Journal of Neurosurgery: Spine*, *23*(5), 574–580. https://doi.org/10.3171/2015.2.spine14746

Rejc, E., Angeli, C. A., Atkinson, D., & Harkema, S. J. (2017). Motor recovery after activity-based training with spinal cord epidural stimulation in a chronic motor complete paraplegic. *Scientific Reports*, *7*(1). https://doi.org/10.1038/s41598-017-14003-w

Riddell, J. S., Jankowska, E., & Eide, E. (1993). Depolarization of group II muscle afferents by stimuli applied in the locus coeruleus and raphe nuclei of the cat. *The Journal of Physiology*, *461*(1), 723–741. https://doi.org/10.1113/jphysiol.1993.sp019538

Rizzolatti, G., Cattaneo, L., Fabbri-Destro, M., & Rozzi, S. (2014). Cortical mechanisms underlying the organization of goal-directed actions and mirror neuron-based action understanding. *Physiological Reviews*, *94*(2), 655–706. https://doi.org/10.1152/physrev.00009.2013

Robinson, G. A., & Goldberger, M. E. (1985). Interfering with inhibition may improve motor function. *Brain Research*, *346*(2), 400–403. https://doi.org/10.1016/0006-8993(85)90879-0

Roll, J. P., & Vedel, J. P. (1982). Kinaesthetic role of muscle afferents in man, studied by tendon vibration and microneurography. *Experimental Brain Research*, *47*(2), 177–190. https://doi.org/10.1007/BF00239377

Roll, J.-P., Vedel, J., & Ribot-Ciscar, E. (1989). Alteration of proprioceptice messages induced by tendon vibration in man: a microneurographic study. *Experimental brain research. Experimentelle Hirnforschung. Expérimentation cérébrale*, *76*, 213–22. https://doi.org/10.1007/BF00253639

Röper, J., & Schwarz, J. R. (1989). Heterogeneous distribution of fast and slow potassium channels in myelinated rat nerve fibres. *The Journal of Physiology*, *416*(1), 93–110. https://doi.org/10.1113/jphysiol.1989.sp017751

Rosenberg, E. (1920). *Die verschiedenen formen der menschlichen wirbelsäule und ihre bedeutung.*

Rossignol, S., Bélanger, M., Chau, C., Giroux, N., Brustein, E., Bouyer, L., Grenier, C.-A., Drew, T., Barbeau, H., & Reader, T. A. (2000). The spinal cat. *Neurobiology of spinal cord injury* (pp. 57–87). Humana Press. https://doi.org/10.1007/978-1-59259-200-5_3

Rossignol, S., Dubuc, R., & Gossard, J.-P. (2006). Dynamic sensorimotor interactions in locomotion [PMID: 16371596]. *Physiological Reviews*, *86*(1), 89–154. https://doi.org/10.1152/physrev.00028.2005

Rossignol, S., & Frigon, A. (2011). Recovery of locomotion after spinal cord injury: some facts and mechanisms. *Annual Review of Neuroscience*, *34*(1), 413–440. https://doi.org/10.1146/annurev-neuro-061010-113746

Roy, A., Osik, J. J., Ritter, N. J., Wang, S., Shaw, J. T., Fiser, J., & Hooser, S. D. V. (2016). Optogenetic spatial and temporal control of cortical circuits on a columnar scale. *Journal of Neurophysiology*, *115*(2), 1043–1062. https://doi.org/10.1152/jn.00960.2015

Sanes, J., Mauritz, K., Dalakas, M., & Evarts, E. (1985). Motor control in humans with large-fiber sensory neuropathy. *Human neurobiology*, *4*(2), 101–114. http://europepmc.org/abstract/MED/2993208

Sayenko, D. G., Angeli, C., Harkema, S. J., Edgerton, V. R., & Gerasimenko, Y. P. (2014). Neuromodulation of evoked muscle potentials induced by epidural spinal-cord stimulation in paralyzed individuals. *Journal of Neurophysiology*, *111*(5), 1088–1099. https://doi.org/10.1152/jn.00489.2013

Scheinin, M., Lomasney, J. W., Hayden-Hixson, D. M., Schambra, U. B., Caron, M. G., Lefkowitz, R. J., & Fremeau, R. T. (1994). Distribution of α2-adrenergic receptor subtype gene expression in rat brain. *Molecular Brain Research*, *21*(1-2), 133–149. https://doi.org/10.1016/0169-328x(94)90386-7

Schiavone, G., Fallegger, F., Kang, X., Barra, B., Vachicouras, N., Roussinova, E., Furfaro, I., Jiguet, S., Seáñez, I., Borgognon, S., Rowald, A., Li, Q., Qin, C., Bézard, E., Bloch, J., Courtine, G., Capogrosso, M., & Lacour, S. P. (2020). Soft, implantable bioelectronic interfaces for translational research. *Advanced Materials*, *32*(17), 1906512. https://doi.org/10.1002/adma.201906512

Schieppati, M. (1987). The hoffmann reflex: a means of assessing spinal reflex excitability and its descending control in man. *Progress in Neurobiology*, *28*(4), 345–376. https://doi.org/https://doi.org/10.1016/0301-0082(87)90007-4

Schindler-Ivens, S., & Shields, R. K. (2000). Low frequency depression of h-reflexes in humans with acute and chronic spinal-cord injury. *Experimental Brain Research*, *133*(2), 233–241. https://doi.org/10.1007/s002210000377

Schirmer, C. M., Shils, J. L., Arle, J. E., Cosgrove, G. R., Dempsey, P. K., Tarlov, E., Kim, S., Martin, C. J., Feltz, C., Moul, M., & Magge, S. (2011). Heuristic map of myotomal innervation in humans using direct intraoperative nerve root stimulation: clinical article. *Journal of Neurosurgery: Spine SPI*, *15*(1), 64–70. https://doi.org/10.3171/2011.2.SPINE1068

Segev, I., Fleshman, J. W., & Burke, R. E. (1990). Computer simulation of group ia EPSPs using morphologically realistic models of cat alpha-motoneurons. *Journal of Neurophysiology*, *64*(2), 648–660. https://doi.org/10.1152/jn.1990.64.2.648

Seki, K., Perlmutter, S. I., & Fetz, E. E. (2003). Sensory input to primate spinal cord is presynaptically inhibited during voluntary movement. *Nature Neuroscience*, *6*(12), 1309–1316. https://doi.org/10.1038/nn1154

Sengul, G. (2013). Atlas of the spinal cord : of the rat, mouse, marmoset, rhesus, and human.

Sharpe, A. N., & Jackson, A. (2014). Upper-limb muscle responses to epidural, subdural and intraspinal stimulation of the cervical spinal cord. *Journal of Neural Engineering*, *11*(1), 016005. https://doi.org/10.1088/1741-2560/11/1/016005

Sharrard, W. J. (1964). The segmental innervation of the lower limb muscles in man [PMC2311748[pmcid]]. *Annals of the Royal College of Surgeons of England*, *35*(2), 106–122. https://pubmed.ncbi.nlm.nih.gov/14180405

Shealy, C. N., Mortimer, J. T., & Reswick, J. B. (1967). Electrical inhibition of pain by stimulation of the dorsal columns: preliminary clinical report. *Anesthesia & Analgesia, 46*(4). https://journals.lww.com/anesthesia-analgesia/Fulltext/1967/07000/Electrical_Inhibition_of_Pain_by_Stimulation_of.25.aspx

Shen, K. Z., North, R. A., & Surprenant, A. (1992). Potassium channels opened by noradrenaline and other transmitters in excised membrane patches of guinea-pig submucosal neurones. *The Journal of Physiology, 445*(1), 581–599. https://doi.org/10.1113/jphysiol.1992.sp018941

Sherrington, C. S. (1910). Flexion-reflex of the limb, crossed extension-reflex, and reflex stepping and standing [PMC1533734[pmcid]]. *The Journal of physiology, 40*(1-2), 28–121. https://doi.org/10.1113/jphysiol.1910.sp001362

Shik, M., Severin, F., & Orlovsky, G. (1969). Control of walking and running by means of electrical stimulation of the mesencephalon. *Electroencephalography and clinical neurophysiology, 26*(5), 549. http://europepmc.org/abstract/MED/4181500

Shokur, S., Mazzoni, A., Schiavone, G., Weber, D. J., & Micera, S. (2021). A modular strategy for next-generation upper-limb sensory-motor neuroprostheses. *Med.* https://doi.org/10.1016/j.medj.2021.05.002

Simons, B. (1951). *Röntgendiagnostik der wirbelsäule.*

Sinnamon, H. M. (1993). Preoptic and hypothalamic neurons and the initiation of locomotion in the anesthetized rat. *Progress in Neurobiology, 41*(3), 323–344. https://doi.org/10.1016/0301-0082(93)90003-b

Soloukey, S., Rooij, J. D., Osterthun, R., Drenthen, J., Zeeuw, C. I. D., Huygen, F. J. P. M., & Harhangi, B. S. (2020). The dorsal root ganglion as a novel neuromodulatory target to evoke strong and reproducible motor responses in chronic motor complete spinal cord injury: a case series of five patients. *Neuromodulation: Technology at the Neural Interface, 24*(4), 779–793. https://doi.org/10.1111/ner.13235

Spear, B. B., Heath-Chiozzi, M., & Huff, J. (2001). Clinical application of pharmacogenetics. *Trends in Molecular Medicine, 7*(5), 201–204. https://doi.org/10.1016/s1471-4914(01)01986-4

Squair, J. W., Bélanger, L. M., Tsang, A., Ritchie, L., Mac-Thiong, J.-M., Parent, S., Christie, S., Bailey, C., Dhall, S., Charest-Morin, R., Street, J., Ailon, T., Paquette, S., Dea, N., Fisher, C. G., Dvorak, M. F., West, C. R., & Kwon, B. K. (2019). Empirical targets for acute hemodynamic management of individuals with spinal cord injury. *Neurology, 93*(12), e1205–e1211. https://doi.org/10.1212/wnl.0000000000008125

Squair, J. W., Bélanger, L. M., Tsang, A., Ritchie, L., Mac-Thiong, J.-M., Parent, S., Christie, S., Bailey, C., Dhall, S., Street, J., Ailon, T., Paquette, S., Dea, N., Fisher, C. G., Dvorak, M. F., West, C. R., & Kwon, B. K. (2017). Spinal cord perfusion pressure predicts neurologic recovery in acute spinal cord injury. *Neurology, 89*(16), 1660–1667. https://doi.org/10.1212/wnl.0000000000004519

Squair, J. W., Gautier, M., Mahe, L., Soriano, J. E., Rowald, A., Bichat, A., Cho, N., Anderson, M. A., James, N. D., Gandar, J., Incognito, A. V., Schiavone, G., Sarafis, Z. K., Laskaratos, A., Bartholdi, K., Demesmaeker, R., Komi, S., Moerman, C., Vaseghi, B., . . . Phillips, A. A.

(2021). Neuroprosthetic baroreflex controls haemodynamics after spinal cord injury. *Nature*, *590*(7845), 308–314. https://doi.org/10.1038/s41586-020-03180-w

Squair, J. W., Phillips, A. A., Harmon, M., & Krassioukov, A. V. (2016). Emergency management of autonomic dysreflexia with neurologic complications. *Canadian Medical Association Journal*, *188*(15), 1100–1103. https://doi.org/10.1503/cmaj.151311

Starkey, M. L., Bleul, C., Maier, I. C., & Schwab, M. E. (2011). Rehabilitative training following unilateral pyramidotomy in adult rats improves forelimb function in a non-task-specific way. *Experimental Neurology*, *232*(1), 81–89. https://doi.org/https://doi.org/10.1016/j.expneurol.2011.08.006

Stein, P. (1997). *Neurons, networks, and motor behavior*. MIT Press.

Stein, R. B., & Capaday, C. (1988). The modulation of human reflexes during functional motor tasks. *Trends in Neurosciences*, *11*(7), 328–332. https://doi.org/10.1016/0166-2236(88)90097-5

Stienen, A. H. A., Schouten, A. C., Schuurmans, J., & van der Helm, F. C. T. (2007). Analysis of reflex modulation with a biologically realistic neural network. *Journal of Computational Neuroscience*, *23*(3), 333–348. https://doi.org/10.1007/s10827-007-0037-7

Stokke, M. F., Nissen, U. V., Glover, J. C., & Kiehn, O. (2002). Projection patterns of commissural interneurons in the lumbar spinal cord of the neonatal rat. *Journal of Comparative Neurology*, *446*(4), 349–359. https://doi.org/https://doi.org/10.1002/cne.10211

Stone, L. S., Broberger, C., Vulchanova, L., Wilcox, G. L., Hökfelt, T., Riedl, M. S., & Elde, R. (1998). Differential distribution of α2aand α2cadrenergic receptor immunoreactivity in the rat spinal cord. *The Journal of Neuroscience*, *18*(15), 5928–5937. https://doi.org/10.1523/jneurosci.18-15-05928.1998

Strack, A., Sawyer, W., Marubio, L., & Loewy, A. (1988). Spinal origin of sympathetic preganglionic neurons in the rat. *Brain Research*, *455*(1), 187–191. https://doi.org/10.1016/0006-8993(88)90132-1

Su, C., Haghighi, S., Oro, J., & Gaines, R. (1992). "Backfiring"in spinal cord monitoring. high thoracic spinal cord stimulation evokes sciatic response by antidromic sensory pathway conduction, not motor tract conduction. *Spine*, *17*(5), 504–508. http://europepmc.org/abstract/MED/1621148

Sundt, D., Gamper, N., & Jaffe, D. B. (2015). Spike propagation through the dorsal root ganglia in an unmyelinated sensory neuron: a modeling study [PMID: 26334005]. *Journal of Neurophysiology*, *114*(6), 3140–3153. https://doi.org/10.1152/jn.00226.2015

Surprenant, A., & North, R. A. (1988). Mechanism of synaptic inhibition by noradrenaline acting at α2-adrenoceptors. *Proceedings of the Royal Society of London. Series B. Biological Sciences*, *234*(1274), 85–114. https://doi.org/10.1098/rspb.1988.0039

Sweeney, J., Mortimer, J., & Durand, D. (1987). Modeling of mammalian myelinated nerve for functional neuromuscular stimulation in proc 9th ann conf. *IEEE EMBS Boston M*, *9*, 1577–1578.

Takakusaki, K., Saitoh, K., Harada, H., & Kashiwayanagi, M. (2004). Role of basal ganglia–brainstem pathways in the control of motor behaviors. *Neuroscience Research*, *50*(2), 137–151. https://doi.org/10.1016/j.neures.2004.06.015

Takakusaki, K. (2008). Forebrain control of locomotor behaviors. *Brain Research Reviews*, *57*(1), 192–198. https://doi.org/10.1016/j.brainresrev.2007.06.024

Takakusaki, K. (2013). Neurophysiology of gait: from the spinal cord to the frontal lobe. *Movement Disorders*, *28*(11), 1483–1491. https://doi.org/10.1002/mds.25669

Takakusaki, K., Chiba, R., Nozu, T., & Okumura, T. (2015). Brainstem control of locomotion and muscle tone with special reference to the role of the mesopontine tegmentum and medullary reticulospinal systems. *Journal of Neural Transmission*, *123*(7), 695–729. https://doi.org/10.1007/s00702-015-1475-4

Takakusaki, K., Saitoh, K., Nonaka, S., Okumura, T., Miyokawa, N., & Koyama, Y. (2006). Neurobiological basis of state-dependent control of motor behaviors. *Sleep and Biological Rhythms*, *4*(2), 87–104. https://doi.org/10.1111/j.1479-8425.2006.00210.x

Takeoka, A., & Arber, S. (2019). Functional local proprioceptive feedback circuits initiate and maintain locomotor recovery after spinal cord injury. *Cell Reports*, *27*(1), 71–85.e3. https://doi.org/10.1016/j.celrep.2019.03.010

Takeoka, A., Vollenweider, I., Courtine, G., & Arber, S. (2014). Muscle spindle feedback directs locomotor recovery and circuit reorganization after spinal cord injury. *Cell*, *159*(7), 1626–1639. https://doi.org/10.1016/j.cell.2014.11.019

Talpalar, A. E., Bouvier, J., Borgius, L., Fortin, G., Pierani, A., & Kiehn, O. (2013). Dual-mode operation of neuronal networks involved in left–right alternation. *Nature*, *500*(7460), 85–88. https://doi.org/10.1038/nature12286

Talpalar, A. E., Endo, T., Löw, P., Borgius, L., Hägglund, M., Dougherty, K. J., Ryge, J., Hnasko, T. S., & Kiehn, O. (2011). Identification of minimal neuronal networks involved in flexor-extensor alternation in the mammalian spinal cord. *Neuron*, *71*(6), 1071–1084. https://doi.org/https://doi.org/10.1016/j.neuron.2011.07.011

Thompson, A. K., Pomerantz, F. R., & Wolpaw, J. R. (2013). Operant conditioning of a spinal reflex can improve locomotion after spinal cord injury in humans. *Journal of Neuroscience*, *33*(6), 2365–2375. https://doi.org/10.1523/jneurosci.3968-12.2013

Thompson, A. K., Pudlik, S. D., & Thompson, C. R. (2017). Effects of h-reflex operant conditioning in humans. In J. Ibáñez, J. González-Vargas, J. M. Azorín, M. Akay, & J. L. Pons (Eds.), *Converging clinical and engineering research on neurorehabilitation ii* (pp. 53–57). Springer International Publishing.

Tillakaratne, N. J., Mouria, M., Ziv, N. B., Roy, R. R., Edgerton, V. R., & Tobin, A. J. (2000). Increased expression of glutamate decarboxylase (GAD67) in feline lumbar spinal cord after complete thoracic spinal cord transection. *Journal of Neuroscience Research*, *60*(2), 219–230. https://doi.org/10.1002/(sici)1097-4547(20000415)60:2<219::aid-jnr11>3.0.co;2-f

Tomer, R., Ye, L., Hsueh, B., & Deisseroth, K. (2014). Advanced CLARITY for rapid and high-resolution imaging of intact tissues. *Nature Protocols*, *9*(7), 1682–1697. https://doi.org/10.1038/nprot.2014.123

Toossi, A., Bergin, B., Marefatallah, M., Parhizi, B., Tyreman, N., Everaert, D. G., Rezaei, S., Seres, P., Gatenby, J. C., Perlmutter, S. I., & Mushahwar, V. K. (2020). Comparative neuroanatomy of the lumbosacral spinal cord of the rat, cat, pig, monkey, and human. https://doi.org/10.1101/2020.08.11.246165

Travessa, A. M., Rodrigues, F. B., Mestre, T. A., & Ferreira, J. J. (2017). Fifteen years of clinical trials in huntington's disease: a very low clinical drug development success rate. *Journal of Huntington's Disease*, *6*(2), 157–163. https://doi.org/10.3233/JHD-170245

Tuthill, J. C., & Azim, E. (2018). Proprioception. *Current Biology*, *28*(5), R194–R203. https://doi.org/10.1016/j.cub.2018.01.064

Urbin, M. A., Ozdemir, R. A., Tazoe, T., & Perez, M. A. (2017). Spike-timing-dependent plasticity in lower-limb motoneurons after human spinal cord injury [PMID: 28468994]. *Journal of Neurophysiology*, *118*(4), 2171–2180. https://doi.org/10.1152/jn.00111.2017

Vallery, H., Lutz, P., von Zitzewitz, J., Rauter, G., Fritschi, M., Everarts, C., Ronsse, R., Curt, A., & Bolliger, M. (2013). Multidirectional transparent support for overground gait training. *2013 IEEE 13th International Conference on Rehabilitation Robotics (ICORR)*. https://doi.org/10.1109/icorr.2013.6650512

van den Brand, R., Heutschi, J., Barraud, Q., DiGiovanna, J., Bartholdi, K., Huerlimann, M., Friedli, L., Vollenweider, I., Moraud, E. M., Duis, S., Dominici, N., Micera, S., Musienko, P., & Courtine, G. (2012). Restoring voluntary control of locomotion after paralyzing spinal cord injury. *Science*, *336*(6085), 1182–1185. https://doi.org/10.1126/science.1217416

Viala, G., & Buser, P. (1974). Inhibition des activités spinales à caractère locomoteur par une modalité particulière de stimulation somatique chez le lapin. *Experimental Brain Research*, *21*(3). https://doi.org/10.1007/bf00235747

Voigt, F. F., Kirschenbaum, D., Platonova, E., Pagès, S., Campbell, R. A. A., Kastli, R., Schaettin, M., Egolf, L., van der Bourg, A., Bethge, P., Haenraets, K., Frézel, N., Topilko, T., Perin, P., Hillier, D., Hildebrand, S., Schueth, A., Roebroeck, A., Roska, B., … Helmchen, F. (2019). The mesoSPIM initiative: open-source light-sheet microscopes for imaging cleared tissue. *Nature Methods*, *16*(11), 1105–1108. https://doi.org/10.1038/s41592-019-0554-0

Volpi-Abadie, J., Kaye, A. M., & Kaye, A. D. (2013). Serotonin syndrome [PMC3865832[pmcid]]. *The Ochsner journal*, *13*(4), 533–540. https://pubmed.ncbi.nlm.nih.gov/24358002

Wagner, F. B., Mignardot, J.-B., Le Goff-Mignardot, C. G., Demesmaeker, R., Komi, S., Capogrosso, M., Rowald, A., Seáñez, I., Caban, M., Pirondini, E., Vat, M., McCracken, L. A., Heimgartner, R., Fodor, I., Watrin, A., Seguin, P., Paoles, E., Van Den Keybus, K., Eberle, G., … Courtine, G. (2018). Targeted neurotechnology restores walking in humans with spinal cord injury. *Nature*, *563*(7729), 65–71. https://doi.org/10.1038/s41586-018-0649-2

Wall, P. D. (Ed.). (2003). *Textbook of pain* (4. ed., reprint). Churchill Livingstone.

Wallen, P., Ekeberg, O., Lansner, A., Brodin, L., Traven, H., & Grillner, S. (1992). A computer-based model for realistic simulations of neural networks. II. the segmental network generating locomotor rhythmicity in the lamprey. *Journal of Neurophysiology*, *68*(6), 1939–1950. https://doi.org/10.1152/jn.1992.68.6.1939

Watson, C., Paxinos, G., Kayalioglu, G., & Heise, C. (2009). Atlas of the mouse spinal cord. *The spinal cord* (pp. 308–379). Elsevier. https://doi.org/10.1016/b978-0-12-374247-6.50020-1

Weber, K., Chen, Y., Wang, X., & Parrish, T. (2014). Choice of motion correction method affects spinal cord fmri results. *20th Annual Meeting of the Organization for Human Brain, Hamburg, Germany.*

Weber, K. A., Chen, Y., Paliwal, M., Law, C. S., Hopkins, B. S., Mackey, S., Dhaher, Y., Parrish, T. B., & Smith, Z. A. (2020). Assessing the spatial distribution of cervical spinal cord activity during tactile stimulation of the upper extremity in humans with functional magnetic resonance imaging. *NeuroImage*, *217*, 116905. https://doi.org/https://doi.org/10.1016/j.neuroimage.2020.116905

Weber, K. A., Chen, Y., Wang, X., Kahnt, T., & Parrish, T. B. (2016a). Functional magnetic resonance imaging of the cervical spinal cord during thermal stimulation across consecutive runs. *NeuroImage*, *143*, 267–279. https://doi.org/https://doi.org/10.1016/j.neuroimage.2016.09.015

Weber, K. A., Chen, Y., Wang, X., Kahnt, T., & Parrish, T. B. (2016b). Lateralization of cervical spinal cord activity during an isometric upper extremity motor task with functional magnetic resonance imaging. *NeuroImage*, *125*, 233–243. https://doi.org/https://doi.org/10.1016/j.neuroimage.2015.10.014

Wenger, N., Moraud, E. M., Gandar, J., Musienko, P., Capogrosso, M., Baud, L., Le Goff, C. G., Barraud, Q., Pavlova, N., Dominici, N., Minev, I. R., Asboth, L., Hirsch, A., Duis, S., Kreider, J., Mortera, A., Haverbeck, O., Kraus, S., Schmitz, F., . . . Courtine, G. (2016). Spatiotemporal neuromodulation therapies engaging muscle synergies improve motor control after spinal cord injury. *Nature Medicine*, *22*(2), 138–145. https://doi.org/10.1038/nm.4025

Wenger, N., Moraud, E. M., Raspopovic, S., Bonizzato, M., DiGiovanna, J., Musienko, P., Morari, M., Micera, S., & Courtine, G. (2014). Closed-loop neuromodulation of spinal sensorimotor circuits controls refined locomotion after complete spinal cord injury. *Science Translational Medicine*, *6*(255), 255ra133–255ra133. https://doi.org/10.1126/scitranslmed.3008325

Wernig, A., & Müller, S. (1992). Laufband locomotion with body weight support improved walking in persons with severe spinal cord injuries. *Spinal Cord*, *30*(4), 229–238. https://doi.org/10.1038/sc.1992.61

West, C. R., Phillips, A. A., Squair, J. W., Williams, A. M., Walter, M., Lam, T., & Krassioukov, A. V. (2018). Association of epidural stimulation with cardiovascular function in an individual with spinal cord injury. *JAMA Neurology*, *75*(5), 630. https://doi.org/10.1001/jamaneurol.2017.5055

Windhorst, U. (2007). Muscle proprioceptive feedback and spinal networks. *Brain Research Bulletin*, *73*(4-6), 155–202. https://doi.org/10.1016/j.brainresbull.2007.03.010

Wirz, M. (2001). Long term effects of locomotor training in spinal humans. *Journal of Neurology, Neurosurgery & Psychiatry*, *71*(1), 93–96. https://doi.org/10.1136/jnnp.71.1.93

Wojtusch, J., & von Stryk, O. (2015). HuMoD - a versatile and open database for the investigation, modeling and simulation of human motion dynamics on actuation level. *2015 IEEE-RAS 15th International Conference on Humanoid Robots (Humanoids)*. https://doi.org/10.1109/humanoids.2015.7363534

Won, S. M., Song, E., Reeder, J. T., & Rogers, J. A. (2020). Emerging modalities and implantable technologies for neuromodulation. *Cell*, *181*(1), 115–135. https://doi.org/10.1016/j.cell.2020.02.054

Woolrich, M. W., Behrens, T. E., & Smith, S. M. (2004). Constrained linear basis sets for hrf modelling using variational bayes. *NeuroImage*, *21*(4), 1748–1761. https://doi.org/https://doi.org/10.1016/j.neuroimage.2003.12.024

Woolrich, M. W., Ripley, B. D., Brady, M., & Smith, S. M. (2001). Temporal autocorrelation in univariate linear modeling of fmri data. *NeuroImage*, *14*(6), 1370–1386. https://doi.org/https://doi.org/10.1006/nimg.2001.0931

World Health Organization, & International Spinal Cord Society (Eds.). (2013). *International perspectives on spinal cord injury* [OCLC: ocn871342223]. World Health Organization.

Wu, J.-C., Chen, Y.-C., Liu, L., Chen, T.-J., Huang, W.-C., Cheng, H., & Tung-Ping, S. (2012). Increased risk of stroke after spinal cord injury: a nationwide 4-year follow-up cohort study. *Neurology*, *78*(14), 1051–1057. https://doi.org/10.1212/wnl.0b013e31824e8eaa

Wyndaele, M., & Wyndaele, J.-J. (2006). Incidence, prevalence and epidemiology of spinal cord injury: what learns a worldwide literature survey? *Spinal Cord*, *44*(9), 523–529. https://doi.org/10.1038/sj.sc.3101893

Yakovenko, S., Mushahwar, V., VanderHorst, V., Holstege, G., & Prochazka, A. (2002). Spatiotemporal activation of lumbosacral motoneurons in the locomotor step cycle [PMID: 11877525]. *Journal of Neurophysiology*, *87*(3), 1542–1553. https://doi.org/10.1152/jn.00479.2001

Yaroslavsky, A. N., Schulze, P. C., Yaroslavsky, I. V., Schober, R., Ulrich, F., & Schwarzmaier, H.-J. (2002). Optical properties of selected native and coagulated human brain tissues in vitro in the visible and near infrared spectral range. *Physics in Medicine and Biology*, *47*(12), 2059–2073. https://doi.org/10.1088/0031-9155/47/12/305

Zeisel, A., Hochgerner, H., Lönnerberg, P., Johnsson, A., Memic, F., van der Zwan, J., Häring, M., Braun, E., Borm, L. E., Manno, G. L., Codeluppi, S., Furlan, A., Lee, K., Skene, N., Harris, K. D., Hjerling-Leffler, J., Arenas, E., Ernfors, P., Marklund, U., & Linnarsson, S. (2018). Molecular architecture of the mouse nervous system. *Cell*, *174*(4), 999–1014.e22. https://doi.org/10.1016/j.cell.2018.06.021

Zhang, F., Vierock, J., Yizhar, O., Fenno, L. E., Tsunoda, S., Kianianmomeni, A., Prigge, M., Berndt, A., Cushman, J., Polle, J., Magnuson, J., Hegemann, P., & Deisseroth, K. (2011). The microbial opsin family of optogenetic tools. *Cell*, *147*(7), 1446–1457. https://doi.org/10.1016/j.cell.2011.12.004

Zhang, J., Lanuza, G. M., Britz, O., Wang, Z., Siembab, V. C., Zhang, Y., Velasquez, T., Alvarez, F. J., Frank, E., & Goulding, M. (2014). V1 and v2b interneurons secure the alternating flexor-extensor motor activity mice require for limbed locomotion. *Neuron*, *82*(1), 138–150. https://doi.org/10.1016/j.neuron.2014.02.013

Zhang, Y., Narayan, S., Geiman, E., Lanuza, G. M., Velasquez, T., Shanks, B., Akay, T., Dyck, J., Pearson, K., Gosgnach, S., Fan, C.-M., & Goulding, M. (2008). V3 spinal neurons establish a robust and balanced locomotor rhythm during walking. *Neuron*, *60*(1), 84–96. https://doi.org/10.1016/j.neuron.2008.09.027

Zimmerman, A. L., Kovatsis, E. M., Pozsgai, R. Y., Tasnim, A., Zhang, Q., & Ginty, D. D. (2019). Distinct modes of presynaptic inhibition of cutaneous afferents and their functions in behavior. *Neuron*, *102*(2), 420–434.e8. https://doi.org/10.1016/j.neuron.2019.02.002

Andreas Rowald *July 21, 1992*

andreas.rowald@epfl.ch • +49 (0)911 518 6760 • Linkedin
Hersbrucker Str. 24 • 90562 • Heroldsberg • Germany

Summary

I am a passionate scientist, fascinated by computational modeling and artificial intelligence.

My main interest is developing theoretical tools that support translation of medical technologies, improve diagnostic and rehabilitative efforts and bring them all the way down to the clinic. For this purpose I am currently enrolled at the École polytechnique fédérale de Lausanne as a PhD student, working on computational modelling of spinal sensorimotor circuits for upper and lower limb motor control.

In the future I would like to combine artificial intelligence with computational modeling to combine first-principle analysis with data-driven optimization.

Current

École polytechnique fédérale de Lausanne — LAUSANNE, SWITZERLAND

PhD student in Electrical Engineering — *July '17 – present*

I combined multiple **computational modeling** techniques (e.g. 3D Finite element method, compartmental cable modeling, spiking neural networks, artificial neural networks, musculoskeletal modeling) with **behavioral** and **electrophysiological experiments** in animal models and humans to study the basic interactions between neuromodulation technologies and sensorimotor circuit dynamics and develop computational tools that support innovation and translation of neuromodulation strategies in a clinical context.

Team Black review team of o2S2PARC — ZÜRICH, SWITZERLAND

Member — *March '20 – present*

The **NIH**-funded SPARC SIM-CORE team is developing the online simulation platform o2S2SPARC to accelerate development of therapeutic devices that modulate electrical activity in nerves to improve organ function. Team Black is an **NIH**-instated **review committee** that provides feedback on platform functionality and usability.

Prep2Go – Eurostars — EINDHOVEN, NETHERLANDS

Work package leader — *February '20 – present*

I lead a small team of 3 PhD students at EPFL in an international collaboration with industrial and scientific partners. Our aim is to develop a **cloud-based service** that can **automatically generate fully personalized, anatomically realistic neuro-physical models of the human spinal cord**. This tool aims to guide the implantation strategies for spinal cord stimulation as well as develop novel electrode designs for various neuromodulation purposes, through a combination of **high-resolution MRI acquisition**, **3D finite element modeling** and **compartmental cable modeling**.

Experience

Defitech Center for Interventional Neurotherapies. — LAUSANNE, SWITZERLAND

Leader of Computational Neuroscience Unit — *December '19 – April '21*

I lead the computational neuroscience unit within the Defitech Center for Interventional Neurotherapies. This entailed the **supervision** of a post-graduate researcher, four PhD students and various undergraduate students, the **securing of funds** and the **communication and planning with international partners in various projects**.

Human Brain Project — GENEVA, SWITZERLAND

Deputy — *July '17 – February '21*

We developed **computational models** to understand the **emergence, disruption and restoration of locomotion**. As deputy of the locomotion project within the Human Brain Project my responsibilities stretch beyond the scientific realm into **communications**, **consulting** and **innovations with researchers across Europe**.

RESTORE – Eurostars — EINDHOVEN, NETHERLANDS

Work package leader — *July '17 – August '19*

We developed a **computational framework** with the capacity to develop novel neuromodulation paradigms for the recovery of locomotion after spinal cord injury. I **lead a team of three people** at EPFL and formed a **consortium with industrial and scientific partners** that resulted in the **creation of a novel paradigm termed targeted Epidural Electrical Stimulation** (**tESS**).

École polytechnique fédérale de Lausanne — Lausanne, Switzerland

Scientific Assistant — *April '17 – June '17*

I designed and built a robot for experiments of involuntary motion in rodents.

Master's Thesis — *October '15 – September '16*

I developed a **computational model** to predict the effects of modulation of noradrenergic receptors during locomotion in rodents. Moreover I **assisted in experimental procedures** to recover locomotion in rodents through these predicted pathways and analyzed this data.

Max-Planck-Institut für biophysikalische Chemie — Göttingen, Germany

Trainee — *March '15 – May '15*

I performed Protein-folding simulations on the HIV-Rev-Homodimer.

European Molecular Biology Laboratory — Heidelberg, Germany

Trainee — *September '14 – February '15*

I contributed to the development of an efficient homogeneous illumination and optical sectioning technique for quantitative single-molecule localization microscopy.

Zentrum für Medizinische Physik und Technik — Erlangen, Germany

Summer intern — *June '14 – August '14*

Development of medical stents on the basis of pericardium.

Imperial College London — London, United Kingdom

Research student — *October '13 – June '14*

Development of a novel pulse-shaper for femtosecond laser pulses.

Siemens Healthcare — Forchheim, Germany

Working student — *August '13 – September '13*

Computational modelling of CT-Scanner.

Please refer to my Linked-in profile for a more complete list of work experience.

Education

Friedrich-Alexander University Erlangen-Nuremberg — Erlangen, Germany

Master of Science (honours) Physics - passed with distinction — *October '15 – January '17*

Bachelor of Science Physics — *October '11 – September '15*

I conducted my studies in the elite study programme for physics (in German: **Elitestudiengang Physik mit integriertem Doktorandenkolleg**) funded by the Elitenetwork of Bavaria. My primary focus was computational physics, complex systems and biophysics.

Imperial College London — London, United Kingdom

Erasmus student — *October '13 – June '14*

Staatliche Fachoberschule und Berufsoberschule Erlangen — Erlangen, Germany

High School Diploma - in German: Allgemeine Hochschulreife — *September '10 – June '11*

Grants, Scholarships and Prizes

Contribution to the successful grant proposal Bridging the Gap Plus (BG+) of the Defense Advanced Research Projects Agency (DARPA)	2020 – 2024
Contribution to the successful grant proposal EUROSTARS E! 113969.	2020 – 2022
Fellow of the PROMOS-scholarship	2015 – 2016
Fellow of the Leonardo-Kolleg	2014 – 2017
ERASMUS-scholarship	2013 – 2014
Fellow of e-fellows online scholarship	2012 – 2017
Member of the Elitenetwork Bavaria	2011 – 2017
LGA-Prize for the valedictorian in the discipline technology	2011
Middle Franconian Secondary School Prize for outstanding accomplishments in the category creative work	2007

Social Engagement

Friedrich-Alexander University Erlangen-Nuremberg — Erlangen, Germany

Tutor of the foreign exchange students — *2015*

I ensured that they received all the necessary paperwork to stay in Germany and was their primary source of contact.

Tutor of the freshman in Physics — *2012*

I guided my group of freshmen through their first semester, helped them with applications and gave them feedback on their university performances.

St. Theresien Hospital Nuremberg — Nuremberg, Germany

Volunteer — *2011*

I helped out in the urology department of the hospital, preparing the patients for surgery and ensuring their overall wellbeing.

Skills

General Purpose Programming: Python, C++, C#, Java, Bash, PowerShell

Computational Modelling: Sim4Life, Neuron, NEST, COMSOL, Webots, NRP, Gromacs, ROOT

Design and 3D Modelling: Solidworks, AutoCAD, Blender, Adobe Creative Cloud

Data Science: Matlab, Scipy, Numpy, Pandas

Web-development: JavaScript (MEAN), PHP, MySQL, HTML, CSS, Wix

Embedded Systems: Arduino, Raspberry, Trinamic

Clinical practice: Good clinical practice module 1, 2.1, 3.1

Other: Windows, OS X, Ubuntu, Latex, MS Office

Natural languages: German (*mother tongue*), English (*fluent*), Greek (*elementary proficiency*), French (*elementary proficiency*) and Spanish (*elementary proficiency*).

Peer-reviewed publications:

Andreas Rowald, Salif Komi, Robin Demesmaeker, Edeny Baaklini, Sergio Daniel Hernandez-Charpak, Edoardo Paoles, Hazael Montanaro, Antonino Cassara, Fabio Becce, Bryn Lloyd, Taylor Newton, Jimmy Ravier, Nawal Kinany, Marina D'Ercole, Aurélie Paley, Nicolas Hankov, Camille Varescon, Laura McCracken, Molywan Vat, Miroslav Caban, Anne Watrin, Charlotte Jacquet, Léa Bole-Feysot, Cathal Harte, Henri Lorach, Andrea Galvez, Manon Tschopp, Natacha Herrmann, Moïra Wacker, Lionel Geernaert, Isabelle Fodor, Valentin Radevich, Katrien Van Den Keybus, Grégoire Eberle, Etienne Pralong, Maxime Roulet, Jean-Baptiste Ledoux, Eleonora Fornari, Stefano Mandija, Loan Mattera, Roberto Martuzzi, Bruno Nazarian, Stefan Benkler, Simone Callegari, Nathan Greiner, Benjamin Fuhrer, Martijn Froeling, Nik Buse, Tim Denison, Rik Buschman, Damien Ganty, Jurriaan Bakker, Vincent Delattre, Hendrik Lambert, Karen Minassian, Cornelis A T van den Berg, Anne Kavounoudias, Silvestro Micera, Dimitri Van De Ville, Quentin Barraud, Erkan Kurt, Niels Kuster, Esra Neufeld, Marco Capogrosso, Leonie Asboth, Fabien B. Wagner, Jocelyne Bloch, Grégoire Courtine, Immediate recovery of trunk and leg motor functions after complete paralysis. **In review**, 2021

Claudia Kathe, Frédéric Michoud, Philipp Schönle, **Andreas Rowald**, Noé Brun, Jimmy Ravier, Ivan Furfaro, Valentina Paggi, Kyungjin Kim, Sadaf Soloukey, Leonie Asboth, Thomas H. Hutson, Ileana Jelescu, Antoine Philippides, Noaf Alwahab, Jérôme Gandar, Daniel Huber, Chris I. De Zeeuw, Quentin Barraud, Qiuting Huang, Stéphanie P. Lacour, Grégoire Courtine, Wireless closed-loop optogenetics across the entire dorsoventral spinal cord in ecological environments. **In review**, 2021

Jordan W Squair, Matthieu Gautier, Lois Mahe, Jan Elaine Soriano, **Andreas Rowald**, Arnaud Bichat, Newton Cho, Mark A Anderson, Nicholas D James, Jerome Gandar, Anthony V Incognito, Giuseppe Schiavone, Zoe K Sarafis, Achilleas Laskaratos, Kay Bartholdi, Robin Demesmaeker, Salif Komi, Charlotte Moerman, Bita Vaseghi, Berkeley Scott, Ryan Rosentreter, Claudia Kathe, Jimmy Ravier, Laura McCracken, Xiaoyang Kang, Nicolas Vachicouras, Florian Fallegger, Ileana Jelescu, YunLong Cheng, Qin Li, Rik Buschman, Nicolas Buse, Tim Denison, Sean Dukelow, Rebecca Charbonneau, Ian Rigby, Steven K Boyd, Philip J Millar, Eduardo Martin Moraud, Marco Capogrosso, Fabien B Wagner, Quentin Barraud, Erwan Bezard, Stéphanie P Lacour, Jocelyne Bloch, Grégoire Courtine, Aaron A Phillips, Neuroprosthetic baroreflex controls haemodynamics after spinal cord injury. **Nature**, January 2021, doi:10.1038/s41586-020-03180-w

Giuseppe Schiavone, Florian Fallegger, Xiaoyang Kang, Beatrice Barra, Nicolas Vachicouras, Evgenia Roussinova, Ivan Furfaro, Sébastien Jiguet, Ismael Seáñez, Simon Borgognon, **Andreas Rowald**, Qin Li, Chuan Qin, Erwan Bézard, Jocelyne Bloch, Grégoire Courtine, Marco Capogrosso, Stéphanie Lacour, Soft, Implantable Bioelectronic Interfaces for Translational Research. **Adv. Mater.** March 2020, doi:10.1002/adma.201906512

Fabien B. Wagner, Jean-Baptiste Mignardot, Camille G. le Goff-Mignardot, Robin Demesmaeker, Salif Komi, Marco Capogrosso, **Andreas Rowald**, Ismael Seáñez, Miroslav Caban, Elvira Pirondini, Molywan Vat, Laura A. Mccracken, Roman Heimgartner, Isabelle Fodor, Anne Watrin, Perrine Seguin, Edoardo Paoles, Katrien Van Den Keybus, Grégoire Eberle, Brigitte Schurch, Etienne Pralong, Fabio Becce, John Prior, Nicholas Buse, Rik Buschman, Esra Neufeld, Niels Kuster, Stefano Carda, Joachim von Zitzewitz, Vincent Delattre, Tim Denison, Hendrik Lambert, Karen Minassian, Jocelyne Bloch and Grégoire Courtine, Targeted neurotechnology restores walking in humans with spinal cord injury. **Nature**, October 2018 doi:10.1038/s41586-018-0649-2

Emanuele Formento, Karen Minassian, Fabien Wagner, Jean Baptiste Mignardot, Camille G. Le Goff, **Andreas Rowald**, Jocelyne Bloch, Silvestro Micera, Marco Capogrosso and Grégoire Courtine, Electrical spinal cord stimulation must preserve proprioception to enable locomotion in humans with spinal cord injury. **Nature Neuroscience**, October 2018, doi:10.1038/s41593-018-0262-6

Joran Deschamps, **Andreas Rowald** and Jonas Ries, Efficient homogeneous illumination, optical sectioning for quantitative single-molecule localization microscopy. **Optics Express**, November 2016, 24:28080–28090, doi:10.1364/OE.24.028080

Communications:

Oral Presentation: Targeted epidural spinal stimulation (TESS) after spinal cord injury: personalized, computationally-guided stimulation protocols, WFNR & SOFMER, October 9th 2020, Lyon, France

Oral Presentation: Personalized, computationally-guided targeted epidural electrical stimulation for the recovery of locomotion after spinal cord injury, Center for Neuroprosthetics, February 12th 2020, Saint-Maurice, Switzerland

Oral Presentation: Targeted epidural spinal stimulation after spinal cord injury: Personalized, computationally-guided stimulation protocols, Sim4Life Workshop at Neuroscience 2019, October 21st 2019, Chicago, USA

Poster Presentation: Targeted epidural spinal stimulation after spinal cord injury: Personalized, computationally-guided stimulation protocols, Society for Neuroscience, October 18-24 2019, Chicago, USA

Keynote speech: Personalized targeted neurotechnology restores locomotion in humans with spinal cord injury, 2019 IEEE International Conference on Cyborg and Bionic Systems and HBP Workshop, September 19-20 2019, Munich, Germany

Oral Presentation: Neuroprothesen ermöglichen die Wiederherstellung des Bewegungsapparates nach Verletzungen im Rückenmark: Ein Überblick über die Translation von Tierversuchen zur klinischen Praxis, Joint Symposium LS2/SGV 2019 Tierversuche im Dialog, September 13th 2019, Zurich, Switzerland

Poster Presentation: Personalized And Optimized Targeted Epidural Spinal Stimulation For The Recovery Of Locomotion After Spinal Cord Injury, Swiss society for biomedical engineering, August 27th 2019, Geneva, Switzerland

Oral Presentation: A computational approach to optimizing and personalizing neurotechnologies for spatiotemporal stimulation after spinal cord injury, Neurorestore Symposium, July 4th 2019, Lausanne, Switzerland

Keynote speech: Targeted neurotechnology restores locomotion in humans with spinal cord injury, 5th EU-Japan Workshop on Neurorobotics/ Cognitive systems, June 19-20 2019, Kashiwa, Japan

Poster Presentation: Computational models steering the personalization of targeted spinal cord stimulation to restore motor function in humans with spinal cord injury, Society for Neuroscience, November 3-7 2018, San Diego, USA

Boards, commissions and reviewing activities:

Reviewer: Scientific Reports

Interests

Non-exhaustive and in alphabetical order: Application development, Astronomy, Blockchain, Cosmology, Deep Learning, Game Theory, Grand Strategy Games, Machine Learning, Neuroscience, Poker, Psychology, Science Fiction, Web development